Cohesive Sediment Transport on an Estuarine Intertidal Zone

by

David P. Freeman

A thesis submitted to the Faculty of Engineering of the University of Birmingham for the degree of Doctor of Philosophy

1994

1st January 1994
School of Civil Engineering
Faculty of Engineering
University of Birmingham
P.O.Box 363
Birmingham
B15 2TT

Abstract

A field study of cohesive sediment movements on a muddy intertidal zone (ITZ) at Portishead, Severn Estuary is presented. Five deployments of 1-3 days have been made to improve the understanding of temporal and spatial variations in suspended and bed sediments at a site which is found to be wave dominated. Pressure transducers, electro-magnetic current meters, optical turbidity meters and ultra-sonic bed level transducers are used to monitor the hydro/sediment dynamics in the bottom metre of the water column at two points on the ITZ. A one-dimensional (vertical) k-ε turbulence model has been modified to include bed sediment exchange and density stratification to enable further interpretation of field data.

Sheltering of the ITZ by surrounding headlands reduced main channel tidal currents (up to $2\,m/s$) to below $0.2\,m/s$ on the ITZ. Measured velocities are interpreted as tidal circulations, influencing suspended sediment advection and resuspending bed sediment on calm days. Prevailing Westerly winds are seen to generate waves of significant height over $50\,cm$ and with zero-crossing periods of 3-5 seconds. Temporal variations during a tidal cycle are influenced by tidal range and wave-current interactions. An empirical equation relating (high water) wave height to wind speed is approximated, but is limited by complex interactions between wind direction, tidal and topographical factors. Attenuation of waves due to bottom interaction is not significant for the conditions observed. Breaking waves, tidal range and antecedent bed surface sediments control erosion rates (maximum recorded rates: $1-2\,cm/tide$). Shear (vane) strength (SV) and moisture content (MC) of surface sediment cover a wide range from easily entrained weak beds (SV $< 3\,kPa$, MC $> 160\%$) to over-consolidated muds (SV $> 11\,kPa$, MC $< 70\%$) virtually resistant to erosion (at least from waves of $40\,cm$ in height). Deposition occurs under calm winds conditions, or when blowing offshore, but can be prevented by small waves over $5\,cm$ in height. The vertical distribution of SSC has been conceptualised as three regions: a highly concentrated ($1-5\,g/l$) near bed region up to $10\,cm$ in thickness, below a region influenced by bed generated turbulence extending over $70\,cm$ for waves of height $40\,cm$ which can be identified by correlating bed shear stress with SSC, above which the lowest SSC region, or background concentration ($0.1-0.5\,g/l$) lies.

Modelling results show that the weak current on the ITZ would simply provide a mechanism for diffusing suspended sediment into the upper part of the flow, and does not enhance the wave boundary layer by its presence and cannot actively support suspended sediment. Hence near bed (wave generated) turbulence controls the vertical SSC distribution. A bed model based on bed sediment exchange via critical erosional and depositional shear stresses only predicts high near bed concentrations for some of the hydrodynamic conditions reflected in field data, suggesting hindered settling is an important factor in their formation. The introduction of density stratification reduces near surface SSC creating steeper SSC gradients in the upper half of the flow, for a weak current with waves.

Acknowledgements

I would like to thank SERC and Hydraulics Research, Wallingford for financially supporting this research and Professor J.G. Perry for the use of the facilities of the School of Civil Engineering, University of Birmingham.

Thanks go to Drs. J.R. West, L.E. Coates and Ms. M.C. Ockenden for their time and effort in providing guidance and direction in this study.

Sincere thanks also to the technical staff and all members of the Tidal Waters Research Group, Roy Atkins and Rob from HR, Wallingford who were all subjected to the pleasentries of Portishead in unfavourable conditions. Also thanks to Bill Roberts who wrote much of the modelling code and helped with numerous queries.

Cheers to all those who were unfortunate enough to have spent some time in the TWRG office with me and cope with my sense of humour. You know who you are!

Most of all thanks to everyone who laughed when I told them what I was studying for three years of my life, looked at me strangely....then walked away.

Contents

1 Introduction 1

1.1 Objectives 2

1.1.1 The River Severn 3

1.1.2 Specific Objectives 3

2 Literature Review and Theory 5

2.1 Introduction 5

2.2 Intertidal Zone Hydrodynamics 6

2.2.1 Introduction 6

2.2.2 Wave Theory 6

2.2.3 Wave Generation 9

2.2.4 Wave Propagation 10

2.2.5 Bed Friction, Boundary Layers and Energy Dissipation 13

2.2.6 Steady Currents 19

2.2.7 Friction Factor in Current Flows 21

2.2.8 Wave-Current Interactions 23

2.2.9 Determining Bed Shear Stress in Wave-Current Flows 24

2.2.10 Conclusions 27

2.3 Intertidal Zone Sediment Dynamics 29

2.3.1 Introduction 29

2.3.2 Suspended Sediment and Fall Velocity 29

2.3.3 Vertical SSC Distribution 31

2.3.4 Fluid Mud 33

2.3.5 Settling and Deposition 33

2.3.6 Consolidation 34

2.3.7 Erosion 35

2.3.8 Biotic Influences 37

2.3.9 Conclusions 38

2.4 Modelling 40

2.4.1 Introduction 40

2.4.2 Modelling (Cohesive) SSC Transport in Estuaries 41

2.4.3 Turbulence Modelling 43

2.4.4 Summary of 1-DV Cohesive Sediment Modelling 53

2.4.5 Conclusions 55

3 Methodology **58**

3.1 Field Methodology and Analysis 58

3.1.1 Overview 58

3.1.2 Site Selection 59

3.1.3 Instrumentation and Calibration 60

3.1.4 Data Logging 63

3.1.5 Signal Processing and Analysis 63

3.1.6 Settling Velocity 67

3.1.7 Bed Sediment Measurement and Analysis 67

3.2 Modelling Methodology and Implementation 69

3.2.1 Introduction 69

3.2.2 The Turbulence Model 70

3.2.3 Suspended Sediment and Bed Modelling 74

3.2.4 Numerical Techniques and Boundary Conditions 75

3.2.5 Model Initiation Parameters 77

3.2.6 Model Output Parameters 79

4 Field Results **80**

4.1 29-30/7/91 Deployment 83

4.1.1 Meteorological and Tidal Conditions 83

4.1.2 Experimental Technique 83

4.1.3 Analysis and Results 84

4.1.4 Summary 85

4.2 17/10/91 Deployment 85

4.2.1 Meteorological and Tidal Conditions 85

4.2.2 Experimental Technique 86

4.2.3 Analysis and Results 86

4.2.4 Summary 87

4.3 6-7/11/91 Deployment 88

4.3.1 Meteorological and Tidal Conditions 88

4.3.2 Experimental Technique 88

4.3.3 Analysis and Results 89

4.3.4 Summary 90

4.4 6-7/2/92 Deployment 91

4.4.1 Meteorological and Tidal Conditions 91

4.4.2 Experimental Technique 91

4.4.3 Analysis and Results 92

4.4.4 Summary 94

4.5 5-7/5/93 Deployment 94

4.5.1 Meteorological and Tidal Conditions 94

4.5.2 Experimental Technique 94

4.5.3 Analysis and Results 95

4.5.4 Summary 97

5 Discussion of Field Results 108

5.1 Wave Characteristics 108

5.1.1 Validity of Linear Wave Theory 108

5.1.2 Wave Heights and Periods 109

5.1.3 Wind-Wave Relationship 111

5.1.4 Wave Velocities and Periods via EMCM and Pressure Transducer 112

5.1.5 Wave Breaking 114

5.1.6 Wave Grouping 114

5.2 Wave Attenuation due to Bed Interactions 115

5.3 Tidal Currents on the ITZ 115

5.4 Estimating Bed Shear Stress 117

5.4.1 Reynolds Stress 117

5.4.2 Spectra Splitting 118

5.4.3 Friction Factor 119

5.5 Bed Sediment 120

5.6 Vertical Distribution of SSC 121

5.7 SSC in the Surf Zone 126

5.8 Settling Velocity 127

5.9 Advection of Suspended Sediment by Currents 127

5.10 Resuspension 128

5.10.1 Current Induced Resuspension 128

5.10.2 Wave Induced Resuspension 129

5.11 Deposition and Erosion Rates 130

5.12 Measurement Techniques 131

6 Modelling Results and Discussion **138**

6.1 Introduction 138

6.2 Evaluation of Hydrodynamic Modelling of Field Data 139

6.2.1 Hydrodynamic Test Cases 140

6.2.2 Roughness Length Analysis 143

6.2.3 Non-Colinear Waves 145

6.2.4 Varying Wave Period 145

6.2.5 Conclusions and Implications for Field Results 145

6.3 Evaluation of Sediment Modelling of Field Data 146

6.3.1 Without Bed Model 147

6.3.2 Including Bed Model 149

6.3.3 Changes in Settling Velocity 151

6.3.4 Density Gradient Effects 152

6.4 Simulation of Vertical SSC Distributions in the Field 153

6.4.1 Storm Deployments 154

6.4.2 Calm Deployments 156

6.5 Comparison with other Data and Models 158

6.5.1 Conclusions 159

7 Conclusions and Future Work **161**

7.1 Hydrodynamic Mechanisms 161

7.2 Surface and Suspended Sediment 162

7.3 Modelling 163

7.4 Future Work 166

Plates

Figures

References **169**

List of Figures

Figures marked * are found in the text at the given page number

*Figure 2.1: Definition sketch - Wave Theory (p.6)
Figure 2.2: Wave predictions based on fetch and duration (Carter, 1982)
Figure 2.3: Predicted wave heights at Portishead (HRS, 1984)
*Figure 2.4: Definition sketch - Zero Crossing Waves (p.10)
*Figure 2.5: Definition sketch - Wave Groups and Associated 'Infragravity' Wave (p.10)
Figure 2.6: Breaking wave profiles and classifications (Galvin, 1972)
Figure 2.7: Classification of flow regimes (Davies, 1983)
*Figure 2.8: Definition sketch - Current Boundary Layers (p.19)
Figure 2.9: Variation of z_o/k_s with u_*k_s/ν (Sleath, 1984)
*Figure 2.10: Definition sketch - Three Zones Under Wave-Current Flow (p.23)
Figure 2.11: Log-Log plot of Energy Density Spectra, showing the technique of splitting the wave variance from turbulence developed by Soulsby & Humphery (1989)
Figure 2.12: Linear version of figure 2.11, showing relative magnitudes of the truncated variance (Soulsby & Humphery, 1989)
Figure 2.13: Settling velocity v SSC (Severn Estuary) (Delo & Ockenden, 1992)
Figure 2.14: Settling velocity v SSC (Different sites) (Delo & Ockenden, 1992)
Figure 2.15: Relative concentration profiles calculated from equation (2.61), for varying values of $B = W_s/\sigma_c\kappa u_*$ (Dyer, 1986)
Figure 2.16: Schematic representation of the states of occurrence of mud suspensions, and the links between them (Parker & Kirby, 1977; see Dyer (1986))
Figure 2.17: Idealised profiles of instantaneous vertical concentration and velocity (Mehta, 1989)
Figure 2.18: Measured and simulated instantaneous concentration profiles in the Severn Estuary (after Ross, 1988; see Mehta, 1989)
Figure 2.19: Graphical representation of consolidation stages (Nichols & Briggs, 1985)
Figure 2.20: Growth of the bed in a settling suspension (Delo & Ockenden, 1992)
Figure 2.21: Laboratory test on the erosion rate (M_e) of cohesive sediment with excess shear stress (Delo & Ockenden, 1992)
Figure 2.22: Three-zoned schematic description of bed shear strength profiles with depth and examples of profiles after 1 day and 8 days of consolidation using kaolinite (Parchure & Mehta, 1985)
*Figure 2.23: Definition sketch - Coastal sediment modelling (O'Connor, 1992) (p.41)

Figure 3.1: Map of Bristol Channel and Severn Estuary
Figure 3.2: Portishead site plan showing approximate position of instrument deployment sites (marked 1,2) (a) Transect elevation 19/4/88 (West, 1990)
Figure 3.3: Portishead bed level changes (cm per 30 days) Nov 1988 - Aug 1989 (West, 1990)

Figure 3.4: Portishead moisture content ratio Nov 1988 - Aug 1989 (West, 1990)
Figure 3.5: Portishead surface shear vane readings (kPa) Nov 1988 - Aug 1989 (West, 1990)
Figure 3.6: EMCM Calibration : Head 1-x
Figure 3.7: Example of Partech Calibration Curve : 5-7/5/93
Figure 3.8: Example of Siltmeter Calibration Curve : 5-7/5/93

29-30/7/91

Figure 4.1: Water depth, wave heights, wave periods and wave orbital velocity at upper site (from pressure data, HW $\approx 200\,mins$), 30/7/91
Figure 4.2: Bed shear stress, wave friction factor, Reynolds number and correction factor from bed pressures to surface wave heights at upper site (pressure data, HW $\approx 200\,mins$), 30/7/91
Figure 4.3: SSC at upper site at $z = 17\,cm$ and $36\,cm$ (Partech data, HW $\approx 200\,mins$), 30/7/91
Figure 4.4: Near bed SSC - upper ($z = 7\,cm$) and lower ($z = 10\,cm$) site from siltmeter data ($SSC > 2\,g/l$), HW $\approx 200\,mins$, 30/7/91
Figure 4.5: Four five minute Partech records ($z = 17\,cm$), 30/7/91
Figure 4.6: Four five minute siltmeter records ($z \approx 10\,cm$), 30/7/91
Figure 4.7: Bed level change (HW $\approx 200\,mins$), 30/7/91
Figure 4.8: Particle size distribution, 29-30/7/91

17/10/91

Figure 4.9: EMCM velocity time series (u, w) for whole tide, 17/10/91
Figure 4.10: Water depth and SSC ($z = 15$, $46\,cm$) time series for whole tide, 17/10/91
Figure 4.11: Water depth, wave heights, wave periods and wave orbital velocity (from pressure data, HW $\approx 200\,mins$), 17/10/91
Figure 4.12: Bed shear stress, wave friction factor, Reynolds number and correction factor from bed pressures to surface wave heights (pressure data, HW $\approx 200\,mins$), 17/10/91
Figure 4.13: Comparison between wave periods and orbital velocities from pressure and EMCM data (HW $\approx 200\,mins$), 17/10/91)
Figure 4.14: Comparison between wave orbital velocities from pressure data at EMCM heights using linear wave theory (HW $\approx 200\,mins$), 17/10/91)
Figure 4.15: Mean velocity fluctuations (u', w' - EMCM data) and bed shear stress - a comparison of methods (HW $\approx 200\,mins$), 17/10/91)
Figure 4.16: Example of Souslby & Humphery (1989) spectra splitting technique (15:34), 17/10/91
Figure 4.17: EMCM (Head 1,2 - u,w) Energy density example($h \approx 1\,m$, flood), 17/10/91
Figure 4.18: EMCM (Head 1,2 - u,w) Energy density example ($h \approx 2.2\,m$, HW), 17/10/91
Figure 4.19: EMCM (Head 1,2 - u,w) Energy density example ($h \approx 1\,m$, Ebb), 17/10/91
Figure 4.20: EMCM (Head 1,2 - u,w) Cumulative normalised energy density example ($h \approx 1\,m$, flood), 17/10/91

Figure 4.21: EMCM (Head 1,2 - u,w) Cumulative normalised energy density example ($h \approx 2.2\,m$, HW), 17/10/91
Figure 4.22: EMCM (Head 1,2 - u,w) Cumulative normalised energy density example ($h \approx 1\,m$, Ebb), 17/10/91
Figure 4.23: EMCM - Cospectra examples at three points in the tidal cycle, 17/10/91
Figure 4.24: Example of wave grouping ($h = 1.63\,m$, Flood), 17/10/91
Figure 4.25: Example of wave grouping ($h = 2.12\,m$, Flood), 17/10/91
Figure 4.26: Example of wave grouping ($h = 1.44\,m$, Ebb), 17/10/91

6-7/11/91

Figure 4.27: Water depth, wave heights, wave periods and wave orbital velocity at upper site (from pressure data, HW $\approx$ 230, 780 *mins*), 6-7/11/91
Figure 4.28: Bed shear stress, wave friction factor, Reynolds number and correction factor from bed pressures to surface wave heights at upper site (pressure data, HW $\approx$ 230, 780 *mins*), 6-7/11/91
Figure 4.29: SSC at upper site at $z = 37\,cm$ and 70 *cm* (from partech data, (HW $\approx$ 230, 780 *mins*), 6-7/11/91
Figure 4.30: Water depth, wave heights, wave periods and wave orbital velocity at lower site (pressure and EMCM comparisons, HW $\approx$ 230, 780 *mins*), 6-7/11/91
Figure 4.31: Bed shear stress, wave friction factor, Reynolds number and correction factor from bed pressures to surface wave heights at lower site (pressure data, HW $\approx$ 230, 780 *mins*), 6-7/11/91
Figure 4.32: Near bed SSC ($z = 12\,cm$) at lower site from siltmeter data ($SSC > 2\,g/l$, HW $\approx$ 230, 780 *mins*, 6-7/11/91
Figure 4.33: Particle size distribution, 6-7/11/91

6-7/2/92

Figure 4.34: Water depth and SSC ($z = 10$, 96 *cm*) time series for tide 1, 6-7/2/92
Figure 4.35: EMCM velocity time series ($u - v$, w) for tide 2, 6-7/2/92
Figure 4.36: Water depth and SSC ($z = 10$, 20 *cm*) time series for tide 2, 6-7/2/92
Figure 4.37: Water depth, wave heights, wave periods and wave orbital velocity (from pressure data, HW $\approx$ 156, 537 *mins*), 6-7/2/92
Figure 4.38: Bed shear stress, wave friction factor, Reynolds numbers and correction factor from bed pressures to surface wave heights (HW $\approx$ 156, 537 *mins*), 6-7/2/92
Figure 4.39: Mean current (Head 1, Head 2 and resultant), and wave periods from EMCM (HW $\approx$ 156, 537 *mins*), 6-7/2/92
Figure 4.40: Horizontal wave orbital velocities (U_s) calculated from EMCM - Heads 1, 2 & 3 and resultant (HW $\approx$ 156, 537 *mins*), 6-7/2/92
Figure 4.41: Comparison between horizontal and vertical wave orbital velocities from EMCM (U_s, W_s) and pressure (U_o, W_o) data (HW $\approx$ 156, 537 *mins*), 6-7/2/92
Figure 4.42: Reynold stresses from EMCM data - Head 1 & 2 and resultant (HW $\approx$ 156, 537 *mins*), 6-7/2/92

Figure 4.43: SSC at $z = 10\,20, 96\,cm$ (HW $\approx 156, 537\,mins$), 6-7/2/91
Figure 4.44: Particle size distribution, 6-7/2/92

5-7/5/93

Figure 4.45: EMCM velocity time series (u, v, w) tide 1, 5/5/93
Figure 4.46: SSC ($z = 5, 22, 58, 80\,cm$) time series tide 1, 5/5/93
Figure 4.47: Water depth and bed SSC time series tide 1, 5/5/93
Figure 4.48: SSC ($z = 22, 58, 80\,cm$) time series tide 2, 6/5/93
Figure 4.49: EMCM velocity time series (u, v, w) tide 3, 6/5/93
Figure 4.50: SSC ($z = 5, 7, 22, 58\,cm$) time series tide 3, 6/5/93
Figure 4.51: Bed SSC time series tide 3, 6/5/93
Figure 4.52: SSC ($z = 7, 22, 58\,cm$) time series tide 4, 7/5/93
Figure 4.53: Wave orbital velocities (U_s, W_s) and zero crossing periods calculated from EMCM, tide 1, 5/5/93
Figure 4.54: Mean velocity fluctuations (u', w') and Reynolds numbers calculated from EMCM, tide 1, 5/5/93
Figure 4.55: Bed shear stress comparison using frictor factor and Reynolds stresses calculated from EMCM, tide 1, 5/5/93
Figure 4.56: Wave orbital velocities (U_s, W_s) and zero crossing periods calculated from EMCM, tide 3, 6/5/93
Figure 4.57: Mean velocity fluctuations (u', w') and Reynolds numbers calculated from EMCM, tide 3, 6/5/93
Figure 4.58: Bed shear stress comparison using frictor factor, Reynolds stresses and Souslby & Humphery spectra splitting technique, tide 3, 6/5/93
Figure 4.59: SSC and standard deviation of SSC for tide 3, 6/5/93
Figure 4.60: Fall velocity from Owen tube in surf zone near site, tide 2, 06:20 (t=30)- 6/5/93
Figure 4.61: Fall velocity from Owen tube in surf zone near site, tide 3, 18:45 (t=30)- 6/5/93

Figure 5.1: Wind velocity v wave height scatter plot: Portishead, Severn Estuary
Figure 5.2: Regressions of SSC v τ_o and H_s/h, 30/7/91
Figure 5.3: Regressions of SSC v τ_o and H_s/h, 6-7/11/91
*Figure 5.4: Interpretation of tidal currents on ITZ at Portishead (p.117)
Figure 5.5: Conceptualised regions of SSC over the water column

Figure 6.1: Test case 4W1 - Vertical profiles of instantaneous velocity and shear stress at ten phases through a wave cycle
Figure 6.2: Test case 4W1 - Vertical profiles of instantaneous turbulent kinetic energy and production rate term in k-equation $((\nu_t + \nu_\tau)\left(\frac{\partial u}{\partial z}\right)^2)$ at ten phases through a wave cycle

Figure 6.3: Test case 4W1 - Vertical profiles of instantaneous eddy viscosity and turbulent energy dissipation rate at ten phases through a wave cycle
Figure 6.4: Test case C4W1 - Depth and wave-cycle averaged velocity, turbulent kinetic energy and dissipation rate - from C4 to convergence
Figure 6.5: Test case C4W2 - Depth and wave-cycle averaged velocity, turbulent kinetic energy and dissipation rate - from C4 to convergence
Figure 6.6: Test cases C4, C4W1 and C4W2 - Converged wave-cycle averaged profiles of velocity and turbulent kinetic energy
Figure 6.7: Test cases C4, C4W1 and C4W2 - Converged wave-cycle averaged profiles of eddy viscosity and maximum shear stress in wave cycle
Figure 6.8: Test case C4W1 - Transient wave-cycle averaged profiles of turbulent kinetic energy and shear stress
Figure 6.9: Test case C4W1 - Transient wave-cycle averaged profiles of velocity and eddy viscosity
Figure 6.10: Test case C4W1 - Transient wave-cycle averaged profiles of turbulent energy dissipation rate
Figure 6.11: Test Case C4W1 - Vertical profiles of instantaneous velocity and shear stress at ten phases through a wave cycle
Figure 6.12: Test Case C4W1 - Vertical profiles of instantaneous turbulent kinetic energy and eddy viscosity at ten phases through a wave cycle
Figure 6.13: Test Cases C4 and C4W2 - Vertical profiles of instantaneous production rate term in k-equation $((\nu_t + \nu_r)\left(\frac{\partial u}{\partial z}\right)^2)$ at ten phases through a wave cycle and converged current profile
Figure 6.14: Test case 4W1 - Converged wave-cycle averaged profiles of turbulent kinetic energy and maximum shear stress: varying k_s for fixed z_o
Figure 6.15: Test case 4W1 - Converged wave-cycle averaged profiles of turbulent kinetic energy and maximum shear stress: varying z_o for fixed k_s
Figure 6.16: Test case C4W1 - Converged wave-cycle averaged profiles of turbulent kinetic energy and SSC: varying k_s for fixed z_o
Figure 6.17: Test cases C4, C4W1 and C4V1 - Converged wave-cycle averaged profiles of turbulent kinetic energy and eddy viscosity
Figure 6.18: Test case C4W1 (varying wave period) - Converged wave-cycle averaged profiles of velocity and turbulent kinetic energy
Figure 6.19: Test cases C4W1 and C4W2 - Transient wave-cycle averaged profiles of SSC starting from C4 SSC profile (no bed flux, bulk conc $0.5\,g/l$)
Figure 6.20: Test cases C4, C4W1 and C4W2 - Transient wave-cycle averaged profiles of SSC (no bed flux, bulk conc $0.5\,g/l$)
Figure 6.21: Test cases 4W1, B1 - Ten instantaneous SSC profiles and C4W1, B1 - cycle averaged SSC profiles converging from below and above
Figure 6.22: Test case C4W1 (varying settling velocity) - Converged wave-cycle averaged profiles of SSC; without bed flux and with bed model B1
Figure 6.23: Test case C4W1g (B1) - Depth and wave-cycle averaged velocity, turbulent kinetic energy and dissipation rate - from C4W1 to convergence
Figure 6.24: Test case C4W1g (B1) - Transient wave-cycle averaged profiles of shear stress and eddy viscosity

Figure 6.25: Test case C4W1g (B1) - Transient wave-cycle averaged profiles of turbulent kinetic energy and SSC

Figure 6.26: Test case C4W1g (B1) - Wave-cycle averaged profiles of shear stress and SSC (oscillating around equilibrium)

Figure 6.27: Test case C4W1g (B1) - Wave-cycle averaged profiles of turbulent kinetic energy and Ri_f (oscillating around equilibrium)

Figure 6.28: Test case CL4W1 - Depth and wave-cycle averaged velocity, turbulent kinetic energy and dissipation rate - from CL4 to convergence

Figure 6.29: Test cases CL4, CL4W1 and CL4W1g (all B1) - Converged wave-cycle averaged profiles of velocity and turbulent kinetic energy

Figure 6.30: Test cases CL4, CL4W1 and CL4W1g (all B1) - Converged wave-cycle profiles of maximum shear stress and averaged SSC and Ri_f

Figure 6.31: Test cases C4 and C4W4 - Converged wave-cycle averaged profiles of velocity and turbulent kinetic energy

Figure 6.32: Test cases C4 and C4W4 - Converged wave-cycle averaged profiles of eddy viscosity and maximum shear stress in wave cycle

Figure 6.33: Test case C1W3g (B3) - Depth and wave-cycle averaged velocity, turbulent kinetic energy and dissipation rate - from C1W3 (B3) to convergence

Figure 6.34: Test case C1W3g (B4) - Depth and wave-cycle averaged velocity, turbulent kinetic energy and dissipation rate - from C1W3 (B4) to convergence

Figure 6.35: Test case C1W3g (B2-B6) - Converged wave-cycle averaged profiles of velocity and turbulent kinetic energy

Figure 6.36: Test case C1W3g (B2-B6) - Converged wave-cycle averaged profiles of eddy viscosity and maximum shear stress in wave cycle

Figure 6.37: Test case C1W3 (B2-B6) and C1W3g (B2-B6) - Converged wave-cycle averaged profiles of SSC (includes SSC data from 11/93 field deployment)

Figure 6.38: Test case C1W3 (B7) - Transient wave-cycle averaged profiles of SSC

Figure 6.39: Test case C4W2 (B7 and B7h) - Transient wave-cycle averaged profiles of SSC (B7h retarded settling rate with same bed model parameters as B7)

Figure 6.40: Test case C4W2 $\rightarrow$ 4W2 - Depth and wave-cycle averaged velocity, turbulent kinetic energy and dissipation rate (removing waves from wave-current case)

Figure 6.41: Test case C4W2 $\rightarrow$ 4W2 (B7 and B7h) - Transient wave-cycle averaged profiles of SSC (B7h retarded settling rate with same bed model parameters as B7)

Figure 6.42: Vertical profiles of instantaneous velocity at ten phases through a wave cycle compared with Davies *et al.* (1988) model for a rough bed (below): (a) $U_o = 1.0\,m/s, \overline{u} = 0\,m/s$, (b) $U_o = 1.0\,m/s, \overline{u} = 1.0\,m/s$

Figure 6.43: Vertical profiles of instantaneous shear stress at ten phases through a wave cycle compared with Davies *et al.* (1988) model for a rough bed (below): (a) $U_o = 1.0\,m/s, \overline{u} = 0\,m/s$, (b) $U_o = 1.0\,m/s, \overline{u} = 1.0\,m/s$

Figure 6.44: Vertical profiles of instantaneous turbulent kinetic energy at ten phases through a wave cycle compared with Davies *et al.* (1988) model for a rough bed (below): (a) $U_o = 1.0\,m/s, \overline{u} = 0\,m/s$, (b) $U_o = 1.0\,m/s, \overline{u} = 1.0\,m/s$

Figure 6.45: Vertical profiles of instantaneous eddy viscosity at ten phases through a wave cycle compared with Davies *et al.* (1988) model for a rough bed (below): (a) $U_o = 1.0\,m/s, \overline{u} = 0\,m/s$, (b) $U_o = 1.0\,m/s, \overline{u} = 1.0\,m/s$ (N.B. not all axes logarithmic)

Figure 6.46: Vertical profiles of instantaneous velocity at six phases through a wave cycle compared with Hayashi & Ohashi (1988) data of purely oscillatory flow in a water tunnel (below)

Figure 6.47: Vertical profiles of instantaneous turbulent kinetic energy at six phases through a wave cycle compared with Hayashi & Ohashi (1988) data for purely oscillatory flow in a water tunnel (below)

Figure 6.48: Vertical profiles of instantaneous shear stress at six phases through a wave cycle compared with Hayashi & Ohashi (1988) data for purely oscillatory flow in a water tunnel (below)

List of Tables

2.1 Wave prediction results - Portishead (HRS, 1984) 56

2.2 Typical values of roughness length (z_o) and friction factor (f_c) for differing bottom types. (Modified from Soulsby, 1988) 57

3.1 Summary of hydrodynamic parameters required for a model run 77

3.2 Summary of suspended sediment and bed properties required for a model run . 78

4.1 Summary of field results. Data are given in terms of numbers of tides recorded. Instrument failures are marked (-), for the Upper (U) and Lower (L) deployment sites. 81

4.2 Summary of instrument positioning during field deployments. Instrument notation: EMCM - E, Siltmeter - S, Partech - P, Pressure transducer - PT, for the Upper (U) and Lower (L) deployment sites. Braystokes not shown. 82

4.3 Meteorological Conditions: 29-30/7/92 83

4.4 Meteorological Conditions: 17/10/91 85

4.5 Meteorological Conditions: 6-7/11/91 88

4.6 Meteorological Conditions: 6-7/2/92 91

4.7 Meteorological Conditions: 5-7/5/93 94

4.8 Bed Sediment Shear Vane Profile 98

4.9 Transect analysis: 29/7/91 99

4.10 Transect analysis: 30/7/91 100

4.11 Transect analysis: 17/10/91. MC - Moisture Content, BD - Bulk Density, DD - Dry Density. Bed Change: erosion (-), Deposition (+). 100

4.12 Shear stress calculated from spectra splitting technique, and ratio of (truncated) wave energy to total energy. (HW $\approx 200\,mins$). 101

4.13 Transect analysis: 6/11/91 102

4.14 Transect analysis: 7/11/91. MC - Moisture Content, BD - Bulk Density, DD - Dry Density. Samples with noticable sand content marked (s). 103

4.15 Transect analysis: 6/2/92. (MC - Moisture Content, BD - Bulk Density, DD - Dry Density.) 104

4.16 Transect analysis: 7/2/92. (MC - Moisture Content, BD - Bulk Density, DD - Dry Density) 105

4.17 Surface sediment analysis: 5-7/5/93. (MC - Moisture Content Ratio, BD - Bulk Density, DD - Dry Density) 106

4.18 Shear stress calculated from spectra splitting technique, and ratio of (truncated) wave energy to total energy. (HW $\approx 130\,mins.$) 107

5.1 Bed shear stress in unidirectional flow over muddy beds 133

5.2 Linear wave theory validity: h is depth, λ is wave length, H is significant wave height, taken from figures. For $H\lambda^2/h^3 > 26$ cnoidal wave theory is preferable. The maximum wave height (H/h) cannot exist above 0.78, hence this is an indication of waves which have broken. 133

5.3 Linear wave theory validity: h is depth, λ is wave length, H is significant wave height taken from figures. For $H\lambda^2/h^3 > 26$ cnoidal wave theory is preferable. The maximum wave height (H/h) cannot exist above 0.78, hence this is an indication of waves which have broken. 134

5.4 Linear wave theory validity: h is depth, λ is wave length, H is significant wave height taken from figures. For $H\lambda^2/h^3 > 26$ cnoidal wave theory is preferable. The maximum wave height (H/h) cannot exist above 0.78, hence this is an indication of waves which have broken. 135

5.5 Linear wave theory validity: h is depth, λ is wave length, H is significant wave height taken from figures. For $H\lambda^2/h^3 > 26$ cnoidal wave theory is preferable. The maximum wave height (H/h) cannot exist above 0.78, hence this is an indication of waves which have broken. 136

5.6 Mean energy dissipation rate per unit bed due to non-breaking waves ($\overline{D}_{NB} = \tau_o U_o$) for a range of depths taken from data presented in figures for each deployment. Approximate wave heights at HW (H_{HW}) are given; the second tides are used for November and February. 137

5.7 Mean energy dissipation rate per unit bed due to waves breaking ($\overline{D}_B$ - see equation 2.34) for a range of wave heights H and periods T. Assumes wave of maximum height $H/h = -0.78$. 137

5.8 Classification of breaker types. H_{HW} is significant wave height at HW, λ_{HW} is wave length at HW (taken from site at $\approx 100\,m$, unless stated), β is breaker classification (after Galvin, 1972; equation 2.17; figure 2.6). $\beta > 5 \Rightarrow$ spilling ; $0.1 < \beta < 5 \Rightarrow$ plunging breakers 137

6.1 Model Test Cases. When the same hydrodynamic conditions are used with density stratification effects "g" is added to the code name. 160

6.2 Bed model test cases 160

Notation

A_o	Free stream orbital amplitude
BD	Bulk density
c	Wave celerity, concentration
c_a	Near bed reference concentration (at z=a)
c_g	Group wave speed
c_o	Suspended sediment concentration (at $z = z_o$)
D	Grain diameter
D_{50}	Grain diameter below which 50% of particles occur
D_B	Dissipation of energy under breaking wave
DD	Dry density
D_{NB}	Dissipation of energy under non-breaking wave
E	Turbulent kinetic energy
E_1, E_2	Constants
EMCM	Electro-magnetic current meter
f	Frequency
f_c	Darcy Weisbach friction factor
f_c^*	Current friction factor for combined w–c motion
f_w	Wave friction factor
f_w^*	Wave friction factor for combined w–c motion
f_{wc}	Wave-Current friction factor
g	Acceleration due to gravity
h	Mean depth of water, bed form height
H	Wave height
H_o	Deep water wave height
H_s	Significant wave height
H_{HW}	Wave height at high water
HW	High water
HWM	Mean high water mark
ITZ	Intertidal Zone
k	Wave number, turbulent kinetic energy per unit mass
k_s	Nikuradse roughness length
L	Bed form length
LW	Low water
LWM	Mean low water mark
m	Mass
MC	Moisture Content
M_e	Erosion rate constant
N	Number of data points
P	Instantaneous pressure

p	Fluctuating component of pressure
pH_s	Significant pressure height
P_o	Pressure gradient
ppt	Parts per thousand
RE	Reynolds number
Ri	Gradient Richardson number
Ri_f	Flux Richardson number
RSM	Reynolds stress model
$S_{uu}(f)$	Energy spectrum
s_{ij}	Fluctuating rate of strain
S_{ij}	Mean rate of strain
SSC	Suspended sediment concentration
t	Time
T	Period
T_p	Peak period
T_z	Zero crossing period
u, v, w	Longitudinal, transverse and vertical velocity
u', v', w'	Standard deviation of velocity fluctuations
u_t, v_t, w_t	Turbulent fluctuations
U_o, V_o, W_o	Maximum free stream wave orbital velocity
$\overline{u}$	Depth averaged current
U_s	Significant wave velocity
USt	Ultra sonic transducer
U_w	Wind velocity (knots)
u_*	Shear velocity
W_i	Settling velocity below which i% of particles settle
W_s	Settling velocity
W_{50}	Settling velocity below which 50% of particles settle
x, y, z	Longitudinal, transverse and vertical distance
z_o	Roughness length
z_{oo}	Roughness length incorporating sediment transport
α	Attenuation damping factor, Kolmogorov constant, constant
β	Wave breaking classification parameter
β	Volumetric expansion coefficient, constant
δ	Boundary layer thickness
δ_w	Thickness of wave boundary layer
δ_{wc}	Thickness of wave-current boundary layer
ε	Turbulent energy dissipation rate
η	Free surface
κ	Von Karman's constant
ℓ	Mixing length
λ	Wavelength, molecular diffusivity
ν	Kinematic viscosity
ν_s	Sediment eddy diffusivity
ν_t	Turbulent eddy viscosity
ρ	Density

ρ_s	Density of sediment
ρ_w	Density of water
σ_c	Turbulent Schmidt/Prandtl number
τ	Shear stress
τ_c	Critical shear stress
τ_d	Critical shear stress for deposition
τ_e	Critical shear stress for erosion
τ_o	Bed shear stress
τ_r	Reynolds stress
ϕ	Velocity potential
ω	Wave frequency
$\overline{f}$	Depth average of variable f
$< f >$	Wave-cycle average of variable f

Model Empirical Constants and Functions

C_D, C_k, C_r	Empirical Constants
C_μ, $C_{\epsilon 1}$, $C_{\epsilon 2}$	Empirical Constants
f_r, f_μ, f_ϵ, f_{ed}	Empirical functions
R_k, R_t, R_*	Reynolds numbers
R_o	Settling velocity constant
W_{min}	Minimum settling velocity
ε_t	Total turbulent energy dissipation rate
ν_r	Roughness viscosity
σ_c, σ_k, σ_ϵ	Turbulent Schmidt/Prandtl numbers

Chapter 1

Introduction

Estuaries, and in particular sediment movements in estuaries, have been a source of interest to mankind for centuries. Interest probably first developed due to their use as waterways, and the necessity of keeping channels free from siltation. They also form an ideal site for towns and cities, with reclaimed land being used for industrial and agricultural purposes. More recently, it has been realised that this exploitation needs to be kept in check to preserve the balance between the environmental and human use.

Suspended sediment concentrations (SSCs) in estuaries are high and particles are fine, cohesive and richly organic (Dyer, 1989). The ability of these fine sediments to absorb and desorb contaminants in the water means that tracing sediment movements is equivalent to pollution watching and regions where sediment congregates are of particular consequence. Complex interactions between tidal dynamics, gravitational circulations and physical sediment properties can lead to the generation of a turbidity maximum - an area of higher than average SSC. The transported sediment is continually deposited onto the banks and then subsequently removed and re-deposited on much varying timescales (Parker & Kirby, 1982; Anderson *et al*, 1981). This cycling of sediment can lead to significant build up in areas prone to accretion and sheltered from continual erosion, forming vast areas of mudflats which are rich in food but low in oxygen (McLusky, 1989).

These mudflats, or intertidal zones (ITZ), present the first line of defence to many coastlines. Their ability to absorb wave energy means that coastal erosion can be substantially reduced. This attenuation of waves due to a mud bottom is so great that in the Gulf of Mexico, a place known as Mud Hole is used as an emergency harbour by fishing boats during storms (Dalrymple & Liu, 1978). ITZs are also the living and feeding grounds for a multitude of flora and fauna. In particular, many wading birds rely solely on the rich pickings to be had from the mud. Concern has built up over mankind's ability to alter river and tidal flow by the introduction of barrages and sea walls, so disturbing the ecological balance. No longer can projects be granted approval unless they can show the environmentalists that the wildlife will be unharmed, or simply relocated. Owing to this more modern environmental awareness the

study of cohesive sediment transport on ITZs has become an issue of real importance.

The suspended sediment in an estuary consists of a spectrum of particle sizes, due to the varying tidal energy in the estuary. Particles smaller than about 60 μm are considered fine grained, but cohesion becomes a major influence for particles less than 20 μm in diameter in waters with salinities greater than 2-3 *ppt* (Mehta, 1989). This is because the negative charge, normally carried by mud particles, can be neutralised by free cations present in saline water, allowing the molecular attractive force to dominate, forcing flocculation. Single particles hence become aggregates or 'flocs' with much higher settling velocities. Flocs are periodically deposited and eroded to and from the ITZ, creating a dynamic situation governed by a variety of physical, chemical and biological factors.

Laboratory studies of cohesive sediment transport processes have proved to have limitations (Dyer, 1989), since there are so many different factors to try and incorporate, such as changes in sediment characteristics when removed from the natural environment (Luckenbach, 1986, Amos *et al.*, 1988). Hence the collection of field data is essential in improving the understanding of the processes governing mud movements. There has been little work done on sediment transport to and from muddy ITZs, due in part to the lack of suitable instruments capable of producing useful results and the practical difficulties of working in the muddy zones. Technical advancements in instrument design have produced equipment capable of recording water velocities, suspended sediment concentrations, wave characteristics and bed movements with reasonable accuracy and reliability. Future instrument improvements are likely to make the collection of good quality field data easier and more comprehensive.

Computer advancement in the last decade has permitted the development of numerous complex numerical models which can solve thousands of iterative processes in seconds. The sophistication of models has still to be balanced against computational time, however, and the physical mechanisms being modelled need to be more fully understood. Three-dimensional prediction of dispersion and advection of pollutants, siltation of harbours and waterways, and coastal protection may be the ultimate goal, but this requires the understanding of the mechanisms of importance on a finer scale. Turbulence modelling of vertical profiles has a part to play in the modelling hierarchy, both in terms of improved prediction and in providing additional understanding of the processes involved in complicated hydrodynamic regimes.

1.1 Objectives

The overall objective of this study is to investigate the mechanisms that control cohesive sediment transport on an ITZ, within a tidal cycle under a range of meteorological conditions. This has been addressed by a combination of a field study of an ITZ in the Severn Estuary, and a one-dimensional (vertical) turbulence ('k–ε') model. Part of the initiative for the work comes from a common complaint by mathematical modellers of the lack of sufficient data to validate recently developed models. This study aims to present some new data to modellers

and hopes that the combination of modelling and field experiments will provide some further direction to this area of research.

1.1.1 The River Severn

The Severn is the longest river in Britain (354 km) with the largest catchment area (11420 km^2). The source is Bryn-Cras in Powys, where high rainfalls help to maintain high flows throughout the year. Severn-Trent NRA data indicate that an average baseflow discharge at Haw Bridge is around 30 *cumecs*, with flood discharges of over 400 *cumecs*. Six million people receive water from the Severn, many in areas well beyond its watershed.

Lower down the river the influence of the tide becomes dominant. The Severn Estuary is macro-tidal with a tidal range of over 14 m on equinoctial spring tides. The tidal range can drop to as low as 6 m in the opposite extreme, resulting in some areas which are only covered by water for a relatively short period of the year. In contrast, most intertidal areas are wetted on a twice-daily timescale. These ITZs necessarily consist of a spectrum of sediment types ranging from rocky outcrops to sandy or muddy flats and saltmarshes (Allen, 1987). It is the extensive mudflats of the middle estuary around Bristol which are of interest to this study.

1.1.2 Specific Objectives

(A)

Collect field data to help in determining the relative influence of waves and tides on the spatial and temporal variation of

- relationships between wave characteristics and meteorological conditions
- change in wave characteristics due to shoaling and energy loss either caused by bed friction or dissipation of energy caused by the deforming of the bed
- estuarine topography influence on tidal currents
- bed structure in terms of bulk properties
- deposition and erosion rates
- vertical suspended sediment concentration (SSC) distribution and the transverse variation across the ITZ
- comparison between methods of estimating bed shear stress

(B)

Field results are to be used to identify areas of importance and for which further understanding can usefully be made by the application of a turbulence model. Vertical bed exchange of sediment and density stratification effects are to be added to an existing k–ε model to improve the understanding of the vertical profiles of SSC measured in the field. An evaluation of the suitability of the present model to the field conditions is to be addressed with suggested future improvements.

Chapter two reviews the literature and theory relevant to the study, separating into three main sections of hydrodynamics, sediment dynamics and numerical modelling. In chapter three, site selection, field methodology and experimental techniques are discussed, followed by a description of the numerical model and various initiation parameters. The results of each field deployment are presented by deployment in chapter four, and then discussed in chapter five, addressing the hydrodynamic mechanisms before the sediment dynamics. Based on the field results, an evaluation of the applicability of the model to the site is made in chapter 6, by covering the range of conditions experienced. The sensitivity of the model to various factors is considered followed by direct comparison with vertical SSC profiles from a 'storm' and 'calm' deployment to improve the understanding of the governing processes. Hydrodynamic comparison with other data and models is then made. Conclusions and recommendations for future work follow this in chapter seven.

Chapter 2

Literature Review and Theory

2.1 Introduction

A study of cohesive sediment transport on intertidal zones necessarily covers a wide and multi-disciplinary subject area. Subdividing a review of the theory and literature is not an easy task, and this review has been divided into three main sections. Firstly the hydrodynamic mechanisms on ITZs are considered. These are categorised into wave, current and wave current interactions. This is followed by a review of the sediment dynamics to be expected on an ITZ, focusing on how sediment is cycled between the bed and suspension. Prediction is probably the ultimate goal in studies of sediment transport, and a review of modelling techniques and applications to cohesive sedment are addressed as the final section. Conclusions follow each of these major sections.

2.2 Intertidal Zone Hydrodynamics

2.2.1 Introduction

The sea bed is subject to effects from steady flow (currents) and oscillatory flow (waves). The balance between these two in an intertidal zone (ITZ) is decided by the geography of the estuary. In the upper reaches of an estuary, where the width is narrow, tidally induced currents or freshwater flow are likely to dominate, since waves need a reasonable surface area (the "fetch") to be generated by wind shear (Phillips, 1977; Seymour, 1977). In the lower reaches, estuaries such as the Severn widen to produce enough fetch to allow locally generated wind waves, and also distantly produced swell waves, to cause significant action. Headlands and rock outcrops can further shelter an ITZ from tidal currents, hence producing areas where wave action is the dominating influence.

This part of the literature review looks at the theory behind these hydrodynamic mechanisms. This has been done by categorising into wave, current and combined wave-current flows. On most ITZs in the Severn Estuary wave processes are likely to be dominant, so the focus is towards waves. Wave theory and propagation are followed by the frictional aspects of oscillatory flow with regards to sediment transport. Unidirectional flow is then followed by the combined case, with concluding remarks.

2.2.2 Wave Theory

There are many texts which give a complete description of wave theories (Lamb, 1932; Stoker, 1957; Coulson, 1944), so the derivation will be kept concise. A cartesian co-ordinate system (x, y, z) is taken, with x measured positively in the direction of wave propagation; z measured vertically upwards from still water level and y orthogonal to x and z. The flow is assumed to be two-dimensional in the $x - z$ plane.

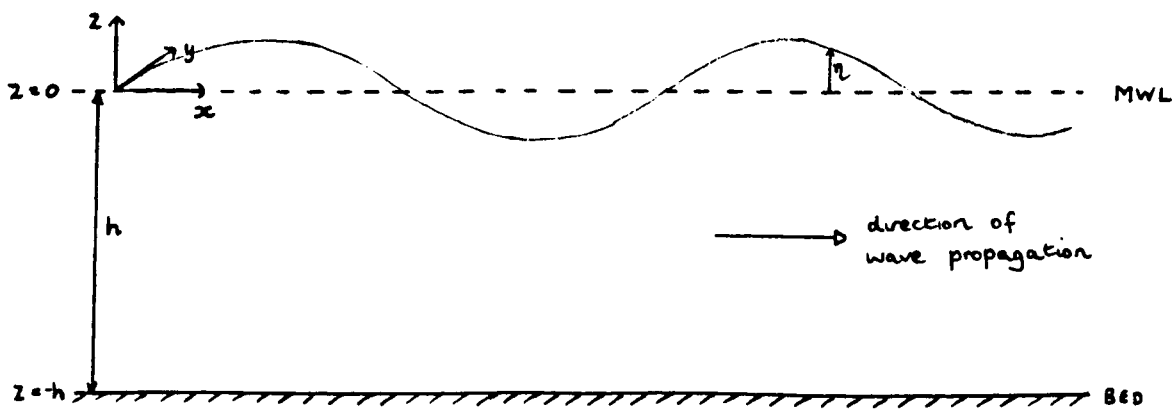

Figure 2.1: Definition sketch - Wave Theory

If it is assumed that water is incompressible, and any viscosity effects are confined to a thin boundary layer at the bed, so making the flow irrotational outside this layer, then the problem is to solve the Laplace equation

$$\nabla^2 \phi = 0 \tag{2.1}$$

for the periodic velocity potential (ϕ) defined by

$$\phi(x,z,t) = \phi(x,z,t+T) \qquad \textit{Periodicity} \tag{2.2}$$

$$u = \frac{\partial \phi}{\partial x}, \quad v = \frac{\partial \phi}{\partial y}, \quad w = \frac{\partial \phi}{\partial z} \tag{2.3}$$

where T is the wave period, subject to the boundary conditions

$$\frac{\partial \phi}{\partial z} = 0 \quad \textit{at } z = -h \qquad \textit{Bed Condition} \tag{2.4}$$

$$\frac{\partial \eta}{\partial t} + \frac{\partial \phi}{\partial x}\frac{\partial \eta}{\partial x} - \frac{\partial \phi}{\partial z} = 0 \quad \textit{at } z = \eta \qquad \textit{Kinematic Surface Condition} \tag{2.5}$$

$$\frac{\partial \phi}{\partial t} + \frac{1}{2}\left[\left(\frac{\partial \phi}{\partial x}\right)^2 + \left(\frac{\partial \phi}{\partial z}\right)^2\right] + \frac{p}{\rho} + g\eta = f(t) \quad \textit{at } z = \eta \qquad \textit{Dynamic Surface Condition} \tag{2.6}$$

Assuming that these equations are valid, the difficulties that remain in finding an exact solution are that the free-surface condition is nonlinear, and that the free-surface ($z = \eta$) is initially unknown.

The most fundamental approach to this problem is to seek linearity by assuming the wave height (H) is much less than both wavelength (λ) and depth (h) and that the free surface is at the still water level (i.e. z=0). This theory is known as small amplitude wave theory, linear wave theory, sinusoidal wave theory or as Airy theory. It is also the first approximation to Stoke's formal perturbation theory (Stoker, 1957) which can be used to gain a higher order small amplitude theory solution. A "separation of variables" technique can be applied to the linear version of the problem resulting in a solution

$$\phi = \frac{gH}{2\omega} \frac{\cosh k(h+z)}{\cosh kh} \sin(kx - \omega t) \tag{2.7}$$

$$\eta = \frac{H}{2} \cos(kx - \omega t) \tag{2.8}$$

$$\omega^2 = gk \tanh kh \qquad \textit{Dispersion Relation} \tag{2.9}$$

where k is the wave number ($k = 2\pi/\lambda$) and ω is the wave frequency ($\omega = 2\pi/T$) in radians. Hence from these equations expressions for orbital velocities and excursions, wave energy, pressures and group velocity can be derived (see e.g. Sarpkaya & Isaacson, 1981).

Linear theory (as it will be referred) is applicable provided

$$\frac{H}{\lambda} \ll 1 \tag{2.10}$$

$$\frac{H\lambda^2}{h^3} \ll 1 \qquad \textit{Ursell Parameter} \tag{2.11}$$

which limits application to small amplitude waves in deep water. When water depth becomes too small relative to wavelength (such as when waves steepen and break), the errors induced by failing to adhere to these limitations may become too large and it may be considered necessary to use a different approach.

Shallow water theory (e.g. cnoidal, solitary waves) simplifies the boundary conditions (equations 2.5 & 2.6) by the opposite approximation to linear theory in assuming that wavelength is long compared to water depth and wave height is small compared with depth. As before, a Taylor's approach can be used to produce very complicated solutions involving Jacobian elliptic functions (see e.g. Wiegel, 1964). A variety of work has been undertaken to discover when shallow water theory gives a better approximation than linear theory (Housley & Taylor, 1957; Dean, 1970; Le Mehaute, 1976) and Le Mehaute suggested that cnoidal theory is preferable when

$$\frac{H\lambda^2}{h^3} > 26 \tag{2.12}$$

Numerical solutions (e.g. Cokelet's (1977) "exact" solution) to the governing equations (2.1-2.6) which give superior results, especially when near wave breaking, are also available.

The extra computational burden with shallow wave theory and numerical methods has to be weighed against the increased accuracy and for this reason linear wave theory is used for most engineering purposes. The errors which arise from using a theory which is on, or over, its theoretical limits need to be considered when conclusions are drawn. Higher order effects which can be observed in steeper waves (see e.g. Sarpkaya & Isaacson, 1981) are a steepening in wave crests and flattening of wave troughs. Also, the particle paths are no longer closed orbits resulting in a net horizontal velocity ("Stoke's drift") which has implications for mass-transport.

2.2.3 Wave Generation

When a wind blows over a length of water surface (the "fetch") for a length of time (the "duration") it exerts a shear stress on the surface and local waves are generated. Once set up these oscillations continue to run across the surface far beyond the direct influence of the wind, and at this stage are known as "swell waves"(Pond & Pickard, 1978). The size and frequency of the waves generated are determined by the fetch and duration (Phillips, 1977; see figure 2.2). A reduced fetch and short duration result in high frequency, small amplitude waves whilst an extended fetch and long duration result in large, long wavelength waves. As a storm progresses the wave heights increase, until a dynamic equilibrium is met, balanced by wind shear and breaking. Typical wave spectra (e.g. JONSWAP) have been created, based on these factors which can be used in subsequent calculations. Driver & Pitt (1979) state that "wave prediction techniques have limited use in shallow water areas, and are a poor substitute for field data." However, in many cases prediction is the only available resource and figure 2.3 and table 2.1 show predicted wave heights near Portishead in the Severn Estuary, taken from HR Report EX1207(1984).

Wind generated waves are obviously not monochromatic, and hence for most practical purposes it is necessary to quantify the whole spectrum of waves in terms of height and period by some statistical property. Much has been written on which quantity to use, (for example, mean height of waves, root-mean-square height, maximum height and significant height) and relationships between the various parameters have been derived (see Longuet-Higgins, 1952). The choice of parameter should depend on the application of the data. If an offshore structure needs to be resistant to waves up to a certain height the maximum wave height may be the best choice, but generally the "significant" wave height (Hs) - defined as the mean height of the highest one-third of all the waves - is used. Similar problems exist in choosing some kind of average period for the wave spectrum, and either the peak of the spectrum (T_p) or more commonly the "zero crossing period" (T_z) is used. This is derived from the definition of a "zero up-cross" wave: a wave passes through the mean line in an upward direction resulting in an up-crossing, and the surface between this and the next up-crossing is an "up-cross" wave. The height of this wave is the distance between the maximum and minimum value taken in this region. The period is the time between consecutive zero-crossings (Tann, 1976).

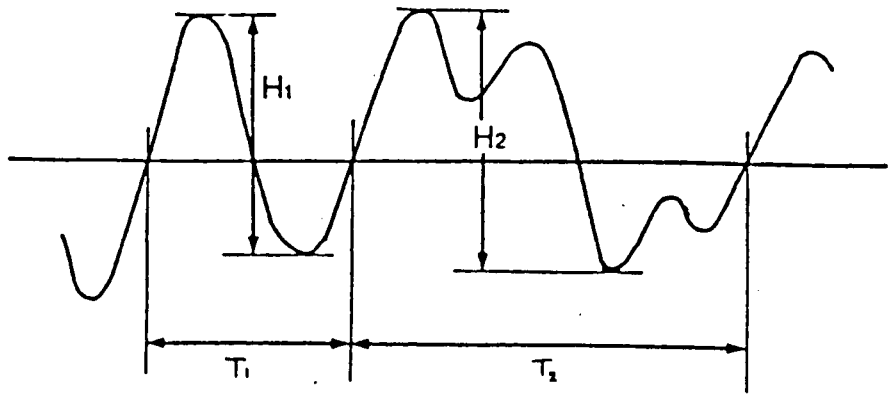

Figure 2.4: Definition sketch - Zero Crossings

The 'significant wave height' (Hs) is defined as the mean height of the highest third of the waves and the zero-crossing period (Tz) is the average of the zero-crossing periods.

2.2.4 Wave Propagation

Wave Grouping

In a train of irregular wind-generated waves grouping can be observed, typically with 4-8 waves in each group.

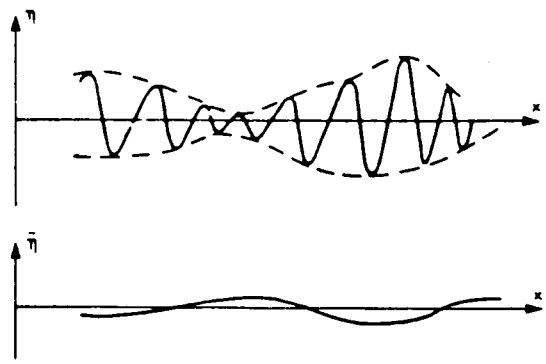

Figure 2.5: Definition sketch - Wave Groups and Associated 'Infragravity' Waves

This is caused by individual waves travelling at different speeds (a consequence of a dispersive process), with the energy propagating at a slower rate known as the 'group velocity'. In deep water the group speed is half the wave celerity and in shallow water is equal to wave celerity. Wave groups have been observed to cause significant additional resuspension of sand in two metres of water depth during a field study by Hayes (1991).

Since a wave group contains waves of different heights then this can give rise to second order waves with length and period of the order of the group. This can be explained by the changes in mean water level created by the need to balance the excess momentum in each propagating wave. Longuet-Higgins & Stewart (1964) defined this excess momentum to be the 'radiation stress' which is a function of wave height, so where waves of differing sizes are grouped, changes in mean water level are created by balancing the radiation stresses. These waves are termed 'infra-gravity' waves owing to the long periods associated with them, and are generally more significant when the wave groups travel into very shallow water where the wave heights increase. In the nearshore often they are referred to as 'surf beat' (Munk, 1948).

Shoaling, Refraction and Reflection

Section 2.2.2 describes the nature of waves at a particular depth (h), but as waves propagate into shallower water they are subject to changes in their characteristics culminating in wave breaking. If wave frequency remains constant then neglecting the effects of bottom friction, and assuming wave power is conserved this gives rise to the process of **shoaling**, which results in changes to the celerity, height and length of the waves

$$\lambda = \lambda_o \tanh \frac{2\pi h}{\lambda} \tag{2.13}$$

$$H = H_o \sqrt{\frac{c_{go}}{c_g}} \tag{2.14}$$

where the subscript o refers to deeper water values, and c_g is the group wave speed $c_g = d\omega/dk$ and can be derived from the dispersion relation (equation 2.9). The height of waves is initially reduced until the reducing wavelength results in steepness increasing more rapidly, and then heights increase until the waves break.

Waves travelling at an angle to the shoreline will be **refracted** more parallel to the shoreline since the waves in the deeper water will travel faster than those in the shallower water. This is a fortunate result which allows measurement techniques to be aligned assuming all waves travel directly up the beach.

Waves hitting the shoreline will be **reflected** as they are when hitting a wall, but with much

reduced amplitudes as much of the energy will have been dissipated in wave breaking. Davies (1983) pointed out that when recording wave heights in the near shore, the recorded heights may be oversized due to the effects of wave reflections, which may have implications on the quantity required e.g. friction factors.

Wave Breaking

The culmination of shoaling is wave breaking, which occurs when the steepness H/λ reaches its critical value, which for a progressive wave in water of constant depth was suggested theoretically by Miche (1944) to be

$$\frac{H}{\lambda} = 0.142 \tanh kh \tag{2.15}$$

This is only approximate, and becomes less accurate in shallower water. Experimentally, the limiting value of H/h for solitary waves in water of constant depth is given by

$$\left(\frac{H}{h}\right) \simeq 0.78 \tag{2.16}$$

Reviews of breaking waves are given by Longuet-Higgins (1976) and Peregrine (1979, 1988). The form of breaking waves is of primary interest since the different type of breaker is likely to have vastly different character and strength (Nielson, 1984). The wave steepness and beach slope are the parameters affecting the type of breaking wave:

spilling low steepness waves which break by continuous spilling of foam down the front face of the wave on gently sloping beaches or in deep water

plunging medium steepness waves on moderately sloping beaches which curl over the water in front

collapsing a transition stage between plunging and surging with foam falling down the face of the wave

surging steep waves on steep beaches where the base of the wave surges up the beach generating considerable foam

Sketches of these descriptions are shown in figure 2.6 together with the parameter β suggested by Galvin (1972) classifying the breaker type

$$\beta = \frac{H_o}{\lambda_o \tan^2\theta} \tag{2.17}$$

where H_o/λ_o is the deep water wave steepness and θ is the beach slope. The transition between breaker type is continual as conditions change, according to Galvin (1972), hence this parameter can only be used as a guide. The turbulence formed in wave breaking is likely to be a major force in bed erosion and sediment resuspension and is an area of study which is not fully understood. Numerical techniques are only just being used to study what was being observed for years (Cooker & Peregrine, 1991). A further discussion on estimating energy dissipation under breaking waves is given in the following section on the frictional aspects of oscillatory flows.

A second order effect which occurs when waves travel into reducing water depth and break, is a process known as 'set-down' and 'set-up', whereby the mean water level is firstly reduced (prior to the breaker zone) and then increased (after breaking). This can be explained by the change in momentum as the waves break, and is caused by the excess flow of momentum due to the presence of waves, defined by Longuet-Higgins & Stewart (1964) as the radiation stress. This change in water level can create strong offshore currents known as 'rip currents'. Waves breaking at an angle to a beach can hence also generate a longshore current flowing parallel to the shoreline by creating transverse variation in water elevation (Komar, 1983).

2.2.5 Bed Friction, Boundary Layers and Energy Dissipation

The Wave Boundary Layer

The previous sections consider the frictionless aspects of oscillatory flow, and are based on the assumption that any viscosity can be confined to a thin layer near the bed, known as the "boundary layer". The boundary layer is an layer of intense velocity shear which allows the flow to go from no velocity at the bed up to the free-stream velocity in a short distance. As will be seen even in fully turbulent flow, in the absence of any current, the thickness of the boundary layer is only a few centimetres (Davies, 1983).

Generating turbulent boundary layers in the laboratory is usually done by artificially increasing the bed roughness, since high velocities cannot be generated, and since the wave climate is invariably sinusoidal the results may not be as applicable to the field as hoped. Determining the thickness of the wave boundary layer in the field is not an easy prospect. Information obtained from laboratory data gives rise to some uncertainty of the thickness to be expected under irregular waves. Work by Jonsson (1966) first classified the flow regimes in terms of the Reynolds Number, (RE) and a "relative roughness" (A_o/k_s)

$$RE = \frac{A_o U_o}{\nu} \tag{2.18}$$

where ν is the kinematic viscosity, A_o is the orbital excursion and U_o the orbital velocity at the wave boundary layer derived from equations 2.3 and 2.7

$$A_o = \frac{H}{2\,sinh\,kh} \tag{2.19}$$

$$U_o = \omega A_o \tag{2.20}$$

The equivalent roughness, k_s, is an important parameter which has no definite classification. Many suggestions have been made relating k_s to grain diameter when there are no bed forms and to the size of the bed forms when they are present (see e.g. Sleath, 1984). Since the bed cannot be observed continually whilst underwater, this leads to some uncertainty as to what value to take. Van Rijn (1982) reviewed the available data, with respect to k_s, but the scatter was too great to show which, if any, of the expressions were correct. On an ITZ where the bed was considered to be fairly smooth and flat (relative to wave propagation direction), West (1990) reviewed the various expressions and found that none changed the categorisation of the flow on the ITZ of study. It can be taken that

$$k_s = D_{50} \qquad \textit{flat bed } (\textit{Grant \& Madsen, 1976; Sleath, 1978}) \tag{2.21}$$

$$k_s = 25\left(\frac{h^2}{L}\right) \qquad \textit{rippled bed } (\textit{Swart, 1976}) \tag{2.22}$$

where D_{50} is the diameter below which 50% of the particles fall, h is the height and L the length of the bed form. For modelling purposes, where the choice of k_s may result in large discrepancies, a sensitivity analysis is suggested.

Slight modifications of Jonsson's (1966) suggestions over the years have produced the delineation shown in figure 2.7 based on his expressions. The flow is categorised into three main areas: laminar, transitional and turbulent. As a further classification the turbulent region is separated into smooth and rough turbulent. The onset of turbulence is defined in terms of RE, but when the transition from laminar to turbulent flow occurs is not clear. Jonsson suggests a value of RE around 10^5, but values as low as 10^4 have been used. The thickness of the wave boundary layer (δ_w), defined by Jonsson to be the distance between the bed and the lowest point at which the velocity equals the free-stream velocity, is given for these different classifications:

$$\frac{\delta_w}{A_o} = \frac{\pi}{2\sqrt{RE}} \qquad \textit{Laminar Flow (Analytical)} \tag{2.23}$$

$$\frac{\delta_w}{A_o} \approx \frac{0.0465}{\sqrt{RE}} \qquad \textit{Smooth Turbulent Flow (Empirical)} \tag{2.24}$$

$$\frac{30\,\delta_w}{k_s} \log \frac{30\,\delta_w}{k_s} = 1.2\,\frac{A_o}{k_s} \qquad \textit{Rough Turbulent Flow (Empirical)} \tag{2.25}$$

From these equations it can be seen that δ_w is a function of RE unless the flow is rough turbulent in which case it is a function of relative roughness. The wave boundary layer does not ever get more than a few centimetres thick, and is typically 2–4 % of the excursion amplitude (Jonsson & Carlson, 1976). On general scaling arguments, Smith (1977) suggested that the thickness of the turbulent wave boundary layer is of the order (u_*/ω) where $u_* = \sqrt{\tau_o/\rho}$ with τ_o the bed shear stress defined in equation 2.26.

Friction Factor and Bed Shear Stress

Bed shear stress is an important parameter, influencing sediment transport, but it is difficult to determine, particularly in the field. Under oscillatory flows, an estimate can be made by using a drag coefficient calculated from laboratory studies of turbulent flow. This drag coefficient, more commonly referred to as a friction factor, is classically found by measuring wave height attenuation in a flume, although this can have its problems: for example side wall influence (Jonsson, 1966). In the field, difficulties arise from wave reflection and refraction (Davies, 1983), and since "no adequate observations of the detailed motions at the seabed appear to have been made to complement the various measurements of wave dissipation rates", the friction cannot be related to the type of bed. Recent field studies (e.g. RRS Challenger Cruise 74B, 1991) have attempted to use bed photography as a method of monitoring sediment transport, which could then be used in combination with spatial wave attenuation measurements to determine friction factors and bed roughness (P.O.L. Cruise Report 11).

The most commonly used definition for the wave friction factor, f_w, is that suggested by Jonsson (1966)

$$\tau_o = \frac{1}{2}\rho f_w U_o^2 \tag{2.26}$$

where τ_o is the maximum bed shear stress, and U_o is the bed orbital velocity (equation 2.20).

The dissipation of energy under a non-breaking wave (D_{NB}) can then be given by

$$D_{NB} = \tau_o U_o \tag{2.27}$$

which is thus a measure of how much energy is transferred to the bed to enable sediment entrainment.

The bed shear stress in laminar flow is defined as

$$\frac{\tau_o}{\rho} = \nu \left(\frac{\partial u}{\partial z}\right)_{z=0} \tag{2.28}$$

From this expression and the linear wave theory velocity distribution (see e.g. Sleath, 1983), it can be shown that in laminar flow the peak values of τ_o lead U_o by $\pi/4$. In turbulent flow the phase difference is less (Jonsson, 1966), and the unknown velocity distribution leads to empirical definitions for f_w, based on the same delineation as for boundary layers (see figure 2.7). The wave friction factor is given by one of these three expressions from Jonsson's (1966) laboratory experiments

$$f_w = \frac{2}{\sqrt{RE}} \qquad \textit{Laminar Flow (Analytical)} \tag{2.29}$$

$$\frac{1}{4\sqrt{f_w}} + 2\log\frac{1}{4\sqrt{f_w}} = \log RE - 1.55 \qquad \textit{Smooth Turbulent Flow (Empirical)} \tag{2.30}$$

$$\frac{1}{4\sqrt{f_w}} + \log\frac{1}{4\sqrt{f_w}} = \log\frac{A_o}{k_s} - 0.08 \qquad \textit{Rough Turbulent Flow (Empirical)} \tag{2.31}$$

For low values of relative roughness ($A_o/k_s < 1.57$) in the rough turbulent regime, the constant value of $f_w = 0.3$ was suggested by Jonsson (1978). This is consistent with other proposals by Bagnold (1946), Kajiura (1968) and Grant & Madsen (1982).

Hence bed shear stress can be calculated using equation 2.26 with the appropriate choice of wave friction factor. Note that the values of bed shear stress calculated in this way will only be valid for those values at which the wave theory deriving bed orbital velocity holds (see section 2.2.2), and values are very sensitive to the estimate of f_w. It is generally assumed that wave friction factors are of the order of 10^{-2} for field applications after the work of Putnam & Johnson (1949). More recent work has suggested much larger values are plausible. Values ranging between 0.02 and 2.32 were obtained by Iwagaki and Kakinuma (1967), for example.

Wave Height Attenuation

Wave shoaling, refraction and reflection are simply geometric processes, caused by waves propagating into water of a different depth, or towards obstacles. Attenuation in wave heights is an effect caused by loss of energy due to bottom interaction – either by bed friction or dissipation due to the creation of a mud wave. The type of loss corresponds to the type of bed over which the waves are travelling. If the bed is rigid, as it would be with no mud layer present, then energy loss is caused by friction. If, however, there exists a layer of soft mud which can easily be deformed, then a mud–wave can be created, which can lead to very strong attenuation. For example, observations made off the southwest coast of India (Wells & Kemp, 1986; MacPherson, 1980) showed that waves could completely disappear over a distance of $4 - 8\lambda$. These observations were made above fluid mud layers $10 - 100\,cm$ thick (Bulk density: $1250\,kgm^{-3}$). In the Mississippi delta, less extreme, but still significant reductions (10%) were reported by Suhayda (1986). An order of magnitude greater in energy dissipation rates was indicated by Tubman & Suhayda (1976) over soft sediments as opposed to an impermeable bed. Despite these differences the simplest way to include attenuation is to assume an exponential decay of wave height with distance travelled for both cases, and use different damping factors (α)

$$H = H_o\, e^{-\alpha x} \tag{2.32}$$

Field studies related to attenuation over a muddy beach have been almost neglected, but damping factors have been calculated in laboratory experiments (Sakakiyama & Bijker, 1989). These laboratory experiments were based on a flume with a constant depth, but by taking a constant damping for all depths on a sloping beach the tendency would be to over estimate initial attenuation and to underestimate attenuation in the shallower water at the top of the beach. The results do highlight the attenuation capabilities of a flexible bed. From field observations and laboratory experiments theoretical shoaling calculations based on water depth alone are unreliable over a flexible bed (Mehta, 1981; Wells & Coleman, 1981).

Energy Dissipation Under Breaking Waves

The turbulence generated by waves breaking has a profound influence on sediment entrainment and erosion, so it is useful to be able to make some estimate of the relative influence of breaking against non-breaking waves. In a review by Peregrine (1988) the major differences in breaker type and how they interact with the bed was considered. Plunging breakers are known to form a jet-like front as they overturn, creating a large impact pressure on the bed, whilst spilling breakers behave more like a bore. Numerical models for calculating impacts from wave-breaking jets are being developed (Cooker & Peregrine, 1990), and a useful estimate of energy dissipation can be made from the similarities between broken wave fronts and hydraulic jumps (Le Mehaute, 1962, see e.g. Fredsoe & Deigaard, 1992). It might be assumed that this is most appropriate for spilling breakers.

By assuming that the energy loss in a hydraulic jump is analogous with the head loss when a wave breaks, and changing the frame of reference to the broken wave (so keeping the broken wave stationary as would a hydraulic jump) the rate of energy loss at each wave front can be found

$$Rate\ of\ Energy\ Loss\ (per\ wave\ front) = \rho g c \frac{hH^3}{4h^2 - H^2} \tag{2.33}$$

where c is wave celerity, h water depth and H breaking wave height. Thus the problem is reduced to deciding on a length scale over which the wave breaks, and a wave height to water depth ratio under breaking. Often the wave length is taken as a length scale, but it can be seen from watching waves break,that waves can break over shorter, or spill over much longer, distances. The wave height to depth ratio may be estimated from equation 2.16. Taking the wave length as the length scale gives a mean energy dissipation per unit bed ($\overline{D}_B$) as

$$\overline{D}_B = \frac{\rho g h H^3}{T(4h^2 - H^2)} \tag{2.34}$$

where T is the wave period. This would probably underestimate $\overline{D}_B$, since the length scale for dissipation is likely to be shorter. A sensitivity analysis is recommended to determine the impact of various possible length scales. This dissipation can then be compared with that under a non-breaking wave ($\overline{D}_{NB} = \tau_o U_o$).

Observations by Kana (1977) showed that plunging breakers were able to entrain almost an order of magnitude more sediment than spilling breakers, and the occurrence of plunging breakers during storm conditions resulted in five times the suspended sediment concentrations than in calm conditions according to Kana & Ward (1979). Hence, this estimate of energy dissipation in breaking should only be viewed as a guideline.

2.2.6 Steady Currents

In estuaries, both freshwater flow and changes in water elevation create currents. Tidal currents are dominant in all but the upper reaches and can obtain speeds of over $2\,m/s$ on high Spring tides. Estuarine topography and bathymetry can alter both the direction and magnitude of currents. Although a tidally induced current is not entirely steady, the fluctuating timescales are long enough to allow this assumption for short periods and steady flow derivations can be used. There are many texts on currents and boundary layers, the following is based on the the summaries given in Sleath (1984) and Dyer (1986).

When a current flows over a surface any slight roughness will induce a boundary layer (δ) to develop, which thickens downstream until it encompasses the whole flow assuming the depth is not infinite and the flow continues for sufficient time. The flow will be turbulent when the Reynolds number ($Re = ux/\nu$) is greater than 5000, where x is the distance from initiation. On an ITZ, and for most practical purposes, this will be the case and the flow is known as "fully developed turbulent flow".

The boundary layer can be split into three main layers:

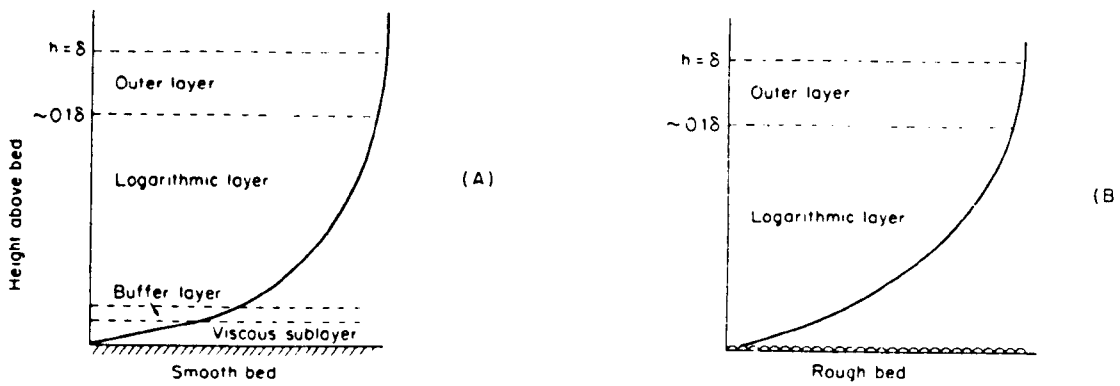

Figure 2.8: Definition sketch - Current Boundary Layers for (A) smooth turbulent, and (B) rough turbulent. Not to scale. (taken from Dyer, 1986)

1. Inner layer (or viscous sublayer) – the thin layer nearest the bed where turbulent eddies are inhibited by the presence of the boundary and viscous stresses dominate.
2. Logarithmic layer
3. Outer layer

A buffer layer between the viscous sublayer and the logarithmic layer can exist when the bed is considered smooth. For rough turbulent flow the fully turbulent layer extends down to the roughness elements, and the viscous sublayer is absent.

Analytical solutions for the velocity distribution in turbulent flow are hampered by not having a satisfactory relationship between shear stress and velocity. There are three ways to solve this problem: assume a velocity distribution, a shear stress distribution or an assumption on the relationship between the two by means of an eddy viscosity (ν_t), (or something analogous to this). Boussinesq (1877) introduced the concept of an eddy viscosity so that friction in turbulent flow is analogous to viscous friction in laminar flow and equation 2.28 is replaced with ν_t

$$\frac{\tau_o}{\rho} = \nu_t \frac{\partial u}{\partial z} \tag{2.35}$$

and then some distribution is assumed for ν_t, the simplest assumption being ν_t is constant.

The approach used by Prandtl and von Karman is analogous to the eddy viscosity technique and was to split the velocity into a mean and a fluctuating component ($u = \overline{u} + u'$) and take a time mean of the Navier Stokes equations, resulting in similar equations as for steady flow but with an additional stress (τ_r)

$$\tau_r = -\rho \overline{u'w'} \tag{2.36}$$

where the overbar indicates a time mean. This term is known as the Reynolds stress. Prandtl assumed an eddy originates at the boundary and travels a distance ℓ, the "mixing length" before dissipating:

$$u' \simeq -\ell \frac{\partial \overline{u}}{\partial z} \tag{2.37}$$

and if

$$w' \propto u' \tag{2.38}$$

then

$$\tau = \rho \ell^2 \left|\frac{\partial \overline{u}}{\partial z}\right| \frac{\partial \overline{u}}{\partial z} \tag{2.39}$$

This is analogous with equation 2.35 where

$$\nu_t = \ell^2 \left|\frac{\partial \overline{u}}{\partial z}\right| \tag{2.40}$$

Some assumption needs to be made about the mixing length, and since the length scale of eddies increases with distance from the boundary

$$\ell = \kappa z \tag{2.41}$$

is taken, where κ is the von Karman constant ($\kappa = 0.4$) (i.e. it is assumed the size of the turbulent eddies varies linearly with distance from the bed).

Using the definition for shear velocity u_*

$$u_* = \left(\frac{\tau_o}{\rho}\right)^{1/2} \tag{2.42}$$

substitution of equations 2.41 and 2.42 into 2.39 gives the logarithmic velocity distribution for the fully turbulent layer:

$$\frac{u}{u_*} = \frac{1}{\kappa} \ln\left(\frac{z}{z_o}\right) \tag{2.43}$$

where z_o is a roughness length and is determined experimentally. Figure 2.9 shows the variation of z_o with a Reynolds number $u_* k_s/\nu$, which is used to categorise the bed into hydraulically smooth or rough. The determination of z_o is of great importance, because the velocity distribution, and hence the bed shear stress, are sensitive to the chosen value.

2.2.7 Friction Factor in Current Flows

As in section 2.2.5 a useful quantity is the drag on the bed and hence the bed shear stress. The most widely used formula for steady flow is the Darcy Weisbach definition of friction factor f_c

$$f_c = \frac{8\,\tau_o}{\rho\,\overline{u}^2} \tag{2.44}$$

where $\overline{u}$ is the depth averaged velocity.

The problem of finding the bed shear stress, is then reduced to getting an estimate for f_c. Using the velocity distribution (equation 2.43) for fully developed steady flow the expression

$$f_c = \frac{1.28}{\ln^2(h/2.72\,z_o)} \tag{2.45}$$

is obtained, where h is the depth and z_o can be taken from figure 2.9. When sediment transport is significant Smith (1977) suggests replacing z_o by

$$z_o = z_{oo} + 26.4 \frac{(\tau_o - \tau_c)}{(\rho_s - \rho)g} \tag{2.46}$$

where z_{oo} is the z_o taken from figure 2.9, ρ_s is the sediment density and τ_c the critical shear stress for motion. For cohesive sediment beds τ_c is given by τ_e (the critical erosion shear stress), which is explained in section 2.3.7.

For hydraulically rough beds ($u_* k_s / \nu > 70$) the Manning Strickler equation

$$f_c = 0.122 \left(\frac{k_s}{h} \right)^{1/3} \tag{2.47}$$

can be used with k_s given either by equation 2.21 or 2.22.

Table 2.2 shows typical values for z_o and f_c taken from Soulsby (1983) for a range of sea bed types. The results are based on measurements 100 cm above the bed.

2.2.8 Wave-Current Interactions

"The presence of a current alters the speed of an ocean wave and thus affects the relationship between the wavelength and the observed wave period. The current also produces changes in other wave properties such as the water particle velocities and accelerations" (Hedges & Lee, 1992). On most ITZs the influence of both currents and waves will be expected, but in differing proportions, so the interactions between the two will be important.

The precise effects of wave–current interactions are complex and are still poorly understood. In a purely oscillatory flow (see section 2.2.5), the turbulence is restricted to a thin boundary layer at the bed only a few centimetres thick (Davies, 1983). In fully developed unidirectional flow, which would probably be the case on an ITZ, the boundary layer extends over the whole depth, hence there is some confusion as to what would happen to the oscillatory and unidirectional turbulent boundary layers for the combined flow. Davies, Soulsby and King (1988) state that in the combined case, the oscillatory boundary layer thickness δ_{wc} is significantly greater than the wave boundary layer thickness δ_w and that within this layer there is interaction between the waves and currents.

There have been many attempts to find analytical solutions for the combined flow (e.g. Grant & Madsen, 1979; Christoffersen & Jonsson, 1985; Fredsoe, 1984), but the lack of sufficient experimental data has resulted in numerous unvalidated models (Tolman, 1992). The problem encountered by modellers is the necessity to make assumptions about the nature of the combined boundary layer, which is poorly understood.

It is generally taken that waves superimposed on a current will enhance the wave boundary layer, with the flow being divided into three zones (Lungren, 1972, see Fredsoe & Diegaard, 1992).

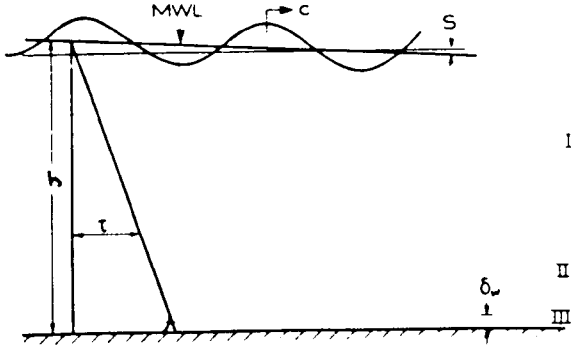

Figure 2.10: Definition sketch - Three Zones Under Wave-Current Flow (Fredsoe & Diegaard, 1992)

In the upper zone the current totally dominates and the turbulent stresses are independent of the waves. Zone II is transitional, where the turbulent viscosity produced by the waves

and current are of roughly equal magnitude. Zone III is wave dominated, although it can be washed out by a strong current (relative to the waves) with the vertical extent of these zones governed by the relative strengths of waves and current (Fredsoe & Diegaard, 1992).

A review by Simons *et al.* (1988) of existing models used to predict bottom shear stresses, concluded that the unidirectional turbulent boundary layer was reduced, and horizontal velocity fluctuations in the boundary layer increased, when waves were superimposed on purely current flow.

Experimental work by Kemp and Simons (1982, 1983) investigated wave–current interactions for a following or opposing current in oscillatory flow over smooth and rough boundaries. Conclusions were that opposing currents increase wave steepness and increase friction factors, and following currents attenuate wave heights and decrease friction factors. The results support the view that turbulent intensities are increased near the bed by the superposition of waves on a current and that the unidirectional turbulent boundary layer is reduced with the addition of waves. Bed shear stresses could be found, to a first approximation, by the linear addition of waves and current stresses for a smooth boundary, but they behaved non-linearly for a rough bed.

2.2.9 Determining Bed Shear Stress in Wave-Current Flows

Bed shear stress (τ_o) is a notoriously difficult parameter to determine under combined wave and tidal flows and a number of methods of estimation can be obtained. Since each method has advantages and disadvantages it is good practice to use more than one method on this understanding (Soulsby & Humphery, 1989). Many of the comments and criticisms made in this following review are based on a paper by Huntley (1988), who reviewed some of the methods of measuring shear stress in wave-current boundary layers. Further references can be obtained from this paper.

Mean Flow Method

By assuming a logarithmic variation in velocity with height above the bed (equation 2.43), u_* and hence τ_o can be found from the gradient. Ideally a number of values of $u(z)$ is required to validate the logarithmic velocity distribution, which is expected to remain valid despite the presence of waves (see e.g. Grant & Madsen, 1984). This method necessarily requires measurements of velocity of sufficient accuracy that differences in velocity between sensor heights can be resolved. Zero drift, or small currents mean that errors in friction velocity are likely (Huntley, 1988).

Reynolds Stress ('Eddy Correlation')

The most direct way of measuring stress is from Reynolds stresses (equation 2.36), which is sometimes known as the 'eddy correlation' method. Although direct, this method suffers from vertical/horizontal sensor alignment errors of the order of 10% per degree of tilt when mean flows are dominant (Huntley, 1988). In theory, when oscillatory flow is present wave orbits should be in quadrature so giving no contribution to $\overline{u'w'}$. However, in practice correlation is enormously increased if there is any sensor misalignment. Huntley (1988) suggested that an accuracy of 0.1 degree is necessary to provide sufficient accuracy and goes on to say that methods of re-aligning vertical axes after data have been logged are at present insufficient. Misalignment errors of between 8-150% per degree were estimated by Soulsby (1988) in field data collected under wave-current interactions in the English Channel.

Inertial Dissipation Method

This method of estimating bed shear stress involves the use of energy spectra and requires the transformation from frequency (f) space to wave-number (k) space where $k = 2\pi f/\overline{u}$. For this method to be valid, the turbulence spectra $\phi(k)$ must contain a range of k for which dissipation balances production, characterised by a $-5/3$ slope. This region is known as the inertial subrange

$$\phi(k) = \alpha\epsilon^{2/3}k^{-5/3} \tag{2.48}$$

where ϵ is the dissipation rate and α is the Kolmogorov constant. If it is assumed that a constant stress layer is present (i.e. bottom stress = local stress) then a substitution of a logarithmic boundary layer (equation 2.43) leads to

$$u_* = \left(\frac{\phi(k)k^{-5/3}}{\alpha}\right)^{1/2}(kz)^{1/3} \tag{2.49}$$

where z is the measurement height. In order that the transfer to k (from f) is valid the Taylor concept of "frozen turbulence" needs to be valid, which can be conceptualised as the time scale for an eddy needing to be much larger than the time for an eddy to be advected past the measurement point (see Tennekes & Lumley, 1972). These restrictions can result in a very small range over which the transfer is valid, as instrument size limitations (see Soulsby, 1980) can often be near the limiting k value.

So primarily this method requires accurate values of $\overline{u}$, which since being a denominator in the transferal of frequency to wave number cannot be too small, and a $-5/3$ slope in the energy

spectra. A more complete description of this method can be found in Huntley (1988).

Spectra Splitting Technique (Soulsby & Humphery, 1989)

Field experiments by Soulsby (1988) in the English Channel over an immobile rough bed of wave and current flow were made to test interaction theories. A number of methods of calculating the bed shear stress were presented. A technique of splitting the spectrum into wave and current sections was used to separate the turbulent fluctuations allowing a comparison between wave and tidal energy.

Measured velocity fluctuations (u_m) are made up from both wave orbits (u_w) and turbulent fluctuations (u_t), and since (by definition) (u_w) is not correlated with (u_t)

$$\overline{u}_m^2 = \overline{u}_w^2 + \overline{u}_t^2 \tag{2.50}$$

with the area under the energy spectrum $S_{uu}(f)$ the total variance $\overline{u}_m^2$. When the energy spectrum is plotted on log-log axes against frequency (see figure 2.11) the wave peak ($\overline{u}_w^2$) can be removed leaving a 'conventional' turbulence spectrum.

Replotting $S_{uu}(f)$ on linear axes (figure 2.12) the corresponding areas $\overline{u}_w^2$ and $\overline{u}_t^2$, can be calculated and the separated turbulent fluctuations (u_t, v_t, w_t) can then be used to estimate bed shear stress from

$$\tau_o = 0.19\rho E \tag{2.51}$$

$$E = \frac{1}{2}\left(\overline{u_t^2} + \overline{v_t^2} + \overline{w_t^2}\right) \tag{2.52}$$

where the constant 0.19 has been observed in a number of flows (Soulsby, 1983). This constant may not be applicable to flow in the shallow water over of an ITZ, as it was observed either in deep water, or in atmospherical boundary layers, by comparing Reynolds stress (equation 2.35) with E.

This method allows a comparison of the relative contribution from turbulent and wave energy, but is time consuming to calculate, as the frequency band of the removed wave energy has to be determined manually from each individual spectrum. It has not been used widely and so a proper validation has not been made yet.

Friction Factors

Equations 2.26 and 2.44 can be used to give estimates of the drag coefficients, and bed shear stress for purely oscillatory and unidirectional flow, respectively. Unless direct measurements

of energy dissipation exist, the drag coefficient under combined wave–current flow can only be estimated. Two commonly used parameterisations relate bed shear stress (τ_o) to velocity

$$\tau_o = \frac{1}{2}\rho f_{wc}(\overline{u} + U_o)^2 \tag{2.53}$$

$$\tau_o = \frac{1}{8}\rho f_c^* \overline{u}^2 + \frac{1}{2}\rho f_w^* U_o^2 \tag{2.54}$$

where $\overline{u}$ is depth averaged current velocity and U_o is bottom wave orbital velocity. In expression 2.53 f_{wc} is defined by

$$f_{wc} = \frac{f_w + \alpha f_c}{1+\alpha} \quad , \quad \alpha = \frac{\overline{u}}{U_o} \tag{2.55}$$

after Jonsson (1967), where f_w and f_c are the purely oscillatory or unidirectional friction factors respectively. In the second expression (2.54), f_w^* and f_c^* are friction factors incorporating both wave and current influences.

A re-analysis of available data by Tolman (1992), suggested that effects of current on bottom friction are much smaller than suggested by the various wave and current models (e.g. Grant & Madsen, 1979) and that the presently best estimate is to ignore influence of waves on current, or *vice versa*. That is, use equation 2.54 with $f_c^* = f_c$, and $f_w^* = f_w$ from the uncombined flow states.

The more commonly used estimate of bed shear stress is to use equation 2.53, but most recently a suggestion by Soulsby (1991) from Delo and Ockenden (1992) is that the combined τ_o can be given by

$$\tau_o = \frac{1}{8}\rho f_c \overline{u}^2 + \frac{1}{2}\rho f_w U_o^2 + \rho B \left(\frac{f_c f_w}{2}\right)^{-1/2} |\overline{u}| U_o \tag{2.56}$$

where B depends on the relative direction of waves and currents. This expression is hence made up from the pure flow forms and an interactive term.

2.2.10 Conclusions

Theory based on either purely oscillatory or unidirectional flow is reasonably well understood, but for the combined flow regime, which is the more common flow on ITZs, is still not completely understood. Wave boundary layers are expected to be enhanced by the presence of

currents, with resulting increases in bed friction and shear stress. On ITZs the flow may be dominated by one of the two flow types, allowing theories based on uncombined flow to be used. There have been very few studies of the hydrodynamics governing a muddy ITZ, hence the theories may only prove to be a rough approximation.

A number of methods of determining bed shear stress under combined flow are presented, but field comparisons between methods are limited. Calculations of bed shear stress based on friction factors are made primarily by some kind of estimate for the "roughness" of the bed. This is an unsatisfactory position to be in since the values of shear stress are sensitive to the choice of friction factor which is dependent on the estimate of "roughness". Almost all work on shear stresses and bed friction has been carried out over beds of non-cohesive sediments with further work needed on classifying the bed roughness scales, particularly over muddy beds.

Attenuation of waves over deformable beds has been restricted to laboratory work, or just field observations and this area deserves some recognition, even if only as a first estimate of relative importance.

Wave breaking is another unknown area, where much research is needed. It is known that breaking waves can entrain considerable quantities of bed sediment, so further knowledge on the turbulence field is required. Different types of breakers probably will need to be addressed separately.

In general there is a lack of field measurements on wave-current interactions, particularly in the near shore region. Measurements of the hydrodynamics on ITZs in combination with sediment properties are needed to investigate the dominant mechanisms in sediment transport.

2.3 Intertidal Zone Sediment Dynamics

2.3.1 Introduction

Sediment transport can crudely be categorised into two mechanisms: bed load transport and transport by suspension. For cohesionless sediments, bed load transport can be defined as individual grains rolling, or jumping (saltating) over each other, and occurs when near bed stresses are close to the critical threshold for motion. For clay sized particles ($d \approx 2\,\mu m$), this concept of individual moving particles does not hold, due to the tendency for particles to adhere to one another. The degree of cohesion is a function of chemical, mineral and physical properties of the mud, making it harder to generalise transport thresholds. This means that cohesive sediment transport can really be classed solely as suspended transport, although the notion of a highly concentrated 'fluid mud' layer which appears to behave in a non-Newtonian manner (see e.g. Mehta, 1989) might be considered separately.

In macro-tidal estuaries, such as the Severn, any fine suspended sediment that is being transported by the estuary can be deposited both in places that are likely to experience erosion from the flow again soon, or can be left to consolidate for longer time periods of weeks, months or even years. This large temporal variation in the consolidation process of deposited sediments can result in large spatial differences in bed surface character, both in terms of resistance to erosion and basic sediment properties. The numerous factors which control these mechanisms of deposition, consolidation and erosion, make cohesive sediment dynamics a complex study. Often the accuracy gained in prediction needs to be weighed against the input effort.

Predicting movements of fine sediment is of major importance on an economical (e.g. preventing siltation of waterways) and an environmental (e.g. water quality and pollution) basis. Teisson (1991) recently summarised "....reliable predictive results are not yet within our reach and model use is often restricted to sensitivity analysis purposes, already very useful. Reasons of relative failure in gaining quantitative results do not come from the numerical techniques, which are well experienced today, but from the incomplete knowledge of basic processes such as deposition, erosion and consolidation of cohesive sediment."

This section highlights the basic knowledge of sediment cycling to and from an ITZ, subdividing the mechanisms into suspended sediment, deposition, consolidation and erosion. Previous studies considered relevant are included, but the author is aware that the review is by no means comprehensive.

2.3.2 Suspended Sediment and Fall Velocity

Particles are held in suspension, if their rate of falling is exceeded (or balanced) by any upward transport mechanism. For the smallest particles Brownian motion is sufficient to keep sediment

in suspension for long periods, but for larger particles turbulence or agitation by waves may prevent settling. The settling velocity of cohesionless sand and silt particles can be reasonably well predicted using empirical equations such as Stokes' Law, which relates size, shape and density to fall velocity (W_s)

$$W_s = \frac{gD^2(\rho_s - \rho)}{18\rho\nu} \tag{2.57}$$

where D is the particle diameter and ρ_s is the particle density. This assumes no interaction between particles and can be applied when the particle Reynolds Number ($W_s D/\nu$) < 0.5.

If this same equation is assumed valid for individual clay particles, $D \approx 2\,\mu m$, $\rho_s \approx 2650\,kg/m^3$ a fall velocity of $0.0035\,mm/s \approx 0.3\,m/day$ results. Since siltation of harbours and waterways by mud is a commonly occurring problem and deposition can be recorded during the relatively short period of time at slack water, it is obvious that mud must settle at a faster rate than the equation implies. The process by which this occurs is known as flocculation.

When mud particles collide in suspension they may stick together, provided the shear in the suspension is not too great, so forming larger particles known as "flocs". The size and shear strength of flocs, in a particular estuary, is determined by the constituent particle size, suspended sediment concentration (SSC), salinity and by the turbulent shear in the water. Flocs are characterised by higher fall velocities, and lower densities than the individual particles due to their increased size. For example, flocs ($D = 200\,\mu m$, $\rho_s = 1070\,kg/m^3$) would have a settling velocity of $1.5\,mm/s$. The effect of SSC on W_s was established by Owen (1970), and reworked by Barton (1992). Higher SSC leads to more collisions and hence larger flocs, with resulting increased W_s. The presence of salt in the water provides additional free ions which encourages attraction, so increasing the strength of the bonds, by affecting the surface chemistry of the particles. The influence of salinity on flocculation is reported to become less with increased salinity. Flocculation is a major influence for particles of less than $20\,\mu m$ in diameter in waters with salinities of 2-3 ppt according to Mehta (1989). Burt & Stevenson (1983) found that changes in salinity above $2\,ppt$ had little effect on W_s.

Since suspended sediment is likely to have a distribution of flocs and particle sizes (Krone, 1986), a median settling velocity (W_{50}) is often used as a classification, whereby half of the sediment settles at a higher rate than W_{50}.

When SSCs become high, hindered settling occurs. Hindered settling, as the name implies, is when settling is slowed by the high concentrations of particles interfering with each other. Krone (1972) estimated that this process commences for concentrations of between 2–10 g/l. Figure 2.13 shows how W_{50} varies with concentration for the Severn Estuary, clearly showing hindered settling. Hindered settling can thus influence near bed fluid mud generated by wave agitation.

In different estuaries the varying chemistry and mineralogy of the mud means that prediction of settling velocities is difficult. Hence direct measurement of settling velocities must be made *in situ* with results necessarily site specific. This task is not simple, since sampling the suspension is likely to change both the hydrodynamic and sediment characteristics. Current research using highly engineered *in situ* instruments capable of recording fall velocity using image analysis techniques are being developed (Fennesy *et al.*, 1993). Owen (1971) developed a tube for sampling a horizontal section of the suspension, which was then rotated vertically to allow the settling velocity to be calculated. Results indicated that W_{50} was an order of magnitude greater than laboratory tests, probably due to the change in size and distribution of the flocs. Barton (1992) recently reworked many of Owen's experiments concluding that a $1\,m$ tube was of sufficient length to allow a correlation between SSC and W_{50} to be made.

The following empirical formula for W_{50} can be used as an approximation

$$W_{50} = K\,c^N \tag{2.58}$$

where K and N are constants, best calculated by field experiments (Delo & Ockenden, 1992). Figure 2.14 gives values for K and N taken from a number of different estuaries.

2.3.3 Vertical SSC Distribution

Suspended sediment transport formula rely on integrating the product of SSC and velocity, either empirically or analytically, which necessarily requires knowledge of the vertical structure of SSC. Profiles of SSC can be obtained by solving the equation of continuity of mass, under certain assumptions. For steady state conditions, with no net vertical velocity ($\overline{w}$) the downward flux ($W_s\overline{c}$) must balance the upward turbulent (Reynolds) flux ($\overline{w'c'}$)

$$W_s\overline{c} = -\overline{w'c'} \tag{2.59}$$

where $\overline{c}$ is the time mean SSC. Analogously to the treatment of Reynolds stress in section 2.2.6, an assumption needs to be made regarding the Reynolds flux for solution. If the Reynolds flux is assumed equivalent to the product of a sediment eddy diffusion coefficient (ν_s) and the concentration gradient

$$W_s\overline{c} = -\nu_s\frac{d\overline{c}}{dz} \tag{2.60}$$

then this can be integrated to give a solution, but still requires a description of ν_s. For unidirectional flow a linear shear stress distribution (with depth) is usually assumed and the

Rouse equation is derived (Rouse, 1932)

$$\frac{c(z)}{c_a} = \left[\frac{(h-z)a}{(h-a)z}\right]^{\frac{W_s}{\sigma_c \kappa u_*}} \tag{2.61}$$

where c_a is a reference concentration at a height, a, above the bed and σ_c is a proportionality constant (turbulent Schmidt or Prandtl number) between the diffusion coefficients for sediment and fluid (see equation 2.74). Usually the diffusion coefficient is taken to be equal to the eddy viscosity ($\sigma_c = 1$), which may be only strictly valid for unstratified flows (further discussion in section 2.4). Figure 2.15 shows the relative concentration profiles for a range of $W_s/\sigma_c \kappa u_*$. A problem arising from this procedure is the need for a particular reference concentration c_a. Smith (1977) gives a further discussion on the difficulties in agreeing a universal value, which should be at the junction between where the suspended and bed load are defined (Dyer, 1986). Under purely oscillatory flow over flat beds, turbulence is confined to the near bed wave boundary layer. If ν_s is taken as a constant then an exponential distribution for time-mean SSC results

$$c(z) = A\, e^{-\alpha z} \tag{2.62}$$

where A, α are empirical constants (Sleath, 1986). If the bed cannot be considered flat then further modifications are necessary (see e.g. Nielson, 1992).

The SSC profiles derived above have been found to compare reasonably with results from both the field and laboratory for non-cohesive sediments. The lower fall velocities and sediment interaction associated with muds mean that these profiles are not usually adequate for predicting vertical cohesive SSC distributions.

Parker and Kirby (1977) have established a qualitative and schematic description of the cohesive sediment distribution based on extensive field studies in the Severn Estuary (see figures 2.16 and 2.17). It was proposed that variations in turbulence levels due to changing tidal energy could classify the SSC into three forms:

- Mobile suspensions - freely moving SSC, with floc size in balance with shear
- Stationary suspensions - gradually settling SSC
- Settled bed - mud forms part of the bed through consolidation

These processes led to layering in the flow, whereby steep gradients (or lutoclines) were formed, separating regions of homogenous SSC. Figure 2.18 shows a measured SSC distribution from the Severn Estuary with a steep lutocline near the bed and a mild lutocline around mid

depth. During a tidal cycle the maximum tidal currents ($2\,m/s$) create a vertically well mixed suspended distribution ($SSC: 2-5\,g/l$), which cannot be supported as the velocity falls. A step in SSC is created near the surface which gets closer to the bed with falling velocity, so forming a highly concentrated layer near the bed at slack water. Some sediment would settle forming part of the bed which may be resistant to erosion by following tides, particularly if tidal range was decreasing. Lutocline development can be likened to the hindered settling process in a settling column (Mehta, 1989). The presence of these steep gradients means that high resolution (with depth) measurements are required if accurate SSC profiles are to be measured. Ross & Mehta (1989) studied lutocline development with a numerical model which is discussed in section 2.4.4.

2.3.4 Fluid Mud

The process of hindered settling has been seen to form thick ($5\,m$ on Neap tides) fluid mud layers (Kirby & Parker, 1983), but also it is known that the oscillatory forces under waves can cause fluidisation. Maa and Mehta (1987) whilst studying erosion of mud in the laboratory under waves, observed that the SSC was noticeably stratified with a highly concentrated layer near the bed. This production of a fluid mud layer has been well noted in the literature (Suhayda, 1986; Macpherson, 1980), but the very nature of fluid mud still needs further understanding, as do the causal mechanisms. The mud responds in both a viscous and elastic manner (Macpherson, 1980), resulting in a breakdown in the structure allowing the bed to be entrained into the flow more easily (Delo & Ockenden, 1992). The behaviour of fluid mud has been likened to pseudoplastics, or Bingham plastics (Maa & Mehta, 1987).

These uncertainties in the formation and structure of fluid muds lead to a subjective definition of the term 'fluid mud' in the literature. Kirby (1988) reviews the previous studies on dense suspensions citing the work of Einstein & Krone (1962) who regard $10\,g/l$ as the lower concentration limit based on when viscous properties are displayed. Lower values of $3.5\,g/l$ and $5.0\,g/l$ are also cited using the point of hindered settling as the definition. An upper limit of $\approx 250\,g/l$ is used by Wells & Kemp (1986) to distinguish between suspended sediment and bed formation.

2.3.5 Settling and Deposition

Deposition of suspended sediment will occur when the fall velocity (W_s) of the particles is greater than any motions which keep the sediment suspended. As has been seen cohesive sediment settling velocities cannot easily be predicted by the size of particle as with sands due to flocculation. Predicting deposition rates is correspondingly hazardous.

The rate of deposition in still water is a function of W_{50} and near bed concentration (c_a), hence as sediment settles out the rate will decrease accordingly. Higher concentrations can be

expected nearer the bed. For flowing water, numerous laboratory tests by a number of authors (see e.g. Delo & Ockenden, 1992) have suggested that the rate of deposition is controlled by a factor of excess shear $(\tau_d - \tau_o)$, where τ_d is the highest (critical) bed shear stress for which deposition occurs. In summary:

$$\frac{dm}{dt} = -c_a W_{50} \qquad \textit{still water} \tag{2.63}$$

$$\frac{dm}{dt} = -\left(1 - \frac{\tau_o}{\tau_d}\right) c_a W_{50} \qquad \textit{flowing water} \tag{2.64}$$

These are empirical approximations based on uniformly distributed sediment (i.e. sediment which can reasonably be described by D_{50}), and hence some sediment will settle even though the bed shear stress is theoretically too great. The sediment can be separated into different classes if necessary and unique W_i can be found for each class i (Delo & Ockenden, 1992). Flume tests by Odd (1988) suggest $0.06 < \tau_d < 0.1\, Nm^{-2}$. This was supported by Einstein and Krone (1962).

The difficulties of working on muddy ITZs mean that depositional studies are relatively few, with most of those being long term studies over periods of months or years. Results tend to be site specific and hence of limited use. Evans (1965) recorded accretion of up to $6\,cm$ in 10 months on the saltmarshes of the Wash. Amos (1974) observed steady but slow accretion on an ITZ with the rate increasing seawards. Significant amounts of deposition occur after the flood phase, but Pestrong (1972) noted that slack water of only 30 minutes duration was insufficient to allow anything but silt-sized particles to settle.

A two year study by West (1990) at two sites in the Severn estuary, and at six further sites for the first year indicates the spatial variation in an estuary. Variations in bed level change, moisture content and bulk density were recorded roughly every month over a transect of each beach. Activity at the sites varied considerably, with rates of bed level changes from between $\pm 50\,cm$ per 30 days (at the most active) to $\pm 5\,cm$ per 30 days (at the most stable). There is a need for *in situ* research into shorter term ($< 1\,day$) deposition rates on ITZs. This would necessarily involve the monitoring of hydrodynamic conditions as well as sediment exchanges.

2.3.6 Consolidation

As a suspension is deposited onto the bed it will begin to consolidate. A bed consolidates under its own weight expelling the pore water and hence increasing in density. Initially a fluid mud layer (high SSC $> 10 g/l$) is formed which increasingly behaves less like a fluid as water escapes until the weight of the bed forces out most of the water (Nicholls & Briggs, 1985; See figures 2.19 & 2.20). Generally, the bed density profile and the shear strength of the sediment

will increase with distance below the surface. From laboratory experiments initial formation dry density of the bed can be expected to be approximately 30–70 kgm^{-3} (Delo & Ockenden, 1992). Laboratory testing by Parchure & Mehta (1985) of the bed shear strength of kaolonite with depth are shown in figure 2.22 after 1 day and 8 days of consolidation. After 8 days the shear strength of bed sediment was found to be constant below 0.5 cm. Mehta (1986) proposed that it is possible for lower density layers to be trapped under higher density layers if a rapid period of deposition is followed by slow deposition. This highlights one of the difficulties of predicting erosion rates, unless detailed bed profiles are obtained.

The process of consolidation can be influenced by numerous physical, chemical or biological factors which can either speed or slow the process. Agitation of the consolidating bed (by waves or an excess shear) can result in a thick near bed fluid mud layer which never properly consolidates (see section 2.3.4). Turbulence in a settling fluid mud can produce an upward flux of SSC slowing the consolidation, and can also plug the micro channels used for dewatering resulting in a decrease in the compaction rate of order 10. This latter process was discovered by Wolanski *et al.* (1992) using microscopes in laboratory tests. Exposure of the bed to the sun and wind can aid the drying process, whereas rain may help to rewater a consolidating bed (Allen, 1987). Moisture contents of surface sediment were lower for areas continually exposed for longer periods (West, 1990). Dessication cracks are caused by sufficiently rapid loss of moisture, leading to shear tension failure in the mud surface, and they can be remarkably regular if no organisms are present in the mud to reduce evaporation (Allen, 1987). These cracks can have the effect of increasing bed roughness, and causing mass erosion of the loosened 'tiles' of mud.

The process of consolidation is complex and difficult to model successfully since settling rates and concentrations vary so much. Outside influences also have a great effect on rates of compaction.

2.3.7 Erosion

Erodibility for non-cohesive sediments is largely a function of particle size, shape and turbulent shear stress. For cohesive sediments the ability of particles to adhere to each other complicates matters, since particles can no longer be considered discrete. Bulk properties such as moisture content, bulk density, dry density, microbial and organic content become the indices of erosion (Amos *et al.*, 1988).

Erosion of cohesive sediment from a muddy ITZ can be categorised into 3 ways:

- surface erosion
- mass erosion
- re-entrainment into a fluid layer by waves

Predicting the commencement of erosion and the quantity which erodes is complicated by the physico-chemical properties of mud. According to Winterwerp *et al.* (1990) eighteen parameters are needed to classify mud, hence empirical or site specific methods are more usually used (Delo & Ockenden, 1992). Recent studies into the development of *in situ* flumes have helped to begin to understand erosion characteristics, and also have highlighted the complexities of the problem (Black, 1991).

Surface erosion is the removal of individual flocs or particles from the bed. "The flocs on the surface of a cohesive sediment bed are bound together by inter-particle attractive forces. To remove a floc by flowing water requires a shear stress sufficient to overcome the attractive forces." (Delo & Ockenden, 1992).

The rate of surface erosion has been related to the excess shear stress $(\tau_o - \tau_e)$, where τ_e is the critical erosion shear stress, after Kandiah (1974)

$$\frac{dm}{dt} = M_e(\tau_o - \tau_e) \tag{2.65}$$

where M_e is a rate constant.

Numerous laboratory studies on unidirectional flow (see e.g. Delo & Ockenden, 1992) have verified equation 2.65, and have more recently been tested in the field. Devries, (1992) used electro-magnetic current meters to measure unidirectional near bed velocities over a cohesive bed monitored by a near bed SSC sensor to verify the expression. Laboratory studies by Maa and Mehta (1987) showed erosion rates were also proportional to $(\tau_o - \tau_e)$, but suggest an exponential formula for freshly deposited beds (Parchure & Mehta, 1985). This formula requires variations in τ_e with depth of bed.

The existence of a single τ_e has been doubted by Lavelle and Mofjeld (1987), but most authors assume a lowest value for erosion to exist. Predicting τ_e is unreliable unless *in situ* measurements can be made. Laboratory work (Delo & Ockenden, 1992) showed τ_e was related to the dry density of the bed by

$$\tau_e = E_1 \rho^{E_2} \qquad \textit{Empirical} \tag{2.66}$$

where E_1 and E_2 are constants. The problem is complicated because as a surface erodes the underlying sediment is likely to have a higher τ_e and so will be less likely to erode, hence reducing erosion rates. In laboratory studies, waves above mud beds can destabilise the bed by producing fluid layers, but prolonged exposure to steady currents in the laboratory produces the opposite effect by enhancing the threshold of motion. This contradicts some field observations, which argues strongly for more *in situ* measurements (Dyer, 1989).

Mass erosion may occur when the shear applied to the bed is well in excess of its critical erosion strength, and is the removal of large chunks or layers of sediment. Mass erosion is poorly understood and there is little field or laboratory data available. Most work has progressed on the understanding of surface erosion and the critical stress at which erosion occurs.

Assuming a critical erosion stress can be found, the problem is reduced to finding a value for the rate constant (M_e). This is dependent on the mineralogy, ion content, temperature, pH, moisture content and biotic content of the mud. An empirical relationship of erosion rate against excess shear stress ($\tau_o - \tau_o$) has been formed from laboratory studies (Delo & Ockenden, 1992; see figure 2.21). Black (1991) found that a time-mean initial erosion rate was of o($10^{-4}\ kgm^{-2}s^{-1}$) from *in situ* flume tests over a mud surface with a mean critical threshold of motion of $0.1\ Nm^{-2}$. The effect of the presence of sand in the flow on erosive rates of a cohesive sediment bed was studied by Kamphuis (1980) in a laboratory flume and conclusions were that the introduction of sands greatly enhanced the erosion rate. Amos *et al.* (1988) studied the effects of exposure and evaporation on τ_e and concluded that this was the dominant factor in sediment resisting erosion, particularly during summer months. If a period of high evaporation occurred at a time when there was no added accretion then a crust could form which was very resistive to erosion. Unless further deposition occurred the bed could withstand much higher shear stresses than the moisture content, or bulk density suggested. This was because the technique of collecting the surface sample for analysis necessarily mixed the top $10\ mm$, which argues that the crust was less than $10\ mm$ thick. Shear vane readings, however, were correspondingly large. Due to these complexities an *in situ* field measurement is suggested by Delo & Ockenden (1992).

Field studies of erosion on muddy ITZs are very limited except for long term (months and years) records of level changes. Monthly readings by West (1990) in a study on the Severn estuary, suggested that erosion could be expected when bed shear stresses exceeded 1 Nm^{-2}, with large spatial variation in erosion rates (max. 30 cm/30 days). Wind (both in direction and magnitude) was concluded to be the dominant factor. Field studies using *in situ* methods are currently being undertaken to measure erosion parameters under controlled shear. There is a lack of field data measuring short term (< 1 day) erosion rates of cohesive sediment under waves, or combined wave-tidal flows. Dyer (1989) in his review on estuarine sediment processes states that the ideal way to measure the flux to and from the bed is by direct measurement of accumulation or erosion rates. The necessary high resolution instrumentation for measuring small changes in elevation is not yet available.

2.3.8 Biotic Influences

The influence of biogenic stabilisation (or destabilisation) on erodibility of cohesive sediments has only recently become an area of much research. It is now realised that biological influences can alter the threshold of erosion (τ_e) by factors of between 25-770% (Paterson & Daborn, 1991).

The populations of benthos are variable on a spatial and temporal (e.g. seasonal) level and hence the erodibliity is equally effected. The variability of biogenic influences is significant and suggests removal of sediment to the laboratory for study (which inevitably alters the biology). However, this results in conditions bearing little resemblance to the field (Luckenbach, 1986).

Biological processes can have both a stabilising and destabilising effect (Heinzelmann & Wallisch, 1991; Paterson & Daborn, 1991). The processes can be coarsely categorised:

Stabilisation	- by particle cohesion
	polysaccharide matrix
	physical networks
	resistance to flow
Destabilisation	- bioturbation (burrowing organisms)
	bed surface roughening
	faecal pellets

According to Brekhovskikh *et al.* (1991) micro-organisms attached to mud particles will lower the settling velocity so reducing deposition and increasing suspended sediment transport.

Modelling biological influences is tremendously complex since so many factors are apparent - tidal rhythms, seasonal and daily conditions and the presence of other benthos. The problem "argues strongly for the use of *in situ* methods to determine the behaviour of sediments under natural conditions" (Paterson & Daborn, 1991).

2.3.9 Conclusions

Sediment transport in estuaries has been found to be complex, and although the basic processes of deposition, consolidation and erosion have been identified qualitatively, research is needed on all aspects, both in the laboratory and in particular the field. Transport of non-cohesive sediment is understood to a much greater extent than is cohesive sediment transport. Profiles of non-cohesive SSC can reasonably be predicted by semi-empirical equations, but are only qualitatively understood for fine sediments. This is partly due to the lack of understanding of the processes of flocculation, fall velocity and erosion rates but also due to the lack of suitable field measurements. Although laboratory work has proved very useful, certain processes have been observed to behave quite differently in their natural environment.

Most sediment studies on ITZs have been long term (days and months), but if improvements in prediction are to be made, shorter term measurements are needed, both as a calibration for models and to understand mechanisms in their own right.

Fluidisation of mud by waves is a particular area of ignorance. Potentially, significant quantities of sediment can be transported by thick fluid mud layers, which are poorly understood both in the rheological and causal sense.

Sediment entrainment in the surf zone can be observed on any muddy ITZ, but has not been quantified. Knowledge of turbulence under breaking waves is required prior to much advancement in this area.

2.4 Modelling

2.4.1 Introduction

Prediction must remain the ultimate goal for researchers in the field of sediment transport. It has therefore become the subject of much interest, with numerous attempts to model both hydrodynamic processes and sediment dynamics since the two are inherently linked. Over the last two decades ever increasing computing power has enabled very complex models to be constructed, attempting to simulate many aspects of the flow. However, models can only ever be as good as the understanding of the physical equations and assumptions on which they are based, and should always be used with their likely limitations on predictive capability in mind.

As an additional tool in understanding the mechanisms of sediment transport they can also be most helpful. Used in conjunction with laboratory or field experiments they can both be validated, and used for guidance in future experiments. There is a tendency to use these empirical results to 'tune' existing models to improve their 'predictive' capability. This can be useful if the model can still be applied to a wide variety of situations, or is being designed for a specific task. There seems little point in adjusting model constants to fit measured data, however, as this defeats the object of prediction and provides only a curve fitting technique.

This review of modelling mainly concentrates on 'turbulence models' which are based around solving the mean-flow equations, by incorporating hypotheses about the turbulent processes to simplify the problem. Hence they do not simulate the details of turbulent motions, but only the effect of turbulence on the mean flow behaviour (Rodi, 1984). Before turbulence modelling is addressed, an assessment of the overall modelling problem is made by considering general aspects of three-dimensional (3-D) cohesive sediment modelling. This allows the reader to see how turbulence modelling fits into the modelling hierarchy. Then the turbulence modelling problem is outlined, before looking towards the different methods of solution in increasing order of complexity. Particular emphasis has been given towards 'two equation' 1-D (vertical) models since this study makes use of this type of model.

Since hydrodynamics are a prerequisite in quantifying sediment movements (Ariathurai & Krone, 1976) many of the models reviewed have solely been tested in clear water. Examples of different models are given throughout as applied to either purely oscillatory, purely unidirectional or combined flows. Emphasis is on the combined case, but the list is by no means comprehensive. Of those models applied to sediment transport, few models have been applied to cohesive sediment movements. Most SSC results from models applied to sand transport, are not necessarily applicable to this study, and therefore only included, where it is felt additional guidance can be gained. Following turbulence modelling, a more specific review of vertical suspended sediment modelling relevant to this study is considered. Finally conclusions are drawn on the current state of research.

2.4.2 Modelling (Cohesive) SSC Transport in Estuaries

As previously described in section 2.1, the hydrodynamics on ITZs are complex with both wave and tidal current flows likely. This combined with the complex cohesive sediment interactions (section 2.2) means that modelling transport processes, which are evidently three dimensional, is a challenging problem. Sediment transport models are usually designed for a specific purpose - for example, to predict worst storm scenarios and their effect on the coastline, or for improvements in long term predictions. For all engineering applications, a model of the whole sediment transport process can be expected to consist of four elements (see figure 2.23), with models classified according to their dimensions and orientation. Choice of the type of model in each element will depend on the physical situation to be modelled and the required accuracy.

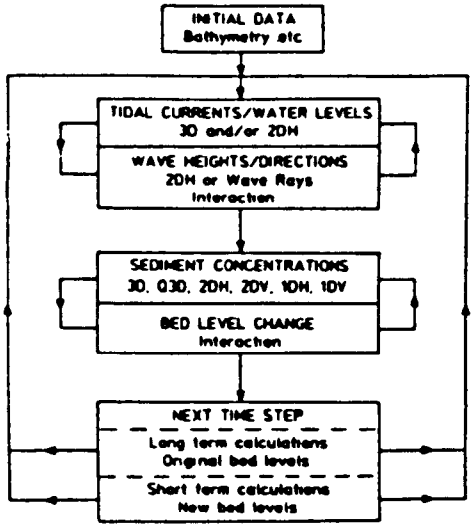

Figure 2.23: Definition sketch - Coastal sediment modelling (O'Connor, 1992)

Ideally an estuarine cohesive sediment transport model should include

- 3-D mean and turbulent currents field
- 2-D surface wave field
- bed surface dynamics - erosion/deposition/consolidation
- flocculation and settling (Sheng, 1984; O'Connor & Nicholson, 1988)

Compromises in physical exactness are necessarily made to enable models to be manageable (O'Connor, 1992). In particular, the number of dimensions is often reduced for a reduction

in computation, and when it is only certain overall characteristics of transport which are important. Another method of minimising time costs is to incorporate some kind of averaging, either in depth or width to reduce the problem.

- 0-D models - A simple mass balance is performed between (time varying) sediment inflow, deposition/erosion and outflow. Only applicable in cases where spatial variability can be ignored.
- 1-DH models - depth and width averaged, giving longitudinal transport. Most applicable to narrow, well defined channels.
- 2-DH, DV models - solve the momentum and concentration equations averaged over depth (H), or width (V). Many examples exist in the literature.
- 3-D models - still in development stage, with increasing capabilities due to improving computer power. Fully describe the flow and density structure (Mehta, 1989).

These models have been divided into two types by O'Connor (1992) - box or continuum models. Box models assume sediment is entrained into the flow quickly, so that maximum transport is reached, necessitating that time steps are chosen carefully, and the flow region is divided into 'boxes' with common boundary conditions. These models are more applicable to coarse sand transport, and for fine sediments a continuum model should be used (O'Connor, 1992). Continuum models usually solve Eulerian diffusion-type equations (e.g. 2.70), although Lagrangian methods have been investigated using random walk techniques. This review confines itself to Eulerian methods in continuum models.

Examples of the application of 2-D models applied to estuaries are Hayter & Mehta (1986) and Teisson & Fritsch (1988), and of 3-D models Nicholson & O'Connor (1986) and O'Connor & Nicholson (1988). 1-D horizontal models are often used to describe the generation of turbidity maxima in estuaries (see e.g. Calverley, 1991).

3-D models are computationally very expensive unless used on a depth or width averaged basis. The complex versions also require extensive calibration to produce accurate results, which is beyond the budget of many engineering projects. Hence, lower cost, averaged models will remain in use for the forseeable future (O'Connor, 1992)

Lower dimensional (and hence computationally less costly) turbulence models providing vertical distributions of velocity and SSC, can also be used to provide boundary conditions for these higher dimension advection-type models (Teisson *et al.*, 1992), and can be used to improve the understanding of physical processes involved. For example, 1-D (vertical) models can be used to study resuspension and deposition (vertically) of suspended sediment. Figure 2.23 shows how these models fit into the overall sediment transport modelling hierarchy.

2.4.3 Turbulence Modelling

The Problem

The exact equations describing almost all practically relevant flows are well known (Navier-Stokes equations), as are numerical methods for solving them. The problem lies in the practical solution of the equations. To solve the exact equations with sufficient accuracy requires a mesh large enough to cover the flow domain, but small enough to resolve the smallest turbulent eddy. The flow domain may be many metres, or even kilometres, but the small scale turbulent motions are typically of the order 10^{-3} smaller (Rodi, 1984). An estimate of the number of grid points required to account for turbulence of the smallest Kolmogorov microscales (see e.g. Tennekes & Lumley, 1972) in a typical three dimensional flow problem is $RE^{11/4}$ where RE is the Reynolds number (Younis, 1992).

Since this is infeasible, either in terms of computer storage, or running costs, some kind of simulation is required. Reynolds (1874) adopted a statistical approach by decomposing the instantaneous values into a mean and fluctuating part. Standard tensor notation, as used by Rodi (1984) has been used throughout this section (where i, j, k represent three orthogonal directions, so that $u_i = u$, $u_j = v$ and $u_k = w$ in the previous notation)

$$U_i = \overline{U}_i + u_i \qquad P = \overline{P} + p \qquad C = \overline{C} + c \tag{2.67}$$

where $\overline{U}_i$ is time averaged velocity, u_i the velocity fluctuation, P the pressure and C is a scalar (in this case concentration).

Since only average values are required by most engineers this idea has become largely adopted as the method of solving the equations of flow. When introduced into the Navier Stokes equations and time-averaged this results in the following set of equations

$$\frac{\partial \overline{U}_i}{\partial x_i} = 0 \qquad \textit{Continuity Equation} \tag{2.68}$$

$$\frac{\partial \overline{U}_i}{\partial t} + \overline{U}_j \frac{\partial \overline{U}_i}{\partial x_j} = -\frac{1}{\rho_w}\frac{\partial \overline{P}}{\partial x_i} + \frac{\partial}{\partial x_j}\left[\nu \frac{\partial \overline{U}_i}{\partial x_j} - \overline{u_i u_j}\right] + g_i \frac{\rho - \rho_w}{\rho_w} \qquad \textit{Momentum Equation} \tag{2.69}$$

$$\frac{\partial \overline{C}}{\partial t} + \overline{U}_i \frac{\partial \overline{C}}{\partial x_i} = \frac{\partial}{\partial x_i}\left[\lambda \frac{\partial C}{\partial x_i} - \overline{u_i c}\right] + \textit{sources} \qquad \textit{Concentration Equation} \tag{2.70}$$

This method has still kept the equations exact in $\overline{U}_i$, $\overline{P}$ and $\overline{C}$, but they are no longer a closed set due to the generation of the unknown correlations in the momentum and concentration equations. Physically these correlations are the turbulent transport of momentum ($\rho\overline{u_i u_j}$), and of mass ($\overline{u_i c}$). They are then referred to as Reynolds stresses (see also section 2.36) and mass fluxes, respectively, and in most flow regions are much larger than their laminar counterparts $\nu\frac{\partial \overline{U}_i}{\partial x_j}$, $\lambda\frac{\partial C}{\partial x_i}$ (Rodi, 1984). The final term in equation 2.69 represents buoyancy, caused by density variations in the flow. The other terms have assumed the density can be taken as the reference density ρ_w.

The problem has thus been reduced to finding a way of closing these governing equations by some determination of the unknown correlations, and hence is termed the 'closure' problem. The set of equations, or formulae used to complete this closure is therefore known as a turbulence model.

A different approach from using the mean flow equations is to solve the exact equations directly, but for large-scale motion only, and to use a model only for smaller scale turbulence. This approach is known as sub-grid modelling and is often referred to as 'large eddy simulation' (see e.g. Moin & Kim, 1982). This technique is computationally expensive, and is still in its development stage (see e.g. Thomas *et al.*, 1992). The following review is restricted to Reynolds (1874) mean flow turbulence modelling technique.

Closure Concepts and Classification

Exact transport equations for the unknown correlations can be derived, but these contain higher order turbulence correlations which are again unknown, and so the the problem still is not closed. This situation gives rise to the classification of turbulence models in terms of their order of solution. Hence if solution is taken by solving the above derived Reynolds stresses and mass fluxes in terms of the mean flow quantities, then this would be termed a first order turbulence model. If, however, exact transport equations are used to solve these first order correlations, giving rise to second order unknown correlations, which are then solved in terms of the lower order terms, then this would be considered a second order turbulence model, and so on.

The most widely used turbulence models are of first order, and closure is based on the Boussinesq (1877) analogy with laminar flow: In laminar flow stress is proportional to the rate of strain with viscosity the proportionality coefficient. Boussinesq proposed that in turbulent flow the Reynolds stresses could be modelled as being proportional to the rate of strain also, with the proportionality coefficient the (turbulent) eddy viscosity (ν_t)

$$-\overline{u_i u_j} = \nu_t\left(\frac{\partial \overline{U}_i}{\partial x_j} + \frac{\partial \overline{U}_j}{\partial x_i}\right) \qquad for\ i \neq j \tag{2.71}$$

ν_t is not a function of the fluid (as in the laminar case), but is a function of the turbulence level. The closure problem has now been shifted to the problem of determining the distribution of ν_t.

A dimensional analysis of ν_t suggests

$$\nu_t = constant \times velocity\ scale \times length\ scale \tag{2.72}$$

So the problem has now been further reduced to choosing an appropriate velocity and length scale. This can be done in a number of ways, and gives rise to a hierarchy of first order turbulence models, by classifying them in terms of the number of transport equations used to evaluate ν_t. The most complete models then use two equations, one to determine the velocity scale, and one for the length scale and are hence known as two equation turbulence models.

In parallel with Reynolds stresses, the mass fluxes need to be closed. The same principle is used, such that the fluxes are related to the concentration gradient

$$-\overline{u_i c} = \nu_s \frac{\partial \overline{C}}{\partial x_i} \tag{2.73}$$

where ν_s is the turbulent diffusivity, analogous to the eddy viscosity, and is also a property of the flow. This analogy between the two, leads to the ratio known as the turbulent Schmidt or Prandtl number (σ_c) being considered

$$\sigma_c = \frac{\nu_t}{\nu_s} \tag{2.74}$$

The present knowledge of (σ_c) is still uncertain. Many models take it to be constant, but recently higher order models which can output the ratio, since they do not use the Boussinesq analogy, have suggested that this is not the case (Teisson *et al.*, 1991). Often the value 1.0 is used, which implies that sediment mixes in the same way as momentum. This ignores stratification of the flow and is only really applicable for low concentrations of suspended sediment (Celik & Rodi, 1984). A further discussion of σ_c and stratification is given in chapter 3.

Before discussing first order turbulence models and examples, it is perhaps pertinent to consider some of the assumptions and hence limitations behind this eddy viscosity/diffusivity approach, apart from the uncertainty of σ_c. The following discussion is considered by Rodi (1984), amongst others. The concept is based on the principle that turbulent eddies are like "lumps of fluid" which, like molecules, collide and exchange momentum. However, turbulent eddies are not rigid bodies which retain their identity, and their path length is not (necessarily)

small when compared to the flow domain as in the molecular analogy. As has been seen, it is also necessary to associate a characteristic length scale for the turbulent motion, which may be adequate for the overall flow characteristics, but does not account for the transport of the smaller scale turbulent Reynolds stresses. Also, in equation 2.71, ν_t has been introduced as a scalar which means that isotropic stresses have been assumed, unless ν_t is prescribed different values for different components. This can be a particular problem near boundaries, where anisotropic dissipation will occur (Chien, 1982). Despite all these limitations predictive turbulence models incorporating the Boussinesq approach have been seen to work in practice. This is because ν_t is a reasonable approximation for many flow situations (see Rodi, (1984) for general applications in hydraulics). In turbulent boundary layer flows (as would generally be found on ITZs) the more complete first order solutions have been shown to work reasonably.

Zero-Equation Models

Zero-equation models do not use any additional transport equations to solve equation 2.71, and ν_t is either prescribed as some algebraic function in terms of flow parameters such as RE, or a mixing length approach is used. This latter method has been described in chapter 2 when deriving the logarithmic velocity distribution. The success of this type of model lies in being able to prescribe the eddy viscosity, or mixing length, relatively simply algebraically (Rodi, 1980) and still represent the flow. Mixing length models favour large-scale motions, where the diffusion or convection of turbulence can be neglected (Tennekes & Lumley, 1972) since these are assumed to be in balance.

Numerous zero equation models have been developed mainly utilising an eddy viscosity which varies with depth, but is held constant in time. The advantage of these models are that solutions are generally analytical, although requiring considerable mathematical skill (Simons *et al.*, 1988). Examples for the combined wave and current case are Lundgren, 1973; Smith, 1977; Grant & Madsen, 1979; Tanaka & Shuto, 1981; Myrhaug 1984; Christoffersen & Jonsson, 1985; Myrhaug & Slaattelid, 1989. The water column is generally separated into either two or three layers, and an eddy viscosity profile is assumed for each layer. The extent of the layers are usually defined in terms of the wave (only) boundary layer thickness, and as a function of friction velocity (u_*), which was a conclusion of the laboratory work by Kemp & Simons (1982) on wave and current interactions. Most of the models tend to be applicable mainly to one end of the combined spectrum (i.e. either a dominant current, or dominant wave). A mixing length approach used by Bakker and Van Doorn (1979) was only applicable to a limited example set and needed numerical solution (Davies *et al.*, 1988). More recently O'Connor *et al.* (1991) have used a 1-D vertical mixing length model in studying sand transport in waves and current. A review of the earlier models is given by Grant & Madsen (1986), and comparison of predicted τ_o for many of the models is made by Simons *et al.* (1988).

Principle conclusions from these models are qualitatively the same. The presence of waves on a current boundary layer enhances the apparent bed roughness, resulting in an increased bed shear stress. These effects have been noted in laboratory studies (see section 2.1; Simons *et al.*

1988). Velocity profiles were expected to be considerably altered, but since eddy viscosities are being defined algebraically this cannot be attained quantitatively for this class of turbulence models.

When modelling sediment transport the eddy diffusivity is taken from equation 2.74 (and hence effectively prescribed in the case of eddy viscosity method) with the problem of choosing σ_c remaining. Buoyancy effects can be included by making ν_t and ν_s a function of the stratification after Munk & Anderson (1948)

$$\nu_t = (\nu_t)_o(1 + \beta\, Ri)^{\alpha} \quad , \quad \nu_s = (\nu_s)_o\,(1 + \beta_c\, Ri)^{\alpha_c} \tag{2.75}$$

where

$$Ri = -\frac{g}{\rho}\,\frac{\partial\overline{\rho}/\partial z}{\left(\partial\overline{U}/\partial z\right)^2} \tag{2.76}$$

Ri is the gradient Richardson number which is a ratio of gravity to inertia effects, and $(\nu_t)_o$ and $(\nu_s)_o$ are the clear water ν_t and ν_t, respectively. The suggested values for the empirical constants α, β, α_c, β_c are -0.5, 10, -1.5, 3.33, respectively (Munk & Anderson, 1948). Variations in these constants have been made over the years (see e.g. Oduyemi, 1987). Rodi (1984) states that σ_c increases in value with increasing Ri and suggests an empirical modification based on the Munk & Anderson approach

$$\sigma_c = (\sigma_c)_o\,\frac{(1 + \beta_c\, Ri)^{\alpha_c}}{(1 + \beta\, Ri)^{\alpha}} \tag{2.77}$$

For mixing length methods, again the Munk & Anderson technique is used with different coefficients for the empirical constants (see e.g. Oduyemi, 1987).

Wolanski *et al.* (1988) and Ross & Mehta (1989) both model cohesive sediment profiles, and investigate density stratification using Richardson number dependent ν_s. These are discussed in detail later. Most non-cohesive sediment studies using zero-equation models found stratification contributed to a decrease in velocity and concentration profiles (e.g. Villaret & Trowbridge, 1991).

The drawback of all these zero-equation models is primarily that both eddy viscosity and mixing length are properties of the flow, and so to work accurately they really need to be prescribed at every position in the flow. All the eddy viscosity models rely on some previous knowledge of the boundary layers, which particularly for the combined wave-current case are still poorly understood. Mixing length methods imply ν_t is zero when the vertical velocity gradient is zero, and as previously stated they also all ignore diffusive and convective turbulent transport. Prediction of profiles can be good, but only when the eddy viscosities/diffusivities have been adjusted empirically. Calculated bed shear stresses can be used to give thresholds

of motion when applied to sediment transport. As a tool for increasing the understanding of interactions, zero-equation models are of limited use.

One-Equation Models

One equation models use a single transport equation for the velocity scale in equation 2.72. This then accounts for some 'history' in turbulence development, since ν_t is no longer necessarily zero when $\frac{\partial \overline{U}}{\partial z}$ is zero (Younis, 1992). The physically most meaningful scale (Rodi, 1984) is to use $\sqrt{k}$, where

$$k = \frac{1}{2}\overline{u_i u_i} \equiv \frac{1}{2}\left(u^2 + v^2 + w^2\right) \tag{2.78}$$

is the kinetic energy of the turbulent motion per unit mass. The equation governing k is derived from the Navier-Stokes equations, by subtracting the time-averaged momentum equation (2.69) from the time dependent Navier-Stokes equations and multiplying the resulting equation for component i with the fluctuating velocity u_j, and *vice versa*. For a more complete derivation (see e.g. Hinze, 1959), or more recently Fredsoe & Diegaard (1992) include a detailed and easy to follow derivation.

$$\underbrace{\frac{\partial k}{\partial t}}_{rate} + \underbrace{\overline{U}_i \frac{\partial k}{\partial x_i}}_{advection} = \underbrace{-\frac{\partial}{\partial x_i}\left[\overline{u_i\left(\frac{u_i u_j}{2} + \frac{p}{\rho} - 2\nu\, s_{ij}\right)}\right]}_{diffusion} - \underbrace{\overline{u_i u_j}\,\overline{S_{ij}}}_{production} - \underbrace{\beta g_i \overline{u_i c}}_{buoyancy} - \underbrace{2\nu\,\overline{s_{ij} s_{ij}}}_{dissipation} \tag{2.79}$$

where

$$s_{ij} = \frac{1}{2}\left(\frac{\partial u_i}{\partial x_j} + \frac{\partial u_j}{\partial x_i}\right) \qquad \textit{fluctuating rate of strain} \tag{2.80}$$

and $\overline{S_{ij}}$ is the time averaged mean rate of strain.

The rate of change is thus balanced by convective, diffusive, productive and dissipative turbulent transport. For high Reynolds numbers, viscous diffusion is neglected and buoyancy terms may also be ignored if density stratification is considered to have little effect. The viscous dissipation term is always a sink term, and is usually assumed isotropic (see Hinze, 1959) so

$$\varepsilon = \nu\,\overline{\frac{\partial u_i}{\partial x_j}\frac{\partial u_i}{\partial x_j}} \simeq 2\nu\,\overline{s_{ij} s_{ij}} \tag{2.81}$$

which is only strictly valid for high Reynolds numbers. Near walls, where viscous dissipation is important, some sort of empirical approximation can be added (see e.g. Chien, 1982).

To make use of this exact equation (2.79) requires solution of the unknown correlations in the diffusive transport term. An analogy to equation 2.73 is made, so that the diffusion flux is proportional to the gradient of k

$$-\overline{u_i\left(\frac{u_i u_j}{2}+\frac{p}{\rho}\right)}=\frac{\nu_t}{\sigma_k}\frac{\partial k}{\partial x_i} \tag{2.82}$$

where σ_k is an empirical diffusion constant (Rodi, 1984) and ε is dimensionally given by

$$\varepsilon = C_D\frac{k^{3/2}}{L} \tag{2.83}$$

where C_D is a constant and L is the length scale, still to be determined. Substituting assumptions (2.71, 2.73, 2.81, 2.82) into equation 2.79 yields the more recognisable k-equation valid for high Reynolds numbers

$$\frac{\partial k}{\partial t}+\overline{U}_i\frac{\partial k}{\partial x_i}=\underbrace{\frac{\partial}{\partial x_i}\left(\frac{\nu_t}{\sigma_k}\frac{\partial k}{\partial x_i}\right)}_{diffusion}+\underbrace{\nu_t\left(\frac{\partial \overline{U}_i}{\partial x_j}+\frac{\partial \overline{U}_j}{\partial x_i}\right)\frac{\partial \overline{U}_i}{\partial x_j}}_{production}+\underbrace{\beta g_i\frac{\nu_t}{\sigma_c}\frac{\partial \overline{C}}{\partial x_i}}_{buoyancy}-\underbrace{\varepsilon}_{dissipation} \tag{2.84}$$

$$\nu_t = C_\mu\sqrt{k}L \qquad Kolmogorov-Prandtl\ expression \tag{2.85}$$

For low Reynolds numbers (e.g. near walls) viscous diffusion can be included and the empirical constants (C_μ, C_D, σ_k) are replaced by functions of turbulent Reynolds number $R_t = \sqrt{k}L/\nu$ (see e.g. Aydin & Shuto, 1988; Chien, 1982; in section 3.2)

As with all one equation turbulence models, there is still left the determination of the length scale (L) in order to close ν_t in equation 2.85. It is this limitation which allows many different models of this class to be formulated, each using a different algebraic expression for L (see Rodi, 1984 for examples). The concentration equation is solved as for zero-equation models, with buoyancy effects included in the same way.

Davies has used one-equation models extensively to model boundary layers under both purely oscillatory flow (1986), and combined wave-current flows (1990b, 1991; Davies *et al.*,1988). He in turn refers to Johns (1977) (waves only), Johns (1978) and Vager & Kagan (1969) (tidal current only). Transient effects of waves added to, or removed from, currents were studied

by Davies (1991). Two methods of modelling currents were used, either holding the depth averaged current constant, or using a constant pressure gradient. Detailed evolution of the mean velocities, turbulent energy, eddy viscosity and shear stress are presented. The question of convergence is discussed. Results have implications on the time to convergence in coastal waters, implying that quasi-steady wave-current conditions may exist in many situations. This conclusion is based on using the constant velocity approach, and time to convergence was found to be much longer (up to 50 hours) if the current was modelled by a constant pressure gradient. The model is applied to sand suspensions (Davies, 1990a), with $\nu_t = \nu_s$, and the sensitivity of the model to time varying reference concentration is assessed. The 'wave related' contribution to the flux $<uc>$ was deemed to dominate transport in the wave boundary layer.

The difficulty in prescribing a suitable length scale in complex flows remains, leading to the next class of model.

Two-Equation Models

The most complete turbulence models employing the Boussinesq approach necessarily use two transport equations: one for the velocity scale and the second for the length scale. The velocity scale is given by the k-equation (2.79), with the same assumptions as for one-equation models if required. Choosing an appropriate length scale is more subjective. It is known that the size of turbulent eddies is controlled by many processes including turbulent convection, dissipation and vortex shedding (Rodi, 1984). Because k is known, any form of $k^m L^n$ can be utilised as the variable in this second transport equation (instead of L). The majority of models use a variable of this form, and the majority use the dissipation (ε) as defined in equation 2.81. For this reason they are known as '$k-\varepsilon$' models. This review will only consider two equation models of this form as they are by far the most popular. For other two equation models using a different length scale see e.g. Rodi (1984).

The exact ε-equation can be derived from the Navier-Stokes in a similar way to the k-equation (see e.g. Tennekes & Lumley, 1972). To simplify matters only the high Reynolds number equation is presented, with low Reynolds modifications discussed afterwards. This can again be derived from the exact equation by the same assumptions as for the k-equation (i.e. equations 2.83, 2.85)

$$\frac{\partial \varepsilon}{\partial t} + \overline{U}_i \frac{\partial \varepsilon}{\partial x_i} = \underbrace{\frac{\partial}{\partial x_i}\left(\frac{\nu_t}{\sigma_\varepsilon}\frac{\partial \varepsilon}{\partial x_i}\right)}_{diffusion} + \underbrace{C_{\varepsilon 1}\frac{\varepsilon}{k}\nu_t\left(\frac{\partial \overline{U}_i}{\partial x_j} + \frac{\partial \overline{U}_j}{\partial x_i}\right)\frac{\partial \overline{U}_i}{\partial x_j}}_{production} + \underbrace{C_{\varepsilon 1}\frac{\varepsilon}{k}\beta g_i \frac{\nu_t}{\sigma_c}\frac{\partial \overline{C}}{\partial x_i}}_{buoyancy} - \underbrace{C_{\varepsilon 2}\frac{\varepsilon^2}{k}}_{dissipation} \tag{2.86}$$

$C_{\varepsilon 1}$, $C_{\varepsilon 2}$, σ_ε are empirical constants calculated from laboratory experiments where one or more term could be omitted (Launder & Spalding, 1972; Rodi, 1984 for specific values). A sensitivity

analysis has suggested that equation 2.86 is sensitive to small changes in $C_{\epsilon 1}$, $C_{\epsilon 2}$ (Rodi, 1984).

Modifications to the high Reynolds number equations can be made to account for low Reynolds numbers (Patel, 1981; Chien, 1982; Aydin & Shuto, 1988) analogously to the k-equation by retaining molecular viscosity, including empirical functions for the constants, and taking into account near boundary anisotropic dissipation effects. Again, as with zero- and one-equation models, the Prandtl/Schmidt number (equation 2.74) is used to close the concentration equation. Buoyancy is already accounted for in the k and ϵ equations. Rodi (1984) discusses the use of another Richardson number dependent constant in the ϵ-equation to effect the buoyancy. Most models for marine boundary layers ignore this constant.

The '$k - \epsilon$' model has been widely used for many hydraulic applications (see Rodi, 1984) with varying success. Failures in the model have generally been blamed on the ϵ-equation and numerous modifications to the empirical constants have been made to improve predictive ability. Applications of the model to purely oscillatory boundary layers include Hagatun and Eidsvik (1986), Justesen (1988), Aydin & Shuto (1988), the latter including low Reynolds number effects. Reasonably good agreement was generally found. Hagatun & Eidsvik (1986) also included sediment modelling, and were able to predict mean velocity and concentration profiles well, and also a reduction in bed friction due to the presence of sediment, which are all generally accepted features from experimental evidence. They also used the model to qualitatively compare results under combined wave and current flows, observing the experimentally predicted increase in bed roughness (as previously mentioned) when waves were added to the current. Aydin & Shuto (1988) used a roughness viscosity to model additional turbulence production due to bed surface roughness (see Chapter 3). The model was compared with the semi-empirical wave friction factors (equations 2.23-25). Good agreement was found particularly for the smooth turbulent flows, with slight modifications introduced for the rough turbulent versions.

Baum & Coponi (1992) used a $k - \epsilon$ model to study the buoyancy effects in the upper ocean. They found that a Richardson number dependent σ_c produced the best results (as in equation 2.77).

In unidirectional flow many applications of the '$k - \epsilon$' model have been made (see Rodi, 1984; Brors & Eidsvik, 1992 for references). Restricting the review to those which have also looked at sediment, Celik & Rodi (1988, 1984) studied concentration profiles in open channel flow, and considered the effect of σ_c on profiles, since it alters the eddy diffusivity. They established that under non-equilibrium conditions, suspended sediment transport was determined by (a) the distribution of eddy diffusivity (equation 2.73), (b) near bed reference concentration (see equation 2.61) and (c) erosion flux. This final condition could be incorporated into (b) since it effectively determines the reference concentration. Eidsvik & Brors (1989) $k - \epsilon$ model was seen to predict most features of turbidity flow reasonably, but when compared to a more recent Reynolds stress model (Brors & Eidsvik, 1992a) could not predict the transfer of turbulent flux through the velocity maximum.

This final point highlights one of the major limitations of two-equation models, or more correctly, in first order closure models. Despite the apparent success in a number of flow situations two-equation models still neglect the transport of turbulent stresses. This type of model can only use one physical scale for velocity and length, so in flow situations where this is likely to be inadequate then so must the model. $k - \varepsilon$ models are likely to remain in use for some time (Younis, 1992) and do offer a good representation of many flows. In wave only boundary layers the model seems to perform reasonably, but is less established for tidal currents, and hence for wave-current interactions. Much of the established experimental knowledge can be well represented, however, and the model does provide additional understanding on that basis, and is not too computationally costly. By using two closure equations it would seem to offer a better description of turbulence, based on the Boussinesq analogy than the lower order models.

Higher Order Models - Reynolds Stress Models

As described in the closure subsection, higher order models can be obtained by direct solution of the transport equations for the unknown correlations (equations 2.71 and 2.73) in the momentum and concentration equations, producing next generation correlations which are then approximated in terms of the lower order variables. Although higher than second order models have been developed (with up to 28 transport equations, see Rodi, 1984) the author is unaware of any testing or application to marine boundary layers, and so the review will be limited to second order models. These second order stress/flux models are usually referred to as Reynolds stress models (RSM), since they solve the Reynolds stress in the mean equations. Algebraic stress models should also be mentioned, but these are simplified versions of RSMs with algebraic expressions for some of the additional transport equations.

RSMs do not have the restriction of a single velocity/length scale, and in actually modelling the transport of stresses and fluxes, are potentially more realistic. They are able to output some of the assumptions made in first order turbulence models, such as σ_c and so might be used to improve predictive capability of the computationally less expensive models. The equations are not presented here but can be found in e.g. Launder, Reece & Rodi, (1975).

RSMs have been developed for some years, but it is only recently that they are beginning to become fully tested. Brors & Eidsvik (1992a, 1992b) have used an RSM for modelling turbidity currents, and oscillatory flows respectively. In the unidirectional case they found the model gave superior results to their two-equation model, but in the oscillatory boundary layer results were similar, although they expected erroneous results from the two-equation model outside the wave boundary layer. Teisson *et al.* (1992) have used an RSM to model cohesive transport in unidirectional flow. They present vertical concentration profiles, and study density stratification effects (discussed in detail in section 2.3.4). Although the model has been validated hydrodynamically, the lack of SSC data means that results from concentration profiles are only qualitative.

Sheng & Villaret (1989) use an algebraic model to examine the effect of stratification on

bed exchange processes (discussed in detail in section 2.3.4). The model was also tested for wave boundary layers using Jonsson & Carlson (1976), predicting velocity and Reynolds stress profiles reasonably, but not as well as the RSM of Sheng (1984). Sheng (1984) suggested the inclusion of a non-Newtonian boundary layer model for the fluid mud system.

The 1-D RSM applied by Teisson *et al.* (1991, 1992) applied to sediment profiles in open channels solves 8 equations on top of the mean flow equations (2.69 and 2.70). Hence in 1-D, the method solves in total 10 partial differential equations as opposed to 4 with a two equation model. This added computational burden remains the major limitation in RSMs, but is likely to be overcome by computer development in future years, making RSMs more feasible for engineering application.

2.4.4 Summary of 1-DV Cohesive Sediment Modelling

Figure 2.16 shows a schematic description of how cohesive sediment is recycled vertically. On an ITZ these sediment dynamics are governed by the hydrodynamic stresses applied by both wave and currents, and sediment interactions both in suspension and at the bed (see section 2.2). 1-DV models can be used to give a direct estimate of sediment transport horizontally by integrating the resulting sediment and velocity (u) fields over the depth. This is not the aim of this study, and so this review does not encompass actual transport prediction based on these models.

Suspension

Only a few models look in detail at cohesive sediment suspensions and their effect on the flow. These are discussed in detail.

Ross & Mehta (1989) and Wolanski *et al.* (1988) used the concentration equation 2.70, and a prescribed eddy diffusivity profile to simulate lutocline and fluid mud formation. Using a Richardson number dependent eddy diffusivity based on the Munk & Anderson (1948) approach they both concluded that these buoyancy effects were the cause of both the lutoclines, and fluid mud. Wolanski *et al.* included a bed flux of sediment by erosion and deposition (equations 2.65, 2.64) and found they needed a saturation concentration ($10\,g/l$) to avoid unrealistic high near bed concentrations, compared with their laboratory experiments. This numerical step was considered to simulate either a limited supply of (erodible) sediment, or a total damping of turbulence preventing erosion. Under waves Ross & Mehta also predicted high concentration near bed layers, but needed to prescribe a different eddy diffusivity based on wave orbital velocity amplitude. Whilst comparing results from field data Ross & Mehta recommend the need for time varying erosional and depositional thresholds, since it is not evident whether sediment is being re-entrained from recently deposited fluid mud layers, or fresh erosion of the bed is occurring. They recognise the difficulties this imposes and the need for precise bed

profiles, and hence only considered quasi-equilibrium representation.

The Sheng & Villaret (1989) algebraic stress model was able to predict a reduction in near bed shear stress due to density stratification, hence reducing erosion rates. Results were compared favourably with laboratory experiments using a 'natural' bed and a 'placed' kaolonite when bed damping was less significant. Stratification, and hence erosion, was found to be strongly influenced by the choice of the fixed settling velocity. For the wave boundary layer tests only hydrodynamic profiles were examined as the SSC distribution was homogenous.

Teisson's *et al.* (1991, 1992) RSM also predicts strong damping effects due to density stratification, causing deformation in mean velocity, concentration and shear stress profiles. They used a fixed settling velocity of $1\,mm/s$, which corresponds to large flocs, and hence suggest that for smaller settling velocities damping might be less extreme. The lack of data meant that results were qualitative. A two phase (momentum and mass separately) model was also used for high concentrations ($> 4\,g/l$), and is to be developed further.

From these results it seems that models which assume decoupling of the concentration and momentum equation are likely to be erroneous. Even at low concentrations $< 1\,g/l$ density stratification influences flow. There has been little work on wave and cohesive SSC interactions, except for the zero-equation approach of Ross & Mehta (1989).

Bed Models and Fluid Mud

Erosion and deposition of sediment is often ignored in modelling suspended sediment profiles (e.g. Teisson *et al.*, 1991; 1992). Presumably this is to enable comparisons to be made with existing models, so a bulk concentration is added and redistributed by the flow. If the Rouse concentration profile is considered (equation 2.61), it is seen that the near bed reference concentration affects the distribution of sediment over the whole water column. Erosion or deposition effectively changes this reference concentration and so will change the distribution of sediment vertically. For non-cohesive sediments the reference concentration is usually altered as a function of the (instantaneous) bed shear stress (e.g. Davies, 1990a). For cohesive sediments, erosion and deposition is usually governed by excess shear stress above a critical value (equations 2.65, 2.64). An example of the use of these equations in a turbulence model is Sheng & Villaret (1989).

One of the problems of including sediment entrainment is the need to model the bed. A layered bed capable of simulating the formation, consolidation and erosion of estuarine sediment was described by Hayter (1986). This was empirical in nature and required substantial laboratory testing of sediment properties for use. Roberts (1991) used a similar bed layered model in a model of the fluidisation of mud by waves. Bed shear stresses under waves (equation 2.26) were used to cause fluidisation, and the flow of fluid mud down slopes was found to be substantial. Lack of field data meant the model could only be assessed qualitatively. Improvements in the modelling of shear induced turbulence were suggested.

2.4.5 Conclusions

Modelling wave and current boundary layers is a topic of much ongoing research. On their own, the boundary layers are reasonably well understood, but interactions between the two are less well comprehended. Introducing sediment transport into the problem complicates the issue further. Turbulence is known to be the factor responsible for maintaining suspensions of fine sediment, but is crudely represented in many transport models.

Although many complex sediment transport models have been developed in recent years, simulation still remains tied to the knowledge of the physical processes (Teisson, 1991). Computer limitations mean that three dimensional models incorporating all the present knowledge are still infeasible, hence depth or width average versions are liable to remain in use for some time (O'Connor, 1992). For both of these reasons one dimensional models can be most useful - in giving increased knowledge of the processes by their higher physical equivalence, and providing boundary conditions for depth averaged models. A whole spectrum of models have developed based on solving the flow equations. Many are based on solving the mean flow equations, by separating the instantaneous velocity into mean and fluctuating parts. These so called turbulence models range from relatively simple eddy viscosity models to high order closure models which can involve the solution of up to 10 partial differential equations.

Few of these models have been applied to cohesive sediment transport and addressed the issue of flow-sediment interactions. Prescribed eddy viscosity models can predict lutocline formation and near bed fluid mud layers if they are made a function of Richardson number. At least a one-equation closure model is required if any further understanding of physical processes is to be gained. Higher order models have also identified sediment stratification as a cause of turbulence damping, and hence deformation of both velocity and concentration profiles. There has been little application of turbulence models to studying cohesive sediment transport under both waves and current as would be expected on ITZs. They have been used more widely to study clear water phenomena with varying success.

Wind Force \ Wind Dir	0	30	60	90	120	150	180	210	240	270	300	330
3	0.27	0.23	0.18	0.12	0.08	0.05	0.09	0.14	0.22	0.29	0.30	0.28
4	0.41	0.39	0.29	0.20	0.15	0.15	0.14	0.20	0.36	0.46	0.47	0.41
5	0.57	0.55	0.41	0.27	0.19	0.15	0.17	0.30	0.52	0.65	0.64	0.58
6	0.73	0.70	0.53	0.34	0.22	0.19	0.25	0.38	0.63	0.80	0.81	0.74
7	0.90	0.83	0.66	0.43	0.28	0.27	0.30	0.47	0.80	1.01	0.99	0.90
8	1.11	1.03	0.81	0.51	0.38	0.35	0.34	0.57	0.98	1.23	1.22	1.11
9	1.31	1.24	0.95	0.61	0.43	0.37	0.40	0.68	1.14	1.44	1.45	1.31
10	1.51	1.43	1.08	0.70	0.47	0.40	0.49	0.77	1.33	1.69	1.68	1.53

SIGNIFICANT WAVE HEIGHT (m)

Wind Force \ Wind Dir	0	30	60	90	120	150	180	210	240	270	300	330
3	1.4	1.3	1.2	1.0	0.8	0.8	0.8	1.0	1.4	1.5	1.5	1.4
4	1.6	1.6	1.4	1.1	0.9	0.8	0.8	1.2	1.7	1.9	1.8	1.7
5	1.9	1.9	1.6	1.2	1.0	0.9	0.9	1.3	1.9	2.2	2.1	1.9
6	2.1	2.1	1.8	1.3	1.0	0.9	1.1	1.5	2.1	2.4	2.3	2.1
7	2.4	2.3	2.0	1.5	1.1	1.1	1.1	1.6	2.3	2.6	2.5	2.3
8	2.6	2.5	2.2	1.6	1.2	1.2	1.2	1.8	2.5	2.9	2.8	2.5
9	2.8	2.7	2.3	1.7	1.3	1.2	1.3	1.9	2.7	3.1	3.0	2.7
10	2.9	2.9	2.5	1.8	1.3	1.2	1.4	2.0	2.9	3.3	3.2	2.9

AVERAGE WAVE PERIOD (s)

Wind Force \ Wind Dir	0	30	60	90	120	150	180	210	240	270	300	330
3	4	4	4	3	2	1	2	4	6	6	6	4
4	3	4	3	2	1	1	1	3	5	5	5	3
5	3	4	3	2	1	1	1	3	5	-	4	2
6	3	4	3	2	1	1	1	3	4	4	4	2
7	3	3	3	2	1	1	1	3	4	4	3	2
8	3	3	3	2	1	1	1	3	4	4	3	2
9	3	3	3	2	1	1	1	3	3	3	3	2
10	2	3	2	2	1	1	1	2	3	3	3	2

REQUIRED STORM DURATION (hr)

Table 2.1: Wave prediction results - Portishead (HRS, 1984)

Bottom Type	Zo (cm)	fc
Mud	0.020	0.0176
Mud/sand	0.070	0.0240
Silt/sand	0.005	0.0128
Sand (unrippled)	0.040	0.0208
Sand (rippled)	0.600	0.0488
Sand/shell	0.030	0.0192
Sand/gravel	0.030	0.0192
Mud/sand/gravel	0.030	0.0192
Gravel	0.300	0.0376

Table 2.2: Typical values of roughness length (z_o) and friction factor (f_c) for differing bottom types. (Modified from Soulsby, 1988)

Chapter 3

Methodology

3.1 Field Methodology and Analysis

3.1.1 Overview

The literature review has identified the lack of field data from muddy ITZs and some of the problems associated with data collection. West (1990) studied deposition and erosion from eight ITZs in the Severn Estuary in terms of monthly averages. Further progress can be made by analysing a single site during a tidal cycle in an attempt to understand the physical processes involved in sediment transport. Spatial variations are recognised from West's work, so results from a single site should be treated as possibly site specific.

To comprehensively tackle the problem of recording wave climate, velocities, SSC and bed level changes over a tidal cycle requires a substantial array of equipment. A combination of instruments from Birmingham University and Hydraulics Research Wallingford (HR) were used in experiments. Instruments were positioned at points on the ITZ at low water, with logging commencing when instruments became covered by the flood tide and finishing when they had re-emerged after the tide had ebbed.

A trial deployment was firstly made to test this methodology, so highlighting many of the potential problems in keeping an undisturbed bed surface and some hardware limitations.

In total five separate deployments were made for a range of meteorological conditions over one to three day periods, allowing recording of usually at least two tidal cycles. This timelength was considered to be a reasonable balance between the minimum time necessary to overcome any technical field difficulties which tended to arise during the logging of the first tidal cycle and the financial constraints. This meant that usually at least one tidal cycle was logged as fully as was possible, given that some instrument failures could not be rectified in a matter of

hours. It was assumed that peak depositional regimes would occur on calm days during Spring tides (providing a maximum sediment supply, HRS (1981)) and maximum wave erosion would occur when wind speeds were greatest and from the Westerly quarter.

The first part of this chapter explains site selection, instrumentation and calibration and post deployment data analysis common to each deployment. Plates 1-10 show examples of the ITZ and the instrument deployments.

3.1.2 Site Selection

A site was chosen which best satisfied a wide ranging number of requirements:

1. close to the main channel and the longitudinal turbidity maximum for a supply of sediment
2. exposed to the prevailing winds for wave generation (NW–SW)
3. reasonably uniform beach of sufficient length ($> 100\,m$) to allow transverse effects to be considered
4. vehicle access to the high water mark is essential since data were to be logged on site
5. dynamic response to erosion and deposition of muds
6. safe working conditions

A two year study by West (1990) on eight ITZ transects in the Severn Estuary was used as a basis for site selection (see figure 3.1 for locations).

Portishead regularly has bed level changes of more than 6 $cm/30$ days at 200 metres from the high water mark (HWM) (see figure 3.3). Wentlooge has less than 3 $cm/30$ days at a similar distance and less than 6 $cm/30$ days at 420 metres down the transect. The higher accretion rates at Portishead probably reflect its closer proximity to the main channel and the high SSC found therein. Sites at Purton and Arlingham have bed level changes of the order of 10 $cm/30$ days, but are subject to outcropping rock and a high proportion of sand respectively.

Battery Point shelters the ITZ at Portishead from ebbing tidal action and from easterly winds, and similarly Black Nore provides shelter from flood tides (see figure 3.2). This allowed the opportunity to study what may be considered a wave dominated beach. The site is readily accessible to the public, hence constant attendance would be required during deployments. The Wentlooge site is similarly protected from tidal action. The 1.5 km width of the ITZ here, probably leads to lower SSC. It is well exposed to the prevailing South-Westerlies, though wave attenuation over the ITZ is probably appreciable.

As instrument cabling is expensive Portishead was considered the most suitable site and would probably produce the better data from short term deployments. Plates 1 and 2 show views across the ITZ taken during two deployments. The upper 30 m of the ITZ consists of either shingle or saltmarsh, with an intermediate rocky/muddy region extending for around 20 m and the rest of the ITZ to the LWM is predominantly mud, although some sand was found (see section 5.5). Bed level changes, moisture contents and surface shear vane readings taken by West (1990) at monthly intervals from Portishead during the period November 1988 – August 1989 are shown in figures 3.3-3.5. The ITZ had a mud cliff halfway down its transect which was observed to erode landwards during the three year study. The ITZ transect elevation for 1988 is shown in figure 3.2a, clearly showing (in dashes) the erosional cliff and also the saltmarsh cliff which extends over the first $10 - 50\,m$ of the transect. The approximate beach slope is 1/20. Approximate distances of instrument deployment positions are measured from MHW using a tape measure.

3.1.3 Instrumentation and Calibration

Instrument development is crucial to the understanding of hydrodynamic and sediment processes in the field. Technical advancements in instruments are presenting data to current experimentalists which workers in the previous years could only have dreamed about. Development is a continuous process and in the years to come hopefully many of the limitations which are present today will be resolved. This section lists the equipment available to the author; the uses and falacies and how instruments were calibrated. Signals from all instruments were cabled back to the instrument electronic boxes which are powered by 12 or 24 volt D.C. supplies and were stored in the logging van. Cabling presented a limitation to equipment use, so maximum cable lengths are given in the text, although some lengths could be shortened when not used at full capacity. Examples of mounted instruments to be described are shown in plates 3-6.

Wave Characteristics and Water Depth

To measure water depth and surface wave characteristics, two bed mounted absolute pressure transducers with cable lengths of 100 m and 500 m were used (see plate 3). These were checked and field calibrated against the rather more primitive wave-staff and stopwatch approach. Pressure transducers record near bed pressure head variations which do not equal the surface fluctuations. To find actual wave heights a transformation is used, which can lead to inaccuracies, since the subsurface dynamic pressures associated with short period waves attenuate more rapidly with depth than long period waves (Wiegel & Kukk, 1957). Before deployments, the transducers were calibrated in a water column in the laboratory and a linear calibration of approximately $1v \equiv 10\,m$ was always found. Instrument resolution was $3\,mm$ water head. Offsets could be calculated in the field when the instrument was in position and before the water covered the instrument and were usually small. Occasional 'jumps' in the offset during logging were observed ($< 0.3\,m$).

Velocity

Current and velocity fluctuations were measured using 5.5 cm diameter electro-magnetic current meters (EMCMs) mounted at set heights above the bed (see plates 3-5). EMCMs are mounted on a bracket fitted with a protractor allowing vertical/horizontal alignment. Fieldwork by Darbyshire (1991) showed that errors in alignment were at most ± 2 degrees. EMCMs work on a similar principle to a dynamo - as the (conducting) water moves through a magnetic field it produces a current proportional to the speed of flow. An EMCM is capable of measuring two components of velocity as the magnetic field is switched between the two orthogonally aligned electrodes. Each switch provides a sample of flow velocity, with the frequency of switching (40 Hz) being a limitation on the number of measurements made. Two manufacturers of EMCM were used - the Colnbrook type being an older model. A single Colnbrook EMCM had a cable length of 500 m and was subject to some offset jumps and to a certain amount of drift. For these reasons it was only used to measure velocity fluctuations and not absolute velocities. A pair of Valeport series 800 2 axis EMCMs had cable lengths of 200 m and were more reliable. Laboratory tests showed that these were not subject to substantial drift ($< \pm 2\, cm/s$ over a day) and did not have offset problems. Calibrations were based on the manufacturers recommendations and were approximately substantiated by some laboratory experiments. A calibration for one channel of EMCM is given in figure 3.6. Any large EMCM offsets could be spotted by checking velocities at high slack water when low currents would be expected.

Braystoke propellor type velocity meters were experimented with as an in-the-field calibration check on the EMCMs and also to provide mean current measurements, but the oscillating velocities under waves prevented any useful data being logged. It was not possible to calibrate a propellor which was being turned at first by water flowing towards it and then by a backwards flow.

Suspended Sediment

SSC was measured over a vertical profile using a mixture of Birmingham University made infra-red optical siltmeters (measure high concentrations $2 - 20\, g/l$) and standard Partech optical sensors (lower concentrations $0 - 5\, g/l$) (see plates 3-5). Three Partechs, each on 100 m of cable, and two siltmeters with 120 m and 200 m of cable were available.

Both Partechs and siltmeters work by a light source and receiver producing a voltage which is reduced when obstructed by mud particles, the reduced signal being a function of the SSC. The range and sensitivity of the instrument is governed by the length of the light path in the head. For the first four deployments the siltmeters had a fixed sensitivity ($> 2\, g/l$), but for the final deployment in May, the sensitivity had been improved by some electronic adjustment in the sensor box. The small size of the siltmeters ($\approx 15\, mm$ diameter) allowed them to be positioned nearer the bed ($5 - 15\, cm$) than the more bulky Partechs (see plate 3).

Partechs were calibrated using a range of formazin solutions on the day of deployment (as given in the manual). Gravimetrically determined SSC were then compared with formazin in the laboratory and a best fit calibration curve was fitted through the points. The Partechs generally had a approximately linear calibration until very high concentrations near the top of their range ($5\,g/l$). Owing to the size of the instrument they were mainly used a reasonable distance from the bed ($> 15\,cm$) and hence concentrations never reached saturation. An exception is in the May deployment when a Partech was positioned $7\,cm$ above the bed.

The siltmeters were calibrated more directly by placing the head in a container of water with different gravimetrically determined SSC kept in suspension by a stirrer. Repetitive calibrations proved this method worked reasonably well. Calibration curves were quite linear over the first $7\,g/l$, and a smooth curve could be fitted through the points. In all but the last deployment (5-7/5/93) the siltmeters had a restricted response to concentrations only above $2\,g/l$.

For both siltmeters and Partechs a cubic best fit curve was used for calibration. Examples of Partech and siltmeter calibration curves are given in figures 3.7 and 3.8, respectively.

Bed Level Change

A combination of accretion/erosion pegs and ultra sonic bed level transducers (USt) was used to monitor bed level change. The USt is an instrument constructed by HR and has been reasonably successful when used in the laboratory for measuring deposition and erosion rates. The USt is positioned approximately $5\,cm$ above the bed surface and 'fires' a beam of ultra sound at the bed which is reflected back and the distance is logged (plates 5 and 6). The results from this device are known to be somewhat subjective and to use the instrument with a fair degree of success requires some experience. It is quite difficult to discern which reflection is the bed, especially under the conditions on an ITZ where wave activity can produce a high concentration fluid mud layer near the bed. To check the instrument is not slipping into the bed, two USt heads are placed side by side with one 'firing' onto a plate positioned on the bed (see plate 6). Periodic checks are made to see if any movement is taking place. For all deployments at this site, no movement was ever detected. Two USts were available with cabling lengths of $100\,m$ and $200\,m$ respectively. Only one of these could be logged at any one time as the logging box was only designed for one instrument. Alternate logging of each USt for short periods of time should be sufficient to quantify bed level changes during the tide.

Accretion/erosion pins (pegs) placed down a transect of the beach were used to provide a definitive check on the overall bed level change during a tide. A transect of pegs was positioned down the ITZ to record spatial variation. Peg 1 was nearest the HWM, $85\,m$ from the sea-wall, with five more pegs spaced at intervals of $20\,m$ down to the furthest one, peg 6, which was $185\,m$ from the sea-wall and is closest to the LWM. Measurements taken from the pegs were considered accurate to the nearest $2\,mm$. This estimate is based on the difficulties of measuring peg heights from a rule on the mudflats.

3.1.4 Data Logging

Ideally all the instruments would be logged continuously for the 6 hours or so they are under water and segments of the record could be analysed later at any sampling rate and timelength. A variety of logging equipment was available (plate 7). Data could be stored on magnetic tape via a Racal Store 4 FM tape recorder either in analogue form (restricted to 4 channels), or could be digitised and multiplexed using a telemetry system so allowing 8 channels to be logged. This had the advantage of permitting effectively continuous recording (tape duration $\approx$ 3 hours), with selected representative segments being analysed at a later stage. On occasions, however, more than 8 channels of data needed to be recorded.

An alternative to storing data on tapes was to directly store digitised data onto the hard disk of a microcomputer. Sixteen channels could be logged in this way, but storage restrictions meant that data could not be recorded continuously and had to be downloaded onto floppy disks at intervals. This process interrupted data logging for approximately 5 minutes.

A combination of these techniques was used during the deployments. Occasional checks were made during recording using an oscilloscope, or a graphics package to see if instruments were functioning. During the trial deployment it was discovered that analogue recording directly onto tape produced spikes on spectra at a number of unexpected frequencies. The magnitude of some of these spikes and the frequencies associated with them, meant that the tape recorder could only be used in conjunction with the digitising telemetry system.

3.1.5 Signal Processing and Analysis

Signals from the instruments were cabled back to the instrument electronic boxes which convert the signals to have a range $-1 \rightarrow +1\,v$. If frequency domain (spectral) analysis is to be used then "aliasing" can become a problem. Aliasing is the name given to signals appearing in spectra at frequencies which are not true signals. This occurs because higher frequency sine waves may be fitted through data which in reality reflects lower frequencies, and these 'alias' signals can be folded back into spectra. Aliasing can be prevented by restricting the highest frequency present in a time series by a low pass filter and sampling at least twice as fast as this frequency. A 10 Hz low pass filter existed on the EMCMs and on collaborative (with HR) deployments a 2.5 Hz low pass filter was used on all instruments. This frequency is still sufficient to measure turbulence with 5.5 *cm* EMCMs and allowed a low frequency sampling rate (5 Hz) to be used (which helped in data storage), without the risk of aliasing problems. On days when the filter box was not used the data were logged onto tape at 40 Hz which allowed for aliasing problems to be dealt with by sampling at more than one rate.

Data were transferred to the DEC Vax mainframe in the School of Civil Engineering and analysed using fortran programs written by the author and various graphics packages. Plots of each raw time series were examined visually to spot faulty instruments and spurious data. This is an

important exercise and can be a time saving operation if instruments failed completely. Once calibrated, data were segmented into shorter sections (after Soulsby, 1980) so that statistical analysis could be performed. Spikes greater than four times the standard deviation from the mean were then replaced by the previous unspiky point. A number of smoothing techniques including weighted averaging were tried by Shiono (1981) and applied to turbulence data from the Tamar Estuary with conclusions that four point averaging was as good as any. Hence to remove high frequency noise and to reduce the number of points in a series for plotting purposes, the data were smoothed by block averaging over four points. Following this, analysis of each instrument was dealt with separately.

Pressure Analysis

The de-spiked and smoothed pressure time series was split up into segments of around 10 minutes and examined visually on this magnified level to make sure the smoothing had had the desired effect of removing high frequency noise, so that genuine zero crossing waves were being used in the next stage. Mean values of water depth were calculated and then a linear trend was removed so that the signal was converted to fluctuations about zero. To calculate wave heights and periods from pressure data a number of methods exist, each resulting in some kind of approximation, and each taking a different amount of calculation. Using the definition of a zero crossing wave as previously described in section 2.2.2, significant pressure heights (pH_s) and zero-crossing periods were calculated from the pressure fluctuations, which were then related to the water surface by a depth correction factor (K_p) (Grace, 1977)

$$H_s = \frac{\cosh kh}{\cosh k(h+z)} pH_s \tag{3.1}$$

where h is water depth and z the instrument height ($z = 0$ is surface, $z = -h$ is bed).

In reality the wave field consists of the whole spectrum of frequencies, but since the wave number (k) has been derived from the dispersion relation using the zero-crossing period (T_z) and the correction factor is effectively being applied to the whole spectrum, this has the effect of increasing low frequency influence and decreasing high frequencies. Hence wave periods are likely to be slightly longer than is true. Comparing zero-crossing periods with periods taken as the peak in the pressure spectrum showed that any differences were small.

Wave orbital amplitudes (U_o) were calculated from (H_s) using linear wave theory (equation 2.20) for Reynolds numbers defined by

$$RE = \frac{U_o^2}{\omega\nu} \equiv \frac{U_o A_o}{\nu} \tag{3.2}$$

Velocity Analysis

The data from EMCMs were truncated into the same size sections as with pressure data and mean velocities were found for the Valeport EMCMs in the two orthogonal directions. A linear trend was then removed to leave velocity fluctuations about zero, so that standard deviations (u'), significant velocity amplitudes (U_s), zero-crossing periods and Reynolds stresses could be calculated from all EMCMs. A number of different velocity scales for U_o can be used: root mean square (U_{rms}), significant velocity (U_s) and maximum velocity (U_{max}) (see e.g. Myrhaug *et al.*, 1992). Statistical analysis has led to the following relationships: $U_{rms} = \sqrt{2}\,u'$, $U_s = 2\,u'$, and $U_{max} = 3u'$. Since the significant wave height had been used as a measure of wave height, to be consistent, the significant velocity was used for U_o. Reynolds numbers from EMCM data were hence defined by

$$RE = \frac{U_s^2}{\omega\nu} \tag{3.3}$$

Some spectral analysis was performed on the velocity data, utilising fourier analysis packages already written by NAG. The velocity records were fed into a fast fourier transform (FFT), composed from a NAG routine, having been truncated into 5–10 minute records to reduce low frequency leakage. Energy density and cumulative normalised energy density could then be plotted against frequency.

Bed Shear Stress Estimation

Bed shear stress (τ_o) is a notoriously difficult parameter to determine under combined wave and tidal flows and a number of methods of estimation can be made, using either velocity or pressure data. Each method has advantages and disadvantages. It is good practice to use more than one method on this understanding (Soulsby & Humphery, 1989). A review of possible methods is given in section 2.2.9.

Since tidal currents were found to be small (see chapter 4), a logarithmic velocity distribution could not satisfactorily be assumed, especially when at most only two differing heights of velocity were being measured. Hence shear stress calculated from the gradient could not be used. Inertial dissipation methods require data transfer from frequency space to wave number space, which entails dividing by velocity. For the small current present this would be infeasible except for one or two short periods during the tidal cycle.

Three final methods were left - friction factor approaches, Reynolds stress estimation and the method of splitting the spectrum described by Soulsby and Humphery (1989). Specific details of their use are given below, with a more comprehensive description of the methods given in section 2.2.9. A further discussion of the merits of these methods in the light of the field results

is given in section 5.4.

Friction Factor

Using either pressure or velocity data an orbital wave amplitude was calculated, which was used in conjunction with a friction factor using Jonsson's (1966) theory to determine (τ_o). From pressure data U_o was calculated from H_s (assuming linear wave theory), or from velocity data U_s was used for U_o (only for 5/93 deployment when no pressure data available). A wave friction factor was calculated from the appropriate equation below

$$f_w = \frac{2}{\sqrt{RE}} \qquad \textit{Laminar flow (Analytical)} \tag{3.4}$$

$$\frac{1}{4\sqrt{f_w}} + 2\log\frac{1}{4\sqrt{f_w}} = \log RE - 1.55 \qquad \textit{Smooth Turbulent Flow (Empirical)} \tag{3.5}$$

where RE was given by either equation 3.2 or 3.3. Bed shear stress (τ_o) could be calculated from

$$\tau_o = \frac{1}{2}\rho f_w \overline{U}_o^2 \tag{3.6}$$

This method is an estimate of maximum bed shear stress. Since this method is solely based on wave energy, despite the presence of a weak tidal current, errors were estimated for the inclusion of the measured current from equation 2.44, using a fixed friction factor of 0.0176 taken from table 2.2.

Reynolds Stress

Reynolds stresses (τ_r) were calculated using the truncated sections of velocity data, having firstly removed linear trends from EMCMs when used in the correct orientation (u-w)

$$\tau_r = -\rho\,\overline{u'w'} \tag{3.7}$$

Spectra Splitting Technique (Soulsby & Humphery, 1989)

Using the segmented velocity data, energy density is plotted against frequency on log-log axes allowing the removal of the wave energy from spectra, leaving the turbulent energy (E). Bed shear stress is then estimated from

$$\tau_o = 0.19\,\rho\,E \tag{3.8}$$

The removed wave frequency range was either defined from a smoothed linear velocity spectrum or from pressure spectra if available. Since this removal is somewhat subjective, it was considered necessary to estimate errors induced by choosing different frequency ranges.

Turbidity Analysis

Mean SSC at each instrument height were calculated from the segmented data.

3.1.6 Settling Velocity

A 1 m Owen tube was used to measure fall velocity (W_s) in the field (Barton, 1992). The nature of an ITZ meant that collecting a sample was problematic because of the practical difficulties in needing to cross a considerable distance with a bulky tube. This could be hazardous to both equipment and person.

Samples were taken in the surf zone near the deployment sites and near the HWM when possible.

3.1.7 Bed Sediment Measurement and Analysis

A surface sample (top 2 cm) of sediment was taken at the beginning and end of the deployment from areas around each of the 6 pegs and from the instrument sites. These samples were kept overnight in sealed plastic bags in a fridge to reduce biological growth and moisture loss. The samples were divided into two so that an average moisture content, bulk density and dry density could be found

$$Moisture\ Content\ (MC) = \frac{water\ mass}{dry\ sed.\ mass} \times 100\% \tag{3.9}$$

$$Bulk\ Density\ (BD) = \frac{wet\ sed.\ mass}{wet\ volume} \tag{3.10}$$

$$Dry\ Density\ (DD) = \frac{dry\ sed.\ mass}{wet\ volume} \tag{3.11}$$

A Pilcon hand operated shear vane (cruciform vane - 50 mm long, 33 mm wide, range 0 – 33 kPa) was used to take a profile every 5 cm over the top 20 cm of sediment, at the same places the samples were taken from. The readings were repeated three times so an average shear could be determined. On the first visit to Portishead a deeper profile was made ($\approx 1\ m$), but since it is surface sediments that are really of interest it was considered unnecessary to take readings so far below the surface on future occasions.

To introduce some kind of conformity, bed measurements and samples were taken when it was low water, since it was considered dewatering of sediment by run off might affect results.

A particle size analysis was performed at HR Wallingford.

3.2 Modelling Methodology and Implementation

3.2.1 Introduction

Numerous complex turbulence models are available for use with modern computers, but still remain an economic burden on processing time. The highest order models, such as Reynolds stress models (RSM) require solution of up to seven partial differential equations to solve for the unknown Reynolds stresses. To accurately predict flows, RSMs may be considered necessary, since lower order models based on the Boussinesq analogy usually require some modification from their standard forms if they are to be successful at prediction (see Rodi, 1980). However, lower order models can still provide useful information on the turbulence and sediment structure and may remain widely used for some time (Younis, 1992). If used as a complement to field data, turbulence models can provide additional understanding of physical mechanisms and permit future direction to field experiments as well as giving some degree of prediction.

The model used in this study is based on the standard "$k-\varepsilon$" model (Jones & Launder, 1972), whereby two partial differential equations are used to describe turbulent development: one in terms of the turbulent kinetic energy (k) and the second in terms of the energy dissipation rate (ε). The two major modifications made by Chien (1982) and more recently by Aydin and Shuto (1988) were to include the influence of molecular viscosity (ν) which is important at low Reynolds numbers, and a wall proximity effect which provides a damping of turbulence at the boundary. In addition a 'roughness viscosity' (ν_r) was introduced to account for extra turbulence production due to surface roughness at low Reynolds numbers. It is considered that this form of the $k-\varepsilon$ model might be applicable to flows over muddy beds. The FORTRAN coding for the hydrodynamical part was written by Bill Roberts of HR and has been tested and supplemented by the author to enable modelling of suspended sediment stratification and fluxes of sediment to and from the bed through erosion and deposition.

The following sections present the equations solved by the model, including a brief description of numerical techniques. The equations for suspended sediment are presented, with details on how the bed surface is modelled. The boundary and initial conditions for implementation of the model for waves and current flows are then described by focusing on the hydrodynamic and sediment parameters separately.

3.2.2 The Turbulence Model

The model described is based on the Aydin & Shuto (1988) model, who in turn refer to Chien (1982) for the basis of their modifications. This was successfully used to compute friction factor and turbulent energy in steady flows and was compared with empirical wave friction factor formulae for smooth and rough turbulent oscillatory flow by Aydin and Shuto (1988) showing particularly good agreement for smooth turbulent flow. Stratification effects have been included in the model by using an additional term in the turbulent equations (after Rodi, 1984).

Equations of Flow

The equations for flow velocity are as follows

$$\frac{\partial u}{\partial t} = \frac{\partial}{\partial z}\left[(\nu + \nu_t)\frac{\partial u}{\partial z}\right] - \frac{1}{\rho}\frac{\partial p}{\partial x} \tag{3.12}$$

$$\frac{\partial v}{\partial t} = \frac{\partial}{\partial z}\left[(\nu + \nu_t)\frac{\partial v}{\partial z}\right] + \frac{\partial}{\partial t}(V_o \sin \omega t) \tag{3.13}$$

where the driving pressure gradient is given by

$$-\frac{1}{\rho}\frac{\partial p}{\partial x} = P_o + \frac{\partial}{dt}(U_o \sin \omega t) \tag{3.14}$$

Hence unidirectional flow is achieved by a fixed pressure gradient in the x direction and wave angle can be varied by altering the ratio of U_o/V_o, the maximum wave orbital velocities, which govern the magnitudes of the oscillatory flow component.

The unknown Reynolds stresses which are created by the time-averaging of the Navier-Stokes equations are represented by the Boussinesq analogy to laminar flow (see section 2.2.6) so the total bed shear stress is given by

$$\frac{\tau}{\rho} = (\nu + \nu_t)\frac{\partial u}{\partial z} \tag{3.15}$$

where the turbulent eddy viscosity (ν_t) is defined as

$$\nu_t = C_\mu f_\mu \frac{k^2}{\varepsilon_t} \tag{3.16}$$

with ε_t the total turbulent energy dissipation rate given by

$$\varepsilon_t = \varepsilon + 2\nu\frac{k}{z^2} \tag{3.17}$$

The second part in ε_t is a near wall effect and is discussed in more detail later.

The Closure Equations

Two partial differential equations for turbulent kinetic energy (k) and turbulent isotropic energy dissipation (ε) are used to 'close' ν_t:

$$\frac{\partial k}{\partial t} = \frac{\partial}{\partial z}\left[\left(\nu + \frac{\nu_t}{\sigma_k}\right)\frac{\partial k}{\partial z}\right] + \underbrace{(\nu_t + \nu_r)\left(\frac{\partial u}{\partial z}\right)^2}_{P} + \underbrace{\beta g \frac{\nu_t}{\sigma_c}\frac{\partial c}{\partial z}}_{G} - \varepsilon - \frac{2\nu k}{z^2} \tag{3.18}$$

$$\frac{\partial \varepsilon}{\partial t} = \frac{\partial}{\partial z}\left[\left(\nu + \frac{\nu_t}{\sigma_\varepsilon}\right)\frac{\partial \varepsilon}{\partial z}\right] + \left(C_{\varepsilon 1}\nu_t\left(\frac{\partial u}{\partial z}\right)^2 + \beta g \frac{\nu_t}{\sigma_c}\frac{\partial c}{\partial z} - C_{\varepsilon 2} f_\varepsilon \varepsilon\right)\frac{\varepsilon}{k} - f_{\varepsilon d}\frac{2\nu\varepsilon}{z^2} \tag{3.19}$$

P is the production of turbulent kinetic energy and G is the buoyancy (or density stratification) term after Rodi (1984). The flux Richardson number is defined as the ratio $Ri_f = -G/P$, and is a measure of stratification. The buoyancy terms are discussed later.

Subscripted σ and C are standard constants and are set to the same as in the Chien model

$$C_\mu = 0.09,\ C_{\varepsilon 1} = 1.35,\ C_{\varepsilon 2} = 1.80,\ \sigma_k = 1.0,\ \sigma_\varepsilon = 1.3,\ \sigma_c = 1.0 \tag{3.20}$$

The turbulent Prandtl/Schmidt number, σ_c, has been fixed at 1.0 as is done by the majority of modellers, but deserves further comment. This is the ratio of eddy to sediment diffusivity and is the subject of much debate. Using an RSM (which is able to output σ_c) Teisson (1992) found that values varied from 0.7–10.0. Rodi & Celik (1988) with a '$k-\varepsilon$' model compared SSC profiles using either 0.5 or 1.0 in channel flow. They found that 1.0 often produced too little mixing and 0.5 sometimes too much, but was generally better at reproducing SSC profiles. Since there seems to be insufficient evidence to assume another value for σ_c, the mixing of

sediment and flow has been assumed to be the same. This restriction should be considered a limitation of eddy viscosity models.

Near Wall Effects

In the near wall region, viscous effects are of comparable magnitudes to turbulent diffusion so for accurate prediction molecular diffusion of k and ε is included by adding ν to the turbulent eddy viscosity. In most high Reynolds number models viscous effects are assumed to be negligible. In addition to this, the dissipation terms in equations 3.18 and 3.19 each have an extra term ($\propto z^2$) which is needed to account for the non-isotropic turbulence experienced in the near wall region (proposed by Chien). These are obtained on dimensional grounds by the need to balance molecular diffusion at the wall (Chien, 1982).

Empirically defined damping functions (subscripted f) were also introduced by Chien (1982) to model low Reynolds number near wall effects. These were formulated in terms of a turbulent Reynolds number R_t:

$$f_\mu = \exp\left(\frac{-4.79}{1.013R_* - 0.156R_*^2 + 0.01R_*^3}\right) \tag{3.21}$$

$$f_\varepsilon = 1 - 0.222\exp\left(-\frac{R_t^2}{36}\right) \tag{3.22}$$

$$f_{ed} = \exp\left(-0.3\sqrt{R_t}\right) \tag{3.23}$$

$$R_t = \frac{k^2}{\nu\varepsilon_t} \tag{3.24}$$

$$R_* = 1 + \frac{R_t}{20} \tag{3.25}$$

Constants in the equations (3.21-3.25) have been obtained by ensuring that the model fits measured velocity profiles for both low and high Reynolds numbers (see Aydin & Shuto, 1988)

Bed Surface Roughness

Bed surface roughness is known to affect turbulent energy throughout the flow. With a low Reynolds number model surface roughness needs to be treated in a different way to high Reynolds number models because of the viscous damping effect which is included. Aydin & Shuto considered a number of ways of adding roughness induced turbulence and decided the introduction of a roughness viscosity, so enhancing the turbulent production in the k-equation was the most suitable. The roughness viscosity (ν_r) is defined by

$$\nu_r = f_\mu f_r u_* k_s \tag{3.26}$$

where f_μ is given by equation 3.21, and f_r is a function which distributes ν_r in such a way that turbulent production is increased in the vicinity of the rough surface, up to a height of $2k_s$ above the bed, where k_s is the Nikuradse roughness and u_* the shear velocity. The peak value of f_r is chosen to occur at $u_* z/\nu = 20$. Numerical experiments by Aydin & Shuto to determine coefficients in this description led to

$$f_r = C_r \, sech \, [C_k(z/z_{20} - 1)] \tag{3.27}$$

where

$$z_{20} = \frac{20\nu}{u_*} \tag{3.28}$$

and C_k is determined depending on relative values of k_s and z_{20} such that

$$\begin{aligned} k_s < z_{20}; \quad & C_k = 4 \\ k_s > z_{20} \begin{cases} z < z_{20}; & C_k = 4 \\ z > z_{20}; & C_k = 4z_{20}/k_s \end{cases} & \end{aligned} \tag{3.29}$$

The constant C_r is a function of u_* and R_k ($= u_* k_s/\nu$) the roughness Reynolds number

$$\begin{aligned} R_k \leq 15; \quad C_r &= \frac{21.6}{\sqrt{u_*}} \\ R_k > 15; \quad C_r &= \frac{31.1 - 8.1 \log(R_k)}{\sqrt{u_*}} \end{aligned} \tag{3.30}$$

3.2.3 Suspended Sediment and Bed Modelling

Suspended Sediment

The following density equation couples the flow and sediment equations (Sheng & Villaret, 1989)

$$\rho = \rho_s c_v + \rho_w(1 - c_v) \tag{3.31}$$

where $c_v = c/\rho_s$ is the volumetric concentration and ρ_w, ρ_s are the densities of water and sediment, respectively. The volumetric expansion coefficient (β), used in the k and ε equations is then defined as

$$\beta = \frac{\rho_s - \rho_w}{\rho_w} \tag{3.32}$$

This parameter has also been used by Teisson (1992) who describes how the value of β affects the concentration profiles in unidirectional flow. With these density definitions, the flow equations can optionally be coupled with following suspended sediment equation and different sediment densities can be considered.

Suspended sediment is modelled by

$$\frac{\partial c}{\partial t} = \frac{\partial}{\partial z}\left[\left(\nu + \frac{\nu_t}{\sigma_c}\right)\frac{\partial c}{\partial z} + W_s c\right] + sources - sinks \tag{3.33}$$

where W_s is the settling velocity and is a function of concentration given by

$$W_s = \begin{cases} W_{min} & \text{if } c < \frac{W_{min}}{R_o} \\ R_o c & \text{if c} \geq \frac{W_{min}}{R_o} \end{cases} \tag{3.34}$$

So a minimum settling velocity has been defined, but otherwise settling is a linear function of concentration, as R_o is a constant. If no settling velocity data exists then a mean value ($R_o = 0.001$) can be taken from figure 2.14.

Bed Model

The sources and sinks in equation 3.33 correspond to erosion and deposition. This flux of sediment to and from the bed is an optional part of the model. Erosion and deposition are governed by the excess bed shear stress, above critical values for both deposition and erosion. Bed shear stress is defined from equation 3.15 at $z = z_o$ and a critical shear stress for either deposition or erosion (τ_d, or τ_e) as given in chapter 2 (equation 2.65, 2.64).

The bed is assumed to consist of a number of layers (N) after Roberts (1991) with erosion only from the uppermost layer. Each layer has an associated τ_e and an entrainable mass of sediment in the layer, described by the dry density and the depth of layer. The bed can experience both deposition and erosion as τ_o varies during a wave cycle. When depositing it is optional to create a new uppermost layer with a reduced τ_e, or just add the sediment to the existing layer with the same τ_e.

It was considered unnecessary to allow for consolidation of the bed or dewatering of layers as the model is to be used to study processes at a fixed depth and for a finite time when these processes might be considered stationary. Any fluidisation of mud is just considered to be a high SSC (i.e. still Newtonian flow in this region).

3.2.4 Numerical Techniques and Boundary Conditions

The equations were transformed into dimensionless form using the following physical scales: wave period (T), wave velocity amplitude (U_o) and molecular viscosity (ν) so that

$$u' = u/U_o \qquad t' = t/T \qquad k' = \frac{k}{U_o^2} \tag{3.35}$$

$$\varepsilon' = \varepsilon\frac{T}{U_o^2} \qquad c' = cTU_o \qquad \nu_t' = \frac{\nu_t}{\nu} \tag{3.36}$$

where f' represents the non-dimensionalised variable (f).

A log-linear depth transformation was applied to allow a grid-mesh with more points nearer the bed, where gradients are expected to be steeper. This transforms the region $z \in [z_o, z_1]$ to $\eta \in [0, 1]$, where z_o is the elevation of the bed and z_1 the surface elevation.

$$\eta = \frac{\log\left(\frac{z'}{z'_o}\right) + \left(\frac{z'-z'_o}{z'_*}\right)}{\log\left(\frac{z'_1}{z'_o}\right) + \left(\frac{z'_1-z'_o}{z'_*}\right)} \tag{3.37}$$

z'_* determines the proportion of linear and logarithmic distribution of points. The time variable is non-dimensionalised from [0,T] to [0,1] so that model run time is defined in terms of number of wave cycles. A grid-size of 50 points, with z'_* set at 0.2 and a time-step of $0.002\,T$ were used for all the model runs presented in this thesis. Variations in these values were experimented with (after Davies & Jones, 1991), but results were found to be consistent using these values.

An implicit Crank-Nicholson finite difference scheme is used to solve the non-dimensionalised and depth transformed variable leading to a set of simultaneous equations in the form of a tridiagonal matrix. A standard Gaussian elimination technique for solving the tridiagonal matrix is used for each time-step.

The system of equations is solved subject to the following boundary conditions:

$$\begin{aligned} &at \quad z = z_0; \quad u = v = k = \varepsilon = 0 \\ &at \quad z = z_1; \quad \frac{\partial u}{\partial z} = k = \varepsilon = 0 \end{aligned} \tag{3.38}$$

These boundary conditions (BC) have been chosen to accommodate sediment particles on the bed (by setting the BCs at z_o and not at $z = 0$) and forcing the turbulence to go to zero which is required for high Richardson number flows when turbulence is expected to be damped out at the bed. These choices may create steep gradients of velocity and turbulence at the bed which could create numerical problems for high Reynolds number flows hence future work might include improvements to the empirical damping functions, and a further evaluation of the choice in boundary conditions.

Physically the two roughness lengths z_o and k_s are linked by an empirical relation (see figure 2.9) but in the model they are interactive and need to be inputted independently. There is a numerical (lower) limitation on the size of z_o (which is affected by k_s), as small values creates tiny grid spacings which are denominators in some of the terms in the equations to be solved. Altering z_* and using small timesteps may be required if results are to remain meaningful. Since ν_r is an empirically derived function of k_s to artificially increase the turbulence production this allows some flexibility in the value used to increase turbulence levels. A further discussion of the choice of z_o and k_s is given in chapter 6.

Convergence is defined by checking depth and wave cycle averaged velocity, turbulent kinetic energy and turbulent dissipation rate such that

$$\left| \frac{<\overline{f}>^i - <\overline{f}>^{i-1}}{<\overline{f}>^i} \right| < 10^{-5} \tag{3.39}$$

where f is replaced by u, k, ε. Depth averages are defined by $\overline{f}$ and wave cycle average of f at time step i is denoted $<f>^i$. A further essential criteria in defining convergence is that bed shear stress is in balance with the pressure gradient P_o (see section 6.2).

Davies & Jones, (1991) discuss numerical techniques for wave and current flows using a one-equation model, including a discussion on grid meshes and timesteps using the implicit Crank-Nicholson scheme. Most of the numerical techniques adopted by the model are examined in some detail in this paper. They concluded that a non-linear grid was an essential requirement, with the number of grid points of order 50 adequate, for suitable resolution. Some time-step instabilities were noted, when the time-step was too large, which sometimes could be stabilised by time filtering. These instabilities were usually observed in the form of time oscillations in various output parameters.

3.2.5 Model Initiation Parameters

Hydrodynamics

A number of physical parameters have been mentioned in the previous description of the model. It is helpful to list the required parameters imposed on the model during a run and a description of their impact on the model.

Model Initiation Parameters	
Parameter	Description
h	Water depth (m)
P_o	Pressure gradient (m/s^2) - governs magnitude of $\overline{u}$
U_o	Free stream wave orbital amplitude (m/s) - parallel to unidirectional flow
V_o	Free stream wave orbital amplitude (m/s) - perpendicular to unidirectional flow
T	Wave period (s) - timescale of one cycle
z_o	Bed roughness length (m) - used in depth transformation
k_s	Nikuradse roughness (m) - affects $\nu_r \Rightarrow$ additional turbulence
Duration	Length of a run (integer) - given as number of wave cycles

Table 3.1: Summary of hydrodynamic parameters required for a model run

The model can be run both from a 'cold' start, whereby no start conditions are assumed, or from a 'hot' start when initial values at each grid point are set up from a previous run. For

combined wave and current flows a converged current profile was firstly obtained and then used as a 'hot' start for a run with waves added. A coarse time-step was used to speed this process up, with a finer time-step to actually converge the current to its final value. A future improvement to the model might be to automate this process as suggested by Davies (1991). Using a constant pressure gradient as the driving force for the current is the most common way of approaching the problem, but it can also be solved by holding $\overline{u}$ as the fixed parameter. Davies (1991) studied the results from both methods, commenting that using the pressure gradient approach was probably more realistic to coastal hydrodynamics. A disadvantage of this method is the larger times to convergence due to the considerable changes in inertia when adding waves (Davies, 1991).

From a 'cold' start it is necessary to initiate computation by giving small values to the turbulent parameters. Specifically, k, ν_t and ε are set at 10^{-6}. The desired $\overline{u}$ can be obtained by varying the pressure gradient for the specified roughness lengths.

Run time for the model on a IBM compatible 486, 33 MHz-DX processor with 4MB RAM is around 18 minutes per 100 cycles for the fully implemented model (i.e. sediment included).

Sediment Dynamics

Sediment can be added to the flow at any stage and can be achieved in a number of ways. Sediment can be added directly into the flow (e.g. by an initial concentration), or entrained from the bed as previously described through erosion. The various input variables are given in table 3.2.

Model Initiation Parameters	
Parameter	Description
c(t=0)	Initial concentration (g/l)
R_o	Settling velocity constant (nominally 0.001) : (equation 3.34)
ρ_s	Sediment density (kgm^{-3}) - if $\rho_s = \rho_w$ then no density stratification effects
β	Volumetric expansion coefficient - controls density stratification
Nlayers	Number of bed layers (integer: max 10)
τ_e^i	Critical erosion shear strength for each layer i (Nm^{-2}) : (equation 2.65)
$mass^i$	Mass of sediment avaliable for entrainment into flow for each layer i (kg)
τ_d	Critical deposition shear strength (Nm^{-2}) : (equation 2.64)
M_e	Erosion rate constant $(kgm^{-2}s^{-1})$: (equation 2.65)

Table 3.2: Summary of suspended sediment and bed properties required for a model run

3.2.6 Model Output Parameters

Any of the variables can be output in either instantaneous or wave cycle averaged form. The following list of output variables are currently outputted for each grid point

Depth and cycle averages - $<\overline{u}>$, $<\overline{k}>$, $<\overline{\varepsilon}>$
Cycle averages - $<u>$, $<k>$, $<\nu_t>$, $<\tau>$, $<\tau_{max}>$, $<c>$, bed mass change
Instantaneous - z, u, v, k, ε, ν_t

The instantaneous values are those required for a 'hot' start. τ and τ_{max} are calculated from equation 3.15. It is a simple task to choose different variables to output either as a maximum or mean value. The number chosen is based on storage restrictions of the data files.

Chapter 4

Field Results

In total five field deployments were made between July 1991 and May 1993, three of which were in collaboration with HR. The five deployments gave the opportunity to study the ITZ under three calm (7/91, 2/92 and 5/93) and two storm (10/91 and 11/91) conditions. Although slight modifications were made to field techniques as experience was gained, the general methodology remained the same.

Data are presented by deployment, and are drawn together by focusing on separate subject areas in the following discussion chapter. Summary tables of field results (tables 4.1 and 4.2) are given as an overall guide to field data collected, with the rest of the chapter defining the conditions experienced, the experimental set up, and the data produced on each deployment in more detail. A brief summary follows each deployment. Analysis techniques were as explained in chapter 3 unless otherwise indicated.

When continuous data logging was used (i.e. via tape recorder), whole tidal cycles have been plotted as a time series. For these figures the calibrated data were kept as raw as possible, by minimising smoothing (within plotting constraints), so allowing the reader to interpret the field data. Gaps in the time series are due to changing tapes; each tape lasts approximately three hours.

Directional notation

displacement	velocity	
y	v	parallel to shoreline (+ve flood)
x	u	transverse to shoreline (+ve HWM-LWM)
z	w	vertical (+ve upwards)

Portishead Deployments - Summary of Results (No. of Tides)											
Instrument	Parameter	29-30/7/91		17/10/91		6-7/11/91		6-7/2/92		5-7/5/93	
		Number of Tidal Cycles									
		L	U	L	U	L	U	L	U	L	U
Pressure	h		1		1	1	2		2		1
	H_s		1		1	1	2		2		-
	T_z		1		1	1	2		2		-
EMCM	u	-	-		1	-	-		1		2
	v	-	-			-	-		1		2
	w										
	u'	-	-		1	2	-		1		2
	v'										
	w'	-	-		1	-	-		1		2
SSC (Partech) and (Siltmeter)	$\simeq 10\,cm$	1	1		1	2			2		2
	$\simeq 20\,cm$		1								4
	$\simeq 30\,cm$		1				2		1		4
	$50+\ cm$				-		2		1		2
USt		1	-			-	2		2		

Table 4.1: Summary of field results. Data are given in terms of numbers of tides recorded. Instrument failures are marked (-), for the Upper (U) and Lower (L) deployment sites.

Portishead Deployments - Summary of Instrument Positioning										
Height above bed (cm)	29-30/7/91		17/10/91		6-7/11/91		6-7/2/92		5-7/5/93	
	Number of Tidal Cycles									
	L	U	L	U	L	U	L	U	L	U
100										
95								P		
90										
85										
80								E3		P
75										
70		P				P				
65										
60										
55				E1		E1				P
50					E3			E2		
45				P				E1		E1
40				S						
35		P				P				
30	E3	E1,E2								
25				E2		E2				
20								P		P
15		P		S						E2
10	S				S	S		S		
5			S							P
0	USt PT	USt PT		PT	USt PT	USt PT		USt PT		S PT, S

Table 4.2: Summary of instrument positioning during field deployments. Instrument notation: EMCM - E, Siltmeter - S, Partech - P, Pressure transducer - PT, for the Upper (U) and Lower (L) deployment sites. Braystokes not shown.

4.1 29-30/7/91 Deployment

4.1.1 Meteorological and Tidal Conditions

The weather was calm with a dying Easterly breeze (hence offshore) during Spring tides of range $\simeq 11.0\,m$. The previous few days had also been calm, but with winds more from the Westerly quarter.

Day	Time	Water Depth	Mean Wind Strength	direction
28th	20:25	12.6 m	6 knts	E
29th	03:14	1.5 m	10 knts	ENE
29th	08:40	12.4 m	15 knts	ENE
29th	15:28	1.6 m	9 knts	ESE
29th	20:56	12.7 m	10 knts	ESE
30th	03:48	1.5 m	7 knts	SSE
30th	09:12	12.5 m	7 knts	SE
30th	15:59	1.7 m	8 knts	SE

Table 4.3: Meteorological Conditions: 29-30/7/92

4.1.2 Experimental Technique

For this first combined deployment two sites were selected - the upper site at approximately $100\,m$, and the lower site at approximately $160\,m$ from the HWM. Erosion/accretion pegs were positioned during the deployment for future use. Different instrument mounting methods and logging techniques were investigated.

Instrumentation

Lower site

- Ultra-sonic bed level transducer mounted $5\,cm$ above the bed
- Infra-red siltmeter (range $2 - 20\,g/l$) mounted $10\,cm$ above bed
- Electro-magnetic current meter (EMCM) orientated to measure u & w velocity components at a height of $30\,cm$ above bed

Upper site

- Ultra-sonic bedlevel transducer mounted 10 cm above the bed
- Bed mounted pressure transducer
- Infra-red siltmeter (range 2-20 g/l) mounted 7 cm above bed
- 2 EMCMs orientated to measure u,v & w velocity components 30 cm above bed
- 3 Partechs (range 0-5 g/l), Partech 1 17 cm above bed, Partech 2 36 cm and Partech 3 70 cm above bed

Instrument Failures

Upper site EMCMs failed due to a leak in the underwater unit, and the uppermost Partech (3) became fouled.

4.1.3 Analysis and Results

The data were logged in two different ways - 8 of the 12 channels continuously onto tape and all 12 were sampled for 5 minutes in every 15 at 10 Hz and recorded directly onto computer and downloaded each time onto floppy disk. Results are plotted against time with time zero (06:43, 30th) the start of recording and time 460 (14:23, 30th) the end of recording.

Mean water depth (h), significant wave heights (H_s), zero crossing periods (T_z), and wave bed orbital amplitudes (U_o) for every five minute section calculated from pressure data at the upper site are presented in figure 4.1. A generally decreasing trend in H_s is seen during the tidal cycle with maximum heights of around $5\,cm$, whilst T_z increase from $2-3.5\,secs$ during the flood phase, before tailing off after HW to around $2.5\,secs$. A mean U_o of around $1.5\,cm/s$ for $h > 2\,m$ is observed, with maximum U_o in the shallow water. Figure 4.2 shows bed shear stress (τ_o), wave friction factors (f_w) (used to calculate τ_o), Reynolds numbers (RE, given by equation 3.2) and the depth correction factor (K_p) to transform bed pressures to surface wave heights (see section 3.5.1). $RE < 10^4$, so friction factors would be calculated from the laminar equation 3.4, with resulting small values for τ_o (for $h > 1\,m$, $\tau_o < 0.05\,Nm^{-2}$).

Figures 4.3 and 4.4 show five-minute SSC means for each site from the Partechs and siltmeters (for siltmeters, SSC $> 2\,g/l$). Examples of five-minute SSC time series are given in figures 4.5 and 4.6 so that different types of event (i.e. in terms of time) can be examined. It can be seen (figure 4.6) that periods of high near bed SSC ($> 2\,g/l$) can be maintained for over five minutes or can just be sustained for short bursts of a few minutes.

Variation in bed level from USt data at the lower site is shown in figure 4.7, with a zero mean bed level change line highlighting changes. Some erosion in the first hour is followed by a steady build up of bed sediment during the rest of the tide, resulting in net accretion of approximately 1 cm.

Only the first four pegs could be put in before the tide had flooded too far on the first day, so the other two were established for later deployments afterwards creating a transect of six pegs across the ITZ. Each peg showed some deposition of between $5 - 15\,mm$ (see tables 4.9 and 4.10). Bed samples were taken from near the pegs over the transect and a particle size distribution ($D_{50} = 9\,\mu m$) from a surface sample taken near the upper site is shown in figure 4.8. Shear vane readings were taken over a metre core, the results of which are shown in table 4.8, and the surface measurements are given in tables 4.9 and 4.10 for the 29th and 30th respectively.

4.1.4 Summary

For this calm deployment during Spring tides, light winds blew offshore creating small ripples. Pressure and SSC data were recorded at the primary deployment site and approximately 1 cm deposition was measured over most of the ITZ.

4.2 17/10/91 Deployment

4.2.1 Meteorological and Tidal Conditions

Near gale force winds were experienced on the day with a Neap tide of range $\simeq 4.2\,m$. The direction of the winds and the continued duration of the storm resulted in a very active wave climate. Wind speeds had been below 5 knots and from the Northeast on the 13th, 14th and 15th with stronger winds on the 16th from the West.

Day	Time	Water Depth	Mean Wind Strength	direction
16th	11:53	9.1 m	20 knts	W
16th	18:12	4.4 m	20 knts	W
17th	00:39	8.7 m	25 knts	W
17th	06:35	4.7 m	20 knts	WNW
17th	13:45	8.9 m	25 knts	WNW
17th	19:42	4.7 m	25 knts	WNW

Table 4.4: Meteorological Conditions: 17/10/91

4.2.2 Experimental Technique

For this independent deployment only a single site was selected $\approx 100\,m$ from the HWM where data were recorded onto tape.

Instrumentation

- Bed mounted pressure transducer
- Green infra-red siltmeter (range $2 - 20\,g/l$) mounted 15 cm above bed
- Blue infra-red siltmeter (range $2 - 20\,g/l$) mounted 41 cm above bed
- Partech (range $0 - 5\,g/l$) mounted 46 cm above bed
- Two EMCMs orientated to measure u & w velocity components at a height of 25 cm (Head 2) and 55 cm (Head 1) above bed

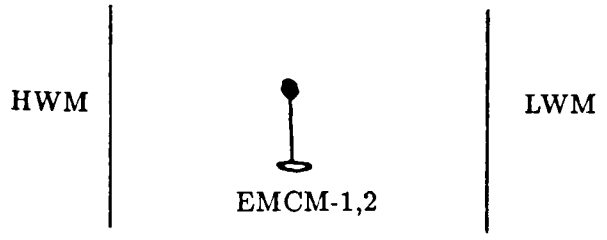

EMCM Orientation

Instrument Failures

The upper siltmeter did not work and there was a problem with the calibration of the Partech. This was a 'double-headed' sensor (two light paths) which can be used to measure low concentrations. It was calibrated after the deployment and was observed to show an increase in voltage with increased SSC (as expected) until $0.75\,g/l$ when the voltage started decreasing with further increasing SSC. This meant that for any one voltage reading there were two possible SSC. Results from this instrument can hence only be qualitative, but are included as they can still provide additional information.

4.2.3 Analysis and Results

Data were recorded continuously onto tape and subsequently segmented into thirteen minute sections of data digitised at 10 Hz. Results are plotted against time with time zero (11:28, 17th) the start of recording and time 400 (18:08, 17th) the end of recording.

Time series of the whole tidal cycle are presented in figures 4.9 (velocity) and 4.10 (h, SSC). The effective digitisation rate is around 0.5 Hz, having been firstly digitised at 1 Hz and then block averaged by two to allow all the data points to be plotted. There appears to be no net current on either EMCM in the deployed orientation. The siltmeter is seen to only show significant response in the shallow water at the beginning and end of data logging. Uncalibrated Partech data are also shown in figure 4.10.

Water depth, H_s, T_z, and U_o calculated from pressure data are presented in figure 4.11. When $h > 1\,m$, $H_s = 60 - 70\,cm$. An increasing trend in T_z from $3.5 - 4.5\,secs$ is observed over the tidal cycle, whilst U_o varies between $50 - 80\,cm/s$. Figure 4.12 shows τ_o, f_w, RE (given by equations 3.2 and 3.3) and K_p. Mean values of RE are 3.0×10^6, $f_w \approx 0.007$ and $\tau_o > 1\,Nm^{-2}$ for the whole tidal cycle.

Figure 4.13 compares zero-crossing periods and wave orbital velocities between both EMCM (U_s) and pressure data (U_o). Figure 4.14 compares wave orbital velocities calculated at the bed and at both EMCM heights, showing little difference in values using linear theory at each height. Mean fluctuations (u') taken from EMCM data and estimations of τ_o are presented in figure 4.15, using friction factor (and U_o), Reynolds stresses and the spectra splitting techniques. An example of the spectra splitting technique applied to the data is shown in figure 4.16. Errors induced by subjectively choosing the wave frequency range to be removed are estimated to be < 15 %. This estimate is based on choosing frequency ranges which over (or under) estimate the wave frequency band (visually). Table 4.12 gives the values of τ_o using this method and also the ratio of the removed wave variance to total variance ($\overline{u}^2$). Over 70% of the total variance (also shown in table 4.12) is wave energy for most sections of the tidal cycle.

Examples of energy density spectra, cumulative normalised energy density, cospectra and wave grouping are presented in figures 4.17-26, taken at three points during the tidal cycle ($h \approx 1\,m$ flood, HW, $h \approx 1\,m$ ebb).

There was a measured bed level change of approximately $2\,cm$ erosion. Moisture content was 134%, bulk density $1370\,kg/m^3$ and dry density $583\,kg/m^3$ at the instrument site after the deployment. These results are summarised in table 4.11. A gravimetrically determined SSC sample of $2.9\,g/l$ was collected from the surf zone around the instrument site. This was the average of three hand collected bottle samples.

4.2.4 Summary

This was the stormiest deployment with near gale force winds creating waves greater than $50\,cm$ in height during a Neap tide. The previous week had seen light winds and $2\,cm$ of mud was eroded from near the deployment site. Pressure, velocity and near bed SSC data were recorded.

4.3 6-7/11/91 Deployment

4.3.1 Meteorological and Tidal Conditions

Near gale force winds were experienced over the two day period with Spring tides of range $\simeq 11.5\,m$. The direction of the winds and the continued duration of the storm resulted in a very active wave climate. The previous few days had been calmer with wind speeds around 10 knots from the North or North-West.

Day	Time	Water Depth	Mean Wind Strength	direction
6th	13:37	1.4 m	10 knts	NW
6th	19:04	13.0 m	25 knts	W
7th	01:58	1.5 m	25 knts	W
7th	07:24	13.1 m	25 knts	W
7th	14:13	1.5 m	22 knts	WSW

Table 4.5: Meteorological Conditions: 6-7/11/91

4.3.2 Experimental Technique

Two sites with reasonably typical bed conditions at $100\,m$ and $175\,m$ from the HWM were selected for this combined deployment. Two tidal cycles were logged.

Instrumentation

Lower site

- Ultra-sonic bedlevel recording device mounted 13.5 cm above the bed
- Bed mounted pressure transducer
- Infra-red siltmeter (range 2-20 g/l) mounted 12 cm above bed
- EMCM orientated to measure u & w velocity components at a height of 53 cm above bed

Upper site

- Ultra-sonic bedlevel recording device mounted 10 cm above the bed
- Bed mounted pressure transducer
- Infra-red siltmeter (range $2 - 20\ g/l$) mounted 12 cm above bed
- 2 EMCMs orientated to measure u & w velocity components at heights of 25 cm and 55 cm above bed respectively
- 2 Partechs (range $0 - 5\ g/l$), Partech A 37 cm above bed and Partech B 70 cm above bed
- 2 Braystoke propellor meters at a height of 55 cm orientated and fixed to measure u velocity

Instrument failures

- The lower site ultra-sonic bed level recorder failed owing to the wrong head being logged
- The lower site pressure transducer only worked for the first tidal cycle
- The lower site EMCM only produced 50% of data due offset problems
- The upper site EMCMs failed due to a leak in the underwater unit
- The upper site siltmeter did not work

Results from Braystoke propellor meters were concluded to be unsatisfactory, because of the problem of reversing oscillatory flow. This meant that the propellers would need to be calibrated for turning both from 'forward' flow and 'backward' flow under waves.

4.3.3 Analysis and Results

The instruments were recorded for 30 minute periods and then downloaded onto floppy disk, a process which took 2-5 minutes, for both tides resulting in 30 files (or runs) of 13 channels of nearly continuous data. Owing to human error there was a break in recording for 30 minutes for the duration of run 9 ($\approx 300\ mins$), hence the figures show a gap during this time. A 30 minute run was split into three 10 minute sections and analysed individually. The results from both tidal cycles are plotted against time, with time zero (15:15, 6th) the start, and time 514 (23:49, 6th) the end of recording of the first tide. Similarly, times 600 - 935 (04:33 - 10:08, 7th) are recording details of the second tide. This second start time (600) does not imply that recording began 86 minutes after the end of the first tide (514), but is simply used to allow both tides to be plotted on the same time axis.

At the upper site, h, H_s, T_z, and U_o for every 10-minute section calculated from pressure data are presented in figure 4.27. H_s are larger on the second tide, varying between $20 - 40\,cm$. An increasing trend in T_z from $3.0 - 5.0\,secs$ is consistent during both tides. Maximum U_o are in the shallow water ($U_o > 30\,cm/s$ for $h < 1\,m$) falling to around $15\,cm/s$ at HW. Again from pressure data, figure 4.28 shows τ_o calculated from equation 3.6 following a similar pattern to U_o with values of around $0.2\,Nm^{-2}$ at HW. f_w varies between $0.008 - 0.02$ and RE between $10^4 - 10^6$ (figure 4.28).

Figures 4.30 and 4.31 show the same parameters as plotted in figures 4.27 and 4.28 but for the lower site. The figures include the limited EMCM data produced at this site where appropriate. The lower site EMCM was affected by a large offset which resulted in some lost data, notably the vertical velocities. This Colnbrook EMCM is not stable enough to give absolute velocities due to excessive zero drift, but velocity fluctuations and zero-crossing periods can be obtained. Pressure data is only available for the first tide, when H_s are observed to increase from around $10\,cm$ at $h = 2\,m$ throughout the tide. A peak in H_s ($\approx 0.5\,m$) is seen at around $400\,mins$ possibly caused by the passing of a large ship.

Figure 4.29 shows SSC variation at the upper site with slightly higher concentrations observed on the second tide. The overall trend is high SSC in the shallow water, decreasing until around HW before increasing again as the tide ebbs and water level drops. At the lower site, SSC at $z = 12\,cm$ is shown in figure 4.32, for concentrations above the instrument lower limit of $2\,g/l$.

Peg heights, and shear vane readings were taken over the transect of the beach prior to the deployment and after the second tide. The pegs showed no overall change in bed level for the two tides. Surface sediment samples were obtained from after the deployment. Tables 4.13 & 4.14 show the results from both days, and figure 4.33 shows a particle size analysis ($D_{50} = 7\,\mu m$) of a sample taken close to the site. A gravimetrically determined SSC sample of $1.98\,g/l$ was taken from the surf zone around the instrument site. This was the average of three hand collected bottle samples.

4.3.4 Summary

During this windy deployment, data from two Spring tides were recorded at two positions on the ITZ. There was no measurable change in bed level, but moisture contents of surface sediment taken after the deployment were low. Pressure data at both sites, some velocities at the lower site and SSC at three heights were measured. The second tide was the windier day and wave heights were correspondingly larger ($\approx 30\,cm$).

4.4 6-7/2/92 Deployment

4.4.1 Meteorological and Tidal Conditions

Near calm wind conditions were experienced over the two day period with Spring tides of range $\simeq 11.5\,m$. The previous week had been very windy with near gale force winds from the west on the 2nd and 3rd, dying out by the 5th and slightly picking up again over the duration of the deployment.

Day	Time	Water Depth	Mean Wind Strength	direction
5th	20:29	12.7 m	5 knts	W
6th	03:12	1.3 m	5 knts	W
6th	08:43	12.9 m	5 knts	WSW
6th	15:31	1.3 m	5 knts	SW
6th	20:57	12.8 m	7 knts	SW
7th	03:42	1.4 m	10 knts	SSW
7th	09:12	12.9 m	7 knts	S
7th	16:00	1.3 m	5 knts	SSW

Table 4.6: Meteorological Conditions: 6-7/2/92

4.4.2 Experimental Technique

A single site was used to enable a more comprehensive deployment over the water column than was possible using two sites over the beach transect as had been done previously (on the July and November combined deployments). The site chosen was approximately $100\,m$ from the HMW.

Instrumentation

- Ultra-sonic bed level transducer mounted $11\,cm$ above the bed
- Bed mounted pressure transducer
- Infra-red siltmeter (range: $2 - 20\,g/l$) mounted $10\,cm$ above bed
- 2 EMCMs orientated to measure u, v & w velocity components at heights of $44\,cm$ (Head 1) and $52\,cm$ (Head 2) above bed
- EMCM orientated to measure u & w velocity components at a height of $82\,cm$ (Head 3) above bed

- 2 Partechs (range: $0 - 5\,g/l$), Partech A $20\,cm$ above bed and Partech B $96\,cm$ above bed
- 3 freely rotating Braystoke propellor meters at heights of $26\,cm$, $49\,cm$ & $69\,cm$ above bed

The orientation of Heads 1 & 2 allows further interpretation of the direction of the tidal current. This orientation, however, implies that the wave orbits normal to normal to the shoreline (U_o) are not being directly measured (as an EMCM allows only measurement across the face) and could result in contaminated data if the angle is too great. Under the calm wave conditions experienced the data collected appear to be good. If the heads were subject to stalling then the horizontal fluctuations would be truncated for part of the wave cycles. Studying the 30 minute runs over smaller time lengths showed that this was not the case.

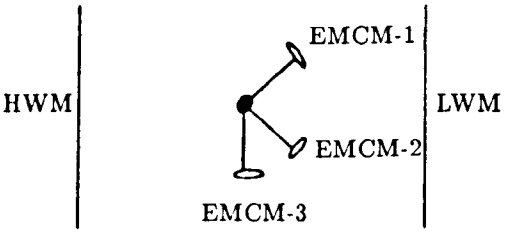

EMCM Orientation

Instrument Failures

Except for the Braystokes, which failed to "freely rotate", all instruments worked for at least some of the time. Various problems including blown fuses and a faulty filter unit resulted in some lost data.

4.4.3 Analysis and Results

The instruments were recorded for 30 minute periods and then downloaded onto floppy disk, a process which took 2-5 minutes, for both tides resulting in 16 files (or runs) of 11 channels of nearly continuous data. A 30 minute run was split into three 10 minute sections and analysed individually. Quantities are plotted against time: the first tide runs from time zero (corresponding to 18:19, 6th; start of run 1) until time 306 (corresponding to 23:25, 6th; end of run 10); and the second tide runs from time 381 (corresponding to 06:36, 7th; start run 11) until time 677 (corresponding to 11:32, 7th; end run 18). The generator stopped once, resulting in a break in recording for 30 minutes for the duration of run 9 (22:37 - 23:05).

Time series of the 30 minute runs for the whole tidal cycle are presented in figures 4.34 (tide 1 - h, SSC) and 4.35 and 4.36 (tide 2 - EMCM and h, SSC). The effective digitisation rate is

around 0.5 Hz, having been firstly digitised at 1 Hz and then block averaged by two to allow all the data points to be plotted.

Water depth, H_s, T_z, and U_o for every 10-minute section calculated from pressure data are presented in figure 4.37. For the first tide $H_s < 3\,cm$ and although larger on the second tide heights are still less than $10\,cm$. Long wave periods are recorded on the first tide, with shorter periods on the second tide ($3.0 - 6.0\,secs$) showing a decreasing trend after HW. U_o are below $2\,cm/s$ for the first tide, and average about $3 - 4\,cm/s$ on the second tide. Again from pressure data, figure 4.38 shows τ_o, f_w, RE and K_p. $RE < 10^4$ and are compared with Reynolds numbers calculated from EMCM data. Values of τ_o are larger on the second tide, and f_w are smaller on the second tide ($0.01 - 0.1$).

EMCM data for the 10 minute sections are presented in figures 4.39-41. The v-component (parallel to shoreline) of the current (figure 4.39) has been calculated from EMCM-1 and EMCM-2 divided by a factor of $cos(\pi/4)$, or $sin(\pi/4)$, respectively. Similarly, if the wave fluctuations are assumed to occur transverse to the shoreline (which would be as expected owing to wave refraction), then horizontal (u) fluctuations can be calculated by dividing the fluctuations by a factor of $sin(\pi/4)$, or $cos(\pi/4)$, respectively. Figure 4.40 shows the horizontal significant velocity (U_s) for each EMCM and a resultant. Figure 4.41 shows the comparison between U_s, W_s and wave orbital velocities calculated from pressure data assuming linear wave theory (equation 2.20), $50\,cm$ above the bed. Reynolds stresses are calculated using the corrected u' and w' and plotted in figure 4.42. Small average values of approximately $0.01\,N/m^2$ are found.

Figure 4.43 presents the mean SSC every 10 minutes from the siltmeter and Partechs. Temporal variations in SSC at each height during the two tides are observed to be quite different. Unfortunately the two Partechs did not work simultaneously; Partech A ($z = 20\,cm$) working for the second tide and Partech B ($z = 96\,cm$) for the first tide. There was little response from the siltmeter throughout the deployment, which had a lower response threshold of $2\,g/l$.

Peg heights, bed samples and shear vane readings were taken over the transect of the beach on both days. Pegs one and six have both been lost, probably due to human interference. Erosion of approximately $1\,cm$ is seen over the whole transect. The instrument site is situated near peg 2. After the deployment moisture contents were lower, with bulk densities and dry densities increased at each sampling site. Tables 4.15 & 4.16 show these results from both days, and figure 4.44 shows a particle size analysis ($D_{50} = 10\,\mu m$) of a sample taken close to the instrument site. Gravimetrically determined SSC samples of $2.9\,g/l$ (19:00, 6th - surf zone near site), $0.4\,g/l$ (09:25, 7th - from HWM), $2.3\,g/l$ (07:30, 7th - surf zone near site) were measured from hand collected bottle samples.

4.4.4 Summary

Light winds blew from the South-West for the two recorded Spring tides. Over the deployment duration wind speeds increased slightly and correspondingly so did wave heights to around $5\,cm$. High moisture contents were noted with around $1\,cm$ of bed sediment was eroded over the two tides. Pressure, velocity and SSC at three heights were successfully logged at a single site.

4.5 5-7/5/93 Deployment

4.5.1 Meteorological and Tidal Conditions

Although quite breezy during the deployment, the direction was generally from North-East and hence offshore. High Spring tides were measured with a range of $\simeq 12.2\,m$. The previous week had seen consistent wind strength ($\approx 10\,knts$), but from a more Westerly-Northern direction. In total four tides were logged, and it was noticeable that during tides 2 and 4 it was windier than for tides 1 and 3.

Day	Time	Water Depth	Mean Wind Strength	direction
5th	00:49	1.3 m	10 knts	E
5th	06:14	13.0 m	10 knts	NE
5th	13:19	1.1 m	20 knts	ENE
5th	18:41	13.2 m	15 knts	E
6th	01:41	0.9 m	10 knts	ENE
6th	07:02	13.4 m	7 knts	NE
6th	14:05	0.9 m	15 knts	NE
6th	19:26	13.5 m	15 knts	E
7th	02:26	0.7 m	10 knts	ENE
7th	07:45	13.5 m	12 knts	NE
7th	14:46	0.9 m	15 knts	NE

Table 4.7: Meteorological Conditions: 5-7/5/93

4.5.2 Experimental Technique

For this final deployment which was independently undertaken (from HR) only a single site was selected $\approx 100\,m$ from the HWM where data were recorded onto tape.

Instrumentation

- Bed mounted pressure transducer
- 'Bed mounted' blue infra-red siltmeter (range $2 - 20\,g/l$)
- Green infra-red siltmeter (range $1 - 15\,g/l$) mounted $5\,cm$ above bed
- Three Partechs (range $0 - 5\,g/l$) mounted 22, 58, and 7 or $80\,cm$ above bed
- Two EMCMs: Head 1 orientated to measure u & w velocity components at a height of $50\,cm$, and Head 2, $16\,cm$ above the bed, measuring u & v velocity components

The 'bed mounted' infra-red siltmeter was pushed into the bed leaving just the sensor head ($1\,cm$ long, $15\,mm$ diameter) protruding above the bed surface. It was hoped that this experiment might lead to a way of either measuring bed level change, or fluid mud formation.

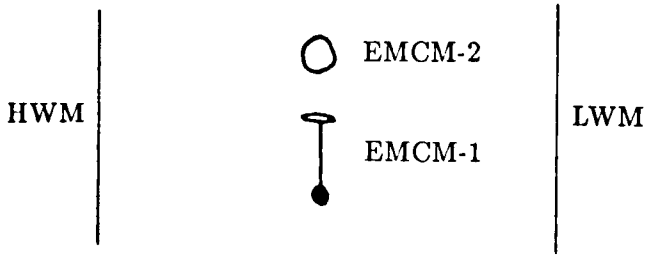

EMCM Orientation

Instrument Failures

Only the pressure transducer failed due to technical difficulties, although this did produce mean water level for most of the third tide. However, human 'interference' resulted in cables being cut on two occasions resulting in no velocity and siltmeter data for tides 2 and 4. The Partechs were spared from this, probably due to having armoured cables.

4.5.3 Analysis and Results

Data were recorded continuously onto tape, and subsequently segmented into thirteen minute sections digitised at 10 Hz. Recording lasted 260 minutes for each tide. Start and end times of the four tides are:

Tide 1 : 17:30 - 21:50, 5th
Tide 2 : 05:50 - 10:10, 6th
Tide 3 : 18:15 - 22:35, 6th

Tide 4 : 06:35 - 10:55, 7th

Time series of the whole tidal cycles are presented in figures 4.45-52. The effective digitisation rate is around 0.5 Hz, having been firstly digitised at 1 Hz and then block averaged by two to allow all the data points to be plotted. Trends in velocity are reasonably consistent, but SSC show different temporal variation during each tide. The bed mounted siltmeter became saturated during part of the first tide, as did the siltmeter at $z = 5\,cm$ during tide 3.

Figure 4.53 presents zero-crossing periods and wave orbital velocities (U_s, W_s) from EMCM data for tide 1. Periods are around 3 *secs* and $U_s < 5\,cm/s$. Velocity fluctuations ($u' < 2\,cm/s$) and RE ($< 10^3$) are shown in figure 4.54. Two methods of estimating τ_o are presented in figure 4.55: using Reynolds stresses and using a friction factor (also shown in figure 4.55) based on using U_s as the wave orbital velocity. Figures 4.56-58 are analogous to figures 4.53-55 but for tide 3. Trends and magnitudes of corresponding data are reasonably similar. Figure 4.58 also shows the spectra splitting technique used to estimate τ_o. Errors induced by subjectively choosing the wave frequency range to be removed are < 5 %. This figure is based on choosing frequency ranges which over (or under) estimate the wave frequency band (visually). Table 4.18 shows τ_o using this method and gives the ratio of the removed wave variance to total energy variance ($\overline{u}^2$). ($\overline{u}^2$ is also shown in the table). Results from the first tide are not included since it was considered repetitive.

Additionally, for tide 3, mean SSC and standard deviations in SSC are plotted against time in figure 4.59. Higher standard deviations are shown in data collected from nearer the bed.

Fall velocities measured using an Owen tube are given in figures 4.60 and 4.61. Both of these samples were taken from in the surf zone around the deployment site. W_{50} of $0.6\,mm/s$ (SSC=$2.41\,g/l$) and $0.15\,mm/s$ (SSC=$0.89\,g/l$) were obtained. Further attempts were made to measure fall velocity from nearer the HWM, but concentrations (and hence W_s) were found to be too low for a $1\,m$ tube to be used (Barton, 1991). These HWM samples did allow SSC of $0.46\,g/l$ on 5/5, $0.42\,g/l$ on 6/5, $0.23\,g/l$ on 7/5 to be recorded.

Table 4.17 shows peg heights, bed surface sample analysis and shear vane readings taken over the transect during the deployment. Pegs one, and four to six have been lost. Deposition occurred on tide 1, erosion on tide 2, deposition again on tide 3 and erosion on tide 4 with $\approx 10\,mm$ being an average level change. Changes in bed level were qualitatively consistent across the transect. Moisture contents (MC), bulk density (BD) and dry density (DD) from surface samples are shown in table 4.17. Two bed samples were taken on 6/5, at 11:30 and 16:00 to investigate the effect of exposure on MC, BD, DD.

4.5.4 Summary

During four Spring tidal cycles, velocity and SSC at four heights were logged. Winds were light and generally offshore. A depositional tide, was followed by erosion, then deposition again preceding erosion. The erosional tides corresponded to visual increases in wave ripples. Unfortunately, some data were lost due to vandalism.

Portishead 29-30/7/91 Shear Vane Strength (Max 33 kPa) (s) indicates sand felt						
Depth (cm)	Peg 1	Peg 2	Peg 3	Peg 4	Peg 5	Peg 6
surface	7.0	6.0	9.0	3.0	0.0	0.0
5	12.0	11.5	11.5	12.5	11.0	13.0
10	13.0	10.0	12.0	12.5	14.0	16.0
15	13.0	14.0	13.0	13.0	13.5	19.0 (s)
20	12.0	11.0	15.0	18.0 (s)	14.5	16.5
25	12.0	12.5	16.0	14.0	14.5	15.0
30	11.0	14.0	12.0	13.0	20.0	24.0 (s)
35	12.0	15.0	14.0	16.5	18.0 (s)	23.0 (s)
40	12.0	13.5	23.0 (s)	19.5 (s)	16.0	25.5 (s)
45	11.5	14.0	15.0	16.0	17.0	28.0 (s)
50	11.0	12.0	16.0	15.0	19.0	22.0
55	12.0	14.0	15.0	21.5 (s)	24.0 (s)	31.0 (s)
60	Bed	17.5 (s)	18.5	29.0 (s)	Bed	29.0 (s)
65		14.0	28.5 (s)	19.0		22.0 (s)
70		12.5	17.0	30.0 (s)		33+ (s)
75		13.5	27.0 (s)	25.5		21.0
80		13.0	17.0	33+		33+ (s)
85		14.0	27.0 (s)	33+		33+ (s)
90		15.0	17.0	33+		Bed
95		20.5 (s)	16.0	Bed		
110		18.5 (s)	21.5 (s)			

Table 4.8: Bed Sediment Shear Vane Profile

Portishead		29/7/91			
Site	Peg Height cm	Moisture Content %	Bulk Density kg/m^3	Shear Vane	kPa
Peg 1	25.7	185	–	surf	7.0
				surf-5	12.0
				surf-10	13.0
Peg 2	19.8	169	–	surf	6.0
				surf-5	11.5
				surf-10	10.0
Peg 3	21.0	178	–	surf	9.0
				surf-5	11.5
				surf-10	12.0
Peg 4	28.0	247	–	surf	3.0
				surf-5	12.5
				surf-10	12.5
Peg 5	–	–	–	surf	–
				surf-5	–
				surf-10	–
Peg 6	–	–	–	surf	–
				surf-5	–
				surf-10	–

Table 4.9: Transect analysis: 29/7/91

Portishead		30/7/91			
Site	Peg Height cm	Moisture Content %	Bulk Density kg/m^3	Shear Vane kPa	
Peg 1	24.2	–	–	surf	–
				surf-5	–
				surf-10	–
Peg 2	19.2	–	–	surf	–
				surf-5	–
				surf-10	–
Peg 3	19.7	–	–	surf	–
				surf-5	–
				surf-10	–
Peg 4	27.3	–	–	surf	–
				surf-5	–
				surf-10	12.5
Peg 5	27.0	272	–	surf	0
				surf-5	11.0
				surf-10	14.0
Peg 6	21.0	290	–	surf	0
				surf-5	13.0
				surf-10	16.0

Table 4.10: Transect analysis: 30/7/91

Portishead				17/10/91	
Site	Bed Change cm	MC %	BD kg/m^3	DD kg/m^3	Shear Vane kPa
Upper Site	−2	135	1370	583	surf –
					surf-5 –
					surf-10 –

Table 4.11: Transect analysis: 17/10/91. MC - Moisture Content, BD - Bulk Density, DD - Dry Density. Bed Change: erosion (-), Deposition (+).

Portishead 17/10/91 Spectra Splitting Data					
Time (mins)	τ_o (Nm^{-2})	$\overline{u}_w^2 : \overline{u}^2$ (variance ratio)	τ_o (Nm^{-2})	$\overline{u}_w^2 : \overline{u}^2$ (variance ratio)	$\overline{u}^2$ $(cm/s)^2$ Average
	Head 1		Head 2		
0	-	-	-	-	-
15	-	-	-	-	-
31	-	-	-	-	-
46	-	-	-	-	-
62	3.21	0.55	4.29	0.46	795
78	1.71	0.75	1.67	0.77	703
94	1.44	0.75	1.72	0.67	669
110	0.98	0.83	0.95	0.82	542
130	0.68	0.85	0.73	0.81	545
144	2.26	0.58	2.22	0.51	414
167	0.53	0.86	0.58	0.76	508
182	0.69	0.80	0.82	0.65	306
198	0.46	0.86	0.47	0.71	294
213	0.46	0.86	0.47	0.71	244
229	0.46	0.87	0.56	0.73	244
244	0.62	0.76	0.50	0.67	275
260	0.59	0.76	0.52	0.60	206
275	0.75	0.78	0.65	0.65	189
291	0.68	0.79	0.58	0.73	267
306	1.41	0.76	1.77	0.67	553
322	2.08	0.72	2.84	0.64	739
353	3.67	0.57	2.73	0.51	585
368	-	-	-	-	-

Table 4.12: Shear stress calculated from spectra splitting technique, and ratio of (truncated) wave energy to total energy. (HW $\approx 200\,mins$).

Portishead		6/11/91			
Site	Peg Height cm	Moisture Content %	Bulk Density kg/m^3	Shear Vane	kPa
Peg 1	23.0	–	–	surf	1.0
				surf-5	10.0
				surf-10	13.5
Peg 2	20.5	–	–	surf	5.5
				surf-5	12.5
				surf-10	12.0
Peg 3	24.0	–	–	surf	11.5
				surf-5	14.5
				surf-10	14.0
Peg 4	34.0	–	–	surf	12.5
				surf-5	13.5
				surf-10	15.5
Peg 5	36.2	–	–	surf	13.0
				surf-5	14.5
				surf-10	14.5
Peg 6	–	–	–	surf	–
				surf-5	–
				surf-10	–
Upper Site	–	–	–	surf	–
				surf-5	–
				surf-10	–
Lower Site	–	–	–	surf	2.5
				surf-5	1.0
				surf-10	7.5

Table 4.13: Transect analysis: 6/11/91

Portishead				7/11/91		
Site	Peg Height cm	MC %	BD kg/m^3	DD kg/m^3	Shear Vane	kPa
Peg 1	23.0	133	1259	540	surf	0
					surf-5	9.5
					surf-10	13.5
Peg 2	20.5	92	1443	751	surf	3.0
					surf-5	11.0
					surf-10	11.5
Peg 3	24.0	69	1537	905	surf	11.5
					surf-5	14.0
					surf-10	14.0
Peg 4	34.0	68	1525	909	surf	12.0
					surf-5	14.5
					surf-10	14.5
Peg 5	35.0	64	1544	950	surf	13.5
					surf-5	14.5
					surf-10	14.5
Peg 6	–	–	–	–	surf	–
					surf-5	–
					surf-10	–
Upper Site	–	97	1316	667	surf	1.5
					surf-5	7.0
					surf-10	11.5
Lower Site	–	36	1673(s)	1228(s)	surf	5.5
					surf-5	7.0
					surf-10	4.5

Table 4.14: Transect analysis: 7/11/91. MC - Moisture Content, BD - Bulk Density, DD - Dry Density. Samples with noticable sand content marked (s).

Portishead				6/2/92	15:30
Site	Peg Height cm	MC %	BD kg/m^3	DD kg/m^3	Shear Vane kPa
Peg 1	*lost*	–	–	–	surf –
					surf-5 –
					surf-10 –
Peg 2	19.5	165	1291	488	surf 2.5
					surf-5 11.0
					surf-10 10.5
Peg 3	29.0	218	1257	395	surf 9.0
					surf-5 13.5
					surf-10 12.0
Peg 4	25.0	252	1259	358	surf 0
					surf-5 2.0
					surf-10 12.5
Peg 5	28.0	179	1295	464	surf 0
					surf-5 10.5
					surf-10 13.5
Peg 6	*lost*	–	–	–	surf –
					surf-5 –
					surf-10 –
Site	–	156	1299	508	surf 2.0
					surf-5 11.0
					surf-10 12.0

Table 4.15: Transect analysis: 6/2/92. (MC - Moisture Content, BD - Bulk Density, DD - Dry Density.)

Portishead				7/2/92	15:00
Site	Peg Height cm	MC %	BD kg/m^3	DD kg/m^3	Shear Vane kPa
Peg 1	*lost*	–	–	–	surf –
					surf-5 –
					surf-10 –
Peg 2	20.5	133	1343	575	surf 4.5
					surf-5 8.5
					surf-10 9.0
Peg 3	30.0	90	1516	798	surf 9.5
					surf-5 12.0
					surf-10 12.0
Peg 4	26.8	172	1389	484	surf 0
					surf-5 5.0
					surf-10 12.5
Peg 5	30.5	138	1372	576	surf 0
					surf-5 11.5
					surf-10 1305
Peg 6	*lost*	–	–	–	surf –
					surf-5 –
					surf-10 –
Site	–	107	1494	721	surf 7.5
					surf-5 11.0
					surf-10 12.0

Table 4.16: Transect analysis: 7/2/92. (MC - Moisture Content, BD - Bulk Density, DD - Dry Density)

Portishead					5-7/5/93 Surface Sediment		
Date,time	Peg Height cm	MC %	BD kg/m^3	DD kg/m^3	Shear Vane kPa	Peg 2 Height cm	Peg 3 Height cm
5/5, 14:00	5.5	220	1215	380	surf 0 surf-5 0 surf-10 7.5	5.5	5.5
6/5, 05:30	4.5	212	1233	395		5.0	5.1
6/5, 11:30	5.2	209	1182	382		4.8	5.0
6/5, 16:00		177	1291	466			
7/5, 06:00	4.0	189	1221	422		4.0	3.5
7/5, 15:00	5.0	135	1360	580		4.8	4.5

Table 4.17: Surface sediment analysis: 5-7/5/93. (MC - Moisture Content Ratio, BD - Bulk Density, DD - Dry Density)

Portishead (Tide 3) 6/5/93 Spectra Splitting Data			
Time (mins)	τ_o (Nm^{-2})	$\overline{u_w^2} : \overline{u^2}$ (variance ratio)	$\overline{u^2}$ $(cm/s)^2$
15	-	-	-
31	-	-	-
46	-	-	-
62	0.0057	0.28	0.36
77	0.0065	0.14	0.23
93	0.0050	0.17	0.26
109	0.0050	0.54	0.49
124	0.0028	0.56	0.26
140	0.0028	0.61	0.31
156	0.0079	0.31	0.55
171	0.0345	0.15	2.07
194	0.0322	0.18	1.93
210	0.0041	0.44	0.32
225	0.0087	0.21	0.53
241	0.0841	0.21	1.75

Table 4.18: Shear stress calculated from spectra splitting technique, and ratio of (truncated) wave energy to total energy. (HW $\approx 130\,mins.$)

Chapter 5

Discussion of Field Results

5.1 Wave Characteristics

As would be expected from an exposed estuary such as the Severn, a prolonged storm can generate a considerable wave climate over a spectrum of frequencies. Wave characteristics are primarily governed by wind speed, direction and duration, since it is the shear exerted by the wind which generates the waves, the direction which determines the area over which the shear is exerted and the duration which controls the length of time for which the shear is applied. Methods of predicting wave heights and periods are thus based on these parameters. However, results from this field study show that in the near shore, interactions with currents and local topography mean that prediction can be difficult.

5.1.1 Validity of Linear Wave Theory

Tables 5.2-5.5 show parameters H/λ, $H\lambda^2/h^3$ ($Ursell parameter$) and H/h which can be used to gauge the validity of linear wave theory (see section 2.2.5). $H/\lambda \ll 1$ is reasonably satisfied by all data. $H/h < 0.78$ is the definition of waves of maximum height, and is an approximation to the breaking criteria (equation 2.15). It is satisfied for nearly all data except the few data in the shallow water at the start and end of recording in 11/91 and 10/91. The Ursell parameter condition ($H\lambda^2/h^3 < 1$) is harder to satisfy except for the calmer deployments of 2/92 and 7/91 (and presumably 5/93), when wave heights are small. The large Ursell parameter values are a consequence of large H/h ratios. Cnoidal theory is suggested for values of the Ursell parameter greater than 26 (see equation 2.12), and linear theory is a better approximation up this value. If this reduced restriction is applied, it is seen that most data now are reasonably suited to linear wave theory. A further validation is the comparison between wave orbital velocities taken either directly from EMCM data, or calculated from pressure data using linear wave theory (discussed in section 5.1.4). It should be noted that there are always limitations

in any wave theory, which should be considered when conclusions are drawn.

5.1.2 Wave Heights and Periods

Significant wave heights calculated from bed mounted pressure transducers at Portishead have covered a range of values. During the 10/91 deployment, wave heights of over 70 *cm* were recorded, in contrast to a calm deployment (e.g. 7/91) when heights were less than 5 *cm*. Zero-crossing wave periods of $2-6$ *secs* have been measured at the site and are consistent with the wave frequency peak in spectra. Wave periods throughout a tidal cycle on the ITZ are significantly longer than those predicted in the main channel at Portishead by a wave ray model (table 2.1: $T = 1-2.5$ *secs*), suggesting wave-current interactions may be an important influence. If predicted wave periods were required in sediment transport calculations (e.g. to estimate bed shear stress) errors could be large. Temporal variations in height and period during tidal cycles can crudely be categorised into 'calm' and 'storm' deployments.

On calm deployments (7/91, 2/92, 5/93), the underlying trend in wave height is decreasing over the tidal cycle (see figures 4.1 and 4.37). Wave periods are observed to increase on the flood until around HW, followed by a decrease on the ebb (figures 4.1 and 4.37). Data from the first tide in 2/92 (figure 4.37) are an exception, when it is suggested that the resolution of the pressure transducer is insufficient to measure the small pressure fluctuations associated with these small waves (discussed further in this section). The periodic trends during a tidal cycle can also be observed in pressure spectra by a shift in frequency ($f = 1/T$) of the wave peak, hence this is not a problem of analysis technique (not included, but can be inferred from energy density spectra, shown at three points during the tidal cycle for the 10/91 data (figures 4.17-19; $T_p \approx 3.3-4.2$) if compared with zero-crossing periods ($T_z \approx 3.5-4.5$) shown in figure 4.11.

The obvious explanation for a decrease in wave height is a decrease in wind speed. However, since the decreasing trend can be seen during each calm deployment, it seems unlikely that the wind dropped on each occasion and the wind data do not imply this to be the case, so another mechanism is involved. The smaller wave heights on the ebb tide could be explained by interactions with this relatively opposing current. Visual observations at the site noted a 'front' between the main channel faster water and the slacker water above the ITZ, as the current is diverted by Portishead Point during the ebb tide (see plate 10); the surface of the slacker water appearing calmer than the faster water. The ebbing tide opposes waves generated by prevailing Westerlies possibly causing wave height attenuation in the main channel resulting in smaller wave heights on the ITZ. Kemp & Simons (1982, 1983) laboratory work concludes that an opposing current serves to increase wave height attenuation, so there is some evidence to support this hypothesis.

Since the variation in wave period correlates with water depth (figures 4.1 and 4.37) there are three main possibilities for explanation. The large tidal range in the Severn Estuary (up to 14 m) means that considerable extra surface water area is produced at HW, as well as

reducing the influence of areas that are shallow at LW - this might be thought of as creating a better quality fetch. At Portishead, for example, the wetted estuary cross-section at HW is approximately 50% wider. This could allow longer period waves to be generated and allow them to propagate further. However, increased periods would probably be coincident with increased wave heights if this was the cause.

Secondly, current interactions with waves are known to vary the wavelength and hence period, so both flood and ebb tidal currents could interact with the waves changing the wave period. The lack of dominant shorter frequency waves ($< 1\,sec$) as predicted by table 2.1, can also be explained by interactions with opposing currents. Waves with periods below about 1 *sec.* would not be able to propagate against a current of around $2\,m/s$ (i.e. max. Spring tide current). Hence the current could serve to filter out the higher frequency waves.

Thirdly, a calculation of pressure attenuation with depth, based on a small wave of $5\,cm$, $1sec$ (i.e. high frequency) in both $1\,m$ and $4\,m$ water depth shows that the resolution of the pressure sensor is near its limit in the deeper case. This limitation (due to the small wave size) could manifest itself as an apparent increase in period at HW. This final explanation is used to explain the particularly long periods during the first tide in 2/92 (figure 4.37) - the waves are so small that pressure fluctuations can hardly be resolved and the period is unrealistically high (up to 10 *secs*). Larger waves with smaller periods on the following tide support this argument.

It is therefore suggested that on calm days the tidal current serves to prevent high frequency waves ($T_z < 1\,sec$) from reaching the ITZ with the ebb current attenuating wave heights. The resolution of the pressure transducer is insufficient to measure wave periods accurately when water depths increase much above $1\,m$ for these small waves ($H_s < 5\,cm$) so causing an apparent increase in period as a function of water depth.

On windier deployments (10/91, 11/91; see figures 4.11 and 4.27) wave heights show no significant trends once the ratio of wave height to water depth has exceeded around 0.5, or the Ursell parameter has exceeded around 50 (see tablees 5.3 and 5.4). This is when the waves are near breaking or broken, and linear wave theory is less applicable, and explains why the wave heights appear to be reduced in the shallow water at the start and end of recording (see figure 4.11). Wave periods are observed to increase throughout the tidal cycle from around $3-5\,secs$ on both occasions (figures 4.11 and 4.27).

Although the increasing periodic trend can be explained by increased storm duration or intensity, this is contradicted by the two 'identical' periodic patterns in 11/91 on consecutive tides. Also similar periods at each stage in the tidal cycle, at this site, have been found to be consistent on almost every deployment. Increased storm intensity probably accounts for the larger wave heights on the second tide in 11/91, but it seems more likely that periodic trends during a tidal cycle are governed by the larger fetch at HW and by wave-current interactions. The larger fetch at HW allows the generation of longer waves which are now able to propagate onto the ITZ continuing into the ebb phase. This may be enhanced by the influences of the tidal currents, which can prevent high frequency waves from propagating onto the ITZ,

as previously discussed. The ebb tide is more opposing wave propagation, hence periods are increased.

It is proposed that, in general, current interactions on the ebb attenuate wave heights, the effects of which are more observable for small waves $< 10\,cm$. Larger storm waves ($30 - 50\,cm$) seem to have less difficulty in propagating against the ebb current than the smaller waves of the calm deployments and the increased fetch at HW allows longer period waves to develop. Both flood and ebb tidal currents seem to 'filter' the wave period by preventing shorter period waves from propagating onto the ITZ, an effect which is more dominant during the ebb tide. This explains why wave periods were consistently measured from $3 - 5\,secs$ and periods are longer than predicted in table 2.1. The upper limit would be bound by the restricted fetch of the estuary (and by storm duration).

5.1.3 Wind-Wave Relationship

Predicted wave climates for Portishead main channel (see table 2.1) provide quite unrealistic wave characteristics in the near shore, particularly for the wave periods which have been observed to be much longer. Wave heights taken from the table are very sensitive to wind direction, making it difficult to compare the predicted heights with the results from this field study, unless very accurate wind data are acquired. Direction and strength of the wind data in this study are based on an average of data from Cardiff made at three hourly intervals. This is insufficient to test whether the table provides good estimates of wave height. Predictions based on fetch and duration (see figure 2.2) are really aimed at coastal or offshore structures (minimum $H_s = 0.5\,m$, $T_z = 2\,secs$) and hence are not scaled down enough for the short period, small height waves to be found in an estuary. If significant wave heights and periods were required for sediment transport modelling purposes a higher degree of accuracy would almost certainly be required.

Field data collected at Portishead show that any wind blowing from the Westerly quarter (SW-NW) is capable of producing waves which can influence erosion. During the 5/93 deployment quite high winds (up to $20\,knots$) were experienced but did not generate waves greater than a few centimetres due to their direction (Easterly) resulting in no fetch. The limited data (SW-NW) are plotted as (high water) wave height (H_{HW}) against wind speed (U_w) in figure 5.1. A best fit regression line has a correlation of 0.86

$$H_{HW} = 2.56\,U_w - 11.0 \qquad U_w > 5\ knots \tag{5.1}$$

where H_{HW} is in centimetres, and U_w is the average wind speed in knots. To improve the resolution in direction more field studies need to be made. Equation 5.1 is cautiously suggested to be applicable for winds from the Westerly quarter of duration of over 6 hours. Wave periods have been consistently measured at around $3 - 5\,secs$ both from pressure and EMCM data.

5.1.4 Wave Velocities and Periods via EMCM and Pressure Transducer

Before comparing data from these two instruments it is worth looking at the statistical relationships between EMCM velocity data. Many researchers use statistical relations to relate different surface wave parameters and, assuming that a similar reasoning can be applied to velocities (see e.g. Myrhaug *et al.*, 1992), then it is expected that the standard deviation (u') should be half the significant velocity (U_s). The 10/91 data (compare figures 4.15 and 4.13) and 5/93 data (figures 4.53 and 4.54 (tide 1) and figures 4.56 and 4.57 (tide 3)) show u' and U_s, respectively, and it can be seen that this ratio between standard deviation and significant velocity does not hold and instead larger ratios are found. A mean ratio U_s/u' of 4.0 is found for 10/91 data and 3.0 is found for 5/93 data. It is proposed that this is due to wave grouping. The larger waves in a group will tend to fall into the upper third of wave heights, once sorted into increasing order of height, so that the significant velocity will effectively be a measure of these larger waves giving a larger value than in a 'random' sea. The standard deviation will take account of all waves measured, thus being a measure of considerably smaller magnitude resulting in larger ratios of U_s/u' than expected. Hence on the ITZ (when grouping is present) the usual statistical relationships between wave data cannot be used with any confidence and comparisons between velocity data from different sources using alternative definitions of velocity should be made with these considerations in mind.

Data from 10/91 and 2/92 can be used for comparison of wave orbital velocities and periods between EMCMs and pressure transducers. Data from the 11/91 deployment also allow some comparison (figure 4.30), but these EMCM results are taken from the Colnbrook EMCM, which has been found to be less reliable than the Valeport EMCMs. In particular, zero-crossing periods can be suspect due to occasional zero offset jumps. These data are therefore excluded from the following discussion, although both orbital velocities and periods compare quite well (better than a factor of two) with pressure data.

Wave periods taken from EMCM and pressure data from the 10/91 deployment compare favourably (figure 4.13). This figure also shows comparison between wave bed orbital velocities from pressure data (U_o) and significant velocities (U_s) calculated from EMCMs at the two heights (25 cm and 55 cm). Figure 4.14 compares wave orbital velocities calculated from pressure data using linear wave theory at the two EMCM heights with the bed value (U_o), showing that differences are small ($\approx 2\,cm/s$) at each height, except in the shallow water (up to $20\,cm/s$). This implies it is reasonable to compare U_o with U_s taken from either height. However, it can be seen (in figure 4.13) that U_o compare much better with the upper EMCM-1 (55 cm) and there are considerable (up to 40% at HW) differences between the two EMCM measuring heights with better agreement in shallower water. The resolution of EMCMs is such that this is not an error of measurement. When the vertical fluctuations are studied (figure 4.15) it is noted that, in contrast, the vertical wave velocities are greater for the lower EMCM. Vertical velocities are very sensitive to sensor alignment, so these anomalies could be explained by horizontal velocities contaminating the vertical velocities. The fact that there is such a large difference in horizontal wave orbital velocities ($\approx 25\%$) in the two heights at HW is difficult to explain simply by sensor misalignment, as this would require around 12 degrees

error. Previous fieldwork with this system (Darbyshire, 1991) has estimated errors to be less than 5 degrees, suggesting an alternative explanation is likely. This could possibly be explained by the existence of a wave-current boundary layer. To confirm this hypothesis requires further vertical profiles of velocity (at least three points) for large wave conditions. Another possibility is periodic vortex shedding from bed forms reaching the lower EMCM but dissipating energy with height so not reaching the upper EMCM. Although the bed is generally considered flat, runnels down the beach have been observed on occasions. Shed vortices would manifest as an increase in the energy in the wave frequency band of energy density spectra at the lower measuring height, and would be more noticeable in the w component since the magnitude of vertical velocities is much smaller than u velocities. Differences in turbulent energy would, however, also be expected at the two measuring heights. Although slightly larger values of turbulent energy are observed in the 10/91 data at the lower height, this increase falls within error estimations of the truncation technique and could be just leakage from the wave peak. Since the additional (vertical) variance at the lower height is mostly confined to the wave frequency band, this explanation also seems unlikely. A further possibility is that although the sensors are actually aligned well in a vertical plane, the beach slope has an influence on the resultant vertical and horizontal velocity direction. This boundary condition would have greatest effect nearer the bed. This seems the most satisfactory explanation, as this is then a mechanism for enhancing misalignment (which all the 'symptoms' suggest) but requires further experiments for confirmation.

EMCM data from the 2/92 deployment are shown in figures 4.40 and 4.41. The EMCMs were orientated at 45 degrees to the shoreline as shown in section 4.4.2 (both approximately 50 cm above the bed), hence to rotate them into the u and v components the velocities were divided by a factor of $1/\sqrt{2}$ as discussed in section 4.4.3, with the resultant the mean of the two EMCM values. Figure 4.40 shows separate horizontal significant velocities and their resultant and figure 4.41 compares the resultant U_s and W_s from EMCM data with U_o and W_o at 50 cm calculated from pressure data. EMCM-1 measures larger horizontal velocities than EMCM-2 (figure 4.40 - nearly double at times), which are probably associated with the orientation relative to wave direction (see section 4.4.2), but vertical velocities are smaller than EMCM-2 (figure 4.41). This may be due to vertical misalignment with EMCM-2, with better alignment for EMCM-1. Vertical velocities would be quite sensitive to contamination from (order of magnitude larger) horizontal velocity component due to misalignment, which would also have the effect of reducing horizontal velocities. A misalignment of 6 degrees would create the necessary difference of 1 cm/s in vertical velocities. The overall comparison of the 2/92 data, shows that EMCM significant velocities are slightly larger (0-20%) than U_o calculated from pressure data, suggesting a possible underestimate in U_o used in subsequent shear stress calculations. Considering the averaging of the two heads and the assumption that maximum horizontal wave velocities are $\pi/4$ to the EMCM orientation, these differences are considered reasonable.

The 5/93 data (figures 4.53-tide 1 and 4.56-tide 3) show only small ($< 1\ cm/s$) differences in the velocities at the two EMCM heights (16 and 50 cm). This is to be expected since the waves are small.

Using linear wave theory to calculate wave orbital velocities from pressure data has been shown to be comparable to significant wave orbital velocities calculated from EMCM time series. The height of the EMCM relative to the bed has been shown to be significant in terms of both horizontal and vertical wave velocities. Significant velocities made 50 *cm* above the bed are within 20% and mostly within 5% of orbital velocities calculated from pressure data. A number of possible explanations have been suggested for the variations in velocity data at each measuring height and it is concluded that the influence of beach slope on sensor misalignment is the most likely cause of differences.

5.1.5 Wave Breaking

Estimates of energy dissipation under breaking waves (D_B) have been made by applying the bore analogy to breaking waves (see section 2.2; equation 2.34), which are then compared with energy dissipation under non-breaking waves ($D_{NB} = \tau_o U_o$). Table 5.6 gives approximate values of D_{NB} from each deployment at three depths during the tidal cycle. A range of wave heights and periods are used to construct table 5.7 giving estimates of D_B considered to cover the different deployments. Comparing values from the two tables it can be seen that D_B is between $10^2 - 10^3$ times larger than D_{NB}.

The values of D_B should be viewed as a first approximation, and it should be noted that the bore analogy has been applied irrespective of breaker type, which have been both plunging and spilling (see table 5.8). It might be considered that the method is more appropriate to spilling breakers, as these are more analogous to a bore. Also, the length scale of breaking has been taken as the wave length, and it is possible that values of D_B could be even larger if the distance over which the waves break is smaller. However, the overriding implication that the rate of dissipation of energy as waves break is so much larger than under non-breaking waves, means that significant erosion can be expected to occur at this time if the bed surface is sufficiently weak. Even when waves are little more than ripples (5 *cm*), dissipation rates when breaking are as large as non-breaking 60 *cm* waves in 1 *m* of water. These results (with antecedent surface sediment conditions) help to explain why the erosion rate due to the small waves during 2/92 was almost as large as those during the stormy deployment of 10/91.

5.1.6 Wave Grouping

As described in section 2.2.4, groups of waves have been observed to form. Examples of wave grouping can be seen in velocity data for the 10/91 deployment shown in figures 4.24-4.26. This phenomenon is mentioned at this stage, since it has been observed in data and hence could be an additional mechanism in sediment transport on ITZs. The calculations of significant wave heights and periods are based only on variations from the mean, so "groupiness", and the effects on sediment transport are not being considered. Correlating resuspension with the grouping frequency has only been attempted on a visual basis by comparing time series of SSC

and H_s without obvious identification of any influence, although effects are probably most significant in the surf zone. Future work might consider this aspect.

5.2 Wave Attenuation due to Bed Interactions

Attenuation of waves due to interactions with the bed as they propagated over the ITZ proved to be less significant than expected, although the data set is limited. From observations made in the field during all deployments wave height attenuation as waves propagated across the ITZ was visually undetectable. This is in contrast to some reported attenuation observations discussed in section 2.2.5, when waves were seen to be totally attenuated within $4 - 8\,\lambda$ (for example). During the 11/91 deployment when two pressure transducers were used successfully, wave heights can be seen to be maintained over the $75\,m$ between sites (compare figures 4.27 and 4.30). Wave lengths are approximately $20 - 25\,m$.

Dynamic attenuation by bed deformation must require that the bed is suitably flexible, but not so weak that it is eroded and entrained into the water column. During the 11/91 deployment when wave heights at two nodes were recorded, the bed had been eroded down to the over consolidated clay, which would probably be too strong to deform. Presumably attenuation would be greatest when a sustained period of accretion allowed the build up of a thick surface layer of high moisture content. The observations described in Chapter 2 all were made above fluidised bed layers $10 - 100\,cm$ thick. At Portishead shear vane profiles never suggested that any fluidised mud could extend more than a few centimetres. Measured SSC, also, did not suggest that any high concentration suspensions $> 10\,g/l$ existed, or if they did then they did not extend more than a few centimetres from the bed. For these reasons attenuation results at this site for the range of conditions observed were perhaps not unexpected.

More research into this area is needed to quantify attenuation rates and at preferably more than two nodes for a wider range of antecedent bed conditions. However, from these initial results and observations, the engineering significance may not warrant the scientific interest at this site.

5.3 Tidal Currents on the ITZ

Estuarine topography is observed to influence both the direction and magnitude of tidal currents significantly. In the main channel near Portishead tidal currents of over $2\,m/s$ were recorded during Spring tides, and during Neap tides maximum velocities of around $0.75\,m/s$ were also measured during tidal surveys of the Severn Estuary (HRS, 1981). On the ITZ at Portishead much lower velocities were measured due to the sheltering effects of the two protective headlands - Portishead Point and Black Nore. Components of the current are u^+ down ITZ transect and v^+ parallel to shoreline, flood direction. Current data were recorded in 10/91

(Neap - figure 4.9), 2/92 (Spring - figures 4.35, 4.39) and 5/93 (Springs - figures 4.45 (tide 1), 4.49 (tide 3)). The most continuous data are from the 5/93 deployment. An analysis of the tidal current on the ITZ has emerged based on the interpretation of the various data measured at a point approximately 100 m from MHW.

During the two Spring tides recorded in 5/93 (figures 4.45 and 4.49), a weak current ($< 5\,cm/s$) was measured during the **flood** tide in the opposite direction to the main channel flood (v^+) except for a period of around 20 $mins$ at $t = 30\,mins$ when velocities were larger (up to $10\,cm/s$). There was no measurable current in the u-direction at either instrument height (16 and 50 cm) during the flood phase. These results correspond to data from 2/92 when velocities were again small on the flood (figure 4.35). On this occasion the current shows more variation in strength and direction, which may be explained by the EMCM orientation for this deployment not being ideal to measure this transverse current.

Velocities are approximately zero **at HW** and are followed by an acceleration period as the tide **ebbs**. This causes an increase in velocity both in the u and v directions lasting around $30 - 45\,mins$ (see figures 4.45 and 4.49). The v component is positive and so is against the main channel ebb direction, and the u component is from HWM - LWM. This is consistent with the 2/92 data (figure 4.35), when only EMCM-1 is orientated correctly to measure this resultant direction. There appears to be two acceleration periods on this occasion, which is as yet unexplained. From the 5/93 data (EMCM-2) the more dominant direction appears to be the v component. These results suggest the assumption that the current was longshore (see section 4.4) when calculating the resultant current from the two EMCMs for the 2/92 data (figure 4.39) are incorrect.

The 10/91 data (figure 4.9) show no significant current at any time during this Neap tide. The orientation of the EMCM (see section 4.2.2) means that any acceleration after HW would be difficult to detect and since the maximum measured velocities on the Spring tides have only been 15 cm/s this is perhaps not unexpected, due to the reduced main channel current. These data are useful in confirming that the EMCMs are subject to little zero drift.

The combination of velocity data is interpreted as two tidal eddies forming over the ITZ created by the headlands Black Nore and Portishead Point (see figure 3.1) on the flood and ebb tide, respectively. A sketch is shown below. The proximity of the site position explains why the ebb eddy is more vigorous as it is nearer to Portishead Point. These tidal currents can have both advective, depositional and resuspension influences (see sections 5.9 and 5.10).

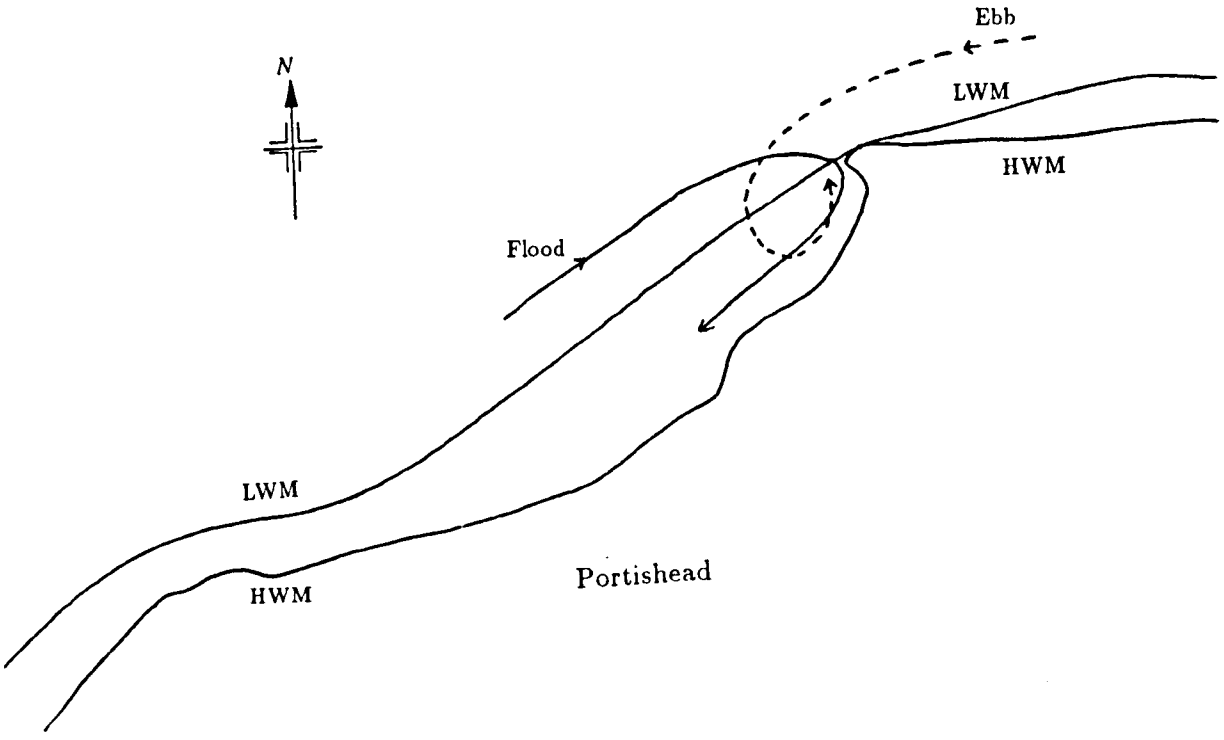

Figure 5.4: Interpretation of tidal currents on ITZ at Portishead

5.4 Estimating Bed Shear Stress

Three methods of estimating bed shear stress have been used. These are outlined in sections 2.2.9 and 3.1.5 and will be referred to as friction factor, Reynolds stresses and Soulsby & Humphery (1989) spectra splitting method.

5.4.1 Reynolds Stress

Reynolds stresses have been evaluated when velocity data were available and are shown in figures 4.15 (10/91), 4.42 (2/92) 4.55 and 4.58 (5/93). The stresses are solely based on $\overline{u'w'}$ correlation, hence take no account of $\overline{v'w'}$. Other workers have commented on the sensitivity of Reynolds stress to sensor misalignment (Soulsby, 1989; Huntley, 1988 - discussed in section 2.2.9). Huntley mentions attempts at re-aligning the axes during subsequent analysis, concluding that none are reliable as yet. These problems are enhanced for these data, since currents are so small. Considerable efforts were made to try and minimise vertical misalignment when instruments were deployed, although it is recognised that the accuracy of alignment necessary

quoted by Huntley (< 0.1 degree) will never be attainable in the field. A further problem may be the effect of the beach slope on resultant directions as discussed earlier (section 5.1.4).

The assumption that vertical and horizontal wave velocities are in quadrature, potentially means that the method can be used successfully. However, cospectra (examples in figure 4.23) show that this is not the case as there is a prominent peak in the wave frequency band. For both 2/92 and 5/93 data, Reynolds stresses are small ($< 0.01\, Nm^{-2}$), when compared with other methods. The 10/91 data show that Reynolds stresses calculated at the two EMCM heights are quite different with the lower EMCM giving around 4 times the magnitude of the upper EMCM-1. This is caused primarily by the larger w-velocities measured by the lower instrument. When the wave peak is removed from the energy density spectra the remaining (turbulent) variances at the two heights are the same. This is known from the estimates of bed shear stress from the spectra splitting technique (which use the remaining spectra) which are virtually the same at either height (see figure 4.15). This means that the additional correlations measured by the lower head must be contained in the (removed) wave peak frequency band. These results contradict the quadrature argument.

Conclusions. Reynolds stresses are the most direct method of measuring shear stresses and are known to work well in unidirectional flow. When significant waves are present this study has shown they are unreliable and error estimation is difficult. This is in agreement with previous results by other workers in the field of wave-current interactions (e.g. Huntley, 1988).

5.4.2 Spectra Splitting

This technique has been applied to 10/91 and 5/93 (tide 3) data. Figure 4.16 shows a typical example of energy density spectra before and after truncation. The method requires turbulent kinetic energy (E) consisting of both u, v, and w variances. In each case only u and w variances were used as two EMCMs (of differing orientation) were not deployed at the same height. This means that E is an underestimate of the total energy. If the turbulence in the truncated spectrum was unaffected by wave turbulence, then ratios of $\overline{u}^2 : \overline{v}^2 : \overline{w}^2 \simeq 1.9^2 : 2.4^2 : 1.2^2$ might be expected (Soulsby, 1989). These ratios are based on steady boundary layer ratios (Soulsby, 1983). For the 10/91 data the ratio of $\overline{u}^2 : \overline{w}^2$ was found to vary between 10:1 and 20:1 and for the 5/93 data between 2:1 and 10:1, implying that turbulence is affected by waves. Since this means there is no way if estimating $\overline{v}^2$, it can be expected that τ_o calculated from this method is an underestimate of up to 100%. These ratios also bring into doubt the validity of the method for this site, where waves are dominant and unidirectional flow is small.

Figure 4.15 compares results with the other shear stress methods for 10/91, with table 4.12 giving the ratios of the truncated part of the spectra and the total variance for each EMCM. Similarly figure 4.58 and table 4.18 present the 5/93 data. Results from the two EMCMs in 10/91 are very consistent, despite the difference in height (25, 55 cm), which implies that turbulent intensity outside the wave frequency band at the two heights is similar. The total energy in 10/91 is around 10^3 times higher than 5/93 energy and the proportion of wave energy

removed is 75 – 85%, compared to 15 – 50% from the 5/93 data (see tables 4.12 and 4.18). These differences are an indication of the wave dominance in kinetic energy at Portishead. The only recognisable increase in τ_o for the 5/93 deployment is between ($t = 160, 200$), due to the current acceleration after HW. The removed wave peak is only 15% of the energy at this time, and is therefore the only time when current generated turbulence dominates. This effect is harder to discern in the 10/91 data, although there is a small drop in the proportion of the truncated wave peak at a corresponding time.

Conclusions: The Spectra splitting method is time consuming to perform, since each wave frequency band has to be identified manually. The method is empirically based on the eddy dissipation method, which requires a significant current to validate the assumptions made in the transferal to wave number space. If expected ratios of orthogonal variances from steady boundary layer flows are much different then results become suspect as turbulence is affected by waves. At this site wave energy is dominant and currents are weak, hence the method is not really suitable. It is probably better suited to sites where waves are less of an influence, and turbulence generated by currents dominates. Wave energy has been shown to be successfully removed by the method. Trends in shear stress do follow those of other methods and the method is useful in identifying the frequency distribution of energy for these data. This can also be done from cumulative energy density (examples from 10/91 - figures 4.20 - 4.22).

5.4.3 Friction Factor

For every deployment except 5/93, the wave orbital amplitude was calculated from pressure data. Owing to the lack of pressure data in the 5/93 deployment, the significant orbital velocity U_s taken directly from EMCM time series was used. Section 5.1.4 discusses the comparison between orbital amplitudes measured from the two instruments.

One of the main advantages of the friction factor method to the engineer is its ease of application. The validity of linear wave theory to calculate orbital amplitudes can be questioned, as can the use of semi-empirical friction factors based on laboratory turbulence measurements. Validity of linear theory for these data has been discussed earlier (section 5.1.1). A consistent pattern of τ_o can be seen in all data, with highest stresses in shallow water as expected (see figures 4.2, 4.12, 4.28 & 4.38). Values greater than $1\,Nm^{-2}$ can occur for waves with significant height $60\,cm$ in water of depth $2\,m$.

This method is based only on wave velocities. It has been shown that a small current can exist on the ITZ, so shear stress estimates for a current alone and a friction factor (taken from table 2.2) are shown in table 5.1. For the low current on the ITZ it can be seen that the linear addition of this associated shear stress would have little effect on the total value of τ_o. The interaction term mentioned in equation 2.56 has not been included as there is not enough evidence to support this concept (Tolman, 1992).

Conclusions. The method can be easily implemented and results follow the general trends of

other methods as water depth changes (see e.g. figure 4.15). The absolute values are suspect in the shallow water at the start and end of recording when the validity of linear wave theory is in doubt. It is the only method which is designed with waves as the primary source of bed shear stress (the other methods are derived from unidirectional results). The method of estimating wave orbital velocity could change the magnitude of shear stress considerably. In using an orbital velocity based on the significant wave height this has consistently given larger values than other shear stress methods. Following the unsuitability of the other methods of estimating bed shear stress mentioned, empirical modifications such as those suggested to Soulsby (1992) (equation 2.56) are likely to remain the most productive avenue for wave-current flows.

5.5 Bed Sediment

Tables 4.8–4.17 present bed sediment data from Portishead for the five deployments in terms of their bulk quantities. Surface sediment at Portishead is found to be predominantly mud, although nearer the LWM sand is present in increasing proportions. Surface samples from the upper part of the ITZ (around the primary instrument site) consistently show median particle diameters of approximately $10\,\mu m$ (figures 4.8, 4.33 and 4.44).

A $1\,m$ shear vane profile (table 4.8) reveals that $10\,cm$ or more below the surface, highly consolidated clay is present ($SV > 11.0\,kPa$). This is only interrupted by intermittent layers of sand, before apparently hitting bed rock at depths of between $60\,cm$ and over $1\,m$. A cross section of the transect at any particular depth below the surface shows that consolidated sediment is generally stronger towards LWM. This is not necessarily the case for more recently deposited surface sediment (see tables 4.8-4.17).

A surface layer ($0 - 10\,cm$) of sediment lies above the consolidated clay. Samples taken from the top $2\,cm$ are seen to vary considerably in moisture content (MC), shear vane strength (SV), bulk density (BD) and dry density (DD) on the different deployments. Ephemeral fluid muds with MC over 200% are associated with $SV \approx 0\,kPa$, $BD < 1250\,kg/m^3$ and $DD < 400\,kg/m^3$. The highly consolidated clays have low MC (< 70%) and associated $BD > 1500\,kg/m^3$ and $DD > 900\,kg/m^3$. The surface sediment varies between these two extremes, primarily dependent on recent wave climates which are governed by wind conditions. Periods with little wave activity (e.g. 7/91, 5/93 deployments) allow sediment to be deposited, creating a near fluid mud surface layer. This is contrasted with continuous storms (e.g. 11/91) when the clay was exposed over much of the transect. It has also been seen that a single erosional tidal cycle can alter surface sediment considerably (compare tables 4.15 and 4.16 (2/92); table 4.17 (5/93 - tide 4)) reducing moisture contents by up to 50%. Tidal range and other meteorological factors (e.g. precipitation) are also considered to be secondary influences on the surface sediment by changing the supply of sediment. Advection of SSC by currents, followed by deposition may be a cause of spatial variability of bed sediment.

Surface samples were generally collected at LW to try and introduce conformity. During the

5/93 deployment when surface sediment was near fluid mud, two samples were taken between tides 2 and 3, to check the effects of exposure on bulk properties (at 11:30 and 16:00 - 6/5/93, table 4.17). Some consolidation had occurred decreasing all bulk properties by as much as 15%. This infers large errors are possible when taking samples, making it difficult to relate bulk properties to erosion rates to produce reliable empirical formulae.

5.6 Vertical Distribution of SSC

Few field measurements of SSC profiles over muddy beds under waves and combined wave-current flows exist. Highly concentrated near bed (fluid) mud suspensions, generated either by wave oscillations or hindered settling have been widely reported but are still poorly understood. Based on the present hydrodynamic knowledge of wave-current interactions and from studies of cohesive SSC distributions in individual flow situations (i.e. current or waves alone) certain qualitative results might be expected with highest concentrations forming in the regions of highest turbulence. These regions can be identified as the wave boundary layer, throughout the water column when large currents are present and the surf zone. The existence of a combined wave-current boundary layer may be an additional mechanism for stratifying the vertical SSC distribution.

The initial part of this discussion looks at the temporal variations of SSC measured in a vertical profile for each separate deployment. This is followed by a summary of the vertical distribution of SSC at Portishead and how the various field data either support or contradict these mechanistic vertical distributions. Further insight is gained from the results of the turbulence model discussed in chapter 6.

29-30/7/91: Spring, calm

SSC at 17 and 36 cm follow a similar pattern except in the shallow water when the lower Partech picks up a marked increase in SSC as the muddy surf zone passes (up to $0.65\,g/l$ at $t = 60\,mins$; figure 4.3). Concentrations tail off (from $0.5 - 0.2\,g/l$ at $z = 17\,cm$) during the tidal cycle as sediment is deposited, although there are periods of increased SSC, some caused by increased wave activity (e.g. $t = 160\,mins$; see section 5.10.2) and others probably just due to advection of 'patches' of higher SSC (see section 5.9). Selected five-minute SSC time series from Partechs (figure 4.5) and siltmeters (figure 4.6) show that periods of increased concentration near the bed (siltmeters) can persist for both short ($< 5\,mins$) and long periods of time. Mean SSC is $0.3\,g/l$ at $17\,cm$, and $0.2\,g/l$ at $36\,cm$. There is little correlation (correlation coeffts: -0.1, 0.15) with H_s/h or bed shear stresses calculated from friction factor technique (figure 5.2), implying bed generated turbulence is not dominant at these heights above the bed. Nearer bed SSC ($z = 7\,cm$, upper; $z = 10\,cm$, lower site) show a more concentrated region ($> 2\,g/l$) existing in this near bed region (figure 4.4). High concentrations are seen to persist longer at the lower site which is closer to the source of SSC in the main channel and bed surface moisture contents

(taken at LW) are higher.

17/10/91: Neap, storm

SSC data are limited from this deployment due to instrument failures. The siltmeter at 15 cm (figure 4.10) shows an increase in SSC to between $2 - 5\,g/l$ when water depths are below $0.5\,m$, but otherwise concentrations are below $2\,g/l$ (the instrument cut off). Uncalibrated data from the Partech (46 cm) are also included in this figure and can be interpreted as high concentrations ($1 - 5\,g/l$) in the shallow water, with reasonably constant SSC of between 0.65 and $0.85\,g/l$ for the rest of the cycle. This range in SSC is deduced from the calibration of the instrument, discussed in section 4.2.2., which was found to increase in voltage for concentrations up to $0.75\,g/l$, but drop from this value as concentration increased. These results imply the water column is quite well mixed, as temporal variations in SSC during the cycle cover a smaller range than on other deployments.

6-7/11/91: Spring, storm

Again SSC at 37 cm and 70 cm have consistent patterns, with mean SSC of $0.5\,g/l$ and $0.4\,g/l$, respectively (figure 4.29). Highest SSCs in the shallow water are 300% larger than HW concentrations at both heights. Correlating SSC with bed shear stress (from friction factor) or H_s/h, produces high correlations (figure 5.3 - coefficients $\approx$ 0.8, 0.9). This suggests that there is a region of SSC influenced by wave generated turbulence extending from the bed to above the upper instrument height. Since instruments are positioned well above the purely oscillatory boundary layer, this could be explained by an extended wave boundary layer due to currents, or by waves shedding vortices from bed forms (discussed in section 5.1.4) or simply diffusion of near bed higher SSC. Spectral analysis techniques cannot be applied very successfully to elucidate these hypotheses, since variations in SSC are dependent on the SSC gradient. Near bed SSC ($z = 12\,cm$) at the lower site (figure 4.32) show sporadic increases in SSC above $2\,g/l$ which can be correlated with times of increased wave activity (see section 5.10.2).

6-7/2/92: Spring, calm

Figures 4.34 and 4.36 show SSC data as blocks of continuous times series, but are also plotted together as ten minute averages in figure 4.43. The Partechs did not work simultaneously and the data show completely different temporal trends at the two heights during each tide. Wave heights were larger during the second tide (see figure 4.37). There is a wide range in SSC during the tidal cycle at both heights, with the upper instrument (96 cm) showing a peak concentration of $0.6\,g/l$ at around HW and a low of $< 0.1 g/l$ (figure 4.43). During the second tide, (only at 20 cm; figure 4.43) SSC generally decrease after a peak of around $1.2\,g/l$. Another peak occurs in the ebb phase when the water depth is about $2.0\,m$ ($t \approx 630\,mins$). These peaks do not

appear to correlate with increases in wave climate, unless there is a delayed effect as sediment diffuses, suggesting they are caused by advection of 'patchy' more concentrated suspensions or current-induced resuspensions. The near bed siltmeter (at $10\,cm$; figure 4.34 and 4.36) shows little response, except for a peak after HW during the first tide ($t \approx 180\,mins$; figure 4.34), caused by current resuspension (see section 5.10.1).

5-7/5/93: Spring, calm

Continuous time series of SSC at up to four heights are shown in figures 4.46, 4.48, 4.50, and 4.52 for the four tidal cycles in 5/93, respectively. In addition to this a 'bed mounted' siltmeter provides data for the first and third tides (figure 4.47 and 4.51). The differing SSC scales should be noted to avoid confusion. They were necessary owing to the wide range in SSC at the differing heights. Definitive trends for the different tides are difficult to identify. Certain similarities are obvious, such as high SSC at the start of logging during the flood, and an increased suspension period after HW. Mean concentrations at HW are approximately $0.25\,g/l$ at all heights above $22\,cm$ for tides 1-3, and $1\,g/l$ at $7\,cm$. During tide 4 concentrations are larger at all depths, with HW mean SSCs of $0.5\,g/l$ at 22 and $58\,cm$, and $1.5\,g/l$ at $7\,cm$. This is probably due to an increased (visually detectable) wave climate but cannot be verified due to instrument vandalism.

Gradients of SSC from $22-80\,cm$ are small ($\approx 0.3\,g/l/m$) compared to the gradient between 7 and $22\,cm$ (tides 3 and 4). Between these latter two heights SSC is more than halved throughout the cycle (mean SSC: $7\,cm \approx 1.5\,g/l, 22\,cm \approx 0.4\,g/l$; figures 4.50 and 4.52) giving a gradient of around $6\,g/l/m$. For tide 3, 10 minute means and standard deviations are also plotted in figure 4.57. These make it clear that SSC is quite well mixed above $20\,cm$ with correspondingly larger standard deviations nearer the bed. It is interesting to note that following the resuspension at $t = 150-175\,mins$ standard deviations are the same at all three heights (7, 22 and $58\,cm$) implying the suspension is temporarily fairly well mixed throughout the bottom metre.

Near bed ($5, 7\,cm$) measurements of SSC indicate a high concentration region of $1-5\,g/l$ persisting for most of the cycle (figures 4.46, 4.50 and 5.52). The Partech at $7\,cm$ shows that for much of the time concentrations are varying between $1-2\,g/l$ (figures 4.50 and 4.52), which may explain the problems in detecting the near bed layer on some previous deployments when siltmeters (measuring only $> 2\,g/l$) were placed $10\,cm$ above the bed.

Data from the 'bed mounted' siltmeter can be used to infer deposition or resuspension. During the first tide, it is known that deposition of $\approx 1\,cm$ occurred (from pegs - table 4.16). The siltmeter (figure 4.47) shows a build up of SSC during the first hour, followed by a sudden removal of the sediment at $t \approx 70\,mins$. This coincides with a small peak in the wave orbital velocity (figure 4.53) and a small increase in SSC at all heights (figure 4.46, slightly delayed). It is concluded that the sudden change in the siltmeter reading is due to this temporary increase in wave climate but it is unclear why high concentrations do not reappear, except for a resuspension event after HW (discussed section 5.10.1), despite the instrument being found

virtually buried from sight by new accretion at LW. It is possible that the measuring path was not completely obstructed by sediment. Hence subjective analysis is required when this method is used to monitor deposition based on other information (i.e. net bed level change, wave/current climate).

During tide 3 (figure 4.51) a similar build up of sediment is noted with saturation occurring after $120\,mins$, which remains until resuspended by the current (section 5.10.1) after HW ($t \approx 150\,mins$). It is difficult to assess whether saturation of SSC measured by the siltmeters during the cycle are due to a very high SSC ($> 20\,g/l$) or in fact actual deposition is occurring. The information from peg data is taken to imply actual deposition, but a further possibility is that most actual deposition forms as the muddy surf zone retreats down the ITZ and the high concentrations monitored during the tide are in fact suspensions.

Summary

Data from each deployment (except 10/91) support the generation of high SSC ($1 - 5\,g/l$) near the bed for at least part of a tidal cycle, due to a combination of the stirring effect of waves over surface sediment with high MC ($> 150\%$) and some hindered settling. On most occasions this region is probably restricted to only a few centimetres, occasionally reaching thicknesses greater than $10\,cm$ and for much of the cycle concentrations are between $1 - 2\,g/l$. It is possible that hindered settling is the more important factor in the formation of these high concentrations and density stratification is helping to prevent the layer from being further entrained into the flow. Intermittent increases in SSC to around $5\,g/l$ can occur at times of increased energy either from waves or currents. During the 10/91 deployment the position of the siltmeter ($15\,cm$) may be too high above the bed to measure any high concentrations or waves breaking in relatively deep water could be providing additional turbulent mixing so preventing the formation, or causing the dispersion, of any high SSC region.

Temporal variability in thickness is thought to be affected by local bed erodibility, advection across the ITZ and proximity to the main channel. High concentrations have been observed to form for extended periods during Spring tides when bed surface moisture contents are around 200% under small waves. This is generally indicative of a depositional regime when there is a large sediment supply, again suggesting that hindered settling is an important factor. Comparison between data from different deployments suggest that if bed surface moisture content is around 100% then the thickness of the layer will be less than $10\,cm$ and may not exist if associated with an erosional tidal cycle. The presence of a highly concentrated region means that steep SSC gradients of order $5 - 50\,g/l/m$ can be found near the bed ($0 - 20\,cm$). A more gradual SSC gradient of order $0.1 - 0.5\,g/l/m$ exists over the rest of the bottom metre and presumably continues to the surface.

The identification of a transitional region above any near bed SSC region has been made by correlating SSC with either τ_o or H_s/h (figures 5.2 and 5.3). These results suggest a limit (or boundary layer) is likely to exist defined as the maximum height SSC is influenced by bed

generated turbulence. The depth of this layer is dependent on the size of parameters τ_o or H_s/h, but can extend at least to $70\,cm$ for waves of $\approx 30\,cm$ (figure 5.3). On calm days the resolution in vertical instrument profiles mean that the thickness of any transitional region cannot be identified, thus the SSC distribution is basically divided into a near bed region $< 10\,cm$ and an upper region with small SSC gradients.

The vertical distribution of SSC under the weak current and varying wave energy has been thus conceptualised as three regions (see figure 5.4):

- A highly concentrated region $(1 - 5\,g/l)$ can form in the bottom few centimetres, maintained for extended periods by small oscillatory forces.
- A bed influenced region $(0.2 - 1.0\,g/l)$ extends above this, and can be identified by correlating SSC with bed shear stress. This can extend to above $70\,cm$ in depth for waves $20 - 40\,cm$ in height, far beyond the hydrodynamic definition of a pure wave boundary layer.
- Above this the lowest concentration region $(0.1 - 0.5\,g/l)$ extends to the surface and is not influenced by the bed generated turbulence. This may be considered the wash load, or background concentration.

This overall description agrees reasonably with previous expectations and regions have been quantified in terms of thickness and concentration to some extent by the field data and for a range of situations. The extent of these regions is dependent on the hydrodynamic conditions and surface sediment, so that distinct regions are not necessary, and any one, or two, may almost dominate the SSC distribution. Antecedent meteorological factors and tidal range are expected to control the background concentration, which in turn affect the magnitude of SSC in other regions.

Temporal variations in SSC during a tidal cycle at a particular height above the bed can be categorised into one of three trends. Near to the bed, or probably almost throughout the water depth on stormy days, highest concentrations occur when the water is shallowest. During Spring tides, even under large waves there is probably a period of deposition around HW (due to large SSC supply and the deep water) and a 'V' shaped SSC distribution is observed - a typical pattern is shown in figure 4.29.

During Neap tides with large waves this distribution tends more towards a 'U' shape as more of the sediment in the water column remains in suspension.

On calmer days during Spring tides, or in the higher part of the water column the pattern is less distinct and highest concentrations can occur around HW. This is probably due to advection of patchy regions of higher SSC being more dominant. When deposition was recorded, generally a decreasing trend in SSC through the tidal cycle can be observed as sediment is deposited (e.g. figure 4.3). Subtle changes in wave climate can alter these trends as seen from the differences in the 5/93 SSC data (figures 4.46, 4.48, 4.50 and 4.52).

The different mechanisms considered important in the determination of SSC profiles are considered in the following sections - wave breaking, settling velocity, advection by tidal currents and resuspension both by waves and currents.

5.7 SSC in the Surf Zone

Turbulence under breaking waves does generate high SSC on each deployment, although the extent of this region varies considerably as a function of wave climate. The muddy zone is observed to move up and down the ITZ with the tide and could be an important mechanism in sediment transport. On stormy days the approximate width of this region can be identified by the the response of turbidity meters at differing heights together with the beach slope ($\tan\alpha \approx 0.06$). On calmer days it is harder to identify whether SSC peaks in the shallow water are actually due to small waves breaking, or due to current influences as these also can create high SSC (see section 5.10.1). It has been assumed that concentrations measured by instruments positioned at a fixed at height above the bed should be monotonically increasing with time, as water depth gets shallower, if high SSC are solely due to small waves breaking and not current induced affects.

During the 7/91 deployment ($H_s \approx 4\,cm$) a SSC peak in the flood surf zone is measured at the lower Partech height ($17\,cm$), but not at the upper one ($36\,cm$) (figure 4.3), implying the high SSC region extends between 3 and $6\,m$ back from the waters edge into deeper water. During the 10/91 ($H_s \approx 60\,cm$) and 11/91 ($H_s \approx 30\,cm$) deployments, surf zone SSC peaks extend to the uppermost instrument (10/91 - $46\,cm$, figure 4.10 and 11/91 - $70\,cm$, figure 4.29) hence the high SSC region is greater than 8 and $12\,m$, respectively. Data logging whilst the water was shallow on the flood was missed for the 2/92 ($H_s \approx 6\,cm$) deployment (second tide) and on the ebb there was only a measurable peak in SSC for the siltmeter near the bed (i.e. not at $20\,cm$) implying the surf zone is narrow ($< 3.5\,m$). For the SSC data from 5/93, it is unclear whether a noticeable high SSC surf zone exists, except for the response of the siltmeter at $5\,cm$ on tide 3 as current induced resuspension in the shallow water on the flood occurs. Visual observations from both 2/92 and 5/93 suggested the surf zone was indeed narrow ($< 2\,m$).

SSC Peaks are usually larger in the flood surf zone. This is probably due to two factors. On calm days the waves are larger on the flood (discussed in section 5.1.2) and on storm days, most easily erodible sediment will be removed on the flood making it harder to increase SSC again in the ebb surf. Hand collected samples from near the deployment site suggest that SSC in the surf zone are of order $1 - 3\,g/l$. This is consistent with peaks in SSC measured in the shallow water by turbidity meters during each deployment (e.g. figure 4.29). Variability in SSC measured in the surf zone by turbidity meters from each deployment will be affected both by instrument position above the bed and bed surface sediment. Comparison between SSC in the surf zone and SSC at HW, approximately $50\,cm$ above the bed, show values are between 2-10 times higher (e.g. figure 4.29). Again this ratio is consistent with hand collected samples taken from near the HWM (where the beach is shingle) which were less than $0.5\,g/l$, and with

samples collected from the surf zone near the instrument site.

The influence of small waves breaking in the surf zone as the tides ebbs (creating a small peak in SSC) may be an important mechanism in determining whether net deposition or erosion occurs over a tidal cycle during calm deployments. This balance between erosion and deposition has been seen to be an unstable equilibrium (e.g. 5/93 deployments, when erosion and deposition alternate on consecutive tides despite similar hydrodynamic conditions). If there is a very small SSC peak then deposition has usually occurred (e.g. 7/91, figure 4.3) and when there is a large peak (over 100% increase, e.g. 11/91, figure 4.29) then net erosion is recorded. Turbulence generated in the ebb surf zone may thus be sufficient to resuspend both sediment deposited during that tidal cycle, and previously deposited sediment, with the size of the breaking waves being the critical process determining the bed level change. As the water retreats across the ITZ sediment is held in suspension thus transporting it back towards the main channel where the stronger currents can disperse it. Evidence from the 5/93 deployments shows that this SSC peak (at $z = 22\,cm$) is more prominent when erosion occurs (tide 2, figure 4.48; tide 4, figure 4.52) than on the depositional tides (tide 1, figure 4.46; tide 3, figure 4.50). Further experiments are needed to determine the significance of these results, as a contradictory example is the 2/92 deployment when there is no observable increase in SSC (figure 4.36, tide 2 at $z = 20\,cm$) yet erosion occurs. Suspended sediment load may be a controlling mechanism.

5.8 Settling Velocity

Attempts to measure settling velocity are restricted to the 5/93 data. Any samples taken near the HWM were found to have too low settling velocity to be measurable using the Owen tube technique (Barton, 1992). Concentrations of these samples were below $0.5\,g/l$. Figures 4.60 and 4.61 give settling velocities for two samples taken from the surf zone near the site at the start of logging of tide 2 and 3, respectively. Settling velocities (0.61 and $0.15\,mm/s$) compare reasonably with previous values from the Severn Estuary plotted in figure 2.14. Data are too few to allow further comment, but to a first approximation confirm it would be reasonable to assume this relationship is valid for modelling purposes.

5.9 Advection of Suspended Sediment by Currents

Weak tidally induced circulations caused by the main channel currents being diverted by the sheltering headlands around the ITZ (see section 5.3) would provide a mechanism for both supplying sediment onto the ITZ by drawing in suspended sediment from the main channel and advecting it (and any additionally eroded sediment) across and possibly back off the ITZ. The lack of correlation of shear stress with SSC on calmer deployments gives strong support to this hypothesis of advection of patchy SSC by currents. These effects will necessarily be more

observable on days with small wave climates when suspensions are less vertically well mixed. This mechanism would create spatial variation in bed sediment, since it is likely (based on the available data) that certain parts of the ITZ experience different proportions of the available energy due to topographical influences. To identify regions prone to deposition and erosion would require a much larger field data collection exercise.

5.10 Resuspension

Data were examined for possible resuspension events. These can be indicated by an increase in SSC at a point above the bed, corresponding to an increase in energy in some form. Both tidal currents and waves are seen to cause resuspension at the site. For a particular tidal range, waves dominate the overall vertical SSC distribution and current induced resuspension can only be observed on days when wave activity is low. Resuspension of bed sediment is a function of the surface sediment, making it difficult to quantify critical shear stresses for resuspension.

5.10.1 Current Induced Resuspension

The 5/93 time series data (figures 4.45-4.52) show continuous response to changes in SSC and velocity during tidal cycles for a small wave climate. A period of resuspension can be observed due to the acceleration on the ebb ($t \approx 150 - 180\,mins$) varying in intensity and duration on each tide. Examining tide 3 in detail (figures 4.49-4.51) the low velocities and small waves allow sediment to be deposited during the flood tide. This is interpreted from the decrease in SSC at each instrument height above 5 cm and from the increase in the 'bed mounted' siltmeter and the siltmeter at 5 cm which both become saturated by high concentrations. As the ebb accelerates at around $t = 150\,mins$ (see figure 4.49), both siltmeters become unsaturated and an increase in SSC is observed at all heights (figures 4.50 and 4.51). The larger increases are nearer the bed, where SSC gradients are steeper. These high SSCs last for around 20 $mins$, before SSCs drop to values which might be interpreted as the values they would have been without the intervening resuspension. This implies that this is resuspension of sediment that has recently settled (during the tidal cycle), or is near settling and is not actual resuspension of the original bed sediment. This resuspension event thus creates a temporary increase in SSC for advection by the current, which would have implications on the spatial distribution of sediment on the ITZ. This mechanism can also hinder deposition and hence bed consolidation, since the previous highly concentrated values measured by the siltmeters do not reappear and may limit total deposition of suspended sediment during a cycle at the site.

This resuspension event can be observed in all the tidal cycles from 5/93. Temporal and overall magnitude variations are considered to be dependent on subtle changes in the wave climate, which influence SSC throughout the water column. In the other calm deployments, there is evidence for the same increases in SSC at a corresponding time in the tidal cycle. During the

2/92 deployment the SSC time series (tide 1 - figure 4.34, tide 2 - figure 4.36) also increase at a corresponding time ($t \approx 175\,mins$) but only at the lower height ($10\,cm$) during the first tide. The Partech (at $96\,cm$) is probably too far from the bed to be affected by this resuspension. This shows that the effects of this current induced resuspension are possibly limited in terms of depth, or that SSC gradients are so weak higher in the water column that the effects cannot be observed. There is only a small response in SSC at $20\,cm$ during the second tide between $t = 550 - 600\,mins$ (figure 4.36) which again is considered to a result of the larger waves reducing SSC stratification during this tidal cycle.

A similar current induced suspension event can be seen in the 5/93 data, around $t = 45\,mins$ near the start of recording (see figures 4.45-4.52). The current is purely across the ITZ (v-direction) against the flood direction. This mechanism could also account for the peak SSC observed in the 2/92 data (figure 4.43, $t = 460\,mins$). It is harder to imply this directly from the velocity data (figure 4.35) due to the non-continuous recording and EMCM orientation. It appears that EMCM-2 may show an increase in velocity in this direction.

5.10.2 Wave Induced Resuspension

The most dominant period of resuspension by waves is in the surf zone due to breaking waves. SSCs in the surf zone are discussed separately in section 5.7. Increases in SSC due to non-breaking waves have been noted during the 7/91 deployment (compare figures 4.1 (H_s) and 4.3 (SSC) at $t = 150\,mins$) with a 30% increase in SSC at both heights (17 and $36\,cm$). Other examples include 2/92 (compare figures 4.37 (H_s) and 4.43 (SSC) at $t = 450\,mins$) and a number of examples in 11/91 (e.g. at $t = 400, 700\,mins$ - compare figures 4.30 (H_s) and 4.32 (SSC)). These events are not all necessarily due to resuspension of previously deposited bed sediment present as some events occur on days when net deposition was measured, but may be an increase in SSC caused by resuspension of sediment deposited during the (current) tidal cycle or due to higher concentrations in the lower part of the water column temporarily lifted higher in the water by increased wave activity. As previously mentioned, high correlation coefficients are found between SSC and τ_o (or H_s/h) indicating that increases in SSC are caused by increased wave heights.

There is insufficient evidence to conclude whether throughout a tidal cycle non-breaking waves are actively eroding the bed. This is due to the failure in ultra-sonic bed level transducer data when waves were present. There seems no doubt that even small waves can prevent deposition by keeping sediment in suspension.

5.11 Deposition and Erosion Rates

At Portishead erosion and deposition rates for a tidal cycle are primarily governed by the wave climate and the bed surface sediment. Peg heights are given in tables 4.8–4.17 and presented

in the results from each deployment in chapter 4.

Deposition has been seen to be prevented by small waves (5 cm) generated by a westerly wind (e.g. 2/92), but accretion of around 1 cm has occurred when winds are light (e.g. 7/91) or blow offshore (e.g. 5/93) during Spring tides. Subtle changes in a small wave climate appear to be able to dictate accretion/erosion (e.g. see consecutive tides during 5/93 deployment), implying that there is a critical wave size at the site which is capable of preventing accretion. This may be affected by the quantity of suspended sediment in the water column at that time. The concept of a critical wave height is similar to the concept of a critical depositional shear stress associated with waves alone, but takes no account of wave period. At this site, zero-crossing periods have consistently varied between $3 - 5\,secs$ on each deployment (see section 5.1.2). This consistency allows the idea of a critical wave height to be acceptable, as if there were larger differences in the period of waves propagating onto the ITZ then this would effect the shear felt at the bed. At sites where wave period is more varied it may be better to use a more traditional critical shear stress. To prevent accretion at this site, a critical wave height is estimated to be around 5 cm at HW. In a depth of 4 m and $T_z \approx 4\,sec$ this applies a shear stress of approximately $0.03\,Nm^{-2}$ to the bed. When breaking, a wave with these characteristics has a dissipation rate of approximately $1.5\,Nm/s$ (per unit bed area) which is more than a (non-breaking) 60 cm wave does in a water depth of 2 m (based on tables 5.6 and 5.7; see section 5.1.5).

Since accretion occurs during Spring tides when unidirectional velocities are at a maximum, the tidal current is not sufficient to actually *prevent* deposition but periods of increased velocity may slow the process down. Peak measured quantities of deposition are of the order 1 cm in a tidal cycle, which could correspond with longer timescale peak rates at the site of 25 cm/30 days (see figure 3.3). From the limited USt data (7/91, figure 4.7) it seems that after the initial turbulence created by small waves breaking, deposition can occur on calm days reasonably steadily through a tidal cycle. A further mechanism for deposition which has been ignored is how the muddy 'surf zone' reacts with the bed surface as the water retreats. To discover whether any accretion is occurring whilst this is being dragged over the surface, an instrument which is capable of monitoring the bed either submerged or exposed needs to be developed. Small waves breaking during this time may also prevent net deposition during a tidal cycle as sediment is held in suspension, or resuspended.

Comparing bed shear stress values (friction factor technique) in shallow water (figures 4.1, 4.38, 4.55 and 4.58) for both erosional and depositional tidal cycles (from 7/91, 2/92 and 5/93) a tentative value for τ_d at this site is suggested at 0.05 Nm^{-2}. This is slightly lower than the bottom of the range of values found by Odd (1988) in flume tests ($0.06 < \tau_d < 0.1\,Nm^{-2}$). This is perhaps not unexpected as in the field hydrodynamic conditions are likely to be more temporally variable than in the laboratory, resulting in a lower average value being estimated.

Erosion rates and critical erosional shear stresses (τ_e) are complicated by the shear strength of the surface sediment to be eroded. Antecedent surface bed sediment with high moisture contents and low shear vanes measurements on days with any wave activity are indicative of high erosion rates, but an empirical formula requires considerably more data. Quantifying

τ_e is similarly difficult, but a range is given as $0.1 < \tau_e < 1\,Nm^{-2}$, varying inversely with MC. Highly consolidated cohesive bed sediment with MC< 70%, SV> $11\,kPa$ is seen to be virtually resistant to erosion (from waves of 40 cm, 11/91), but weak sediment with MC> 160%, SV< $3\,kPa$ will be eroded by any Westerly wind generated waves > $5\,cm$ in height as they break (e.g. 2/92).

More data are required to try to produce a more precise result, or an empirical formula relating τ_e to bulk quantities. This is due to the complexities of cohesive sediment involving biotic and mineral content, exposure and particle size as well as the bulk properties.

From the comparisons of dissipation rates under breaking and non-breaking waves given in section 5.1.5 it is apparent that the majority of this erosion probably occurs as waves break, so increasing SSC in the surf zone as discussed in section 5.7. Since consistent erosion rates of $1\,cm/tide$ have been found on each occasion that erosion was observed (despite different wave heights), it is suggested that the combination of beach slope and tidal range may be an important mechanism in restricting this total amount of erosion as these factors govern the time of exposure to breaking waves. Since small waves breaking ($H_s \approx 5\,cm$) have these same erosion rates this has implications to the formation and maintenance of ITZs.

The slope of an ITZ and the tidal range will determine the time length of exposure to breaking waves at a point on the ITZ during a tidal cycle, with the tidal range also controlling how much of the ITZ is exposed to these waves. A steep slope and small tidal range will allow waves to break at a point for longer than a shallower slope as the tide either floods or ebbs. This has particular consequence for the smaller waves which have been seen to cause as much erosion as larger waves if the bed surface is suitably weak as it is likely that these may be present for much of the year. ITZs with shallow slopes would experience only a relatively short period of time when small waves breaking could cause resuspension so allowing larger accumulations of sediment and longer periods of consolidation before being exposed to storms. This mechanism could be preventing the formation of thick ($> 2\,cm$) surface ephemeral fluid muds as can be observed at other sites in the Severn (West, 1991).

5.12 Measurement Techniques

Collecting field data from muddy ITZs is a difficult and tiring operation. Specially designed mountings requiring the minimum of fixing and positioning are required to reduce the time spent on the mudflats, with a single pole pushed through a bed plate providing a good form of mounting. Instruments need to be positioned above an undisturbed bed, so attaching the instruments to the pole before moving the whole rig a few metres to an untouched area is recommended.

Although ultra-sonic bed level transducers have been reasonably successful at monitoring bed level in the laboratory, field results have been less rewarding. Data have only been presented

from the 7/91 deployment although they have been used on other occasions but results were found to be inconsistent with changes measured from pegs (Freeman, 1992). Parker (1993) suggested that waves creating air bubbles and sounds in the frequency band of the instrument are a likely cause of error. This would explain why results were good from the 7/91 deployment when the wave climate was so small. This was the only depositional regime when the USts were used, so it is also possible that the interface between bed and water is better defined. The transducers can potentially be used to record the presence of fluid mud, and have been successfully used for monitoring the bed in other situations (Parker, 1993).

Optical siltmeters can measure near bed SSC successfully, the size of the siltmeters allowing positioning down to $5\,cm$ above the bed. The development of smaller devices would be an improvement for nearer bed measurements, especially under storm conditions when bed scour is likely if instruments are too large.

A siltmeter pushed into the bed, with the light path just above the bed surface, has been experimented with to monitor bed level change under depositional regimes in the 5/93 deployment. Resuspension of any deposited sediment and near bed fluidisation could be identified using this technique. Further experiments with this method may prove worthwhile.

Ideally, logging of data should be continuous, but if storage is a problem the longest lengths of recording possible are recommended, since changes in near bed suspension, for example, can be short term (see example figures 4.6). Thirty minute runs are adequate.

f_c	$\overline{u}$ (m/s)	τ_o (equation 2.44) (Nm^{-2})
0.0176	0.01	0.0002
0.0176	0.05	0.0055
0.0176	0.1	0.0220
0.0176	0.2	0.0880

Table 5.1: Bed shear stress in unidirectional flow over muddy beds

Linear wave theory parameters - 29-30/7/91			
h (m)	H/λ	$H\lambda^2/h^3$	H/h
0.45	0.016	11.05	0.140
1.05	0.007	1.48	0.043
1.66	0.006	0.55	0.027
2.22	0.004	0.33	0.018
2.71	0.001	0.02	0.002
3.15	0.003	0.14	0.011
3.49	0.005	0.15	0.016
3.76	0.002	0.13	0.008
3.87	0.001	0.01	0.001
3.88	0.002	0.12	0.008
3.74	0.001	0.13	0.006
3.45	0.003	0.15	0.010
3.01	0.003	0.18	0.012
2.51	0.002	0.28	0.012
1.95	0.002	0.35	0.010
1.36	0.003	0.71	0.018
0.72	0.004	2.25	0.032
0.17	0.005	47.56	0.106

Table 5.2: Linear wave theory validity: h is depth, λ is wave length, H is significant wave height, taken from figures. For $H\lambda^2/h^3 > 26$ cnoidal wave theory is preferable. The maximum wave height (H/h) cannot exist above 0.78, hence this is an indication of waves which have broken.

Linear wave theory parameters - 17/10/91			
h (m)	H/λ	$H\lambda^2/h^3$	H/h
0.23	0.042	712.046	1.074
0.43	0.048	199.658	0.777
0.69	0.052	117.135	0.679
0.93	0.048	70.699	0.547
1.16	0.054	47.739	0.515
1.37	0.050	34.899	0.441
1.54	0.048	33.544	0.425
1.74	0.047	22.971	0.367
1.86	0.051	20.932	0.377
2.05	0.042	18.295	0.319
2.15	0.043	16.518	0.311
2.18	0.040	18.405	0.309
2.18	0.038	17.744	0.297
2.12	0.041	18.972	0.318
2.01	0.036	21.330	0.302
1.88	0.039	28.107	0.346
1.70	0.037	33.773	0.357
1.51	0.038	34.031	0.363
1.26	0.040	60.833	0.457
0.98	0.041	108.436	0.563
0.44	0.037	374.555	0.805

Table 5.3: Linear wave theory validity: h is depth, λ is wave length, H is significant wave height taken from figures. For $H\lambda^2/h^3 > 26$ cnoidal wave theory is preferable. The maximum wave height (H/h) cannot exist above 0.78, hence this is an indication of waves which have broken.

Linear wave theory parameters - 6-7/11/91 Tide 2 (similar results for tide 1)			
h (m)	H/λ	$H\lambda^2/h^3$	H/h
0.25	0.031	652.916	0.863
0.70	0.029	72.885	0.401
1.18	0.021	25.358	0.221
1.87	0.024	12.697	0.193
2.26	0.016	10.749	0.140
2.64	0.017	5.320	0.113
3.18	0.013	4.615	0.093
3.47	0.015	4.445	0.100
3.74	0.014	3.167	0.085
4.06	0.012	2.210	0.067
4.18	0.011	2.415	0.066
4.26	0.013	2.112	0.071
4.29	0.013	2.913	0.080
4.21	0.011	3.480	0.074
4.05	0.012	3.781	0.083
3.65	0.011	3.960	0.075
3.34	0.015	6.172	0.112
2.99	0.013	7.966	0.110
2.40	0.014	12.040	0.134
1.99	0.014	15.010	0.146
1.56	0.015	29.211	0.185
0.96	0.013	44.782	0.200
0.54	0.015	117.890	0.310
0.14	0.022	2000.068	0.984

Table 5.4: Linear wave theory validity: h is depth, λ is wave length, H is significant wave height taken from figures. For $H\lambda^2/h^3 > 26$ cnoidal wave theory is preferable. The maximum wave height (H/h) cannot exist above 0.78, hence this is an indication of waves which have broken.

Linear wave theory parameters - 6-7/2/92 Tide 2 (similar results for tide 1)			
h (m)	H/λ	$H\lambda^2/h^3$	H/h
0.38	0.008	51.928	0.145
0.84	0.006	12.435	0.075
1.29	0.003	3.836	0.034
2.14	0.003	1.535	0.022
2.51	0.003	1.950	0.027
2.86	0.003	1.295	0.020
3.45	0.002	0.842	0.017
3.71	0.002	0.831	0.015
3.93	0.002	0.862	0.014
4.16	0.002	0.775	0.014
4.24	0.002	0.851	0.016
4.26	0.002	0.638	0.013
4.18	0.001	0.687	0.009
4.02	0.001	0.794	0.009
3.79	0.001	0.839	0.010
3.45	0.001	1.156	0.012
3.11	0.002	2.513	0.019
2.74	0.002	1.839	0.016
2.01	0.002	1.631	0.015
1.59	0.002	2.186	0.017
1.16	0.002	5.485	0.023
0.52	0.003	12.779	0.047
0.12	0.004	2360.574	0.328

Table 5.5: Linear wave theory validity: h is depth, λ is wave length, H is significant wave height taken from figures. For $H\lambda^2/h^3 > 26$ cnoidal wave theory is preferable. The maximum wave height (H/h) cannot exist above 0.78, hence this is an indication of waves which have broken.

Deployment		29-30/7/91	17/10/91	6-7/11/91	6-7/2/92
$H_{HW}(m)$		0.03	0.6	0.25	0.05
h (m)	1.0	0.004	1.5	0.24	0.006
	2.0	0.0005	0.7	0.1	0.002
	4.0	0.0002	-	0.03	0.001

Table 5.6: Mean energy dissipation rate per unit bed due to non-breaking waves ($\overline{D}_{NB} = \tau_o U_o$) for a range of depths taken from data presented in figures for each deployment. Approximate wave heights at HW (H_{HW}) are given; the second tides are used for November and February.

H (m)		0.02	0.05	0.1	0.2	0.4	0.6	0.8
Period	3	0.3	1.8	7.3	29.1	116.4	261.8	465.5
(secs)	5	0.2	1.1	4.4	17.5	69.8	157.1	279.3

Table 5.7: Mean energy dissipation rate per unit bed due to waves breaking ($\overline{D}_B$ - see equation 2.34) for a range of wave heights H and periods T. Assumes wave of maximum height $H/h = -0.78$.

Portishead Deployments - Breaker type classification							
	29-30/7/91	17/10/91	6-7/11/91			6-7/2/92	
			1st tide	2nd tide	Lower site	1st tide	2nd tide
H_{HW}	0.03	0.65	0.25	0.35	0.2	0.02	0.06
λ_{HW}	14	16	24	25	38	40	30
β	0.7	12.4	3.2	4.2	1.6	0.2	0.6

Table 5.8: Classification of breaker types. H_{HW} is significant wave height at HW, λ_{HW} is wave length at HW (taken from site at $\approx 100\,m$, unless stated), β is breaker classification (after Galvin, 1972; equation 2.17; figure 2.6). $\beta > 5 \Rightarrow$ spilling ; $0.1 < \beta < 5 \Rightarrow$ plunging breakers

Chapter 6

Modelling Results and Discussion

6.1 Introduction

In section 3.2 the equations solved by the turbulence model and various initiation parameters were presented. This chapter presents results for a number of different physical situations considered relevant to the field conditions and discusses critically the performance of the model. None of the empirical constants in the equations or the boundary conditions were changed for any run, although it is recognised from modelling literature that slight variations could improve data fit considerably.

If the model is to accurately simulate the field observations at a point on the ITZ it would be necessary to model the temporal changes in depth, wave climate, tidal current and SSC during a tidal cycle. It is not the intention to use this 1-D turbulence model as a predictive tool for such a complex 3-D flow on the ITZ, but to use it to provide additional understanding of the mechanisms determining the observed vertical distribution of suspended sediment. This has been addressed by simulating 'snapshots' of the cycle by considering a number of fixed depths for a range of wave/current ratios and sediment conditions.

The first part of this chapter (section 6.2) addresses general aspects of the model in a wave, current and wave-current situation considered to cover the range of flow conditions observed in field experiments. This is followed by a discussion of the implications of the possible methods of introducing sediment into the flow; firstly by introducing sediment directly into the flow and assuming no bed flux and then with reference to the bed model described in section 3.2.3. Following this (in section 6.4) direct attempts to simulate results from the fieldwork are made for water depths of $1\,m$ and $4\,m$ for storm (large waves) and calm (small waves) deployments. These results are used as an aid to interpreting the field data. The final section (6.5) compares hydrodynamic results from the model with other models and laboratory data, making recommendations for future improvements. Various units have been used to keep numbers small, as there are variations of several orders of magnitude (e.g. in length).

6.2 Evaluation of Hydrodynamic Modelling of Field Data

The field study has revealed the basic hydrodynamic properties on the ITZ at Portishead. A weak tidal current has been measured, which although showing some temporal variation through the tidal cycle, is generally of the order of a few centimetres per second $50\,cm$ above the bed during Spring tides, with occasional peaks in velocity of up to $15\,cm/s$ lasting around $30\,mins$. Wave energy varies on each deployment and winds of over $20\,knots$ from the West have been able to generate wave heights of up to $70\,cm$, with wave periods consistently between $3-5\,secs$ on each deployment. The depth of water at a point $\approx 100\,m$ from MHW is around $4\,m$ at HW during Spring tides.

As well as these driving hydrodynamic factors, estimates of k_s and z_o are required which describe the bed surface. When there are no bed forms present the grain size (d_{50}) is usually taken for k_s as discussed in section 2.2.5. At Portishead, d_{50} has consistently been measured at around $10\,\mu m$ (see chapter 5) so this has been used for the following test cases. This may seem a small value to use as the concept of using the grain size as a roughness length is generally applied to non-cohesive beds where individual particles are a real concept (see section 2.3). Floc size may be somewhat larger, so increasing the estimate of k_s, but the consolidation process could also result in a smoother bed. The log-linear depth transformation requires that the boundary conditions are defined at $z = z_o$. It is important that a realistic value for z_o is used as this defines the height above the bed where velocity and turbulence are zero. Soulsby (1983) lists values of z_o for different bed types quoting a value of $z_o = 0.2\,mm$ for muddy beds (see table 2.2). Owing to the uncertainties in the choice of z_o and k_s a sensitivity analysis has been included. These choices for k_s and z_o are found to give satisfactory results when running the model, as they have been found to interact with each other for certain cases causing crashes in the model. These problems are discussed in section 6.2.2 and 6.5.

It is important that a clear formulation of the problem is made, as this defines how the model will react from a stable position, if confronted by changes in momentum and energy (by the addition of waves, for example) in trying to re-seek equilibrium. Since the pressure gradient (P_o) is held constant, convergence will be satisfied when it is in balance with the shear stress. Integrating equation 3.12 with respect to both time and depth shows that this will be the case when

$$(h - z_o).P_o = \frac{\tau_o}{\rho} \tag{6.1}$$

where $\tau_o = \tau$ at $z = z_o$ defined by equation 3.15. Hence the addition of waves to a converged current profile cannot enhance cycle-averaged bed shear stress (as is generally conceived in the literature), except as a transient process in seeking convergence but will result in changes in other parameters in the governing equations (i.e. turbulence) to compensate. The associated changes in turbulent energy create different velocity gradients, which in turn affect both shear stress and the production of turbulence which will then take time to correct as the shear stress

works to rebalance equation 6.1. The timescales involved are real in as much as the model represents reality. For example, when modelling combined wave and current flows, this is modelled by suddenly superimposing waves on a steady current. If there is a physical situation where a train of monochromatic waves are suddenly superimposed on a steady current then the time to reach equilibrium in the model represents the physical convergence timescale. These timescales can be thus interpreted as determining the quasi-equilibrium status in coastal waters (see Davies, 1991).

6.2.1 Hydrodynamic Test Cases

Results in this section are presented with a water depth of $4\,m$, for a weak current (test case C4 - $\overline{u} = 0.1\,m/s$) and two wave sizes (test case 4W1 - $U_o = 0.5\,m/s$ and 4W2 - $0.05\,m/s$) with period $4\,secs$.. These two wave conditions can be used to assess the applicability of the model to the field data, as they approximately represent the two measured extremes in wave energy. When these two waves sizes are superimposed on the current (C4) the test cases are C4W1 and C4W2. Results are also given for a larger current CL4 - $\overline{u} = 0.5\,m/s$ and with waves added CL4W1 - $U_o = 0.5\,m/s$. Table 6.1 shows the complete hydrodynamic test case parameters with results plotted on a logarithmic depth scale from $z = z_o$ to $z = h$ and presented in figures 6.4-6.13 for the weaker current. Figures 6.28-6.30 show the results from the larger current cases which are referred to for comparison when appropriate.

The following hydrodynamic discussion of the changes in various parameters is kept concise, since the trends are well established and it is the effects on SSC that are of primary interest. The reader is referred to Davies (1991, 1990b) or Davies *et al.* (1988) for an essentially similar discussion of how a (one-equation) turbulence model performs under combined wave and current flow.

Waves Only

Figures 6.1-6.3 show instantaneous vertical profiles of velocity (u), shear stress (τ), turbulent kinetic energy (k), non-dimensionalised turbulent production rate ($[\nu_t + \nu_\tau]\left(\frac{\partial u}{\partial z}\right)^2$ - term in k-equation 3.18), eddy viscosity (ν_t) and turbulent dissipation rate (ε) at ten points though a wave cycle for case 4W1. Qualitatively similar results are obtained for the smaller wave 4W2. The wave cycle $[0 - T]$ proceeds from the point of maximum velocity (0 T) through the decelerating phase to zero velocity (0.25 T) before accelerating to maximum negative velocity (0.5 T).

The figures (6.1-6.3) clearly show the formation of a wave boundary layer extending to around $2.5\,cm$ (defined where velocity is within 1% of U_o). There is no turbulence generated or diffused into the upper part of the water column. During a wave cycle it can be seen from the figures that the accelerating and decelerating phases are quite different, and that production

of turbulence is therefore also cyclic (as observed experimentally e.g. by Jonsson & Carlson, 1976; Hayashi & Ohashi, 1982). There are periods of near zero production in a cycle (see figure 6.2), which have been described (e.g. by Aydin & Shuto, 1988) as a time of re-laminarisation of the boundary layer. There is a double structure in eddy viscosity and turbulent kinetic energy caused by double curvatures in velocity profiles (Aydin & Shuto, 1988). Maximum τ_o and k during the cycle are $1.9\,Nm^{-2}$ and $73\,cm^2s^{-2}$ with maximum turbulent production occurring at the start of the deceleration phase ($t = 0,\, 0.5\,T$).

The relative magnitudes of energy between the two wave cases (4W1, 4W2) can be gauged from the combined cases C4W1 and C4W2 shown in figures 6.6 and 6.7, as the wave boundary layer is largely unaffected by the small current. Reynolds numbers (equation 2.18) for the two cases (4W1 - 1.6×10^5; 4W2 - 1.6×10^3) imply that the smaller wave is essentially laminar ($RE < 10^4$), hence will have very small levels of turbulent kinetic energy. The wave boundary layer thickness is the same in both cases, as the wave period is the same and it is this which influences the development of the boundary layer (see equations 2.23-2.25). Peaks in k and τ_o are $3.5 \times 10^{-3}\,cm^2s^{-2}$ and $0.06\,Nm^{-2}$ for case W2. Hence k is four orders of magnitude smaller than for case 4W1 and τ_o is around 30 times smaller. The small values of k are anticipated to be caused by the tiny turbulent production which is six orders of magnitude smaller than turbulent production for larger wave.

Current Only

Converged current profiles (C4) of u, k, τ, ν_t are included in figures 6.6-6.9 for the combined wave-current cases, since they are the starting conditions for these runs. A logarithmic velocity profile is obtained from around $10\,cm$ above the bed up to the free surface (figure 6.6), with a near bed region ($0 - 1\,mm$) influenced by the viscous and damping functions. A buffer region joins the two regions, appearing quite extensive for this small current. Velocity profiles over silty-sand measured by Chriss & Caldwell (1982) also show a viscous and buffer region extending to around $1\,cm$ for small currents ($\approx 10\,cm/s$, $20\,cm$ above bed). Test cases with larger currents (CL4 - see figure 6.29) have resulted in a logarithmic profile from virtually the bed to the free surface. Depth-averaged turbulent kinetic energy is $9\,cm^2/s^2$ for this case compared to $0.6\,cm^2/s^2$ for the smaller current (C4). Larger roughness lengths have also been found to remove any viscous layer. A near linear shear stress distribution is maintained with a maximum of $0.036\,Nm^{-2}$ at the bed, which is within 1% of the expected value to balance equation 6.1 (figure 6.8). Eddy viscosity has a characteristic distribution with a maximum at mid-depth (figure 6.7), and turbulent kinetic energy is reasonably constant for the depth region $1 - 600\,mm$ tailing off to zero at both the free surface and the bed (figure 6.6) due to the boundary conditions. A slight peak in k occurs $0.5\,mm$ above the bed where the velocity gradient is altered by the viscous forces and hence there is a small peak in turbulent production (can be seen in figure 6.13; case C4W2).

Current and Waves

In this section waves are added to converged current profiles and run until convergence criteria (equation 3.39) are again satisfied. This simulates the sudden introduction of a train of monochromatic waves on a steady current. Depth and wave-cycle averaged values of k, u, ε can be seen for the two cases (C4W1 and C4W2) in figures 6.4 and 6.5 during convergence, respectively. For case C4W1, $<\overline{k}>$ is increased from the current (C4) values of $0.60\,cm^2s^{-2}$ to $0.65\,cm^2s^{-2}$ by the addition of waves, but for case C4W2 was decreased to $0.53\,cm^2s^{-2}$. It is perhaps at first sight surprising to find that for the smaller wave case convergence takes longer to achieve, as it would seem natural that a smaller change in momentum would take less time to achieve equilibrium (C4W2: 1498 cycles $\approx 100\,mins$, as opposed to C4W1: 989 cycles $\approx 65\,mins$). It is also surprising to find that the converged depth and cycle averaged velocity for the combined case is increased slightly from the current only case; (C4W1 - by 2%, C4W2 - by 8%). For fully developed rough turbulent flow this is not generally the case, as the addition of waves causes a reduction in mean velocity (Davies, 1991) as additional turbulent energy introduced by the waves is diffused into the upper part of the flow. This has also been found to be the case with this model for runs with stronger currents (see figure 6.29), and can also be the case with larger waves or roughness lengths.

The increases in $<u>$ in the upper part of the flow correspond with decreases in $<k>$ in the same region. Transient and equilibrium wave-cycle averaged profiles for case C4W1 are shown in figures 6.8-6.10. The addition of waves (immediately) creates an increase in k in the wave boundary layer (1 cycle) but just above the upper edge of the boundary layer, after 1 cycle k is reduced (figure 6.8) and ε is increased (figure 6.10). The changes are perhaps best identified in the eddy viscosity profiles (in figure 6.9) which show a reduction from above $1\,cm$. Figure 6.13 shows turbulence production rate for case C4W2 at ten points through a cycle and also turbulence production rate due to the current only (C4). The smaller wave case is shown, as this allows both wave and current induced production to be plotted in one figure, however, qualitatively results are similar for the larger wave case. It can be seen that production is in fact decreased from the current only case for much of the cycle. To keep the governing equations in balance, the decreases in k result in an increase in u. These changes are, however, quite small $< 10\%$ in general and will have a minor effect on the SSC distribution. So interactions between the hydrodynamic parameters control the overall changes in $<u>$ and for larger energy cases, a decrease from current only values at all depths can be expected by the addition of waves, but for lower energy cases the addition of waves can cause an increase in the upper part of the flow. At the bed there is always a reduction in $<u>$ corresponding to an increase in $<k>$.

Both reductions and increases in mean velocity have been observed in laboratory tests depending on wave orientation relative to the flow. Kemp & Simons (1982, 1983) found that waves propagating with the current created a reduction, and opposing waves an increase, in depth-averaged velocity. Near the bed, the mean velocity was reduced irrespective of wave direction if the bed surface was hydraulically rough. However, above a smooth bed, an increase in near bed velocity was always observed. It should be noted that in a turbulence model of this kind,

the waves are purely sinusoidal and hence have no 'direction' relative to the current, except for the angle of alignment by choosing different ratios of $U_o : V_o$.

Comparison of cycle averaged quantities between cases C4, C4W1 and C4W2 is shown in figures 6.6-6.10. A reduction in velocity in the near bed region due to the addition of waves can be seen for both C4W1 and C4W2 cases, although more extensive for the larger wave (up to around $10\,cm$) (see figure 6.6). The increase in velocity in the upper part of the water column can also be seen as previously discussed. The gradient of the velocity in the logarithmic region is slightly less for the larger wave, implying an enhancement of z_o. Instantaneous profiles of velocity at ten phases in the wave cycle, show that velocities are largely unaffected in the wave boundary layer, with the current effects superimposed above this region (figure 6.11). Significant enhancement of the wave boundary layer by the weak current is thus not obvious, as has been observed in many combined flow situations (see e.g. Davies *et al.*, 1988). This is a consequence of the magnitude of the weak current, as a larger current can indeed enhance the boundary layer thickness. Maximum shear stresses in a wave cycle are shown in figure 6.7, with instantaneous profiles though the wave cycle in figure 6.11. Bed shear stresses are dominated by the waves due to the associated larger velocity gradients, with maximum values of $1.95\,Nm^{-2}$ for C4W1 and $0.15\,Nm^{-2}$ for C4W2. For the larger wave value this is almost the linear addition of the wave and current shear stresses, as found by Kemp & Simons (1982) in flows over smooth beds. For the smaller wave case the combined stress is larger than the linear addition, but since the values are so small it is difficult to draw any conclusions from this result.

$<\nu_t>$ is decreased by about 10% over the (formerly) current boundary layer as a consequence of the reduction in k when either wave size is added (figure 6.7). Nearer the bed eddy viscosities are reduced at the edge of the wave boundary layer and slightly enhanced below this by the additional k from the waves (figure 6.7), which is exemplified by the instantaneous profiles through a wave cycle in figure 6.12. At the upper edge of the wave boundary layer the eddy viscosity is 'pulled' to a larger value by the current, than it was for waves only (compare figure 6.12 with figure 6.3).

6.2.2 Roughness Length Analysis

A sensitivity analysis of changes in z_o and k_s has been performed for both the waves only (4W1) and combined wave-current case (C4W1). It is simpler to test the effects on the purely oscillatory case (4W1) as the convergence is so much quicker and the implications of the effects can still be understood. Figures 6.14 and 6.15 show wave-cycle averaged k and maximum τ in a wave cycle (for 4W1) as these are considered to be representative of the important hydrodynamic parameters in the determination of SSC profiles.

Keeping z_o fixed at $0.2\,mm$ and decreasing k_s to zero has only a small effect (e.g. 10% decrease in k peak) on either k or τ_o (figure 6.14). Thus the chosen value of surface roughness in the previous tests is having only a small input into turbulence production as required and the

bed can be considered fairly smooth. Doubling the value of k_s to $20\,\mu m$ has a similar effect (10% increase in k peak) but increasing k_s further has a larger influence which starts to effect the size of the boundary layer if $k_s > 50\,\mu m$. Bed shear stress is increased by nearly 50%. This is when roughness viscosity begins to dominate over eddy viscosity in the turbulent production term and the boundary condition ($k = 0$ at z_o) starts to be contradicted by the formulation of roughness viscosity, which is controlled by the choice in k_s. This increase in k_s creates additional turbulent production and hence k near the bed but the boundary condition satisfies $k = 0$. It is anticipated that this contradiction leads to large gradients of k resulting in unrealistically large diffusion terms in the governing equations. Increasing k_s still further causes the model to crash. This shows a limitation of the model at present and requires a reconsideration of using a roughness viscosity to increase turbulent production, due to surface roughness with the present boundary conditions, if rough beds are to be successfully modelled (see chapter 7).

Increasing or decreasing z_o ($1 - 0.01\,mm$) for the fixed k_s has little impact (<5%) on the k and τ_{max} (see figure 6.15). Obviously, moving the boundary means that the viscous region is extended or partly removed. Increasing z_o to very large values ($10\,mm$) does affect the flow considerably as the viscous region has then been totally removed. Decreasing z_o further has no more influence than the decrease to $0.01\,mm$, but can cause numerical difficulties due to very small grid spacing near the bed. Decreasing the time step and decreasing z_* (to put more points nearer the surface and hence increase the size of the grid spacing near the bed - see section 3.2.4) improves results but the required resolution means that additional running time is high.

The same tests for the wave and current case show small changes in all parameters higher in the water column and similar changes near the bed as for the waves alone. Small alterations in depth averaged velocities and turbulent kinetic energy and dissipation rate necessarily occur due to the near bed changes. Figure 6.16 compares cycle averaged values of k for case C4W1 (with $z_o = 0.2\,mm$, $k_s = 2, 60\,\mu m$) which caused the largest changes for the wave only case. The increase in k decreases u and starts to apparently 'enhance' the wave boundary layer as previously discussed. As can be seen the changes in the upper part of the flow are small and for the other tests are virtually unnoticeable (< 1%). The effect on SSC (figure 6.16) is therefore also far more than for any of the other sensitivity analysis cases, which showed small changes (< 1%) in SSC above the wave boundary layer but is still not that large. This test was conducted using bed model B1 (see section 6.3) allowing mass of sediment in the flow to be changed by erosion or deposition. The relatively large changes in SSC are caused by the substantial increases in bed shear stress (50%) as seen in figure 6.14.

These results show that for the range of conditions associated with the field data, changes in z_o and small changes in k_s have no major effect on hydrodynamic factors which in turn mean that sediment profiles are relatively unchanged (max. <10%). However, if surface roughness is a major influence ($k_s > 50\,\mu m$ for $z_o = 0.2\,mm$) then profiles are altered considerably by contradictions between boundary conditions and the present roughness viscosity formulation. Further comment is made on this subject after comparison with other data and models (section 6.5).

6.2.3 Non-Colinear Waves

Although the model can be used to represent waves at an angle to the unidirectional flow, test cases have been kept to a minimum. This is because, as has been seen in the fieldwork, the site is wave dominated and it has been found that when attempting to model the results the current serves mainly as a mechanism of providing *some* turbulence in the upper part of the flow. This allows sediment to diffuse into this region which it is unable to do if the flow is purely oscillatory and hence direction is of little importance. Bed model interactions are also controlled by the wave (only) shear stress as the bed shear stress associated with the weak current is so small. Future work might consider the differences between colinear and non-colinear waves in this turbulence model.

Converged wave-cycle averaged turbulent kinetic energy and eddy viscosity (ν_t) results are presented in figure 6.17 for an orthogonal wave and current flow (C4V1) and compared with the colinear case (C4W1) and current only (C4). Combined flow peaks in k and ν_t are within 10% in each case with the slightly smaller values for the orthogonal case. This has little effect on the vertical SSC distribution.

6.2.4 Varying Wave Period

Varying wave period from 3-5 seconds (the range of zero-crossing periods found in field data) has a minimal (5%) effect on the magnitudes of k and u but does change the thickness of the wave boundary slightly (figure 6.18). However, the changes are small (<5%) so it is reasonable to assume that the results presented with a period of 4 seconds are representative of the wave periods at Portishead.

6.2.5 Conclusions and Implications for Field Results

The addition of waves to the weak current is seen to create no increase in wave boundary layer thickness. Hence the concept of an enhanced wave-current boundary layer in the field is unlikely if the model sufficiently represents reality. The thickness of this boundary layer is much less than the instrument measuring heights, hence estimates of wave orbital velocity at each height should be similar, as predicted by linear wave theory. A sensitivity analysis of the bed parameters in the model (z_o and k_s) shows that changes make only small differences (<10%) in turbulence in the flow although the model has been shown to have limitations for large values of k_s.

Current generated turbulence is small (for this weak current), hence it is not surprising to find that estimates of bed shear stress based on unidirectional flow methods are unreliable. Again, the only way of inducing significant additional turbulence is to increase the roughness beyond

the point of reality. Thus methods of estimating bed shear stress based on friction factors, or eddy viscosities (if they could be calculated) probably are the most useful measure of bed shear stress for this combined wave-current situation (in agreement with field discussion). The linear addition of current and maximum wave bed shear stress is probably a reasonable approximation of total maximum bed shear stress for this site based on the model results. This is in agreement with laboratory measurements over smooth beds and with Tolman's (1992) recent paper on the best way of estimating shear stress based on present knowledge. Current only bed shear stress is 1-20% of the maximum bed shear stress (for the range of waves, $U_o = 0.05 - 0.5\,m/s$) hence in many cases it would also be a reasonable approximation to use only the bed shear stress associated with waves in calculations of sediment transport rates.

6.3 Evaluation of Sediment Modelling of Field Data

The sediment modelling can be divided into two areas - suspended and bed sediment. Interactions between the hydrodynamical conditions and the choices of these sediment characteristics control the vertical distribution of sediment. Field data have shown that SSCs generally vary between $0.1 - 1.0\,g/l$ over the bottom metre, with higher SSC in the near bed ($< 10\,cm$) region (up to $5\,g/l$) on occasions. Limited settling velocity data has suggested that using the relationship with concentration (c) given by figure 2.14 (i.e. $W_s = 0.001\,c$) is a reasonable first approximation, with a sensitivity analysis to assess the influence on SSC profiles. The bed surface strength has varied considerably on each deployment; from an easily erodible layer of near fluid mud to a surface virtually resistant to erosion. Therefore, both the erosion rate and critical erosional shear stress will have a wide range of values (τ_e: $0 - 1\,Nm^{-2}$). A critical depositional shear stress has been tentatively suggested to be around $0.05\,Nm^2$. The bed model has a number of parameters given in section 3.2.5, which formulate the bed type. The effects on SSC due to variations in these parameters are considered critically.

Sediment can be added into the flow in a number of ways - either directly into the flow, or via the bed through erosion. Many turbulence models solve the concentration equation (e.g. Teisson, 1991) without the source and sink terms, hence the most common method used by modellers is to introduce an initial homogenous SSC distribution, allowing redistribution by the flow but retaining the total mass of sediment in suspension. Initial tests are discussed using this method (section 6.3.1), which also allowed solving of some numerical problems which can result in loss of total mass of suspended through rounding off errors. Losses due to numerical techniques with the present model are less than 0.5% in 1500 cycles. This is followed by the effects of allowing erosion and deposition as described in section 3.2.3. All the preliminary tests in sections 6.3.1-6.3.3 are made with concentration and momentum equations uncoupled, before addressing the influence of density gradients (section 6.3.4). To assess the performance of the model with respect to the field data, the previous hydrodynamic situations given in table 6.1 and discussed in section 6.2 have been used in the preliminary tests.

In section 2.3.3, analytical solutions to the concentration equation (e.g. Rouse equation 2.61)

showed that SSC profiles are basically a function of three factors - turbulence, settling velocity and near bed reference concentration. This simplified concept has been used in the following discussions to help in the explanation of various results.

6.3.1 Without Bed Model

Two intial homogenous (bulk) concentrations of 0.5 and 0.25 g/l were used, giving a total mass of sediment (per m^2) in 4 m water depth of 2 kg/m^2 and 1 kg/m^2, respectively. The settling velocity is taken as $W_s = R_o c$ with $R_o = 0.001$ with a minimum settling velocity of 0.1 mm/s, hence when concentrations are below 0.1 g/l this minimum value is used. SSC profiles for current only cases are presented as initial conditions (0 wave cycles) in the cases with waves added.

Waves Only

If an intial homogenous SSC distribution over the whole depth is assumed, then since there is no mechanism of turbulence generation outside the wave boundary layer (as shown in section 6.2.1), then all sediment attempts to settle into this near bed region. This can cause numerical difficulties, due to the steep gradient of SSC at the upper edge of the boundary layer and the large concentrations contained therein. There is little point in presenting results for this case, unless some sediment is allowed to 'escape' by deposition, as the magnitudes of concentrations are simply representative of the choice of initial SSC.

Current Only

An initial homogenous SSC distribution redistributes to form a relatively constant SSC gradient over most of the water depth for a current (C4) only for either bulk concentration of 0.25 g/l and 0.5 g/l (see figure 6.20). The SSC gradient is dependent on the initial choice in bulk concentration. For the smaller bulk concentration (0.25 g/l), the SSC gradient is almost zero as the downward settling flux is small (due to low concentrations) compared with the upward turbulent flux (see equation 3.33). The SSC gradient is steeper for the larger bulk concentration (0.5 g/l) and some sediment collects in the near bed viscous region.

Current and Waves

The effect of the addition of waves on the weak current only SSC profile is shown in figure 6.19 through the stages to convergence for both cases C4W1 and C4W2 using the bulk concentration of 0.5 g/l. In both cases the effect of waves is to immediately start increasing SSC in the wave

boundary layer, at the expense of the sediment just above this region. In time, the added energy in the wave boundary layer creates larger concentrations from the bed up to around $80\,cm$ for C4W1, and slightly smaller concentrations (than for C4) above this. The thickness of this increased SSC region is around $1\,m$ for in both cases C4W2. Thus the influence of the waves on SSC profiles extends far greater than the hydrodynamic definition of wave boundary layer thickness shown in figures 6.6-6.8 (i.e. a few cm).

In figure 6.20, SSC profiles for C4, C4W1 and C4W2 with both bulk concentrations of $0.25\,g/l$ and $0.5\,g/l$ are shown for comparison. Qualitatively, results are similar for either initial concentration. As has been mentioned (see figure 6.20) it is seen that the SSC profile is largely unchanged from C4 above $\approx 1\,m$ by the addition of waves and for the smaller concentration the profiles are unchanged as low as $10\,cm$. This contradicts the results when a bed flux of sediment is assumed, when SSC is affected throughout the flow by wave magnitude. The two different wave sizes create quite different distributions in the near bed region if sufficient sediment is available in the flow (i.e. with $0.5\,g/l$), however, due to the differing magnitudes of turbulence in these regions. The larger wave has a more pronounced boundary layer, as opposed to a more gradual increase in SSC nearer the bed with the smaller wave.

Conclusions

It has been seen that when the model is run without any bed flux of sediment, so that total mass in suspension is retained, then results are necessarily dependent on this choice in bulk concentration. This implies that SSC models which are formulated in this way and have no bed model, will only produce SSC profiles reflecting this initial condition and can hence only simulate limited physical situations. This is because in most natural situations any choice in initial SSC distribution for a particular flow will tend to fall into one of two categories -

- the flow 'wants' to deposit sediment to the bed, but cannot, and hence the reference concentration is being kept artificially high so influencing SSC profiles.
- the flow 'wants' to erode sediment from the bed and increase its total load, but cannot, hence redistributes SSC based on the limited sediment available.

The first situation is the more unrealistic, as in any flow deposition should be permitted as governed by the turbulence levels for a particular settling velocity. Without a depositing flux, for example, it would be possible to create a distribution with bulk concentration of over $1\,g/l$ despite having virtually zero turbulence if this was the initial choice in SSC. This is because the reference concentration is controlling the distribution. If the flow falls into the latter category, then this can at least represent the physical problem of a limited sediment budget (i.e. bed resistant to erosion). Prediction in either of these cases is an unrealistic concept unless the total input of suspended sediment is known.

6.3.2 Including Bed Model

Careful consideration must be given to the values assigned to the parameters in the bed model, since erosion and deposition are being instigated by critical values in bed shear stress. During a purely oscillatory or a combined wave and current flow, bed shear stresses vary considerably during a wave cycle (see section 6.2.1), but must still retain a maximum value. For a current only case, bed shear stress is a constant. If the critical depositional shear stress is not zero (i.e. sediment is allowed to deposit for at least part of a wave cycle), but the erosional shear stress is above the maximum bed shear stress generated by the hydrodynamic conditions, then eventually all sediment will deposit. This can be thought of as continually reducing the reference concentration until it is zero, hence the rest of the SSC profile must become zero. Similarly if the depositional shear stress is above the maximum bed shear stress in a cycle, then the flow will continually erode sediment if available, and provided $\tau_o > \tau_e$ for at least part of the wave cycle.

Thus to obtain equilibrium profiles it is sensible to choose a critical erosional shear stress below the maximum bed shear stress and above the depositional shear stress. In a current only situation, since the bed shear stress is constant then the only option is to use the retained mass approach and ignore bed influence. For this reason the rest of this chapter is devoted to waves only or combined wave-current flows. If SSCs dropped below $0.05\,g/l$ in a depositional regime then the test case was not run until convergence because the large computational times in getting final convergence profiles were unwarranted, since the significance of a profile of $0.05\,g/l$ was considered irrelevant compared to some of the large concentrations measured during the field experiment.

Table 6.2 lists the different bed models (B1-B7) used in the following sections. Critical erosion shear stresses vary between $0 - 1\,Nm^{-2}$ and critical depositional shear stress of $0.05\,Nm^{-2}$ and $0.1\,Nm^{-2}$ have been used. Erosion rates given in the literature (Mehta, 1987; Delo & Ockenden, 1992) show a wide range (over two orders of magnitude) since they are (generally taken to be) a function of (excess) shear stress (see section 2.3.7) making the interpretation of a sensitivity analysis difficult. Values of 0.0002 and $0.001\,kgm^{-2}s^{-1}$ have been used.

A sensitivity analysis of bed parameters is restricted to section 6.4 where the bed model is directly related to the field data as every situation warrants a separate analysis as each parameter interacts dynamically with the others depending on the hydrodynamic conditions. As an extreme example, increasing the erosion rate (M_e) only has an influence if any erosion can actually take place (i.e. when $\tau_o > \tau_e$). Each parameter has the potential to alter the SSC by over an order of magnitude under the correct situation. The influences of settling velocity and density gradients are addressed at this stage, however, as these are dependent on the actual SSC values which are reasonably representative of field data.

In the following preliminary test cases using C4W1 and 4W1 a single layered bed with an unlimited sediment budget has been used. This section shows results only using bed model B1: $\tau_e = 1.2\,Nm^{-2}$, $\tau_d = 0.06\,Nm^{-2}$, $M_e = 2.0\times10^{-4}\,kgm^{-2}s^{-1}$. These bed model parameters

have been chosen to produce SSC profiles which can be used for testing the influence of settling velocity and density gradient affects without concentrations becoming too large. They also give SSC profiles with similar orders of magnitude as field data. Tests using the smaller wave case (C4W2 and 4W2) found that all suspended sediment was deposited for any of these bed models. A further discussion of the implications of this is given in section 6.4.

Convergence of SSC Profiles

Experiments with (automatic) convergence criteria based on checking total mass of sediment in suspension proved to be quite dangerous in terms of predicting convergence prematurely owing to low deposition and erosion rates and the considerable time to redistribute suspended sediment from initial conditions in some cases. To be certain that converged SSC profiles (within 1%) had been obtained, checks were made both by adding and removing some suspended sediment to apparently converged SSC profiles and allowing the sediment to redistribute again to equilibrium.

Waves Only

Figure 6.21 shows ten instantaneous SSC profiles through a wave cycle for case 4W1, which can be compared with the hydrodynamic profiles in figures 6.1-6.3. During a cycle there is little variation in SSC ($< 1\%$), with slightly more variation in the bottom $1\,mm$ (up to 10%). This is a product of a small settling flux, with insufficient time (wave period) to have any influence. The cycle-mean concentration is almost constant $1\,g/l$ throughout the depth of the wave boundary layer ($\approx 0-3\,cm$). The influence of SSC extends further than the hydrodynamic definition of the wave boundary layer to around $10\,cm$ due to small levels of turbulence found at the edge of the boundary layer. This shows that it only requires the mere presence of turbulence (i.e. $k \neq 0$) to permit some sediment diffusion. Steep SSC gradients are found at the edge of this 'SSC boundary layer' between 5 and $10\,cm$.

Current and Waves

In figure 6.21, convergence of SSC profiles to an equilibrium profile is shown starting from the converged SSC profiles shown in figure 6.20 for case C4W1 without bed fluxes with both initial bulk concentrations of $0.5\,g/l$ and $0.25\,g/l$. The time to reach this equilibrium profile is large from either starting profile ($\approx 5000\,cycles = 5\,hours$ for SSC at each grid point to get within 10%) indicating that on the ITZ suspended sediment profiles are unlikely to be in equilibrium, even if hydrodynamic conditions could remain quasi-steady. This time to convergence is a function of both the settling velocity and weak current generated turbulent kinetic energy. Further checks were made to ensure that the same equilibrium profile was obtained by starting from zero initial concentration and allowing sediment into suspension only by erosion from the

bed. This important result means that any initial SSC can be used to speed up the process of convergence without influencing final SSC profiles provided bed parameters are chosen sensibly (i.e. $0 < \tau_d < \tau_e < \tau_{max}$).

SSC near the bed follow those of the wave only case (both shown in figure 6.21) until above the wave boundary layer and the total mass remaining in suspension is $1.51\ kgm^{-2}$.

For the smaller wave case (C4W2) any initial suspension (as a starting condition) is deposited despite changes in bed model parameters to allow more erosion (decrease τ_e, increase M_e), as there is insufficient upward turbulent flux to balance the settling flux. This implies that near bed turbulent kinetic energy is a controlling mechanism in the SSC profile over the whole water column (and not just the wave boundary layer) when any current is present and provided there is a small amount of energy in the upper flow domain (i.e. a weak current is present) then 'high' SSC profiles are possible if wave energy is sufficient. The balancing factor determining the magnitude of concentration will then be the rates of deposition and erosion relative to the wave generated bed shear stress and settling velocity discussed next.

6.3.3 Changes in Settling Velocity

Changes in SSC profiles with settling velocity (more specifically R_o where $W_s = R_o c$) are shown in figure 6.22, both with and without a bed flux of sediment. It should be noted that the changes in R_o are quite large (factor of two) compared with most estimates of W_s (as a function of concentration; see figure 2.14), hence the effects are somewhat exaggerated. It is recognised that settling velocity is a complex function of sediment properties (see e.g. Fennesy *et al.*, 1993) and is crudely modelled by this equation.

Without any bed flux (retaining mass in suspension), varying the settling velocity has the effect of altering the overall SSC gradient: larger W_s creating steeper gradients (figure 6.22). Doubling R_o to 0.002 creates very large concentrations ($> 100\ g/l$) in the near bed region for the bulk concentration of $0.5\ g/l$ by pushing suspended sediment from the upper (current dominated) flow. Reducing R_o to 0.0005, creates a weak SSC gradient and the SSC distribution approaches well mixed conditions.

If settling and erosion is permitted then doubling or halving W_s decreases or increases overall concentrations, changing the total mass in suspension from $1.51\ kgm^{-2}$ to either $0.87\ kgm^{-2}$ and $2.45\ kgm^{-2}$, respectively. This is due to changes in the rate of deposition which is a function of near bed concentration. The SSC gradients in the profiles are, however, unchanged as a consequence of the resultant changes in concentration at the bed. This is in complete contrast to the results when sediment is held in suspension. These fundamental differences mean that SSC profiles produced by models of this kind should always be related to the bed sediment boundary conditions.

Settling velocity (as a function of concentration) thus has the capability of causing large changes in total mass of sediment in suspension which is of obvious consequence in calculations of sediment transport rates. The profiles are unaltered in structure however, provided enough time is allowed to reach convergence and a bed flux of sediment is permitted. Large convergence times for the lower settling velocities are required unless reasonably accurate initial conditions can be chosen. If the SSC profile obtained by using $R_o = 0.001$ is used as an initial condition for the case with $R_o = 0.0001$ over 10000 cycles ($\approx 10\ hours$) are needed to converge values at each grid point to within 5%.

6.3.4 Density Gradient Effects

Figures 6.23-6.27 show the effect of coupling the sediment and momentum equations by equation 3.31 as described in section 3.2.3. As a starting condition the converged hydrodynamic and SSC profiles from test case C4W1 with bed model B1 are used to observe the transitory effects of introducing density gradient effects. This initial profile are therefore included in the figures. Other examples of density gradient effects are discussed in section 6.4.

Depth and wave-cycle averaged velocity ($<\overline{u}>$), turbulent kinetic energy ($<\overline{k}>$) and turbulent dissipation rate ($<\overline{\varepsilon}>$) are shown in figure 6.23 for 5500 cycles ($\approx$ 6 hrs). Numerical convergence is never actually achieved and $<\overline{k}>$ and $<\overline{\varepsilon}>$ oscillate periodically (period $\approx$1200 cycles) around the values without density gradients effects after around 2000 cycles. Figures 6.24 and 6.25 show the transitory effects on τ, ν_t, k and c during the first 768 cycles. Figures 6.26 and 6.27 show the various parameters during a period of this oscillation between 3328-4224 cycles. Flux Richardson numbers (Ri_f) defined as the ratio of production and dissipation by buoyancy in the k-equation (see section 3.2.2; equation 3.18) are shown in figure 6.27.

The introduction of density effects firstly damps much of the turbulence in the current dominated part of the flow (figure 6.25) which reduces eddy viscosity and hence shear stress (figure 6.24). After around 1000 cycles the linear shear stress distribution has been limited to the bottom 1.5 m with 50% reductions in overall magnitude at the bed (figure 6.24). The effect this has on suspended sediment is considerable, forcing sediment into the near bed boundary layer and increasing gradients throughout the depth and in particular reducing concentrations in the upper half of the water column (figure 6.25). Having therefore disturbed the balance between shear stress and pressure gradient the model then starts to react and attempt to recreate the (wave-cycle averaged) linear shear stress profile which is required for quasi-equilibrium. It is suggested that because of the small total energy in the system, due to the weak current, equilibrium is never achieved as the balance is quite critical and an oscillation develops with shear stress continually over- and under-shooting the equilibrium position (see figure 6.26). Efforts to improve this by altering timesteps and grid spacing had little effect. Based on the results of other examples (C1W3g; see figures 6.33 and 6.34) the oscillations can dampen in time, but in this case they appeared to be maintained indefinitely (at least for 20000 cycles). The same oscillation cycling can be seen in k and Ri_f, shown in figure 6.27 (although variations in Ri_f are small), with the upper part of the flow most affected. Variations in in concentration shown

in figure 6.26 are also small (<10%), hence general aspects of the density gradient alterations to the SSC profile can be discussed. Overall, density damping has reduced concentrations from above 10 cm to the water surface ($h = 4\,m$) (by 50% at surface) which can be directly correlated with Ri_f. The point at which damping plays a role is close to the critical vale of 0.15 suggested by Ellison (1966). Near the surface the values of Ri_f become large (> 1) because of small turbulence production which is a denominator in the definition of Ri_f. Although in the upper part of the flow SSCs are reduced significantly for this water depth ($4\,m$), in the field measuring region ($0.05 - 1\,m$) changes due to density damping are small (<5%).

In figures 6.28-6.30 a similar comparison between density effects with a larger current (CL4W1: $\overline{u} = 0.5\,m/s$; $U_o = 0.5\,m/s$) is made, showing a case when convergence was achieved. Damping effects are negligible for this larger current (order of magnitude large k) for the same sediment parameters fairly well mixed SSC distribution (figure 6.30). Flux Richardson numbers are much smaller (< 0.1) for the whole of the flow rising above the critical value of 0.15 (Ellison, 1966) only at the surface when the boundary condition forcing k and hence ν_t to zero create virtually zero production as previously discussed.

6.4 Simulation of Vertical SSC Distributions in the Field

The intention of this section is not to use the model to *predict* SSC profiles, but to use it to attempt to justify and explain some of the observations made in the field by simulating them. There are too many (uncalibrated) degrees of freedom with the model to allow it to be used as a completely predictive tool as yet, although results are encouraging in at least creating profiles which resemble field measurements for physically realistic bed parameters. In the discussion of field results (chapter 5) two mechanisms which received attention were the formation of highly concentrated ($1 - 5\,g/l$) near bed suspensions and the correlation (or non-correlation) of bed shear stress with SSC measured at various heights above the bed. The results from this model provide some additional insight into explaining these processes.

Previous research (see section 2.3.4) has suggested that either fluidisation of bed sediment by waves or hindered settling can create high concentrations near the bed but from the fieldwork alone it is unclear which of these mechanisms is more important. The field observations have shown that high concentration regions can form for extended periods of time during Spring tides when surface sediment is very weak ($< 3\,kPa$) and moisture contents are high (>200%) under small waves ($U_o < 5\,cm/s$). They have also been recorded during storm conditions (11/91) but more intermittently. The thickness of this near bed region is less than 10 cm on most occasions and with concentrations of between $1 - 2\,g/l$. Proximity to the main channel (sediment supply) has also been a governing factor in temporal variations. On each deployment there are spasmodic periods of high concentration in the bottom 10 cm which can be correlated with high energy events (increases in current or wave size).

The following test cases are made for two water depths of $1\,m$ and $4\,m$ considered to provide

information on SSC profiles to be expected for a range of scenarios and have been separated into storm and calm days. The results presented in section 6.4.1 for test case C1W3 (figures 6.33-6.39) show a sensitivity analysis of the various parameters in the bed model and consider the effects of density stratification for a water depth of $1\,m$. In the deeper water ($4\,m$) test cases are made independently of density stratification as this has been seen (in section 6.3.4) mainly to reduce SSC near the water surface ($1 - 4\,m$) which is above instrument measuring heights.

6.4.1 Storm Deployments

The most complete data for storm conditions are from 11/93 when there was no net erosion measured despite quite large ($40\,cm$) waves with associated shear stresses (given by friction factor technique) in excess of $1\,Nm^{-2}$ when near breaking. Figures 4.27 and 4.28 show the variation of orbital velocity and shear stress during the two tidal cycles from the field study. During the second tide when water depth (h) was $\approx 1\,m$, $U_o = 0.33\,m/s$ and at around HW ($h \approx 4.0\,m$) $U_o = 0.2\,m/s$. These two wave sizes with a weak current ($\overline{u} = 0.1\,m/s$) are used as the test cases (C1W3 and C4W4) in this section. The complete test parameters are given in table 6.1.

Water Depth: 1 m, test case C1W3

SSCs measured during the 11/93 deployment 37 and $70\,cm$ above the bed for this water depth are approximately 0.62 and $0.45\,g/l$, respectively. Bed shear stresses (given by friction factor method; figure 4.28) of around $0.5\,Nm^{-2}$ are found at this depth.

Converged wave-cycle averaged k, τ_{max}, u, ν_t for test case C1W3 ($\overline{u} = 0.1\,m/s, U_o = 0.33\,m/s$) are shown in figures 6.35 and 6.36. In these figures profiles with density gradient effects included are also shown for the same hydrodynamic conditions with various bed models. Maximum bed shear stresses are $1.05\,Nm^{-2}$ (figure 6.36) and the peak in k is more than double the value in $4\,m$ water depth (compare figures 6.35 and 6.31).

Based on the field study information a reasonably resistive bed model with parameters $\tau_e = 1.0\,Nm^{-2}$, $\tau_d = 0.05\,Nm^{-2}$, $M_e = 1.0 \times 10^{-3}\,kgm^{-2}s^{-1}$ (table 6.2 - bed model B2) was formulated with the resulting SSC profile shown in figure 6.37. Concentrations at the measuring heights are approximately 50% less than the field values (shown as circles in the figure) so a number of other profiles given by other bed models (B3-B6) are also presented in the same figure providing a sensitivity analysis of the bed model for this situation. The relevant parameters for each bed model are given in table 6.2. All bed models have a single layer (with unlimited available sediment) so equilibrium profiles have been obtained when the settling and erosion during a wave cycle are in balance and not due to limitations on sediment supply. Hence either by lowering the critical erosional shear strength, increasing the erosion rate or increasing the

depositional shear stress slightly better agreement with field data has be found. None of the profiles, however, give concentrations greater than $2\,g/l$ $10\,cm$ above the bed implying a near bed high concentration layer does not exist assuming the bed can be modelled in this way. A further test was made for a bed with a low τ_e and high M_e (B7 - $\tau_e = 0.1\,Nm^{-2}$, $M_e = 0.001\,kgm^{-2}s^{-1}$; table 6.2) starting from a homogenous SSC distribution of $0.5\,g/l$ and run for 1500 cycles ($\approx 100\,mins$). The transient results are shown in figure 6.38 and concentrations increase to over $> 5\,g/l$ at the bed. This has not been run until convergence as concentrations become so large, but shows that high near bed concentrations could be possible if an easily entrainable sediment layer overlaid a more resistant layer.

If a multilayered bed model is used with different critical erosional shear stresses and sediment budget in each layer then this provides the bed model with the capability of producing any of these profiles by effectively controlling the value of the reference concentration. In reality sediment strength is a function of bed depth (Mehta & Parchure 1985; figure 2.22) so to produce equilibrium profiles using a single layer is unrealistic. However, predictive capability is removed unless detailed bed profiles can be obtained.

The same tests (C1W3g) have been made with momentum and concentration equations coupled (i.e. including density stratification effects) with each bed model (B2-B6) which produces converged wave-cycle averaged profiles given in figures 6.35-6.38. Convergence is achieved despite initial small equilibrium oscillations developing (see figures 6.33 and 6.34 - C1W3g with bed models B3 and B4, respectively). Profiles of $<u>$ and $<k>$ (figure 6.35) and $<\nu_t>$ and $<\tau>_{max}$ (figure 6.36) show the same effects as discussed in section 6.3.4 with small increases in $<u>$ and decreases in $<k>$ above the wave boundary layer. Maximum bed shear stress are unchanged from the case without density effects. The SSC profiles (figure 6.37) are similar to those without density effects in the wave boundary layer. They reflect the measured SSCs much better by reducing concentrations in the upper part of the flow and creating larger SSC gradients than were previously produced.

Implications of all these results are three-fold. Firstly, in all cases significant sediment is retained in suspension for any 'natural' choices in bed parameters, hence SSC well above the wave boundary layer are responding to bed shear stress. This explains the high correlation of shear stress with SSC on the storm deployment (figure 5.3) and is simply a result of suspended sediment diffusing into the steady boundary layer and not the result of any enhancement of the wave boundary layer by currents.

Damping of SSC by density stratification above the wave boundary layer could be responsible for the measured gradients of SSC. Gradients are under predicted without density damping. Any of the bed models tested produce SSC profiles with correct (to within an order of magnitude) concentrations (for the limited data). In each of these cases a dynamic equilibrium between deposition and erosion is maintained. In the field SSC profiles are dependent on both the amount of sediment already in suspension and bed conditions. These effects can be simulated by affecting sediment in suspension using a multilayered bed model, which can physically represent an upper sediment layer with small shear strength above a resistant bed. If sediment deposits then it forms part of this easily entrained layer and is thus easily resuspended.

Near bed high concentrations can be simulated with these large waves but do not reach concentrations greater than around $2\,g/l$ unless there is a suitable supply of bed sediment with low shear strength (i.e. bed model B7). This can be interpreted as either needing a large amount of sediment in suspension or an easily entrainable bed. Predicted concentrations approximately $10\,cm$ above the bed are around $1\,g/l$, hence siltmeters which only measure above $2\,g/l$ when positioned this far above the bed were unlikely to respond for long periods as was found in field experiments.

Water Depth: 4 m, test case C4W4

SSC measured at 37 and $70\,cm$ during the 11/91 deployment for this water depth are approximately 0.45 and $0.3\,g/l$, respectively (figure 4.29).

Converged wave-cycle averaged k, τ_{max}, u, ν_t for test case C4W4 ($\overline{u} = 0.1\,m/s$, $U_o = 0.2\,m/s$) are shown in figures 6.31 and 6.32. The results fall between those of the earlier test cases (C4W1 and C4W2) and maximum bed shear stresses are $0.49\,Nm^{-2}$ and therefore 50% less than stresses in the shallower water. For any of the bed models with $\tau_e \geq 0.5$ used in the previous tests (B1-B3, B5 and B6, see table 6.2) all suspended sediment is deposited as maximum shear stresses do not exceed this value. For the two bed models with smaller $\tau_e = 0.1\,Nm^{-2}$ (B4 and B7) all suspended sediment is still deposited as the settling rate is still larger than erosion rate.

To maintain a non-zero equilibrium SSC profile requires physically unrealistic bed model parameters. Increasing erosion rates to $0.001\,kgm^{-2}s^{-1}$ and decreasing critical erosion shear stress to zero can maintain suspensions in the upper part of the flow, however, these still cannot produce high concentrations ($> 1\,g/l$) $5 - 10\,cm$ above the bed. This is because of the small bed shear stresses associated with these hydrodynamic conditions. It is concluded that the flow would be depositing sediment for this water depth.

6.4.2 Calm Deployments

During the calm ($H_s < 5\,cm$) deployments of 7/91 (figure 4.4) and 5/93 (e.g. figure 4.46) the formation of a high SSC near bed region $1 - 5\,g/l$ is seen for much of the tidal cycle. Concentrations in the rest of the flow generally decrease during the cycle until midway through the ebb phase when they (generally) are at a minimum at all measuring heights. As the water decreases in depth further, then in the very shallow ($< 0.5\,m$) water concentrations can be increased slightly as the small waves break resuspending some of this deposited sediment (e.g. figure 4.49).

When modelling these small waves, since the wave orbital velocities are small they have been taken simply as $U_o = 0.05\,m/s$ allowing use of earlier results for test case C4W2 (depth $4\,m$;

see figures 6.5-6.7). In figure 6.7 it is seen that maximum bed shear stresses associated with these velocities are small $\approx 0.15\,Nm^{-2}$. Further tests for the same waves and current in $1\,m$ water depth were made, but results are similar to those in the deeper water to be discussed as shear stresses are the same, hence figures are not included and results concentrate on the water depth of $4\,m$.

At both depths of $1\,m$ and $4\,m$ no sediment can be retained in suspension despite reducing τ_e to zero and increasing M_e to $0.01\,kgm^{-2}s^{-1}$ which is large based on the maximum excess shear stress of $0.15\,Nm^{-2}$ (see figure 2.21). This is because the excess shear stress used in erosion formula is so small for these waves. Starting from an initial homogenous concentration of $0.5\,g/l$ with bed model B7 the transient depositional profiles for C4W4 are shown in figure 6.39 for 2000 cycles ($\approx 135\,mins$). As can be seen, there is no formation of any near bed high concentration region with this bed model approach suggesting that hindered settling is a necessary factor in determining fluid mud formation. As was seen in the tests without any bed flux (see figure 6.20) high concentrations were formed when the sediment had no mechanism for escape which then means concentrations at the bed are high enough to possibly give rise to hindered settling.

Hindered settling has been observed to occur for concentrations as low as $3.5\,g/l$ (see Kirby, 1988) so this mechanism could indeed be responsible as concentrations above this value are suggested to exist in the bottom $1\,cm$ by the measurements $5\,cm$ above the bed. The bed model was modified to reduce the deposition rate by altering the near bed concentration (c_o) which is one of the parameters in the settling rate (see equation 2.64). This was done simply by setting it to the depth average concentration $\approx 0.5g/l$ as to complicate matters further was considered unwarranted based on the data available. This concept of a 'retarded' deposition was then used with test case C4W2 with the same bed model parameters as in B7 (as before). This bed model is coded B7h. The resulting transient profiles are shown in figure 6.39, again as they vary with wave cycles from an initial homogenous distribution of $0.5\,g/l$ up to 2000 cycles. This time much higher concentrations can form but still remain below $1\,g/l$, $10\,cm$ above the bed.

A further factor that might be considered is that as the tidal current decreases around HW then this might also cause increases near bed concentrations. This was modelled by removing the pressure gradient when the waves are added but using the same homogenous SSC distribution. The reduction in depth averaged current, approximately $0.1 - 0.075\,m/s$ in 1500 wave cycles, is shown in figure 6.40. The corresponding transient SSC profiles are shown in figures 6.41, both for the original bed model (B7) and with retarded settling (B7h). The concentrations are increased throughout the depth in both cases, in particular in the retarded settling case, creating SSC just over $1\,g/l$, $10\,cm$ above the bed.

It is concluded that small wave oscillations alone are probably not capable of maintaining high concentrations in the near bed region and that both a sufficient SSC supply and some form of hindered settling are also required. As the tidal current reduces in magnitude to leave purely oscillatory flow, high concentrations are more likely to form and based on earlier results with larger waves could then be enhanced temporarily (in thickness) by intermittent increases in

wave energy.

6.5 Comparison with other Data and Models

There are insufficient suitable data to compare SSC profiles produced by the model with other wave-current environments. Some validation has been given by the comparison with the limited field data and reasonable agreement with SSC profiles has been found. However, it is important to compare the hydrodynamic profiles as these control the SSC distribution.

The model boundary conditions (BC) were formulated in an attempt to be suitable for modelling flows over muddy beds where both viscous and turbulent viscosity are likely to be of importance. This has meant choosing the bed BC at z_o but retaining the low Reynolds number approach by making $k = 0$ at z_o (see section 3.2.4). However, the choices in BCs mean that the model may have become specific to the intended purpose and comparison with other data is required to establish the generality of the model. The method of generating unidirectional flow by a constant pressure gradient (allowing velocity to vary, and holding wave cycle-averaged shear stress the same, when waves are added) used by the model makes it unsuitable for comparison with laboratory wave-current data where the current is kept constant (effectively changing the pressure gradient) and shear stress is enhanced by the addition of waves. Hence, comparison between the model and Davies *et al.* (1988) well established one-equation turbulence model for flow over rough beds, which is the basis of the more recent models of Davies (1990a, 1990b and 1991), is made. Also, comparison with measurements of a turbulent oscillatory boundary over a horizontal wall using a large oscillating water tunnel by Hayashi and Ohashi (1982) highlight limitations in the present model, necessitating future work should reconsider the present BCs and damping functions if predictive capability is to be improved.

Davies *et al.* (1988) Turbulence Model

Detailed comparison of the values of u, k, τ and ν_t with Davies *et al.* (1988) model is made for a wave and a combined wave-current case ($U_o = 1.0\,m/s$, $\overline{u} = 1.0\,m/s$) over a rough bed $z_o = 5\,mm$ ($k_s = 150\,mm$). When these values of z_o and k_s were used, the formulation of roughness viscosity (a function of k_s; see section 3.2.2) meant that large values of k were produced near the bed contradicting the BC, $k = 0$ at $z = z_o$. It is anticipated that although turbulence levels at the bed were correct in magnitude, large gradients of k created large diffusion terms which caused the model either to crash, or produce 'strange' results through the majority of the water column. Smaller values of k_s ($0 - 10\,mm$) produced qualitatively similar results to the Davies *et al.* model, underpredicting k and τ. In figures 6.42-6.45 instantaneous values of u, k, τ and ν_t are shown at ten phases through the wave cycle and compared with the Davies *et al.* results for both wave only and wave-current cases using $k_s = 10\,mm$. This value of k_s was the maximum value that still produced qualitatively correct results with smaller values underpredicting hydrodynamic values still further (by another 50%

for $k_s = 0$). As can be seen, qualitative comparison is good and boundary layer thickness is the same, but peaks in k are half those of Davies *et al.* model and τ_o are smaller by 25%. Enhancement of the wave boundary layer by currents is correctly predicted and values of ν_t are of similar magnitude (figure 6.45). In this figure results could not be plotted on a logarithmic scale (with this model, for comparison) since values of ν_t are zero at the surface and bed. Only the wave alone case is shown as values of ν_t cover three orders of magnitude when a current is included and on a linear scale cannot be plotted for comparison.

Hayashi and Ohashi (1982) Oscillatory Boundary Layer Measurements

Measurements by Hayashi and Ohashi (1982) in a purely oscillatory turbulent boundary layer over a horizontal wall using a large oscillating water tunnel are also compared with model results. Oscillations of period 9.8 *secs* and $U_o = 59\,cm/s$ with a Stokes boundary layer thickness ($\delta = (2\nu/\omega)^{1/2} = 2.1\,mm$) were produced, and velocities, turbulent kinetic energy and Reynolds stresses are plotted non-dimensionalised in figures 6.46-6.48, respectively at three points during both the acceleration $(0 - \pi/2)$-(a) and deceleration $(\pi/2 - \pi)$-(b) part of the cycle. Similarly results from the model are shown in the same figures, which have been produced using $z_o = 0.05\,mm$ (the smallest value that can be used without causing numerical difficulties; see section 6.2.2) and $k_s = 0$ (no surface roughness). These choices in z_o and k_s need to reflect the smooth wall conditions but are limited by this minimum value for z_o required in the log-linear depth transformation. Qualitative agreement is found in all figures with boundary layer thickness correctly reproduced. Velocities compare quantitatively correctly, but turbulent kinetic energy (two-fold) and shear stress (six-fold) are over-predicted (note differing scales in figures). It is anticipated that these over-predictions are due to under-damping of near wall turbulence created by the boundary conditions being set at z_o as opposed to the wall ($z = 0$).

6.5.1 Conclusions

The model has been found to perform qualitatively correctly for a wide range of cases. Quantitative performance is less satisfactory. In particular the model tends to underestimate the levels of turbulent kinetic energy and shear stress as compared with rough flows and overestimate for smooth laboratory tests. Under certain regimes the additional production of turbulence due to surface roughness interacts with bed boundary conditions, so creating numerical problems due to steep gradients. This is most noticeable when considering rough beds and leads to the conclusion that the best way to view this empirical approach to surface roughness with the present BCs is to select the largest value of k_s below the physically correct value, such that it enhances the turbulence without altering the rest of the flow domain. Future work should address BCs and damping functions in an effort to improve this situation (see section 7.4).

Model Initiation Parameters for Test Cases										
Test case	C4	C4W1	C4W2	CL4	CL4W1	C4V1	4W1	4W2	C1W3	C4W4
h (m)	4	4	4	4	4	4	4	4	1	4
P_o (cm/s^2)	0.0009	0.0009	0.0009	0.0136	0.0136	0.0009	-	-	0.005	0.0009
$\overline{u}$ (m/s)	0.1	0.1	0.1	0.5	0.5	0.1	-	-	0.1	0.1
U_o (m/s)	-	0.5	0.05	-	0.5	0	0.5	0.05	0.33	0.2
V_o (m/s)	-	0	0	-	0	0.5	0	0	0	0
T (s)	4	4	4	4	4	4	4	4	4	4
z_o (cm)	0.02	0.02	0.02	0.02	0.02	0.02	0.02	0.02	0.02	0.02
k_s (cm)	0.001	0.001	0.001	0.001	0.001	0.001	0.001	0.001	0.001	0.001
Converge (N)	-	989	1498	-	2510	1010	5	5	542	1204

Table 6.1: Model Test Cases. When the same hydrodynamic conditions are used with density stratification effects "g" is added to the code name.

Model Initiation Parameters for Bed Model Test Cases							
Bed Model	B1	B2	B3	B4	B5	B6	B7
R_o	0.001	0.001	0.001	0.001	0.001	0.001	0.001
Nlayers	1	1	1	1	1	1	1
τ_e (Nm^{-2})	1.2	1	0.5	0.1	0.5	0.5	0.1
τ_d (Nm^{-2})	0.06	0.05	0.05	0.05	0.1	0.05	0.05
M_e $(kgm^{-2}s^{-1})$	0.0002	0.001	0.0002	0.0002	0.001	0.001	0.001

Table 6.2: Bed model test cases

Chapter 7

Conclusions and Future Work

A field study of an ITZ at Portishead, Severn Estuary and a one-dimensional (vertical) $k-\varepsilon$ turbulence model have been used to improve the understanding of sediment and hydrodynamic spatial and temporal variations during tidal cycles. The following conclusions have been made.

7.1 Hydrodynamic Mechanisms

Tidal currents and waves create complex hydrodynamic conditions on ITZs. Estuarine topography, both on a large scale (e.g. headlands, bays) and a finer scale (e.g. bed surface) is an important influence on sediment transport.

1. Winds blowing from the Westerly quarter (up to 25 *knots*) have been observed to generate waves on the ITZ with zero-crossing periods consistently in the range 3–6 seconds and with significant heights up to 70 *cm*. A best fit regression line correlating wave height and wind velocity (from SW-NW) has been estimated (equation 5.1). Predicted wave climates for Portishead main channel using a wave ray model (see table 2.1) and wave characteristics based on fetch and duration (see figure 2.2) are unsuitable for estimating wave characteristics on the ITZ due to the complex influences of wind direction, fetch, duration and wave-current interactions. Hence, if estimates are needed for engineering purposes it would be recommended to conduct a field survey.

2. Although mud bed deformation has been observed to dynamically attenuate waves in the field (Wells & Kemp, 1986; MacPherson, 1980), attenuation in wave heights at Portishead due to bottom interaction has proved to be less significant than expected. These previous field observations were made at sites which had fluid mud (BD$<$ 1250 kg/m^3) layers 10–100 *cm* thick. At Portishead a layer of this density (MC$>$150%) has only been of order 1 *cm* in thickness for the conditions observed. This depth of deformable bed sediment has probably been insufficient to absorb wave energy.

3. Estuarine topography has been seen to effect both the direction and magnitude of tidal currents significantly. Mean velocity data have been interpreted as tidally induced circulations (max. velocity 15 cm/s 50 cm above the bed) forming over the ITZ at Portishead with much reduced magnitude of the main channel current (max. velocity 2 m/s). These are caused as the main channel current is diverted by the two headlands which protect the embayment. During the flood tide the current is small and predominantly longshore ($< 5\,cm/s$, $\Rightarrow \tau_o < 0.01\,Nm^{-2}$) and against the main channel flood direction (estimates of τ_o based on table 5.1). This has not been observed to have any influence on sediment resuspension but would provide an advective transport mechanism both in transporting additional SSC onto the ITZ from the main channel and transporting SSC laterally. As the tide ebbs, a more circular eddy structure is perceived which is of sufficient vigour for a period of 15–45 minutes ($15\,cm/s$, $\Rightarrow \tau_o \approx 0.07\,Nm^{-2}$) to resuspend sediment deposited previously in the tide on calm days. Increases in SSC can be measured in the bottom 50 cm during this period.

4. Kinetic energy at the site is dominated by waves and methods of estimating bed shear stress based on unidirectional results have therefore been found to be unsuitable. At present, the most productive avenue for improvement in bed shear stress estimation in accounting for wave-current interactions is suggested to be empirical alterations to friction factor methods when waves are significant.

7.2 Surface and Suspended Sediment

1. Surface bed sediment at Portishead is predominantly mud, although nearer the LWM sand is present in increasing proportions. The median particle diameter (d_{50}) is approximately 10 μm. Moisture content, bulk density and shear vane strength vary considerably on daily timescales depending on erosion and deposition.
MC: 50 – 300 %, SV: 15 – 0 kPa, BD: 1700 – 1200 kgm^{-3}

2. Erosion at this site is dominated by breaking waves and the antecedent bed condition. Small waves ($H_s \approx 5cm$) have been observed to remove 1 cm of recently deposited surface sediment (MC > 160 %, SV < 3 kPa) during a tidal cycle. If previous stormy days have resulted in a resistant surface being exposed (MC< 70 %, SV >11 kPa) moderate waves ($H_s \approx 20 - 40\,cm$) have little effect. Since MC has been seen to be an index of erosion rate, an empirical relation would be useful. However, this would require significantly more data because of the numerous factors involved. Beach slope and tidal range may be important in determining erosion rates as these control the length of time that a point on the ITZ is exposed to breaking waves.

3. Deposition has been observed during Spring tides on days of little wave activity ($H_s <$ 5 cm). Peak rates of around 1 cm in a tidal cycle of sediment (BD: 1250 kgm^{-3}, MC: 200%) have been recorded. This could correspond with longer timescale peak rates at the site of 25 $cm/30\,days$ (West, 1990) but it is expected that higher rates might occur if calm Spring tides follow a storm.

4. Suspended sediment has been found to be patchy, varying both transversely and vertically. SSCs at HW range from 0.1–0.5 g/l approximately 50 cm above the bed. Tidal range, antecedent meteorological factors and current/wave climate all influence SSCs.

   (a) Transverse variations in SSC are caused by varying water depth and antecedent bed sediment. A muddy surf zone region (SSC $1 - 3\,g/l$) created by turbulence generated by waves breaking can extend over $10\,m$ for waves over $40\,cm$ in height. Concentrations in the surf zone are 2–10 times the magnitude of HW values. The retreat of this muddy surf zone as the tide ebbs on calm days may be a significant transport mechanism with small breaking waves keeping sediment in suspension, thus preventing deposition.

   (b) The vertical distribution of SSC under the weak current and varying wave energy has been conceptualised as three regions (see also figure 5.4):

   - A highly concentrated region ($1 - 5\,g/l$) can form in the bottom few centimetres, maintained for extended periods by small oscillatory forces and hindered settling.
   - A bed influenced region ($0.2 - 1.0\,g/l$) extends above this and can be identified by correlating SSC with bed shear stress from the friction factor technique (or H_s/h). This can extend to above $70\,cm$ in depth for waves $20 - 40\,cm$ in height, far beyond the hydrodynamic definition of a wave boundary layer.
   - Above this the lowest concentration region ($0.1 - 0.5\,g/l$) extends to the surface and is not influenced by bed generated turbulence. This may be considered the wash load or background concentration.

   Hence steep SSC gradients of order $5 - 50\,g/l/m$ can exist in the bottom $0 - 20\,cm$ with much reduced gradients of order $0.1 - 0.5\,g/l/m$ in the overlying metre. The extent of these regions is dependent on the hydrodynamic conditions and bed surface sediment, so that distinct regions are not necessary, and any one, or two, may almost dominate the SSC distribution. Tidal range and antecedent meteorological factors are expected to control the supply of SSC, affecting the magnitudes of SSC in each region.

7.3 Modelling

The concentration equation in a low Reynolds number $k-\varepsilon$ model has been modified to include density stratification effects and sediment exchanges to and from a bed model, with sediment exchange governed by critical erosional and depositional shear stresses. A weak current ($\overline{u} = 0.1\,m/s$) and differing wave sizes ($U_o = 0.05 - 0.5\,m/s$, $T = 4\,secs$) in $4\,m$ and $1\,m$ water depth have been used to provide additional insight into field measurements. The complexities of breaking waves have not been considered. As a first approximation, settling velocity has been assumed to be function of SSC, without any particle interaction (e.g. flocculation).

1. Qualitatively the model has worked well for a number of different flows without changing any empirical coefficients, functions or boundary conditions in the model. Boundary layer thickness and the overall turbulent and shear stress structure during the acceleration and deceleration phases of oscillatory flow are correctly predicted. In comparison with other data and models, quantitative results are less satisfactory. The model under-predicts turbulence and bed shear stress in rough oscillatory flows and over-predicts when compared with smooth bed laboratory experiments. Various improvements are suggested (see section 7.4), but a more extensive set of field data might be appropriate as a precursor to this investigation.

2. Flows with waves only result in sediment congregating in the wave boundary layer. This is due to no turbulent kinetic energy being generated above this region, hence there is no mechanism able to support suspended sediment. Numerical instabilities can be created if an homogenous SSC profile is used as an initial condition, since eventually a severe SSC gradient is created at the edge of the wave boundary layer as sediment is redistributed. Without bed sediment exchange concentrations are simply functions of the initial mass in suspension, and with bed exchange are controlled by the balance between settling and erosion.

3. The inclusion of a weak current provides a carrier for sediment to be diffused into the upper part of the water column. Wave size controls the magnitude of SSCs throughout the depth but for small waves, $U_o = 0.05\,m/s$, equilibrium SSC profiles cannot be maintained above $0.05\,g/l$ in either $1\,m$ or $4\,m$ of water depth for any 'realistic' choice in bed model parameters. The same is true in $4\,m$ water depth with larger waves $U_o = 0.33\,m/s$ (corresponding to $40\,cm$ waves). It is therefore concluded that sediment would be depositing throughout the tidal cycle on calm days, and there would also be a period of deposition on storm days if tidal range is sufficient. Thus, the current alone is insufficient to support sediment in suspension.

4. No enhancement of the wave boundary layer ($\approx 2.5\,cm$ for $T = 4\,secs$) is predicted by the addition of this weak current to the waves. However, SSCs are affected well above this purely hydrodynamic definition of wave boundary layer thickness. The correlation of SSC with bed shear stress found in field results for larger waves could therefore be explained simply by sediment diffusion.

5. High concentrations (above $1\,g/l$) in the bottom $10\,cm$, as observed in field experiments, can be produced for large waves ($U_o = 0.33\,m/s$; c.f. 11/91 deployment) in shallow water ($1\,m$) with suitable choices in bed model parameters. However, in deeper water, or for smaller waves ($U_o = 0.05\,m/s$) the smaller oscillations are insufficient to support high concentrations unless the bed model is modified to include a form of 'retarded' settling rate. This suggests hindered settling plays a significant part in their formation in the field.

6. The inclusion of density stratification reduces concentrations in the upper part of the water column, corresponding with flux Richardson numbers above the critical value of 0.15 suggested by Ellison (1966). The resulting steeper SSC gradients are more comparable with the limited field data. Introducing density stratification effects into an equilibrium

wave-current situation creates transitory reductions in shear stress through the water column (up to 50% at the bed).

7.4 Future Work

Field results have shown that predicting the transport of cohesive sediment on ITZs where both wave and current influences are present is complex. Numerous hydrodynamic and sediment factors mean that it may remain necessary to complete a detailed field study when accurate prediction is required for engineering or environmental purposes. The understanding of the temporal change in SSC during a tidal cycle as a function of depth has been improved quantitatively, but further field studies are needed to improve the spatial resolution. In has been seen that significant quantities of sediment can be transported during a tidal cycle, with the near bed region containing a high proportion of suspended sediment under suitable hydrodynamic conditions.

Field Work

Future field work should be aimed at quantifying the near bed ($< 10\,cm$) region, necessarily requiring both turbulence and sediment measurements. It may be necessary to develop smaller instruments to address this fully. The role of steep near bed SSC gradients in damping turbulence, thus reducing bed shear stress needs attention.

To produce an empirical relation linking erosion rates with bed sediment properties requires significantly more data from a wide range of sites. It is important to be able to monitor bed level changes throughout the tidal cycle if significant progress is to be made in this area. Again, instrument development may be required.

A detailed comparison between this field study and a wider, flatter ITZ more exposed to tidal currents (e.g. Wentlooge, Severn Estuary) may provide useful information on processes governing longer term (months/years) accretion/erosion rates and elucidate the hypothesis that (frequently available) small breaking waves are crucial in controlling sedimentation on ITZs.

Processes on ITZs

Further understanding of the turbulence beneath breaking waves and the impact on suspensions is essential to improving knowledge of sediment transport on ITZs. The retreating of the muddy surf zone, created by small waves breaking as the tide ebbs could be a significant transport mechanism. An instrument capable of monitoring the bed level change when both submerged and exposed would provide information on this concept. Work should include the comparison between Spring and Neap tides as tidal range controls the advance of the surf zone across the ITZ.

Formation of fluid mud layers needs further research under a range of wave-current ratios and for a number of antecedent bed conditions. This should improve the knowledge of the mechanisms controlling their creation - oscillatory forces and hindered settling.

More research into wave attenuation by soft mud beds is needed to quantify attenuation rates and at preferably more than two nodes. However, from the results and observations of this field study the engineering significance may not warrant the scientific interest at this site.

Measurement Techniques

Collecting field data from muddy ITZs is a difficult and tiring operation. Specially designed mountings requiring the minimum of fixing and positioning are required to reduce the time spent on the mudflats, with a single pole pushed through a bed plate providing a good form of mounting. Instruments need to be positioned above an undisturbed bed so attaching the instruments to the pole before moving the whole rig a few metres to an untouched area is recommended. Ideally, logging of data should be continuous, but if storage is a problem the longest lengths of recording possible are recommended, since changes in near bed suspension, for example, can be short term. Thirty minute runs are adequate.

Although ultra-sonic bed level transducers (USts) have been reasonably successful at monitoring bed level in the laboratory, field results have been less rewarding. Potentially USts could be used to monitor the presence of fluid mud. Bed level monitoring using USts provides an ideal method of recording bed level changes during the submerged part of the tidal cycle without disturbing the bed and further research in perfecting the technique might be profitable.

An optical siltmeter pushed into the bed, with the light path just above the bed surface, has been used to monitor bed level change under a depositional regime (tide 1 and 3, 5/93 deployment). Resuspension of any deposited sediment can be identified, but further experiments with this method are required to allow a proper evaluation.

Modelling Improvements

If advection models are to be used as a predictive tool, they will need to be able to model the presence of a near bed highly concentrated region if they are to accurately simulate cohesive sediment transport. The modelling has shown that the choice of bed exchange parameters controlling the supply of sediment into the flow affects SSC profiles considerably, but the present understanding of near bed mechanisms is limiting further progress. There are many areas where improvements to the present model might improve predictability, however, the continued advancement in computing power means that higher order models which represent the physical conditions more realistically (e.g. Reynolds Stress Models) may become more feasible on a wider basis.

To improve the current model may require a larger data set, however, certain areas would benefit from further investigation. Contradictive interactions, under certain regimes, between the formulation of the roughness viscosity, in simulating the additional production of turbulence due to surface roughness, and the boundary conditions at $z = z_o$ need addressing. It may prove better to set the boundary conditions at $z = 0$ by changing the depth transformation as Aydin & Shuto (1988) did, although this may worsen the under-estimation of shear stress and turbulent kinetic energy for rougher flows. It may also be found that there is an upper limit to surface roughness over which an empirical roughness viscosity can apply.

The boundary conditions at the free surface also may be improved (e.g k=0, $\partial u/\partial z$=0), by experimenting with other conditions avaliable in the literature (e.g. used by Davies, 1991). It is unclear whether these changes would have a significant impact on SSC profiles.

Further improvements to the bed model could be made, by including hindered settling and non-discretising the bed layers into a continuous function of shear strength with depth. However, this would again require suitable available data to test the validity.

Improvements in the modelling of suspended sediment dynamics could be made by including particle to particle interactions, so adjusting settling velocities. Richardson number dependent Prandtl/Schmidt numbers could also allow for wider application of the model (see Rodi, 1984).

Priorities should be the investigation of bed boundary conditions and to allow unidirectional flow to be controlled by a constant depth-averaged velocity (instead of constant pressure gradient). This will make the model suitable for comparison with laboratory flows on wave-current interactions.

Plate 1 : View from MHW across Portishead ITZ towards Portishead Point (17/10/91)

Plate 2 : View from MHW across Portishead ITZ towards Black Nore at LW (7/11/91)

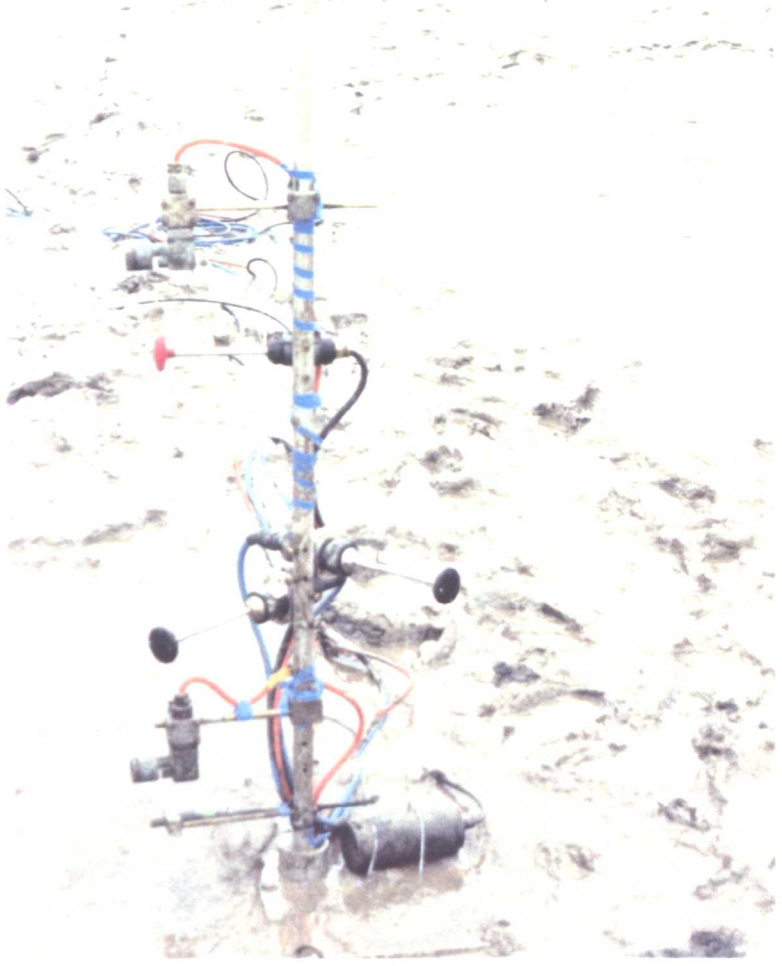

Plate 3 : Instrument profile (from bed to surface) - Pressure transducer, siltmeter, Partech, EMCM, EMCM, EMCM and Partech (6-7/2/92)

Plate 4 : Upper instrument site (from left to right) - USt, Partechs/EMCMs/siltmeter and Braystoke propellers (6-7/11/91)

Plate 5 : Lower instrument site showing USt and EMCM/siltmeter (background) above near fluid mud bed surface (29/7/91)

Plate 6 : USt detail: Two USts are used, one 'fires' at a plate to check on vertical movements and the other the monitors bed level change (6-7/2/92)

Plate 7 : Logging facility located in van above MHW (29-30/7/91)

Plate 8 : The author attempting to recover a mounting pole from the upper site (29-30/7/91)

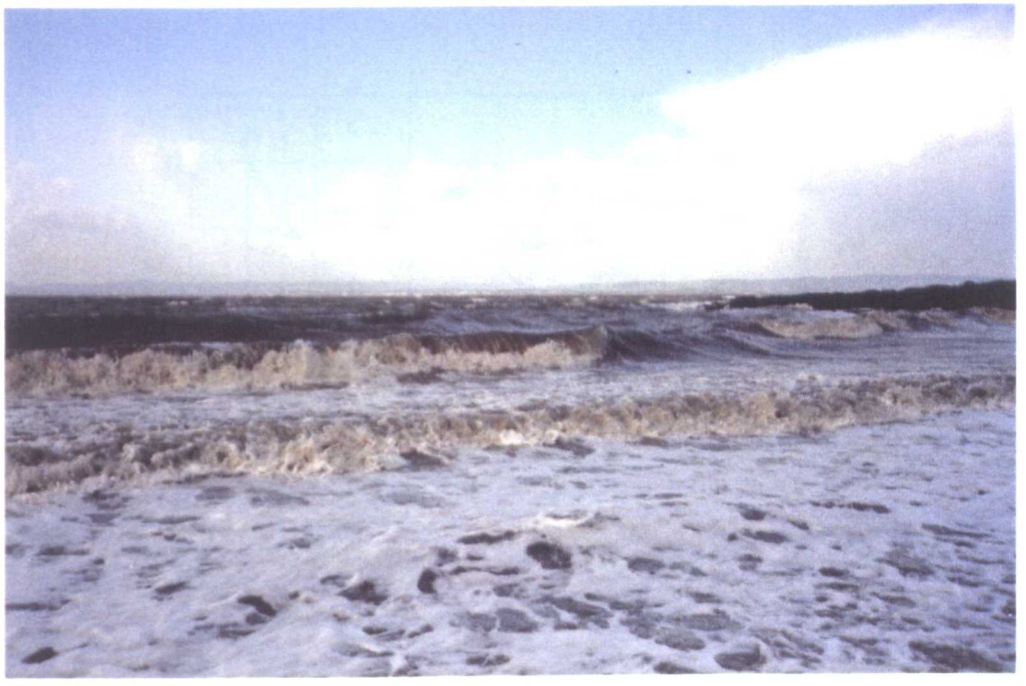

Plate 9 : Breaking waves (17/10/91).

Plate 10: View from Portishead Point towards main channel showing a 'front' between the slacker water above the ITZ created by sheltering and the faster ebbing current in the main channel (6/2/91)

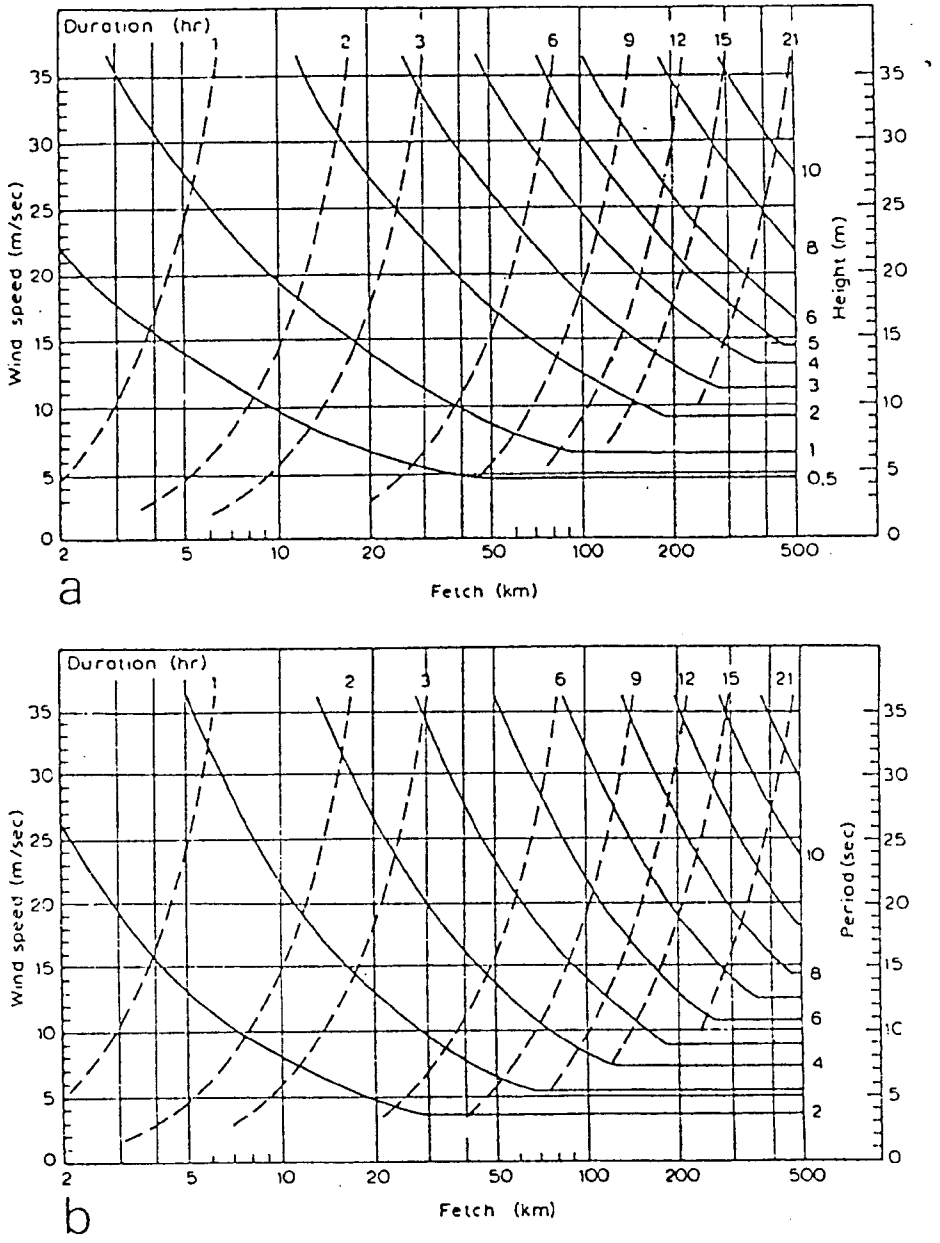

– Graphs for the prediction of (a) significant wave height and (b) zero up-crossing wave period in coastal waters, based on JONSWAP results, from Carter (1982). In (a), enter with wind speed at left-hand side, move across until the limiting fetch or duration (broken lines) is reached, then move down the curve (full line) to the height scale. Similarly in (b), but moving down to the period scale.

Figure 2.2: Wave predictions based on fetch and duration (Carter, 1982)

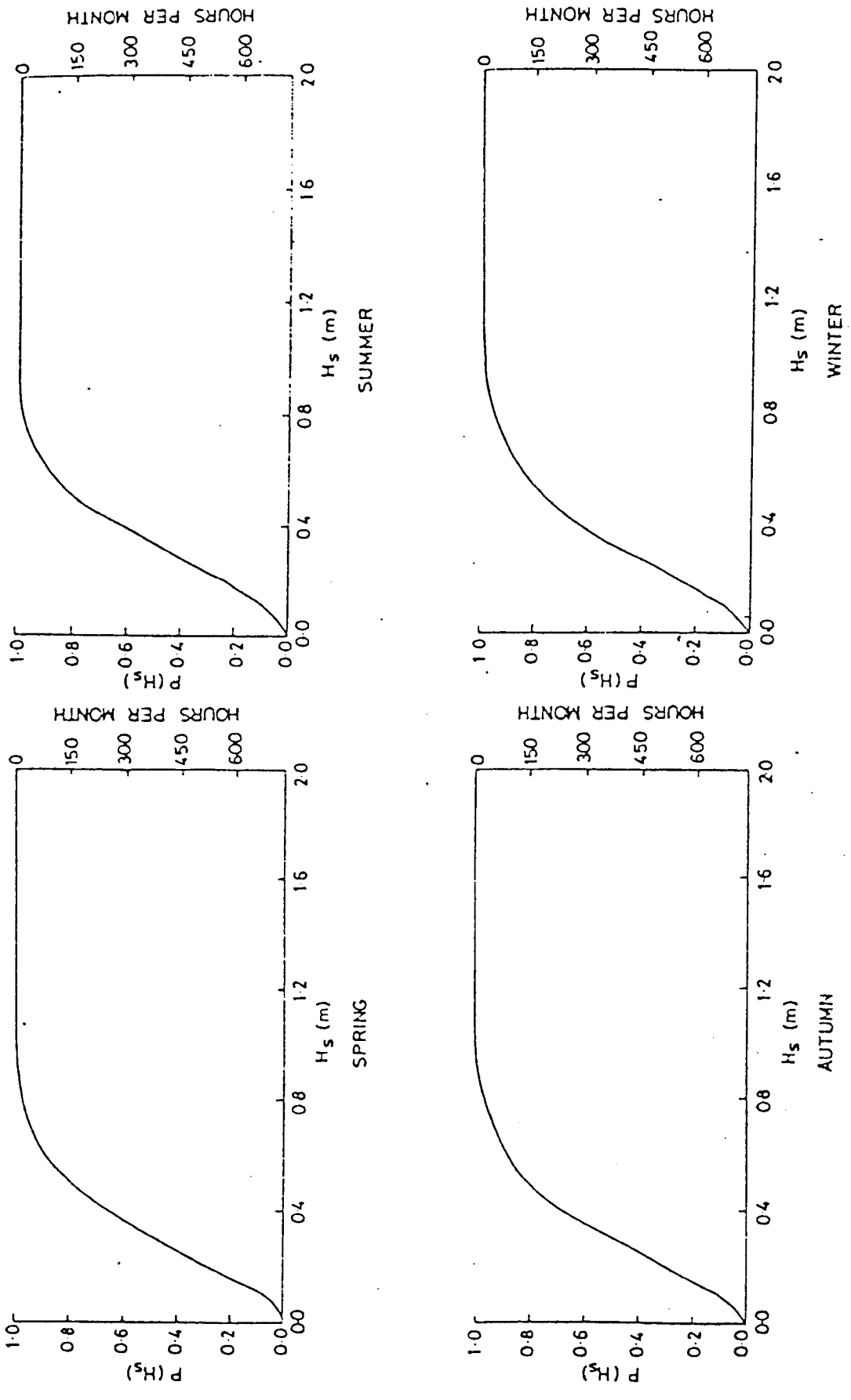

Figure 2.3: Predicted wave heights at Portishead (HRS, 1984)

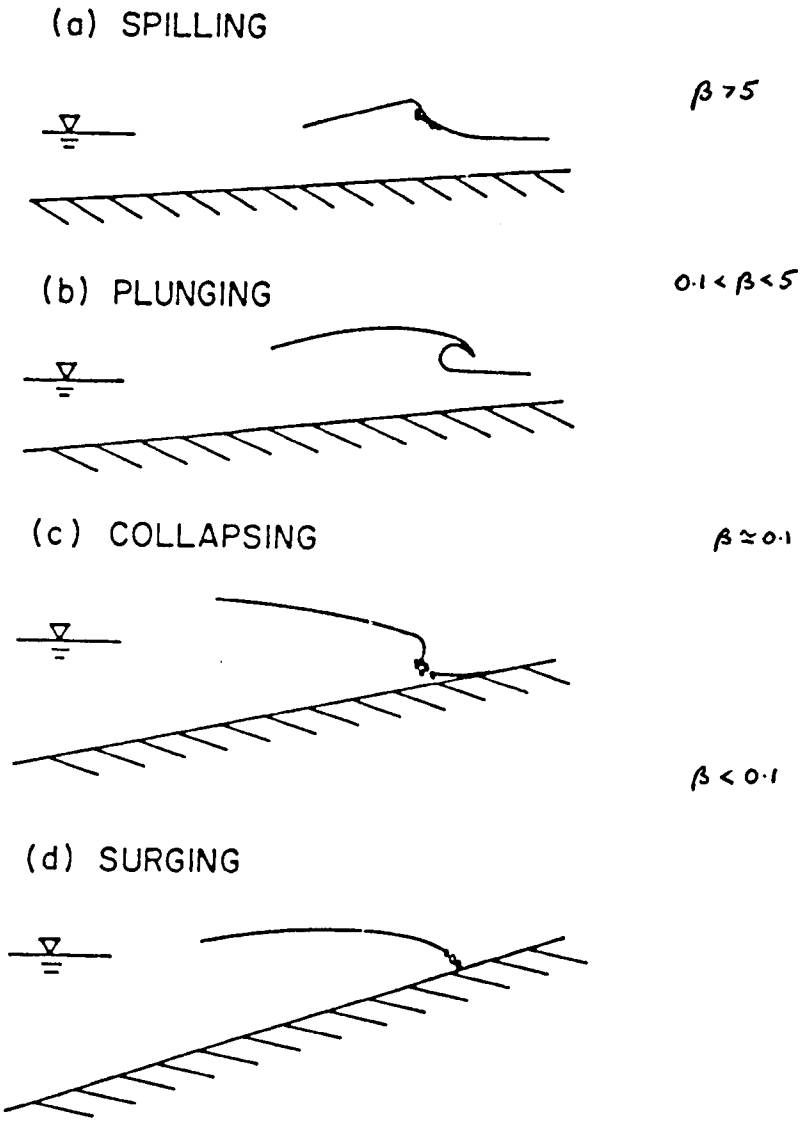

Figure 2.6: Breaking wave profiles and classifications (Galvin, 1972)

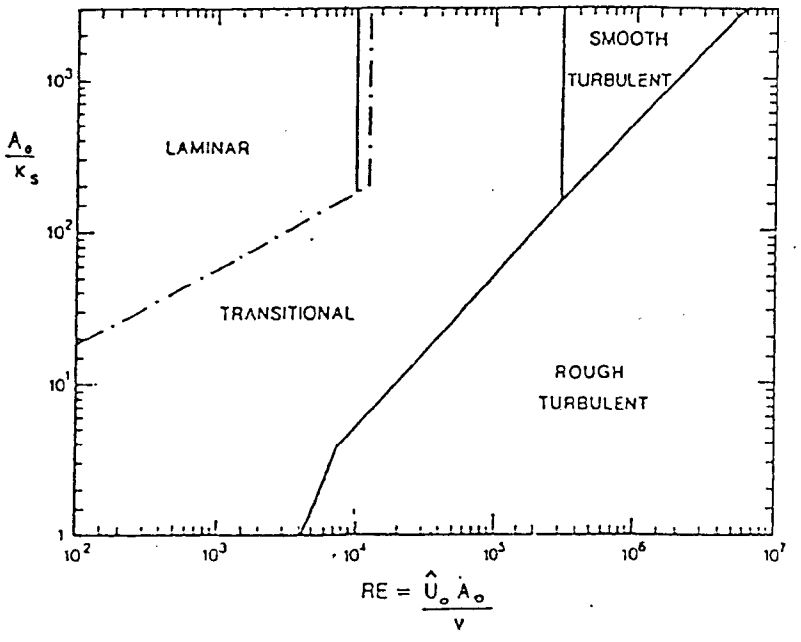

Figure 2.7: Classification of flow regimes (Davies, 1983)

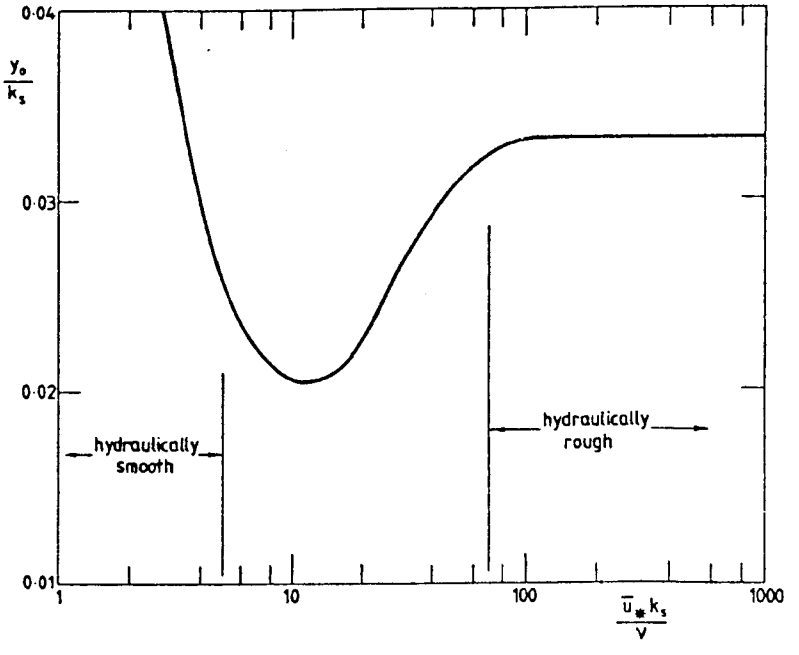

Figure 2.9: Variation of z_o/k_s with $u_* k_s/\nu$ (Sleath, 1984)

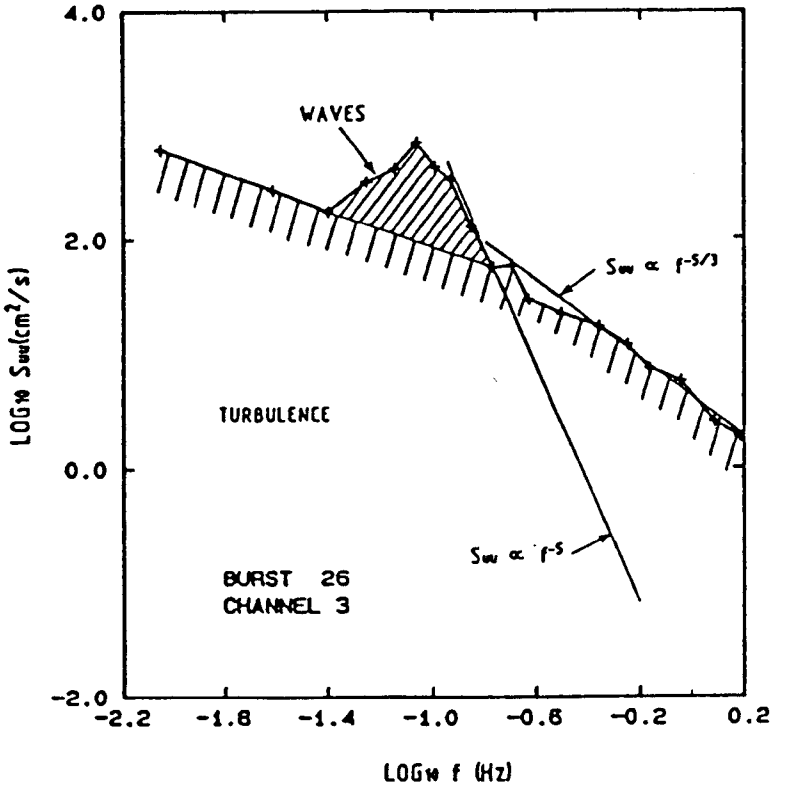

Figure 2.11: Log-Log plot of Energy Density Spectra, showing the technique of splitting the wave variance from turbulence developed by Soulsby & Humphery (1989)

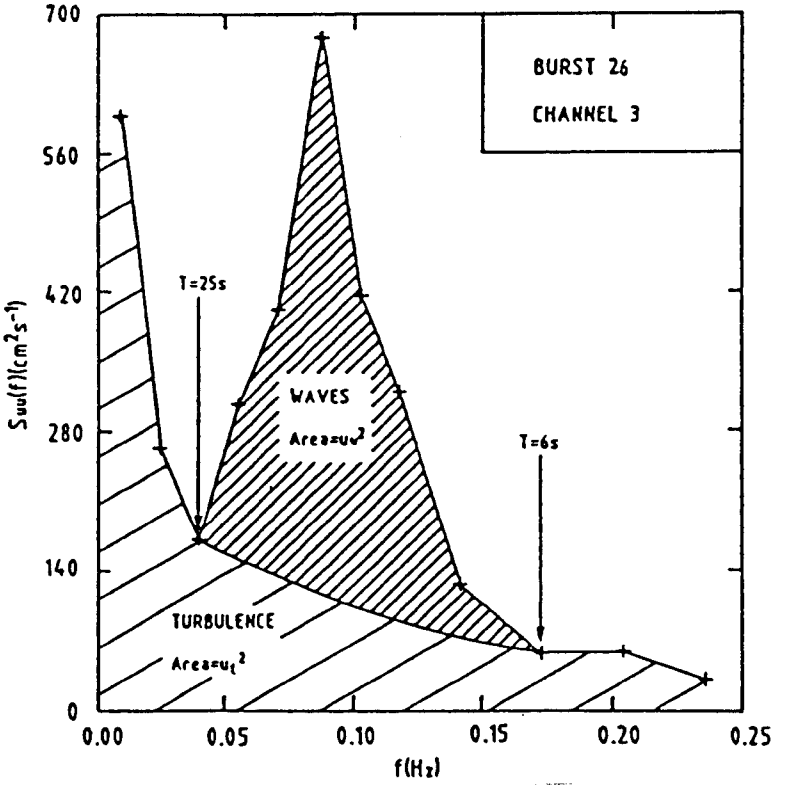

Figure 2.12: Linear version of figure 2.11, showing relative magnitudes of the truncated variance (Soulsby & Humphery, 1989)

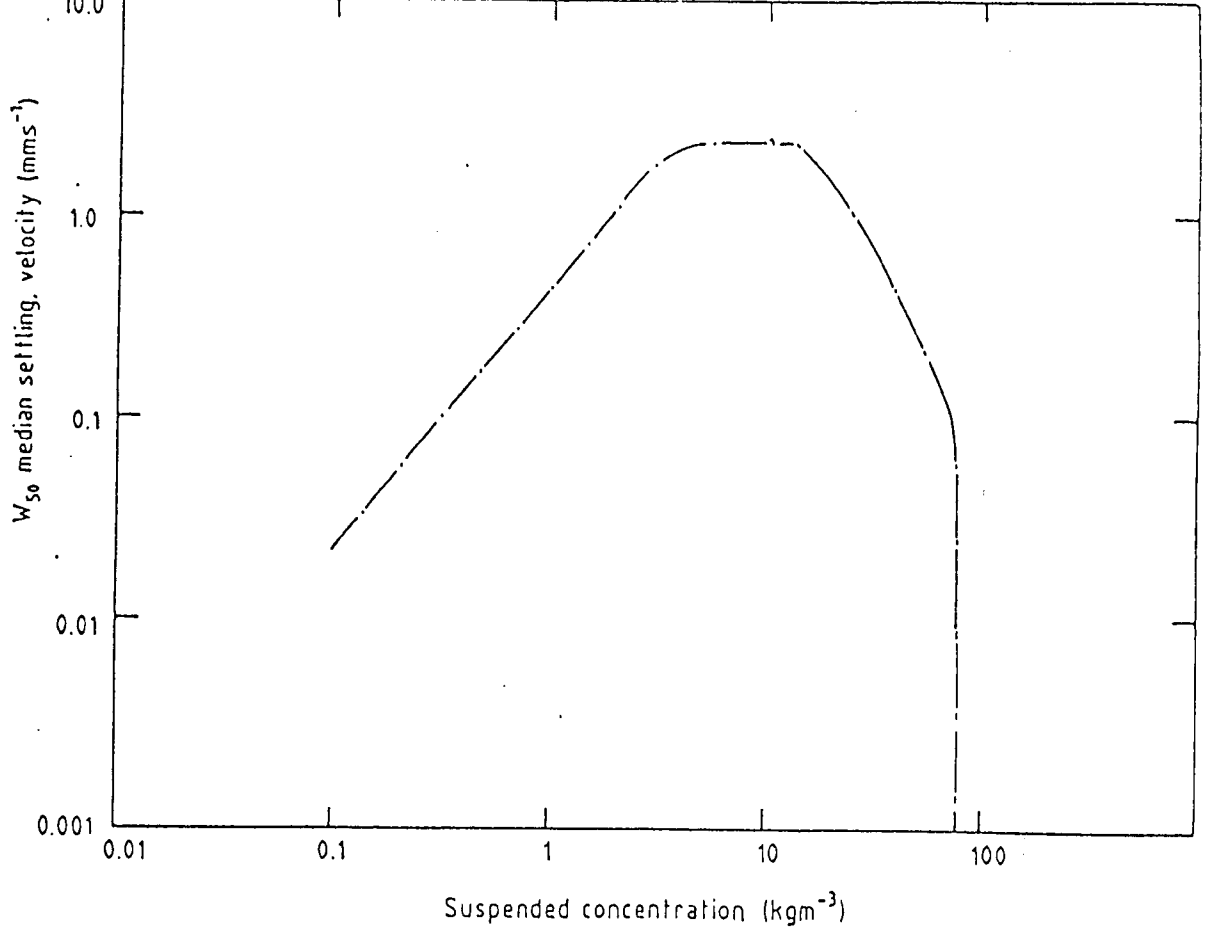

Figure 2.13: Settling velocity v SSC (Severn Estuary) (Delo & Ockenden, 1992)

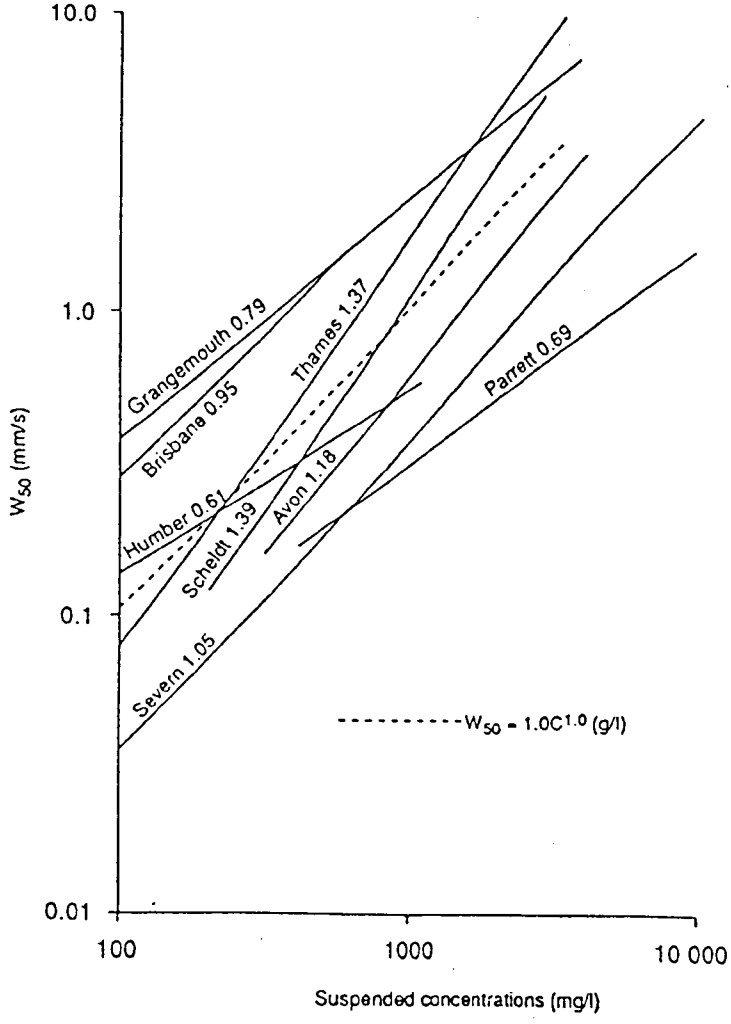

Figure 2.14: Settling velocity v SSC (Different sites) (Delo & Ockenden, 1992)

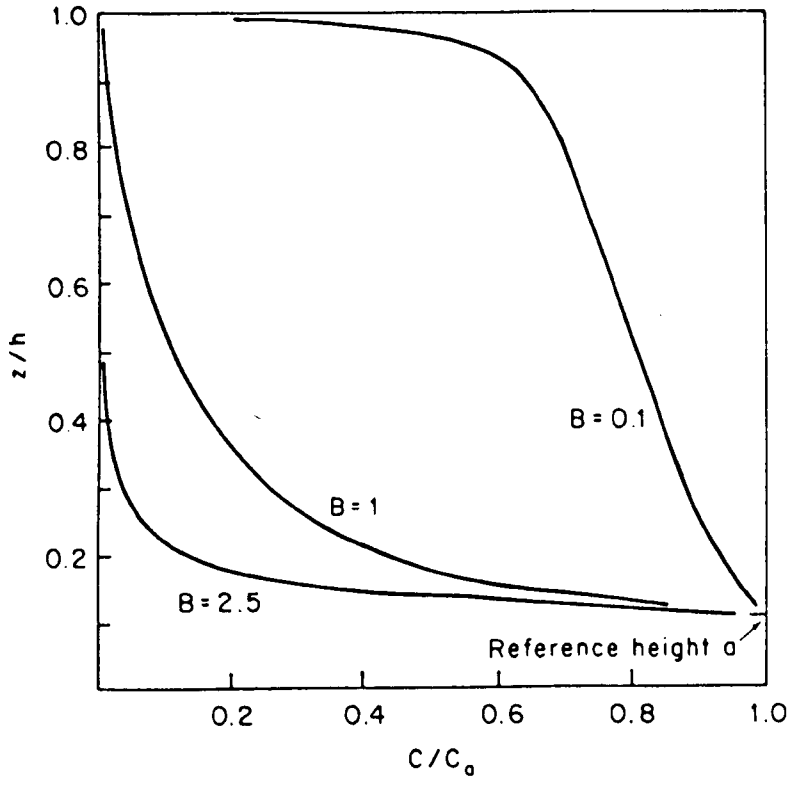

Figure 2.15: Relative concentration profiles calculated from equation (2.61), for varying values of $B = W_s/\sigma_c \kappa u_*$ (Dyer, 1986)

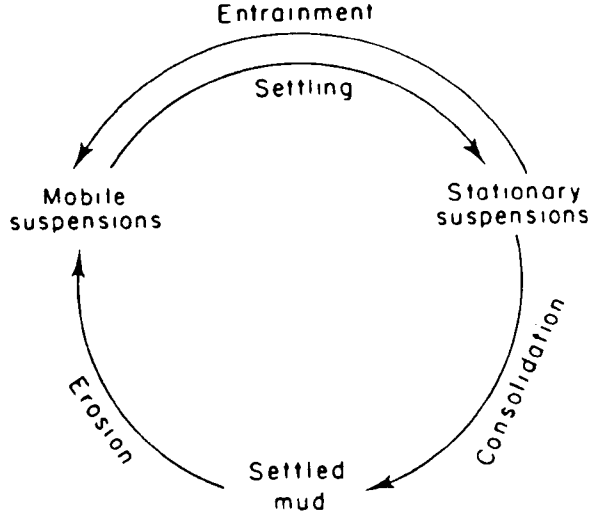

Figure 2.16: Schematic representation of the states of occurrence of mud suspensions, and the links between them (Parker & Kirby, 1977; see Dyer (1986))

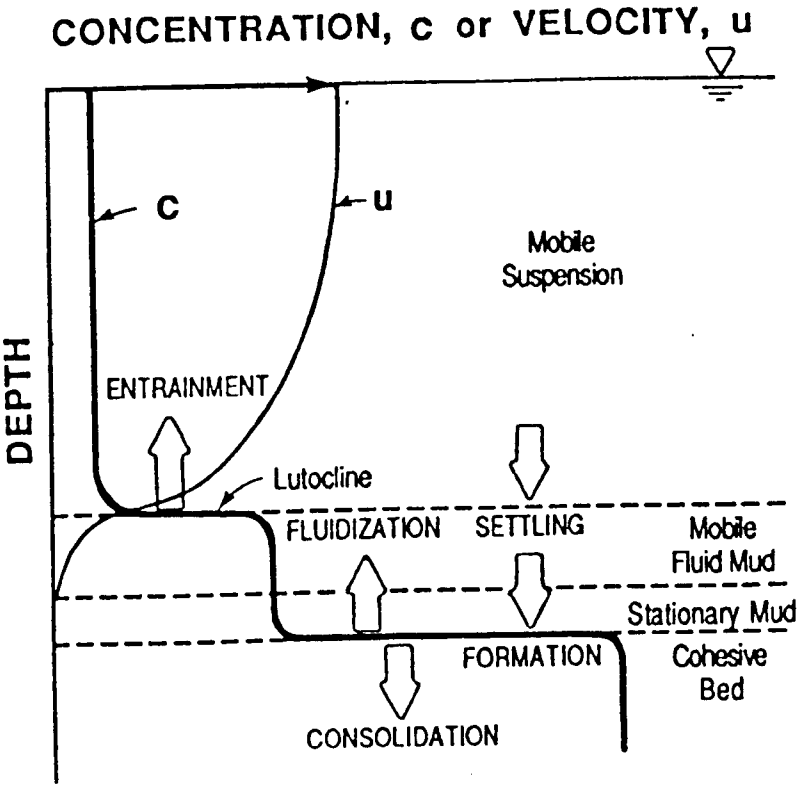

Figure 2.17: Idealised profiles of instantaneous vertical concentration and velocity (Mehta, 1989)

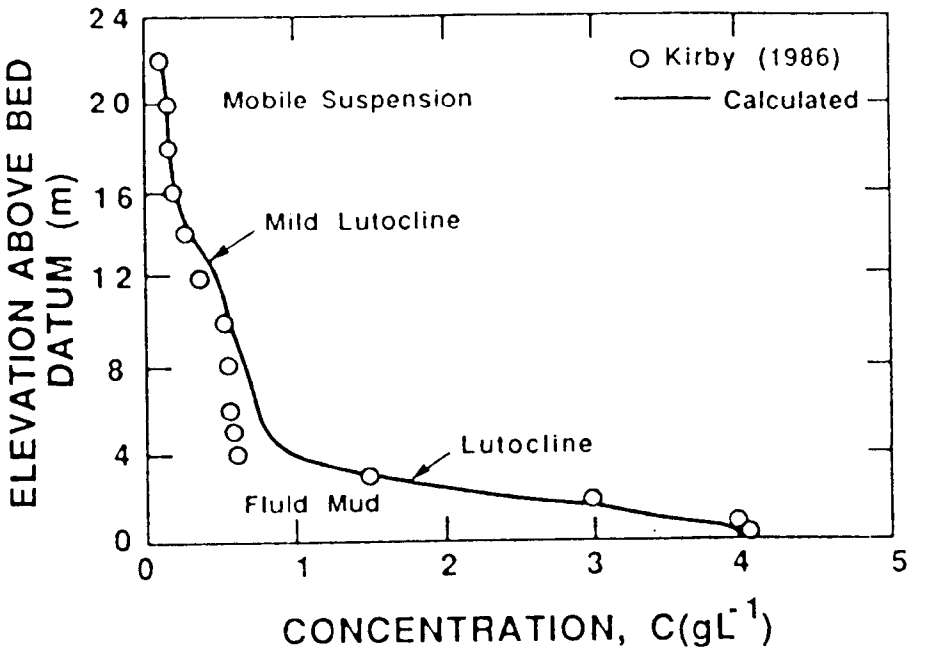

Figure 2.18: Measured and simulated instantaneous concentration profiles in the Severn Estuary (after Ross, 1988; see Mehta, 1989)

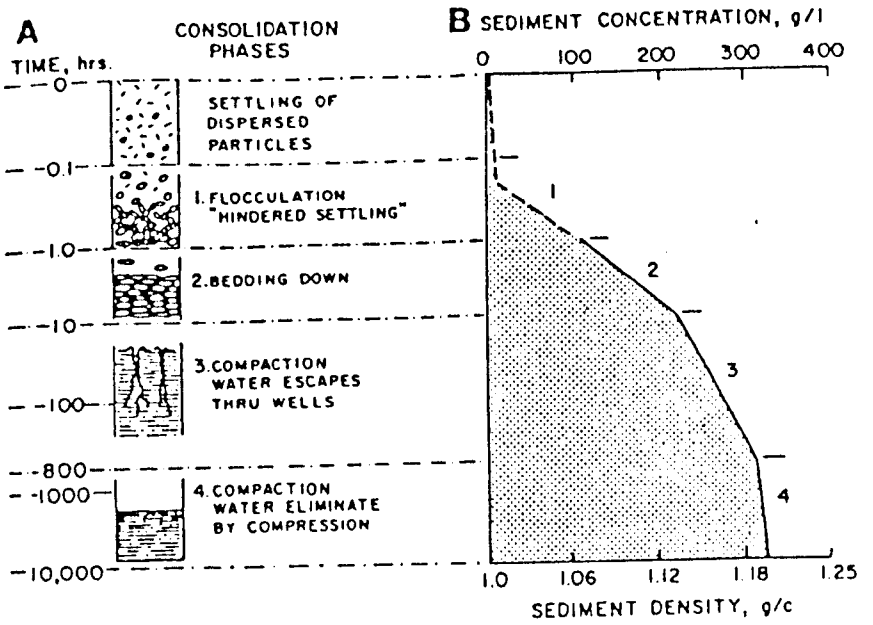

Figure 2.19: Graphical representation of consolidation stages (Nichols & Briggs, 1985)

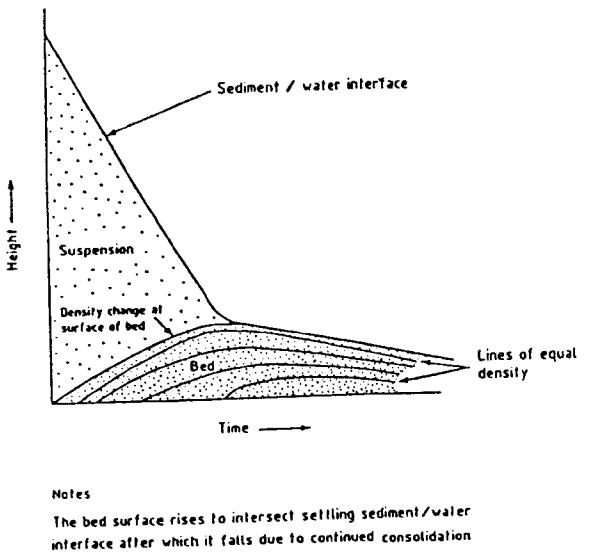

Figure 2.20: Growth of the bed in a settling suspension (Delo & Ockenden, 1992)

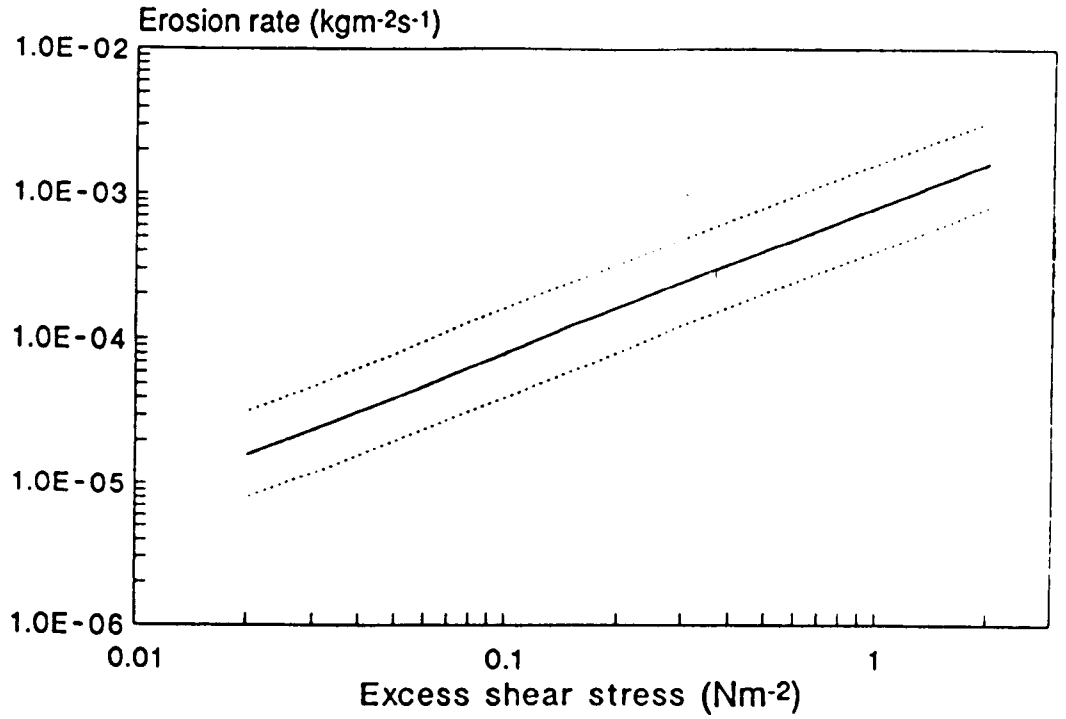

Figure 2.21: Laboratory test on the erosion rate (M_e) of cohesive sediment with excess shear stress (Delo & Ockenden, 1992)

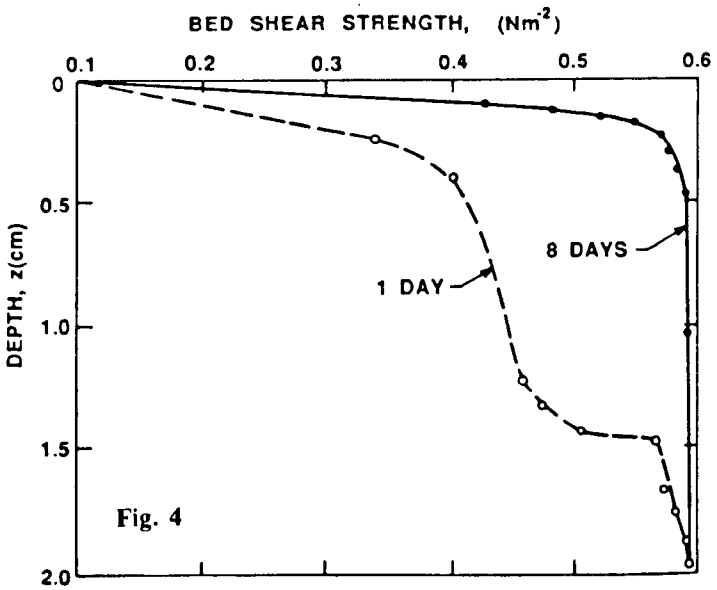

Figure 2.22: Three-zoned schematic description of bed shear strength profiles with depth and examples of profiles after 1 day and 8 days of consolidation using kaolinite (Parchure & Mehta, 1985)

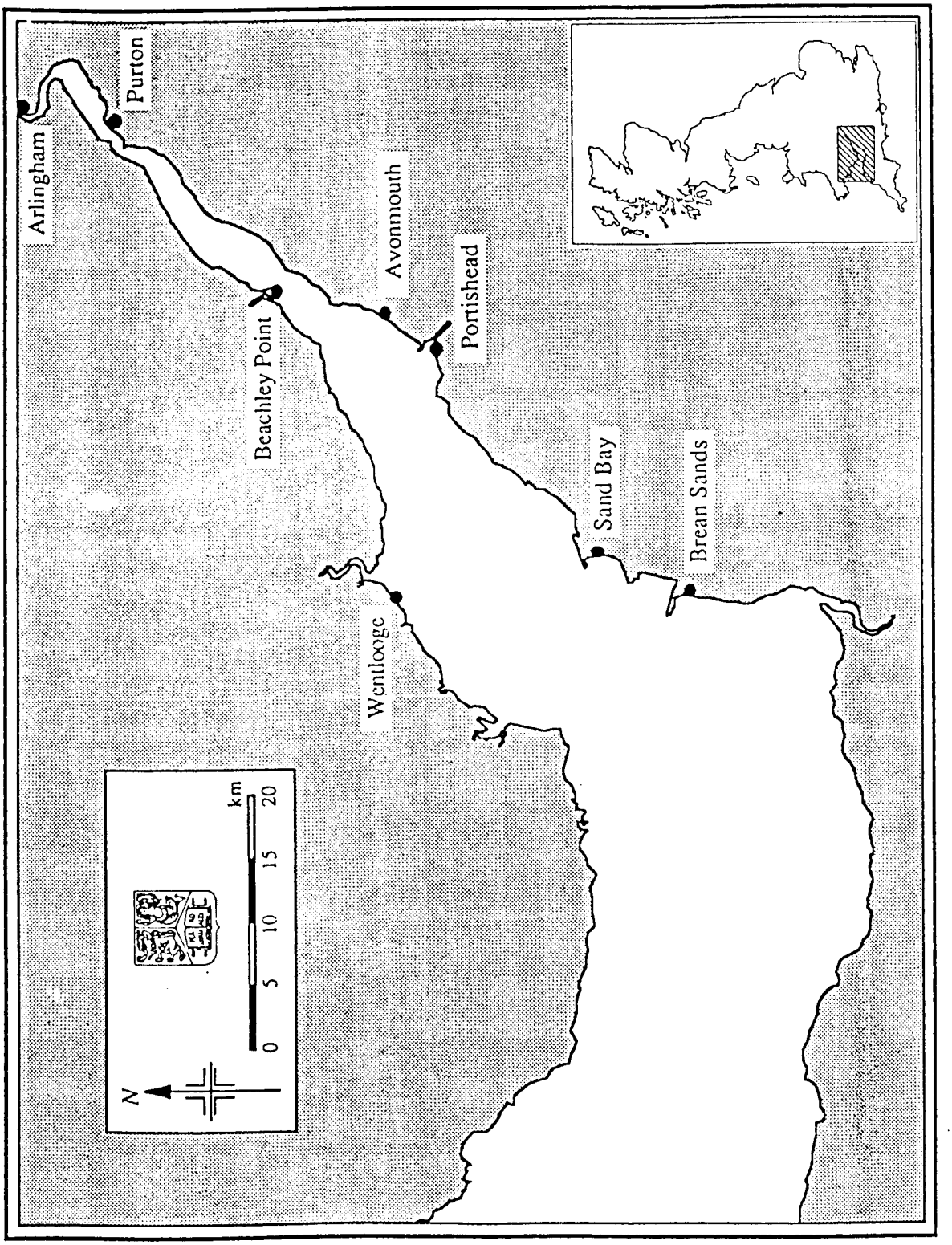

Figure 3.1: Map of Bristol Channel and Severn Estuary

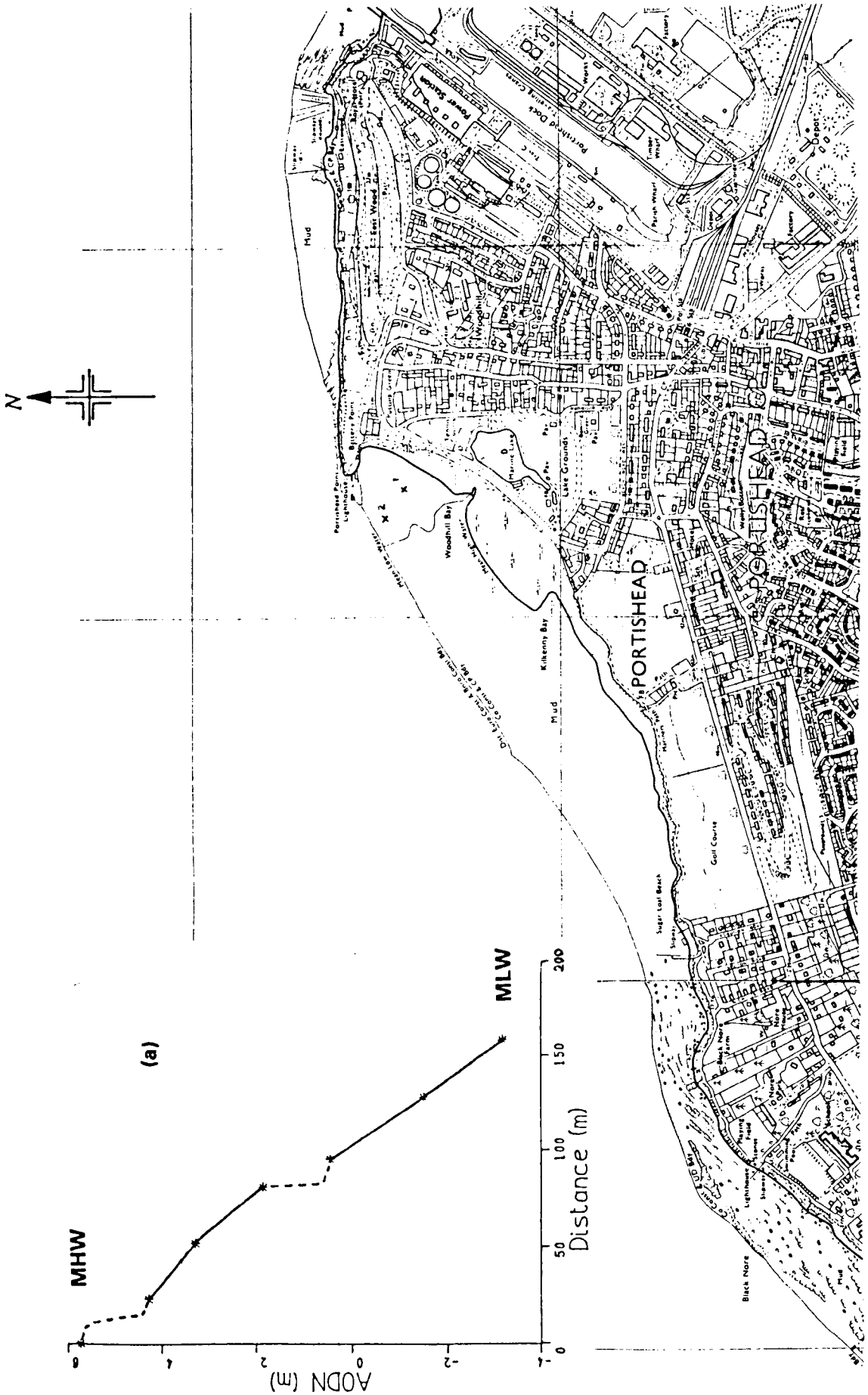

Figure 3.2: Portishead site plan showing approximate position of instrument deployment sites (marked 1,2) (a) Transect elevation 19/4/88 (West, 1990)

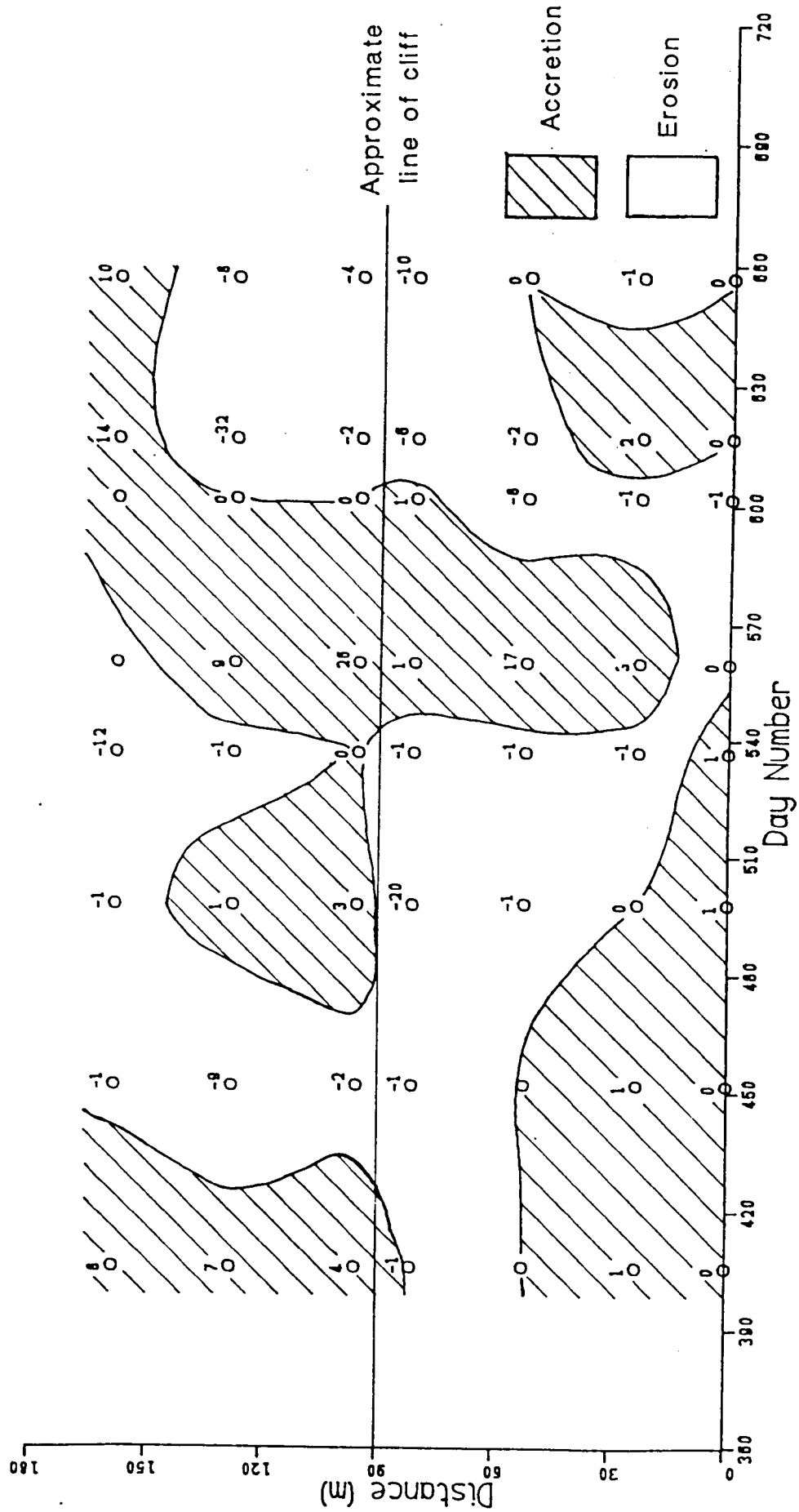

Figure 3.3: Portishead bed level changes (cm per 30 days) Nov 1988 - Aug 1989 (West, 1990)

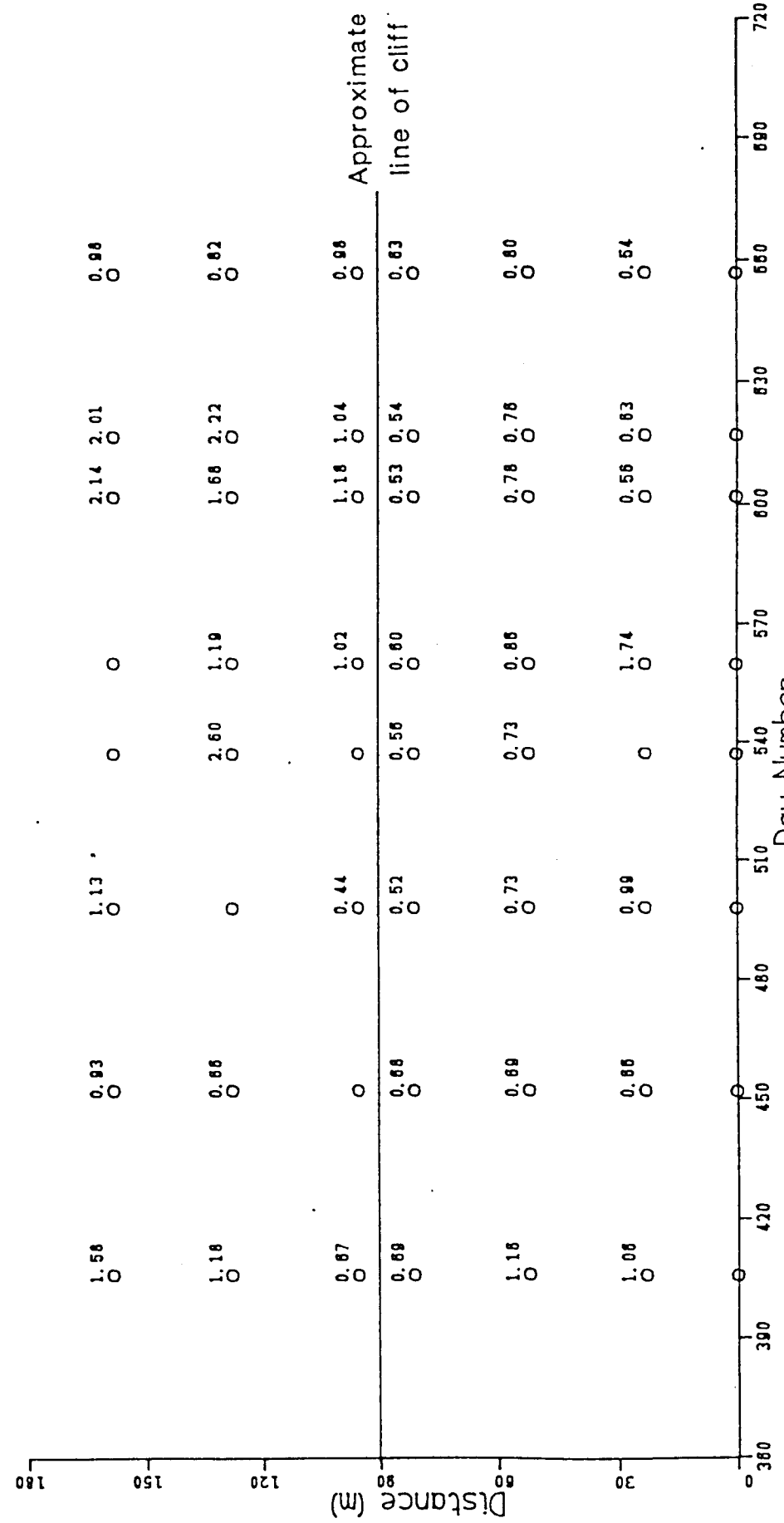

Figure 3.4: Portishead moisture content ratio Nov 1988 - Aug 1989 (West, 1990)

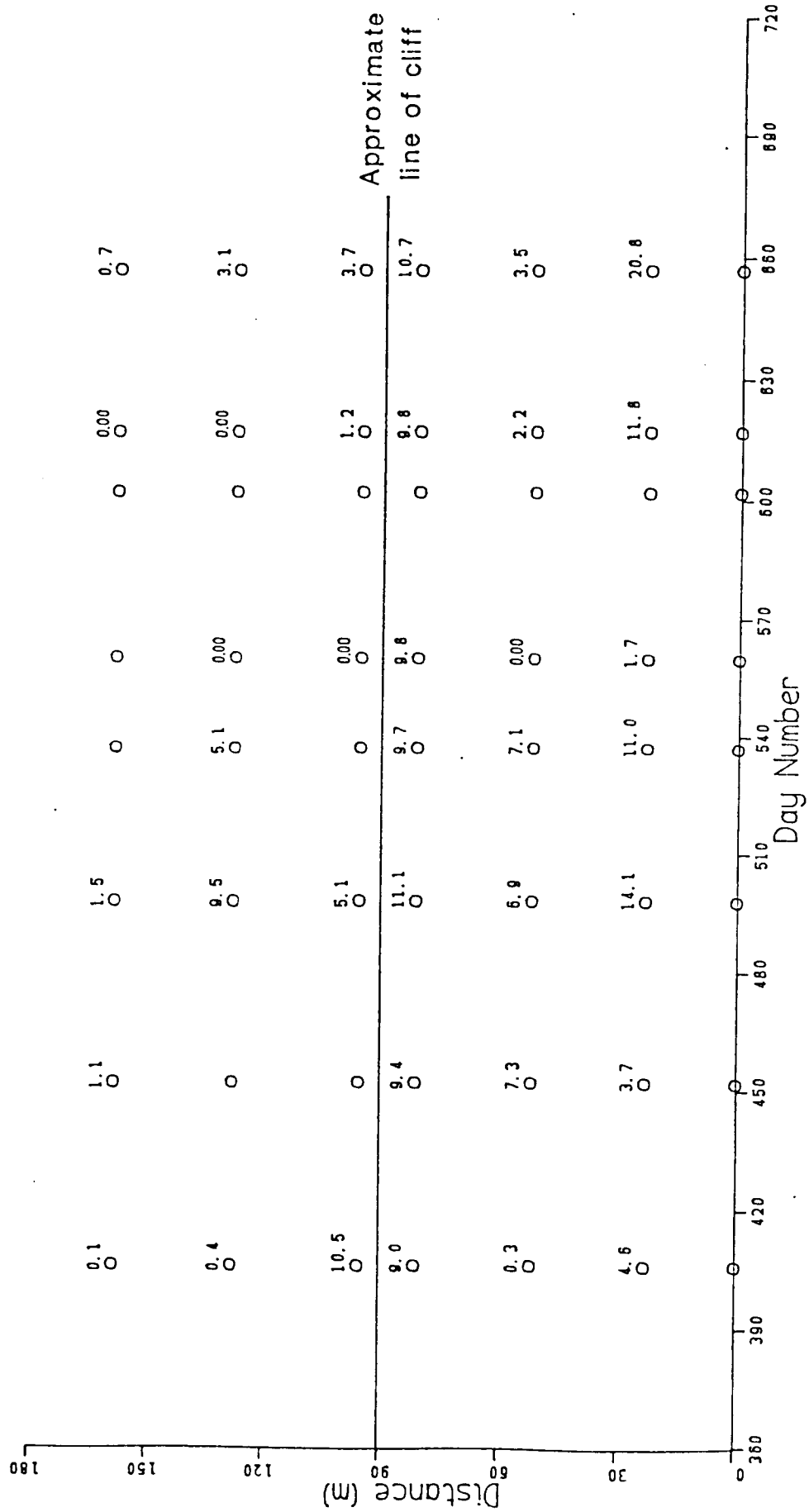

Figure 3.5: Portishead surface shear vane readings (kPa) Nov 1988 - Aug 1989 (West, 1990)

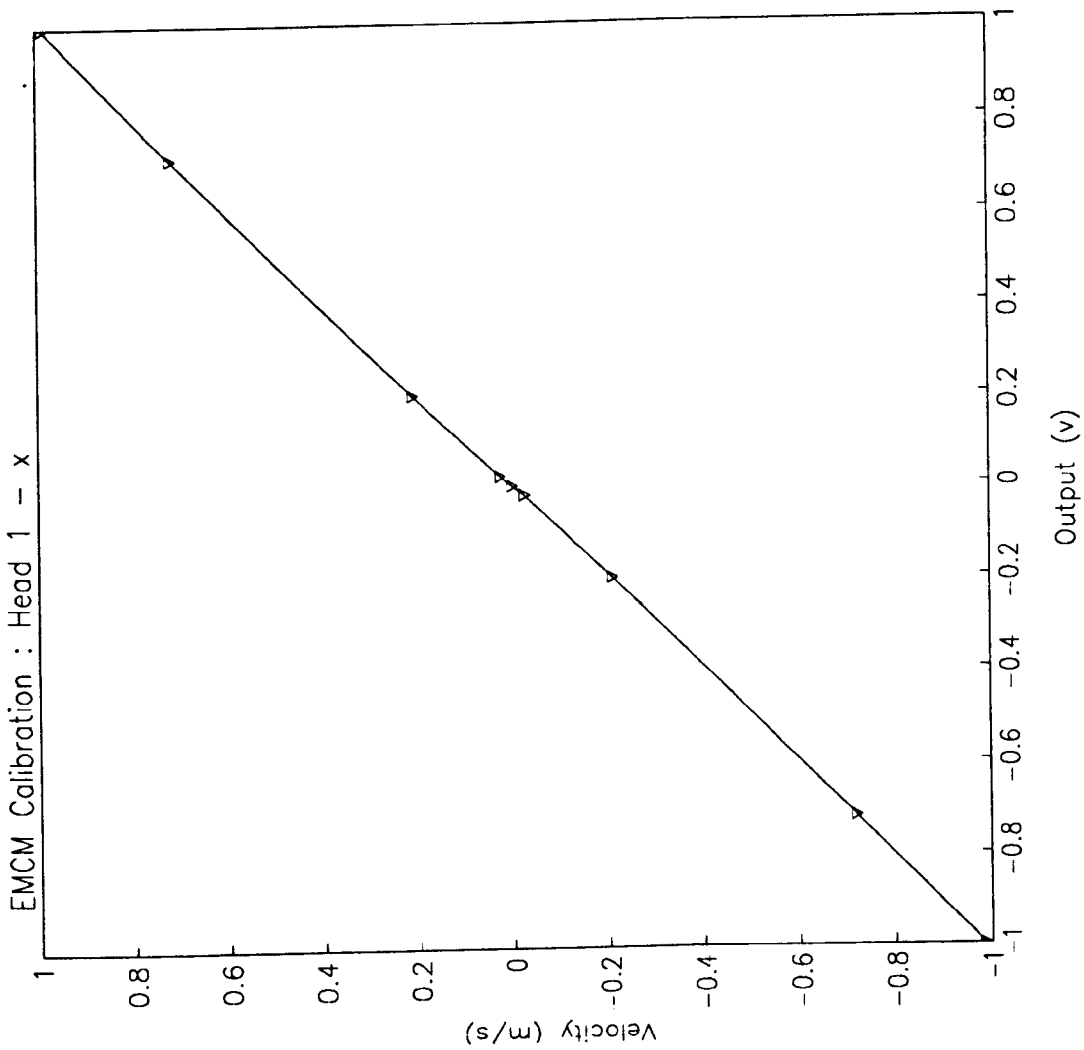

Figure 3.6: EMCM Calibration : Head 1-x

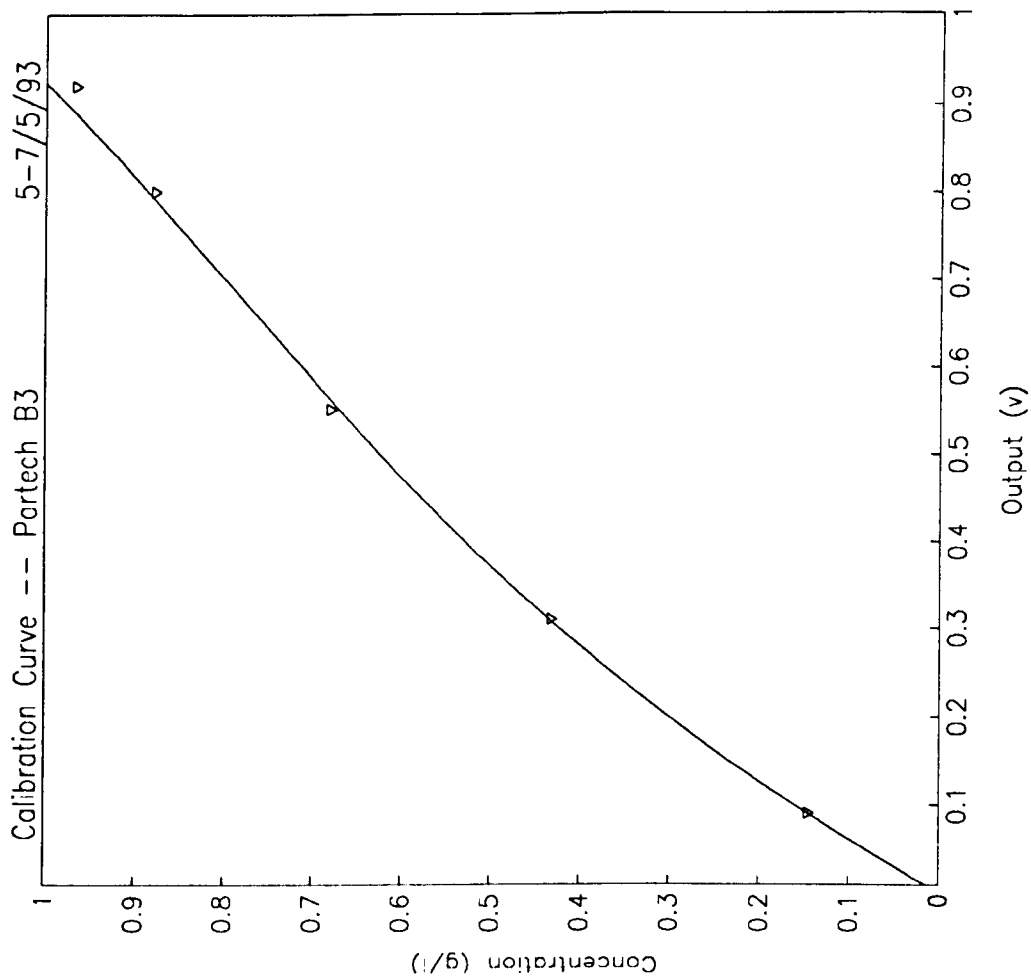

Figure 3.7: Example of Partech Calibration Curve : 5-7/5/93

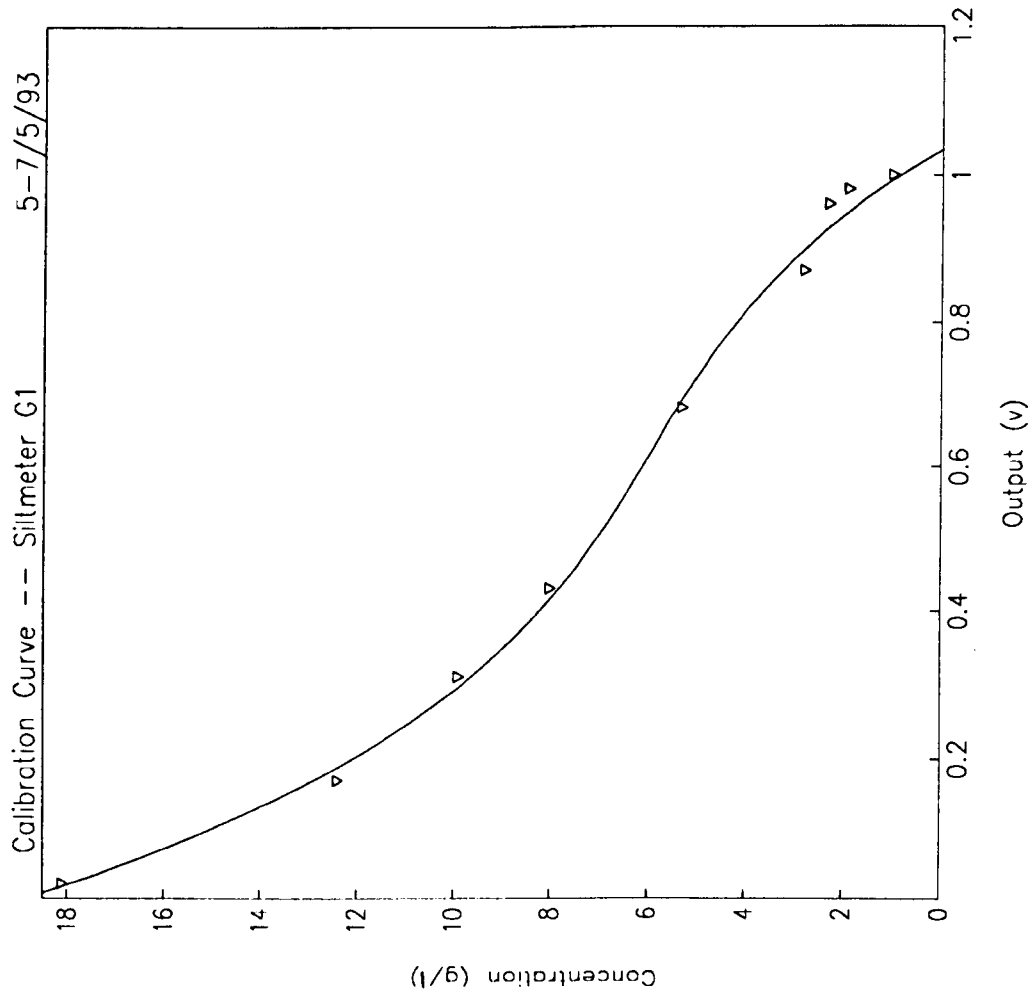

Figure 3.8: Example of Siltmeter Calibration Curve : 5-7/5/93

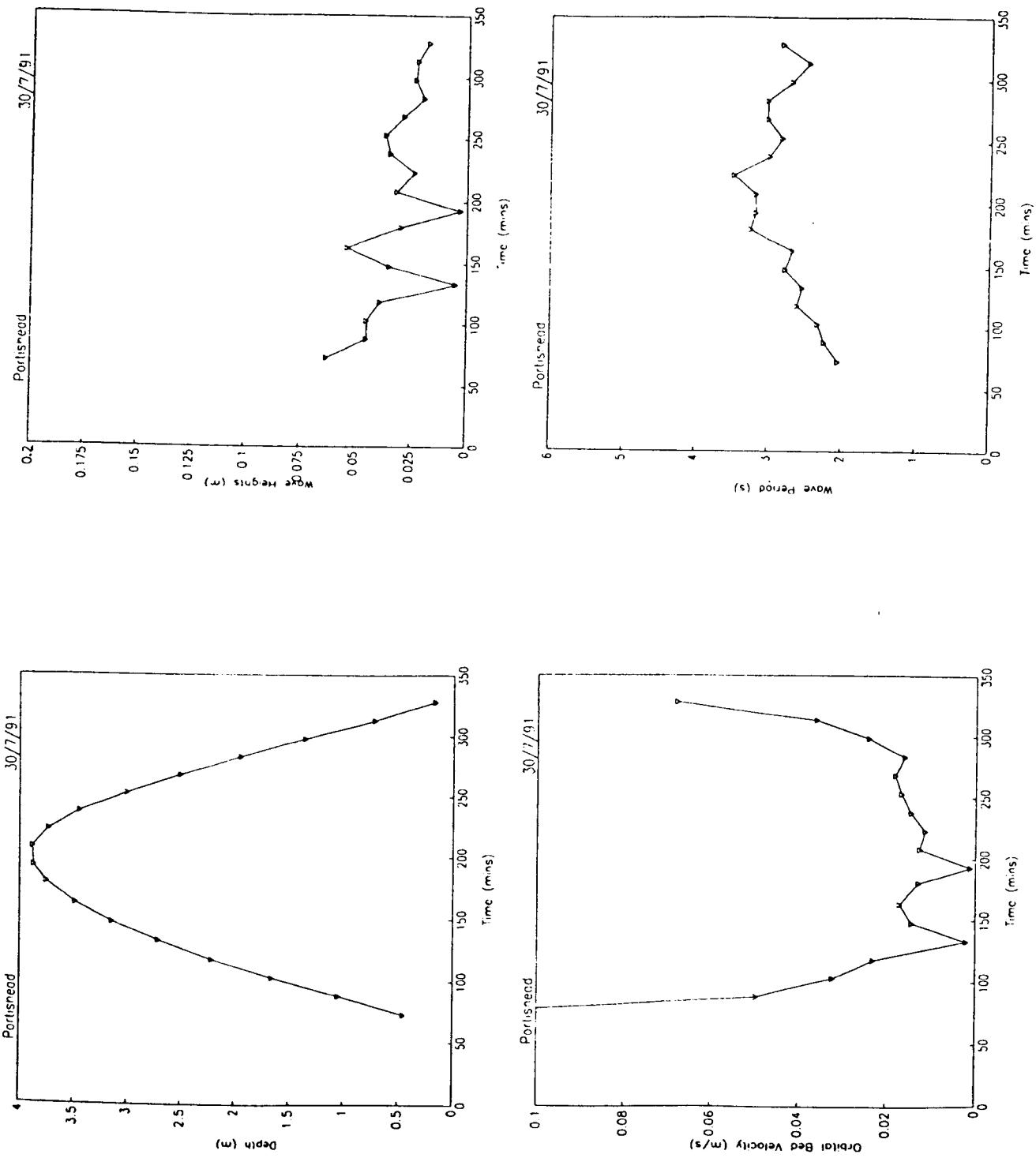

Figure 4.1: Water depth, wave heights, wave periods and wave orbital velocity at upper site (from pressure data, HW $\approx 200\,mins$), 30/7/91

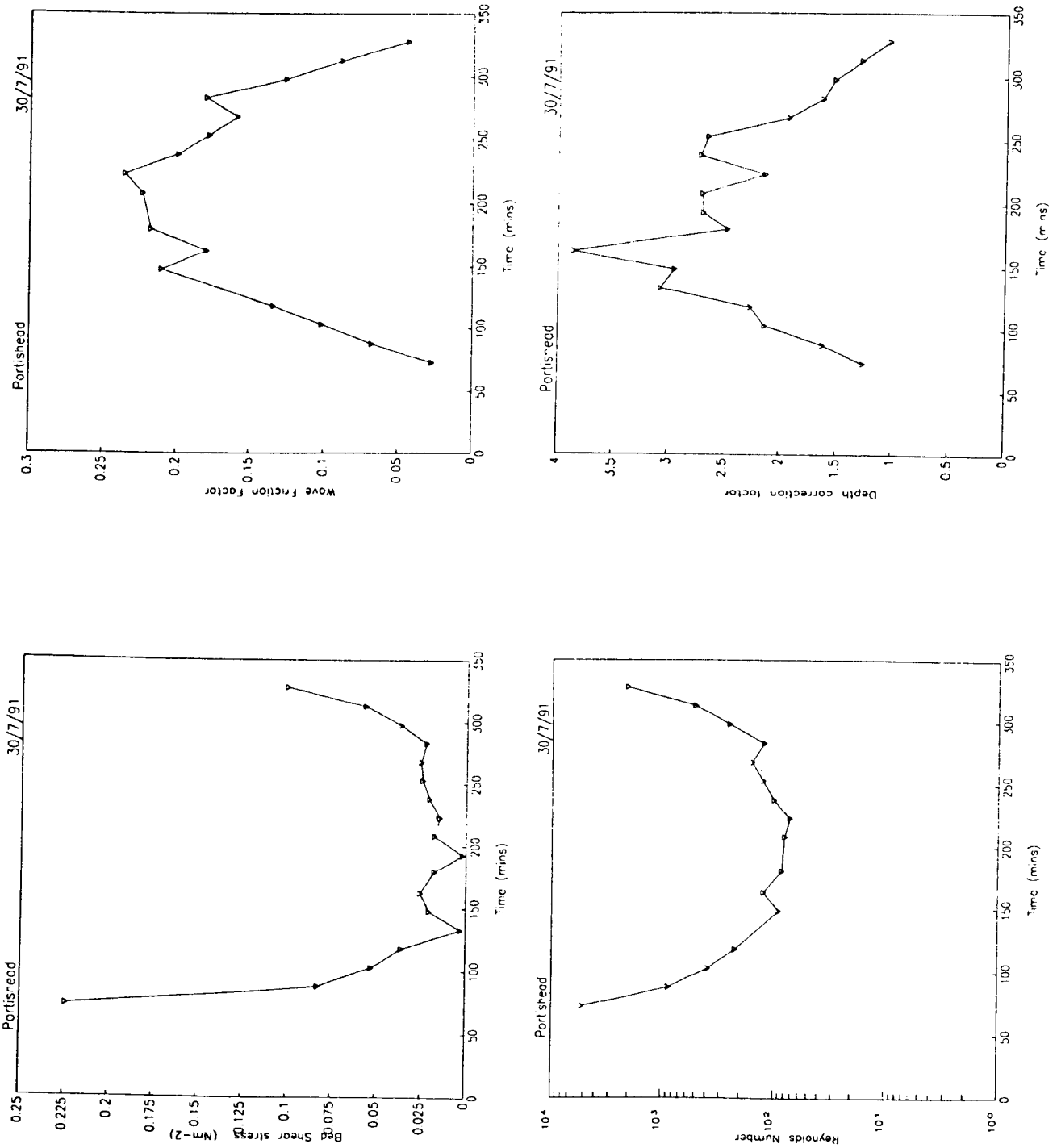

Figure 4.2: Bed shear stress, wave friction factor, Reynolds number and correction factor from bed pressures to surface wave heights at upper site (pressure data, HW $\approx 200\,mins$), 30/7/91

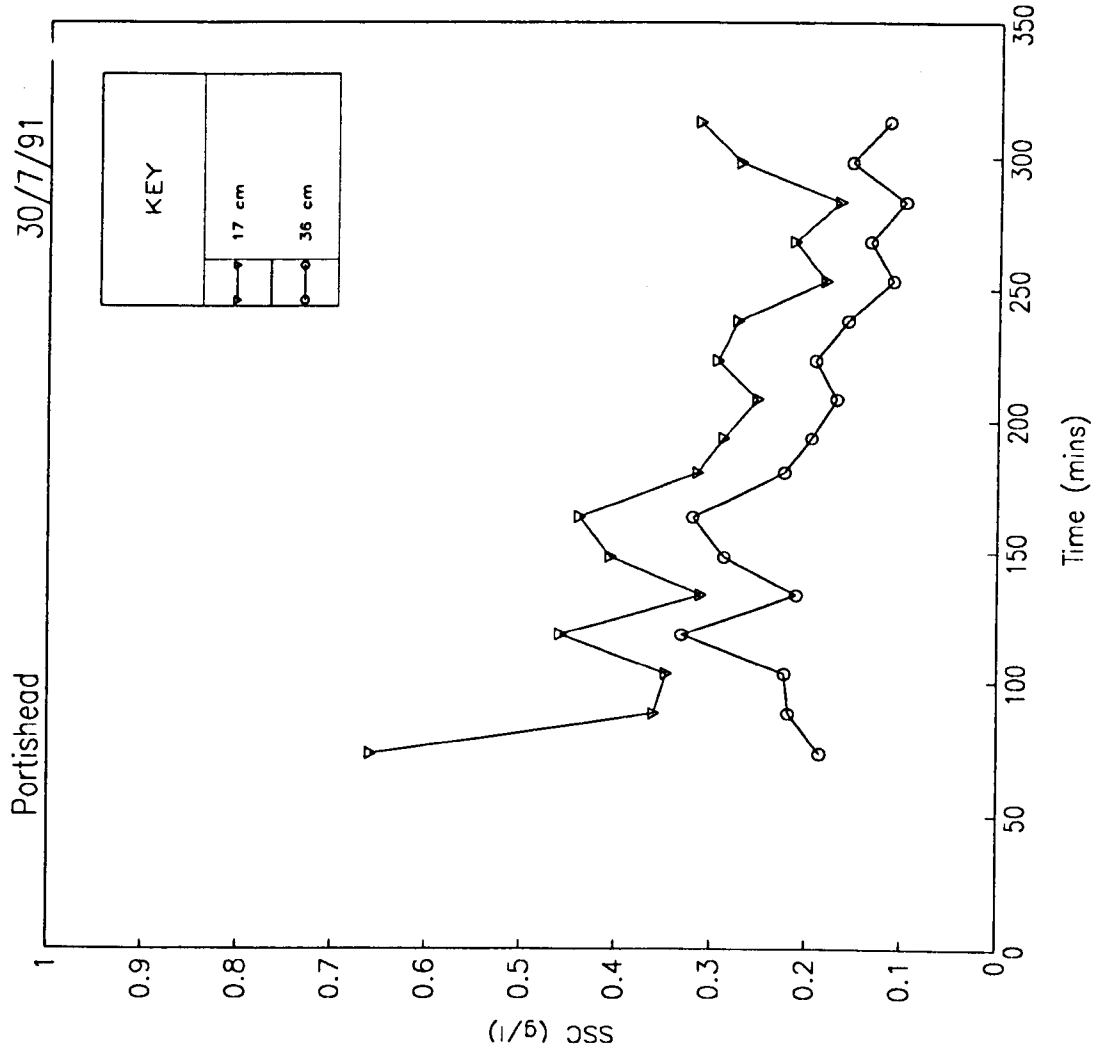

Figure 4.3: SSC at upper site at $z = 17\,cm$ and $36\,cm$ (Partech data, HW $\approx 200\,mins$), 30/7/91

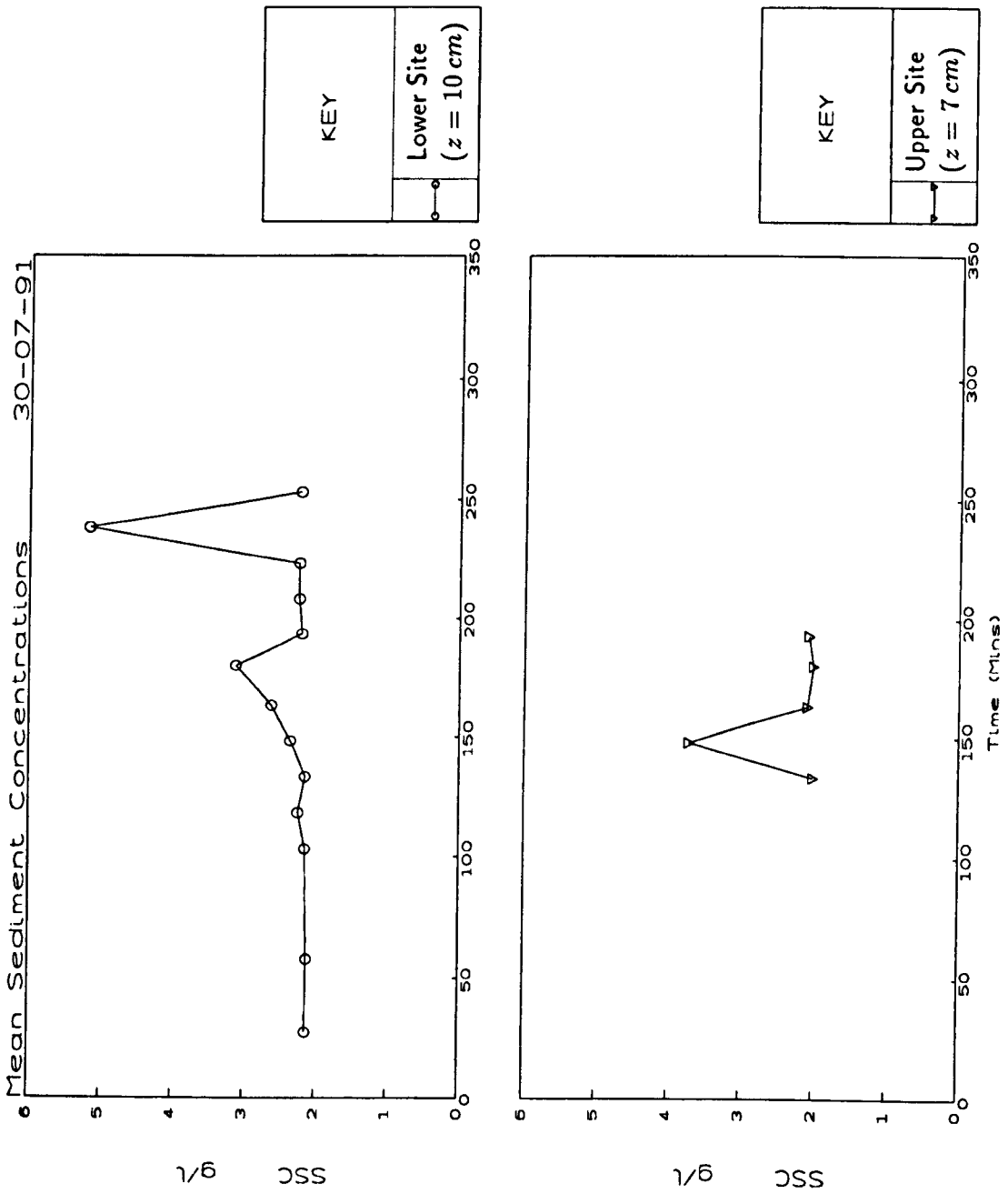

Figure 4.4: Near bed SSC - upper ($z = 7\,cm$) and lower ($z = 10\,cm$) site from siltmeter data ($SSC > 2\,g/l$), HW $\approx 200\,mins$, 30/7/91

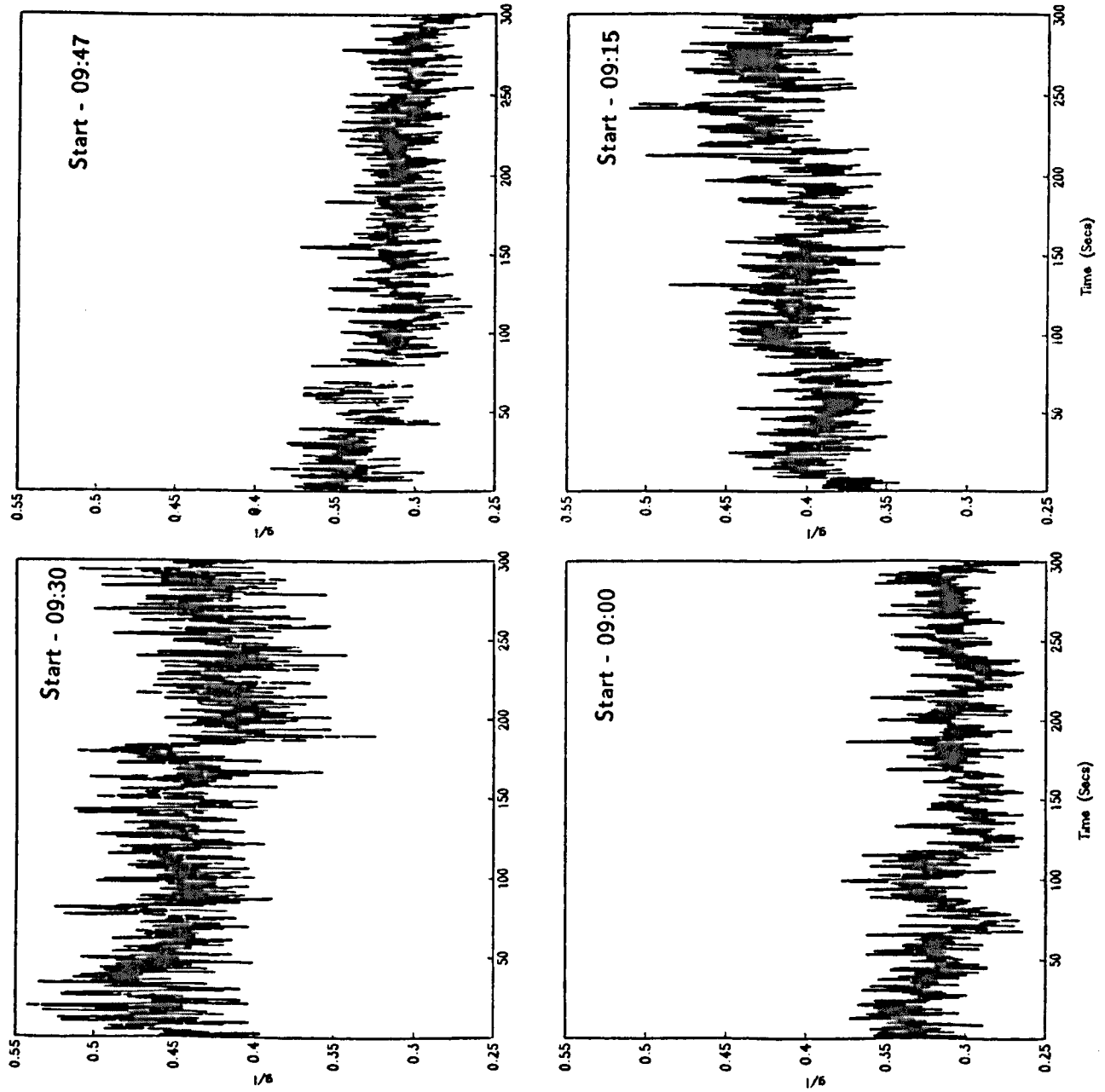

Figure 4.5: Four five minute Partech records ($z = 17\,cm$), 30/7/91

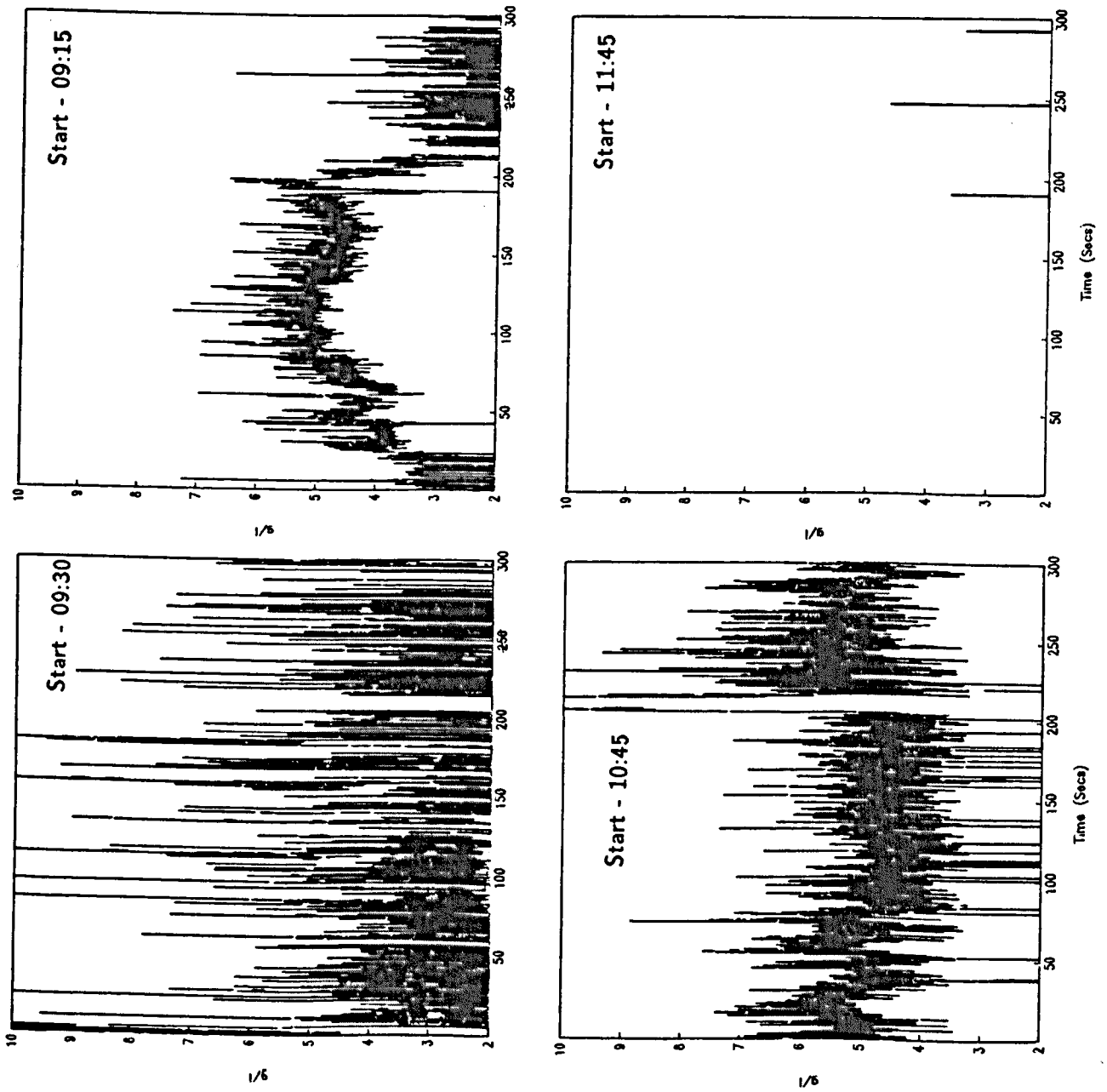

Figure 4.6: Four five minute siltmeter records ($z \approx 10\,cm$), 30/7/91

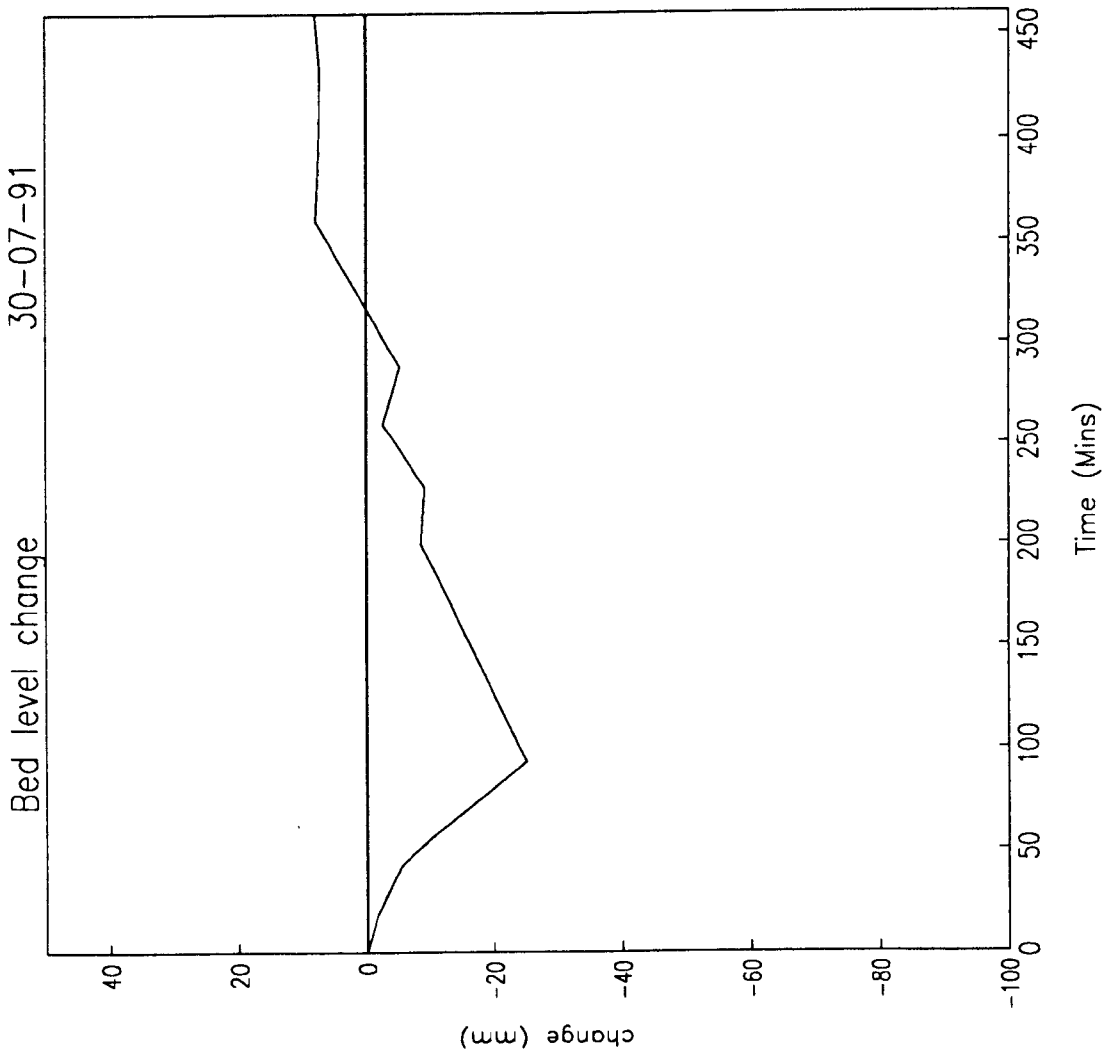

Figure 4.7: Bed level change (HW $\approx 200\,mins$), 30/7/91

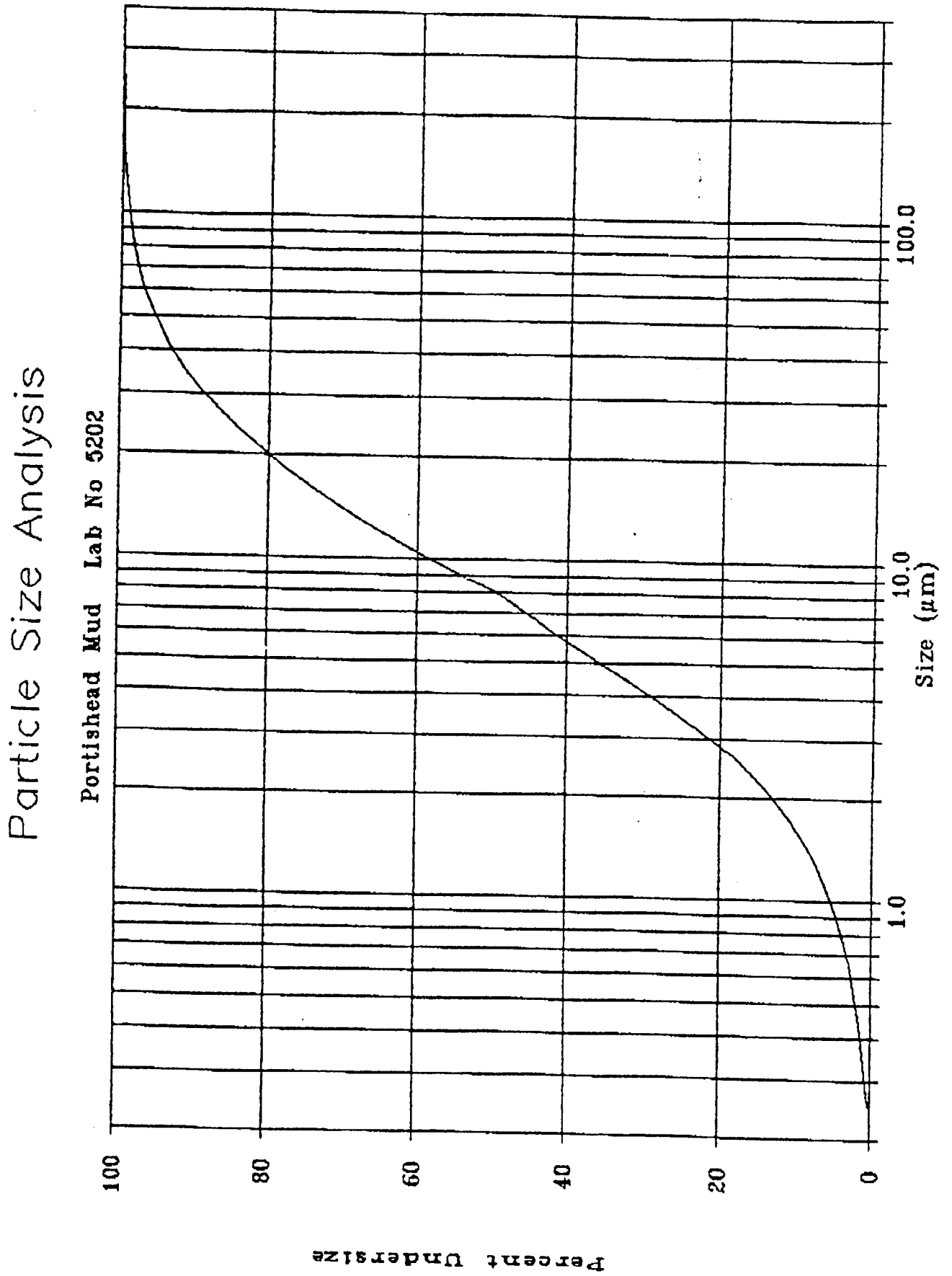

Figure 4.8: Particle size distribution, 29-30/7/91

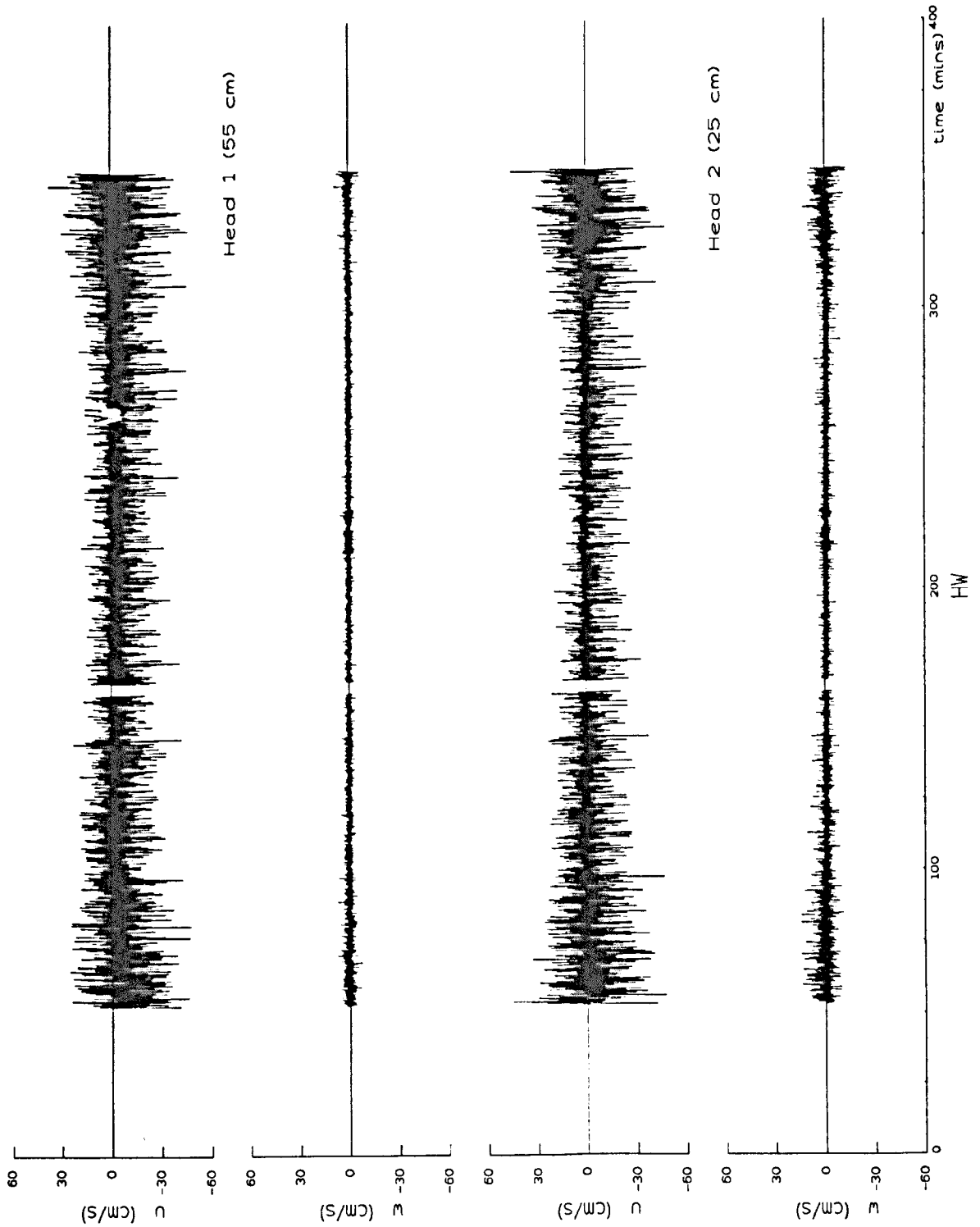

Figure 4.9: EMCM velocity time series (u, w) for whole tide, 17/10/91

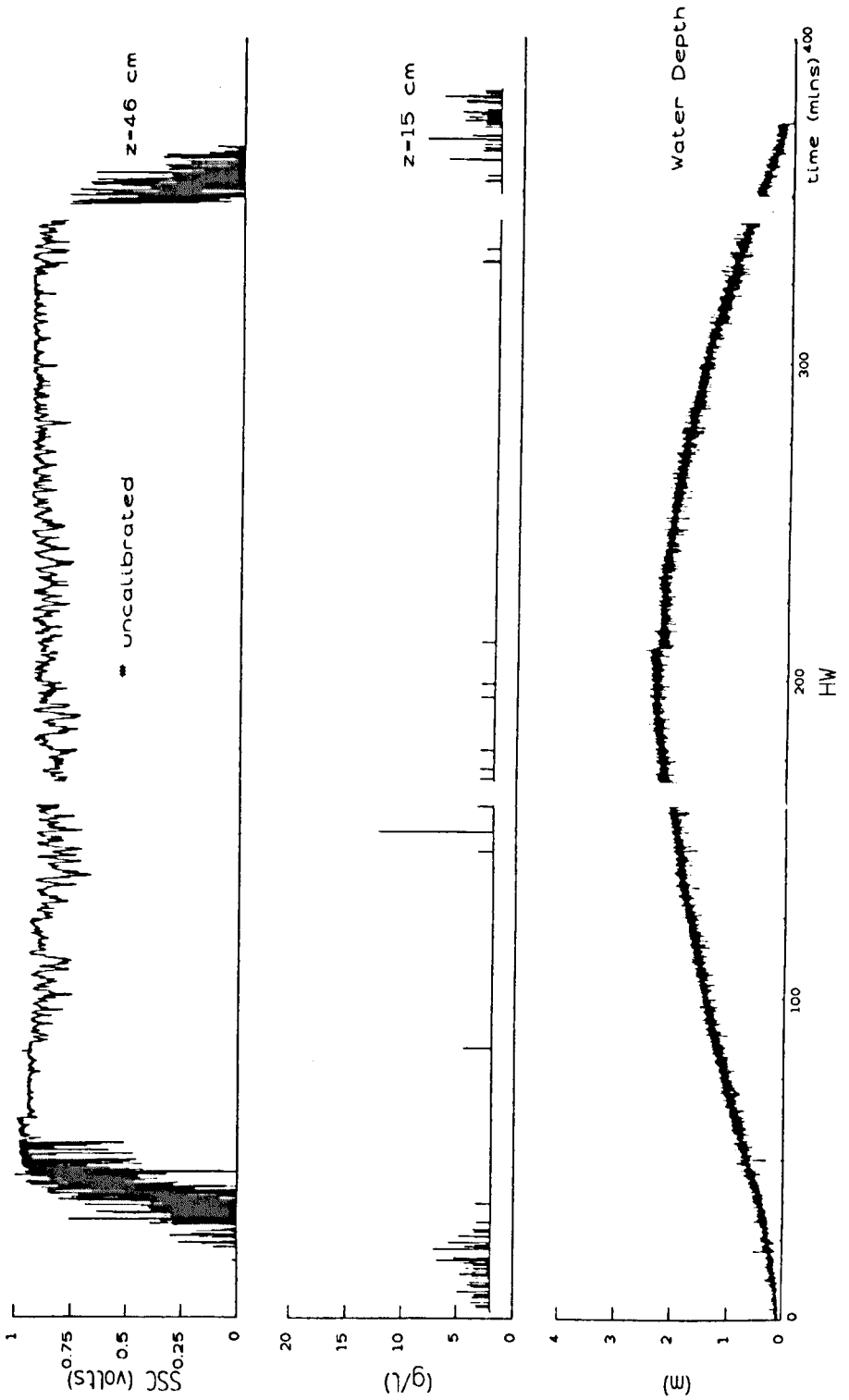

Figure 4.10: Water depth and SSC ($z = 15, 46\,cm$) time series for whole tide, 17/10/91

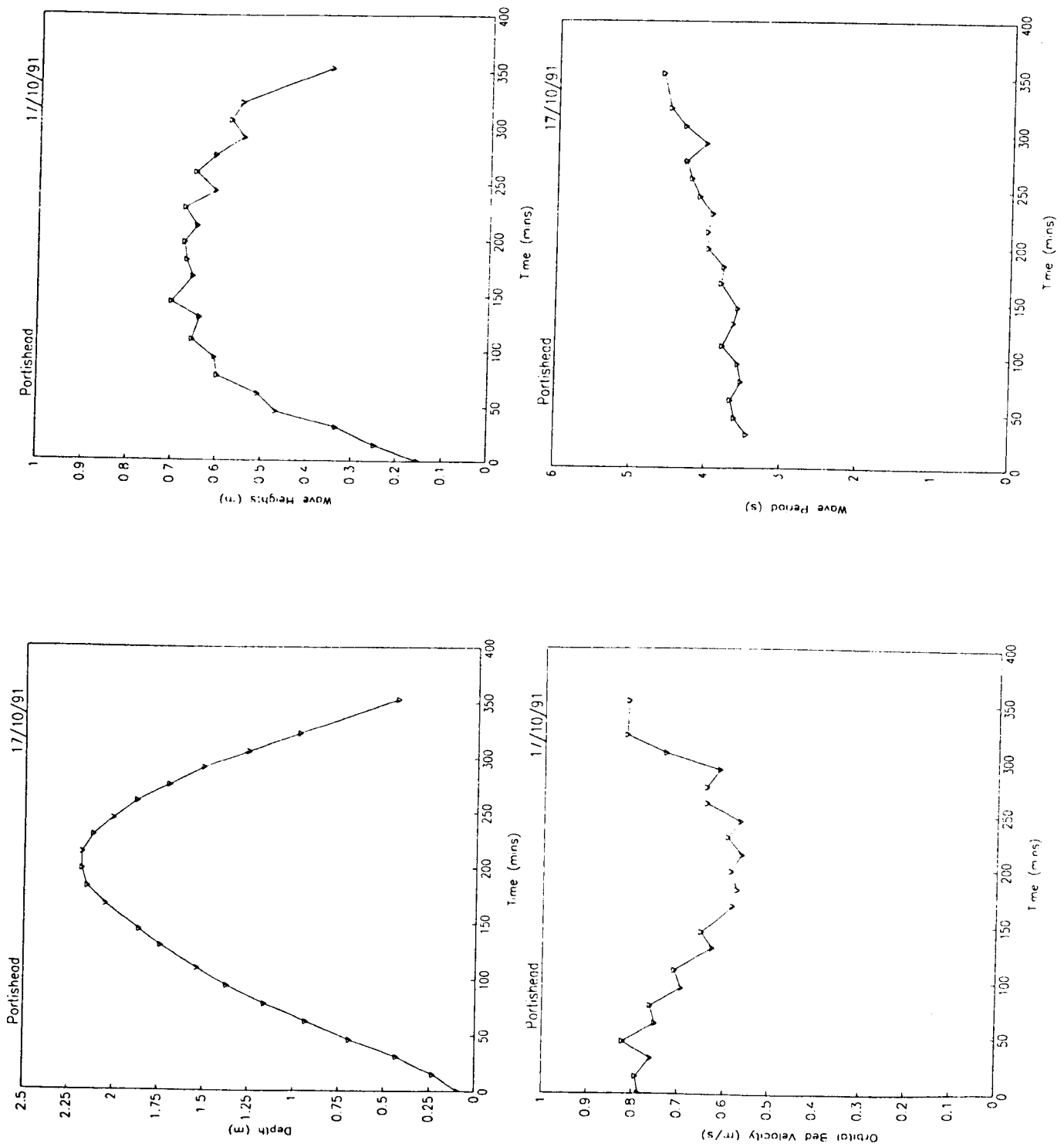

Figure 4.11: Water depth, wave heights, wave periods and wave orbital velocity (from pressure data, HW $\approx 200\,mins$), 17/10/91

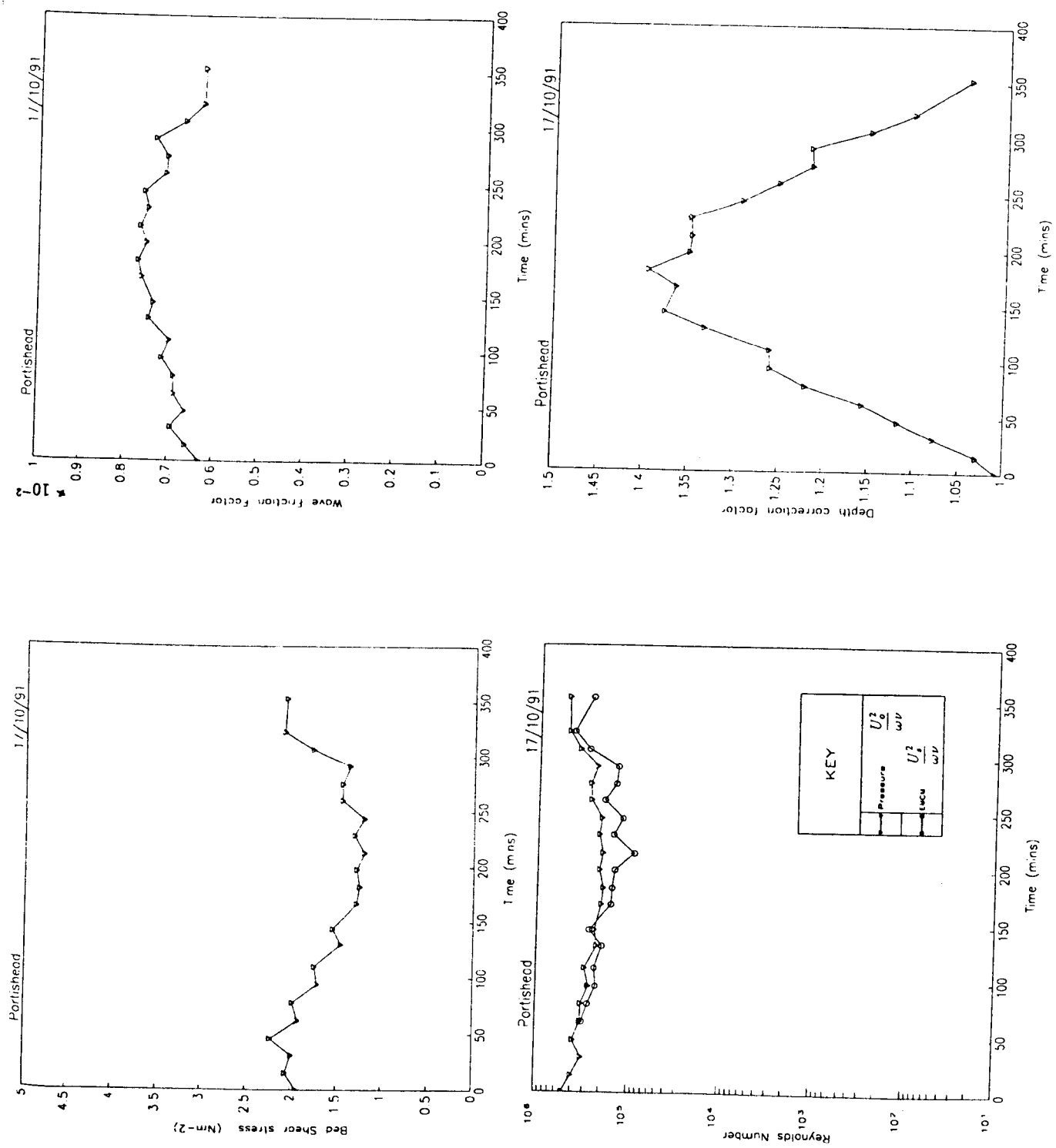

Figure 4.12: Bed shear stress, wave friction factor, Reynolds number and correction factor from bed pressures to surface wave heights (pressure data, HW $\approx 200\,mins$), 17/10/91

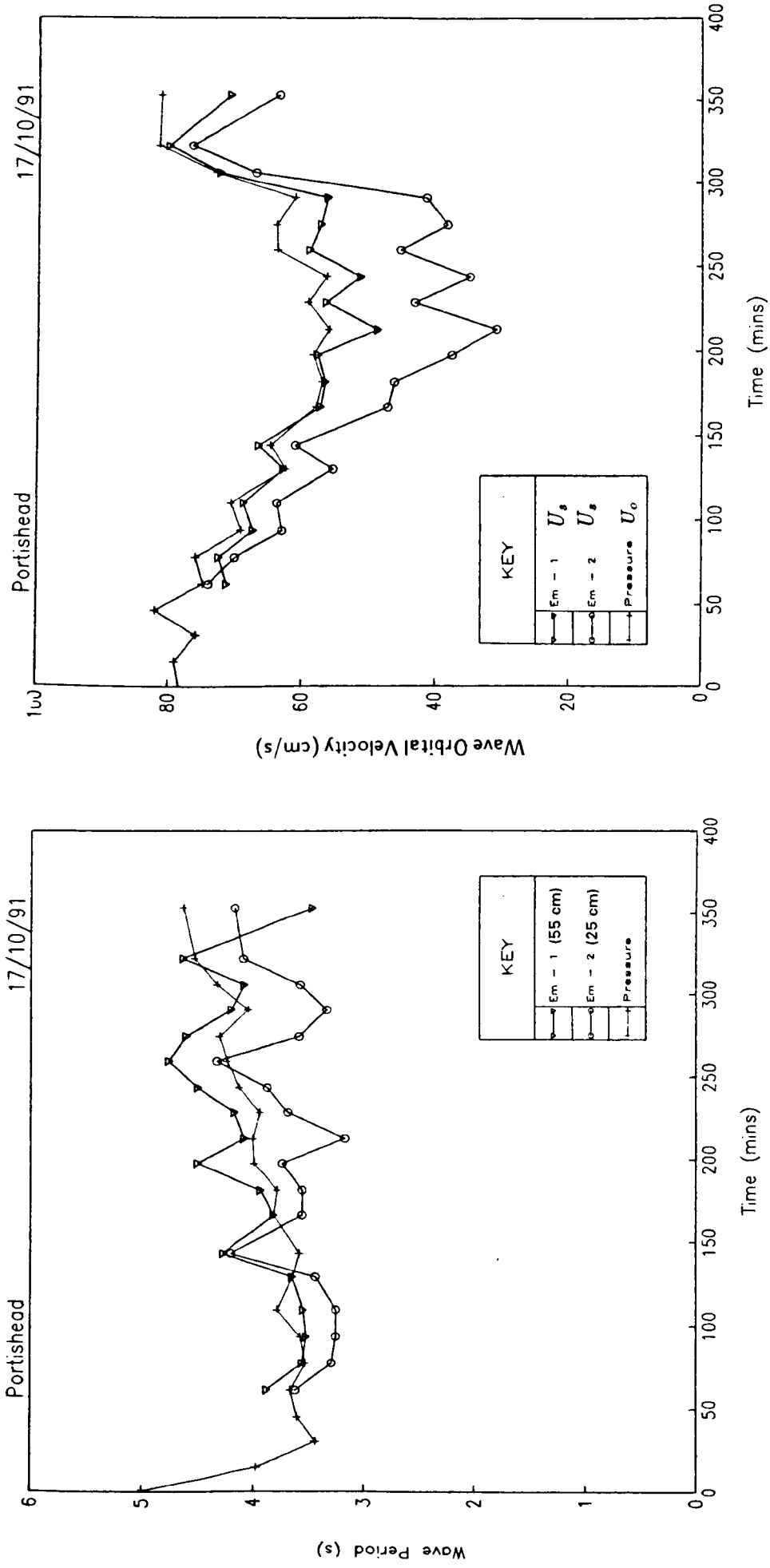

Figure 4.13: Comparison between wave periods and orbital velocities from pressure and EMCM data (HW $\approx 200\,mins$), 17/10/91)

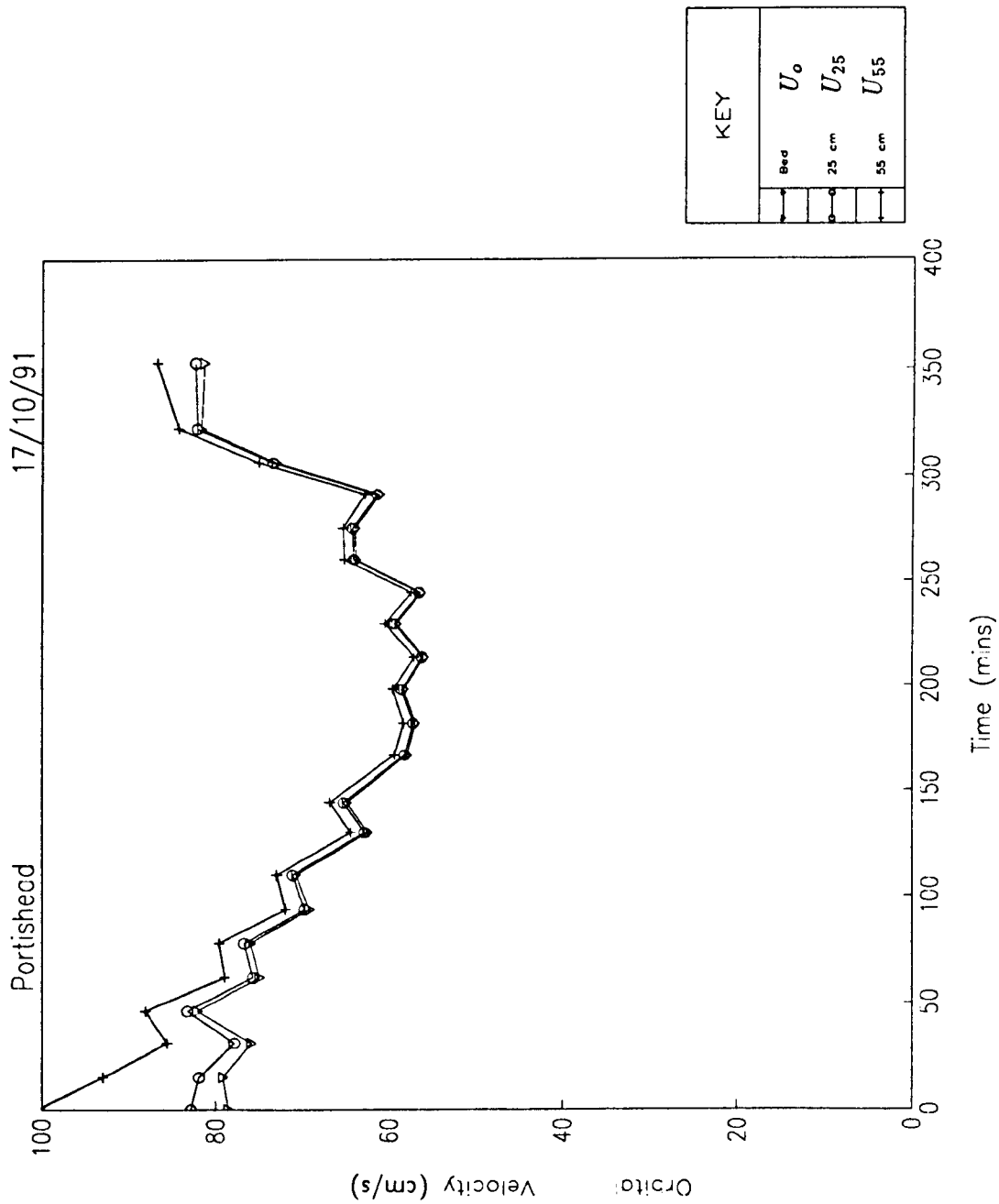

Figure 4.14: Comparison between wave orbital velocities from pressure data at EMCM heights using linear wave theory (HW $\approx 200\,mins$), 17/10/91)

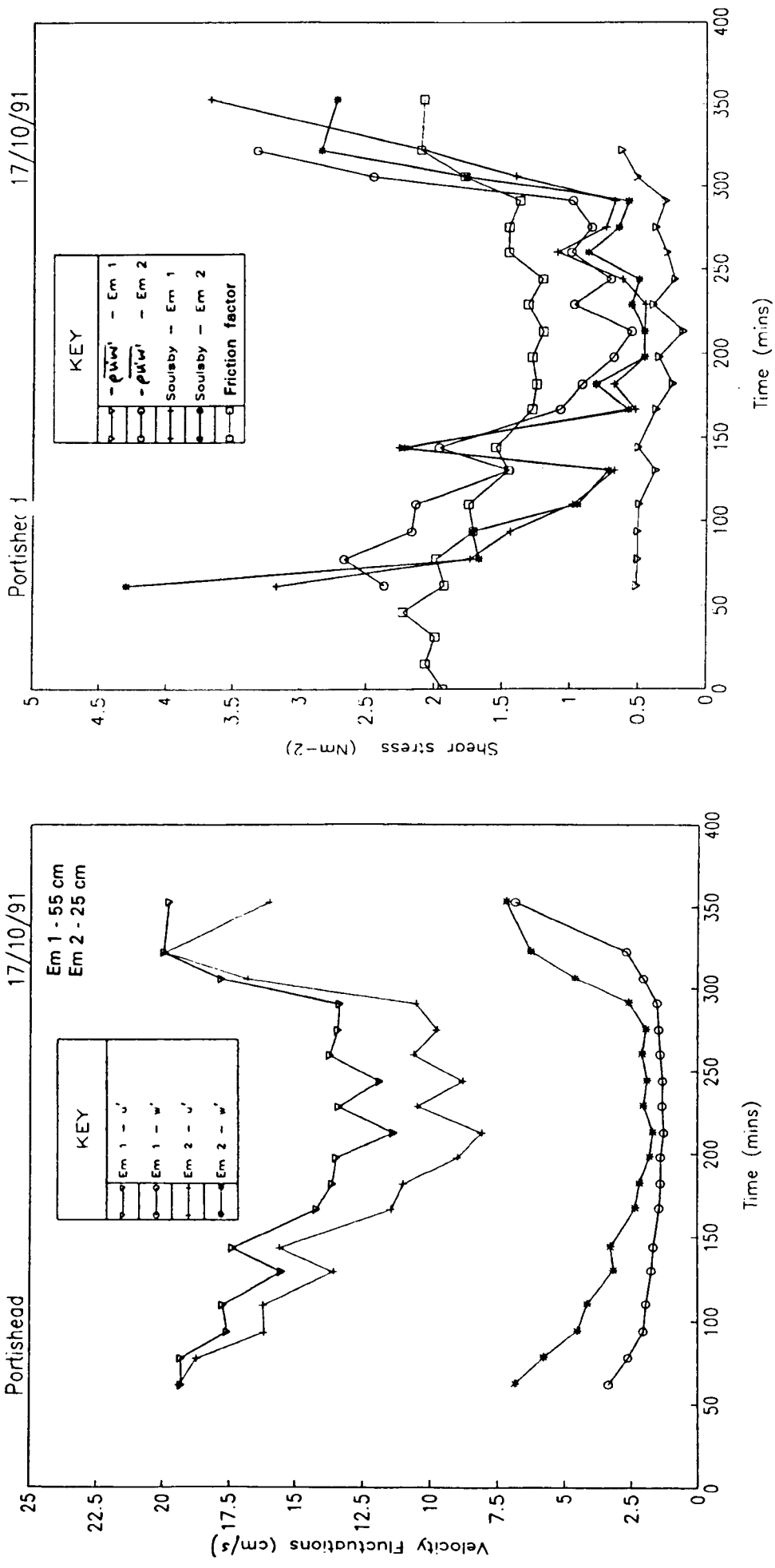

Figure 4.15: Mean velocity fluctuations (u', w' - EMCM data) and bed shear stress - a comparison of methods (HW $\approx 200\,mins$), 17/10/91)

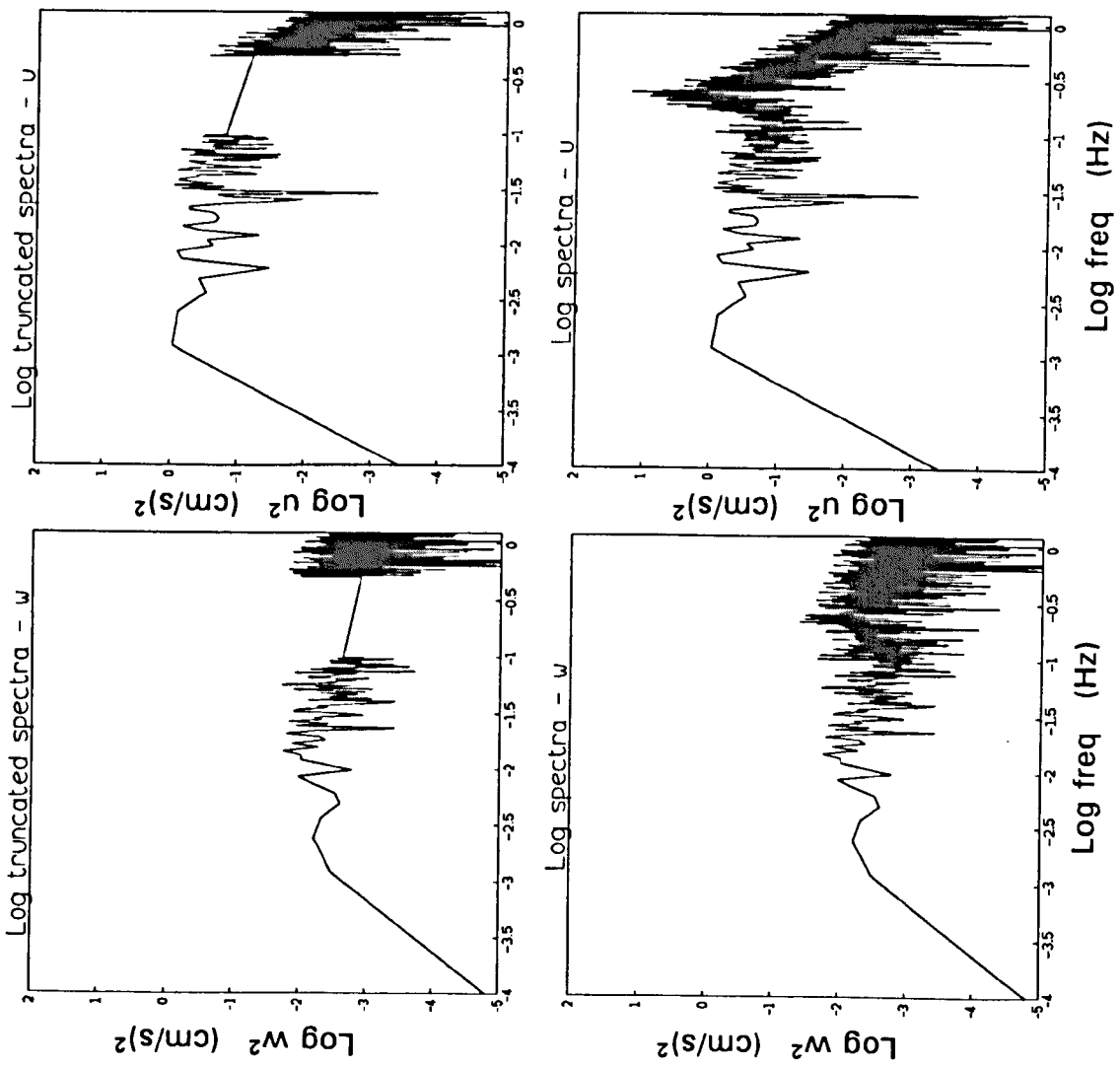

Figure 4.16: Example of Souslby & Humphery (1989) spectra splitting technique (15:34), 17/10/91

Figure 4.17: EMCM (Head 1,2 - u,w) Energy density example($h \approx 1\,m$, flood), 17/10/91

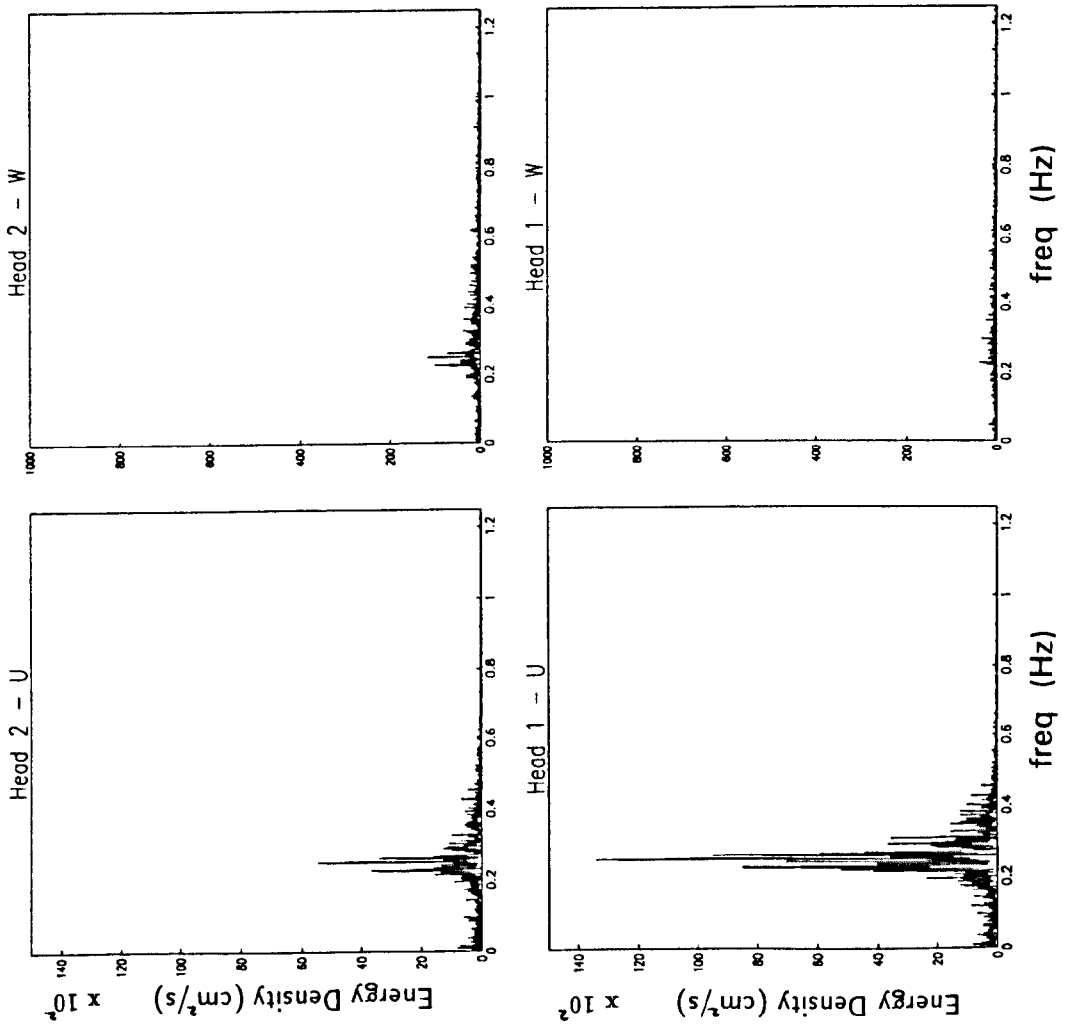

Figure 4.18: EMCM (Head 1,2 - u,w) Energy density example ($h \approx 2.2\,m$, HW), 17/10/91

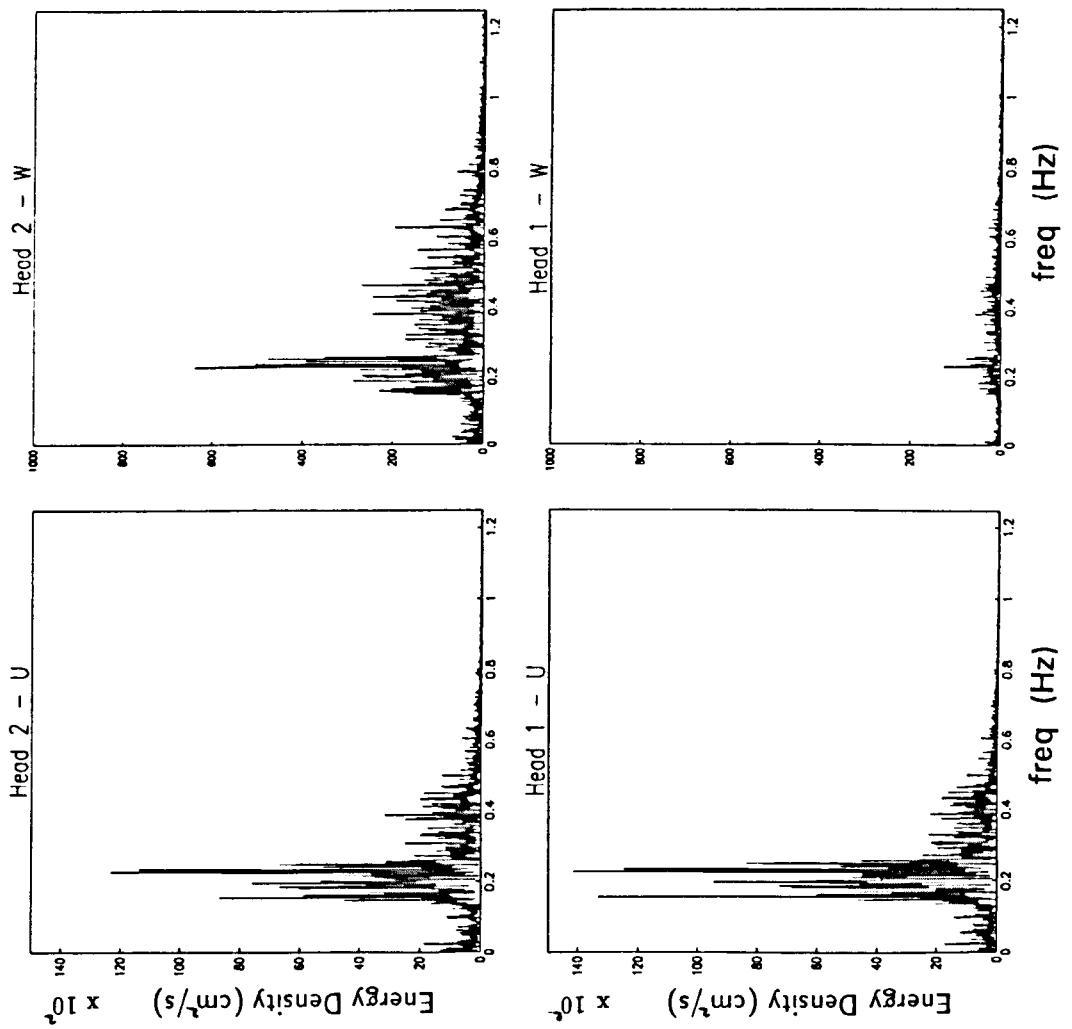

Figure 4.19: EMCM (Head 1,2 - u,w) Energy density example ($h \approx 1\,m$, Ebb), 17/10/91

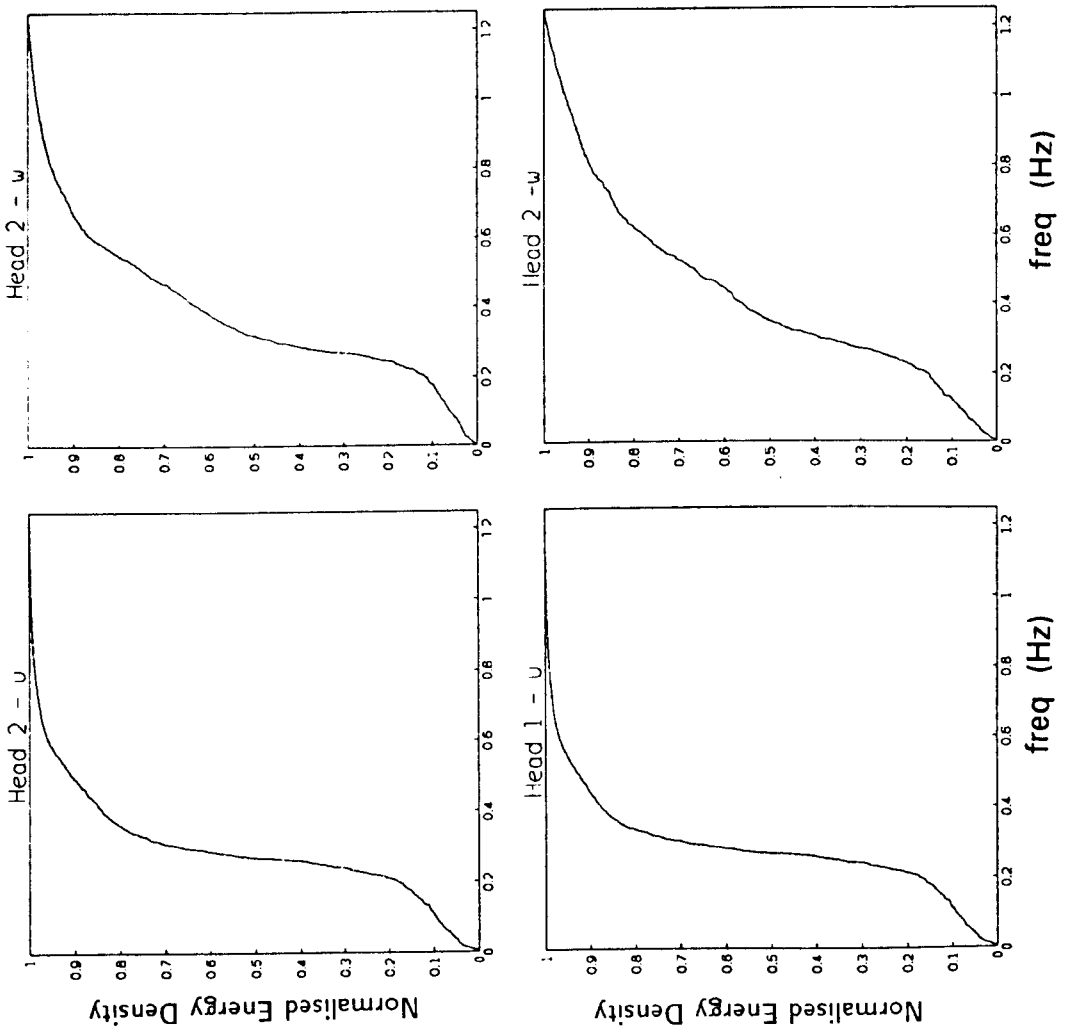

Figure 4.20: EMCM (Head 1,2 - u,w) Cumulative normalised energy density example ($h \approx 1\,m$, flood), 17/10/91

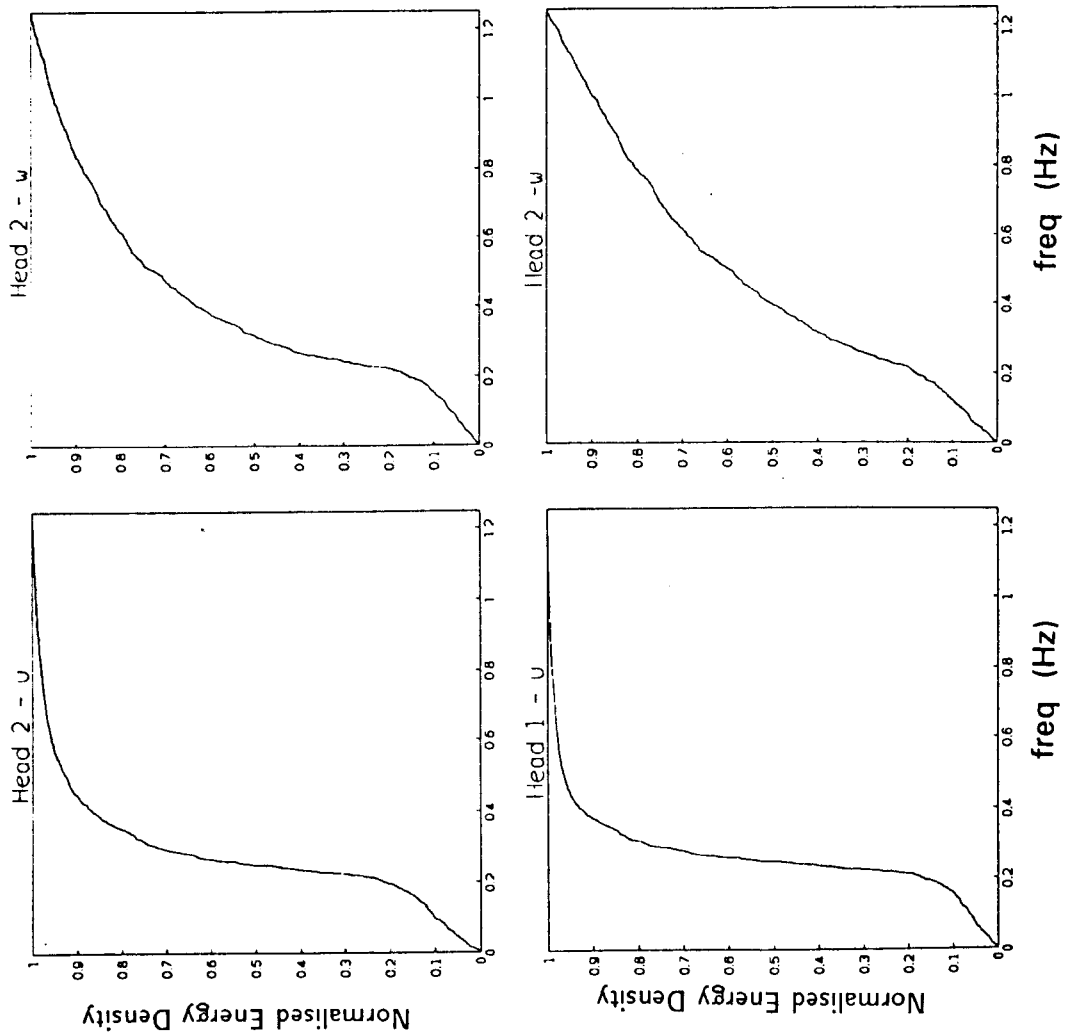

Figure 4.21: EMCM (Head 1,2 - u,w) Cumulative normalised energy density example ($h \approx 2.2\,m$, HW), 17/10/91

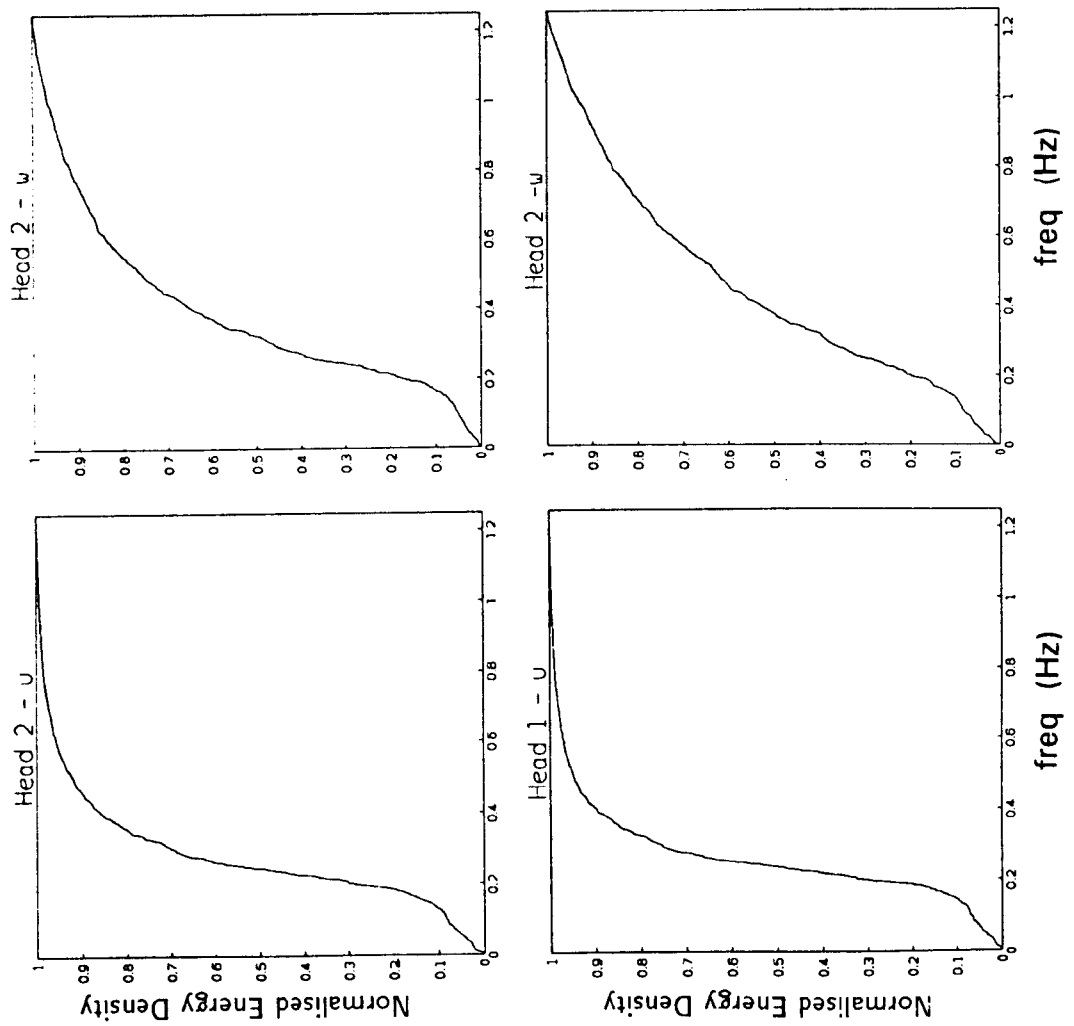

Figure 4.22: EMCM (Head 1,2 - u,w) Cumulative normalised energy density example ($h \approx 1\,m$, Ebb), 17/10/91

Figure 4.23: EMCM - Cospectra examples at three points in the tidal cycle, 17/10/91

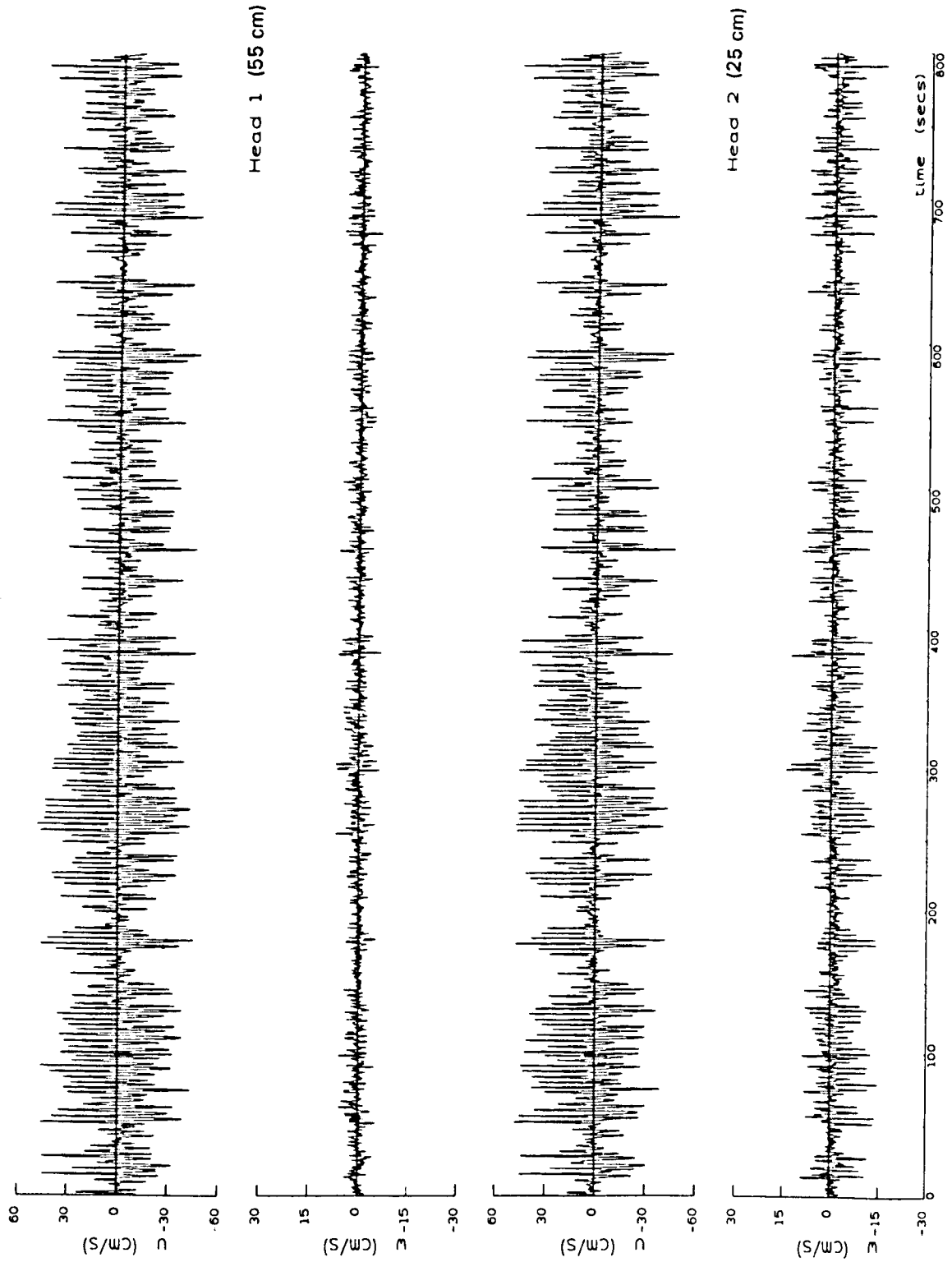

Figure 4.24: Example of wave grouping ($h = 1.63\,m$, Flood), 17/10/91

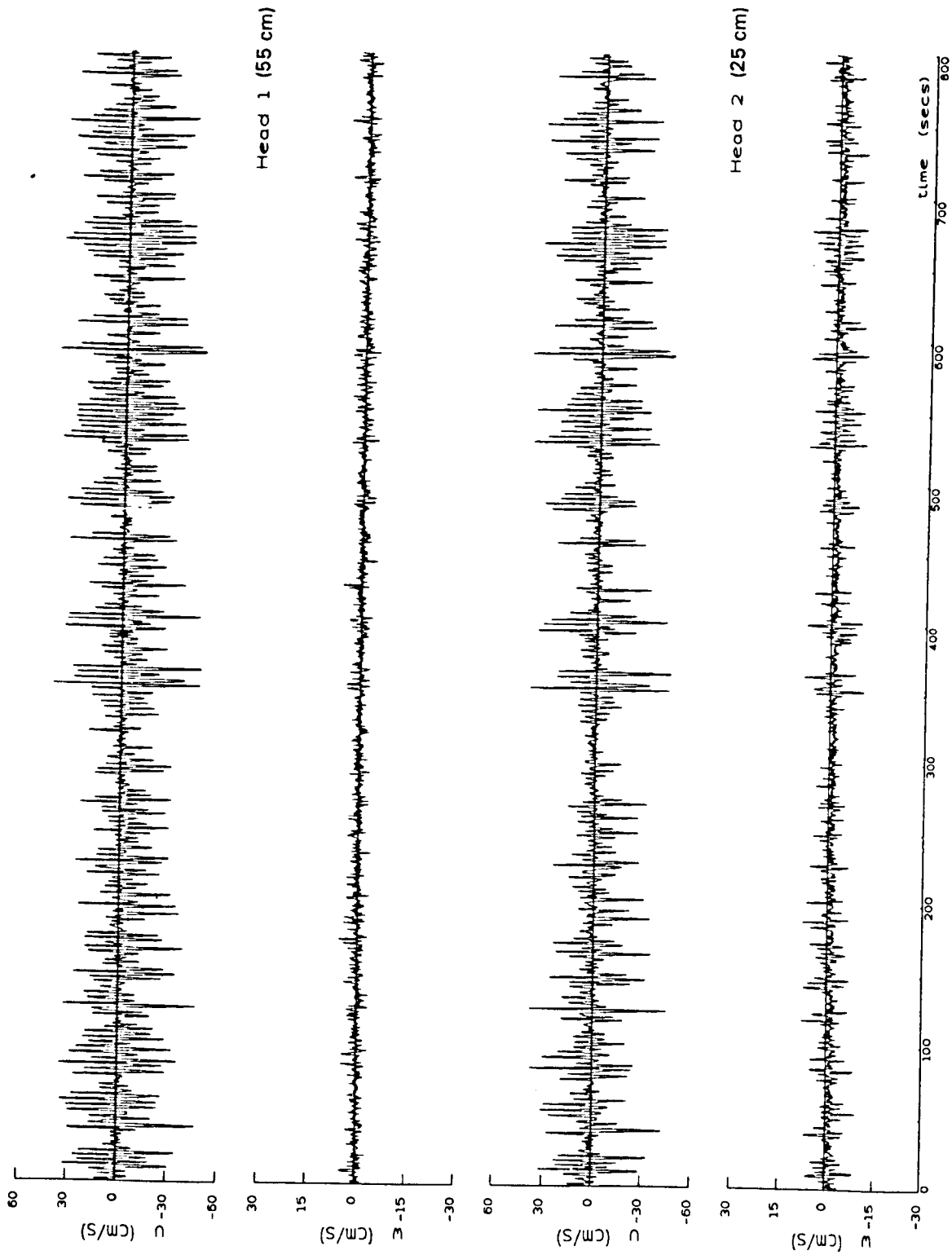

Figure 4.25: Example of wave grouping ($h = 2.12\,m$, Flood), 17/10/91

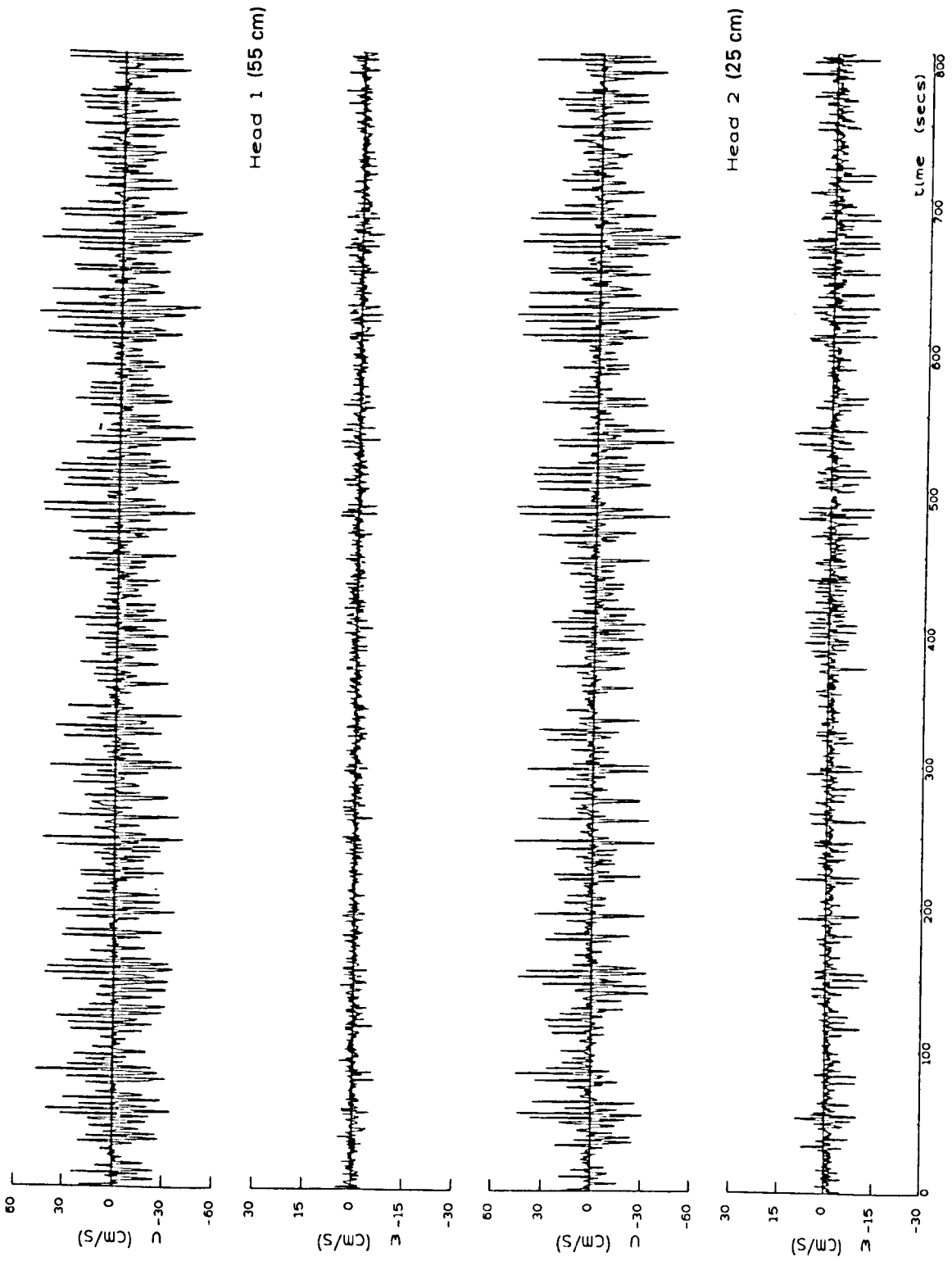

Figure 4.26: Example of wave grouping ($h = 1.44\,m$, Ebb), 17/10/91

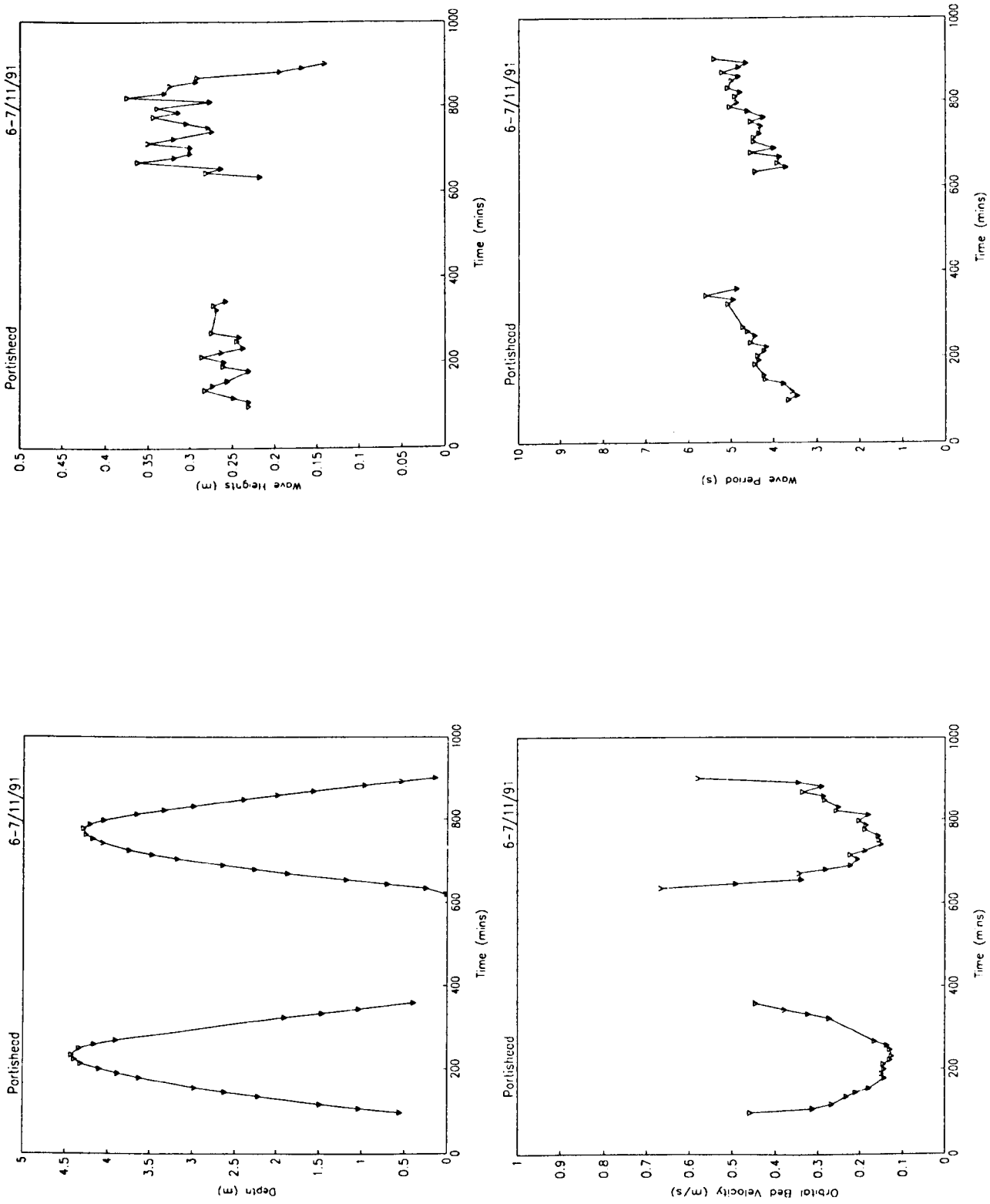

Figure 4.27: Water depth, wave heights, wave periods and wave orbital velocity at upper site (from pressure data, HW $\approx$ 230, 780 *mins*), 6-7/11/91

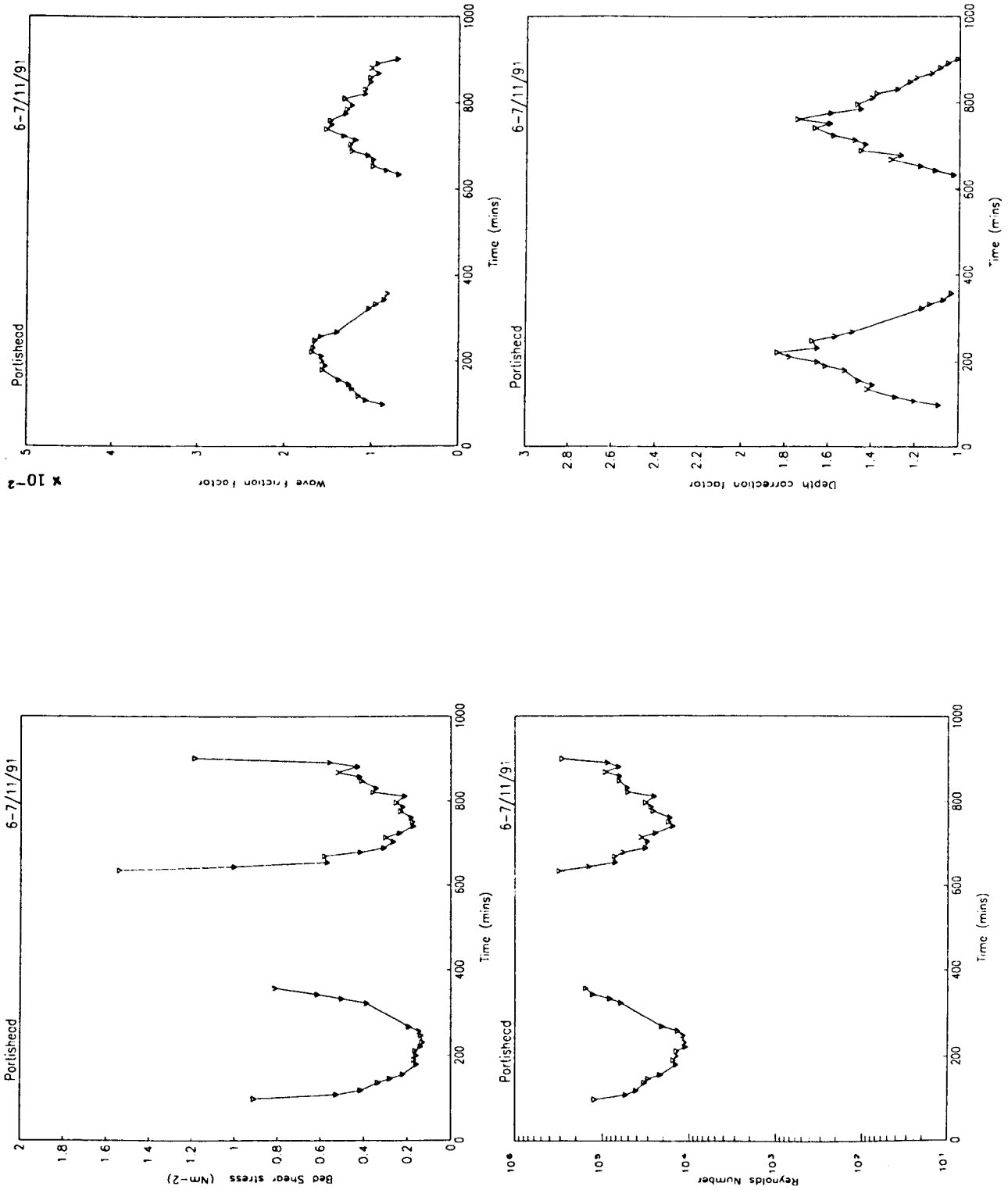

Figure 4.28: Bed shear stress, wave friction factor, Reynolds number and correction factor from bed pressures to surface wave heights at upper site (pressure data, HW $\approx$ 230, 780 *mins*), 6-7/11/91

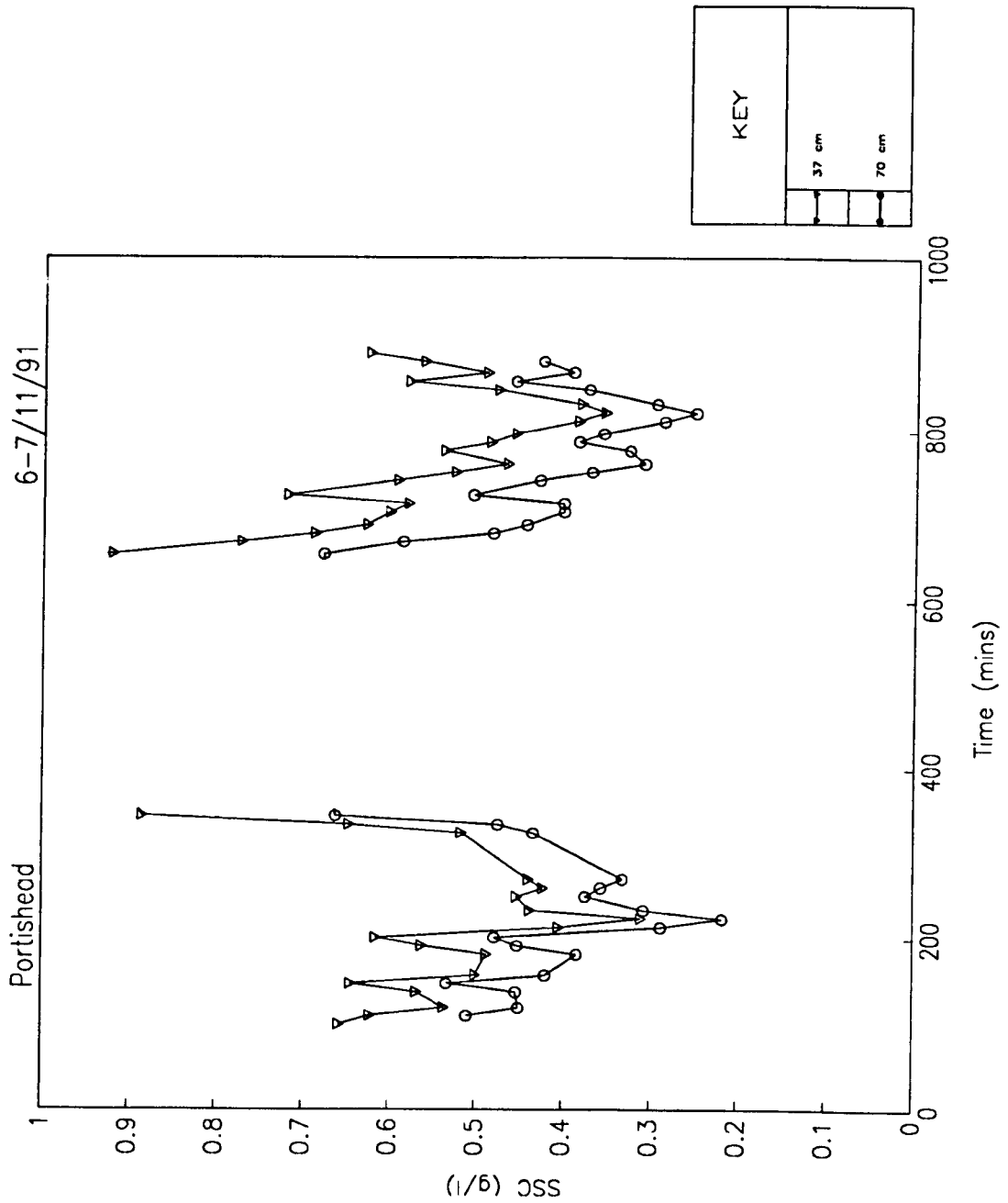

Figure 4.29: SSC at upper site at $z = 37\,cm$ and $70\,cm$ (from partech data, (HW $\approx$ 230, 780 *mins*), 6-7/11/91

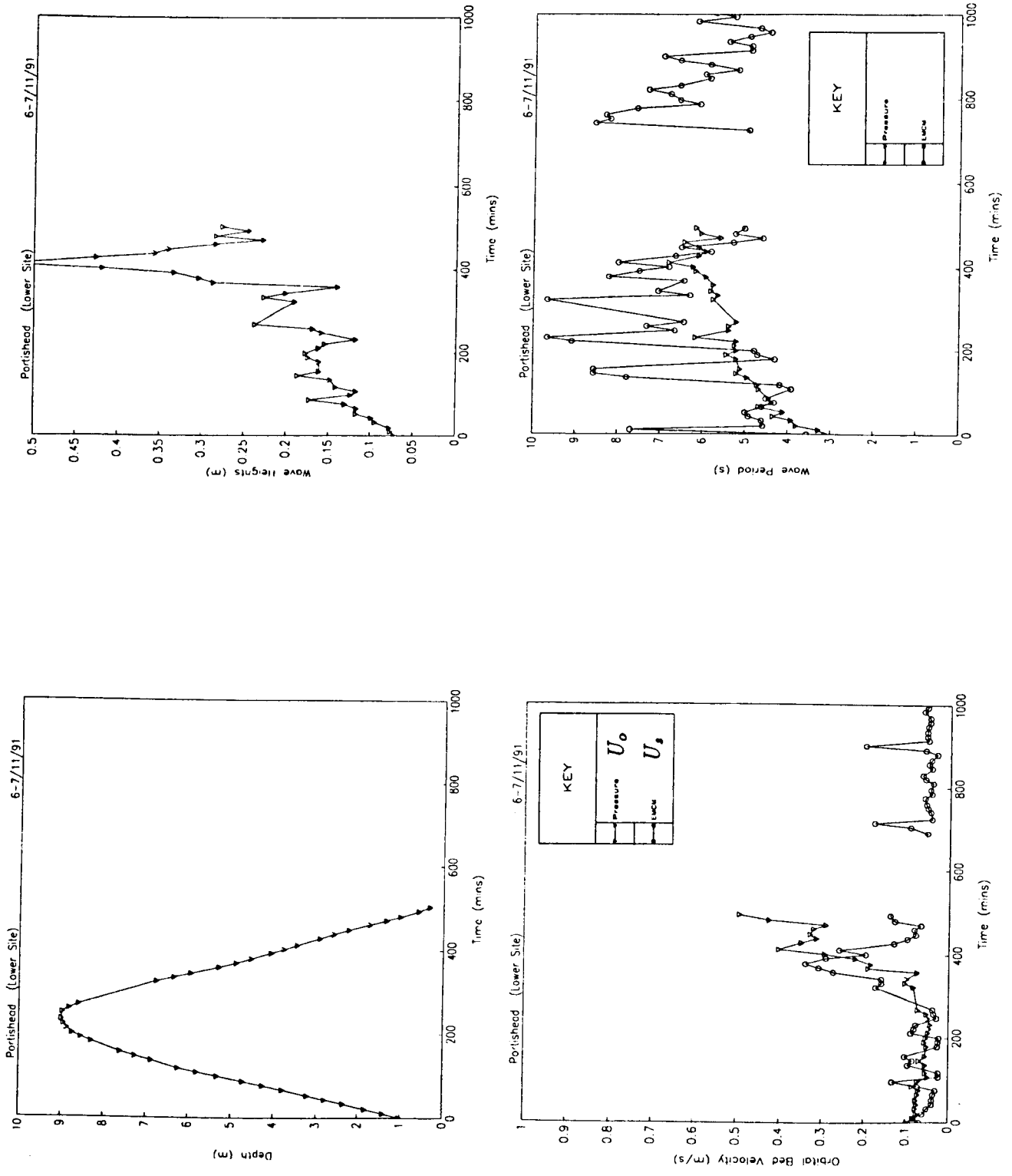

Figure 4.30: Water depth, wave heights, wave periods and wave orbital velocity at lower site (pressure and EMCM comparisons, HW $\approx$ 230, 780 *mins*), 6-7/11/91

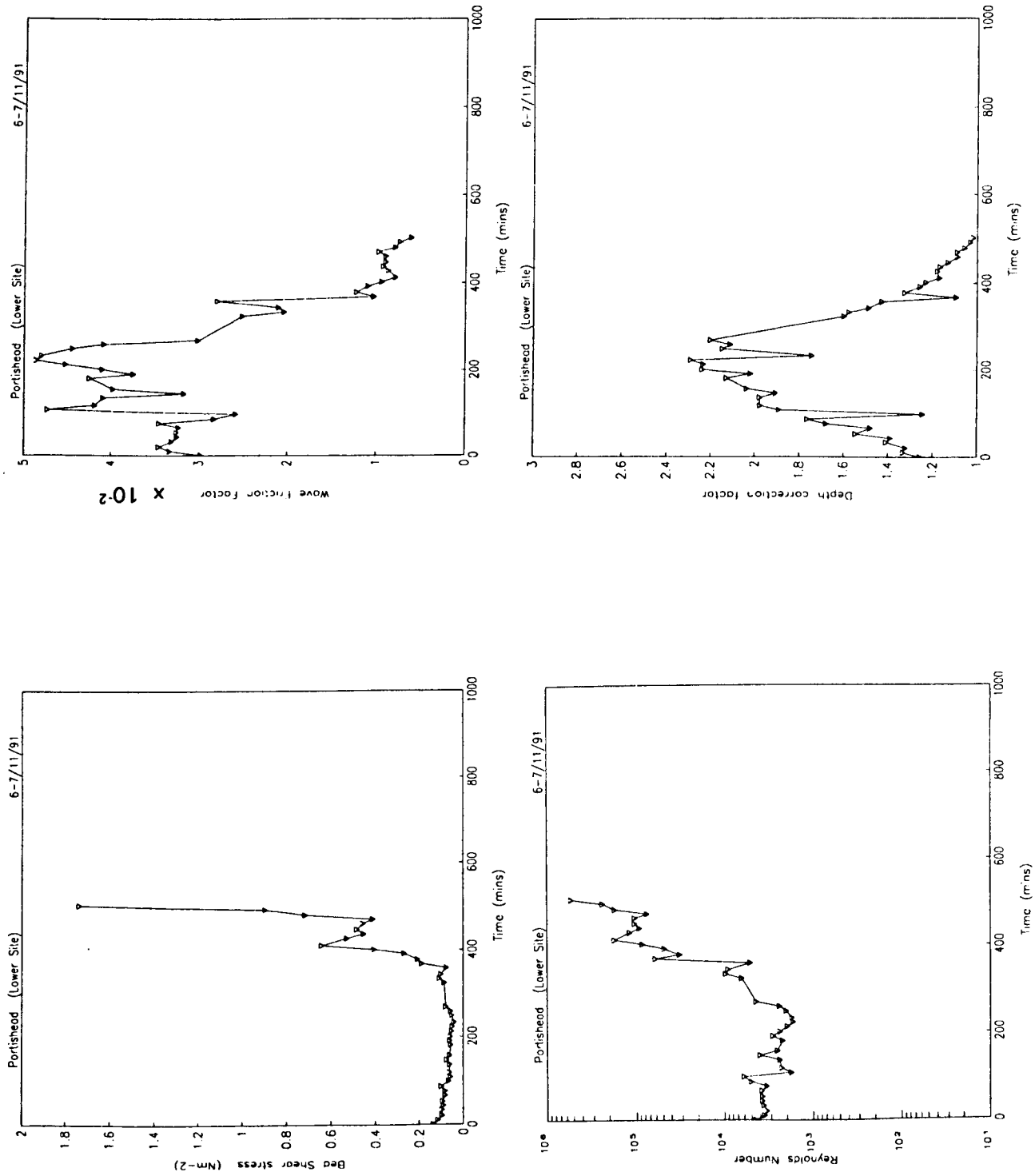

Figure 4.31: Bed shear stress, wave friction factor, Reynolds number and correction factor from bed pressures to surface wave heights at lower site (pressure data, HW $\approx$ 230, 780 *mins*), 6-7/11/91

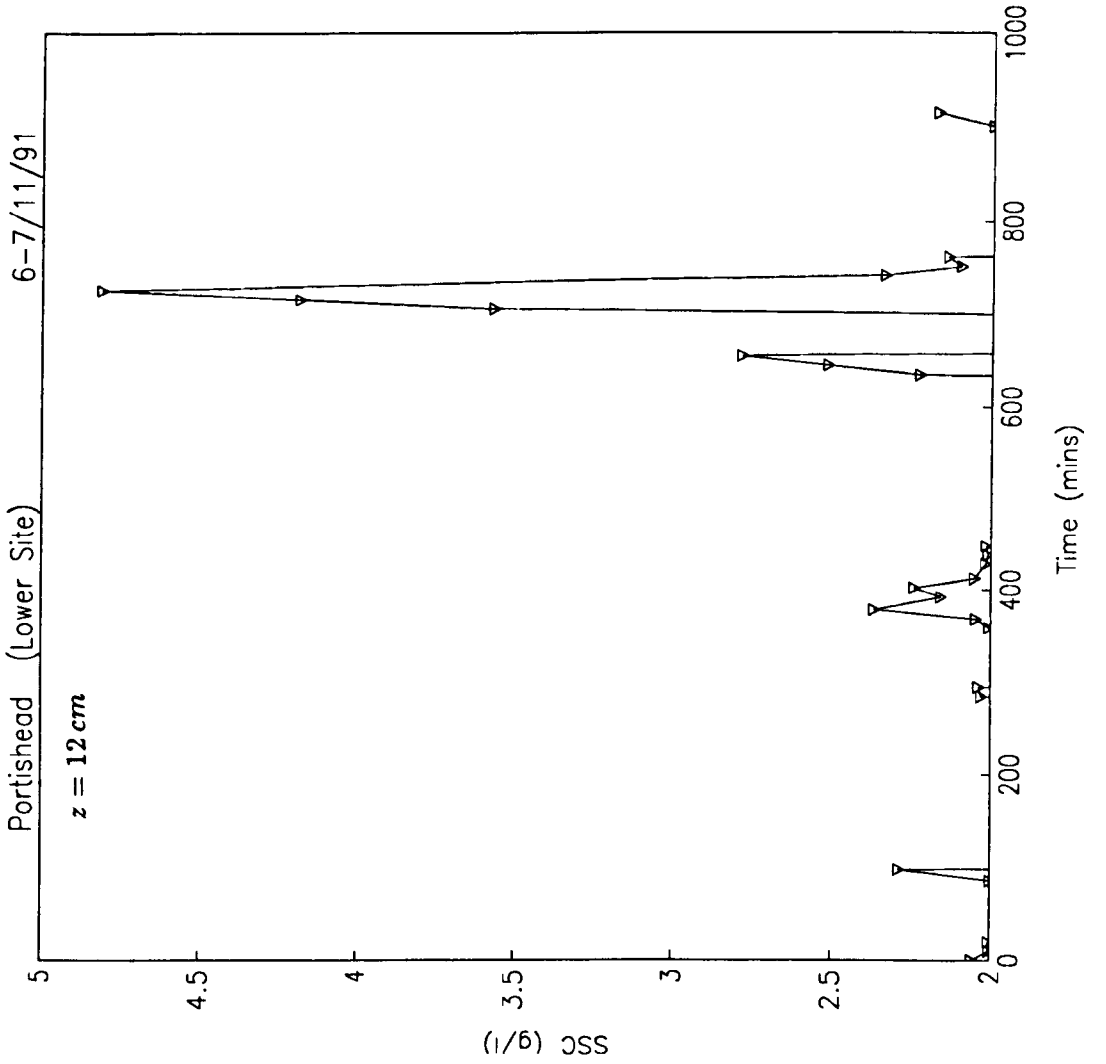

Figure 4.32: Near bed SSC ($z = 12\,cm$) at lower site from siltmeter data ($SSC > 2\,g/l$, HW $\approx$ 230, 780 *mins*, 6-7/11/91

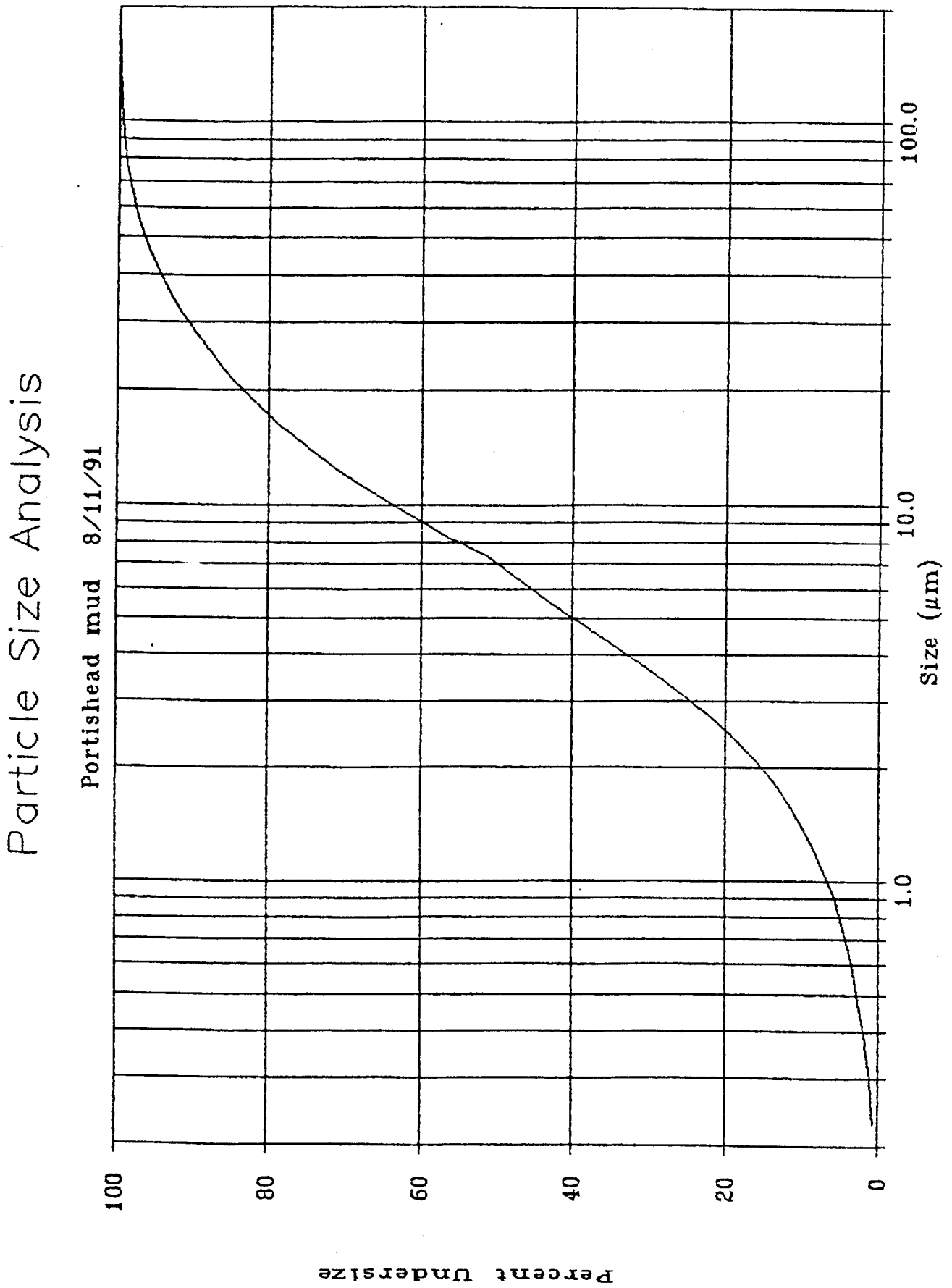

Figure 4.33: Particle size distribution, 6-7/11/91

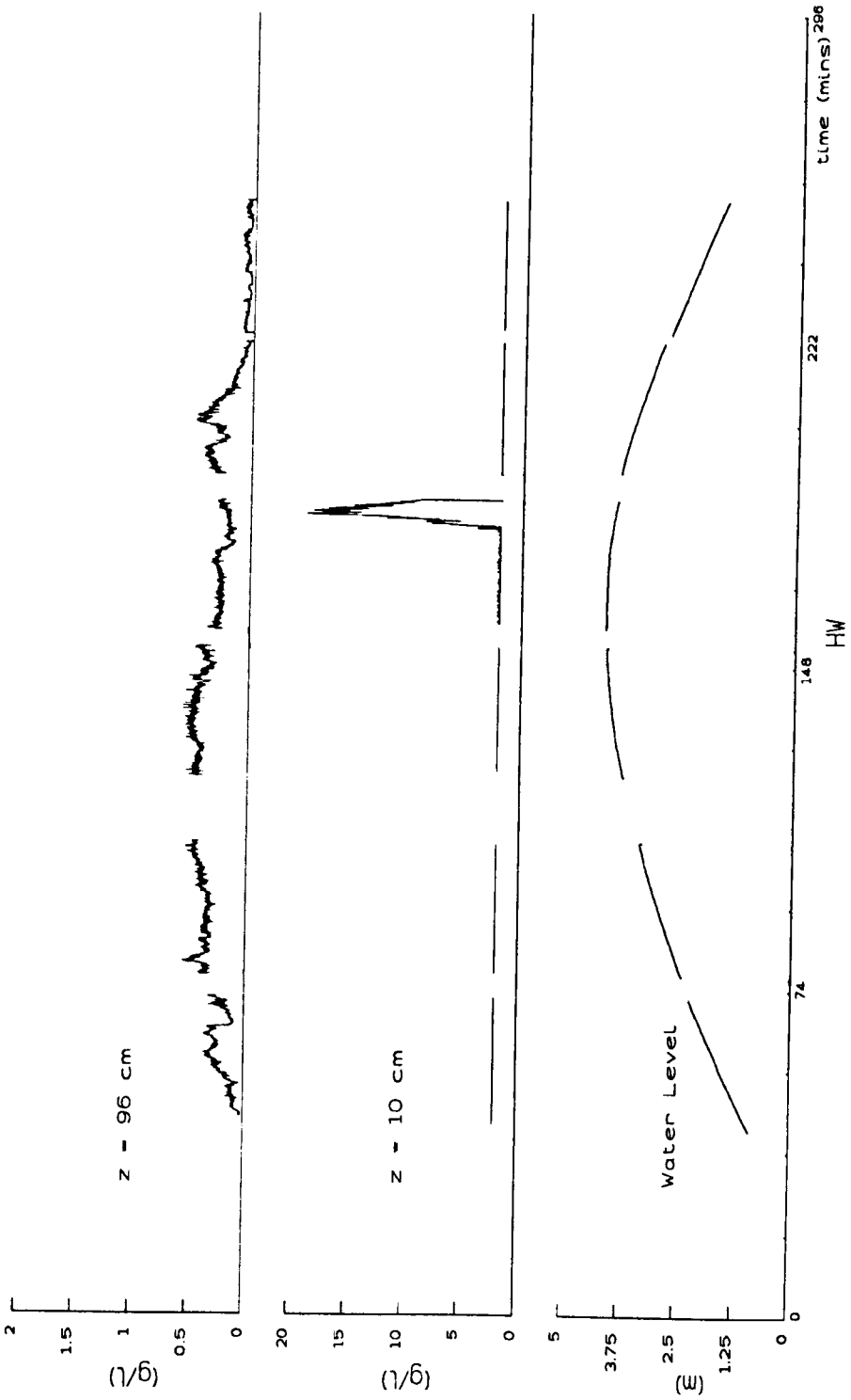

Figure 4.34: Water depth and SSC ($z = 10, 96\,cm$) time series for tide 1, 6-7/2/92

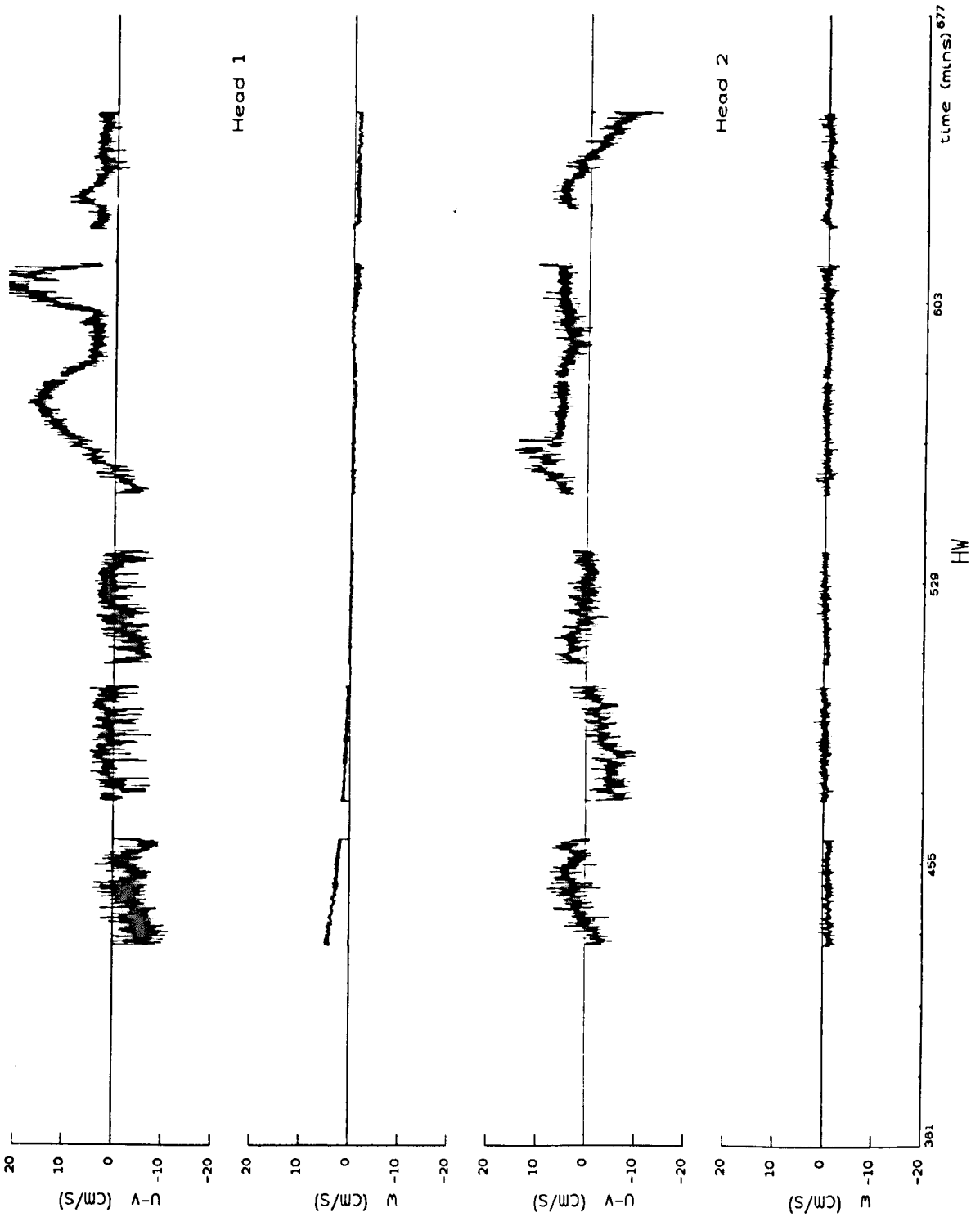

Figure 4.35: EMCM velocity time series ($u - v$, w) for tide 2, 6-7/2/92

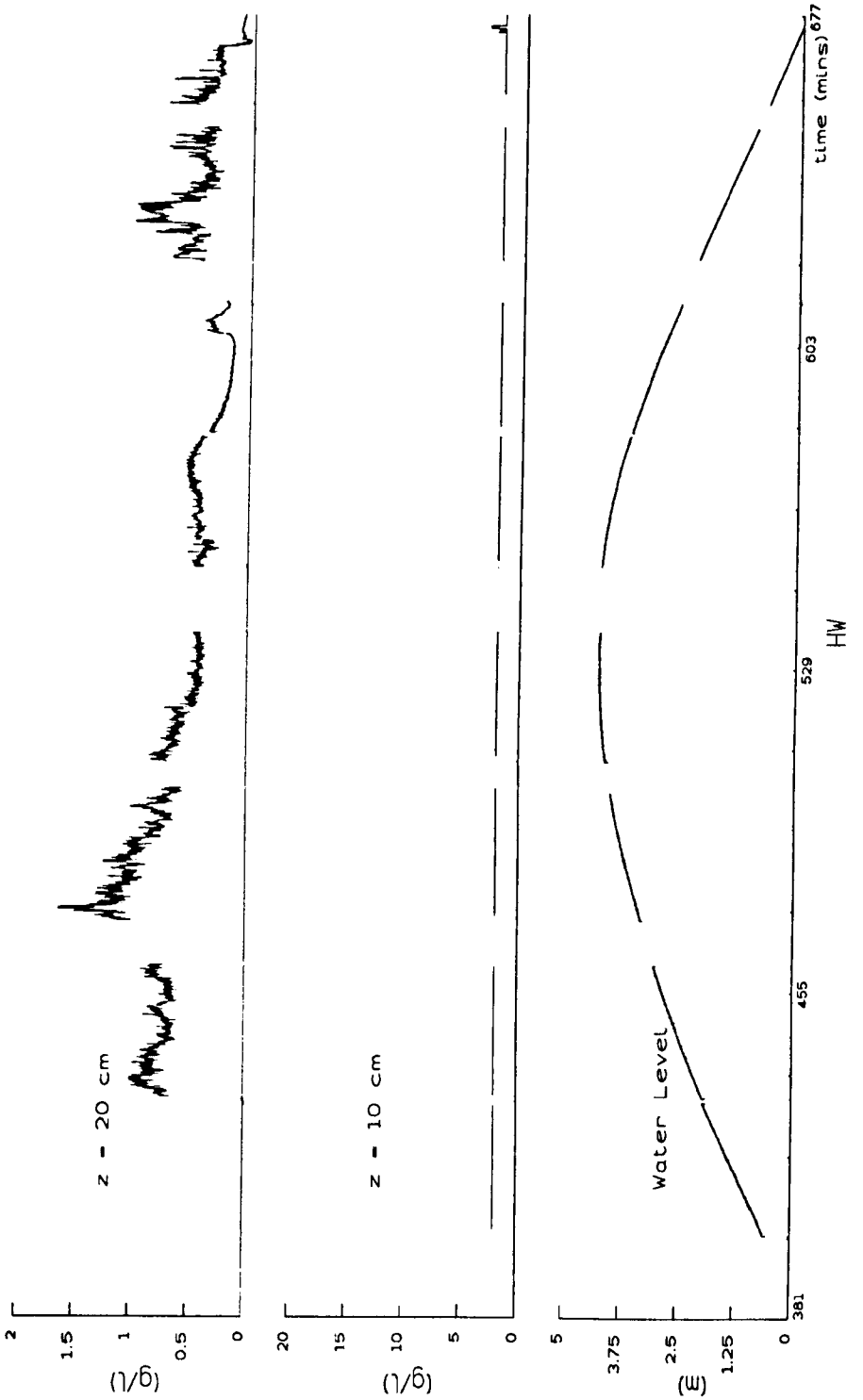

Figure 4.36: Water depth and SSC ($z = 10, 20\,cm$) time series for tide 2, 6-7/2/92

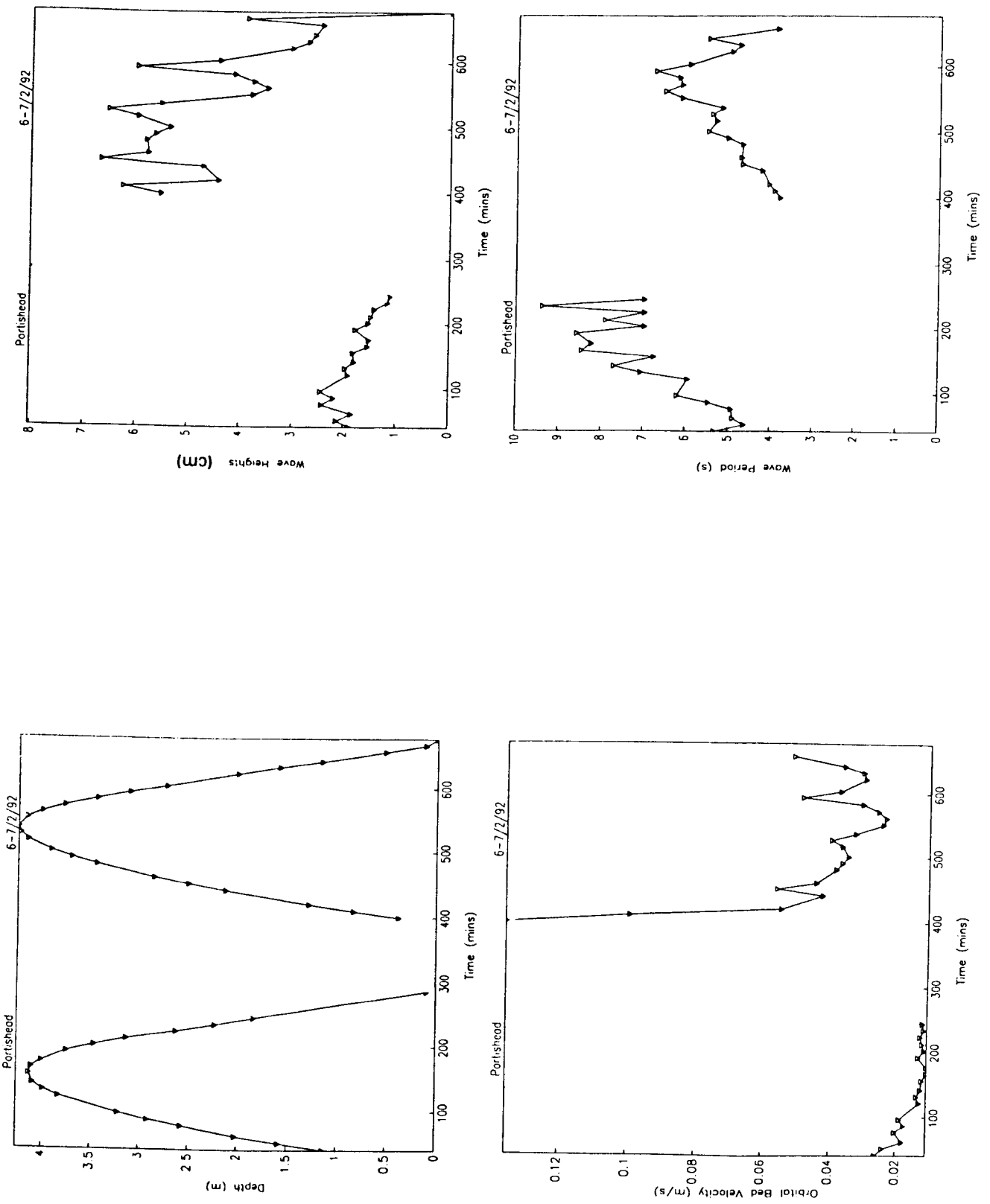

Figure 4.37: Water depth, wave heights, wave periods and wave orbital velocity (from pressure data, HW $\approx$ 156, 537 *mins*), 6-7/2/92

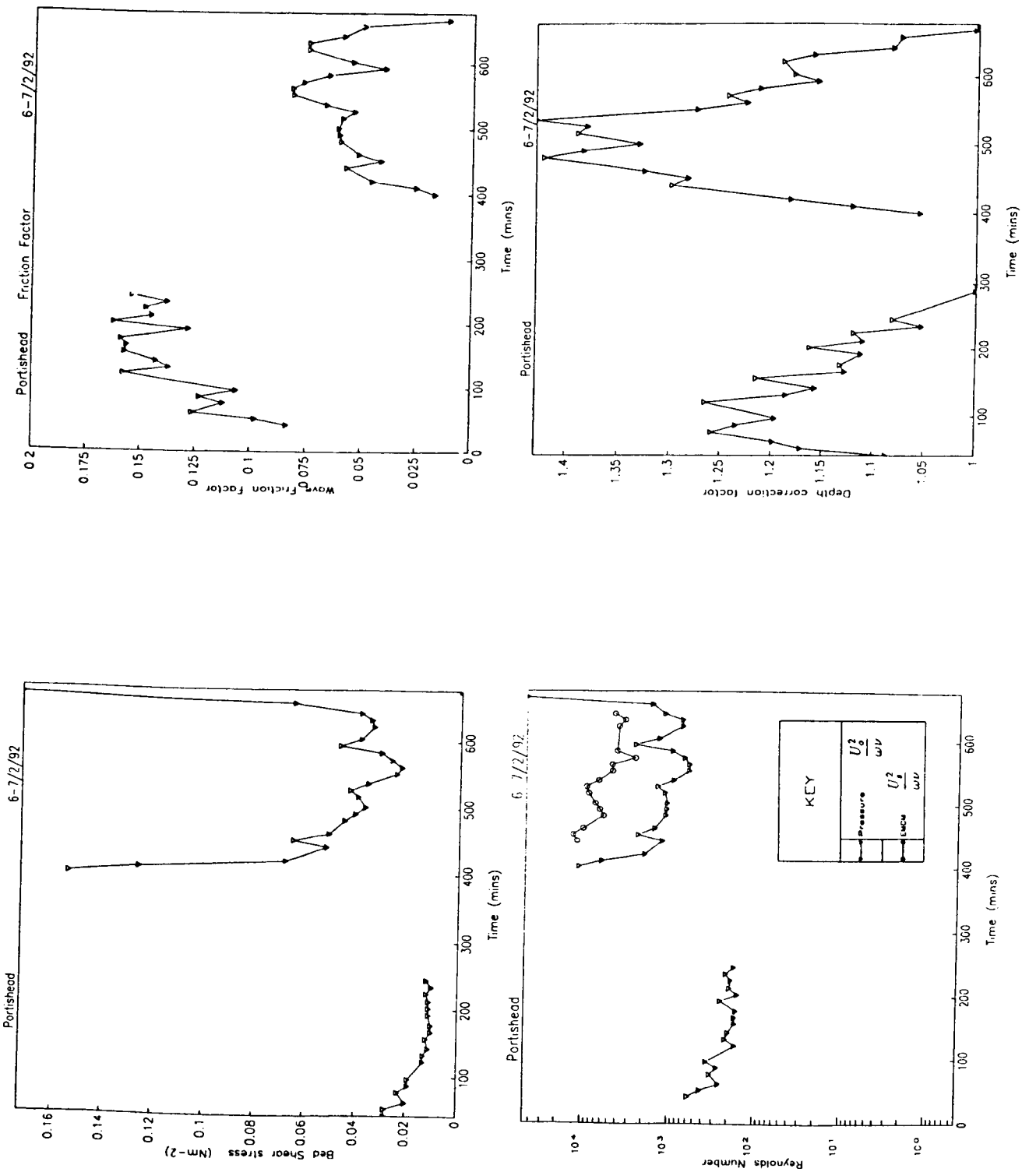

Figure 4.38: Bed shear stress, wave friction factor, Reynolds numbers and correction factor from bed pressures to surface wave heights (HW $\approx$ 156, 537 *mins*), 6-7/2/92

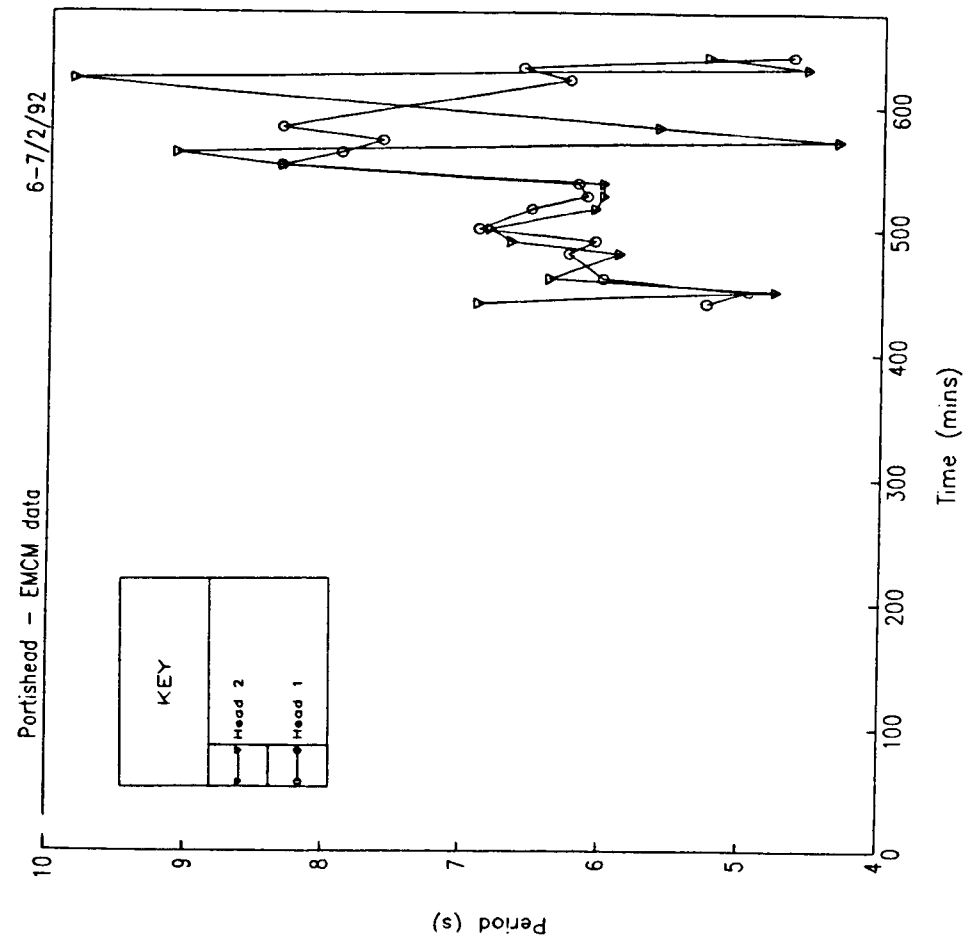

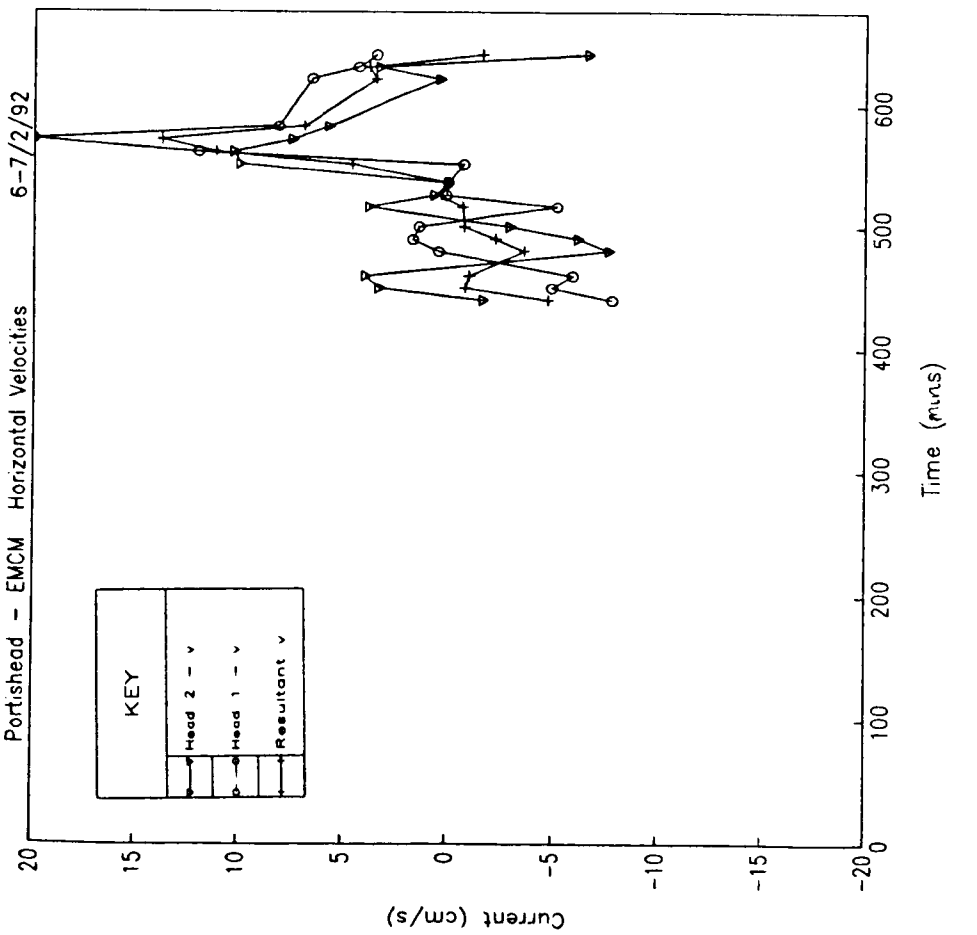

Figure 4.39: Mean current (Head 1, Head 2 and resultant), and wave periods from EMCM (HW $\approx$ 156, 537 *mins*), 6-7/2/92

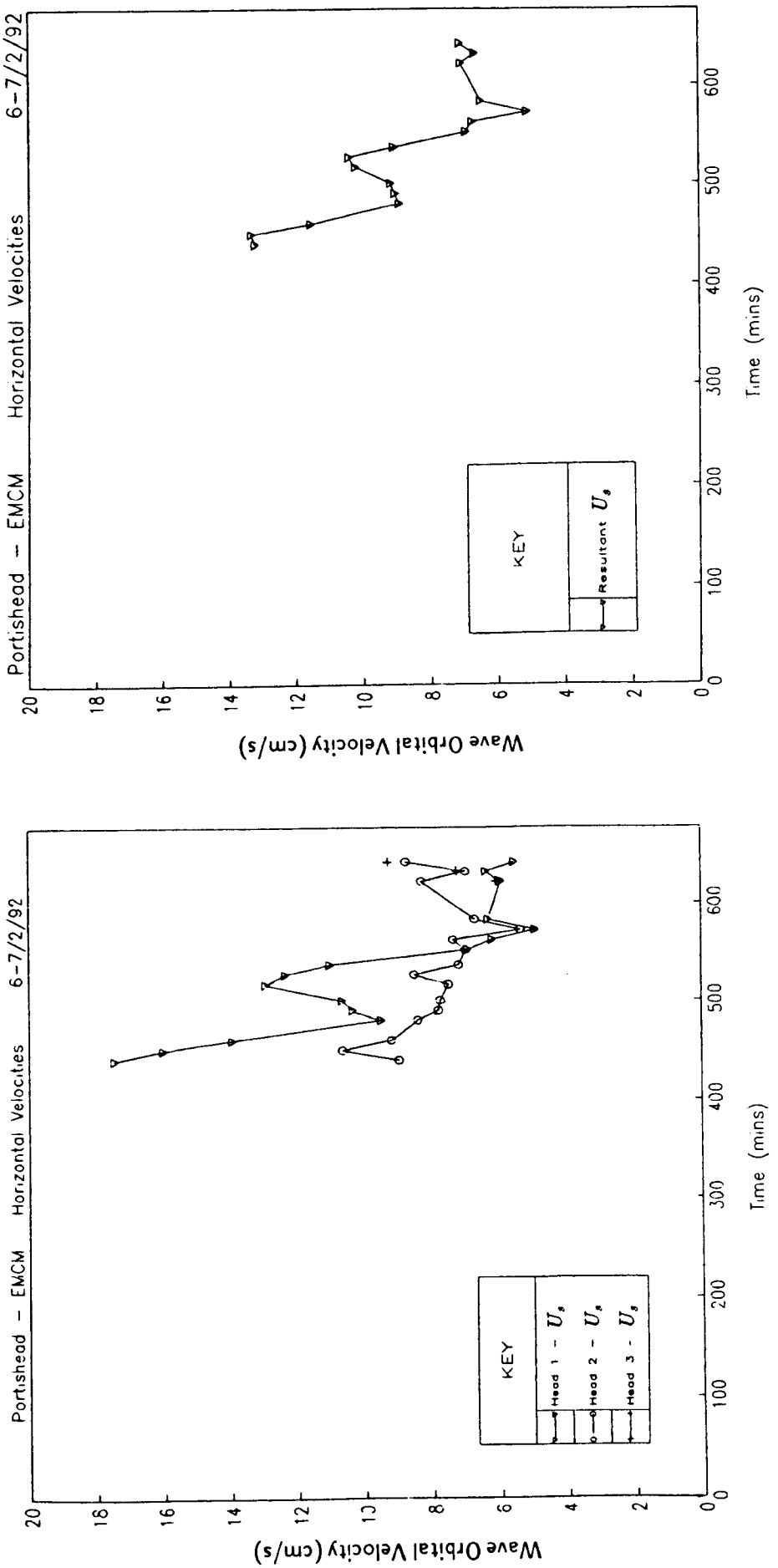

Figure 4.40: Horizontal wave orbital velocities (U_s) calculated from EMCM - Heads 1, 2 & 3 and resultant (HW $\approx$ 156, 537 *mins*), 6-7/2/92

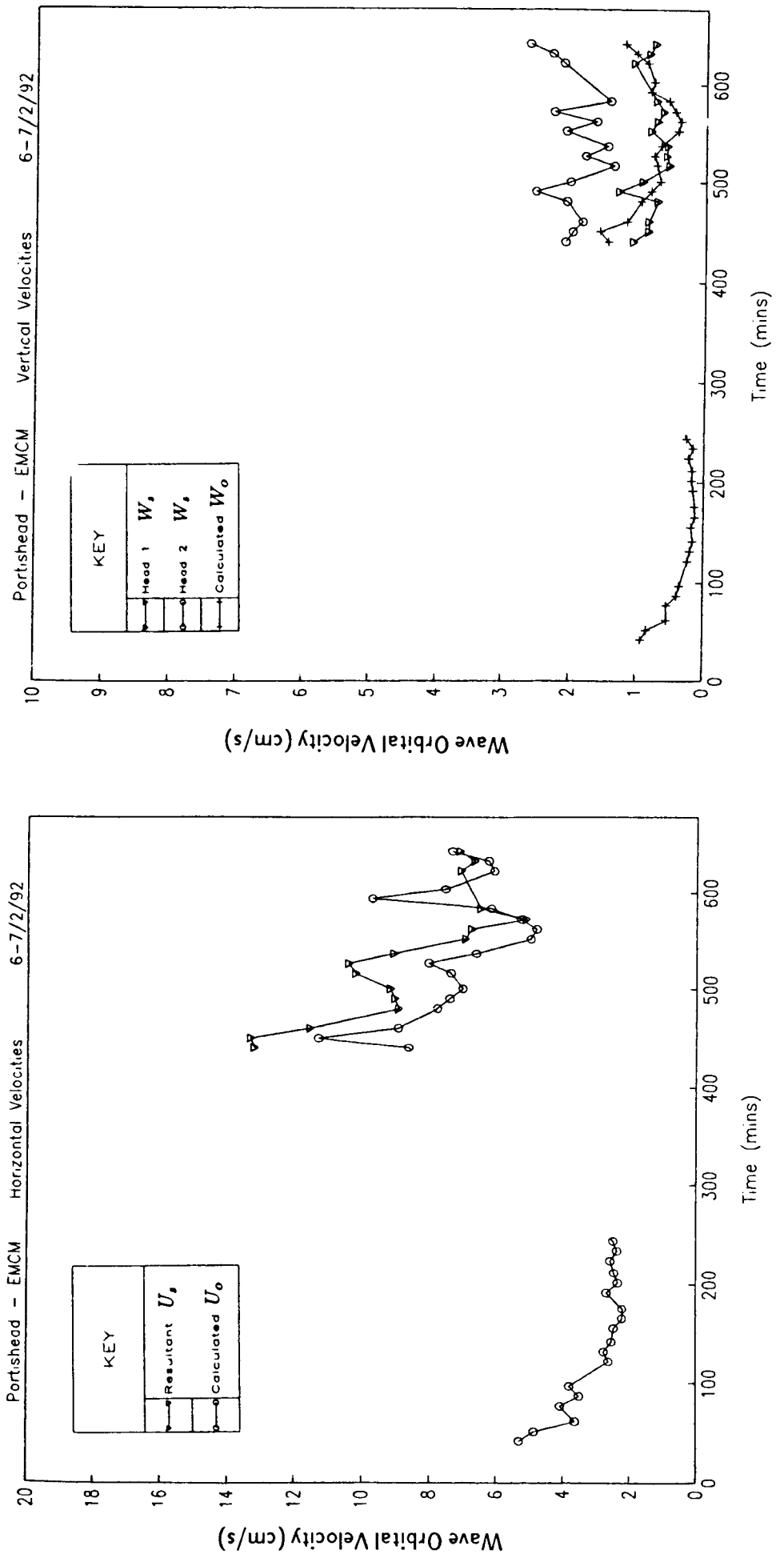

Figure 4.41: Comparison between horizontal and vertical wave orbital velocities from EMCM (U_s, W_s) and pressure (U_o, W_o) data (HW $\approx$ 156, 537 *mins*), 6-7/2/92

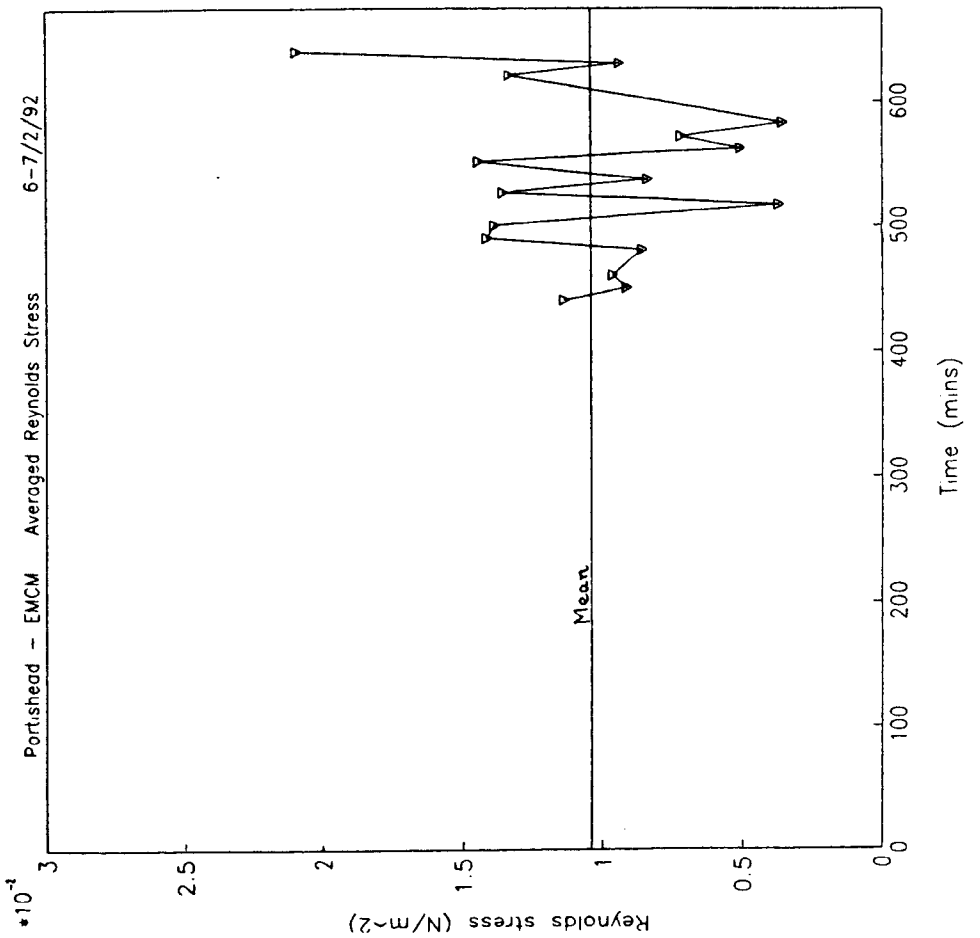

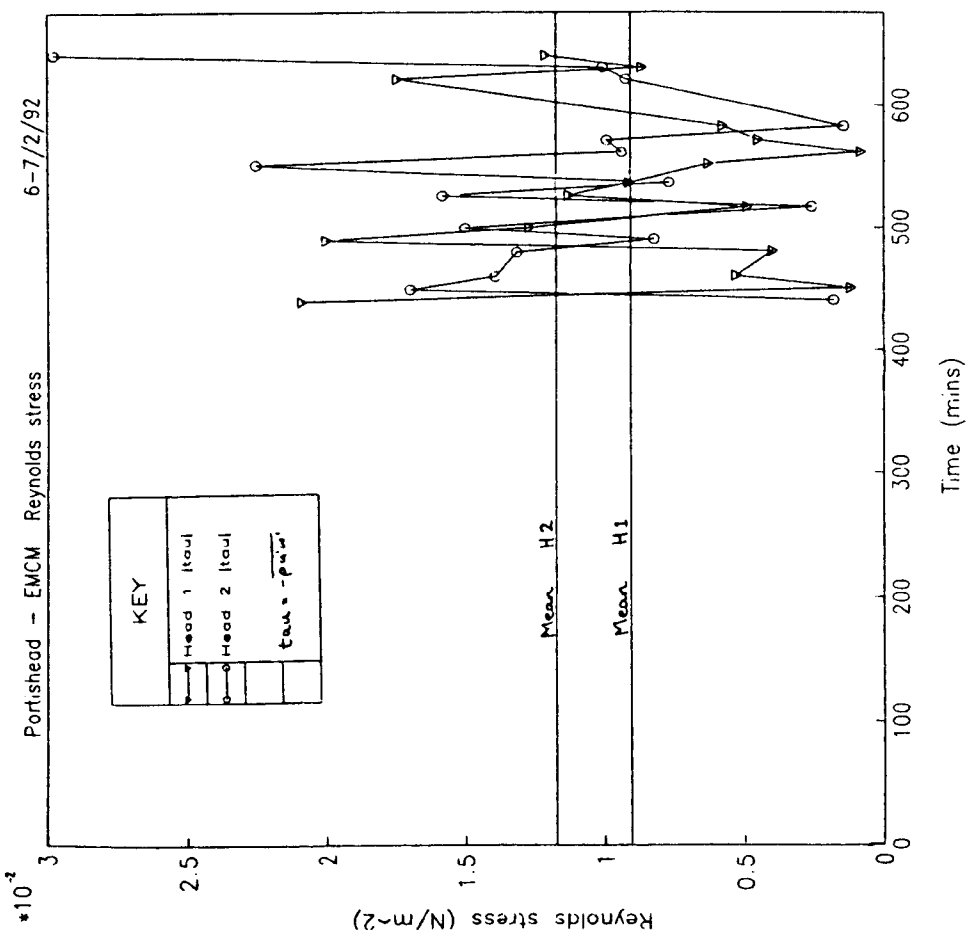

Figure 4.42: Reynold stresses from EMCM data - Head 1 & 2 and resultant (HW $\approx$ 156, 537 *mins*), 6-7/2/92

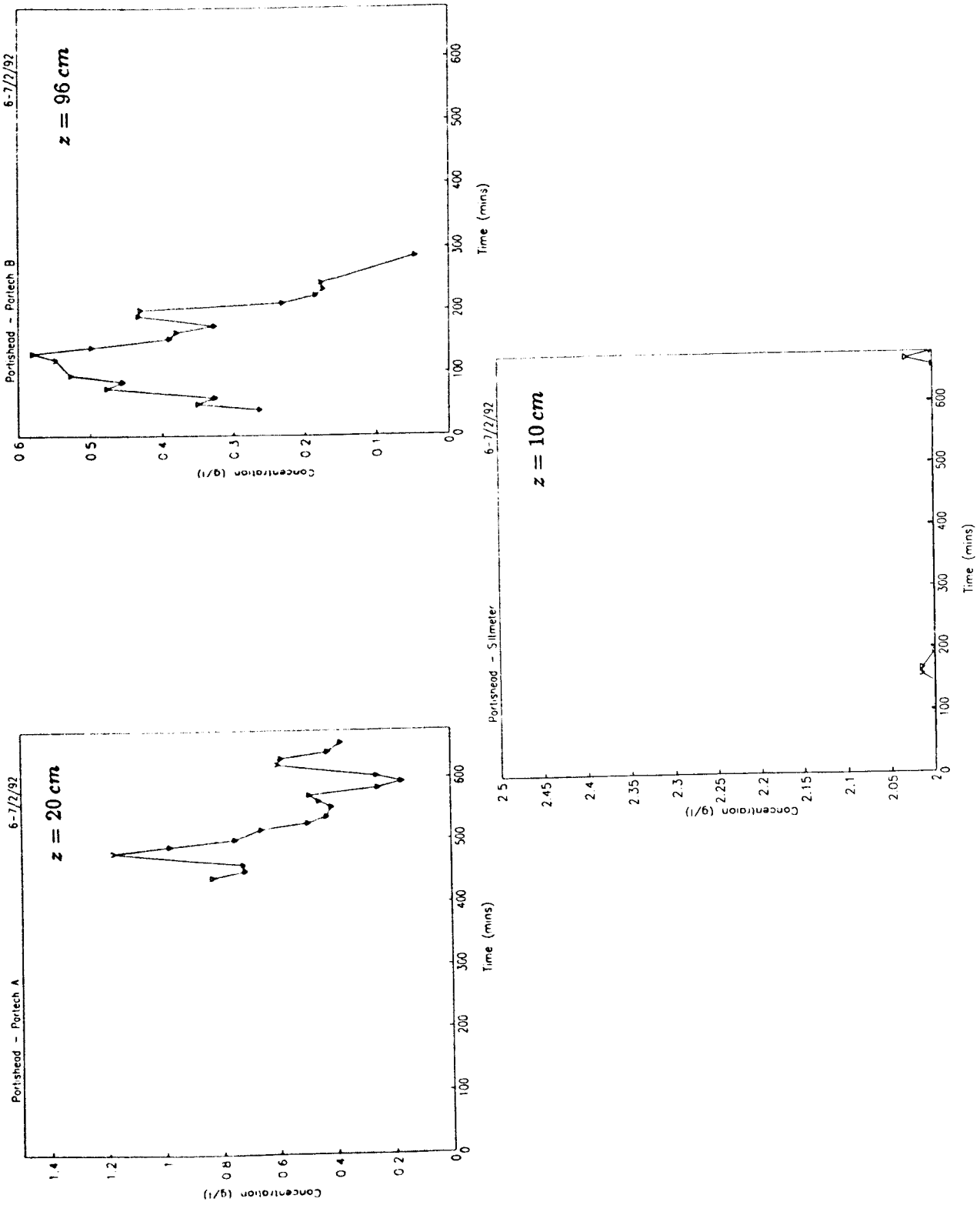

Figure 4.43: SSC at $z = 10\,20, 96\,cm$ (HW $\approx 156, 537\,mins$), 6-7/2/91

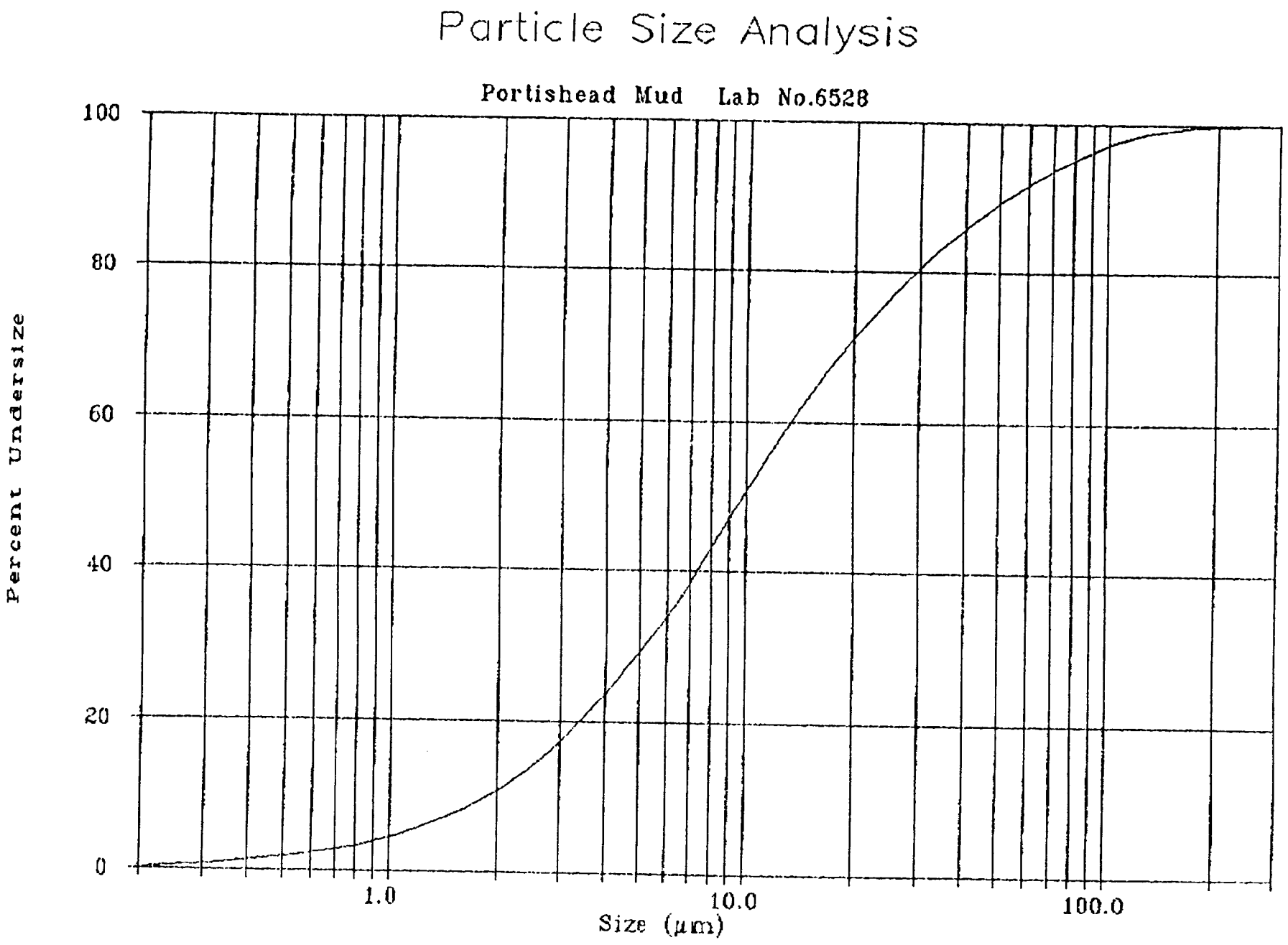

Figure 4.44: Particle size distribution, 6-7/2/92

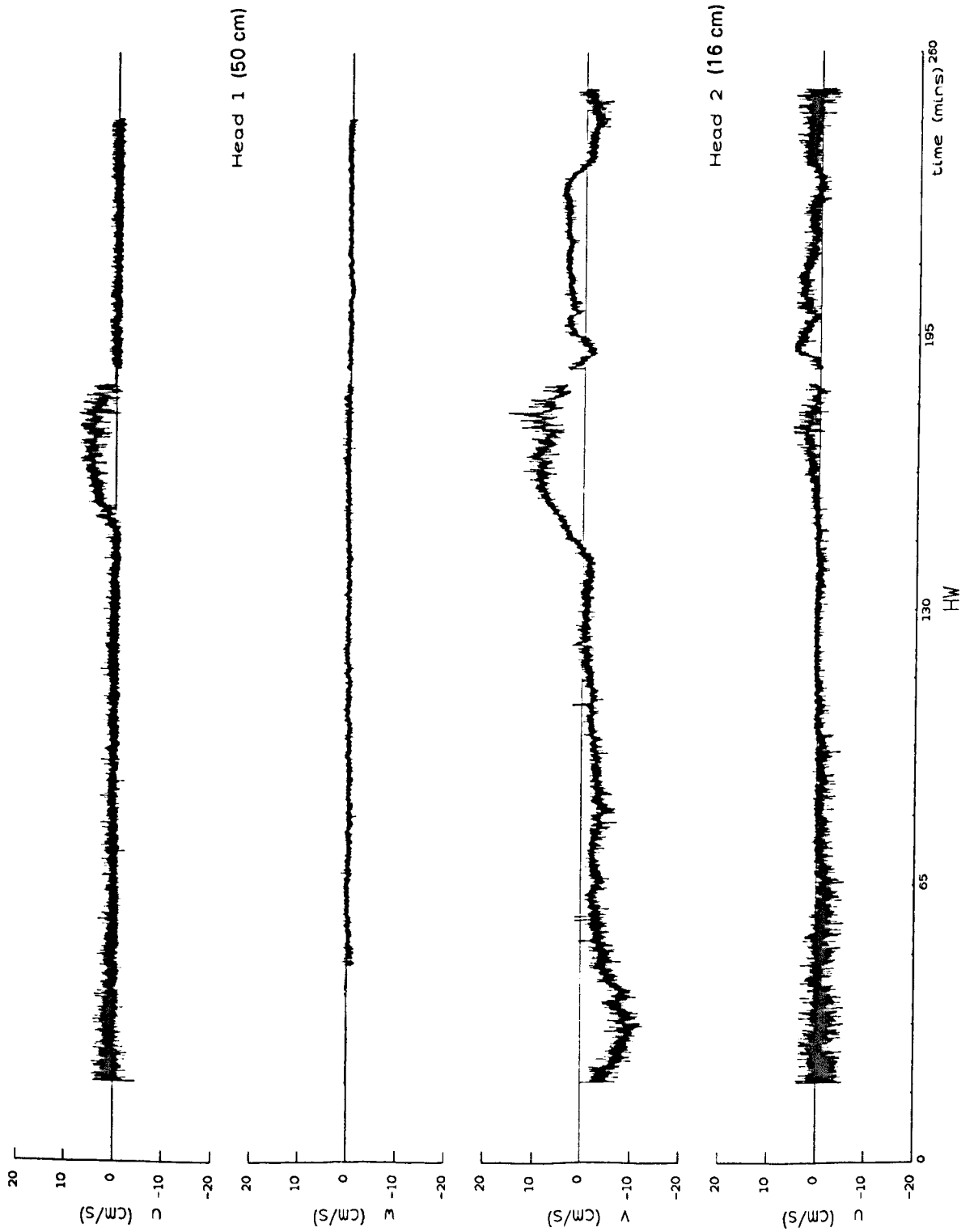

Figure 4.45: EMCM velocity time series (u, v, w) tide 1, 5/5/93

Figure 4.46: SSC ($z = 5, 22, 58, 80\,cm$) time series tide 1, 5/5/93

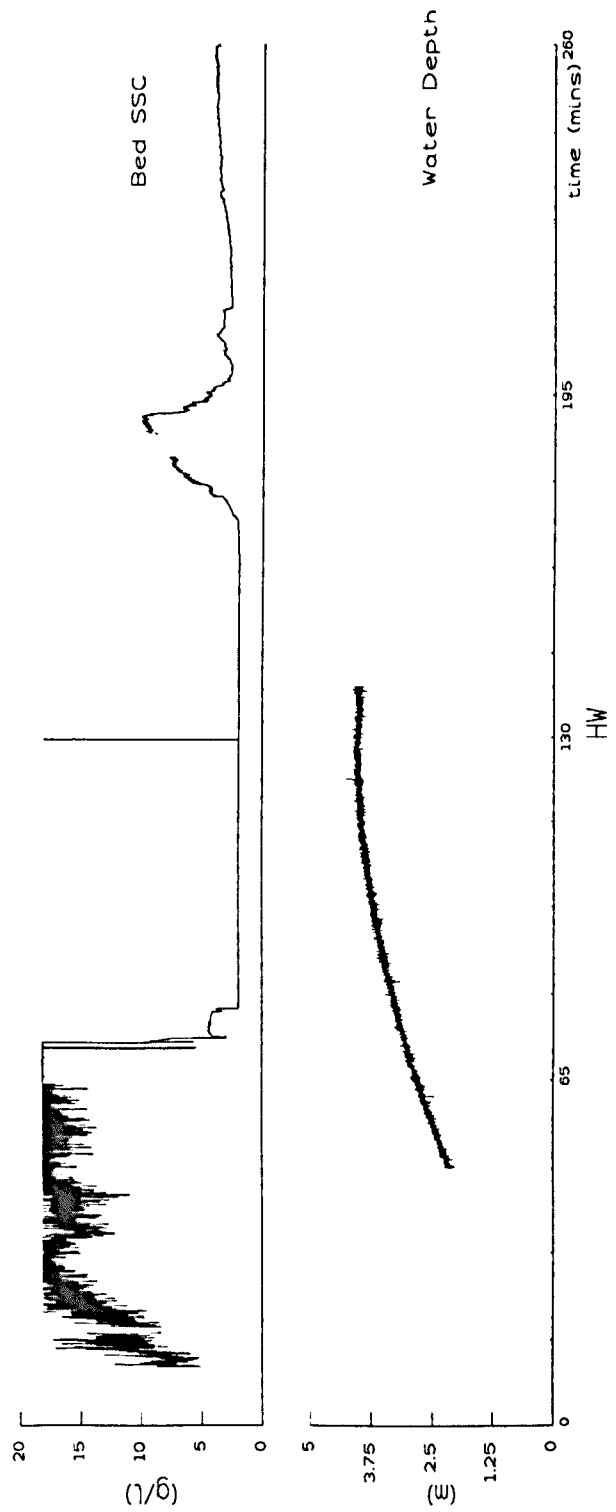

Figure 4.47: Water depth and bed SSC time series tide 1, 5/5/93

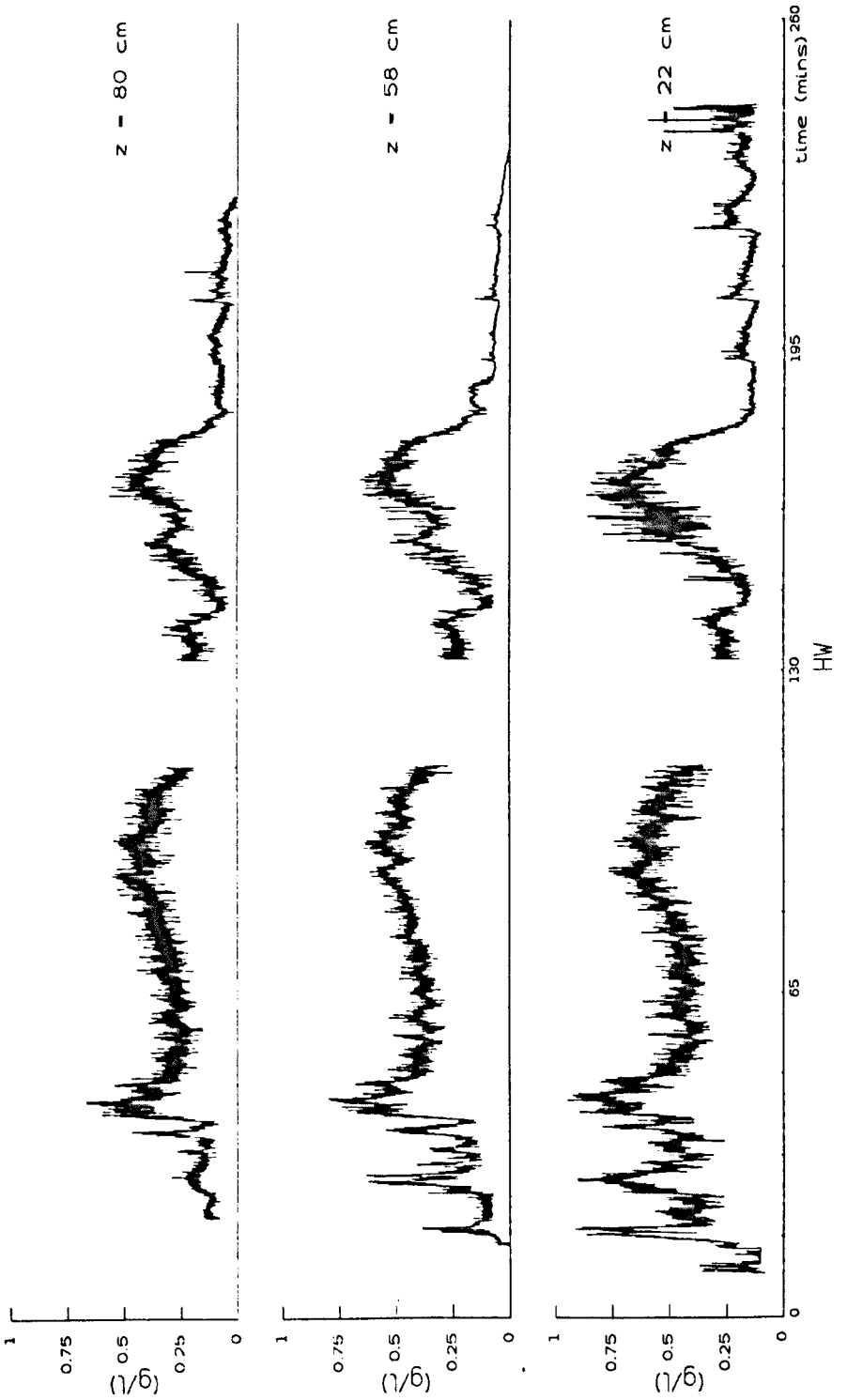

Figure 4.48: SSC ($z = 22, 58, 80\,cm$) time series tide 2, 6/5/93

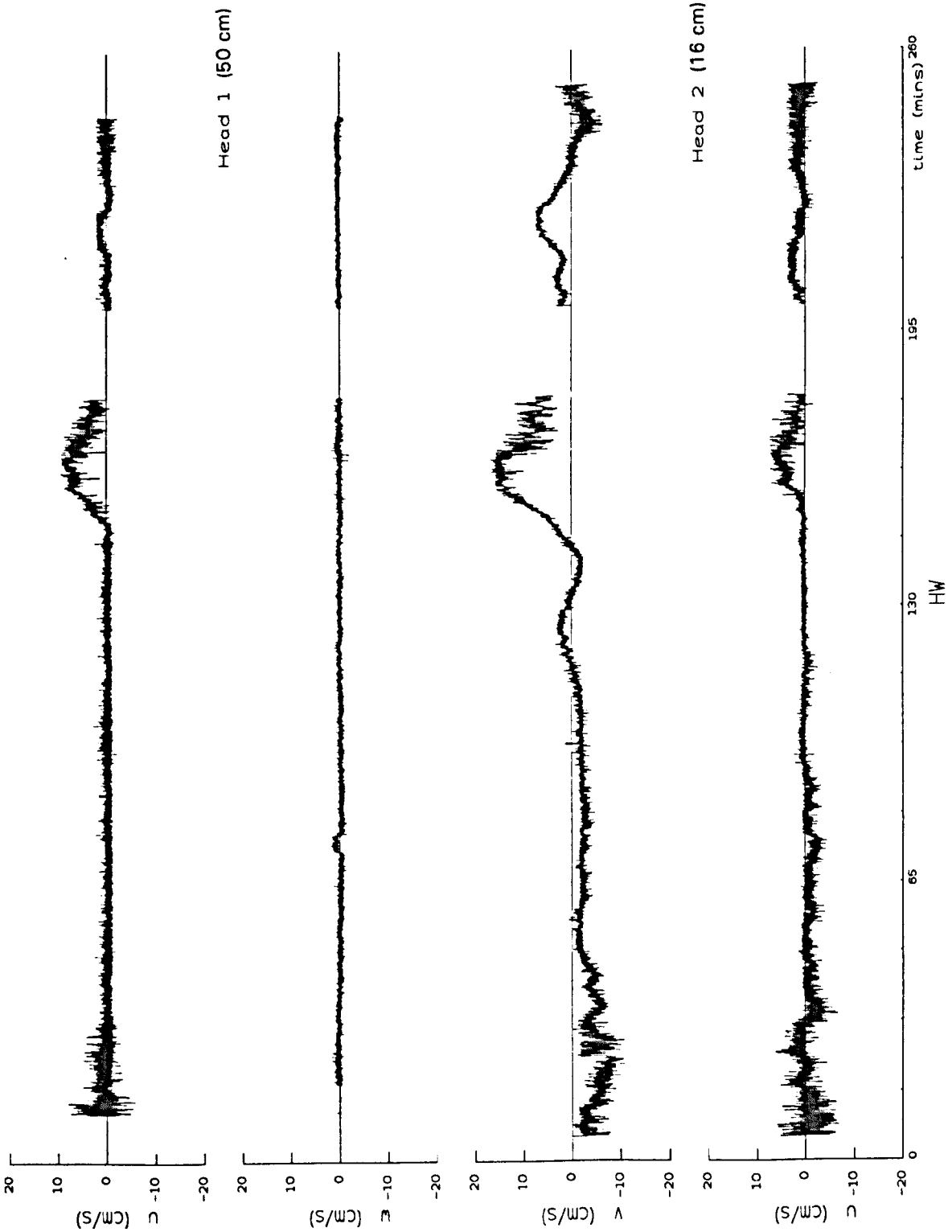

Figure 4.49: EMCM velocity time series (u, v, w) tide 3, 6/5/93

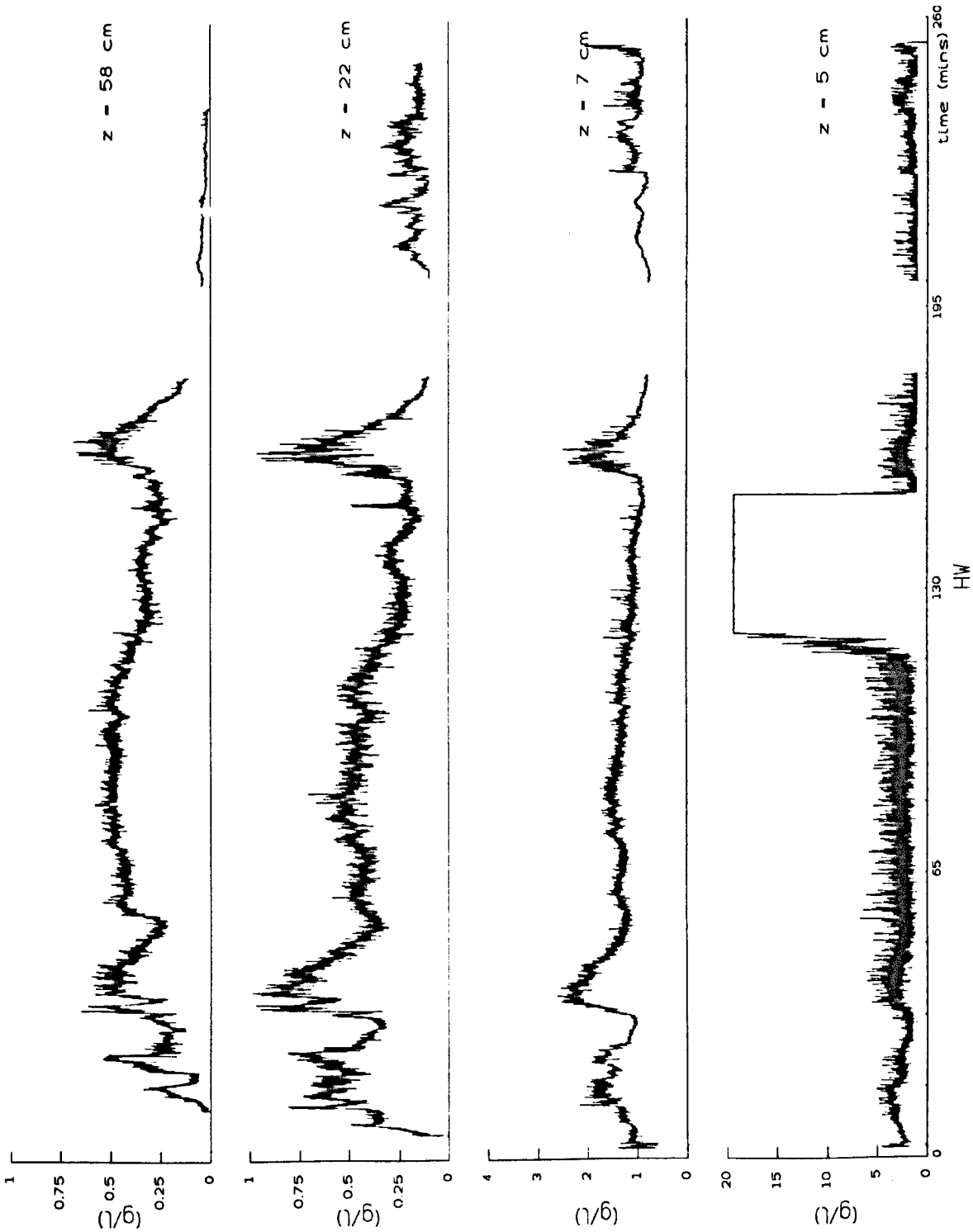

Figure 4.50: SSC ($z = 5, 7, 22, 58\,cm$) time series tide 3, 6/5/93

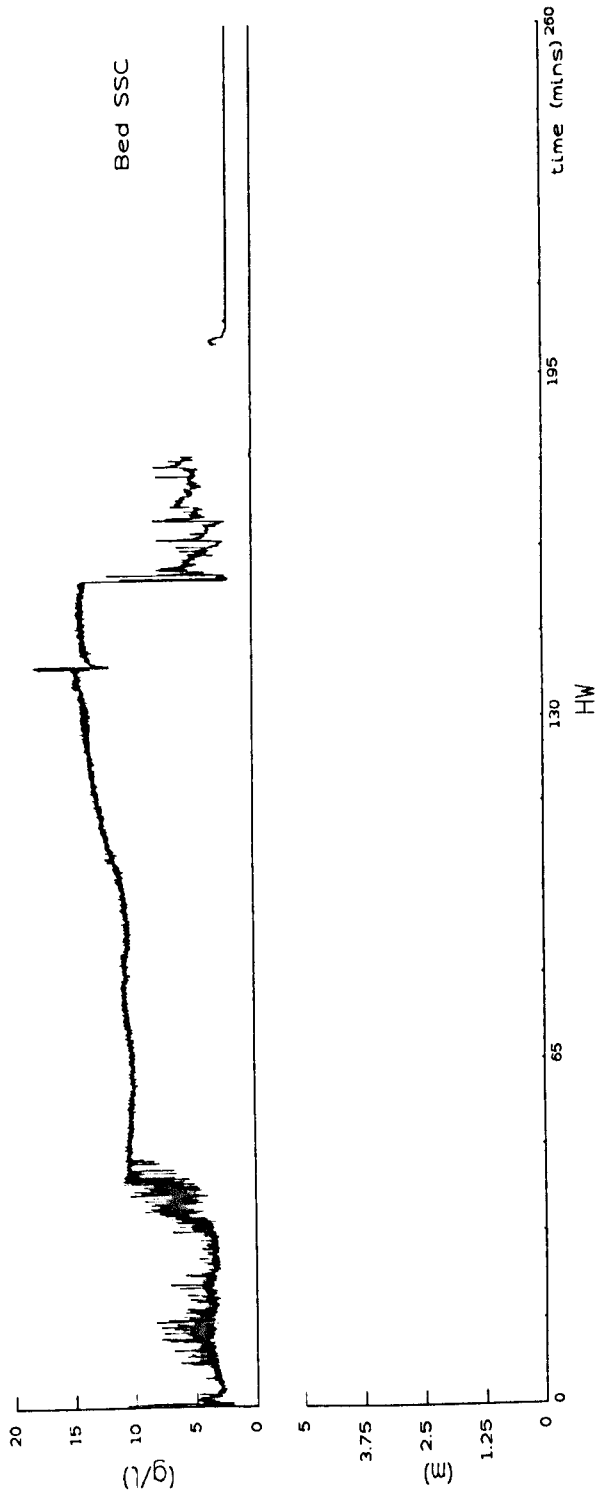

Figure 4.51: Bed SSC time series tide 3, 6/5/93

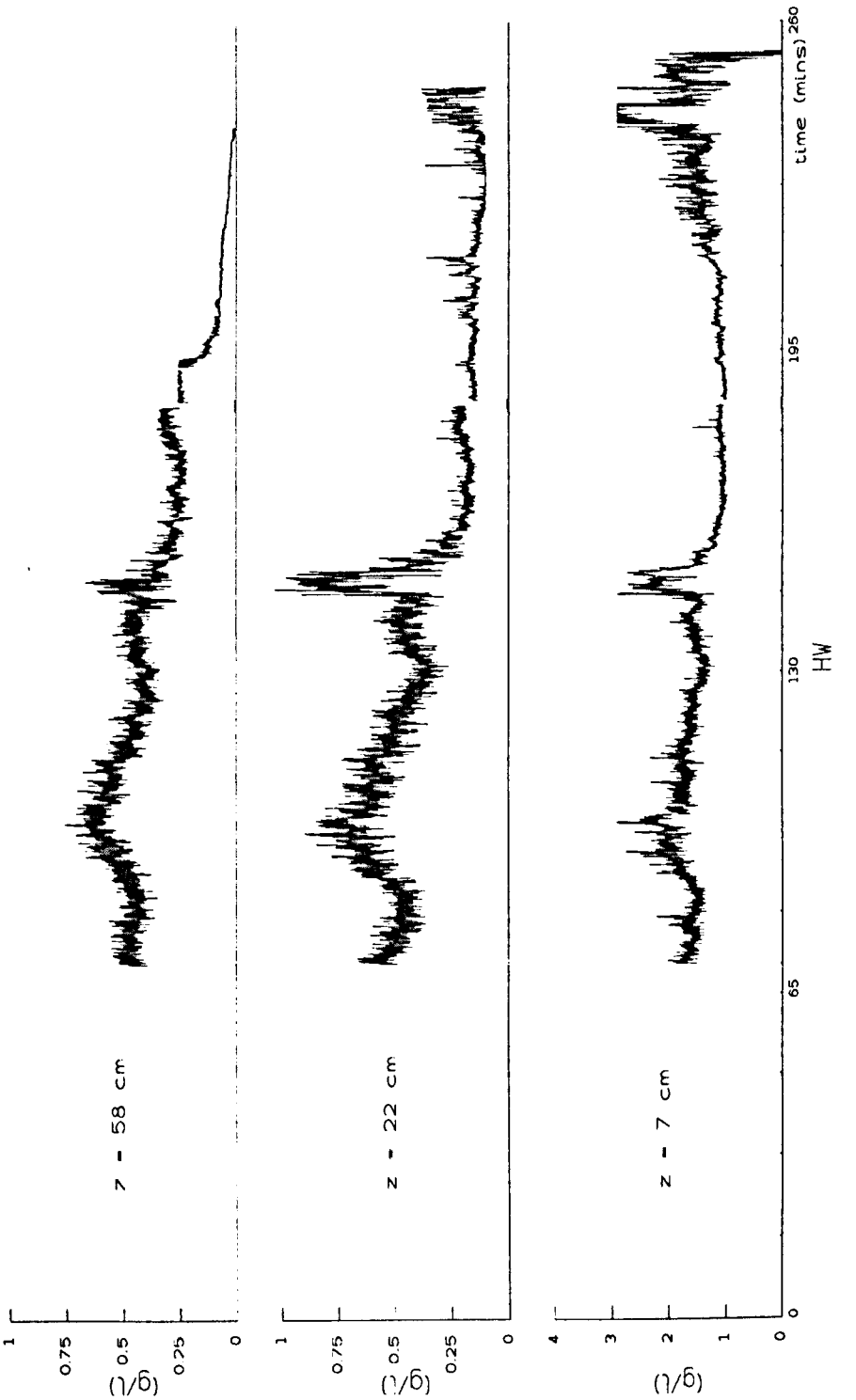

Figure 4.52: SSC ($z = 7, 22, 58\,cm$) time series tide 4, 7/5/93

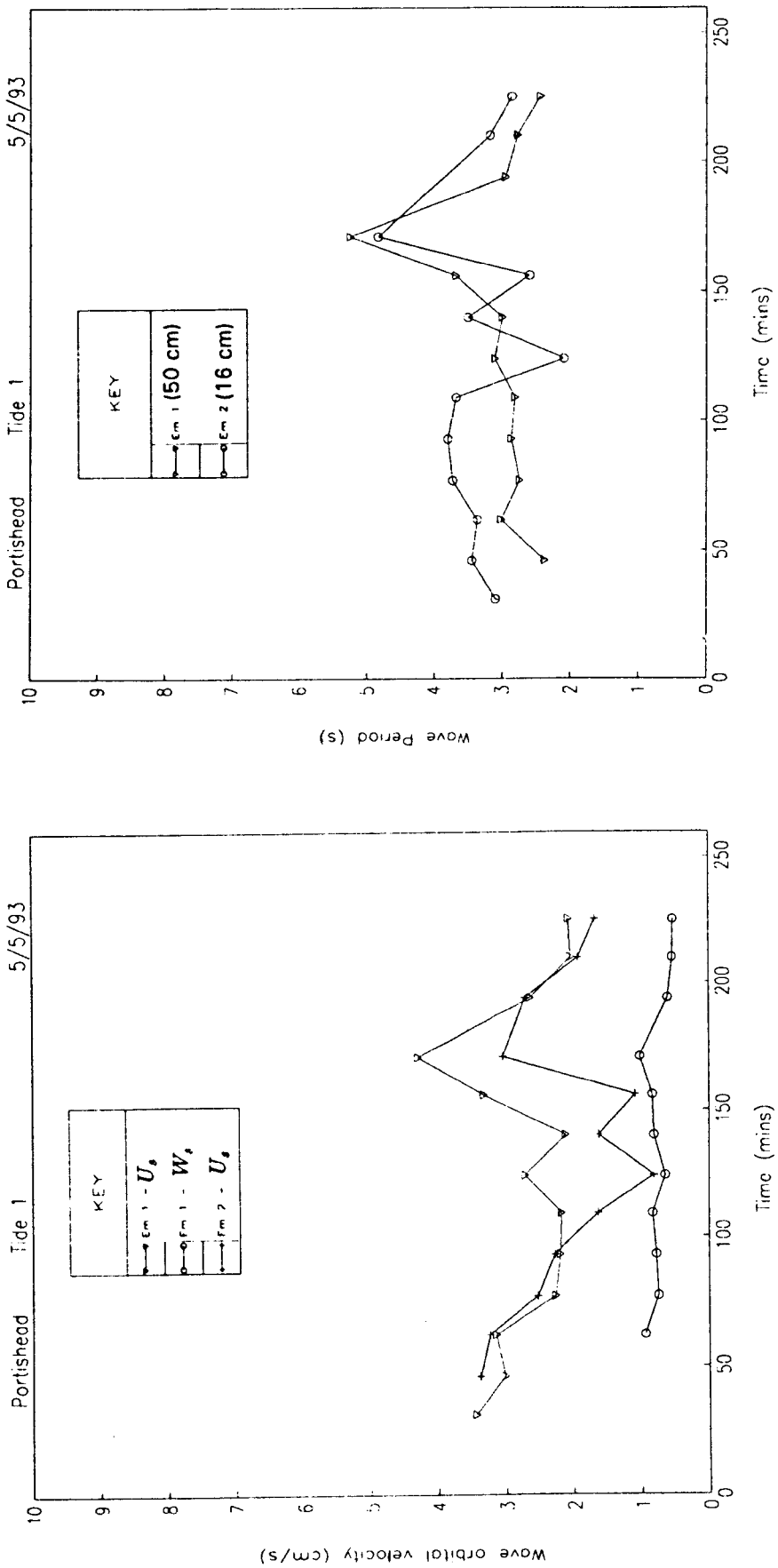

Figure 4.53: Wave orbital velocities (U_s, W_s) and zero crossing periods calculated from EMCM, tide 1, 5/5/93

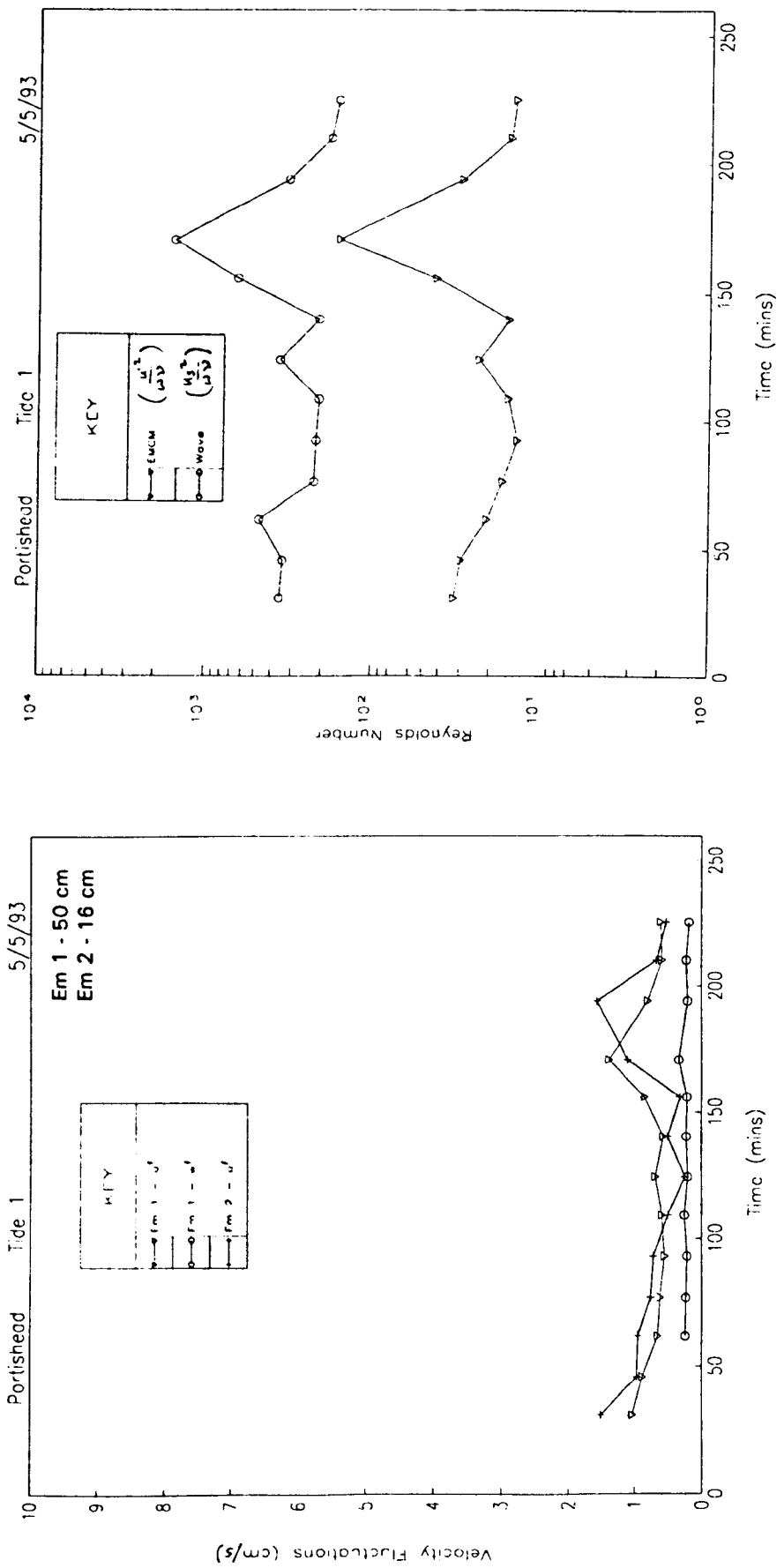

Figure 4.54: Mean velocity fluctuations (u', w') and Reynolds numbers calculated from EMCM, tide 1, 5/5/93

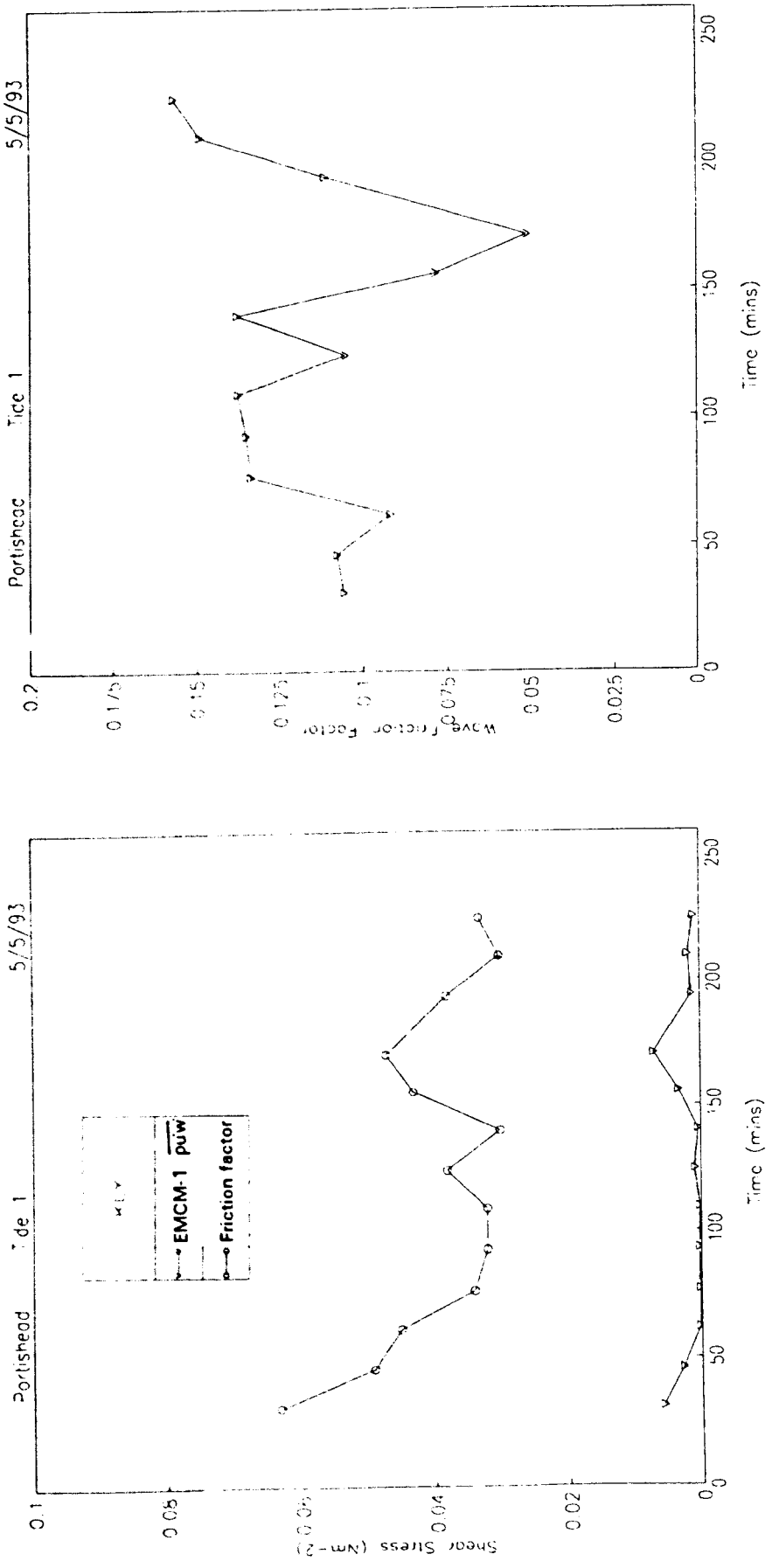

Figure 4.55: Bed shear stress comparison using frictor factor and Reynolds stresses calculated from EMCM, tide 1, 5/5/93

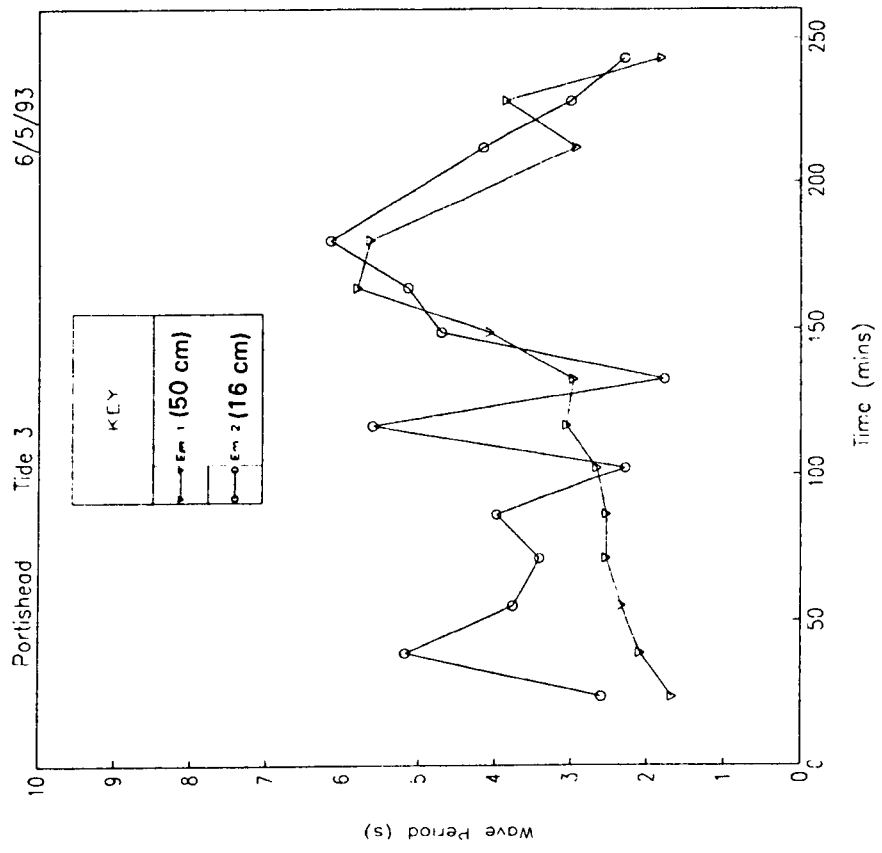

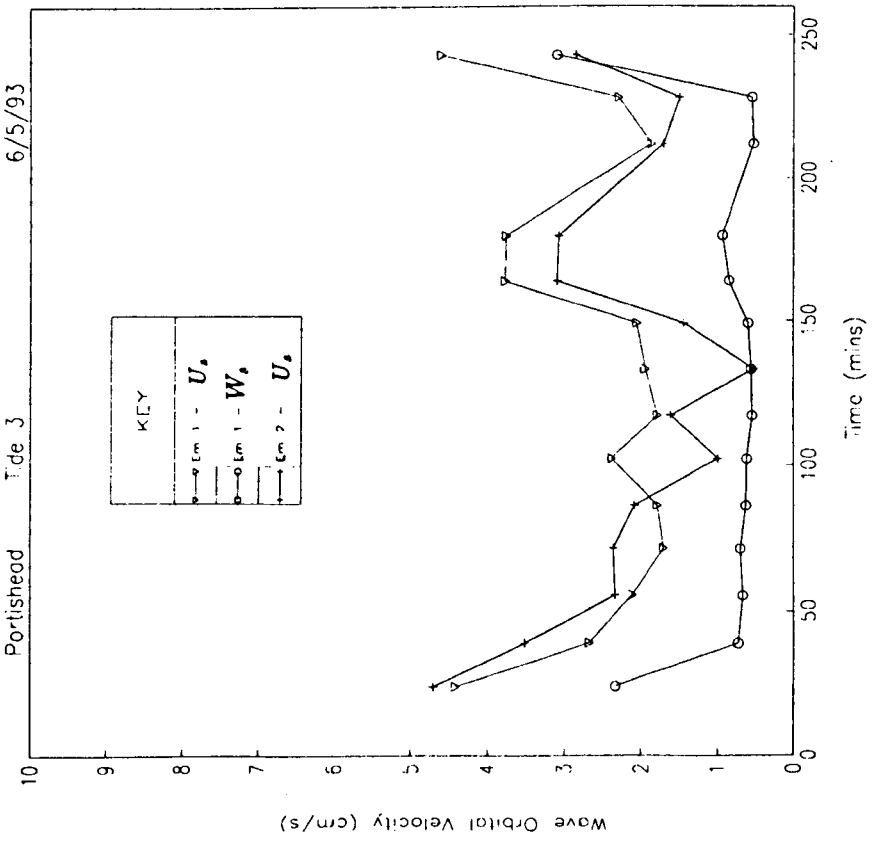

Figure 4.56: Wave orbital velocities (U_s, W_s) and zero crossing periods calculated from EMCM, tide 3, 6/5/93

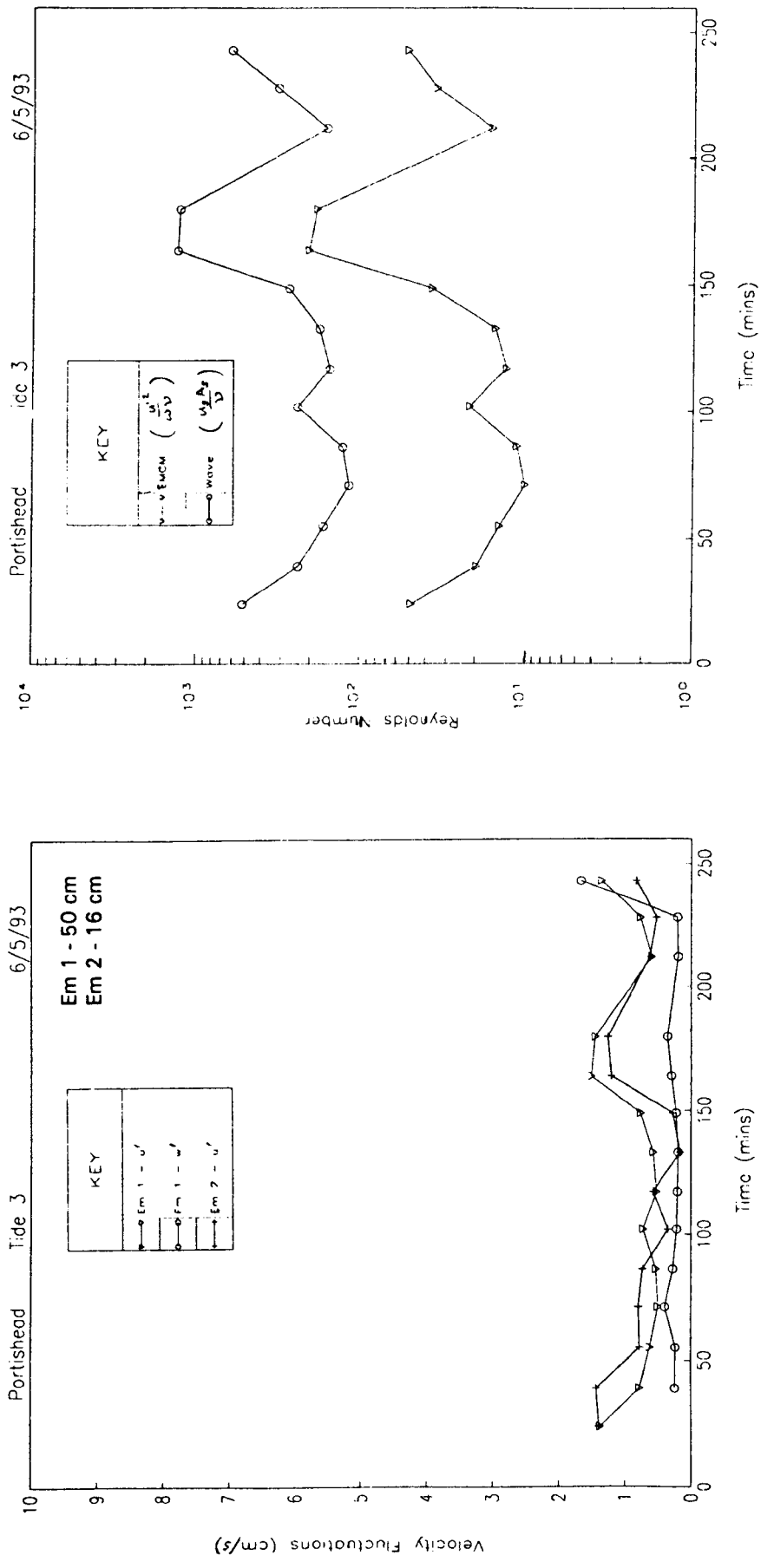

Figure 4.57: Mean velocity fluctuations (u', w') and Reynolds numbers calculated from EMCM, tide 3, 6/5/93

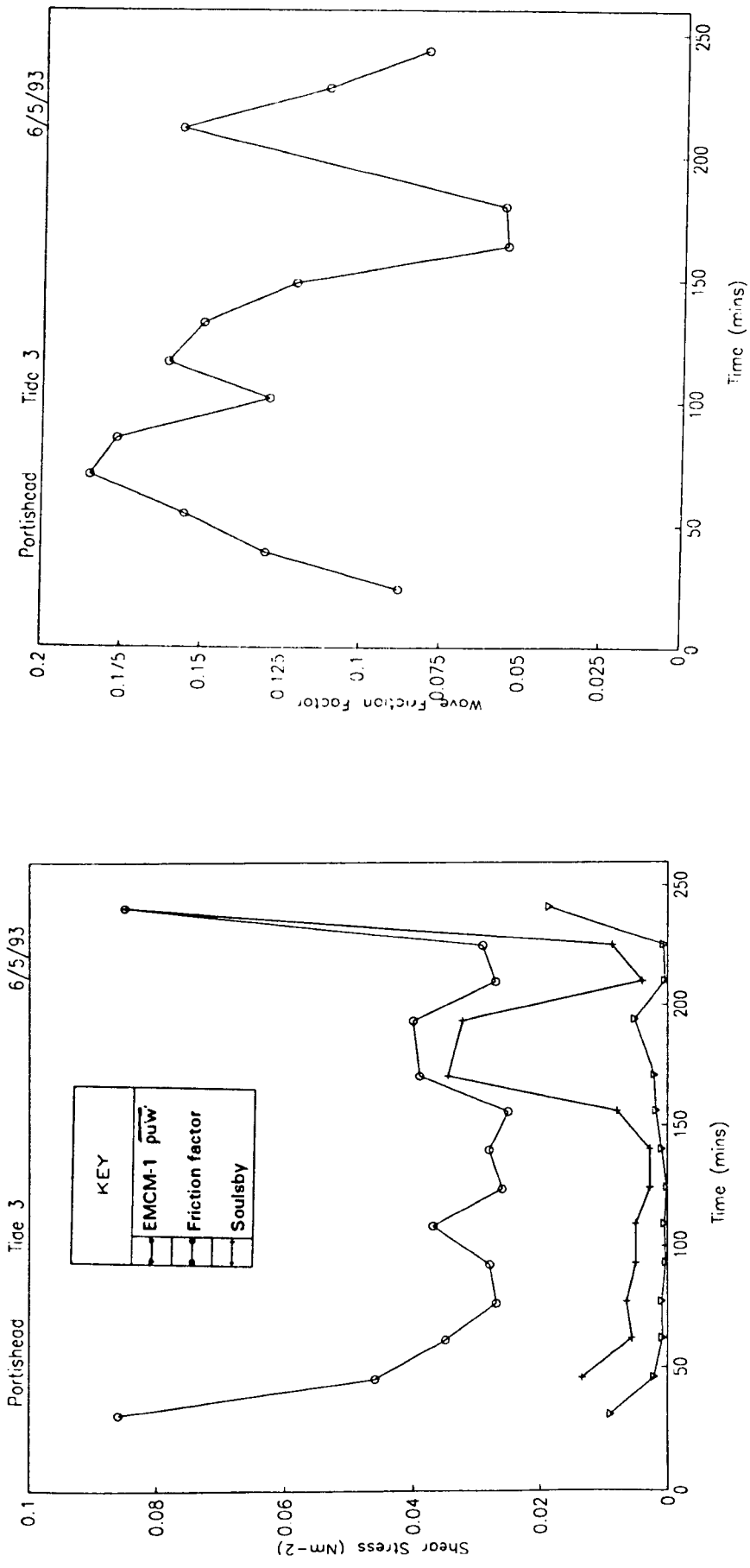

Figure 4.58: Bed shear stress comparison using frictor factor, Reynolds stresses and Souslby & Humphery spectra splitting technique, tide 3, 6/5/93

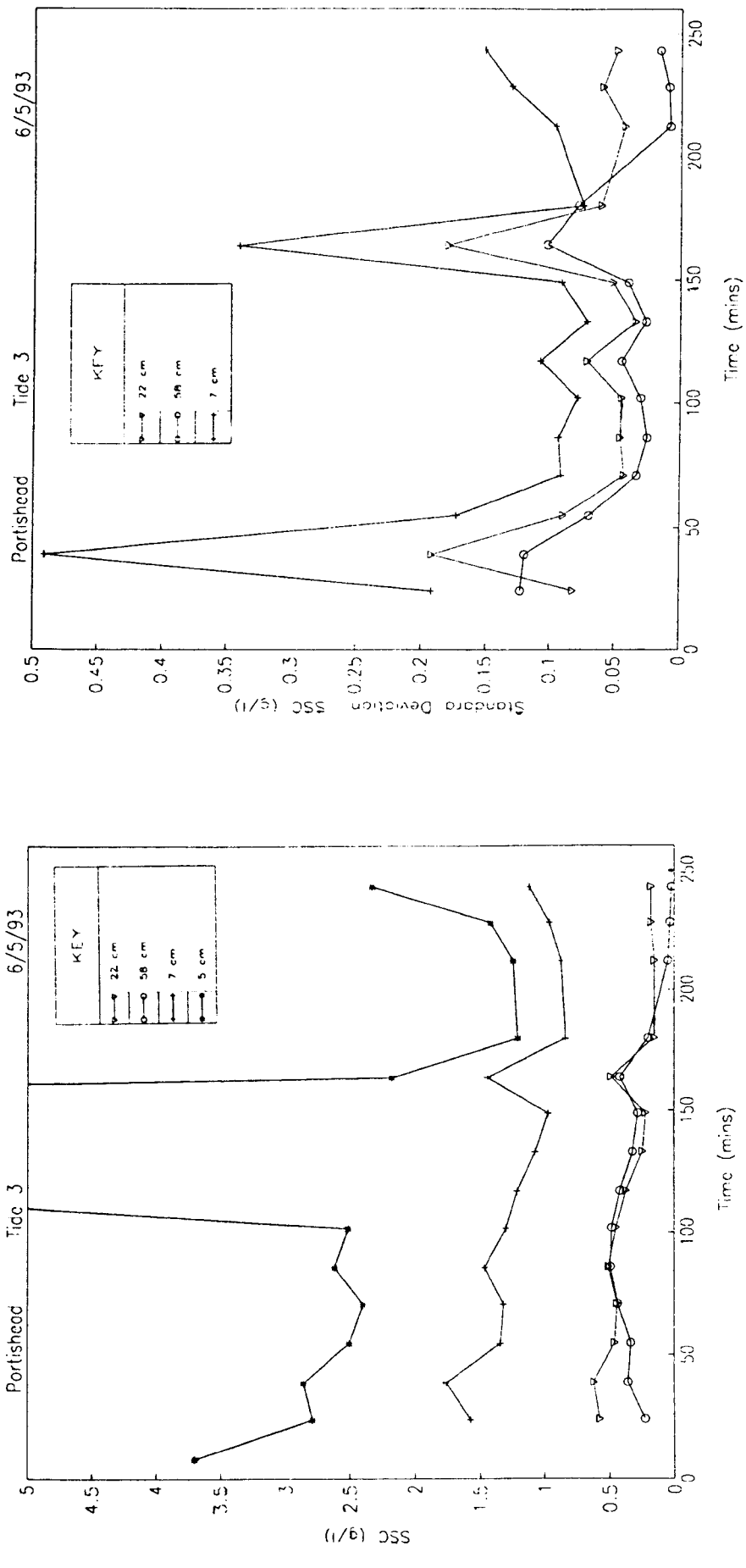

Figure 4.59: SSC and standard deviation of SSC for tide 3, 6/5/93

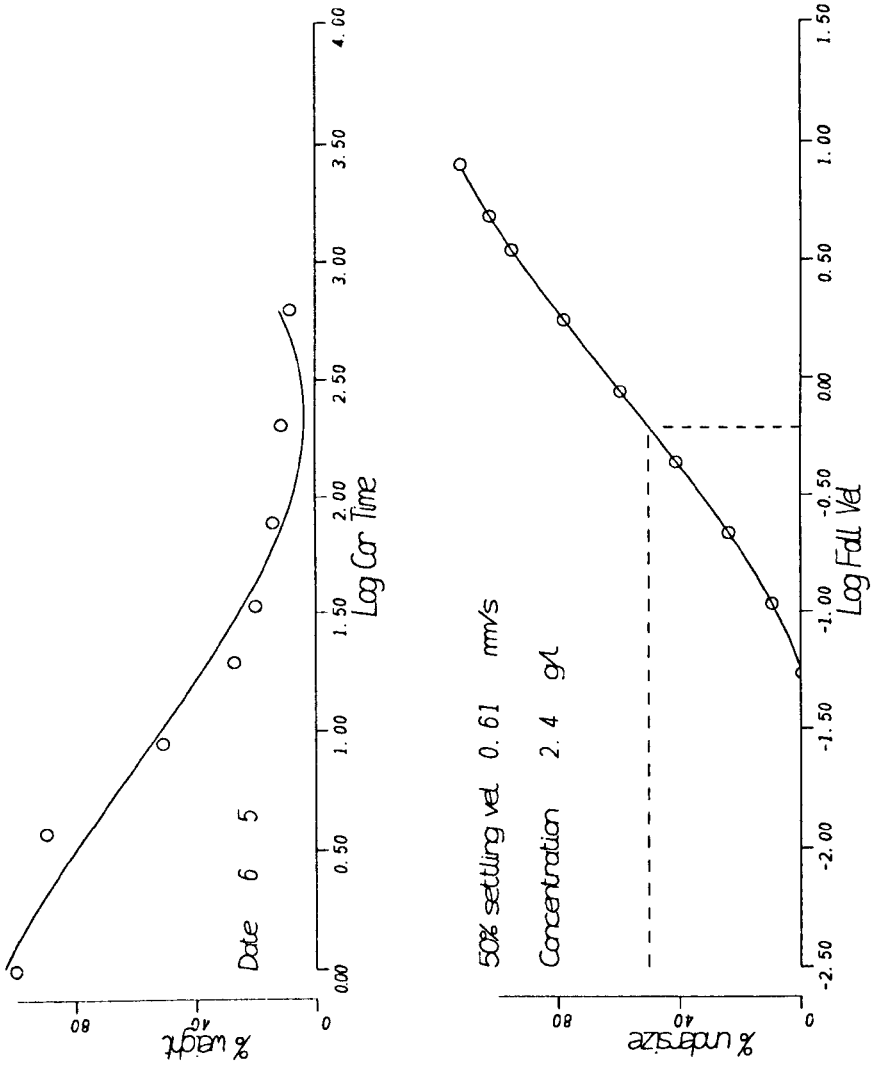

Figure 4.60: Fall velocity from Owen tube in surf zone near site, tide 2, 06:20 (t=30)- 6/5/93

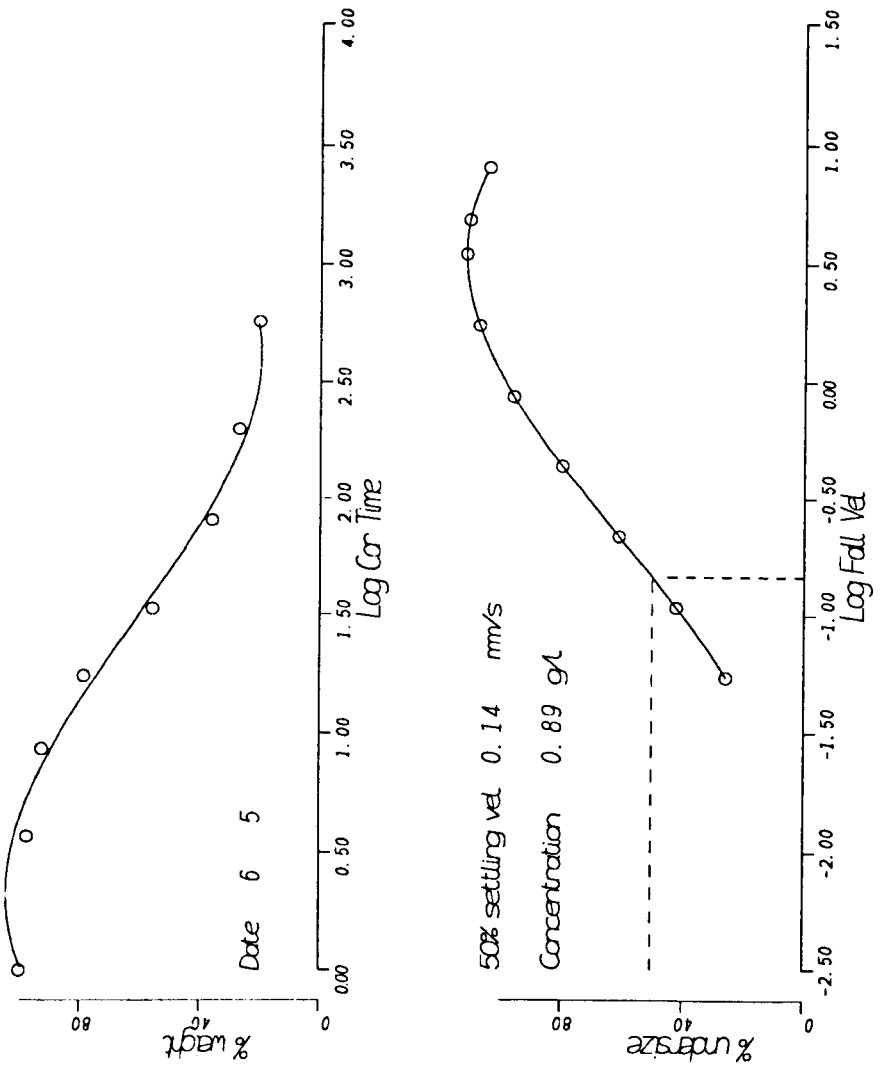

Figure 4.61: Fall velocity from Owen tube in surf zone near site, tide 3, 18:45 (t=30)- 6/5/93

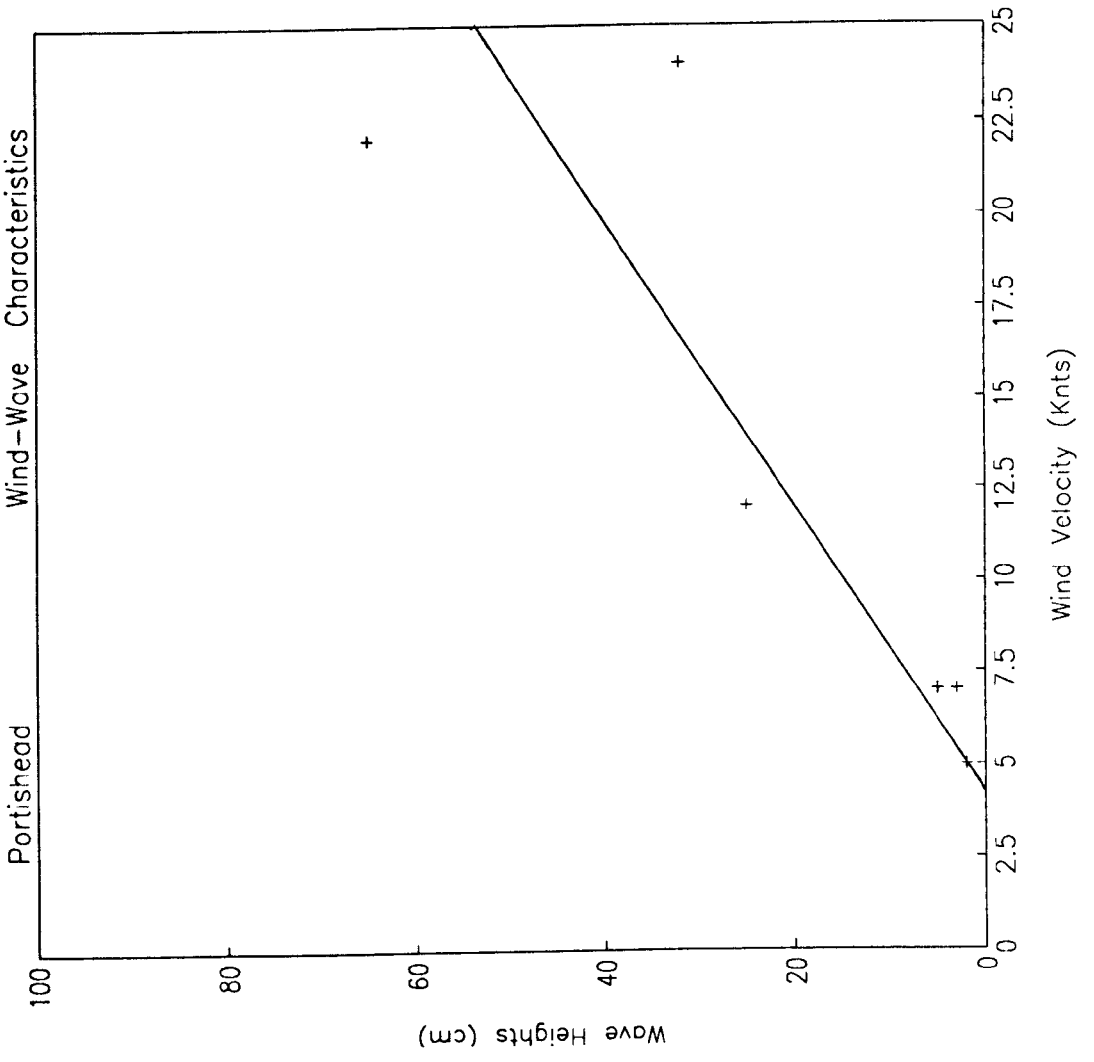

Figure 5.1: Wind velocity v wave height scatter plot: Portishead, Severn Estuary

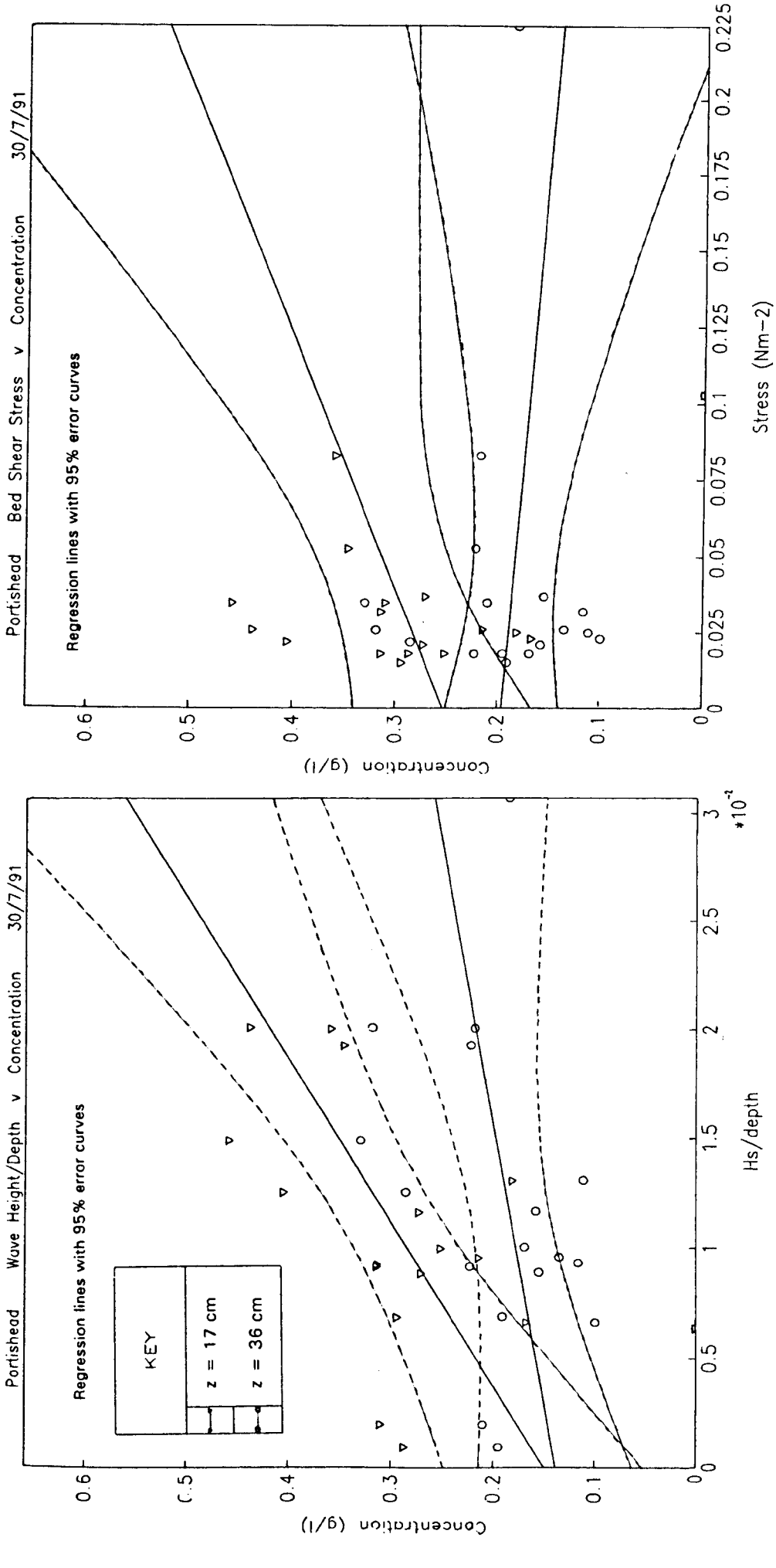

Figure 5.2: Regressions of SSC v τ_o and H_s/h, 30/7/91

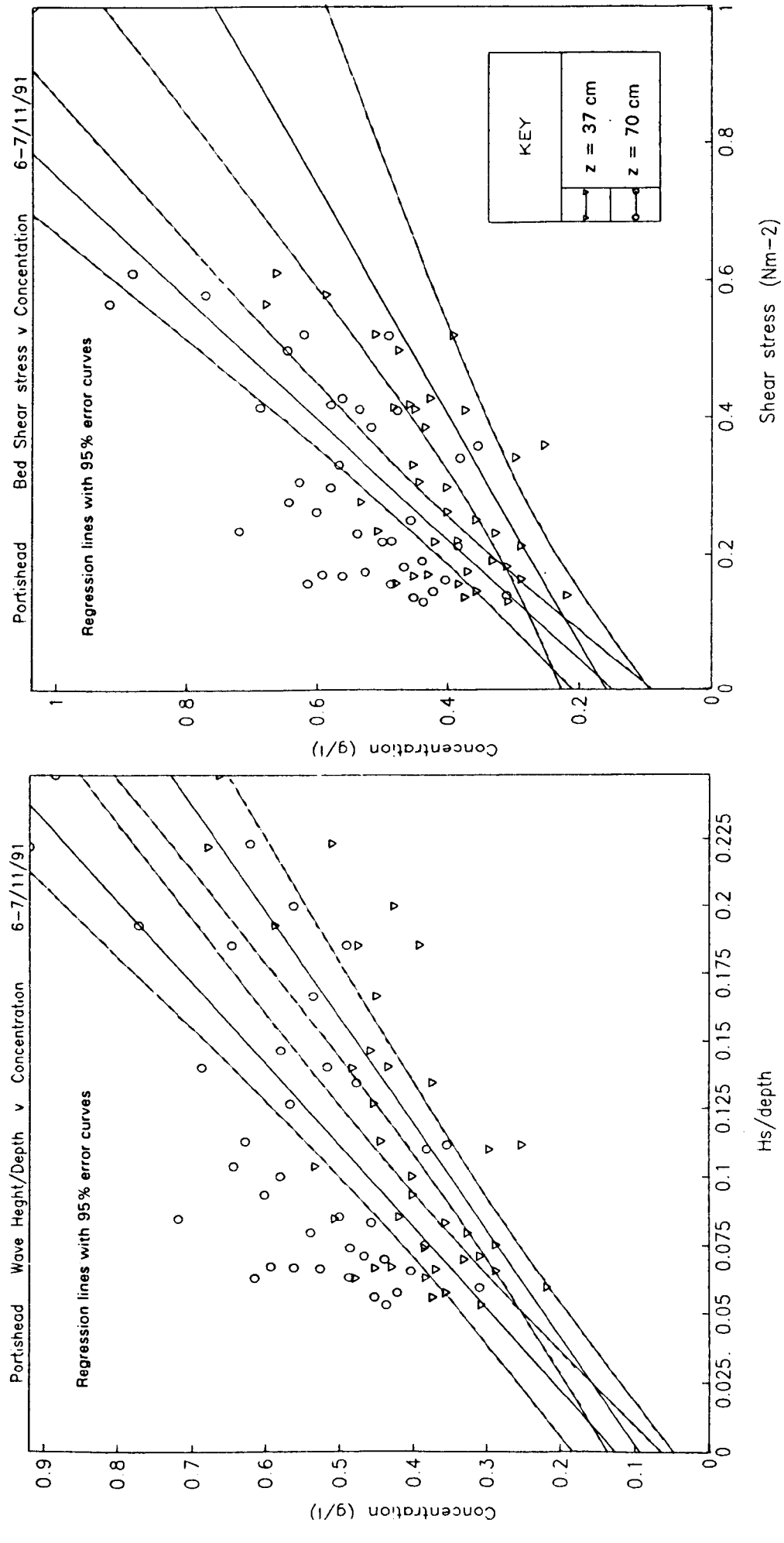

Figure 5.3: Regressions of SSC v τ_o and H_s/h, 6-7/11/91

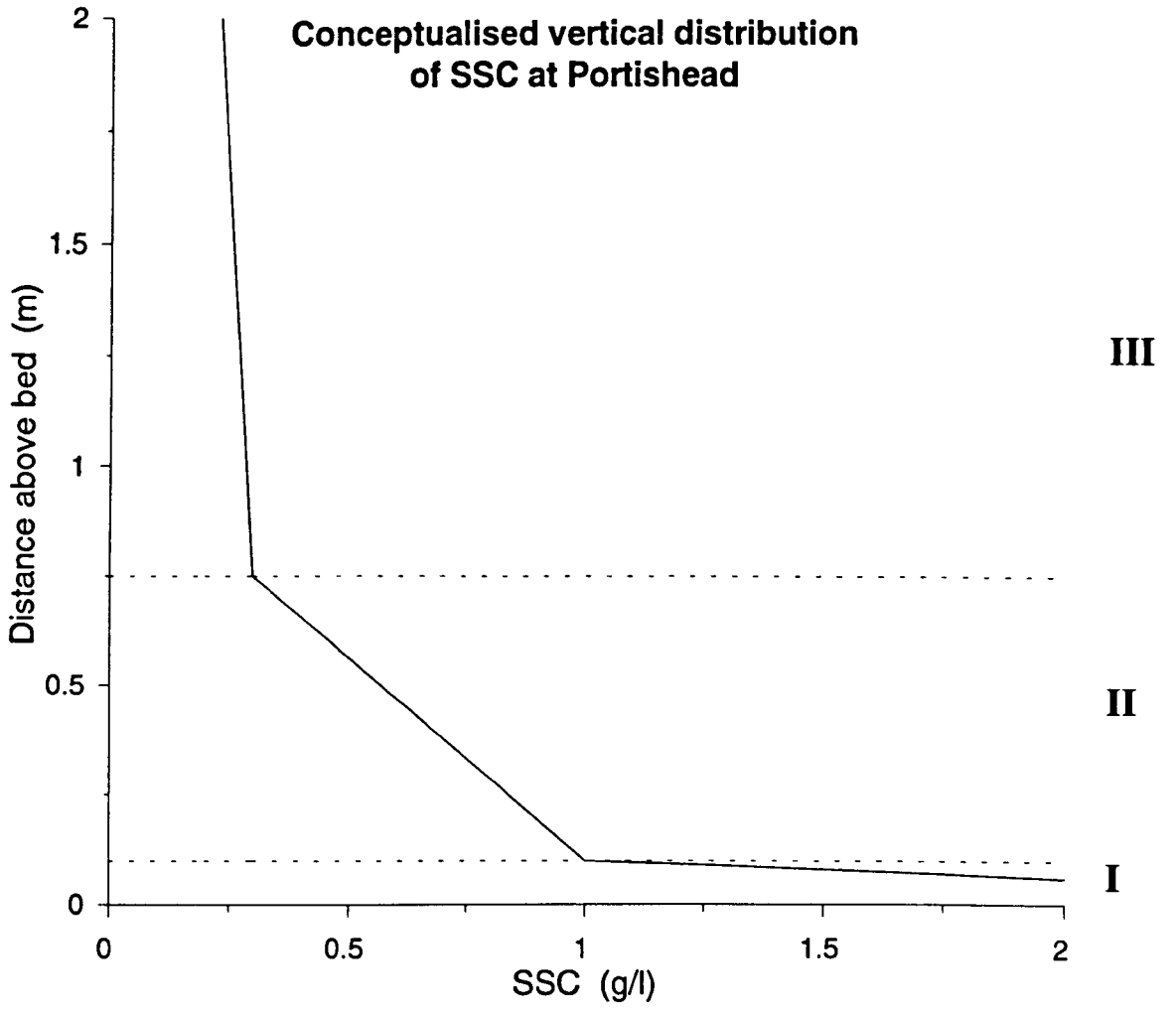

Figure 5.5: Conceptualised regions of SSC over the bottom two metres at Portishead ITZ. Three regions (I - III) have been identified, as described in section 5.6. The depth of each region is determined by the wave magnitude, and under small waves region II is much reduced.

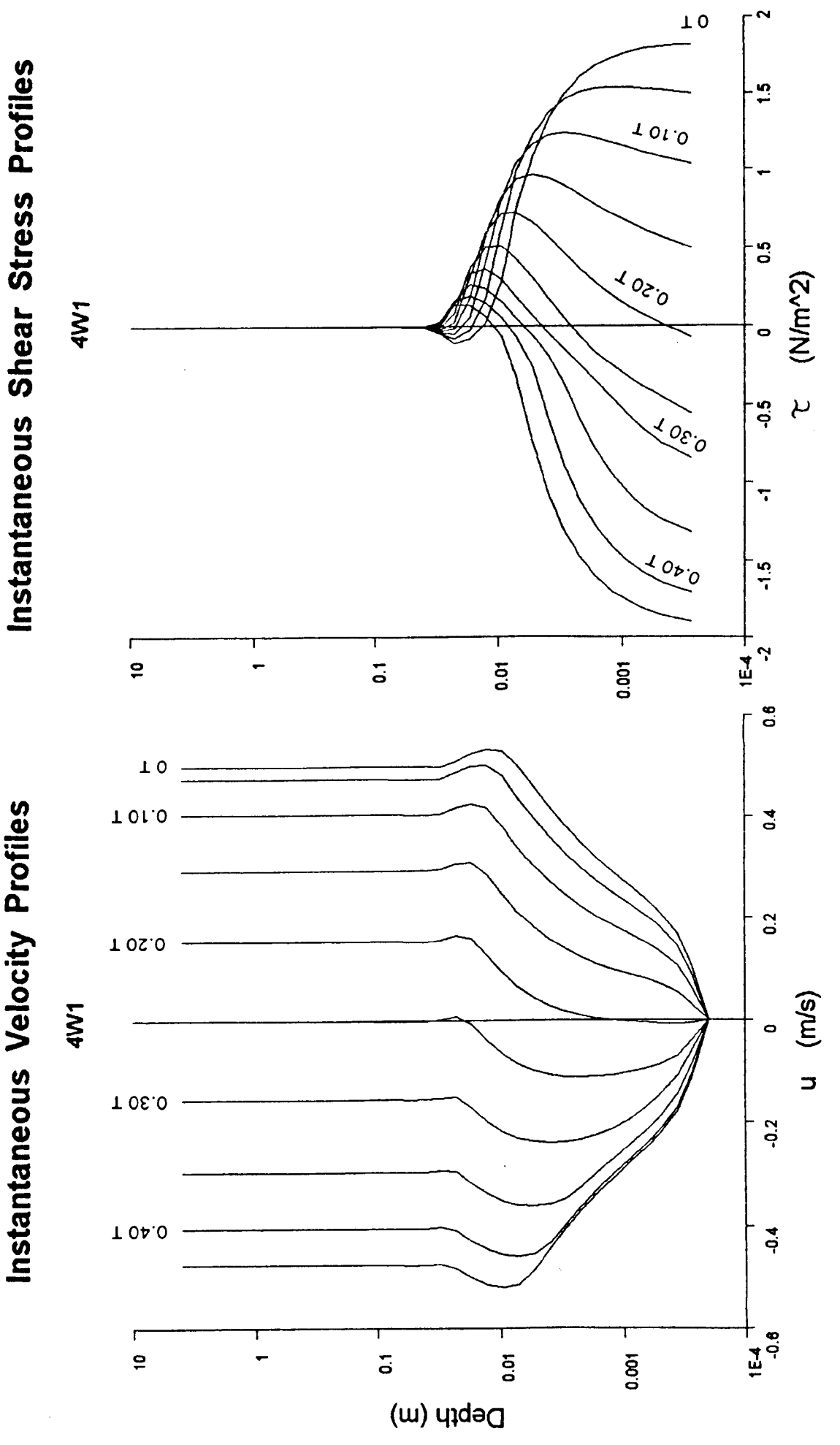

Figure 6.1: Test case 4W1 - Vertical profiles of instantaneous velocity and shear stress at ten phases through a wave cycle

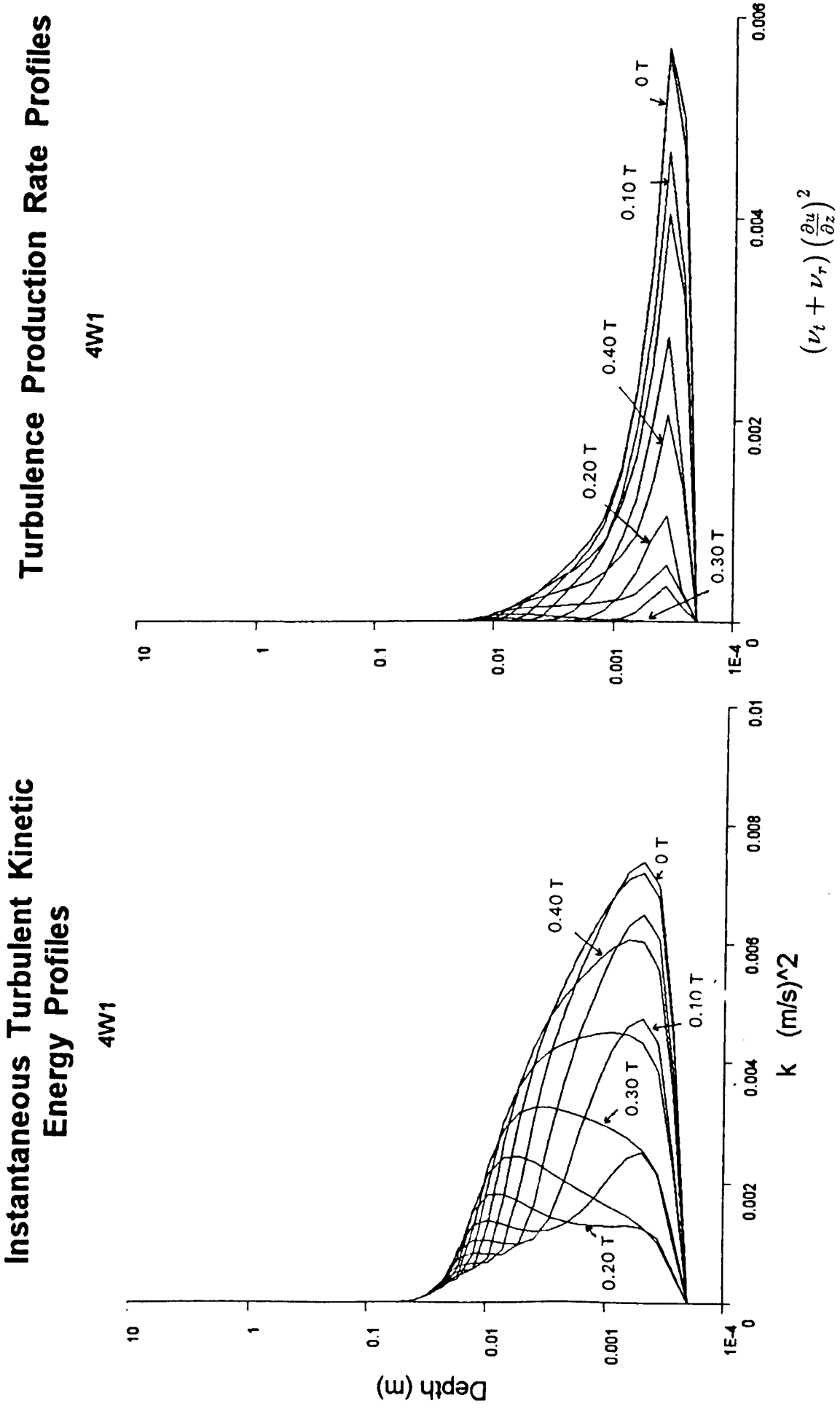

Figure 6.2: Test case 4W1 - Vertical profiles of instantaneous turbulent kinetic energy and production rate term in k-equation $((\nu_t + \nu_r)\left(\frac{\partial u}{\partial z}\right)^2)$ at ten phases through a wave cycle

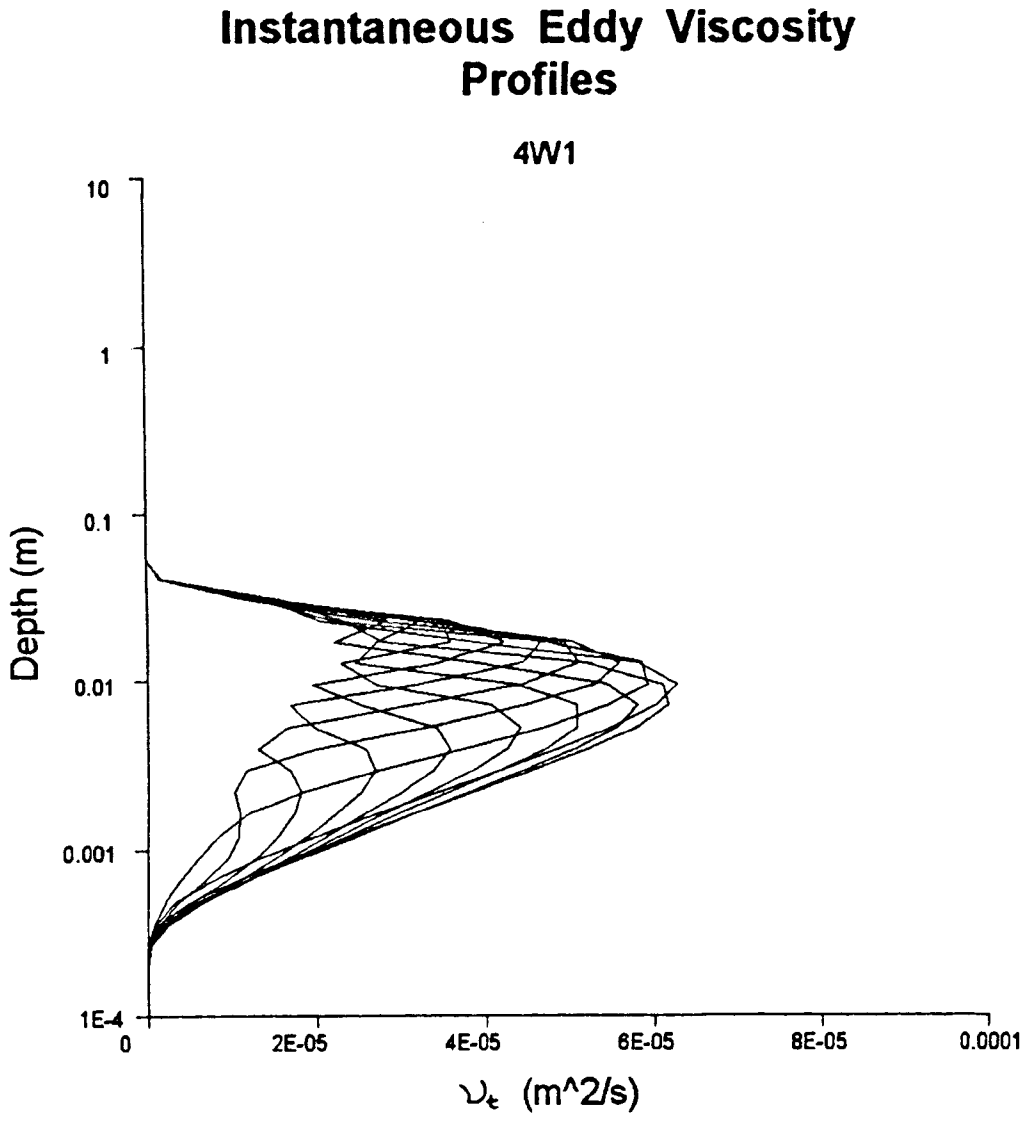

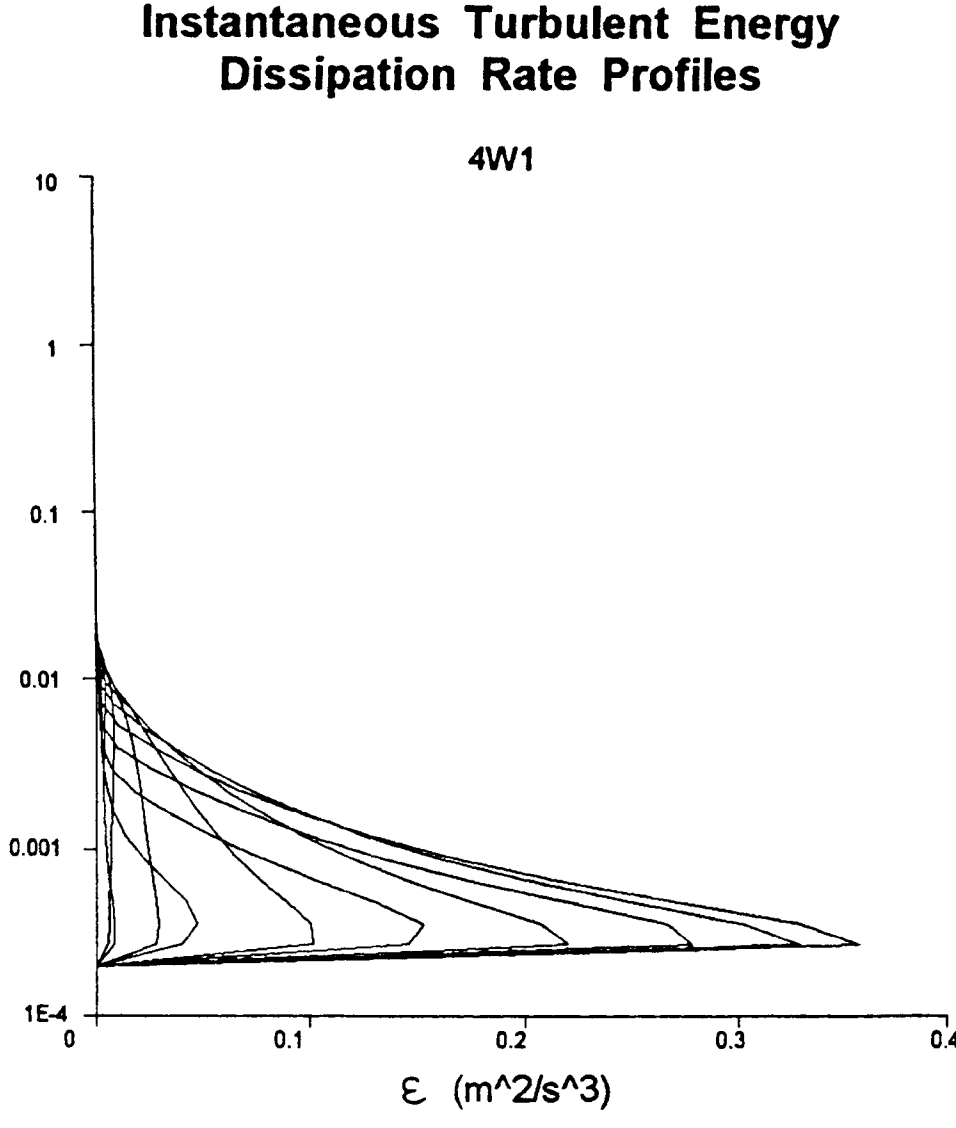

Figure 6.3: Test Case W1 - Vertical profiles of instantaneous eddy viscosity and turbulent dissipation rate at ten phases through a wave cycle

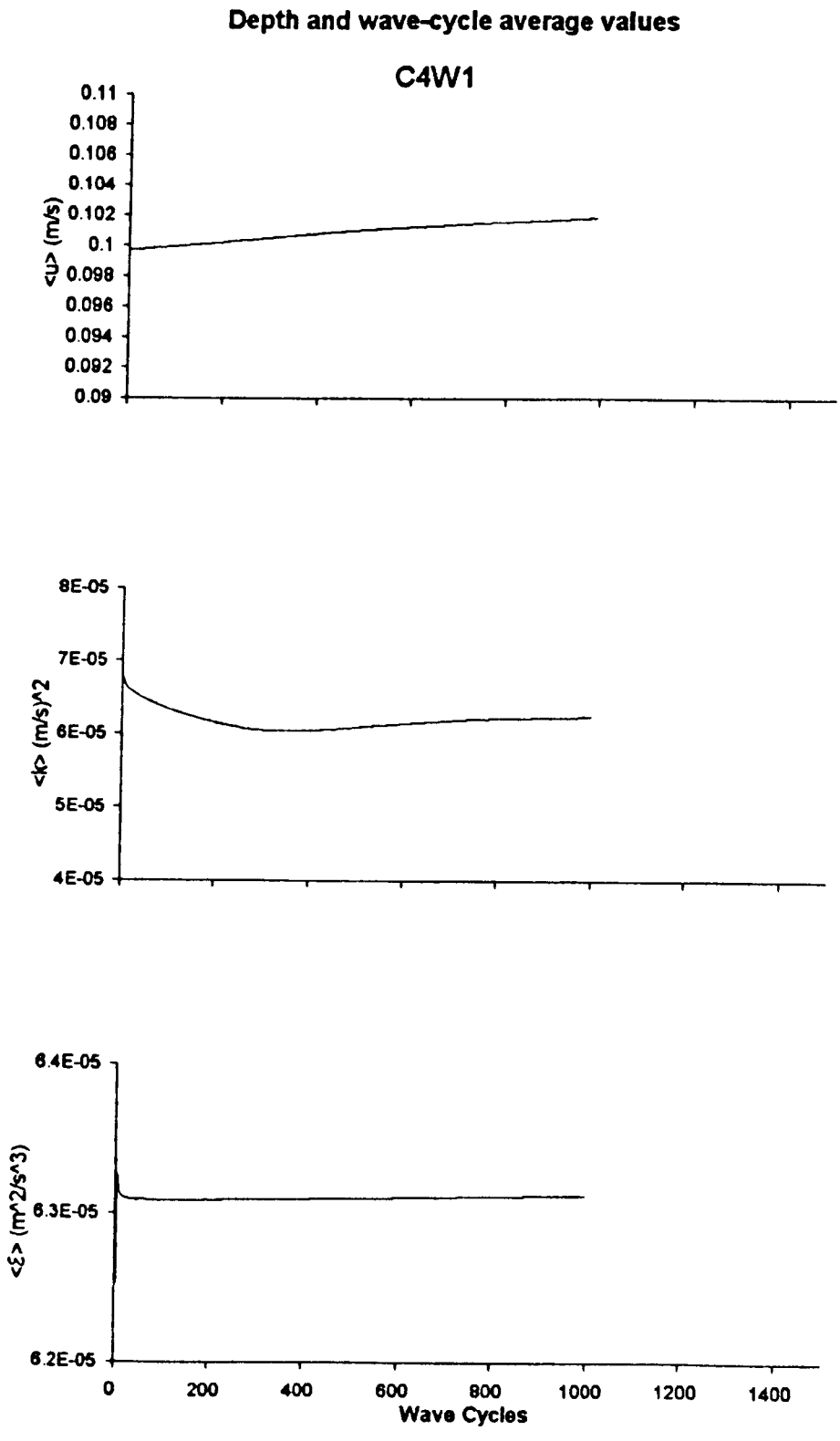

Figure 6.4: Test case C4W1 - Depth and wave-cycle averaged velocity, turbulent kinetic energy and dissipation rate - from C4 to convergence

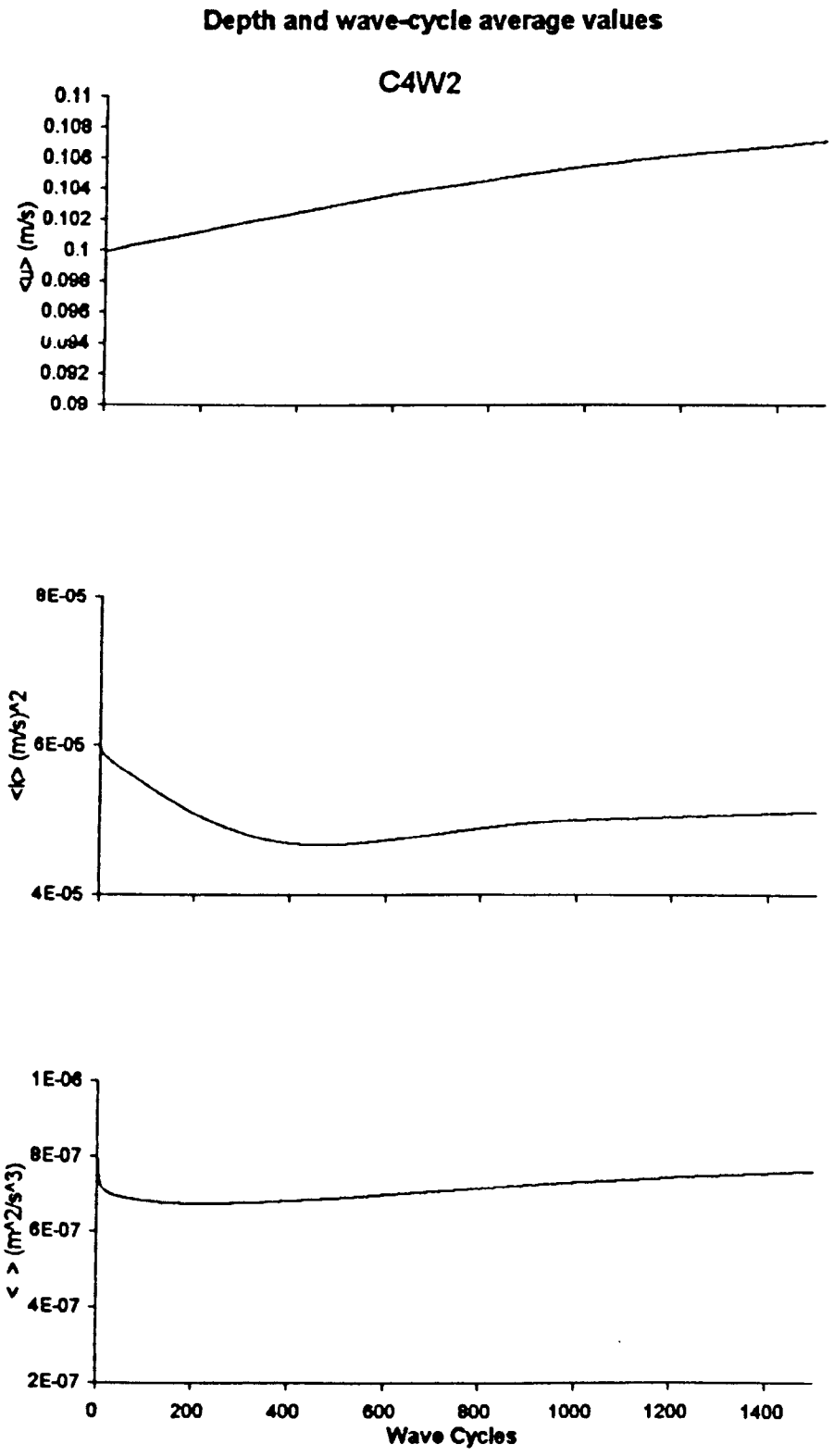

Figure 6.5: Test case C4W2 - Depth and wave-cycle averaged velocity, turbulent kinetic energy and dissipation rate - from C4 to convergence

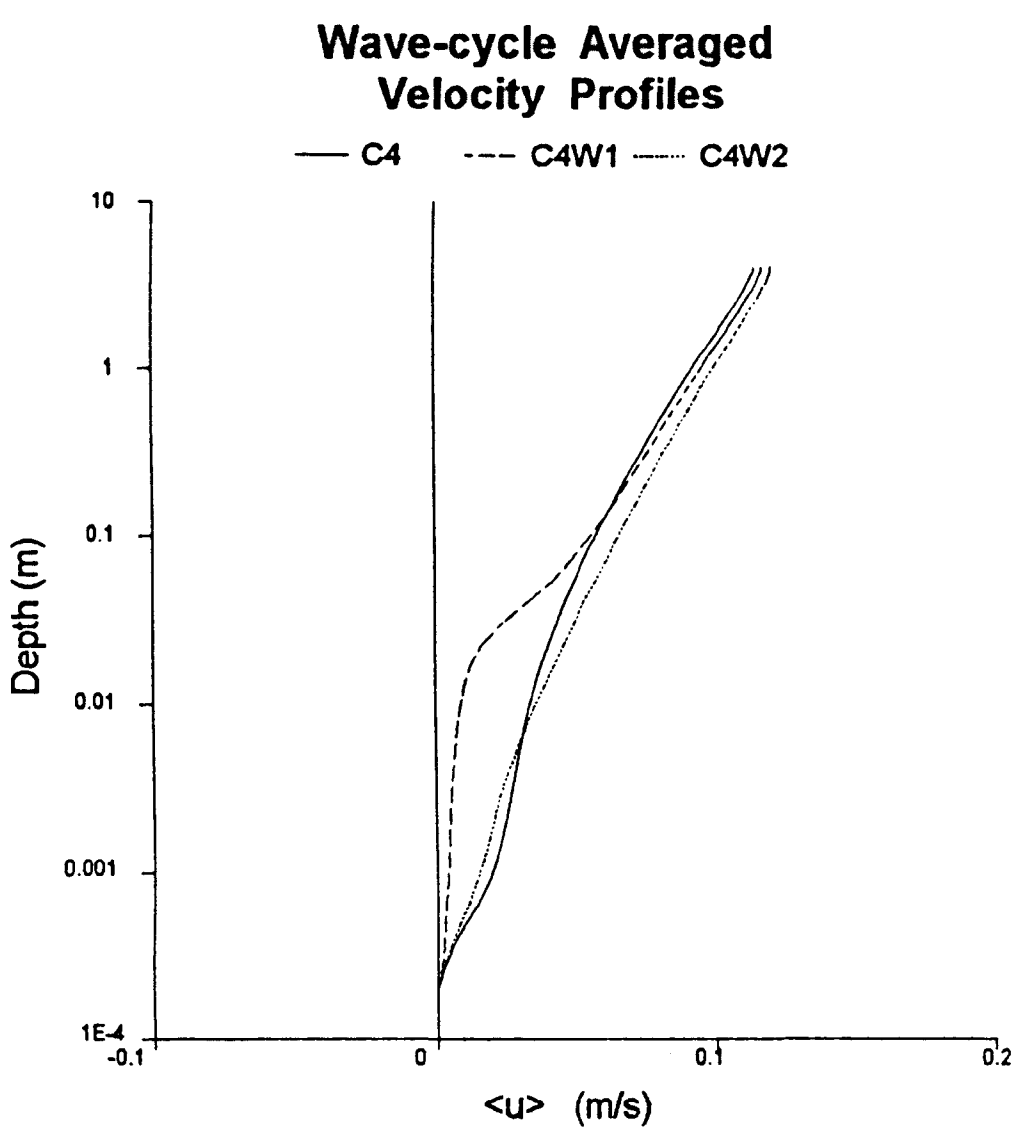

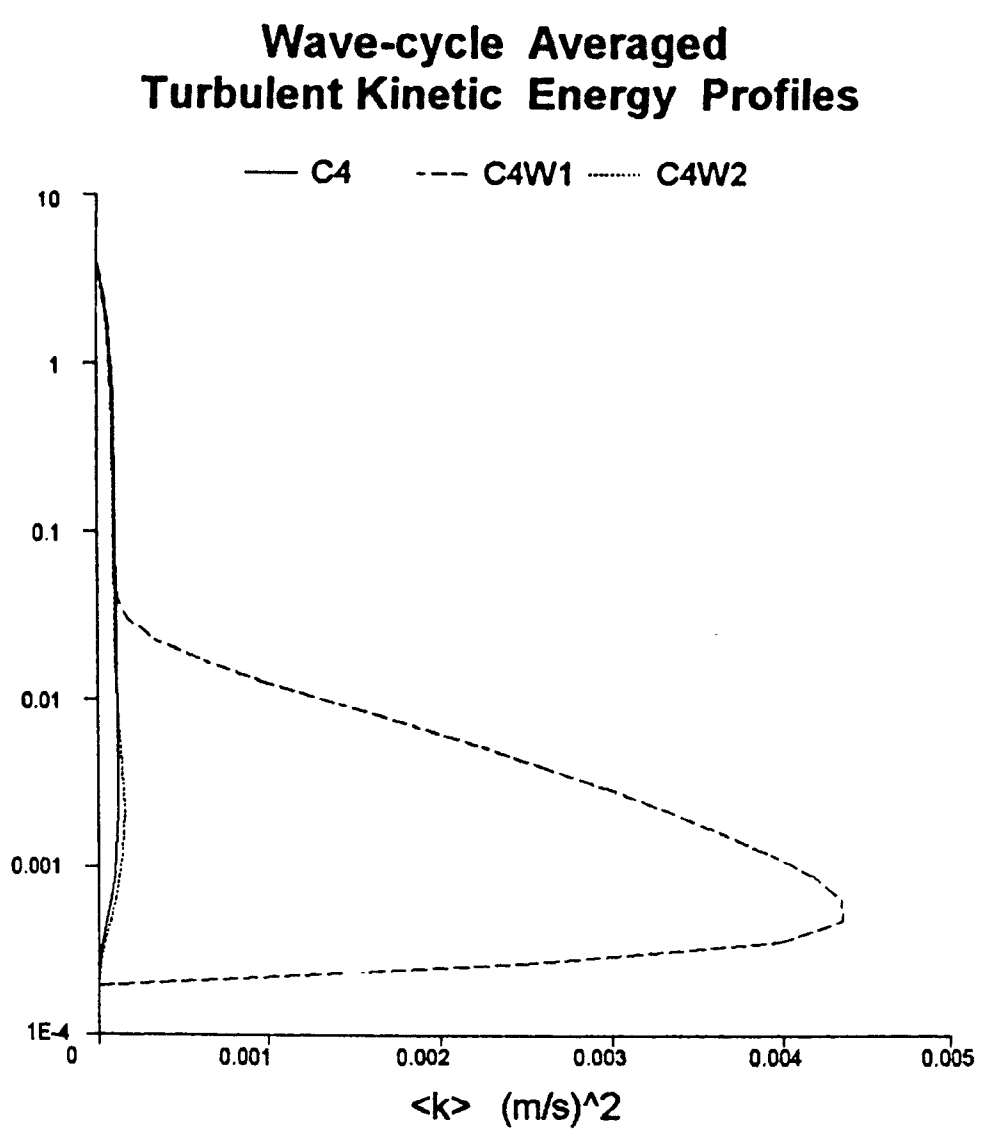

Figure 6.6: Test cases C4, C4W1 and C4W2 - Converged wave-cycle averaged profiles of velocity and turbulent kinetic energy

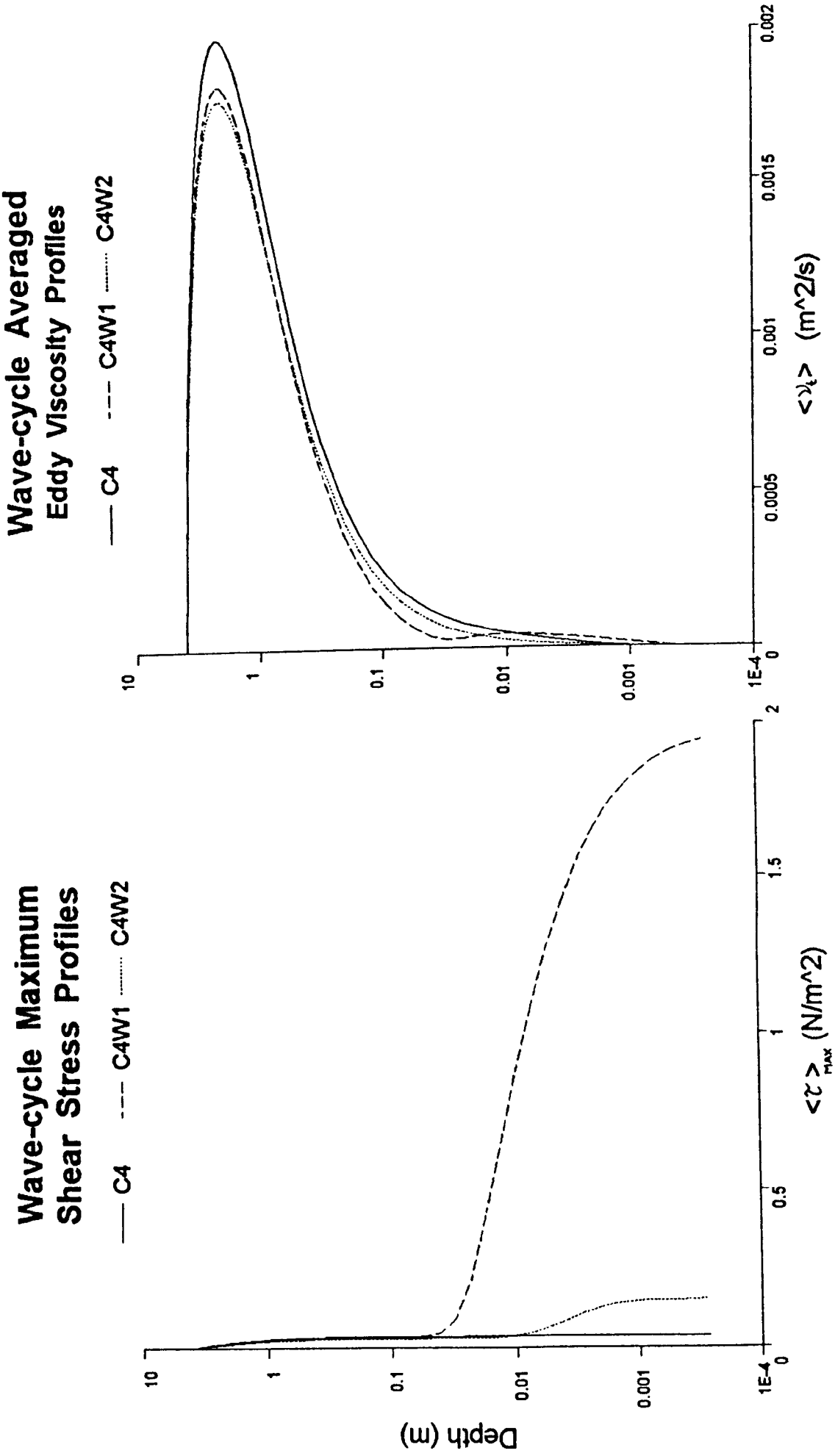

Figure 6.7: Test cases C4, C4W1 and C4W2 - Converged wave-cycle averaged profiles of eddy viscosity and maximum shear stress in wave cycle

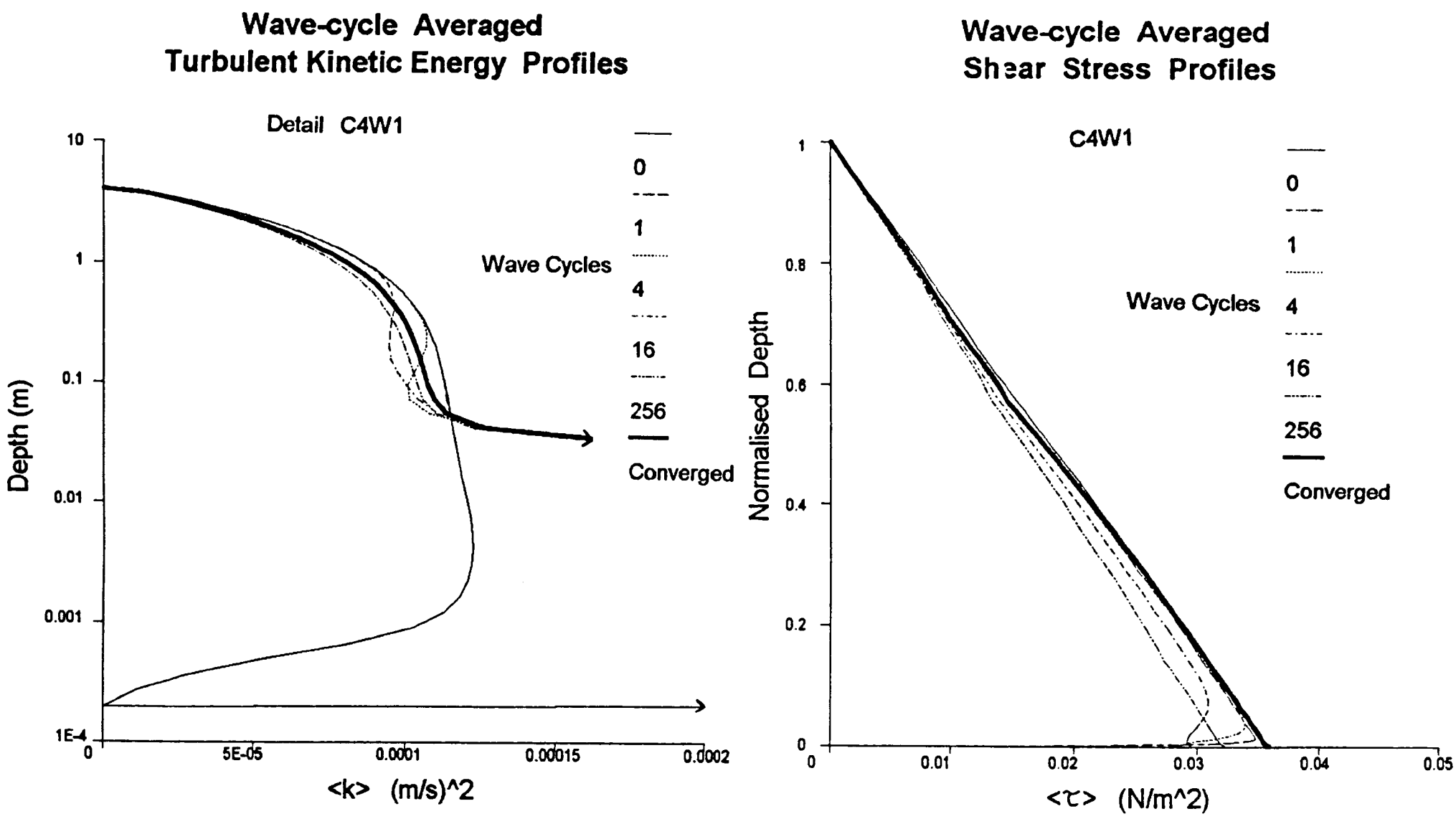

Figure 6.8: Test case C4W1 - Transient wave-cycle averaged profiles of turbulent kinetic energy and shear stress

Figure 6.9: Test case C4W1 - Transient wave-cycle averaged profiles of velocity and eddy viscosity

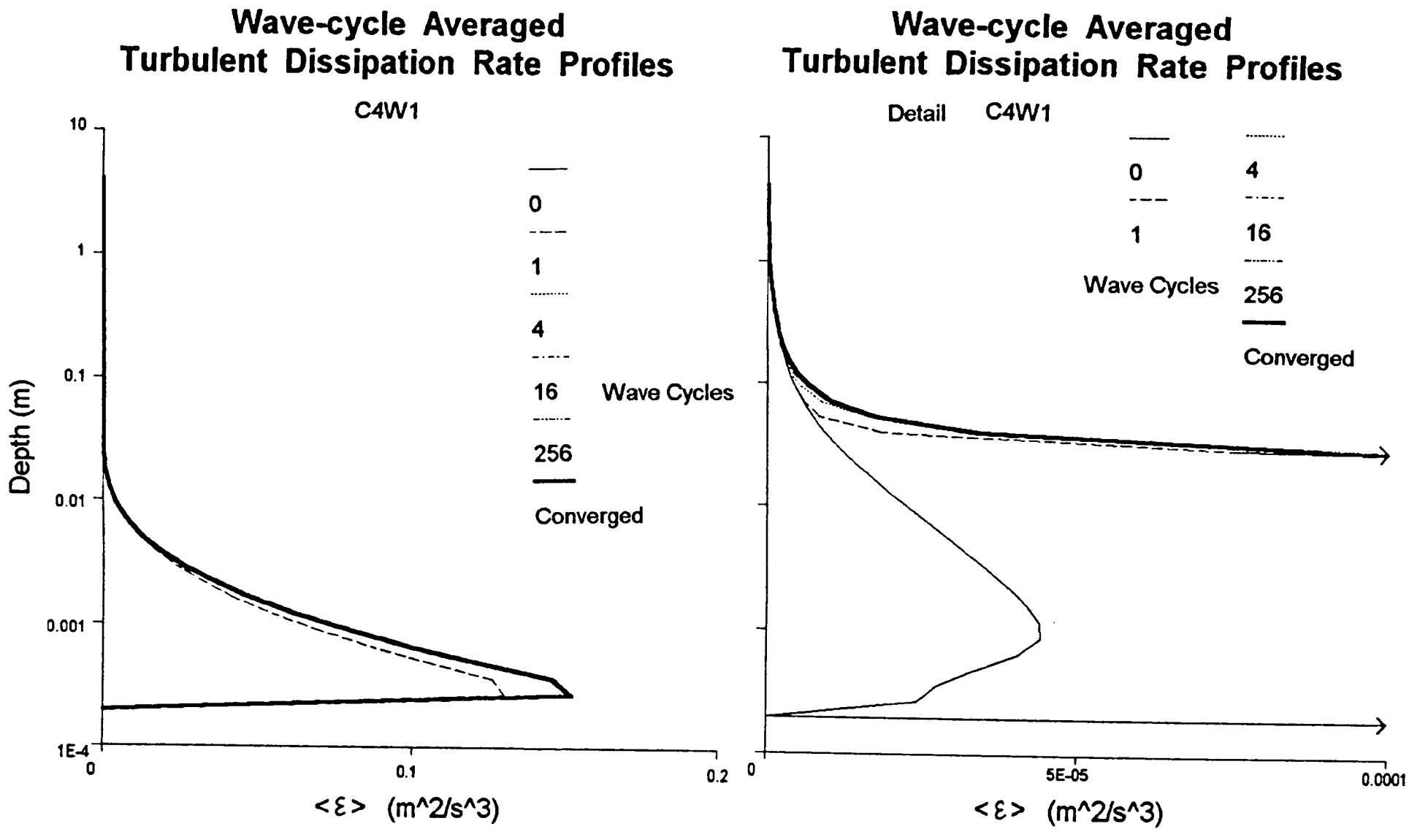

Figure 6.10: Test case C4W1 - Transient wave-cycle averaged profiles of turbulent energy dissipation rate

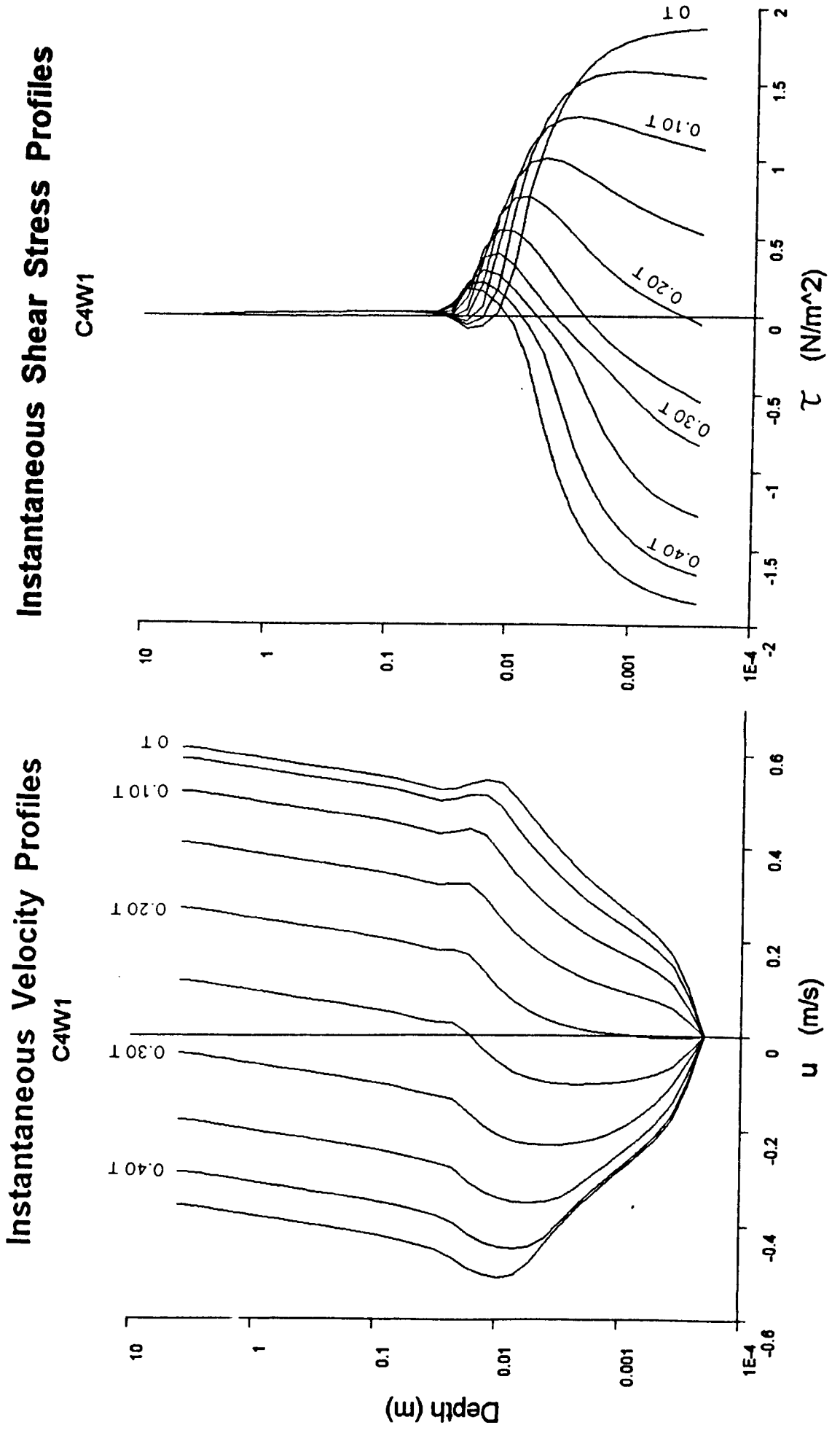

Figure 6.11: Test Case C4W1 - Vertical profiles of instantaneous velocity and shear stress at ten phases through a wave cycle

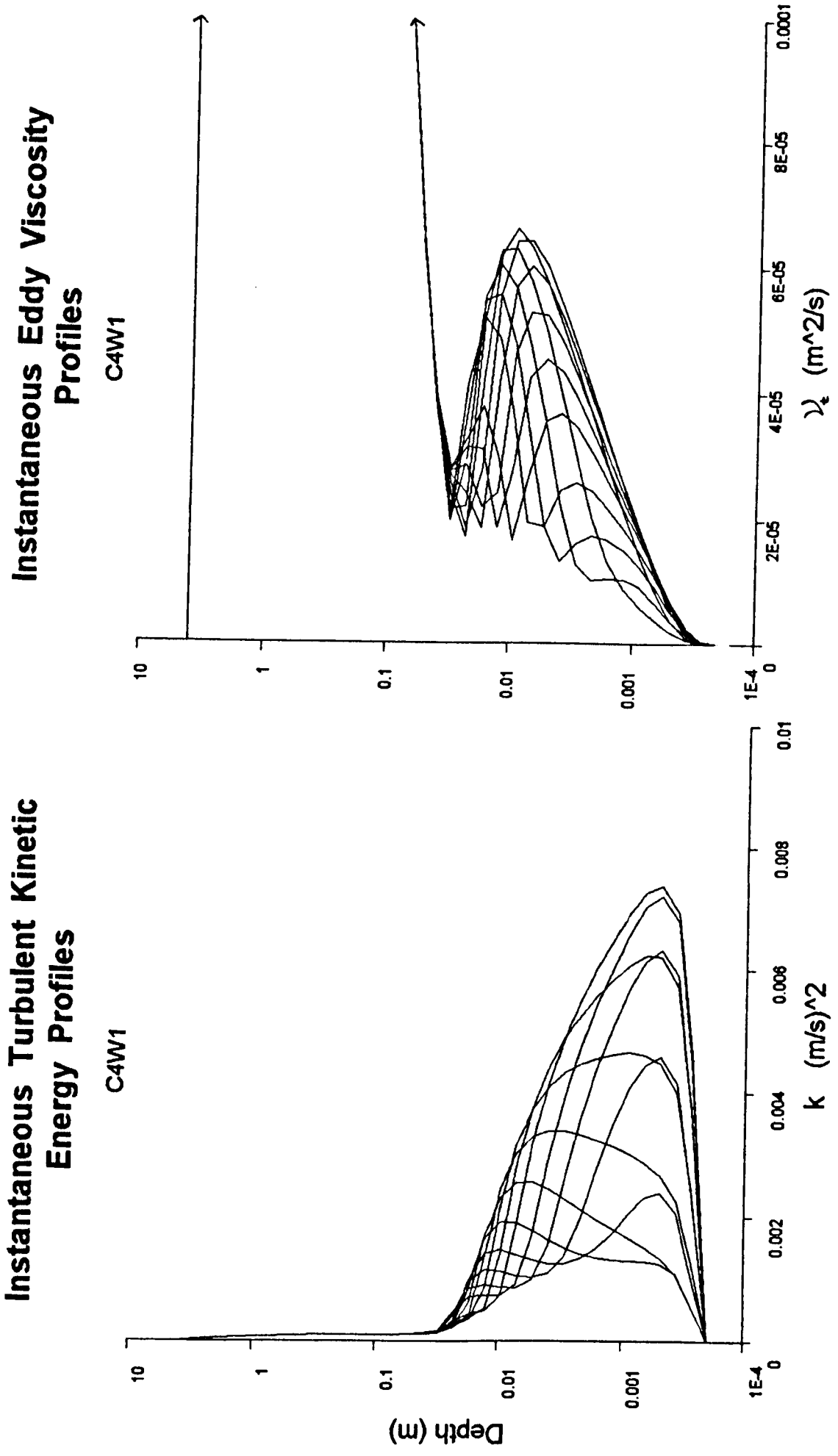

Figure 6.12: Test Case C4W1 - Vertical profiles of instantaneous turbulent kinetic energy and eddy viscosity at ten phases through a wave cycle

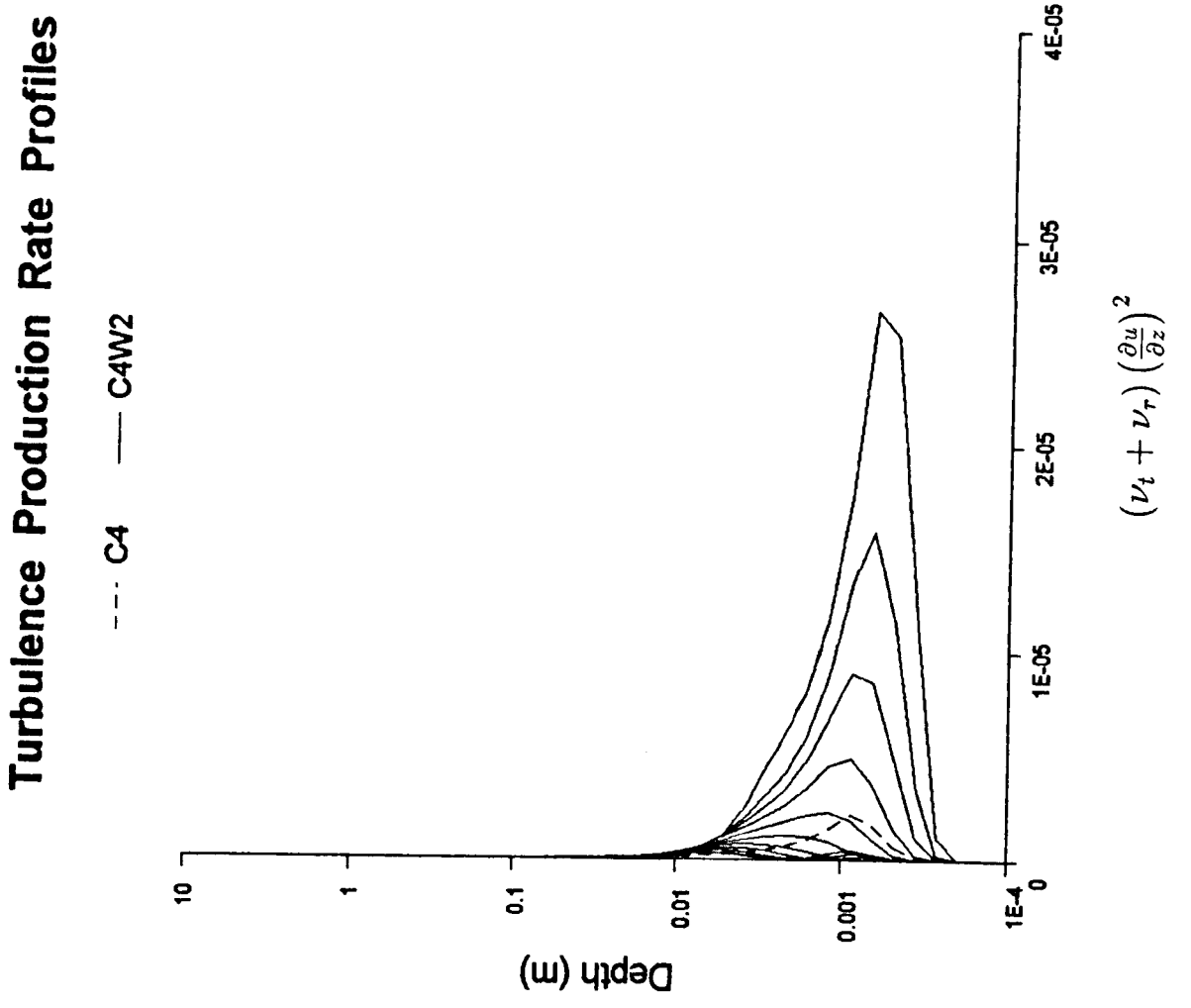

Figure 6.13: Test Cases C4 and C4W2 - Vertical profiles of instantaneous production rate term in k-equation $\left((\nu_t + \nu_r)\left(\frac{\partial u}{\partial z}\right)^2\right)$ at ten phases through a wave cycle and converged current profile

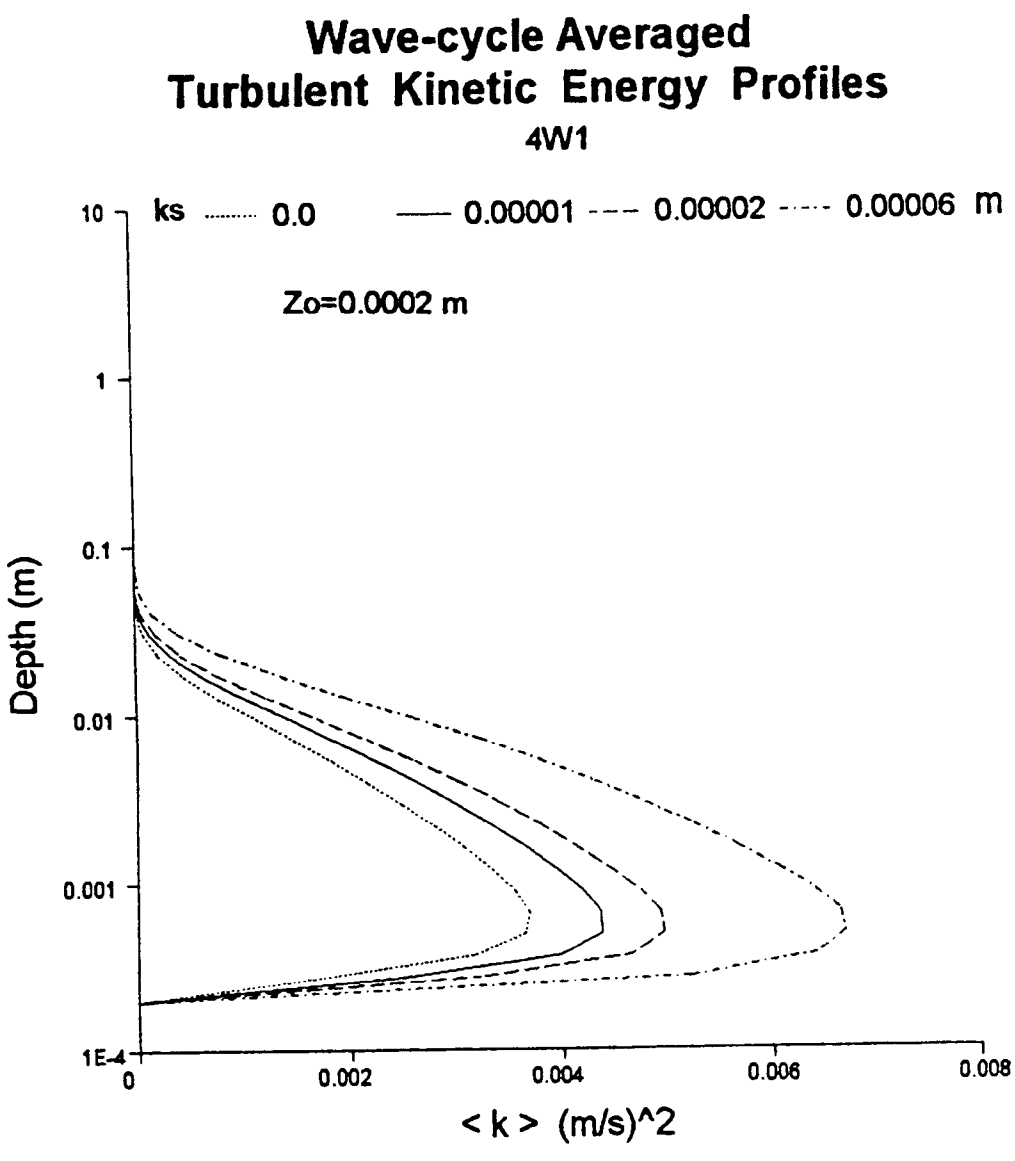

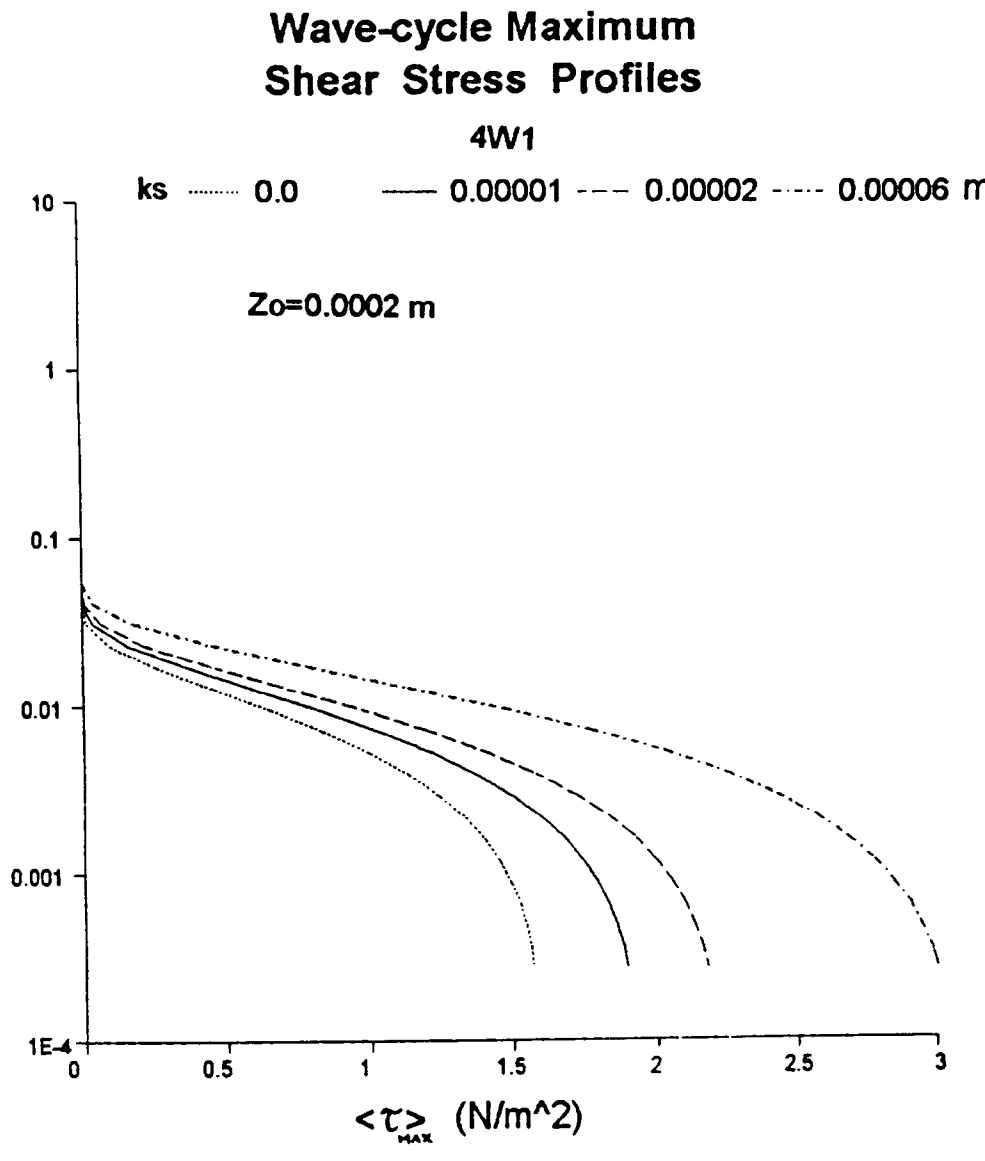

Figure 6.14: Test case 4W1 - Converged wave-cycle averaged profiles of turbulent kinetic energy and maximum shear stress: varying k_s for fixed z_o

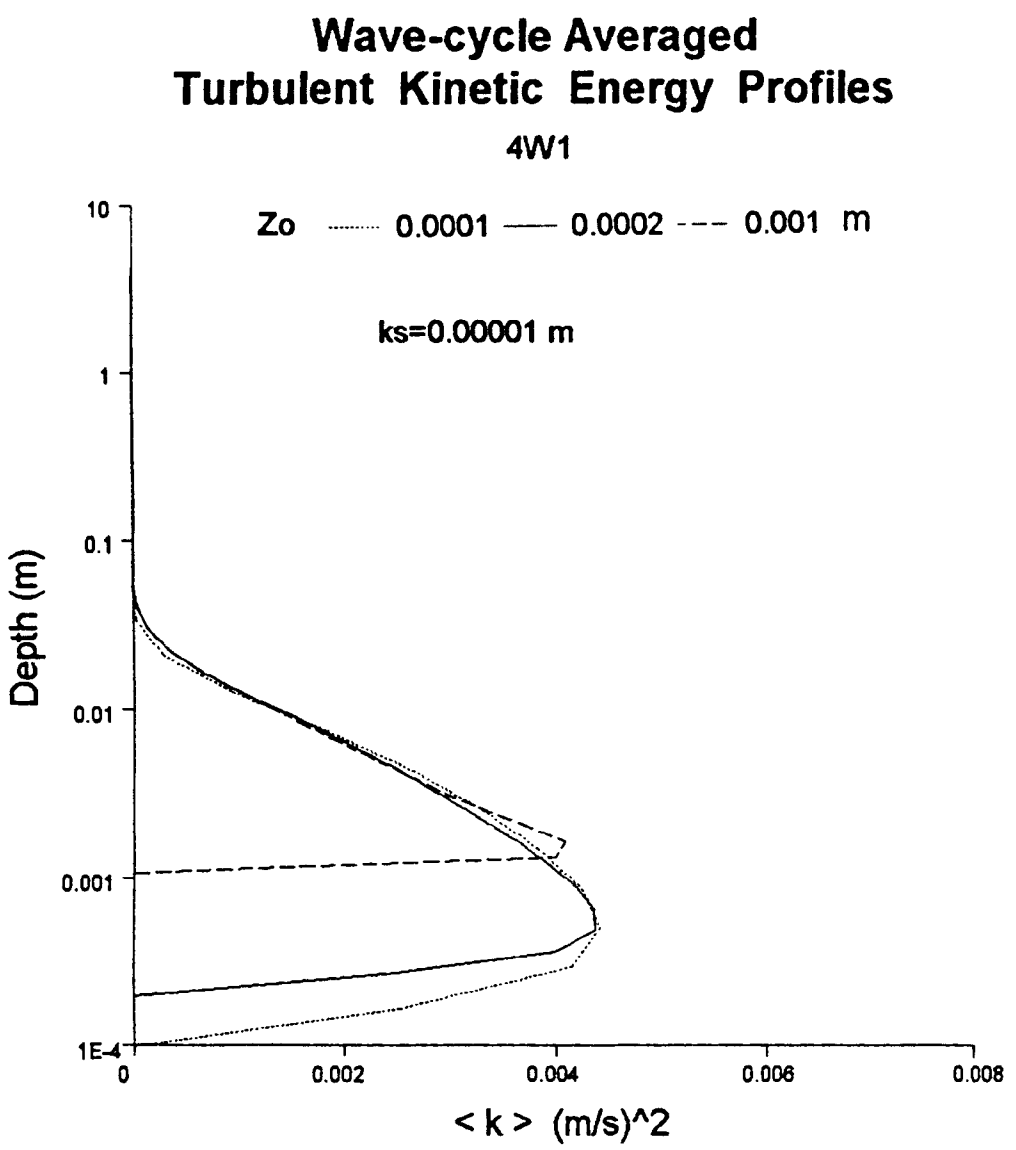

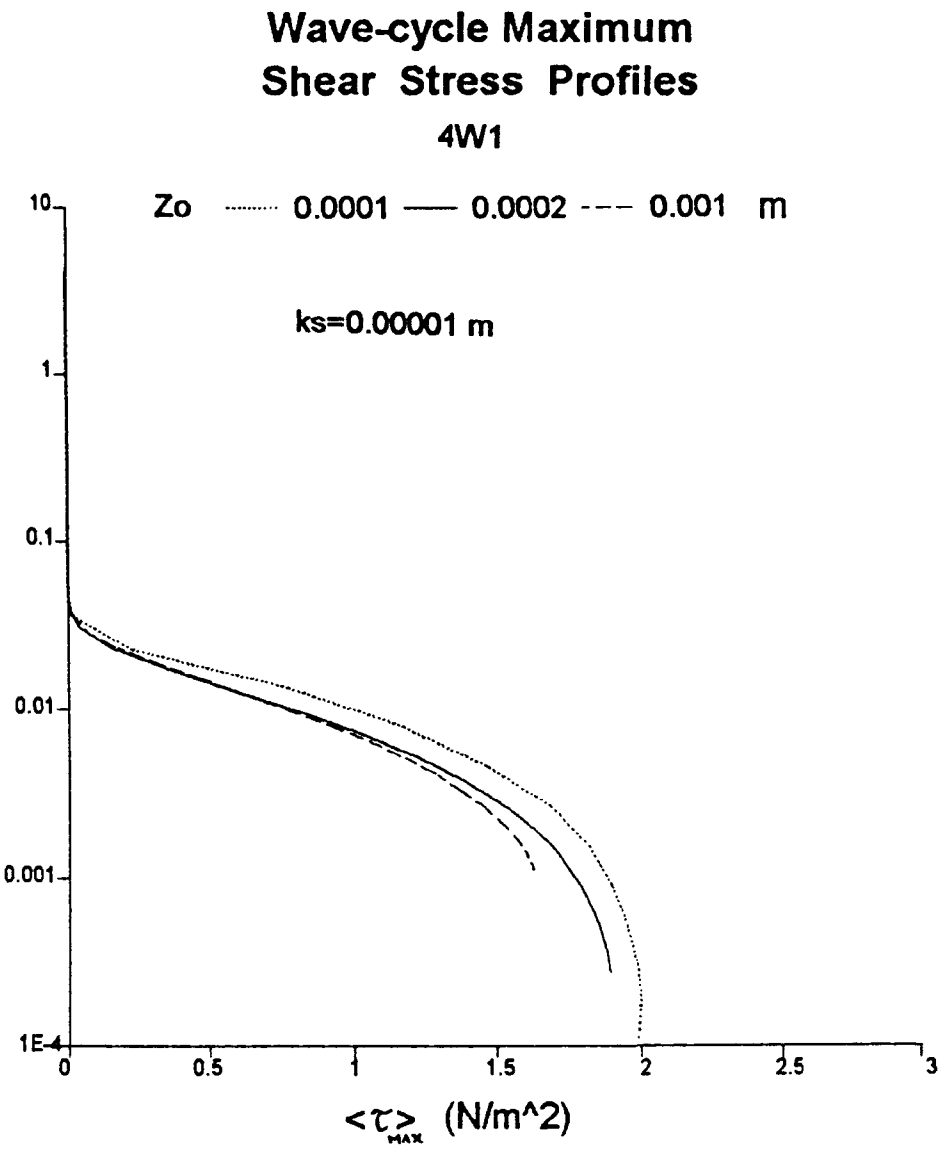

Figure 6.15: Test case 4W1 - Converged wave-cycle averaged profiles of turbulent kinetic energy and maximum shear stress: varying z_o for fixed k_s

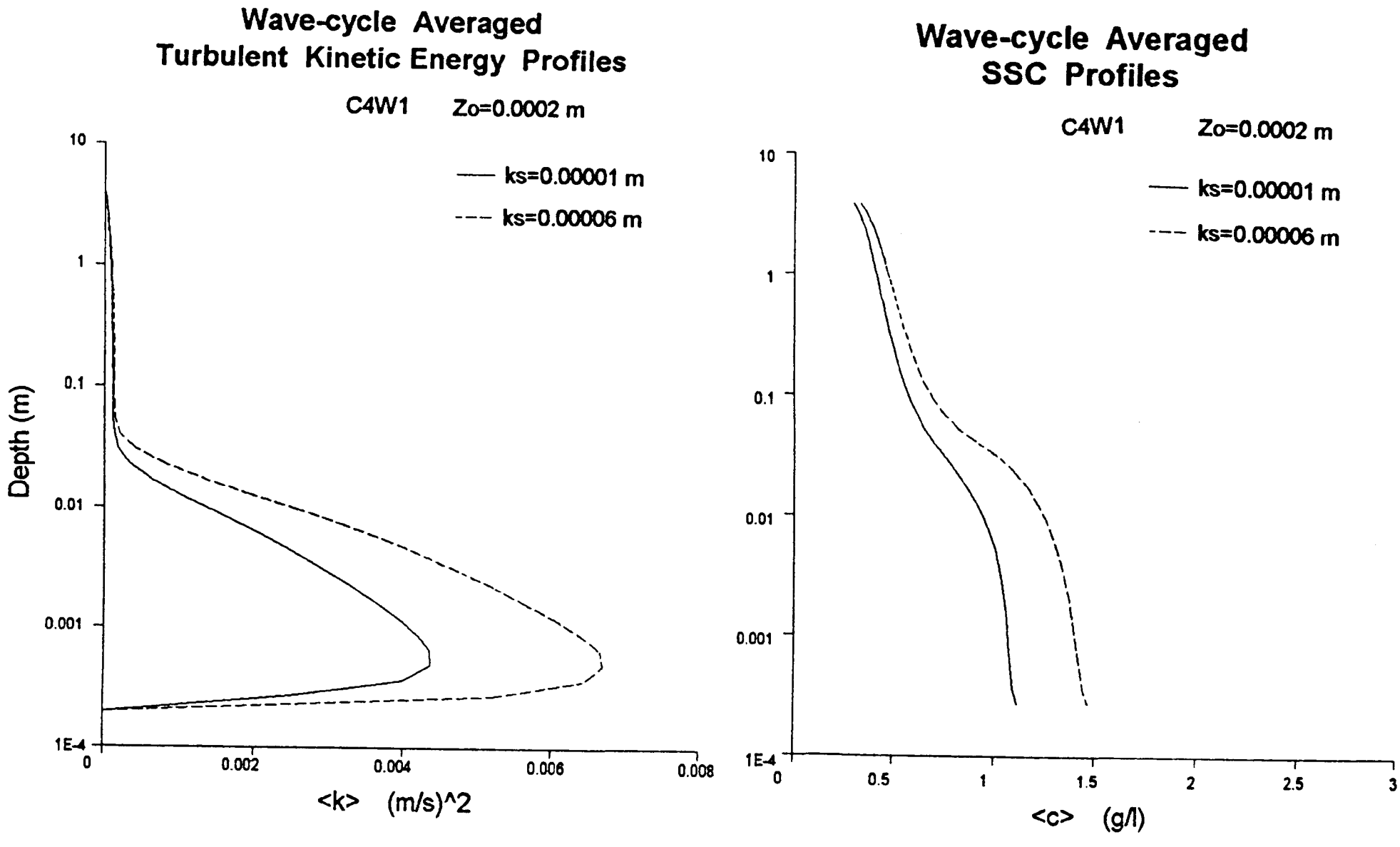

Figure 6.16: Test case C4W1 - Converged wave-cycle averaged profiles of turbulent kinetic energy and SSC: varying k_s for fixed z_o

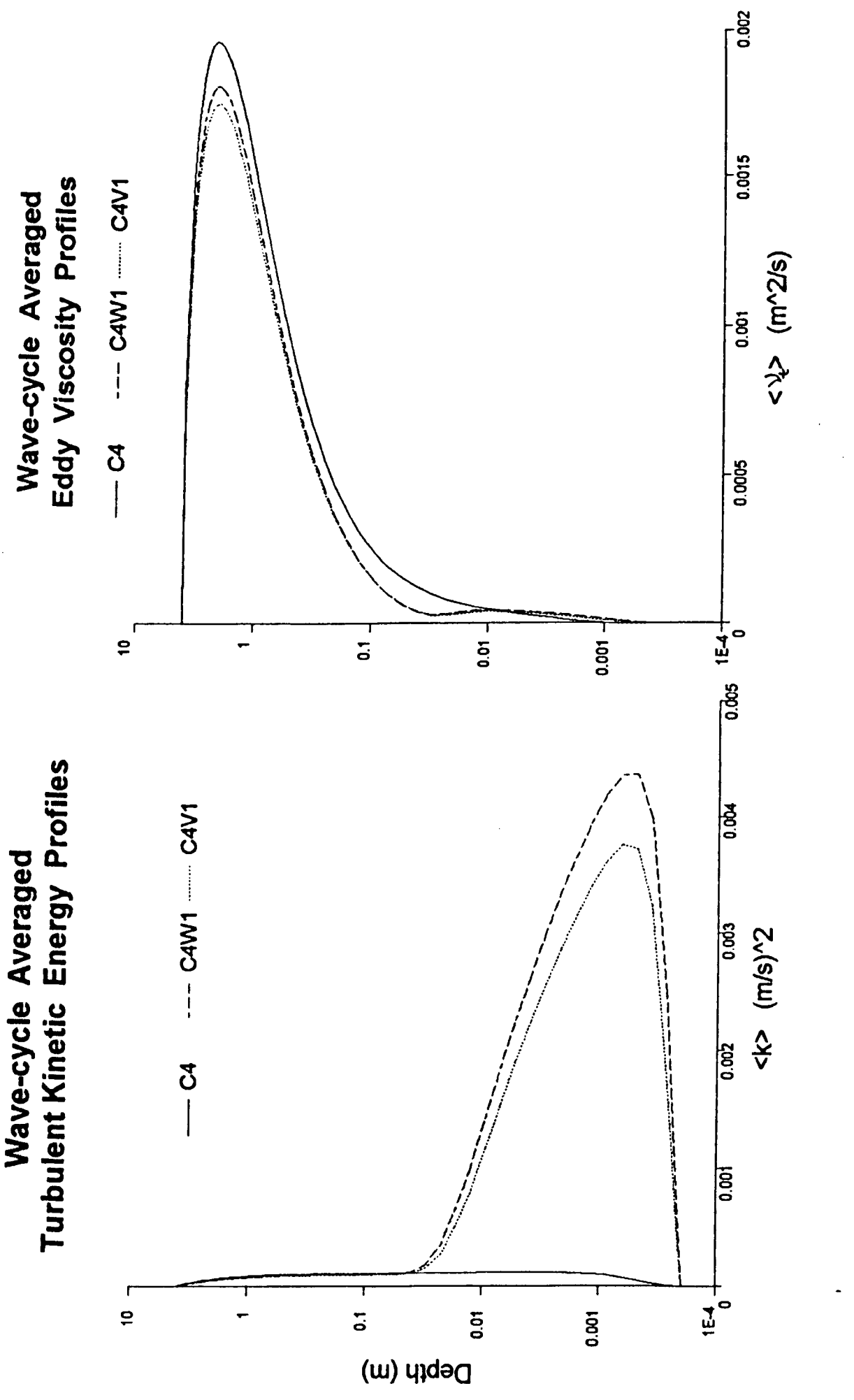

Figure 6.17: Test cases C4, C4W1 and C4V1 - Converged wave-cycle averaged profiles of turbulent kinetic energy and eddy viscosity

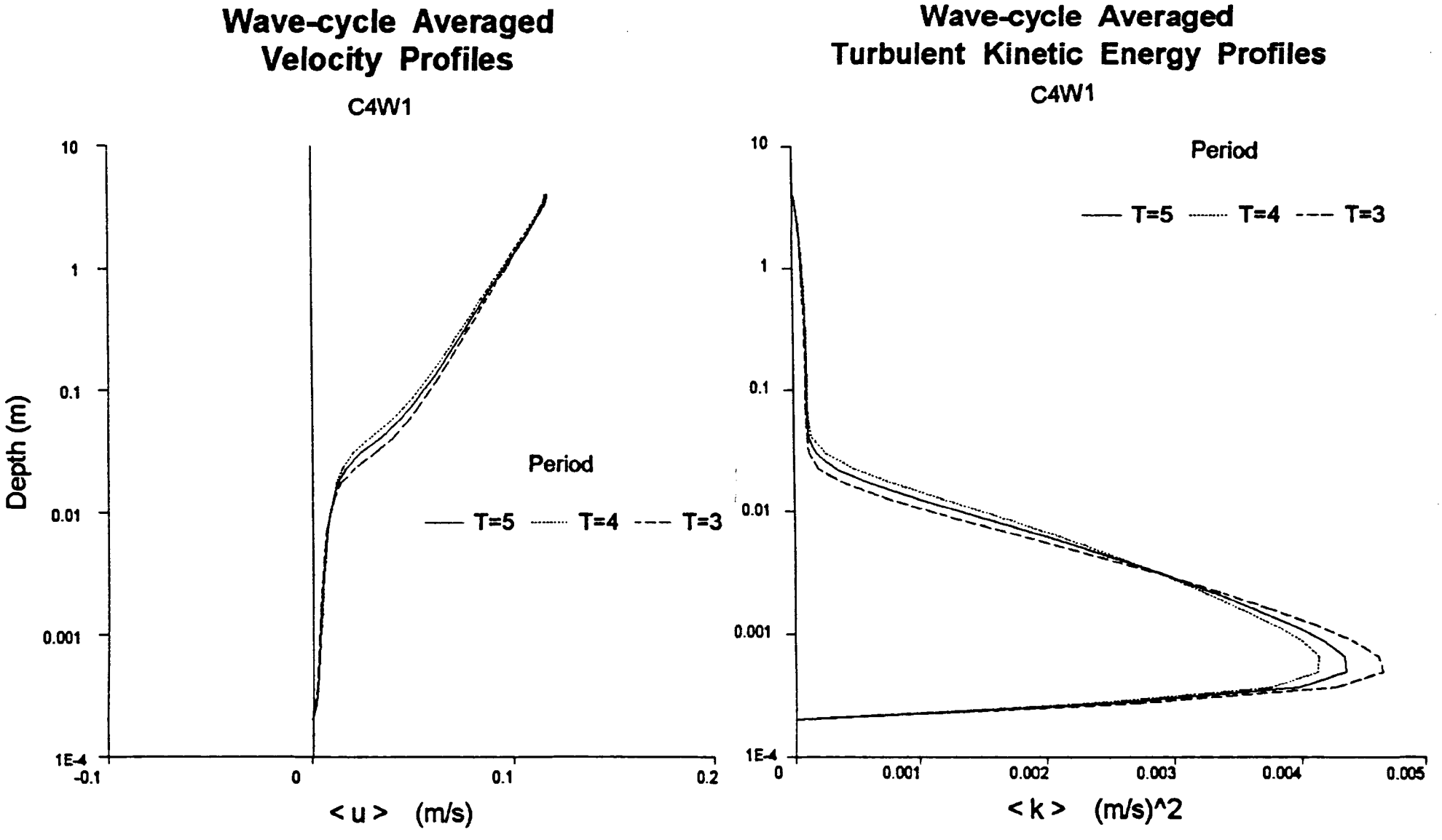

Figure 6.18: Test case C4W1 (varying wave period) - Converged wave-cycle averaged profiles of velocity and turbulent kinetic energy

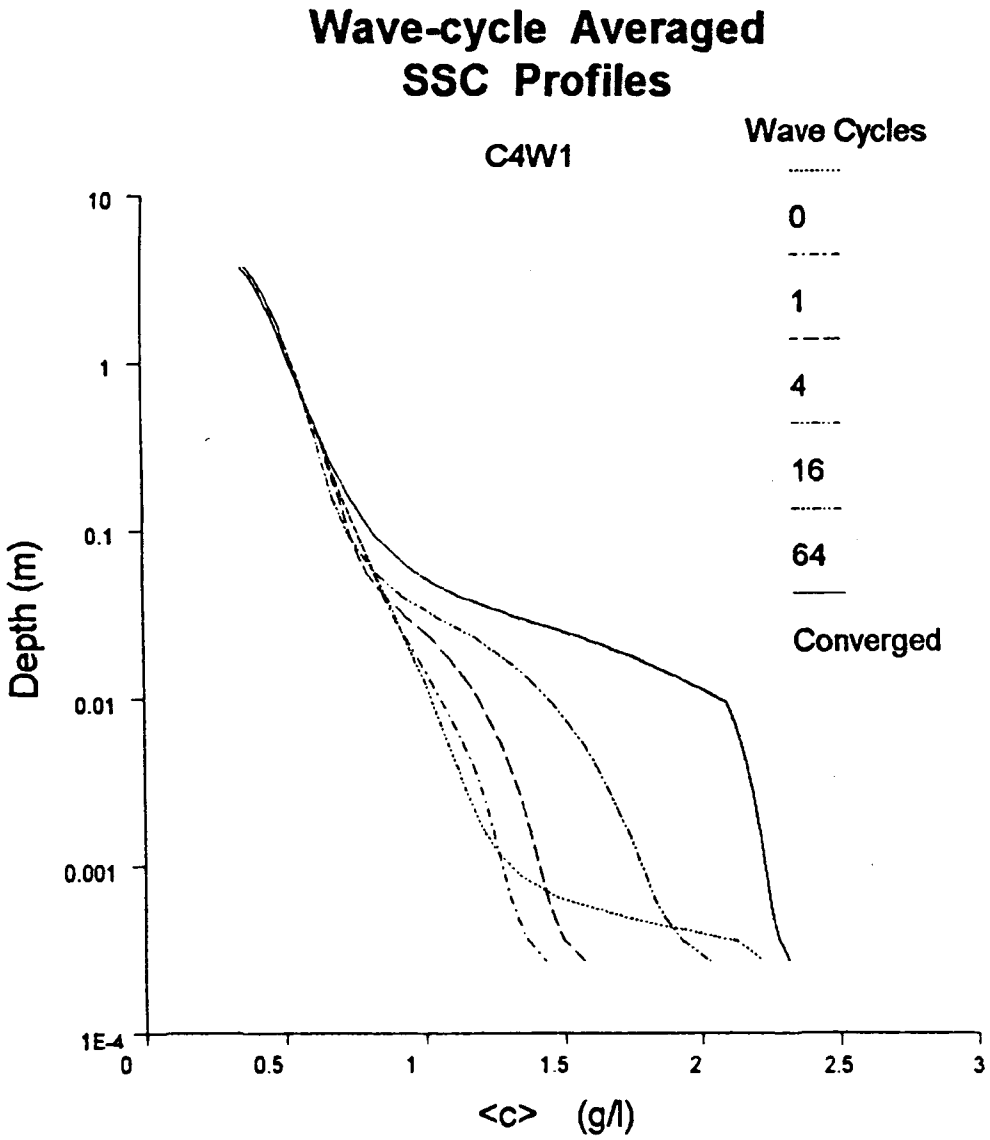

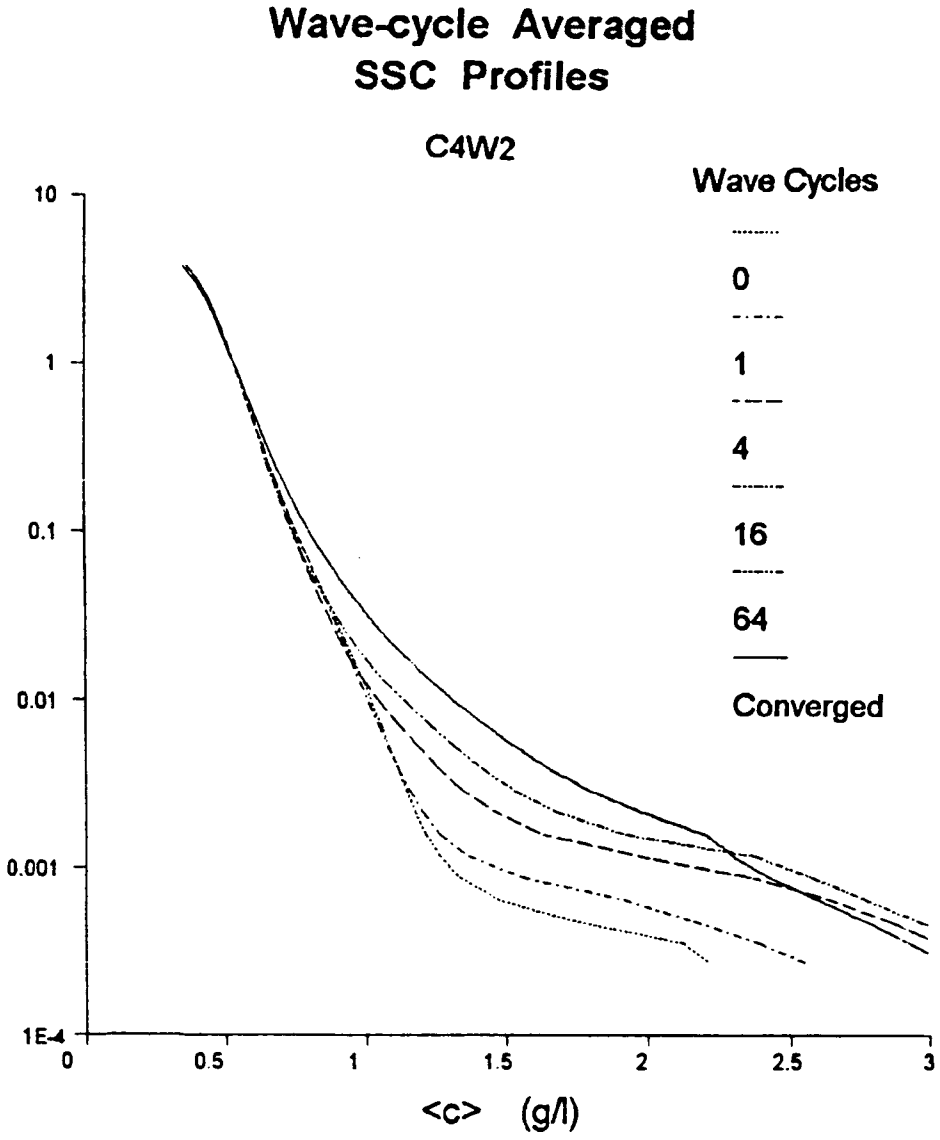

Figure 6.19: Test cases C4W1 and C4W2 - Transient wave-cycle averaged profiles of SSC starting from C4 SSC profile (no bed flux, bulk conc 0.5 g/l)

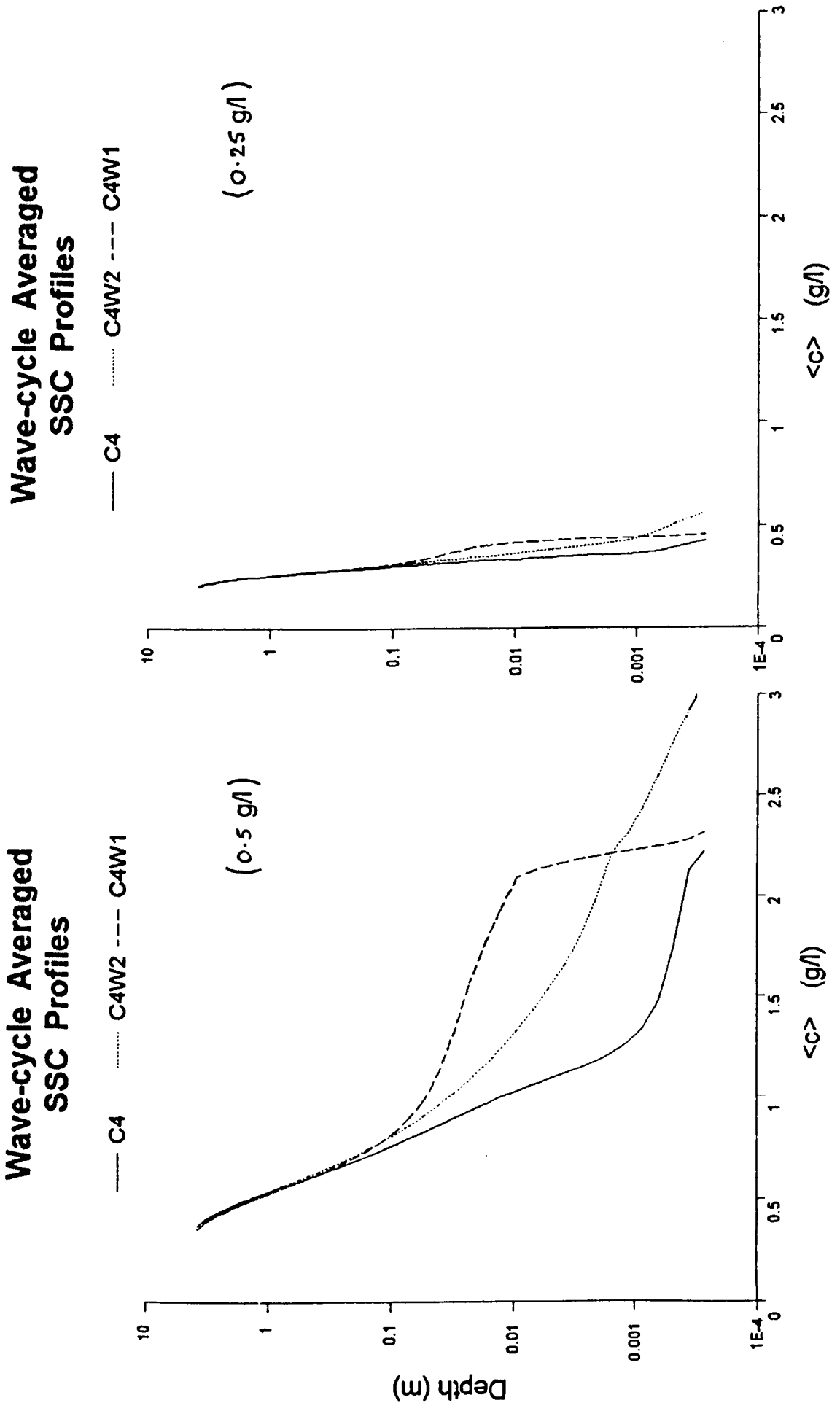

Figure 6.20: Test cases C4, C4W1 and C4W2 - Transient wave-cycle averaged profiles of SSC (no bed flux)

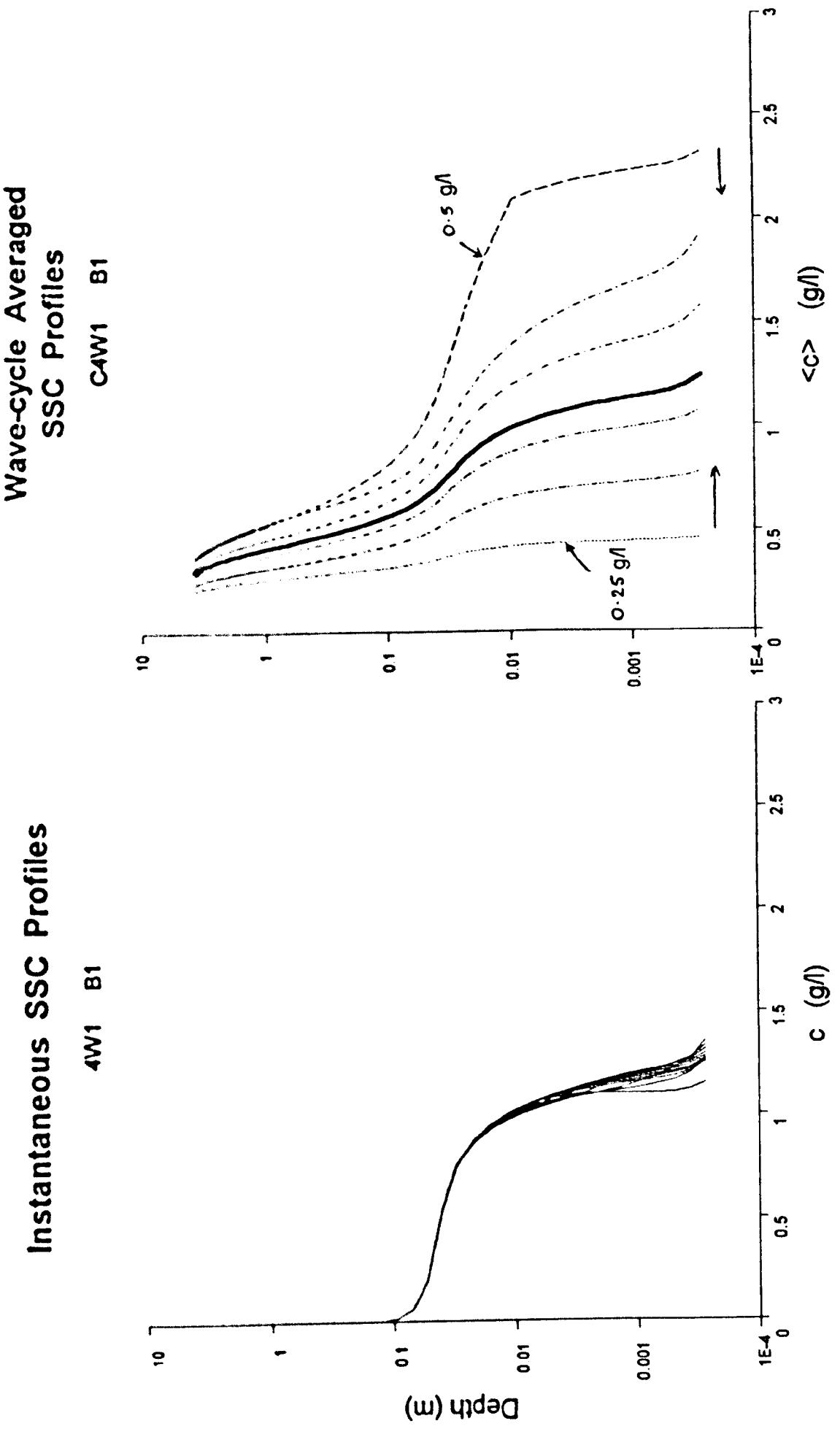

Figure 6.21: Test cases 4W1, B1 - Ten instantaneous SSC profiles and C4W1, B1 - cycle averaged SSC profiles converging from below and above

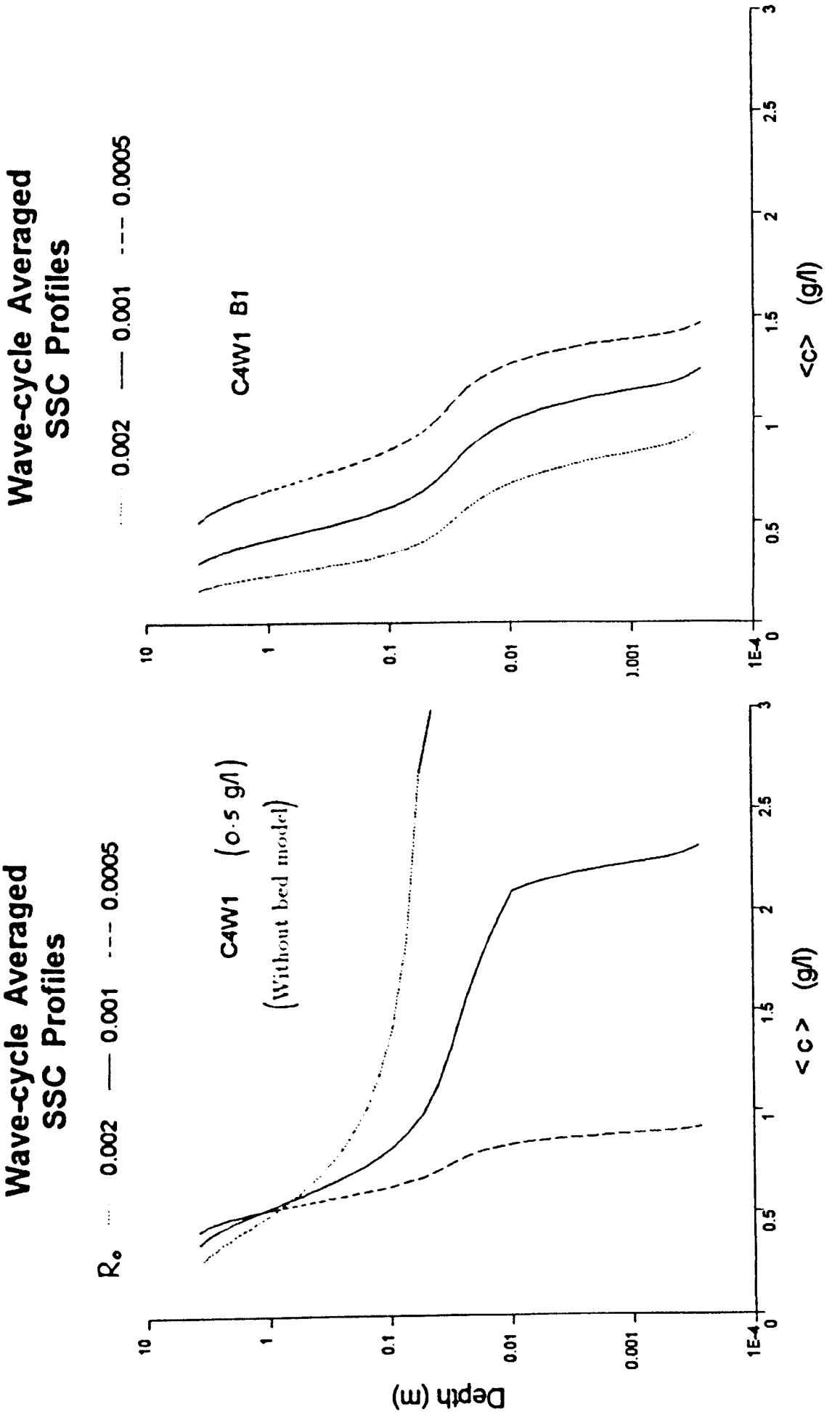

Figure 6.22: Test case C4W1 (varying settling velocity) - Converged wave-cycle averaged profiles of SSC; without bed flux and with bed model B1

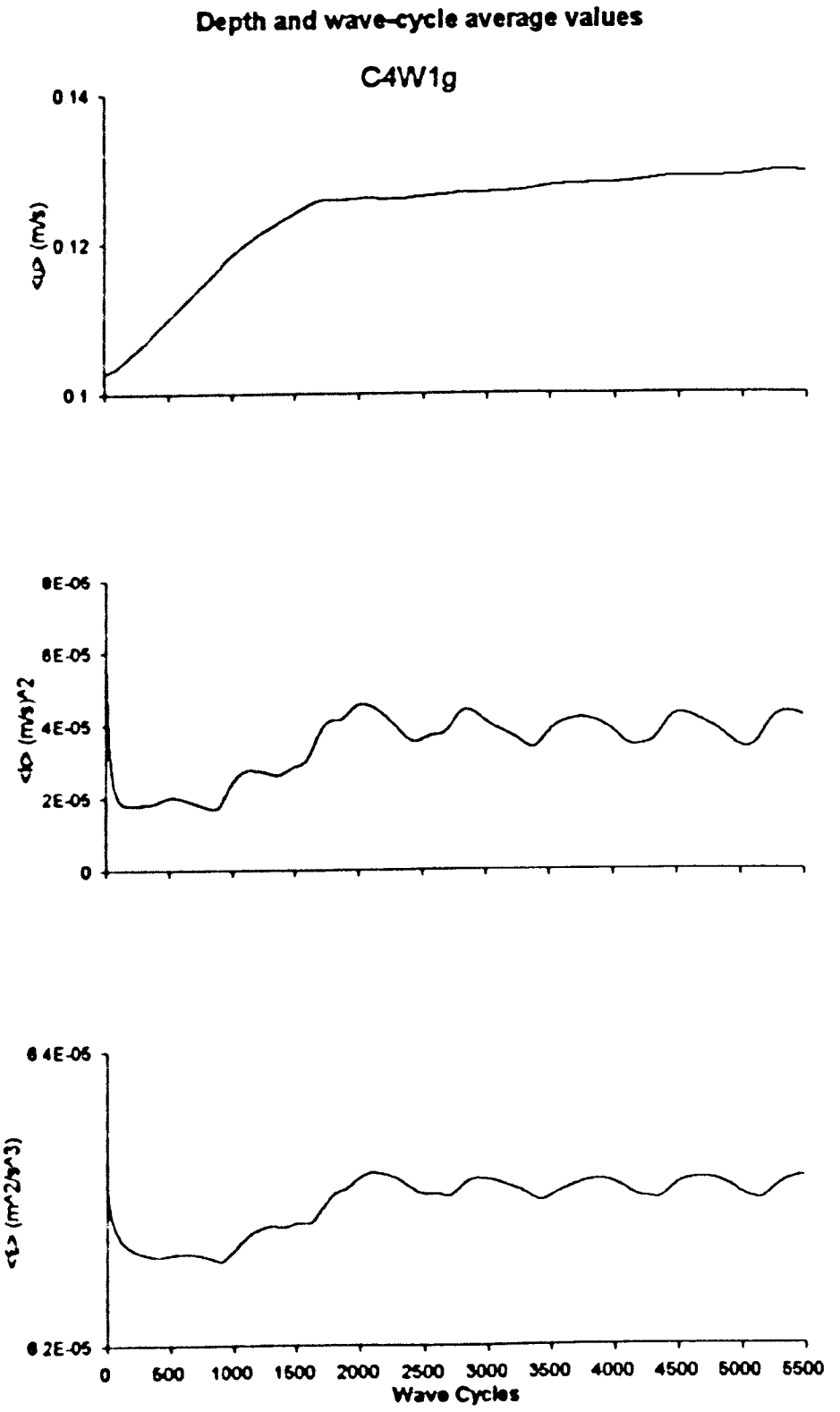

Figure 6.23: Test case C4W1g (B1) - Depth and wave-cycle averaged velocity, turbulent kinetic energy and dissipation rate - from C4W1 to convergence

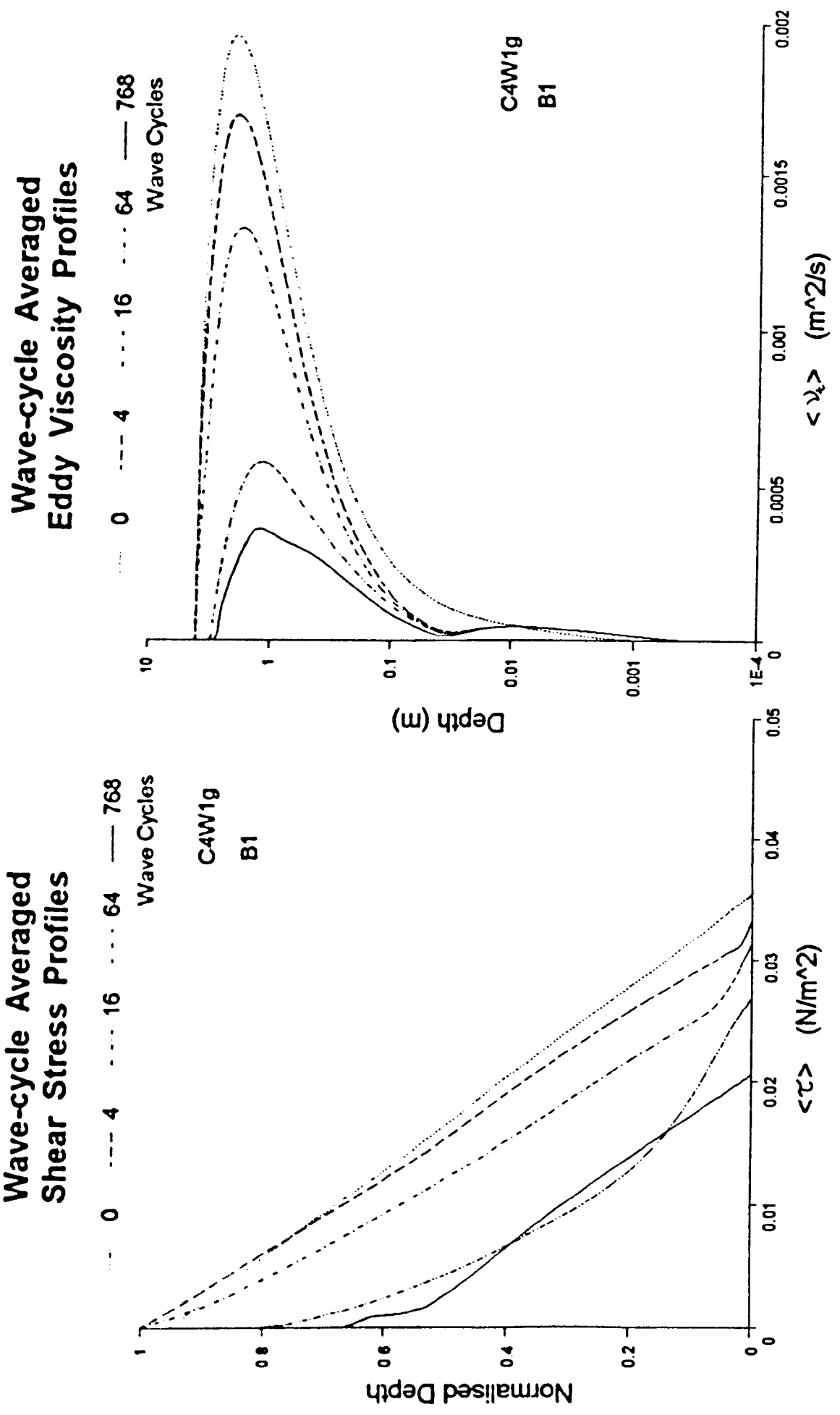

Figure 6.24: Test case C4W1g (B1) - Transient wave-cycle averaged profiles of shear stress and eddy viscosity

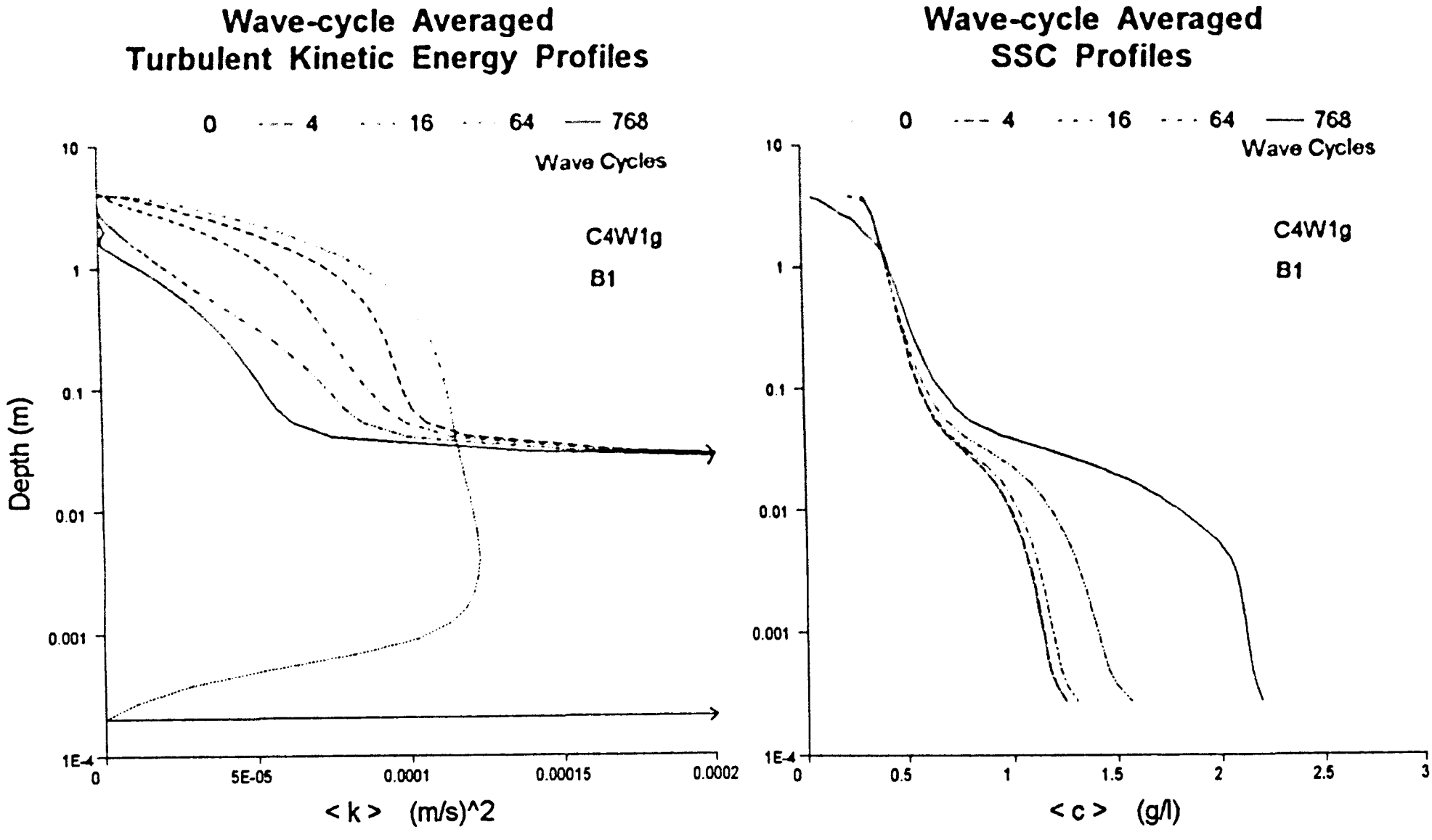

Figure 6.25: Test case C4W1g (B1) - Transient wave-cycle averaged profiles of turbulent kinetic energy and SSC

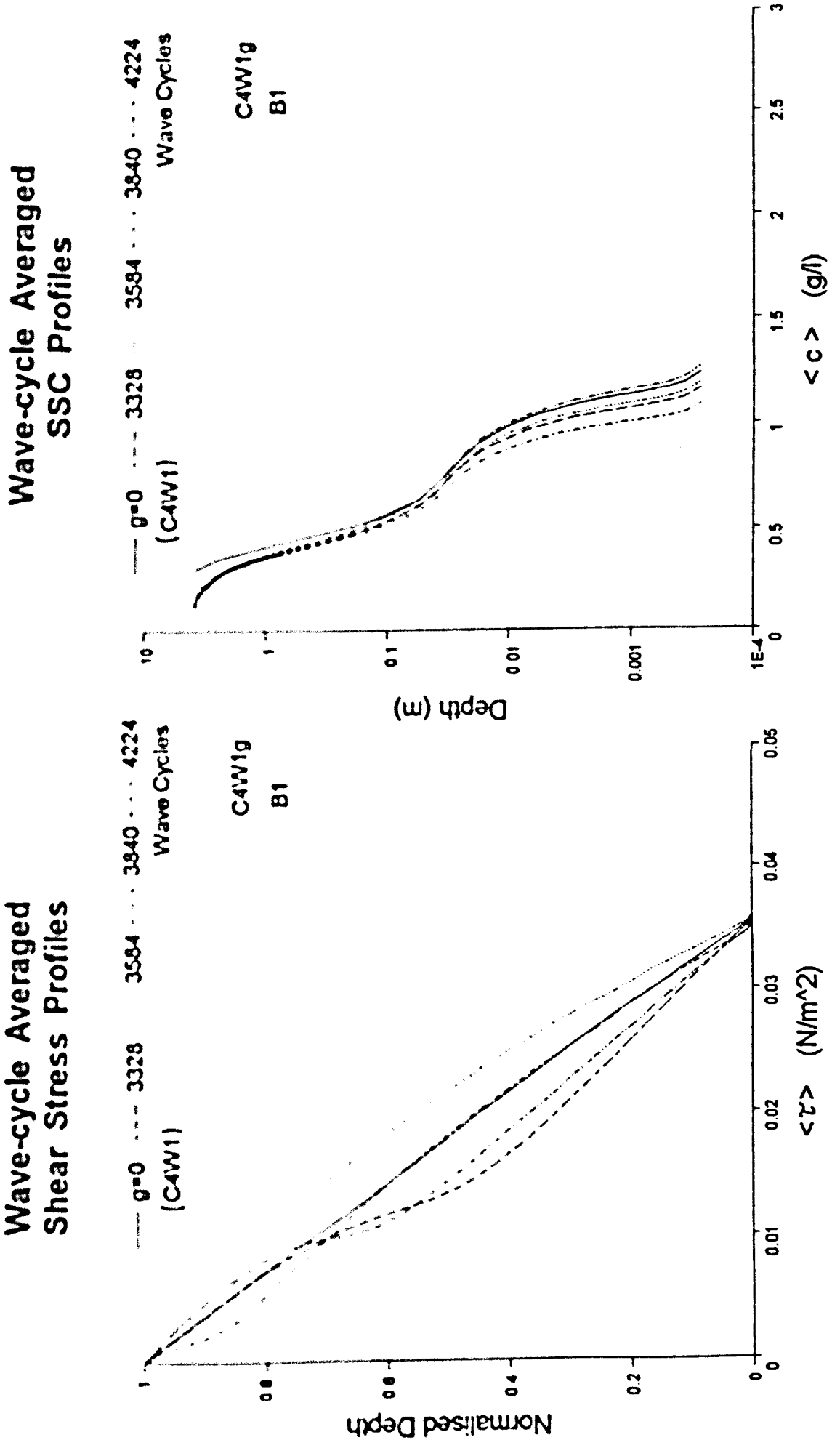

Figure 6.26 Test case C4W1g (B1) - Wave-cycle averaged profiles of shear stress and SSC (oscillating around equilibrium)

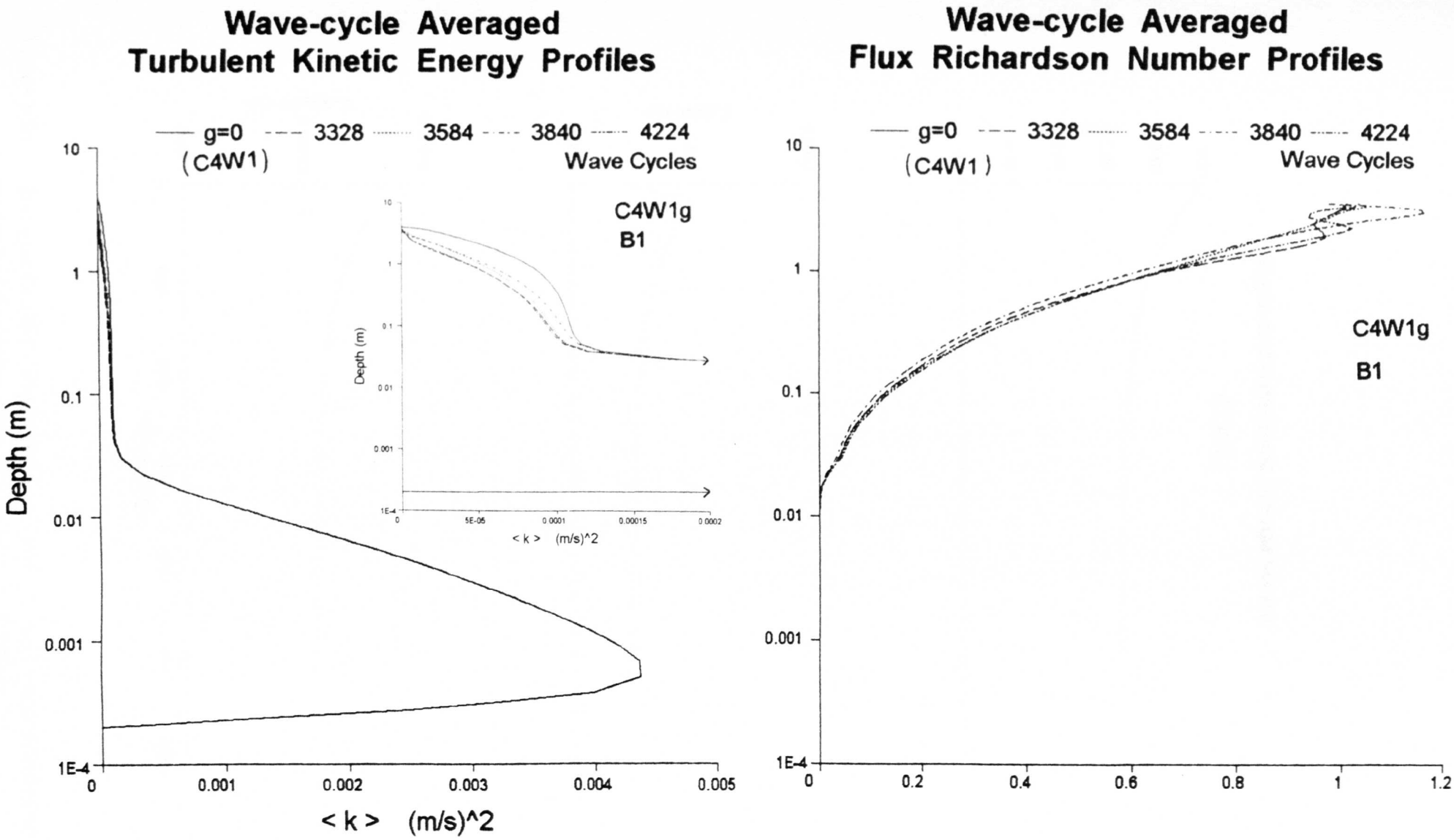

Figure 6.27: Test case C4W1g (B1) - Wave-cycle averaged profiles of turbulent kinetic energy and Ri_f (oscillating around equilibrium)

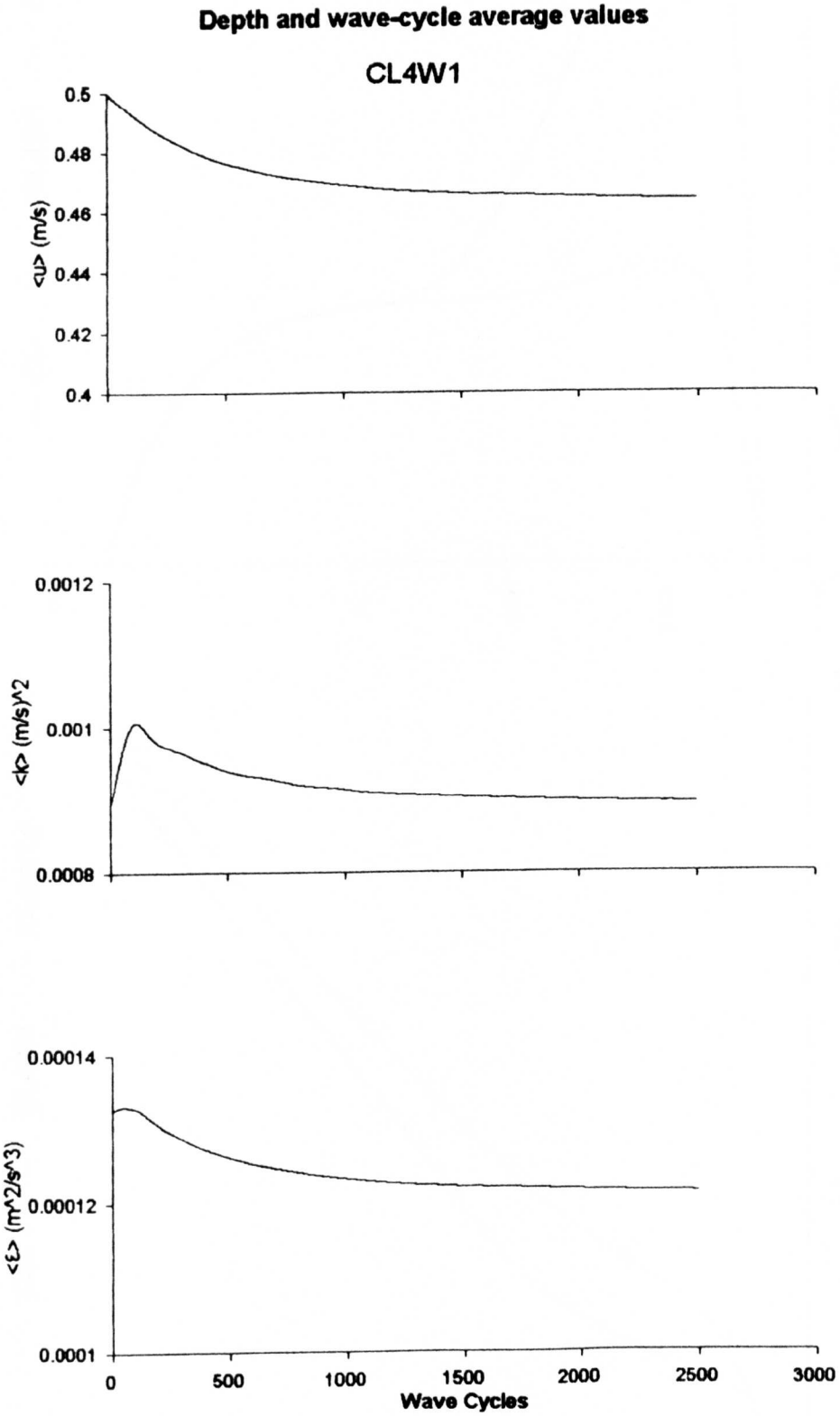

Figure 6.28: Test case CL4W1 - Depth and wave-cycle averaged velocity, turbulent kinetic energy and dissipation rate - from CL4 to convergence

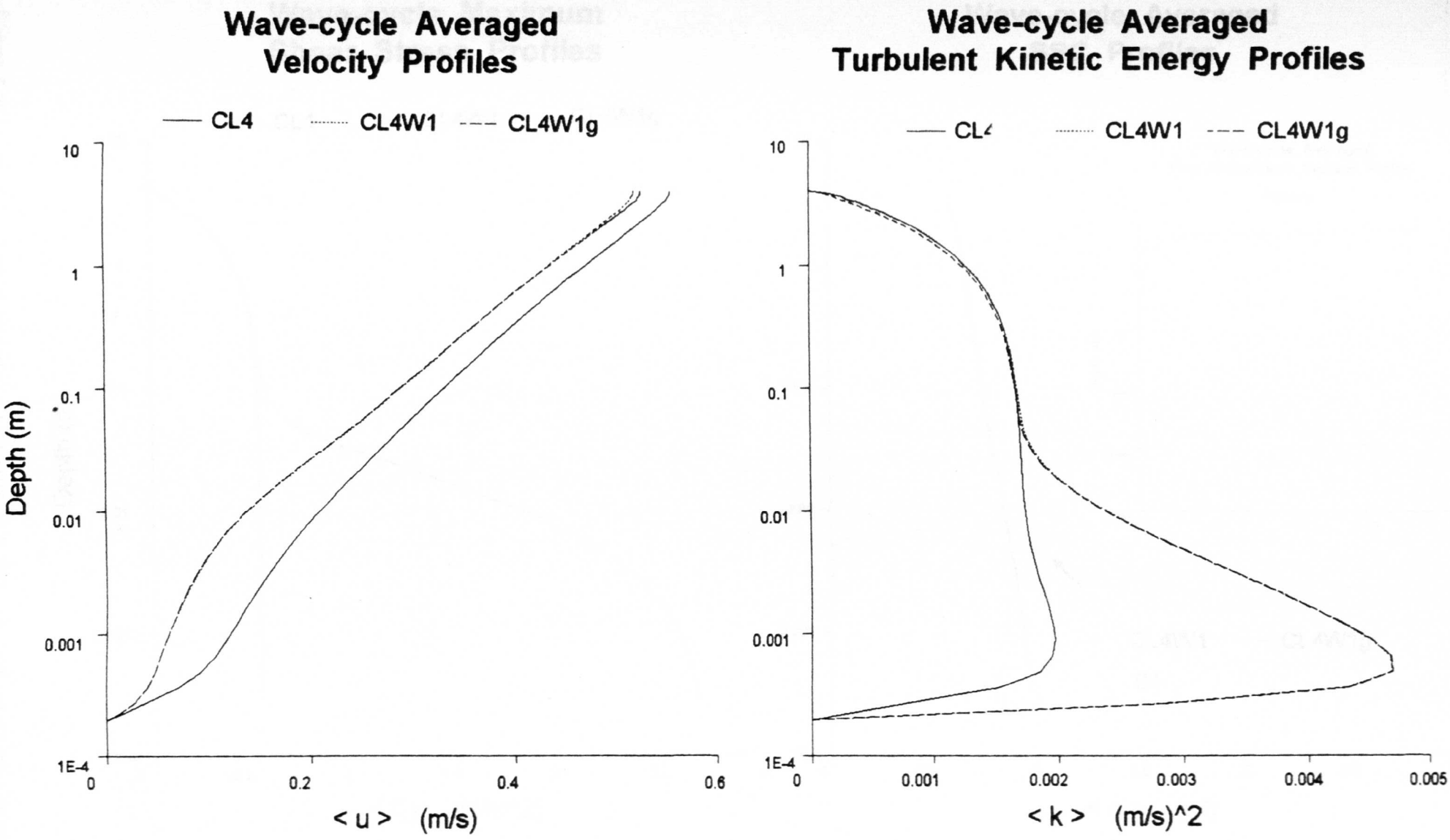

Figure 6.29: Test cases CL4, CL4W1 and CL4W1g (all B1) - Converged wave-cycle averaged profiles of velocity and turbulent kinetic energy

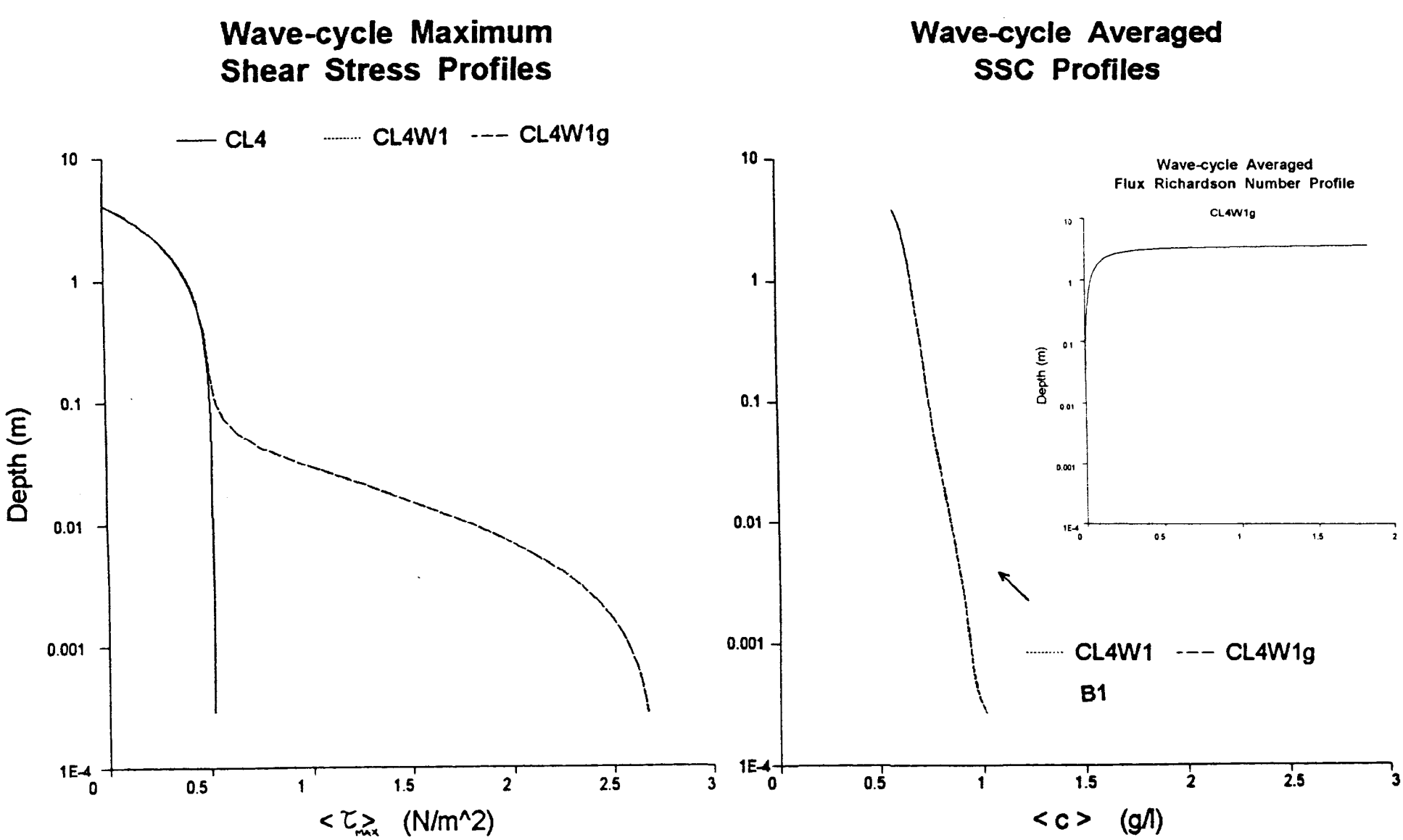

Figure 6.30: Test cases CL4, CL4W1 and CL4W1g (all B1) - Converged wave-cycle profiles of maximum shear stress and averaged SSC and Ri_f

Figure 6.31: Test cases C4 and C4W4 - Converged wave-cycle averaged profiles of velocity and turbulent kinetic energy

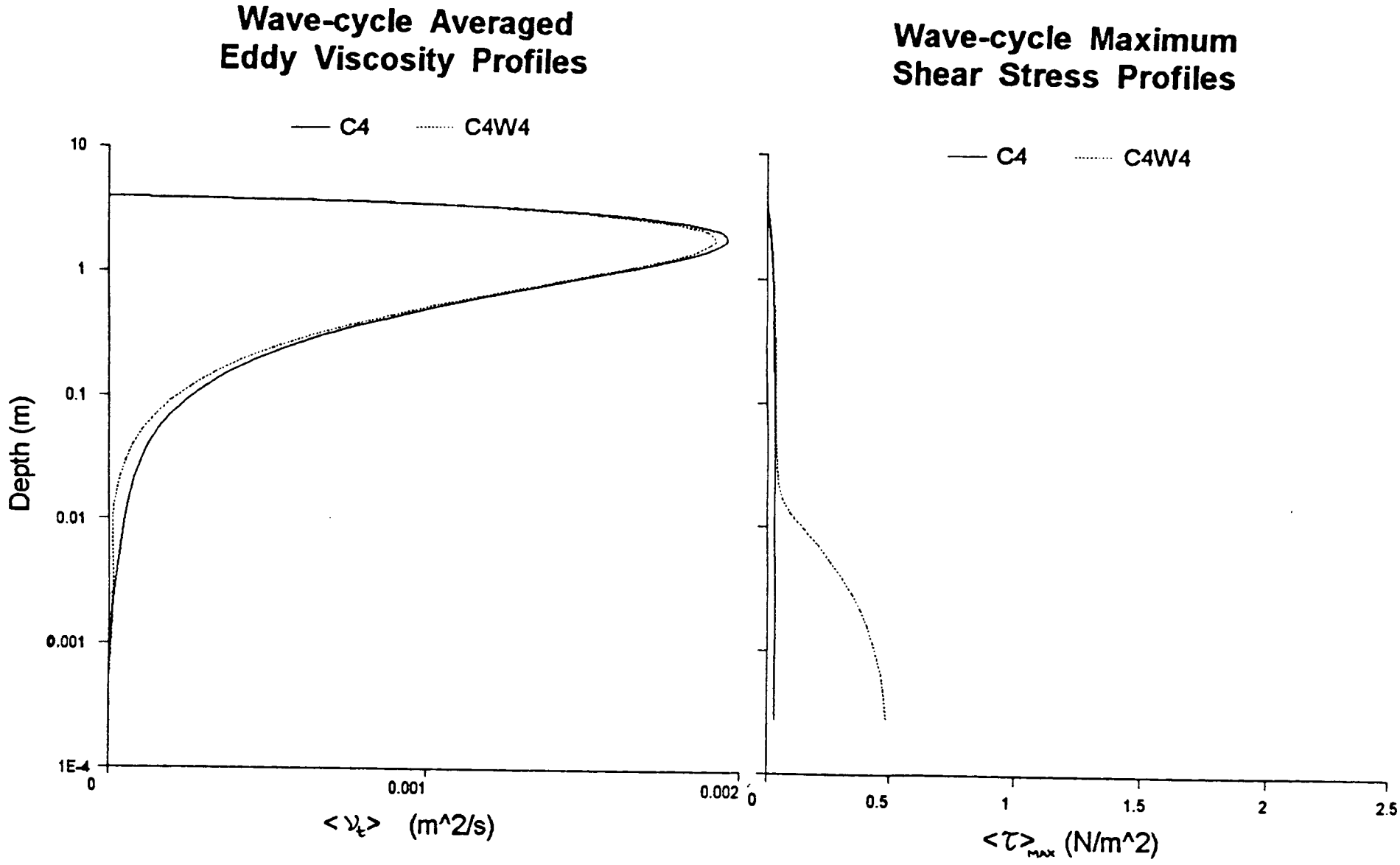

Figure 6.32: Test cases C4 and C4W4 - Converged wave-cycle averaged profiles of eddy viscosity and maximum shear stress in wave cycle

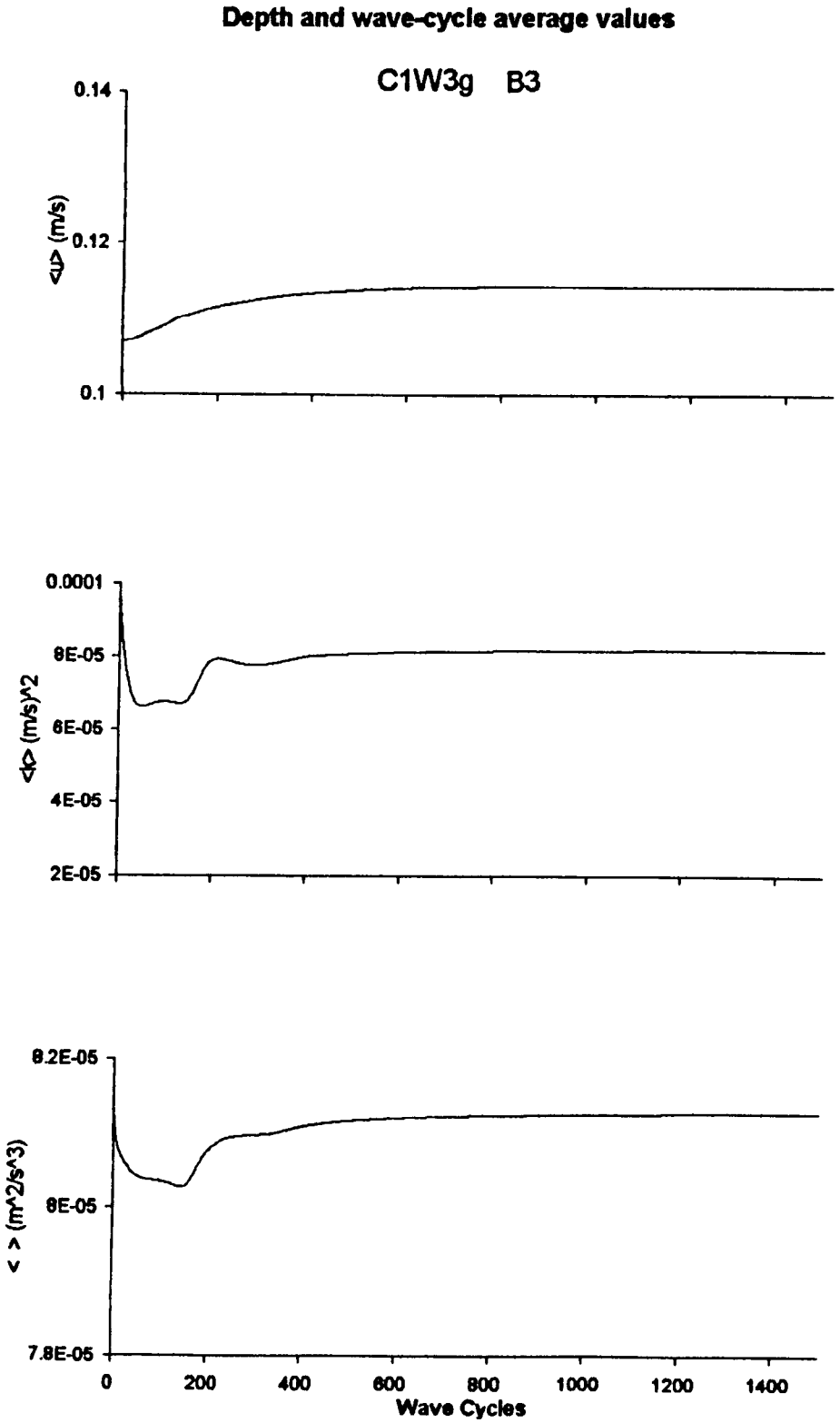

Figure 6.33: Test case C1W3g (B3) - Depth and wave-cycle averaged velocity, turbulent kinetic energy and dissipation rate - from C1W3 (B3) to convergence

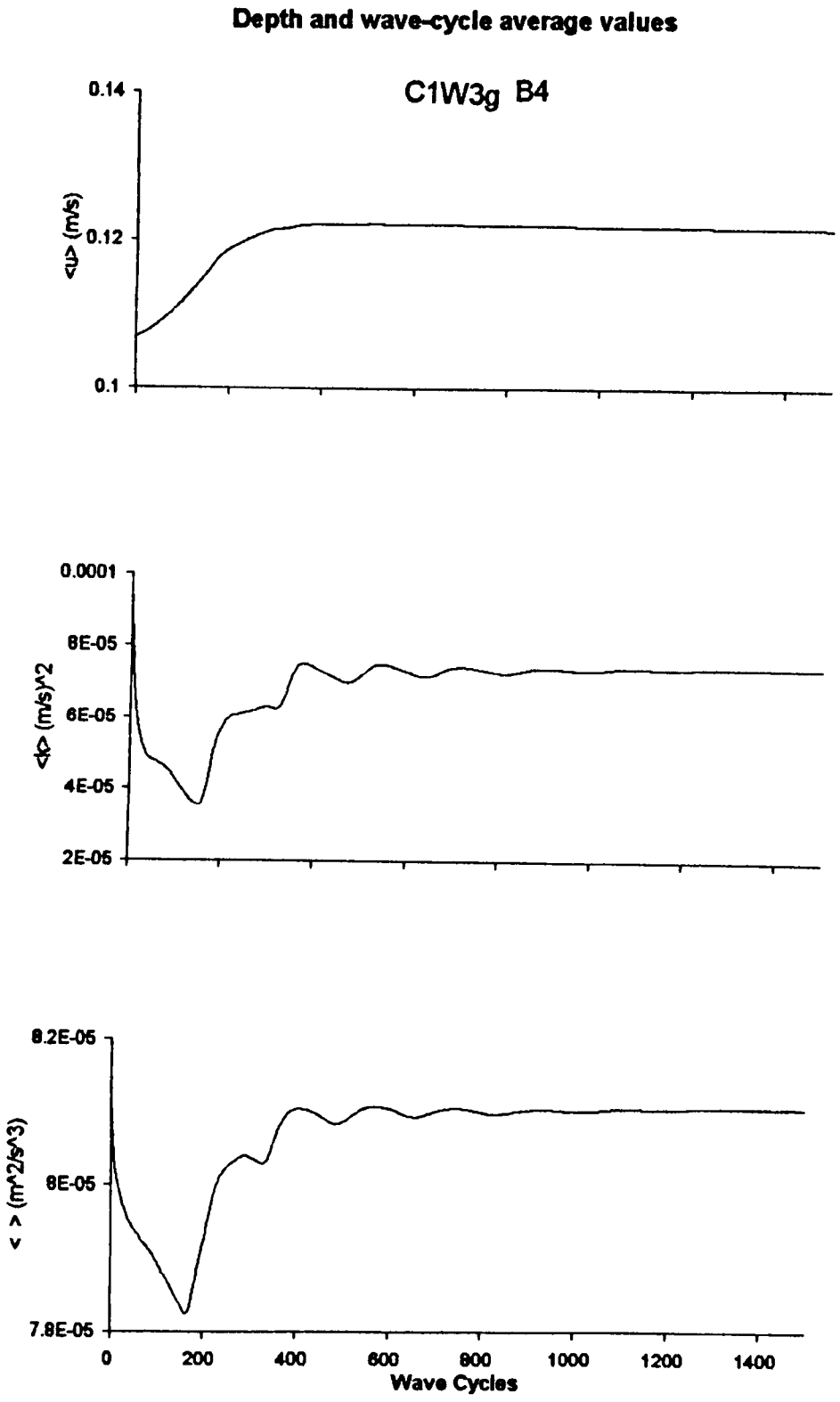

Figure 6.34: Test case C1W3g (B4) - Depth and wave-cycle averaged velocity, turbulent kinetic energy and dissipation rate - from C1W3 (B4) to convergence

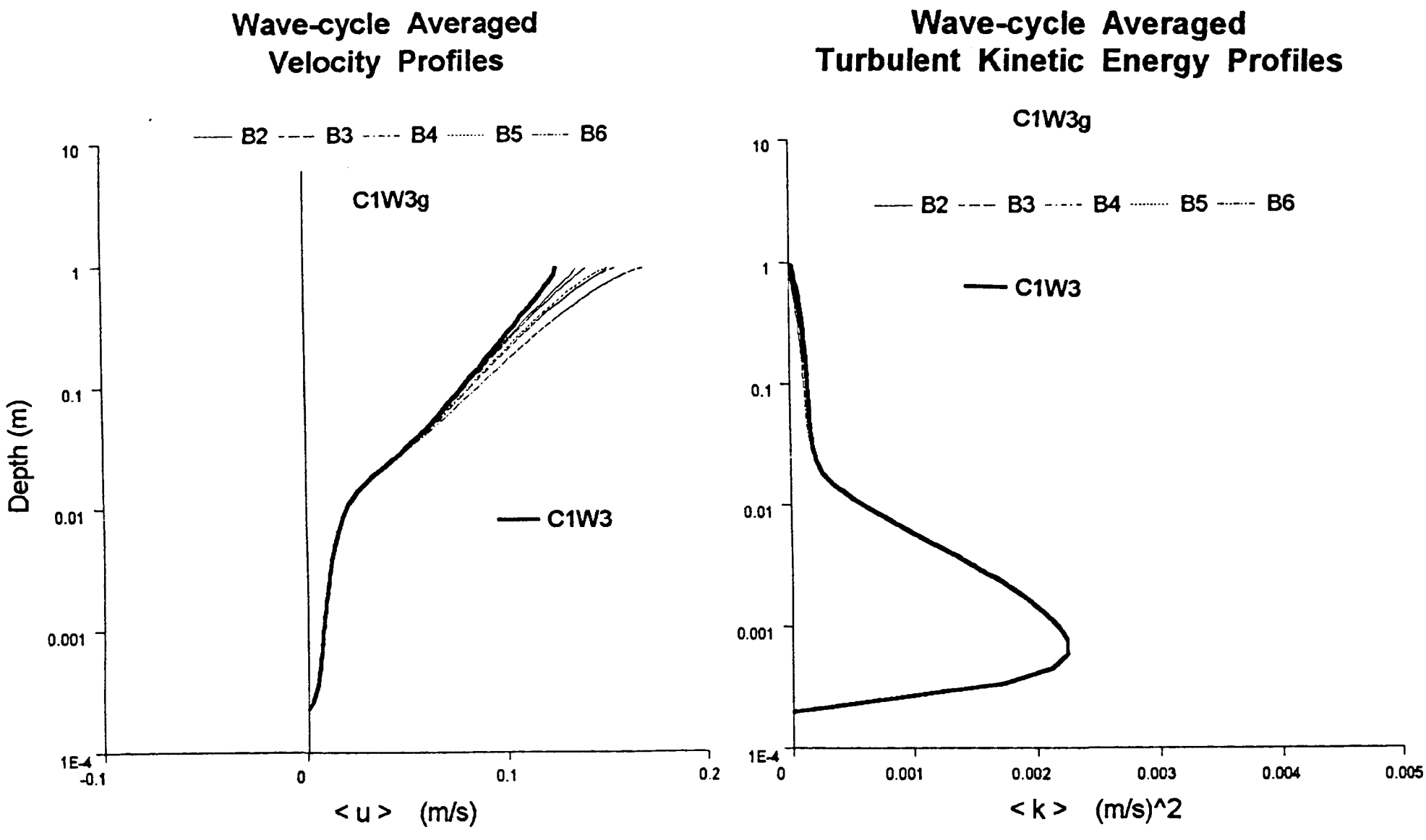

Figure 6.35: Test case C1W3g (B2-B6) - Converged wave-cycle averaged profiles of velocity and turbulent kinetic energy

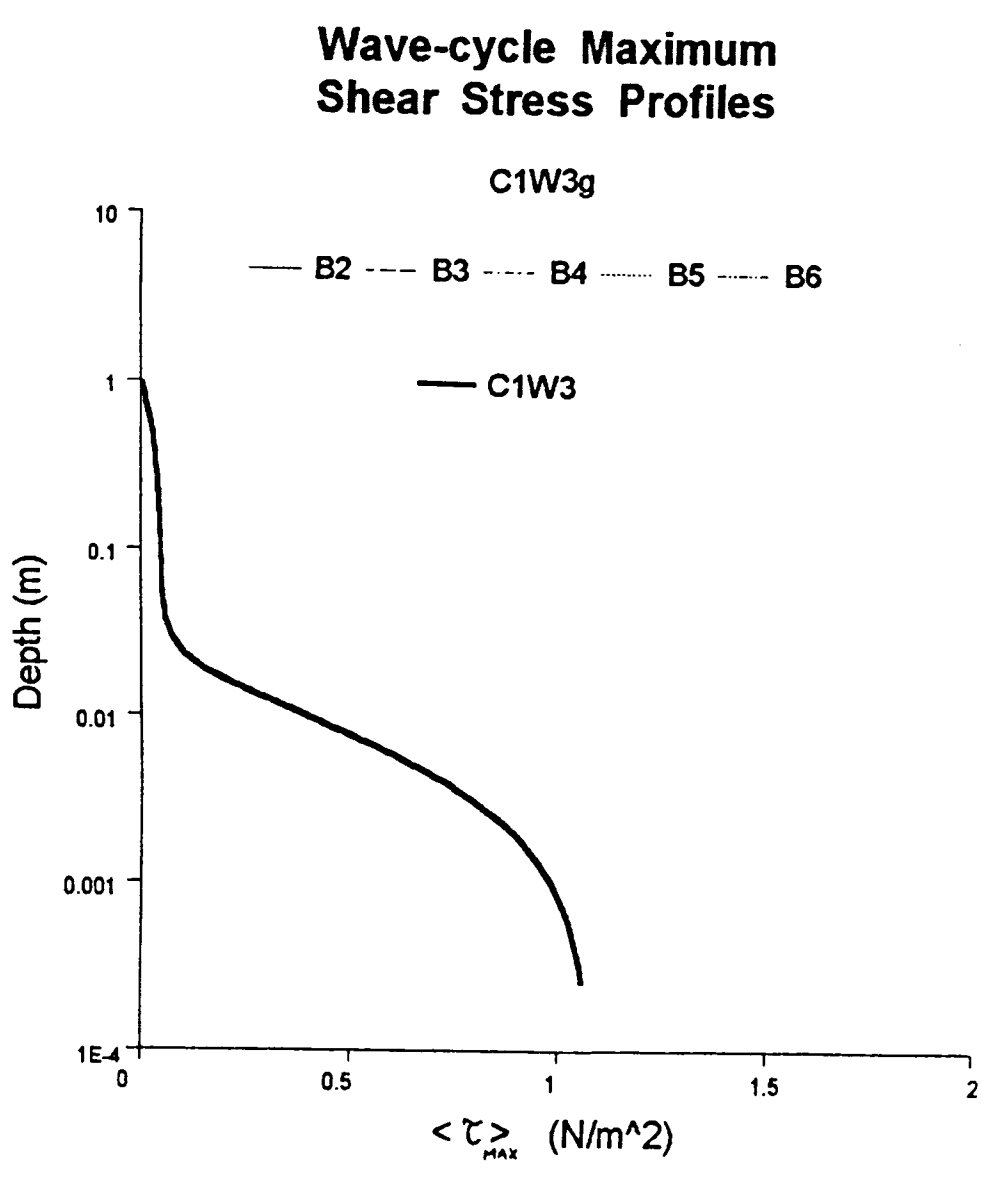

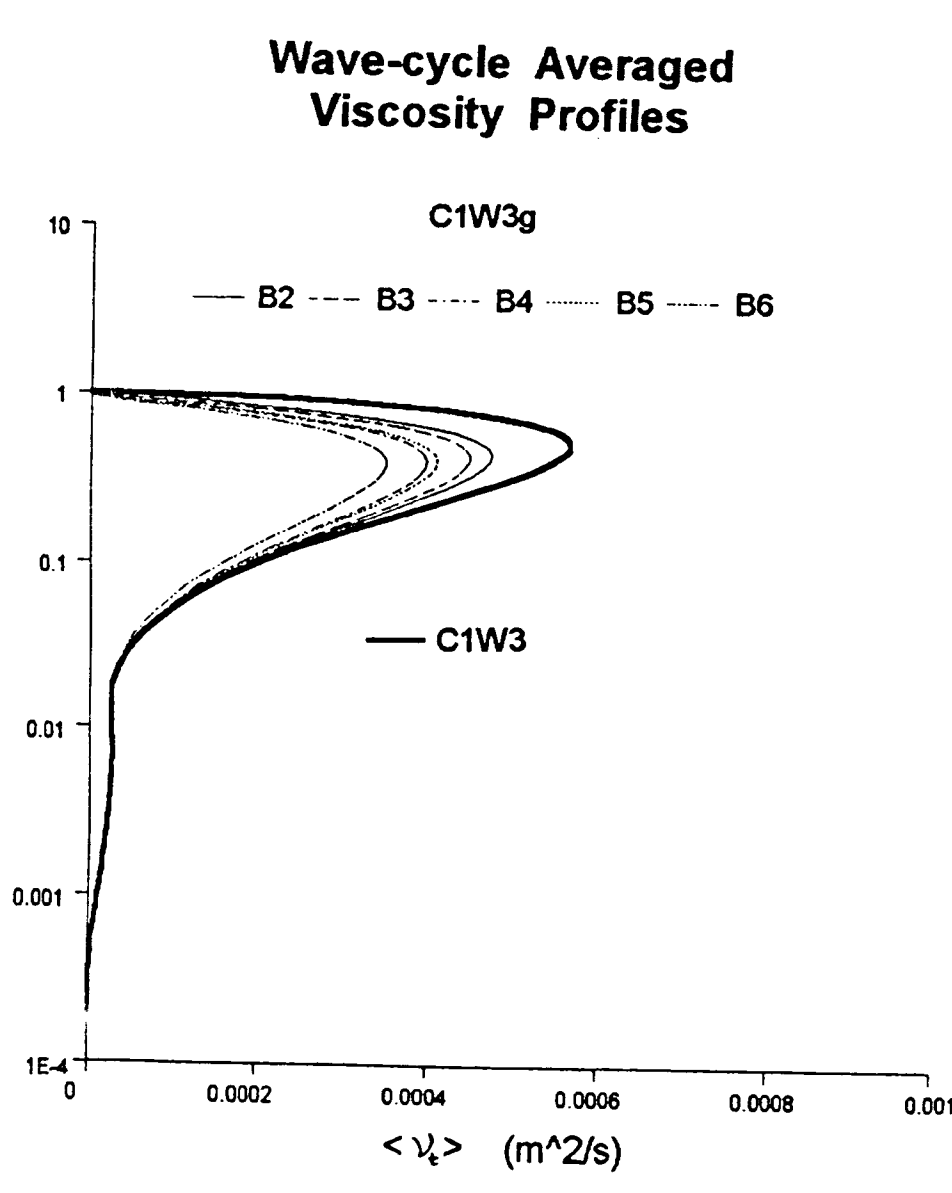

Figure 6.36: Test case C1W3g (B2-B6) - Converged wave-cycle averaged profiles of eddy viscosity and maximum shear stress in wave cycle

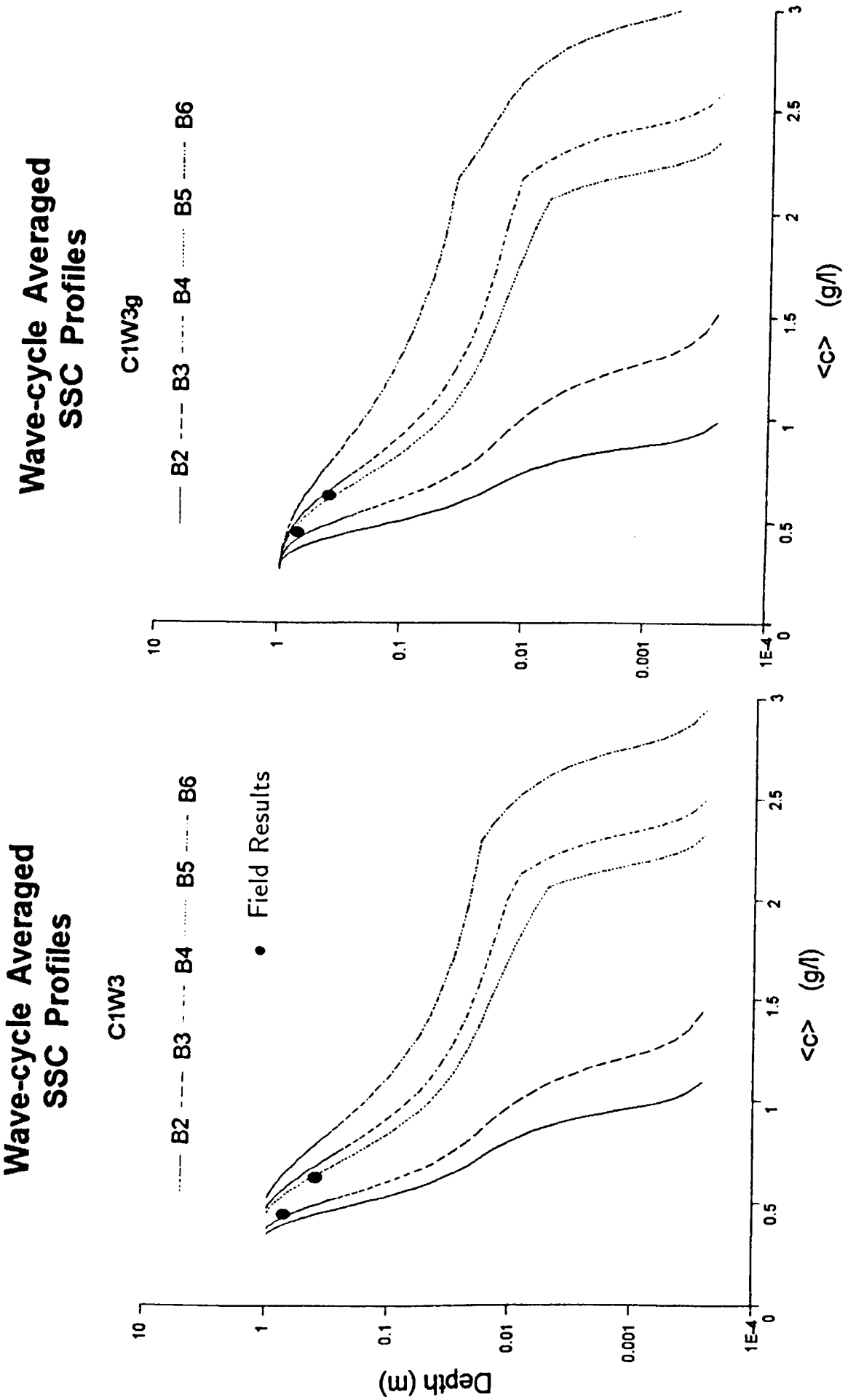

Figure 6.37: Test case C1W3 (B2-B6) and C1W3g (B2-B6) - Converged wave-cycle averaged profiles of SSC (includes SSC data from 11/93 field deployment)

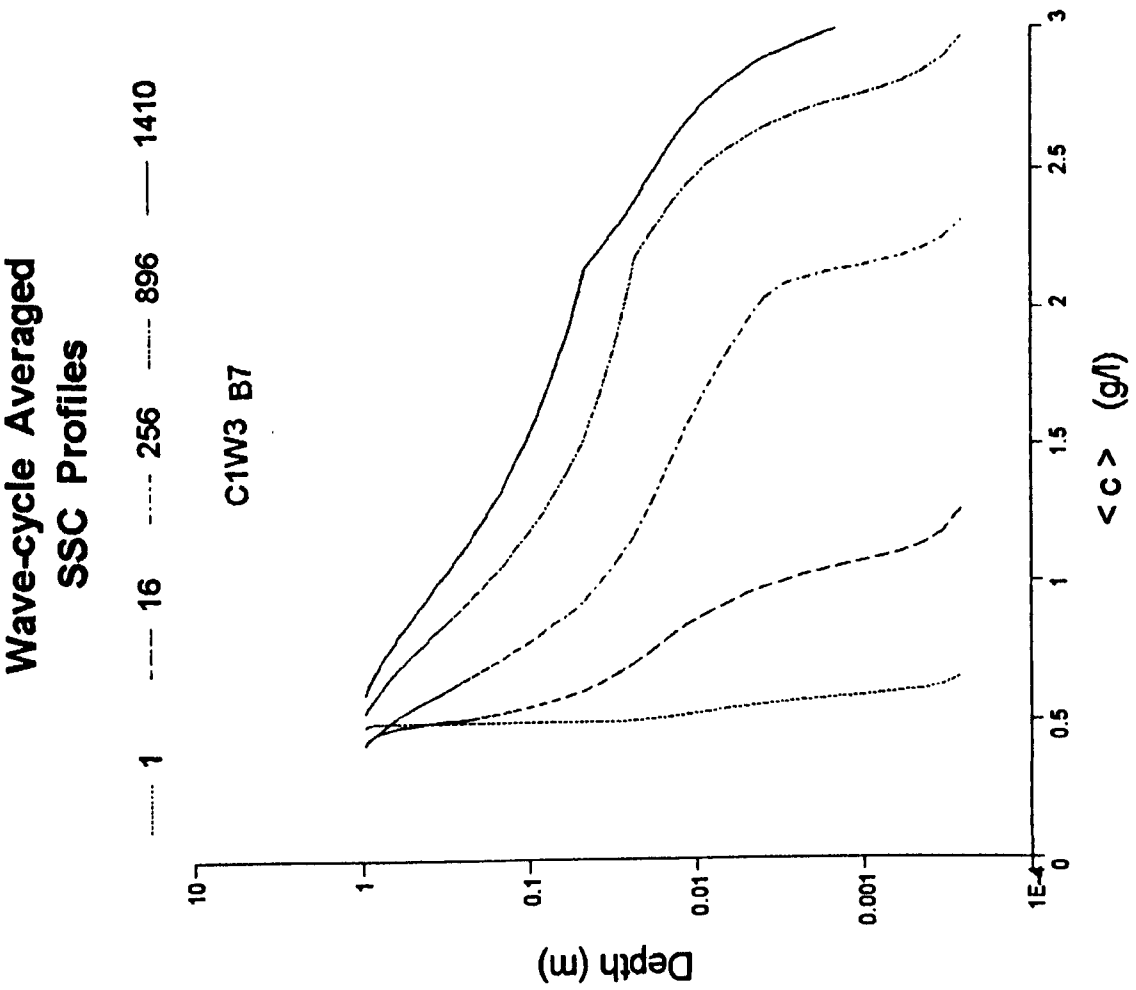

Figure 6.38: Test case C1W3 (B7) - Transient wave-cycle averaged profiles of SSC

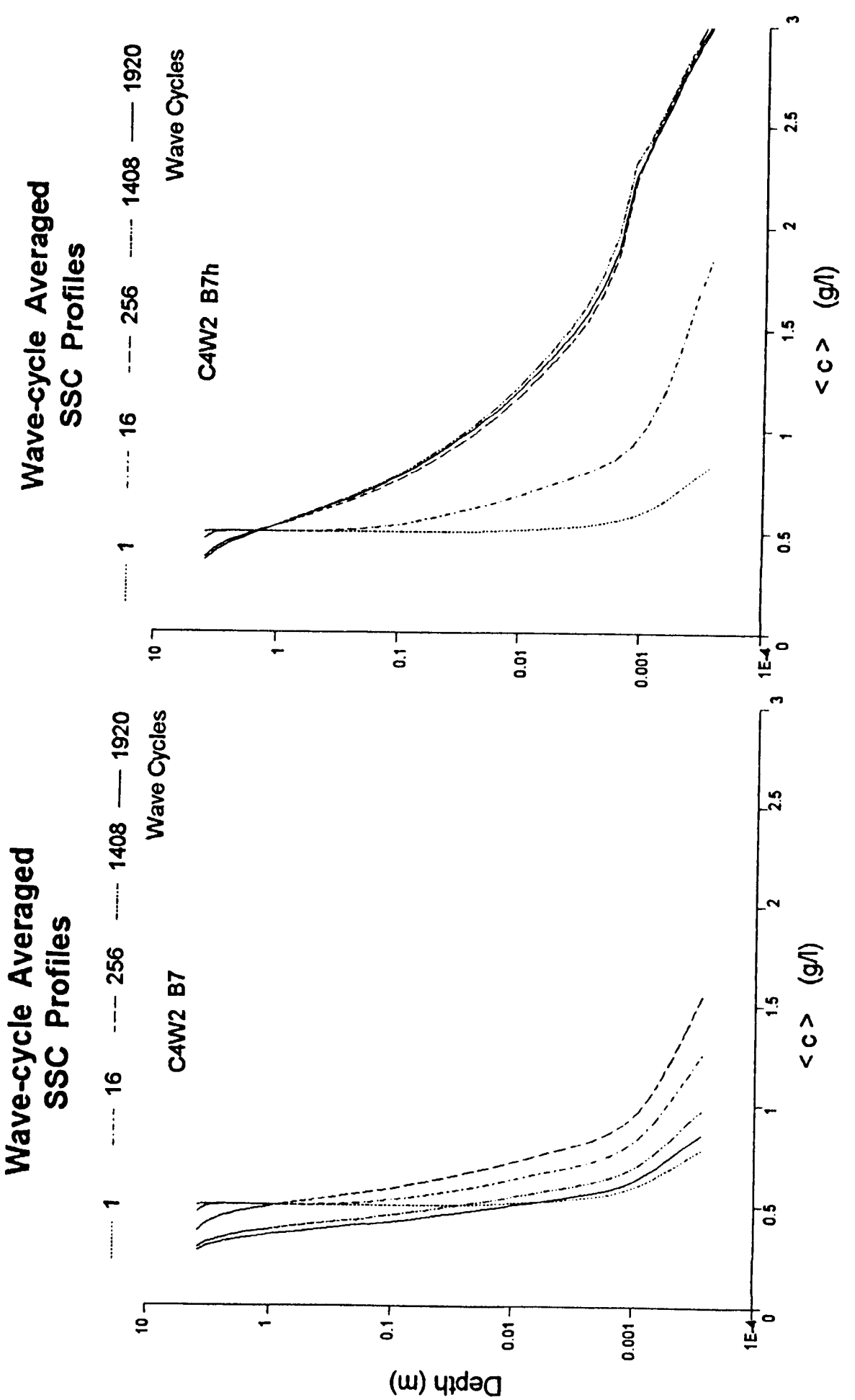

Figure 6.39: Test case C4W2 (B7 and B7h) - Transient wave-cycle averaged profiles of SSC (B7h retarded settling rate with same bed model parameters as B7)

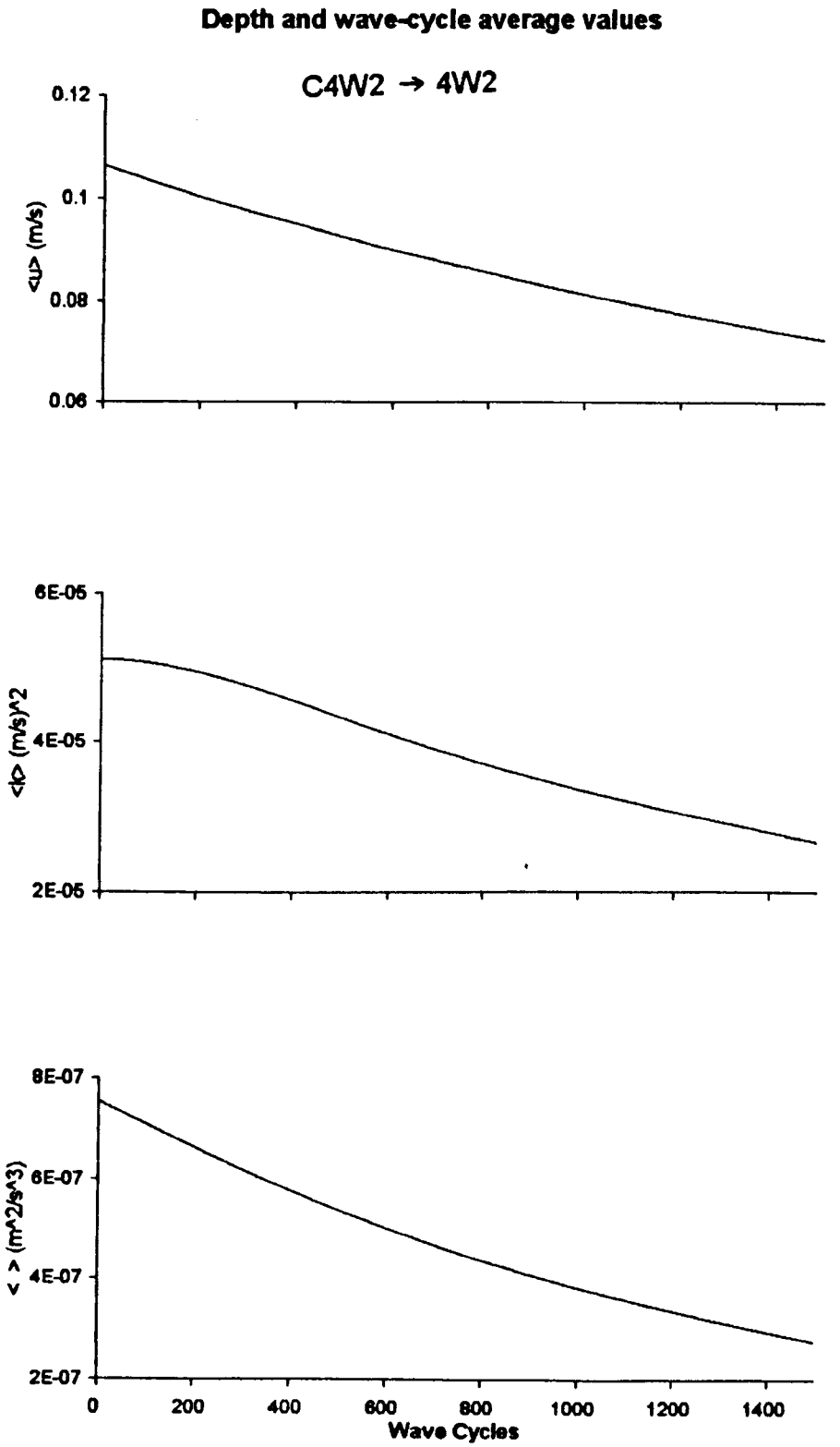

Figure 6.40: Test case C4W2 → 4W2 - Depth and wave-cycle averaged velocity, turbulent kinetic energy and dissipation rate (removing waves from wave-current case)

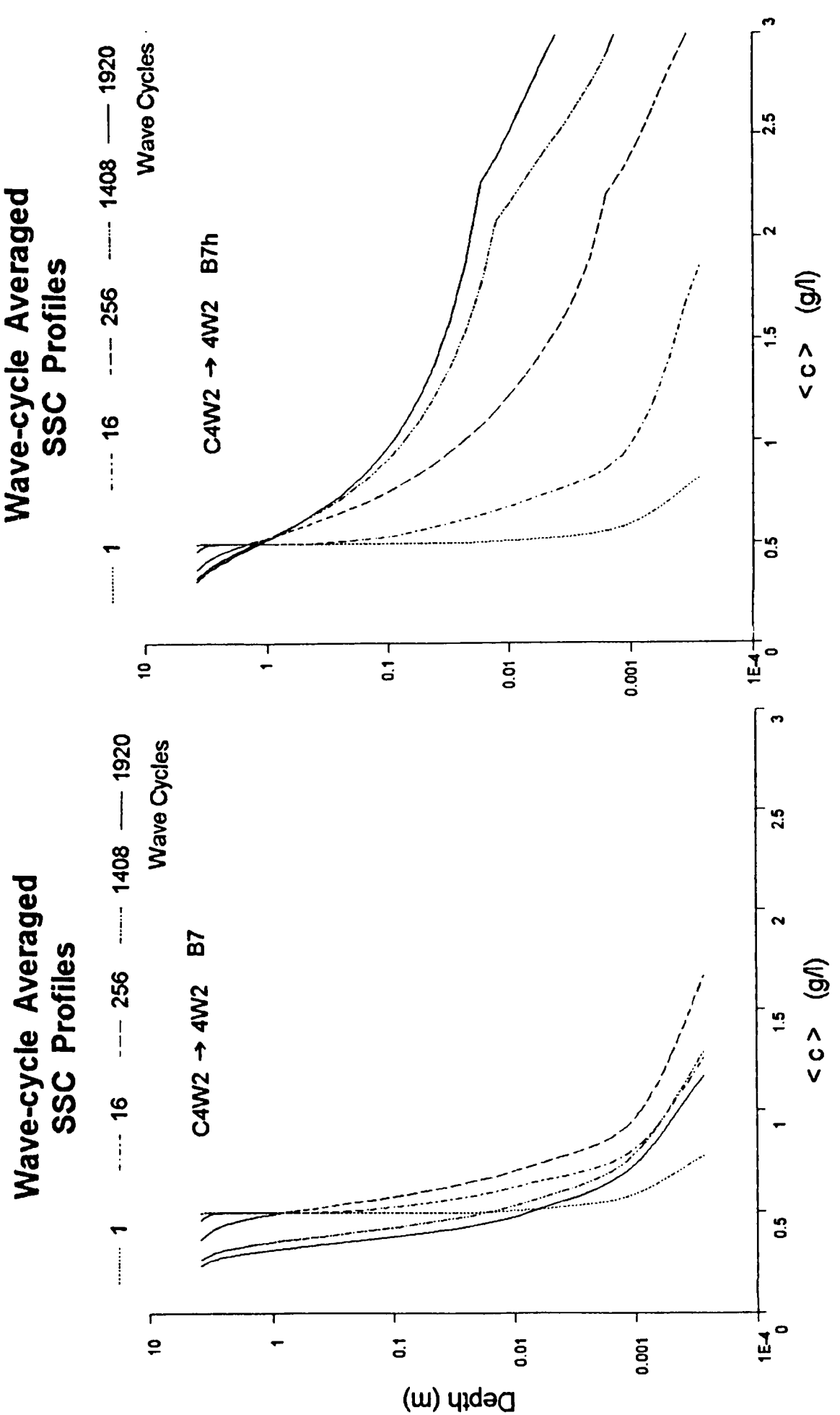

Figure 6.41: Test case C4W2 → 4W2 (B7 and B7h) - Transient wave-cycle averaged profiles of SSC (B7h retarded settling rate, with same bed model parameters as B7)

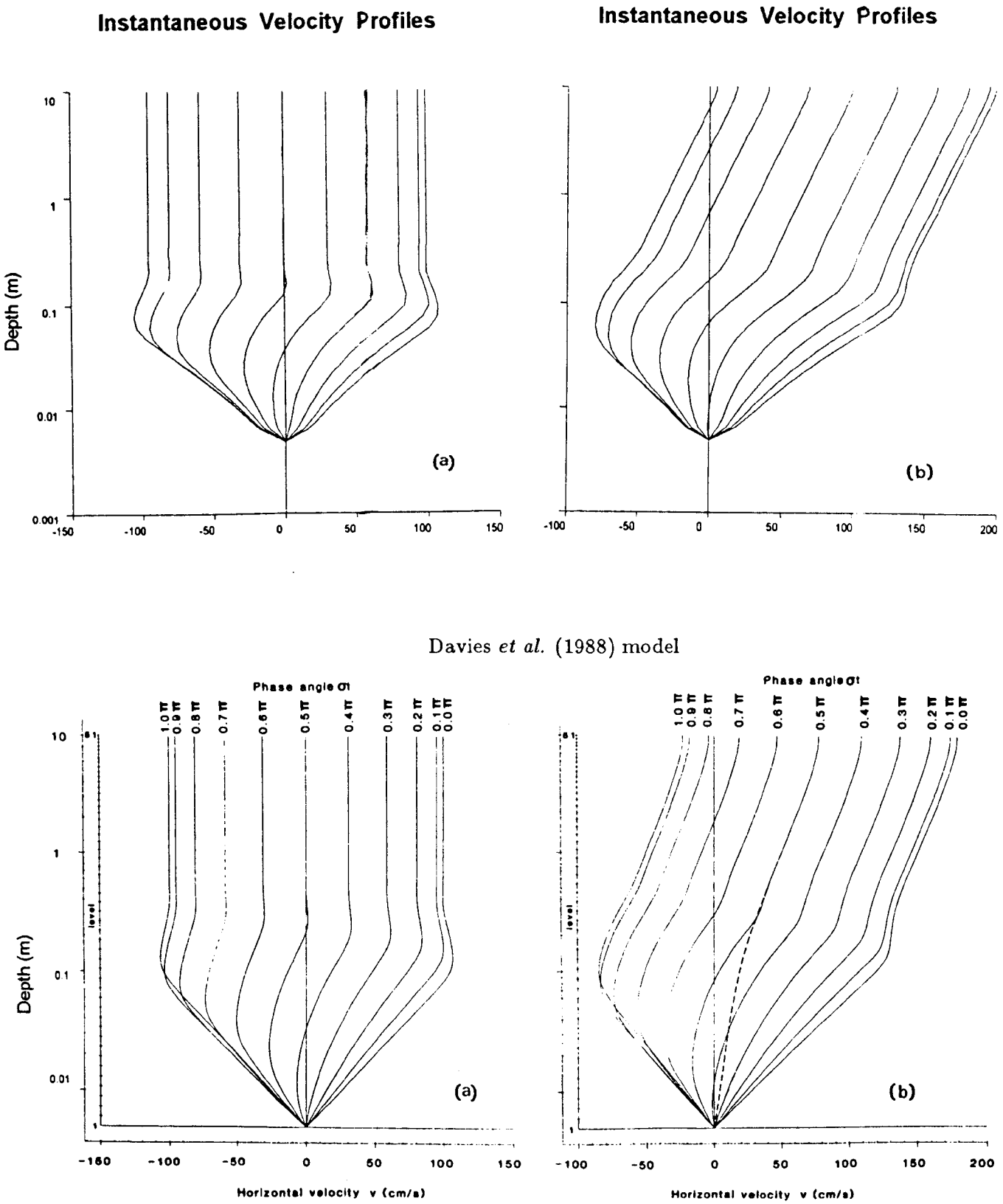

Figure 6.42: Vertical profiles of instantaneous velocity at ten phases through a wave cycle compared with Davies *et al.* (1988) model for a rough bed
(a) $U_o = 1.0\,m/s$, $\overline{u} = 0\,m/s$, (b) $U_o = 1.0\,m/s$, $\overline{u} = 1.0\,m/s$

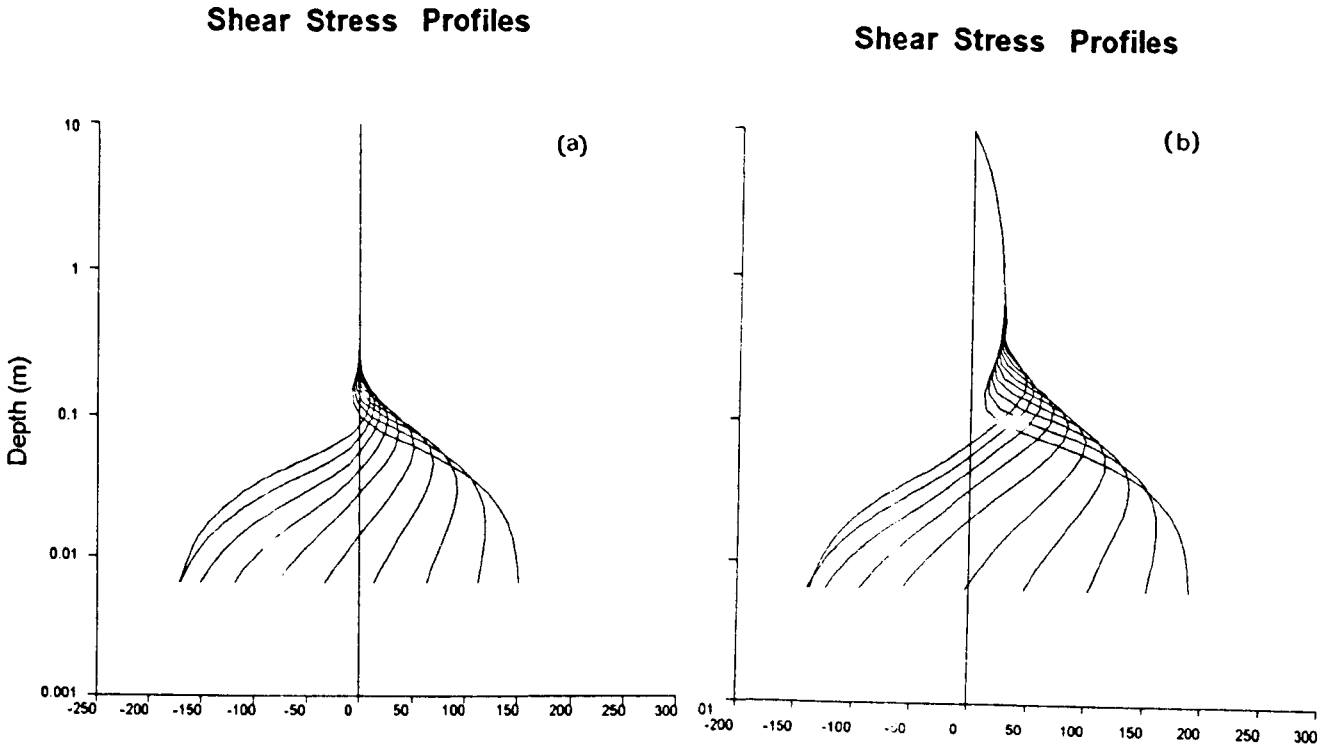

Davies *et al.* (1988) model

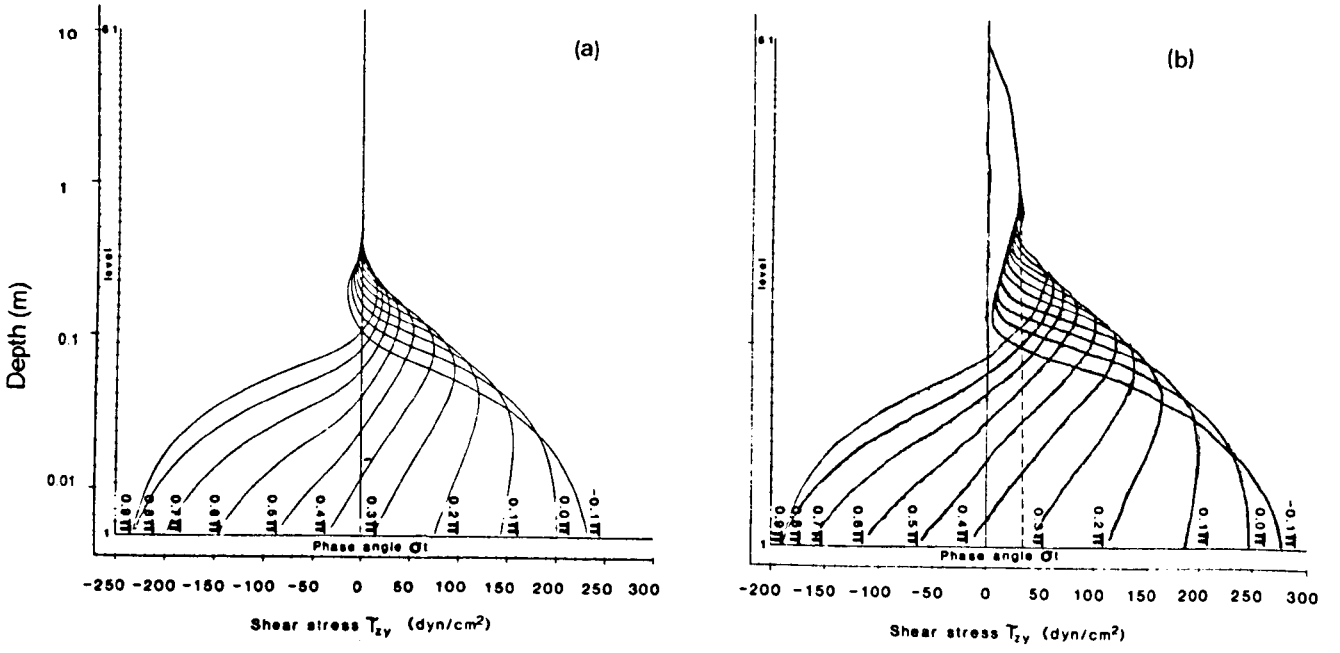

Figure 6.43: Vertical profiles of instantaneous shear stress at ten phases through a wave cycle compared with Davies *et al.* (1988) model for a rough bed
(a) $U_o = 1.0\,m/s$, $\overline{u} = 0\,m/s$, (b) $U_o = 1.0\,m/s$, $\overline{u} = 1.0\,m/s$

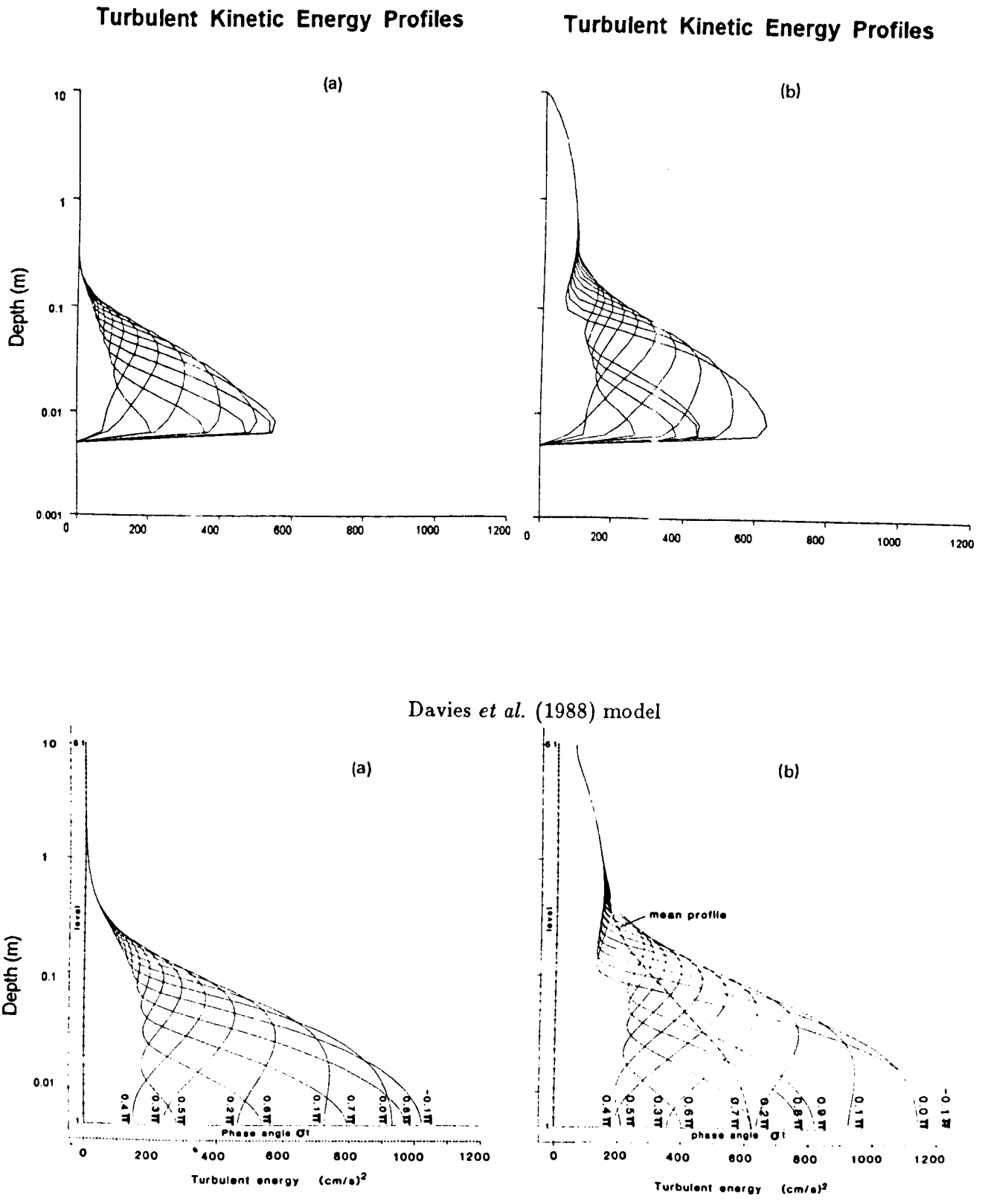

Figure 6.44: Vertical profiles of instantaneous turbulent kinetic energy at ten phases through a wave cycle compared with Davies *et al.* (1988) model for a rough bed (a) $U_o = 1.0\,m/s$, $\overline{u} = 0\,m/s$, (b) $U_o = 1.0\,m/s$, $\overline{u} = 1.0\,m/s$

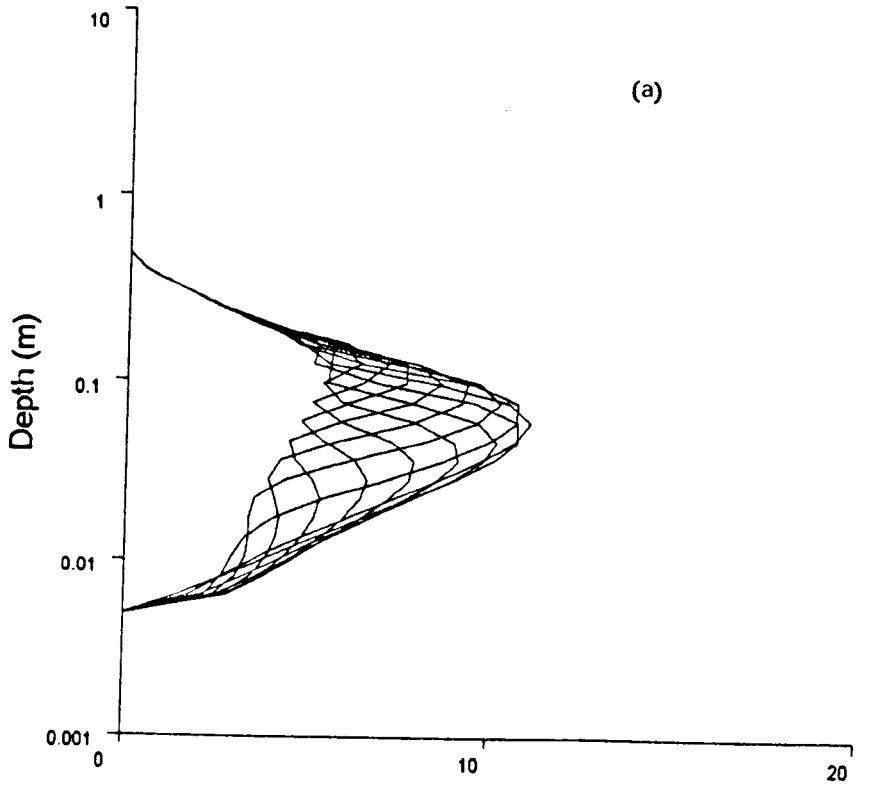

Davies *et al.* (1988) model

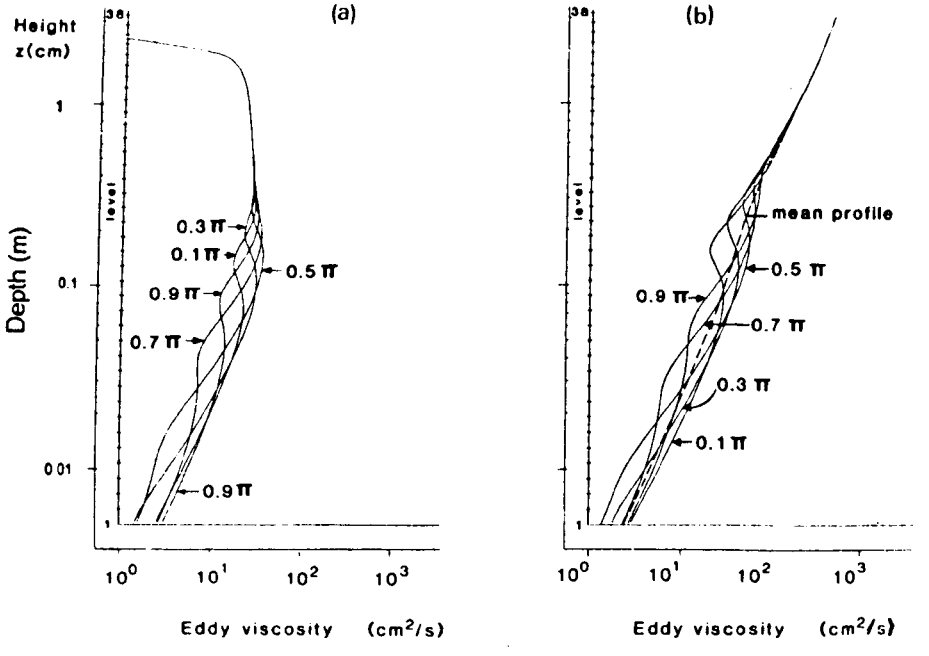

Figure 6.45: Vertical profiles of instantaneous eddy viscosity at ten phases through a wave cycle compared with Davies *et al.* (1988) model for a rough bed (below): (a) $U_o = 1.0\,m/s$, $\overline{u} = 0\,m/s$, (b) $U_o = 1.0\,m/s$, $\overline{u} = 1.0\,m/s$ (N.B. not all axes logarithmic)

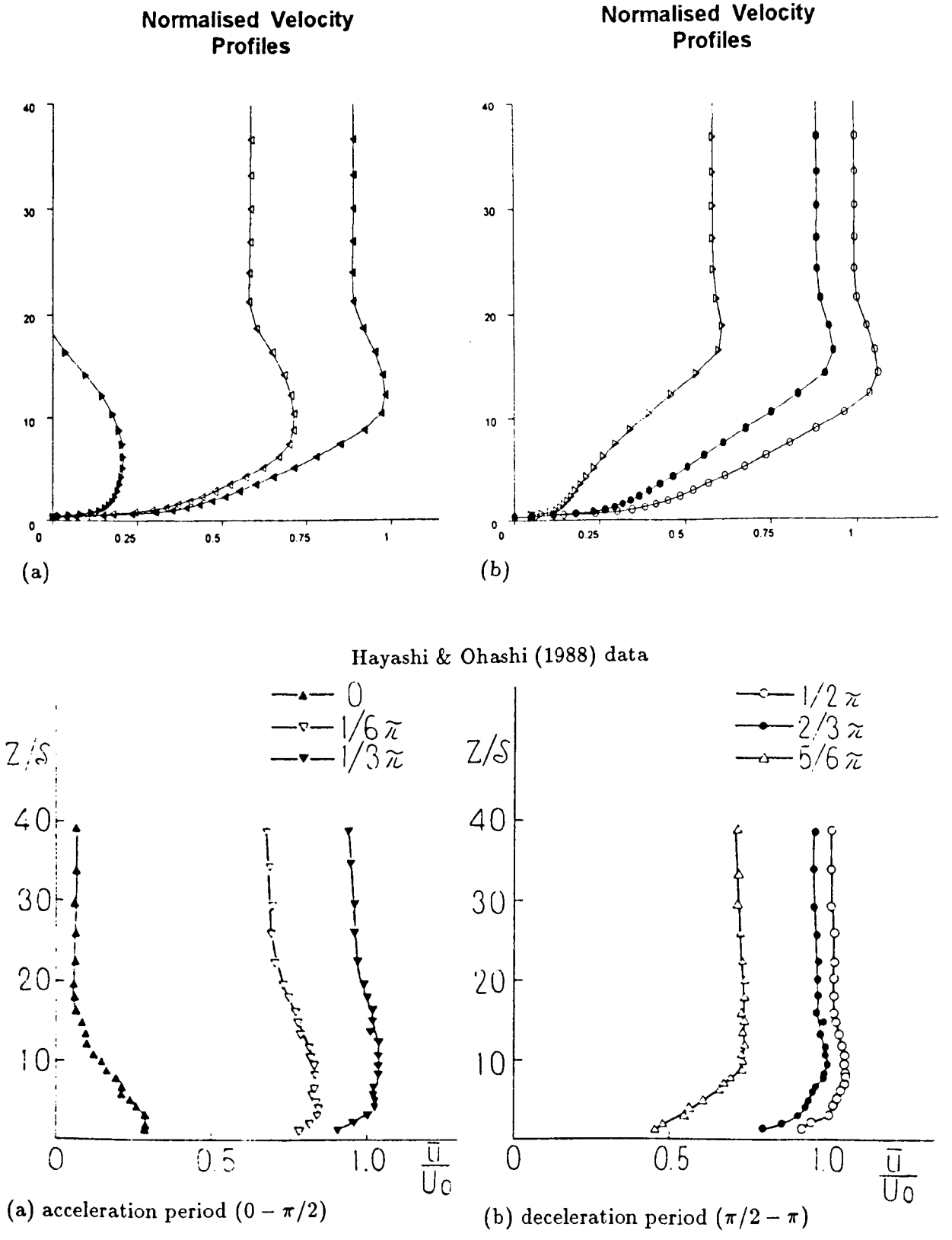

Figure 6.46: Vertical profiles of instantaneous velocity at six phases through a wave cycle compared with Hayashi & Ohashi (1988) data of purely oscillatory flow in a water tunnel

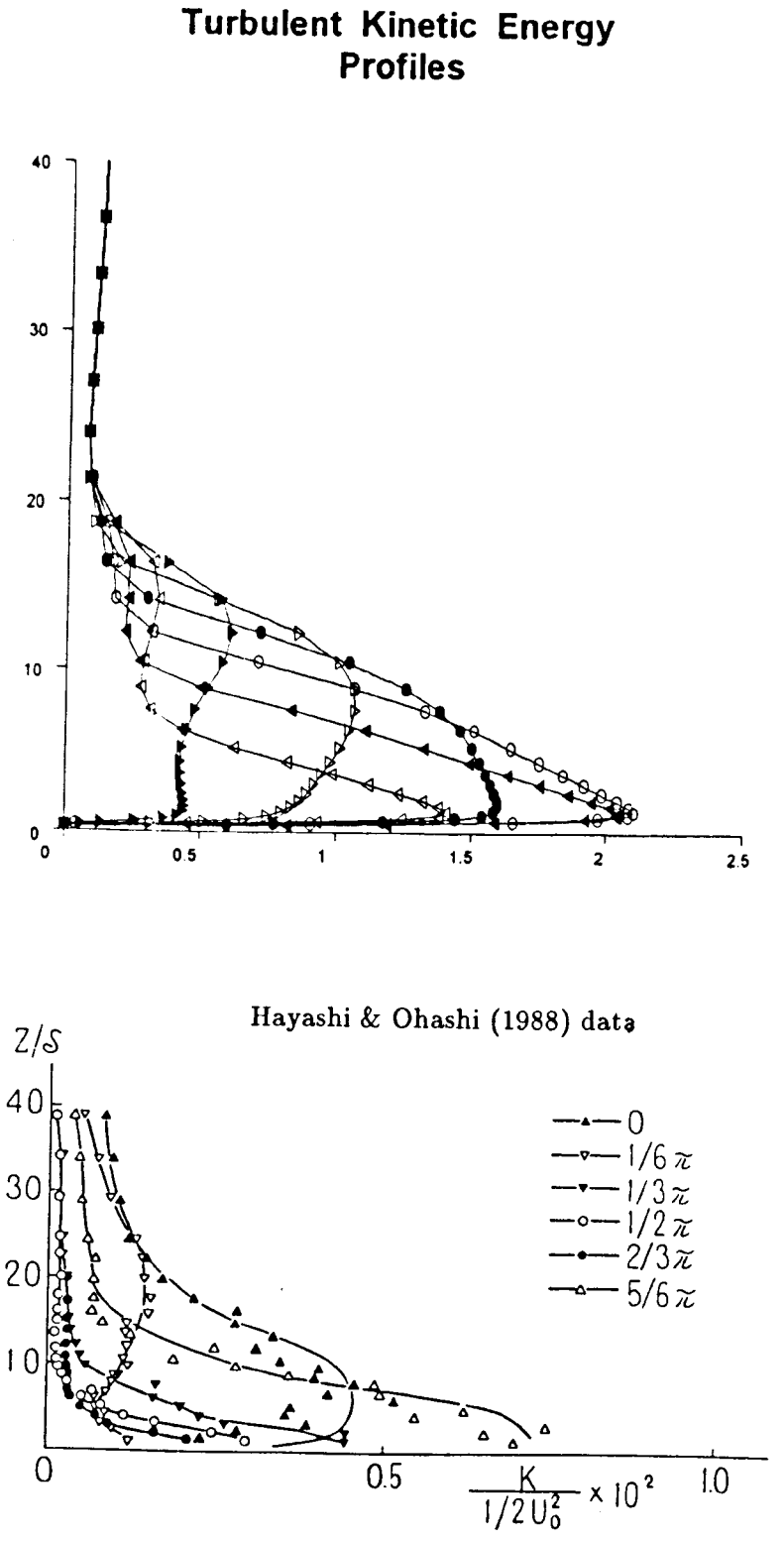

Figure 6.47: Vertical profiles of instantaneous turbulent kinetic energy at six phases through a wave cycle compared with Hayashi & Ohashi (1988) data for purely oscillatory flow in a water tunnel

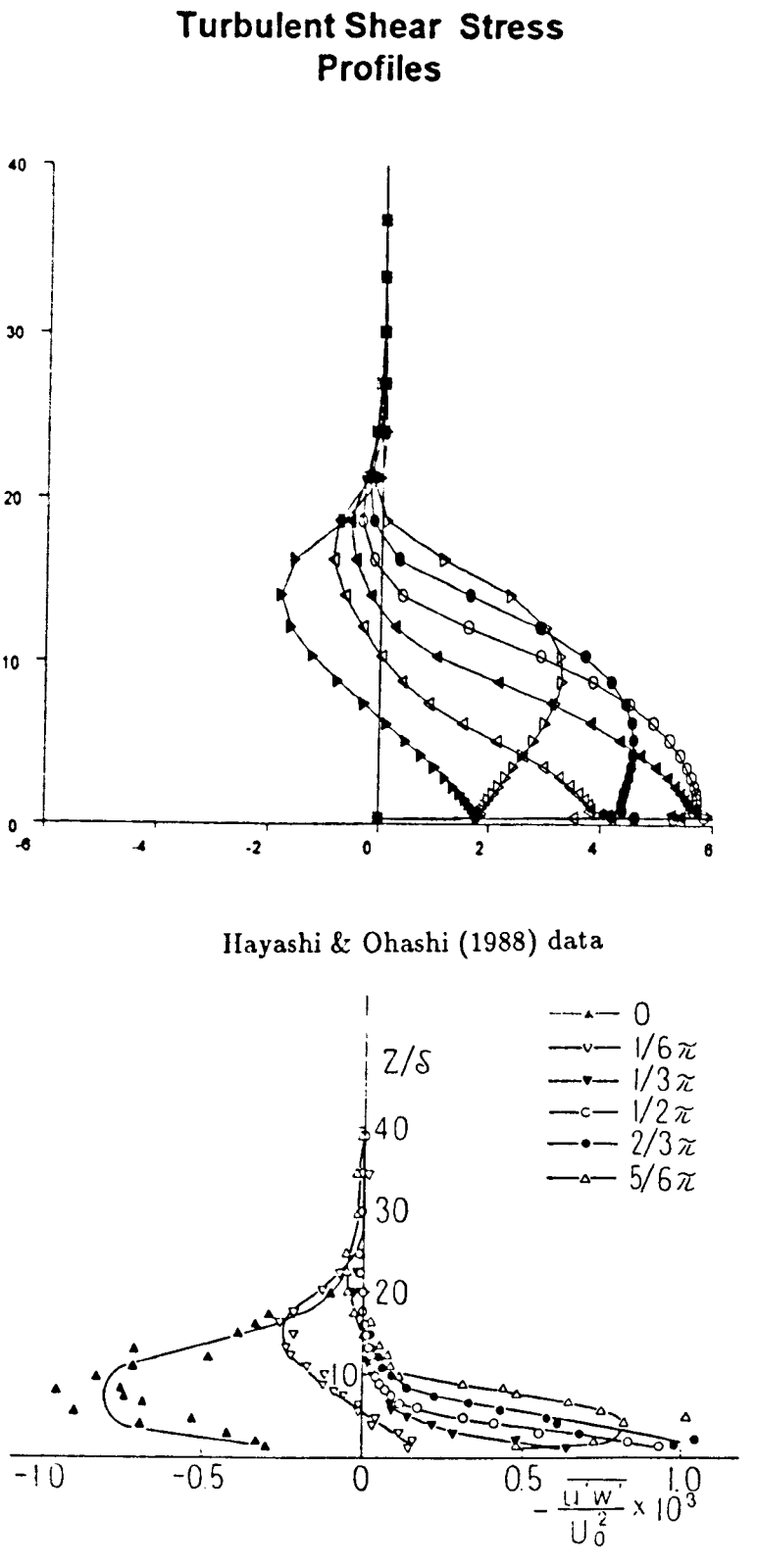

Figure 6.48: Vertical profiles of instantaneous shear stress at six phases through a wave cycle compared with Hayashi & Ohashi (1988) data for purely oscillatory flow in a water tunnel

References

Allen, J.R.L. (1987). Dessication of mud in the temperate intertidal zone: Studies from the Severn Estuary and Eastern England. *Phil. Roy. Soc. Lond.(B)*, **315**, p127–156.

Amos, C.L., Van Wagoner, N.A. & Daborn, G.R. (1988). The influence of subaerial exposure on the bulk properties of fine–grained intertidal sediment from Minas Basin, Bay of Fundy. *Est. Coast & Shelf Sci.*, **27**, p1–13.

Amos, C.L. (1974). Intertidal flat sedimentation of the Wash, E. England. *Unpubl. PhD. thesis, Univ. of London.*

Anderson, F.E., Black, L., Watling, L.E., Mook, W. & Mayer, L.M. (1981). A temporal and spatial study of mudflat erosion and deposition. *J. Sedim. Pet.* **51**, p729–736.

Ariathurai, R. & Krone, R.B. (1976). Mathematical modelling of sediment transport in estuaries. In: Wiley, M. (Ed.) *Estuarine Processes II: Circulation, sediments and transfer of material in the estuary. Acamemic Press*, p98–106.

Aydin, I. & Shuto, N. (1989). An application of the k-ε model to oscillatory boundary layers. *Coastal Eng. in Japan*, **30**(2), p11–24.

Bagnold, R.A. (1946). Motion of waves in shallow water. Interaction between waves and sand bottoms. *Proc. Roy. Soc. London*, **Ser. A, 187**, p1–18.

Bakker, W.T. & van Doorn, T. (1979). Near-bottom velocities in waves with a current. *Proc. 16th Coastal Eng. Conf.*, ASCE, p1394.

Barton, M.L. (1991). Cohesive Sediment Transport Processes in the Tamar Estuary. *Unpubl. PhD thesis, Univ. of Birmingham, England.*

Baum, E. & Coponi, E.A. (1992). Modeling the effects of buoyancy on the evolution of geophysical boundary layers. *J. Geophys. Res.*, **97** (C10), p15513–15527.

Black, K. (1991). The erosion characteristics of cohesive estuarine sediments: some *in situ* experiments and observations. *Unpubl. PhD. thesis, Univ. of Wales.*

Brekhovskikh, V.F. *et al.* (1991). Erosion of cohesive bottom sediments: The influence of benthos. *J. Hydr. Res.*, **29**(2), p149.

Brors, B. & Eidsvik, K.J. (1992a). Dynamic Reynolds Stress Modelling of Turbidity Currents. *J. Geophys. Res.*, **97**(C6), p9645–9652.

Brors, B. & Eidsvik, K.J. (1992b). Oscillatory boundary layer flows modelled with dynamic Reynolds stress turbulence closure. *J. Geophys. Res.*

Calverley, M. (1991). A water quality model of the Blackwater Estuary. *Unpubl. PhD thesis, Univ. of Birmingham, England.*

Celik, I. & Rodi, W. (1984). Simulation of free-surface effects in turbulent channel flows. *Phys. Chem. Hydrodyn.*, **5**(3/4), p217–231.

Celik, I. & Rodi, W. (1988). Modelling suspended sediment transport in nonequilibrium situations. *J. Hydr. Eng.*, **114**(10), p1157–1188.

Chien, K.Y. (1982). Predictions of channel and boundary layer flows with a low Reynolds number turbulence model. *AIAA J.*, **20**(1), p33–38.

Chriss, T.M. & Caldwell, D.R. (1982). Evidence for the influence of form drag on bottom boundary layer flow. *J. Geophys. Res.*, **87** (C6), p4148–4154.

Cokelet, E.D. (1977). Steep gravity waves in water of arbitrary uniform depth. *Philos. Trans. Roy. Soc.*, **Ser. A, 286**, p183–230.

Cooker, M.J. & Peregrine, D.W. (1991). Wave breaking and wave impact pressures. In: Peregrine, D.H. & Loveless, J.H. (Eds.) *Developments in Coastal Engineering, Univ. Bristol.*

Coulson, C.A. (1944). Waves (3rd Edition). *Publ. Oliver and Boyd, Edinburgh.*

Christoffersen, J.B. & Jonsson, I.G. (1985). Bed friction and dissipation in a combined wave and current motion. *Ocean Eng.*, **12**(5), p387–423.

Dalrymple and Liu (1978). Waves over soft muds: a two-layer model. *J. Phys. Oceanogr.*, **8**, p1121–1131.

Darbyshire, E. (1991). Vertical turbulent transport in the Tamar Estuary. *Unpubl. PhD*

thesis, Univ. of Birmingham, England.

Davies, A.G. (1983). Wave interactions with rippled sand beds. In: Johns, B. (Ed.) *Physical Oceanography of Coastal and Shelf Seas.* Elsvier Oceanography Series, **35**, p1–65.

Davies, A.G. (1986). A numerical model of the wave boundary layer. *Cont. Shelf Res.*, **6**(6), p715–739.

Davies, A.G. (1990a). Modelling the vertical distribution of suspended sediment in combined wave-current flow. In: Prandle (Ed.) *Dynamics and Exchanges in Estuaries and the Coastal Zone*, American Geophysical Union.

Davies, A.G. (1990b). A model of the vertical structure of the wave and current boundary layer. In: Davies, A.M. (Ed.) *Modeling Marine Systems*, CRC Press, Boca Raton, Florida, **2**, p263–297.

Davies, A.G. (1991). Transient effects in wave-current boundary layer flow. *Ocean Engng.*, **18**(1/2), p75–100.

Davies, A.G. and Jones, J.E. (1991). On the numerical solution of the turbulence energy equations for wave and tidal flows. *Int. J. Num. Met. Fluids*, **12**, p17–41.

Davies, A.G., Soulsby R.L. and King, H.L. (1988). A numerical model of the combined wave and current bottom boundary layer. *J. Geophys. Res.*, **93**(C1), p491–508.

Dean, R.G. (1970). Relative validities of water wave theories. *Proc. ASCE. J. Waterway, Port, Coastal and Ocean Eng. Div.*, **96**(WW1), p105–119.

Delo, E.A. & Ockenden, M.C. (1992). Estuarine Muds Manual. HR Report SR301.

Devries, J.W. (1992). Field measurements of the erosion of cohesive sediments. *J. Coastal Res.*, **8**(2), p312-318.

Driver, J.S. & Pitt, J.D. (1979). Wind and wave relationship in a shallow water area. *Proc. 14th Coastal Eng. Conf.*, ASCE, **1**, p148–163.

Dyer, K.R. (1989). Sediment processes in estuaries: Future research requirements. *J. Geophys. Res.*, **94**(C10), p14327–14339.

Dyer, K.R. (1986). Coastal and Estuarine Sediment Dynamics. *Publ. J. Wiley & Sons Ltd.*

Eidsvik, K.J. & Brors, B. (1989). Self-accelerated turbidity current prediction based upon

($k - \varepsilon$) turbulence. *Cont. Shelf Res.*, **9**, p617–627.

Einstein, H.A. & Krone, R.B. (1962). Estuarial sediment transport patterns. *J. Hyd. Div., Proc. ASCE*, **87**, p51–59.

Ellison, T.H. (1966). A note on the influence of density stratification on turbulence. *See: Turner, J.S. (1973). Buoyancy effects in fluids.*

Evans, G. (1965). Intertidal flat sediments and their environment of deposition in the Wash. *Q. J. Geol. Soc. Lond.*, **121**, p209–245.

Fennesy, M.J., Dyer, K.R. & Huntley, D.A. (1993). Size/settling velocity spectra of flocs in the Tamar Estuary over a tidal cycle. *Submitted for Publ. Proc. ECSA-23 Symp.: Particles in Estuaries and Coastal Waters, to be in: Netherlands J. Aquatic Ecology*, **28**, 1994.

Fredsoe, J. (1984). The turbulent boundary layer in wave-current motion. *J. Hydr. Engg.*, **110**(8), p1103–1120.

Fredsoe, J. & Deigaard, R. (1992). Mechanics of coastal sediment transport. *Publ. World Scientific Publ. Co. Pte. Ltd.*, Singapore.

Freeman, D.P. (1992). Cohesive sediment transport on an intertidal zone. *Unpubl. MPhil. thesis, Univ. of Birmingham, England.*

Galvin, C.J. (1972). Wave breaking in shallow water. In: Meyer, R.E. (Ed.) *Waves on beaches and resulting sediment transport.* Academic Press, p413–456.

Grace, R.A. (1978). Surface wave heights from pressure records. *Coastal Eng.*, **2**, p55–67.

Grant, W.D. & Madsen, O.S. (1979). Combined wave and cuerrent interaction with a rough bottom. *J. Geophys. Res.*, **84**(C4), p1797–1808.

Grant, W.D. & Madsen, O.S. (1982). Movable bed roughness in unsteady oscillatory flow. *J. Geophy. Res.*, **87**, p469–481.

Grant, W.D. & Madsen, O.S. (1986). The continental-shelf bottom boundary layer. *Ann. Rev. Fluid Mech.*, **18**, p265–305.

Hagatun, K. & Eidsvik, K.J. (1986). Oscillating turbulent boundary layers with suspended sediment. *J. Geophys. Res.*, **91**(C11), p13045–13055.

Hayashi, T. & Ohashi, M.A. (1982). A dynamical and visual study on the oscillatory turbulent

boundary layer. *Turbulent Shear Flows*, Springer-Verlag, p13–33.

Hayes, D.M. (1991). Suspension of sand due to wave groups. *J. Geophy. Res.*, **96**, p8911–8915.

Hayter, E.J. (1986). Estuarial sediment bed model. In : Mehta, A.J. (Ed.) *Estuarine cohesive sediment dynamics : Lecture notes on coastal and estuarine studies*, **14**, Springer–Verlag, p326–359.

Hayter, E.J. & Mehta, A.J. (1986). Modelling cohesive sediment transport in estuarial waters. *Appl. Math. Modelling*, **10**, p294–303.

Hedges, T.S. & Lee, B.W. (1992). The equivalent uniform current in wave-current computations. *Coastal Eng.*, **16**, p301–311.

Heinzelmann, C.H. & Wallisch, S. (1991). Benthic settlement and bed erosion. A review. *J. Hydr. Res.*, **29**(3), p355.

Hinze, O. (1959). Turbulence. *Publ. McGraw Hill, New York.*

Housley, J.G. & Taylor, D.C. (1957). Application of solitary wave theory to shoaling oscillatory waves. *Trans A.G.U.*, **38**(1).

Huntley, D.A. (1988). A modified inertial dissipation method for estimating seabed stresses at low Reynolds numbers, with application to wave/current boundary layer measurements. *J. Phys. Oceanogr.*, **18**, p339–346.

Hydraulics Research Station (1984). Waves Upstream of the Severn Barrage. HR Report, EX1207.

Hydraulics Research Station (1981). The Severn Estuary. HR Report, EX966.

Iwagaki, Y. & Kakinuma, T. (1967). On the bottom friction factors off five Japanese coasts. *Coastal Eng. Jpn*, **10**, p13–22.

Jiang L. & Zhao, Z. (1989). Viscous damping of solitary waves over fluid mud sea-beds. *J. Waterway, Port, Coastal and Ocean Eng.*, ASCE, **115**, p345.

Johns, B. (1977). Residual flow and boundary shear stress in the turbulent bottom boundary layer beneath waves. *J. Phys. Oceanogr.*, **7**, p733–738.

Johns, B. (1978). The modelling of tidal flow in a channel using a turbulence energy closure scheme. *J. Phys. Oceanogr.*, **8**, p1042–1049.

Jonsson, I.G. (1966). Wave boundary layers and friction factors. *Proc. 10th Coastal Eng. Conf.*, ASCE, p127–148.

Jonsson, I.G. (1967). The friction factor for a current superimposed by waves. *Progress rep. 11, Coast Engg. lab.*, Tech. Univ. Denmark.

Jonsson, I.G. & Carlson, N.A. (1976). Experimental and theoretical investigations in an oscillatory boundary layer. *J. Hydraul. Res.*, **14**, p45–60.

Justesen, P. (1988). Prediction of Turbulent Oscillatory Flow over Rough Beds. *Coastal Eng.*, **12**, p257–284.

Kajiura, K.(1968). A model of the bottom boundary layer in water waves. *Bull. Earthquake Res. Inst.*, **46**, p75–123.

Kamphuis, J.W. (1980). Influence of sand or gravel on the erosion of cohesive sediment. *J. Hyd. Res.*, **28**, p43–53.

Kana, T.W. (1977). Suspended sediment transport at Price Inlet, South Carolina. *Proc. Coastal Sediments 1977*, ASCE, p366–382.

Kana, T.W. & Ward, L.G. (1979). Nearshore suspended sediment load during storm and post-storm conditions. *Proc. 17th Coastal Eng. Conf.*, ASCE, p1158–1173.

Kandiah, A. (1974). Fundamental aspects of surface erosion of cohesive soils. *PhD thesis, Univ. of California, Davis.*

Kemp, P.H. & Simons, R.R. (1982). The interaction between waves and a turbulent current: waves propagating with the current. *J. Fluid Mech.*, **116**, p227–250.

Kemp, P.H. & Simons, R.R. (1983). The interaction between waves and a turbulent current: waves propagating against the current. *J. Fluid Mech.*, **130**, p73–89.

Kirby, R. (1988). High concentration suspension (fluid mud) layers in estuaries. In: Dronkers, J. & Leussen van, W. (Eds.) *Physical processes in estuaries*, Springer–Verlag, p463–487.

Komar, P.D. (1983). Nearshore currents and sand transport on beaches. In: Johns, B. (Ed.) *Physical Oceanography of Coastal and Shelf Seas.* Elsvier Oceanography Series, **35**, p67–110.

Krone, R.B. (1972). A field study of flocculation as a factor in estuarial shoaling processes: A final report. *U.S. Army Corps of Eng., Comm. Tidal Hydr., Tech. Bull.*, **19**.

Krone, R.B. (1986). The significance of aggregate properties to transport processes. In : Mehta, A.J. (Ed.) *Estuarine cohesive sediment dynamics : Lecture notes on coastal and estuarine studies*, **14**, Springer-Verlag, p66–84.

Lamb, H. (1932). Hydrodynamics (2nd Edition). *Publ. Cambridge Univ. Press.*

Launder, B.E., Reece, G.J. & Rodi, W. (1975). Progress in the development of Reynolds stress closure. *J. Fluid Mech.*, **68**, p537–566.

Launder, B.E. & Spalding, D.B. (1972). Lectures in Mathematical Models of Turbulence. *Publ. Academic Press, London.*

Lavelle, J.W. & Mofjeld, H.O. (1987). Do critical stresses for incipient motion really exist? *J. Hyd. Eng.*, **113**(3), p370–393.

Le Mehaute, B. (1962). On non-saturated breakers and the wave run-up. *Proc. 8th Coastal Eng. Conf.*, p77–92.

Le Mehaute, B. (1976). An introduction to Hydrodynamics and Water Waves. *Publ. Springer-Verlag, Dusseldorf.*

Longuet-Higgins, M.S. (1952). On the statistical distribution of the heights of sea waves. *J.Mar. Res.*, **11**, p245–266.

Longuet-Higgins, M.S. (1976). Recent developments in the study of breaking waves. *15th Ann. Conf. Coastal Eng., ASCE, Honolulu*, **HI**, p441–460.

Longuet-Higgins, M.S. & Stewart, R.W. (1964). Radiation stress in water waves: a physical discussion with applications. *Deep- Sea Res.*, **11**, p529–549.

Luckenbach, M.W. (1986). Sediment stability around animal tubes: The roles of hydrodynamic processes and biotic activity. *Limnol. Oceanogr.*, **31**(4), p779–787.

Lundgren, H. (1973). Turbulent currents in the presence of waves. *Proc. 13th Coastal Eng. Conf.*, ASCE, **1**, p623–634.

Maa, P.Y. & Mehta, A.J. (1987). Mud erosion by waves: A laboratory study. *Cont. Shelf Res.*, bf 7(11/12), p1269–1284.

MacPherson, H. (1980). The attenuation of water waves over a non-rigid bed. *J. Fluid Mech.*, **97**, p721–742.

McLusky, D.S. (1989). The Estuarine Ecosystem (2nd Edition.), *Publ. Chapman and Hall, New York.*

Mehta, A.J. (1989). On estuarine cohesive suspended sediment behaviour. *J. Geophys. Res.*, **94**(C10), p14303–14314.

Mehta, A.J. (1986). Characterization of cohesive sediment properties and transport processes in estuaries. In: Mehta, A.J. (Ed.) *Estuarine cohesive sediment dynamics: Lecture notes on coastal and estuarine studies*, **14**, Springer–Verlag, p290–325.

Mehta, A.J. (1981). Review of erosion function for cohesive sediment beds. *Proc 1st Indian Conf. Ocean Eng.*, Indian Inst. of Tech., Madras, **1**, p122–130.

Mehta, A.J & Parchure, T.M. (1985). Erosion of soft cohesive sediment deposits. *J. Hyd. Eng.*, **110**(10), p1308–1326.

Miche, R. (1944). Mouvements ondulatoires des mers en profundeur constante ou decroissante. *Annales Ponts Chaussees*, **114**, p25–78, 131–164, 270–292, 369–406.

Moin & Kim (1982). Numerical simulation of turbulent channel flow. *J. Fluid Mech.*, **118**, p341–377.

Myrhaug, D. (1984). A theoretical model of combined wave and current boundary layers near a rough sea bottom. In: Chung, J.S. (Ed.) *Proc. 3rd Int. Symp. Offshore Mech. Arctic Eng.*, ASME, **1**, p559–568.

Myrhaug, D., Lambrakos, K.F. & Slaattelid, O.H. (1992). Wave boundary layer in flow measurements near the seabed. *Coastal Eng.*, **18**, p153–181.

Myrhaug, D. & Slaattelid, O.H. (1989). Combined wave and current boundary layer model for fixed rough seabeds. *Ocean Engng.*, **16**(2), p119–142.

Munk, W.H. & Anderson, E.R. (1948). Notes on the theory of the thermocline. *J. Mar. Res.*, **7**, p276–295.

Nielson, P. (1984). Field measurements of time averaged suspended sediment concentrations under waves. *Coastal Eng.*, **8**, p51–72.

Nichols, M.M. & Briggs, R.B. (1985). Estuaries. In: Davis, R.A.(Jnr) (Ed.) *Coastal Sedimentary Environments*, Springer–Verlag (2nd Edition), p77–186.

Nicholson, J. & O'Connor, B.A. (1986). Cohesive sediment transport model. *J. Hydr. Eng.*,

112(7), p621–640.

O'Connor, B.A. (1992). Suspended sediment transport in the coastal zone. *Dept. Civil Eng., Uni. of Liverpool, UK.*

O'Connor, B.A., Harris, J.M, Kim, H., Wong, Y.K., Oebius, H.U. & Williams, J.J. (1991). Bed Boundary Layers. *Dept. Civil Eng., Univ. of Liverpool, UK.*

O'Connor, B.A. & Nicholson, J. (1988). Mud transport modelling. In: Dronkers, J. & Leussen van, W. (Eds.) *Physical processes in estuaries*, Springer–Verlag, p532–544.

Odd, N.V.M. (1988). Mathematical modelling of mud transport in estuaries. In: Dronkers, J. & Leussen van, W. (Eds.) *Physical processes in estuaries*, Springer–Verlag, p503–531.

Oduyemi, K.O.K. (1987). Turbulent Transport of Sediment in Estuaries. *Unpubl. PhD thesis, Univ. of Birmingham, England.*

Owen, M.W. (1970). A detailed study of the settling velocities of cohesive muds. *Hydraulics Research Station*, Report INT. 78.

Owen, M.W. (1971). Properties of consolidating mud. *Hydraulics Research Station*, Report IT161.

Owen, M.W. (1976). Determination of the settling velocities of cohesive muds. *Hydraulics Research Station*, Report INT. 161.

Parker, W.R. (1993). Personal Communication.

Parker, W.R. & Kirby, R. (1982). Sources and transport patterns of sediment in the inner Bristol Channel and Severn estuary. In : ICE *Severn Barrage*, Thomas Telford Ltd., p181–194.

Patel, V.C. (1981). Evaluation of turbulence models for near-wall and low-Reynolds number flows. *Proc. 3rd Symp. on Turbulent Shear Flows*, Davis, California.

Paterson, D.M. & Daborn, G.R. (1991). Sediment stabilisation by biological action:significance for coastal engineering. In: Peregrine, D.H. & Loveless, J.H. (Eds.) *Developments in Coastal Engineering, Univ. Bristol.*

Peregrine, D.H. (1988). Breaking Water Waves. In: Nonlinear Topics in Ocean Physics. Osborne, R.A. (Ed.) *Italian Physical Soc., Proc. Internat. Sch of Physics. Course 109.*

Peregrine, D.H. (1979). Mechanics of breaking waves – A Review of Euromech 192. In: Shaw, T.l. (Ed.) *Mechanics of Wave-Induced Forces on Cylinders*, Pitman, London, p204–214.

Pestrong, R. (1972). Tidal flat sedimentation at Cooley Landing, Southwest San Fransisco Bay. *Sed. Geol.*, **8**, p251–288.

Phillips, O.M. (1977). The dynamics of the upper ocean (2nd Edition). *Publ. Cambridge Univ. Press.*

Pond, S. & Pickard, G.L. (1978). Introductory Dynamic Oceanography. *Publ. Pergamon Press.*

Putnam, J.A. & Johnson, J.W. (1949). The dissipation of wave energy by bottom friction. *Trans. Am. Geophys. Union*, **30**, p67–74.

Roberts, W. (1991). Fluidisation of mud by waves. *Hydraulics Research, Wallingford. Report SR 296.*

Rodi, W. (1984). Turbulence models and their application in hydraulics - a state of the art review. *IAHR, Delft, The Netherlands.*

Ross, M.A. and Mehta, A.J. (1989). On the mechanics of lutoclines and fluid mud. *J. Coastal Res.*, **5**, p51–61.

Sakakiyama, T. & Bijker, E.W. (1989). Mass transport velocity in mud layers due to progressive waves. *J. Waterway, Port, Coastal and Ocean Eng.*, ASCE, **115**, p614–633.

Sarpkaya, T. & Isaacson, M. (1981). Mechanics of wave forces on offshore structures. *Publ. Van Nostrand Reinhold, New York.*

Seymour, R.J. (1977). Estimating wave generation on restricted fetches. *Proc. ASCE. J. Waterway, Port, Coastal and Ocean Eng. Div.*, **103**(WW2), p251–264.

Sheng, P.Y. (1984). Modelling bottom boundary layer and cohesive sediment dynamics in estuarine and coastal waters. In : Mehta, A.J. (Ed.) *Estuarine cohesive sediment dynamics : Lecture notes on coastal and estuarine studies*, **14**, Springer–Verlag, p360–400.

Sheng, P.Y. & Villaret, C. (1989). Modeling the effect of suspended sediment on bottom exchange processes. *J. Geophys. Res.*, **94**(C10), p14429–14444.

Shiono, K. (1981). Vertical turbulent transport in stratified flows. *Unpubl. MPhil. thesis, Univ. of Birmingham, England.*

Simons, R.R., Kyriacou, A., Soulsby, R.L., Davies, A.G. (1988). Predicting the nearbed turbulent flow in waves and currents. *IAHR Symp. on Math. Mod. Sed. Trans. in the Coastal Zone*, Denmark.

Sleath, J.F.A. (1978). Measurements of bed load in oscillatory flow.*J. Waterway, Port, Coastal and Ocean Eng.*, ASCE, 104(WW4), p291–307.

Sleath, J.F.A. (1984). Sea bed mechanics. *Publ. Cambridge Press.*

Smith, J.D. (1977). Modelling of sediment transport on continental shelves. In: Goldberg, E.D *et al.* (Ed.) *The Sea*, **6**, p538–578.

Soulsby, R.L. (1980). Selecting record length and digitisation rate for near bed turbulence measurements. *J. Phys. Oceanography*, **10**, p208–219.

Soulsby, R.L. (1983). The bottom boundary layer of shelf seas. In: Johns, B. (Ed.) *Physical Oceanography of Coastal and Shelf Seas.* Elsvier Oceanography Series, **35**, p189–266.

Soulsby, R.L. & Humphery, J.D. (1989). Field observations of wave–current interactions at the sea bed. In: Torum, A. (Ed.) *Proc. NATO Adv. Res. Workshop on Water Wave Kinematics, Molde, Norway.*

Stoker, J.J. (1957). Water waves. *Publ. Interscience, New York and London.*

Suhayda, J.N. (1986). Interaction between surface waves and muddy bottom sediments. In : Mehta, A.J. (Ed.) *Estuarine cohesive sediment dynamics : Lecture notes on coastal and estuarine studies*, **14**, Springer-Verlag, p401–428.

Swart, D.H. (1976). Coastal sediment transport. Computation of longshore transport. *Delft Hydraul. Lab. Rep.*, r968(1).

Tanaka, H. & Shuto, N. (1981). Friction coefficient for a wave-current coexistent system. *Coastal Eng. Japan*, **26**, p19–37.

Tann, H.M. (1976). The estimation of wave parameters for the design of offshore structures. *Institute of Oceanographic Sciences, Report No. 23.*

Teisson, C. (1991). Cohesive suspended sediment transport: feasibility and limitations of numerical modelling. *J. Hydr. Res.*, 29(6), p755.

Teisson, C. & Fritsch, D. (1988). Numerical modelling of suspended sediment transport in the Loire estuary. *Proc. IAHR Symp. on Math. Modelling of Sed. Trans. in the Coastal Zone,*

Copenhagen, Denmark.

Teisson, C., Simonin, O., Galland, J.C., Laurence, D., Fritsch, D. (1991). Numerical modelling of cohesive sediment transport: past experience and new research axes. *Int. Symp. Transport of Sed. and its Math. Modelling, Florence.*

Teisson, C., Simonin, O., Galland, J.C., Laurence, D., (1992). Turbulence and mud sedimentation: A Reynolds stress model and a two-phase flow model. *Int. Conf. Coastal Eng., Venice.*

Tennekes, H. & Lumley, J.L. (1972). A first course in Turbulence. *Publ. MIT Press.*

Thomas, T.G., Leslie, D.C. and Williams J.J.R. (1992) Development of a large eddy simulation open channel code. *Submitted to J. Comp. Phys.*

Tubman, M.W. & Suhayda, J.N. (1976). Wave action and bottom movements in fine sediments. *Proc. 15th Coastal Eng. Conf.*, ASCE, **2**, p1168–1183.

Tolman, H.L. (1992). An evaluation of expressions for wave energy dissipation due to bottom friction in the presence of currents. *Coastal Eng.*, **16**, p165–179.

Van Rijn, L.C. (1982). Equivalent roughness of alluvial bed. *Proc. ASCE J. Hydraul. Div.*, **108**(HY10), p1215–1218.

Wells, J.T. & Coleman, J.M. (1981). Physical processes and fine grained sediment dynamics, coast of Surinam, South America. *J. Sedim. Pet.*, **51**(4), p1053–1068.

Wells, J.T. & Kemp, G.P. (1986). Interaction of surface waves and cohesive sediments : field observation and geological significance. In : Mehta, A.J. (Ed.) *Estuarine cohesive sediment dynamics : Lecture notes on coastal and estuarine studies*, **14**, Springer–Verlag, p43–65.

West, M.S. (1990). Aspects of intertidal sediment dynamics in the Severn estuary. *Unpubl. PhD thesis, Univ. of Birmingham, England.*

Wiegel, R.L. (1964). Oceanographical Engineering. *Publ. Prentice-Hall, Englewood Cliffs, New Jersey.*

Wiegel, R.L. & Kukk, J. (1964). Wave measurements along the California Coast. *Trans. Am. Geophys. Union*, p667–174.

Winterwerp, J.C., Cornelisse, J.M. & Kuijper, C. (1990). Parameters to characterize muds. *Intern. workshop on cohesive sediment: towards a def. of mud, Brussels.*

Vager, B.G. & Kagan, B.A. (1969). The dynamics of the turbulent boundary layer in a tidal current. *Isv. Acad. Sci. USSR Atmos. Oceanic Phys., Eng. trans.*, 5(2), p88–93.

Villaret, C. & Trowbridge, J.H. (1991). Effects of stratification by suspended sediments on turbulent shear flows. *J. Geophys. Res.*, 96(C6), p10659–10680.

Wolanski, E. *et al.* (1992). The role of turbulence in the settling of mud flocs. *J. Coastal Res.*, 8(1), p35–46.

Wolanski, E., Chappell, J., Ridd, P. and Vertessy, R. (1988). Fluidization of mud in estuaries. *J. Geophys. Res.*, 93(C3), p2351–2361.

Younis, B. (1992). Some turbulence models. *IAHR Symposium: Is Turbulence modelling of any use?*, Institute of Civil Engs., London.